Solar /electric heating systems for the future energy system

Simon Furbo, Mark Dannemand, Bengt Perers, Elsa Andersen, Jianhua Fan, Peder Bacher, Henrik Madsen, Rasmus Halvgaard, Henrik Aalborg Nielsen, Kristian Pagh Nielsen, Sisse Camilla Lundholm, Bent Hansen Sass, Thomas Engberg Pedersen, Jakob Nymann Rud og Kristian Harley Hansen

Report

Department of Civil Engineering
2013

DTU Civil Engineering Report R-288 (UK)
May 2013

DTU Civil Engineering
Department of Civil Engineering

Solar /electric heating systems for the future energy system

Simon Furbo, Mark Dannemand, Bengt Perers, Elsa Andersen, Jianhua Fan, Peder Bacher, Henrik Madsen, Rasmus Halvgaard, Henrik Aalborg Nielsen, Kristian Pagh Nielsen, Sisse Camilla Lundholm, Bent Hansen Sass, Thomas Engberg Pedersen, Jakob Nymann Rud, Kristian Harley Hansen,

DTU Byg, report R-288

ISBN=9788778773739

Table of Contents

1. Introduction

The project “Solar/electric heating systems in the future energy system” was carried out in the period 2008-2013. The project partners were DTU Byg, DTU Informatics (now DTU Compute), DMI, ENFOR A/S and COWI A/S. The companies Ajva ApS, Ohmatex ApS and Innogie ApS worked together with the project partners in two connected projects in order to develop solar/electric heating systems for laboratory tests. The project was financed by the Danish Agency for Science, Technology and Innovation under the Danish Council for Strategic Research in the program Sustainable Energy and Environment. The DSF number of the project is 2104-07-0021/09-063201/DSF. This report is the final report of the project.

The aim of the project is to elucidate how individual heating units for single family houses are best designed in order to fit into the future energy system. The units are based on solar energy, electrical heating elements/heat pump, advanced heat storage tanks and advanced control systems.

Heat is produced by solar collectors in sunny periods and by electrical heating elements/heat pump. The electrical heating elements/heat pump will be in operation in periods where the heat demand cannot be covered by solar energy. The aim is to use the auxiliary heating units when the electricity price is low, e.g. due to large electricity production by wind turbines.

The unit is equipped with an advanced control system where the control of the auxiliary heating is based on forecasts of the electricity price, the heat demand and the solar energy production. Consequently, the control is based on weather forecasts.

Three differently designed heating units are tested in a laboratory test facility. The systems are compared on the basis of:

- energy consumption for the auxiliary heating
- energy cost for the auxiliary heating
- net utilized solar energy

1.1 Background

Advanced designs and controls of heating units that utilize excess electricity production, e.g. from wind turbines in windy periods and at night when the load on the electricity grid is off peak, can help to even out the load of the power grid. Smarter utilization of the electricity on the grid can lead to reduced CO_2 emissions and possible reductions of cost for the individual household as well as for the society.

DTU Informatics and ENFOR A/S developed prognoses for heat demands for houses and for solar heat production of solar collectors. The prognoses are based on weather forecasts developed by DMI. The weather forecasts include hourly forecast for the ambient air temperature, for diffuse and direct solar radiation for areas down to 3 x 3 km for Denmark.

Hourly electricity prices for electricity on the Nordic marked are listed at the Nord Pool Spot website. http://www.nordpoolspot.com/. The hourly price variations are quite large and the price is low, especially in windy periods where a lot of electricity is generated by wind energy. The low price is typically 10% of the price when it is at the highest.

Appliances that are not required to run at a specific time of the day can therefore be programmed to be in operation where the cost is the lowest. Short term thermal energy storage is a possible application for this strategy. The strategy can benefit the consumer in terms of lower operation cost and it will possibly also help to reduce the daily peaks of electricity production by smoothing out the demand throughout the day hence reducing GHG-emissions from electricity production by fossil fuels. Taxes and other costs do however reduce the relative benefit.

2. Prognoses

2.1 Introduction

The activities on prognoses were carried out at DTU Compute by a PhD project financed by the project: Models for Efficient Integration of Solar Energy, but also a major contribution was given by a DTU financed Ph.D. project: Model Predictive Control for Smart Energy Systems (not completed at the time of writing). The main outcome of the Ph.D. project financed by the project is disseminated in four articles in international scientific journals: [1], [2], [3] and [4], which forms the basis of the Ph.D. dissertation [5]. In addition work was disseminated in several conference papers and co-authoring on reports and journal papers: [6], [7], [8], [9], [10], [11], [12] and [13].
The main results related to the Solar/Electric project achieved in the DTU financed PhD project is documented in the journal papers [14] and [15].
The developed methods can be applied for modeling, forecasting and control of building heating systems based on solar and electric power, especially for optimizing the integration of large amounts of solar and wind energy production. The methods can be used to deal with important aspects for optimized energy use in buildings, especially for enabling buildings as a key player in smart grids and for energy performance improvement of the building stock. The key is to enable a flexible demand, which can adapt to the fluctuating power generation, by using passive thermal storage in buildings. The methods can just as well be applied for enabling a flexible load by cooling of buildings. This can be both in the building structures, i.e. the thermal mass of the interior walls etc., and in a thermal storage device, e.g. a hot water tank for heating or an ice tank for cooling. If the energy is stored in the building structure the important modeling is of the heat dynamics of the building, as described in [2], and the model predictive control (MPC) described in [15] is suited for exactly this task. If the energy is stored in a thermal storage device the control is based on the forecasts described in [3] of the heat load of the building and the MPC described in [14] provides the method for optimal control. Both types of control is based on electricity price control, where a price signal provides the information from the surrounding electricity market, such that the price is low when there is a surplus of electricity and the price is high when there is a shortage of electricity. In the studies the electricity price of Nord Pool Spot is used, reflecting the current price of electricity in the Denmark. Price forecasting as described in [16] is also used. Furthermore, if the heating system includes a solar collector (i.e. fluid based system for space heating and hot water consumption), the method for solar heat forecasting in [6] can be applied and if photovoltaics (PV) is included in the system the methods for solar power forecasting in [1] or [9] can be applied.
The following section outlines the content and results of the studies. In the next section, the methods for solar power forecasting are described. Then follow a section on modeling and control for flexible heating in buildings based on thermal storage in building structures. Thereafter follows a section on forecasting and control for flexible heating in buildings based on energy storage in thermal storage devices. Finally, in the last section the remaining methods and results related to project are presented.

2.2 Solar power forecasting

The developed solar power forecasting methods are based on modelling the power output past data consisting of past measurements and numerical weather predictions (NWPs). The forecast horizons are as long as provided by the NWPs, in the presented applications they are complete up to 42 hours ahead at any time of day.
Two basic approaches have been developed: A two-stage method based on the statistical clear-sky model combined with a linear model, and a one-stage method based on a conditional parametric model. The two-stage approach is applied to forecasting of the total output of 21 PV-systems located in a small village in Denmark, it is described in [1]. The one-stage approach is applied to forecasting of the output of both: a PV-system, as described in [9], and to forecast the output of a solar thermal collector, as described in [6]. Finally, an approach to probabilistic solar power forecasting is outlined in the dissertation [5].
The obtained results from application of the forecasting methods are based on the data described in the papers, together with NWPs from [17], which are provided by the Danish Meteorological Institute.

2.3 Flexible heating with thermal storage devices in buildings and solar collectors

In a system based on electrical heating a simple hot water tank can be used for storage of thermal energy and enable a flexible electrical load. Such a tank is a prerequisite for solar collector systems, as the system developed in the Solar/Electric project. Based on a price signal an MPC is developed based on forecasts of the heat load of the building as outlined in this section.

2.3.1 Heat load forecasting for single family houses

A method for forecasting the load for space heating in a single-family house is presented in [3]. The forecasting model is built using data from sixteen houses located in Sønderborg, Denmark, combined with local climate measurements and weather forecasts. Every hour, the hourly heat load for each house the following two days is forecasted. The forecast models are adaptive linear time-series models and the climate inputs used are: ambient temperature, global radiation and wind speed. A computationally efficient recursive least squares scheme is used. The models are optimized to fit the individual characteristics for each house, such as the level of adaptivity and the thermal dynamical response of the building, which is modeled with simple transfer functions. Identification of a model, which is suitable for all the houses, is carried out. A thorough analysis of results shows that practically all available information available in the climate variables and the heat load is modeled in the forecasts leading to the conclusion that the forecast model cannot be further improved in the current setting. Furthermore, the results show that the forecasting errors mainly are related to: unpredictable high frequency variations in the heat load signal (predominant only for some houses), shifts in resident behavior patterns and uncertainty of the weather forecasts for longer horizons, especially for solar radiation.

2.3.2 Economic model predictive control for heating systems with hot water tanks

In Halvgaard et al. (2012a) model predictive control (MPC) for optimized operation of an electrical heating system with thermal storage in a hot water tank is presented. Further, the heat dynamics of a storage tank is modelled on the basis of data and maximum likelihood methods. The resulting grey-box model is used for Economic Model Predictive Control (MPC) of the energy in the tank. The control objective is to balance the energy from a solar collector and the heat demand in a single family house. The storage tank provides heat in periods where there is low solar radiation and stores heat when there is surplus solar heat. The forecasts of heat load were based on data obtained from meters in a group of single-family houses in Denmark.
The tank is also heated by electric heating and the electricity costs of operating these electric heating elements are minimized. Consequently, the electric heating elements are to the largest possible extend only used in periods with cheap electricity. It is proposed to integrate a price-sensitive control to enable the

storage tank to serve a smart energy system in which flexible demand is expected to help balance fluctuating renewable energy
sources like wind and solar. Through simulations, the impact of applying Economic MPC shows annual electricity cost savings up to 25-30.

2.4 Flexible heating with thermal storage in building structures

For enabling flexible heating using thermal storage in building structures an MPC scheme based on models for the heat dynamics of buildings has been developed and is described in this section.

2.4.1 Models for the heat dynamics of buildings

In [2] models are presented, which can provide detailed knowledge of the heat dynamics of a building from measurements of: heat load, indoor temperature, ambient temperature, and global radiation. The focus of the paper is a procedure for selection of the most suitable model. The models are grey-box models, which are based on a combination of physical and data-driven modelling.
They are based on stochastic differential equations, which allows for extensive modelling of dynamical systems and estimation of parameters which are directly physically interpretable, for example the heat capacity of the building and the UA-value of the building envelope.

2.4.2 Economic model predictive control for building climate control in a smart grid

Model predictive control (MPC) can be used for optimizing the operation of units in energy systems based on fluctuating and climate dependent energy production from renewables. For example in [15] an MPC controller for providing flexible load by optimizing the cost of running heat pumps in residential buildings with a floor heating system is presented. The thermal capacity of the building is used to shift the energy consumption to periods with low electricity prices. In this way the heating system of the house becomes a flexible power consumer in the Smart Grid. A model for a house with a ground source based heat pump used for supplying thermal energy to a water based floor heating system is presented. The model is a linear state space model and the resulting controller is an Economic MPC formulated as a linear program. The model includes forecasts
of both weather and electricity price. Simulation studies demonstrate the capabilities of the proposed model and algorithm. Compared to traditional operation of heat pumps with constant electricity prices, the optimized operating strategy saves 25-35% of the electricity cost excluding taxes and tariffs.

2.5 Modeling for solar energy applications

In this section several studies carried during the project are outlined.

2.5.1 A non-parametric method for correction of global radiation observations

In [4] a method for correction and alignment of global radiation observations based on information obtained from calculated global radiation is presented. The one-hour forecast of global radiation from a numerical weather prediction (NWP) model is used. Systematical errors detected in the observations are corrected. These are errors such as: tilt in the leveling of the sensor, shadowing from surrounding objects, clipping and saturation in the signal processing, and errors from dirt and wear. The method is based on a statistical non-parametric clearsky model which is applied to both the observed and the calculated radiation in order to find systematic deviations between them. The method is applied to correct global radiation observations from a climate station located at a district heating plant in Denmark. The results are compared to observations recorded at the Danish Technical University. The method can be useful for optimized use of solar radiation observations for forecasting, monitoring, and modeling of energy production and load which are affected by solar radiation.

2.5.2 Grey-box models for solar collectors

The need for fast and accurate performance testing of solar collectors is increasing. In [7] a new technique for performance testing which is based on non-linear continuous time models of the heat dynamics of the collector is presented.
It is shown that all important performance parameters can be accurately estimated with measurements from a single day. Modelling the dynamics of the collector is carried out using stochastic differential equations, which is a well proven efficient method to obtain accurate estimates of parameters in physical models. The applied method is described by [18] and implemented in the software CTSM-R 1.
Measurements obtained at a test site in Denmark during the spring 2010 are used for the modelling. The tested collector is a single glazed large area flat plate collector with selective absorber and Teflon anti convection layer. The modelling technique provides uncertainty estimates such as confidence intervals for the parameters, and furthermore enables statistical validation of the results. Such tests
can also facilitate procedures for selecting the best model to use, which is a very non-trivial task.

2.5.3 Open source software for MLR modelling of solar collectors

In [8] a software package for multiple linear regression modelling (MLR) of solar collectors implemented in the free and open source program R2 is presented. Applications of the software package includes: visual validation, resampling and conversion of data, collector performance testing according to the European Standard EN 12975 [19], statistical validation of results, and estimation of collector incidence angle modifier function [20]. The paper gives a demonstration with examples of the applications, based on measurements obtained at a test site in Denmark [21]. The tested collector is a single glased large area flat plate collector with selective absorber and teflon anti convection layer.
The package enable fast and reliable validation of data, and provide a unified implementation for MLR testing of solar collectors. This will furthermore make it simple to replicate the calculations by a third party in order to validate the results. Finally more advanced methods can be implemented and easily shared as extensions to the package, for example methods for estimation of the incidence angle modifier by smooth functions.

3. Weather forecast

This project is the first project in which the DMI numerical weather prediction (NWP) model HIRLAM has been used for forecasting the potentially available solar irradiance at the surface, which is also called global radiation. Within the weather model HIRLAM, this is always calculated, but it has not previously been used for energy forecasting. As it from the start of the project was seen as essential to calculate both the direct and the diffuse component of the global radiation, HIRLAM was modified to output these hourly in the forecast. Here direct global radiation is defined as the downward solar irradiance at the surface coming from the direction of the sun, while diffuse global radiation is defined as the downward solar irradiance at the surface coming from all other directions. The diffuse global radiation is global radiation diffusely transmitted through a cloud, global radiation reflected from a cloud, global radiation scattered from atmospheric molecules (the blue sky), and global radiation scattered from atmospheric aerosols. In HIRLAM, the direct and diffuse global radiation is calculated with respect to a horizontal plane at the surface. If the direction to the sun and the surface albedo are known, it is possible to estimate the global radiation on tilted surfaces given the direct and diffuse components of global radiation. This is relevant, for instance, for solar heating units on tilted roofs.

Besides the components of the global radiation the 2-meter temperature, the 10-meter wind speed and direction, and the downward longwave radiation at the surface were also output from HIRLAM during the project. The DMI HIRLAM version with the highest resolution was used. This covers North-Western Europe

as shown in figure 1. It is run for 54 hours forecasts. All data from model grid-points within the Danish mainland were used.

During the course of the project HIRLAM has been updated five times at DMI. In table 1 the periods during which these were run can be seen. As the partners from DTU IMM preferred that one model version was run throughout the project, the model S05 was run until the end of the project in April 2013 even though this has not otherwise been used operationally since January 2010.

In addition to running regular NWP models, DMI has since 2011 run an ensemble model, which consists of 25 individual HIRLAM models covering the S05 domain (figure 1). These 25 models are run with slight differences in the initial state and in the model physics. The purpose is to estimate both the most likely weather forecast and the uncertainty of this.

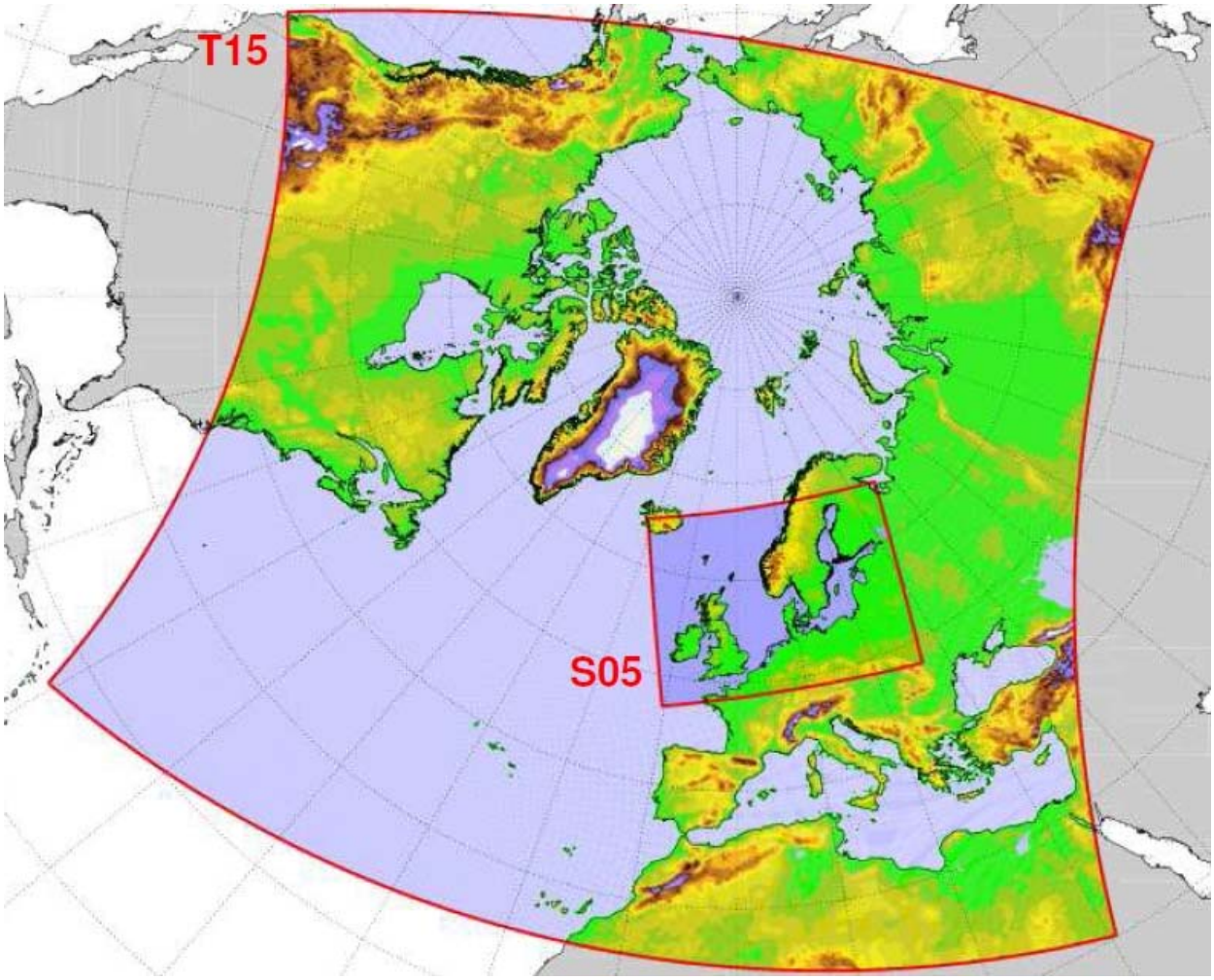

Figure 1. The domains covered by the S05 and T15 HIRLAM models run by DMI.

Start month	Stopped	Model version	Domain name	Model levels
2008-04	*2013-04*	HIRLAM 6.1	S05	40
2010-02	2010-10	HIRLAM 7.1	S03	40
2010-11	2011-12	HIRLAM 7.2	S03	65

2011-08		HIRLAM 7.3 – 25x ensemble	S05	40
2012-01		HIRLAM 7.3	SKA	65

Table 1. Operational models run at DMI during the course of the project.

The main focus of DMI in the project has been to estimate the quality of the global radiation forecasts, and the make improvements of the forecasts of direct and diffuse global radiation. This work has primarily been done in a Ph.D.-project described in a Ph.D. Thesis [22]. In this, the ensemble model, as described above, has been verified against measured data. The main result of this investigation is that the ensemble mean, *i.e.* the average of the 25 ensemble members, has approximately 20% less root mean square error (RMSE) for global radiation forecasts as compared to the regular NWP model. This result is shown in figure 2. It has also been investigated to which degree the spread of the ensemble members reflects the variations in the observed global radiation. In that regard it is optimal that the ensemble spread is large when the measurements are very variable, and vice versa, that the ensemble spread is small when the measurements do not vary much. In general, it was found that the ensemble was under-dispersive, *i.e.* that the ensemble spread was too low.

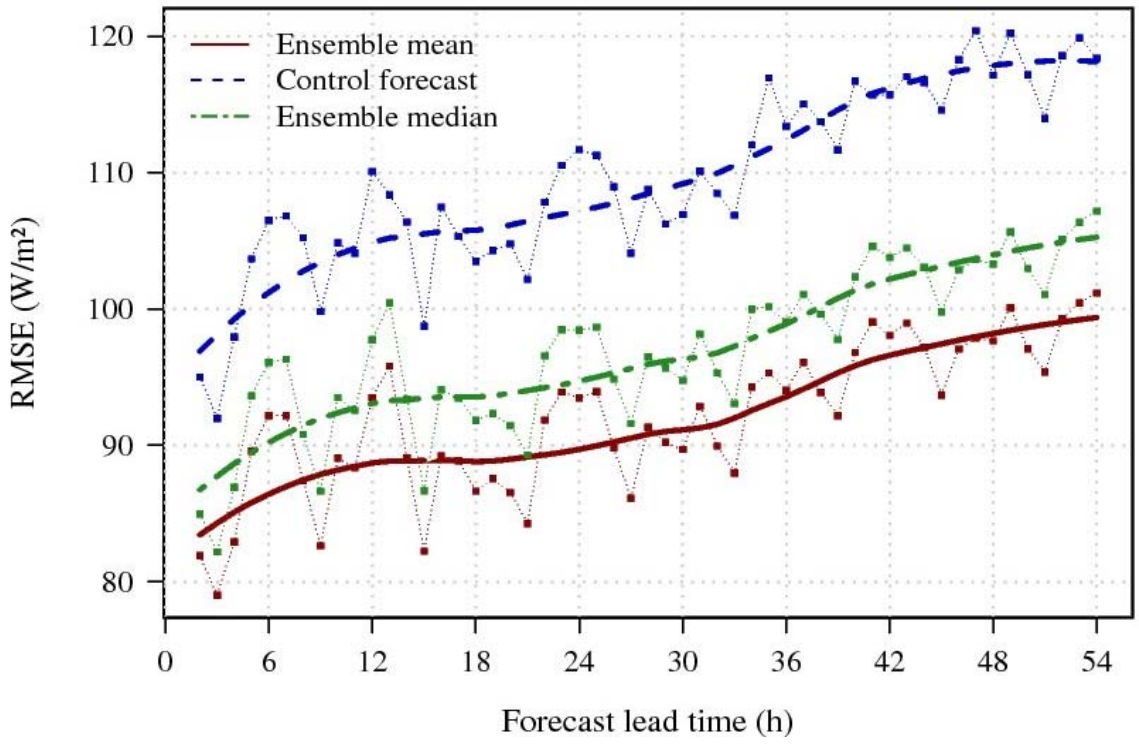

Figure 2. The root mean square error (RMSE) of global radiation forecast as a function of the forecast length. The blue curve shows the results for the control run, the green curve shows the result for the ensemble median, and the red curve shows the result for the ensemble mean.

As a part of the Ph.D. project the parameterizations of the direct and diffuse components of global radiation in HIRLAM were also tested. This was done by comparing the model results with measurements of the global radiation components performed at DTU Civil Engineering. The analysis of the results from this comparison led to two corrections in the parameterization. Firstly, a bug that in some cases caused unrealistic high values of the diffuse global radiation was fixed. Secondly, an error that made all global

radiation transmitted through a cloud into diffuse global radiation was corrected by using the Beer-Lambert law to calculate the cloud transmittance of the direct global radiation component.

Besides the Ph.D. project, work at DMI has been focused on improving the cloud forecasts in HIRLAM. Clouds are clearly the most important meteorological variable affecting the quality of global radiation forecasts. In particularly, forecasting the correct position of the clouds is challenging. Utilizing cloud data derived from images made with the SEVIRI instrument on the Meteosat satellite (MSG), DMI have performed regular verifications of cloud cover, cloud optical thickness and cloud water path throughout the project [23], [24], [25].

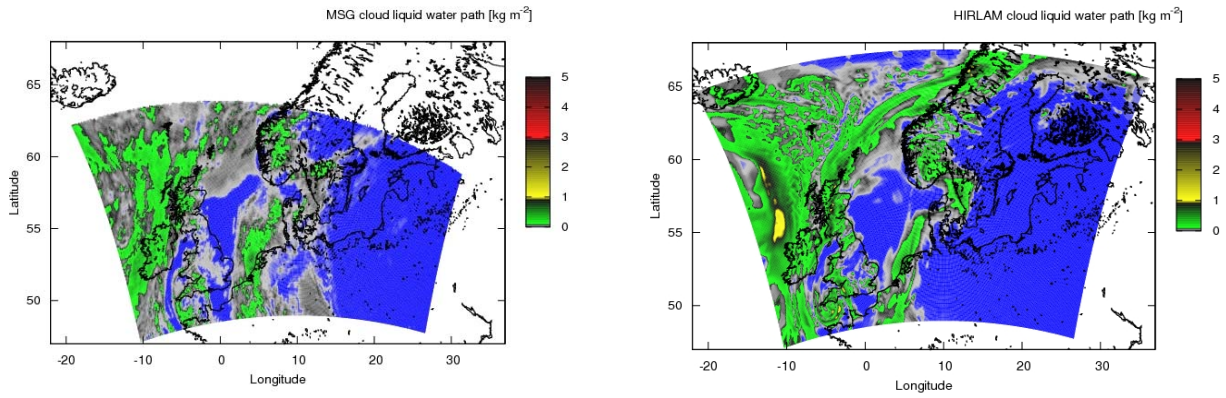

Figure 3. Integrated cloud water path on April 26th 2009 as derived from SEVIRI data (left) and HIRLAM S05 (right).

In figure 1 a comparison of MSG SEVIRI measurements and HIRLAM modeling results for the integrated cloud water path is shown. The colours give the amount of cloud water: In the blue areas there are no clouds or less than 0.01 kg/m² integrated cloud water; in the grey areas there is between 0.01 kg/m² and 0.1 kg/m² integrated cloud water; in the green areas there is between 0.1 kg/m² and 1 kg/m² integrated cloud water. The HIRLAM forecast length in this case is 10 hours. It can be seen that HIRLAM has captured the main features of the cloud cover, but that there are considerable deviations locally, for instance in the southern parts of Denmark and in Germany, where the model has no clouds, while the satellite observes a thin cloud cover.

In addition to real time verification of cloud data as shown in figure 2, verifications of the monthly averages of HIRLAM cloud cover have been performed. These made it clear that HIRLAM during the first years of the project overall underestimated the cloud cover. An example of this from January 2010 is shown in figure 4. In this figure, it can also be seen that HIRLAM at the time had a significant spin up during the first 12 hours of forecast. Spin up occurs when the initial state of a NWP model is out of balance. In such a case the model must use time to reach a balanced state. Here the problem was that the model had too few clouds in the initial state.

After having made successive improvements of the HIRLAM cloud physics at each model update (table 1), the spin up effect for the cloud cover has been almost completely removed in the newer HIRLAM versions. An example from January 2012 is shown in figure 5. Additionally, it can be seen that the monthly average of

HIRLAM cloud cover now is much closer to the monthly average cloud cover observed from the MSG satellite.

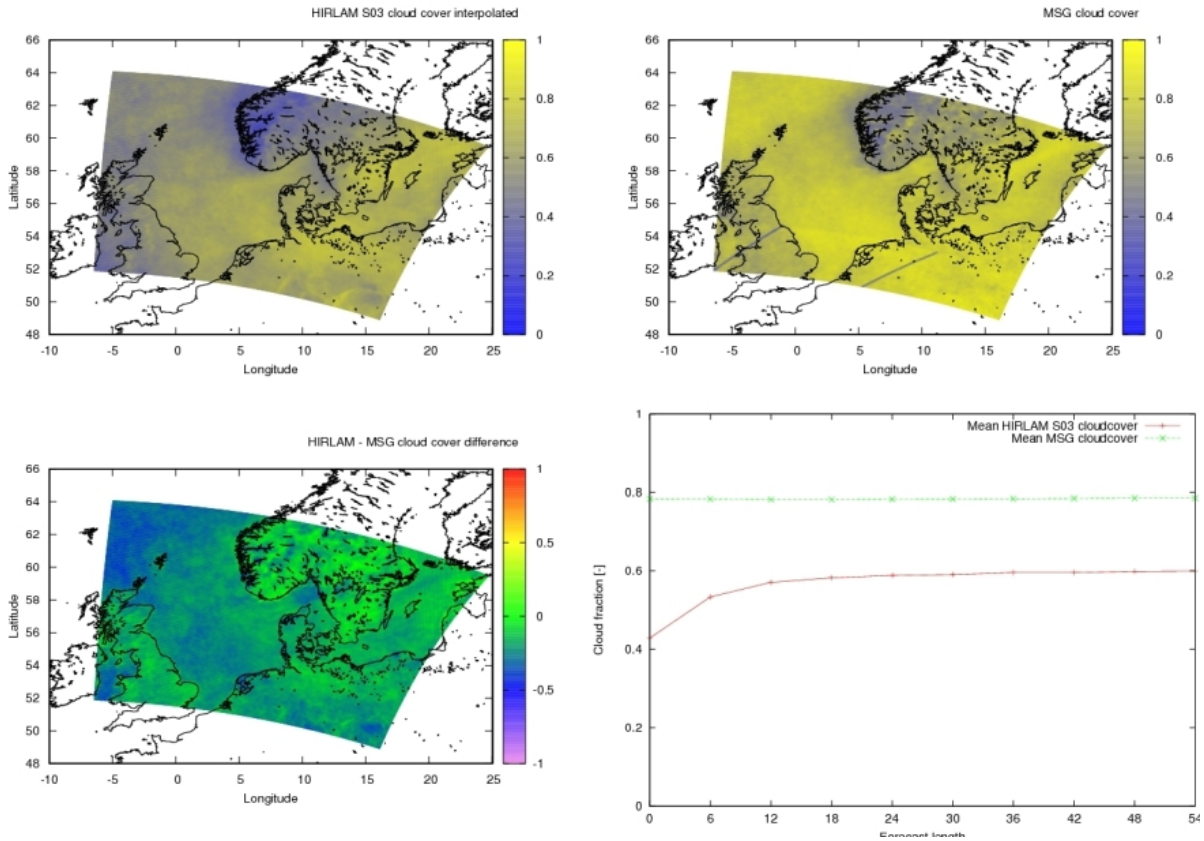

Figure 4: Monthly cloud cover verification of HIRLAM S03 against MSG cloud cover for the month of January 2010. 1 here refers to a cloud cover of 100%. Upper left: Average HIRLAM S03 24 hour forecasts. Upper right: Averages measured with MSG SEVIRI. Lower left: The average difference between HIRLAM and MSG cloud covers. Lower right: Cloud cover as function of forecast length for HIRLAM S03 (red curve) and MSG (green curve).

DMI has also developed a new way of calculating the direct global radiation within NWP models. Until now, global radiation has been calculated in vertical columns in NWP models, as illustrated with the green column in figure 6. As the models are run with higher and higher horizontal resolution, this is increasingly incorrect in cases when the Sun is not directly overhead. The actual column through which the direct global radiation transverses is shown with the purple colour in figure 6. In the modified version of HIRLAM, it is possible to calculate the global radiation in tilted columns. The method and the results have been described in [26].

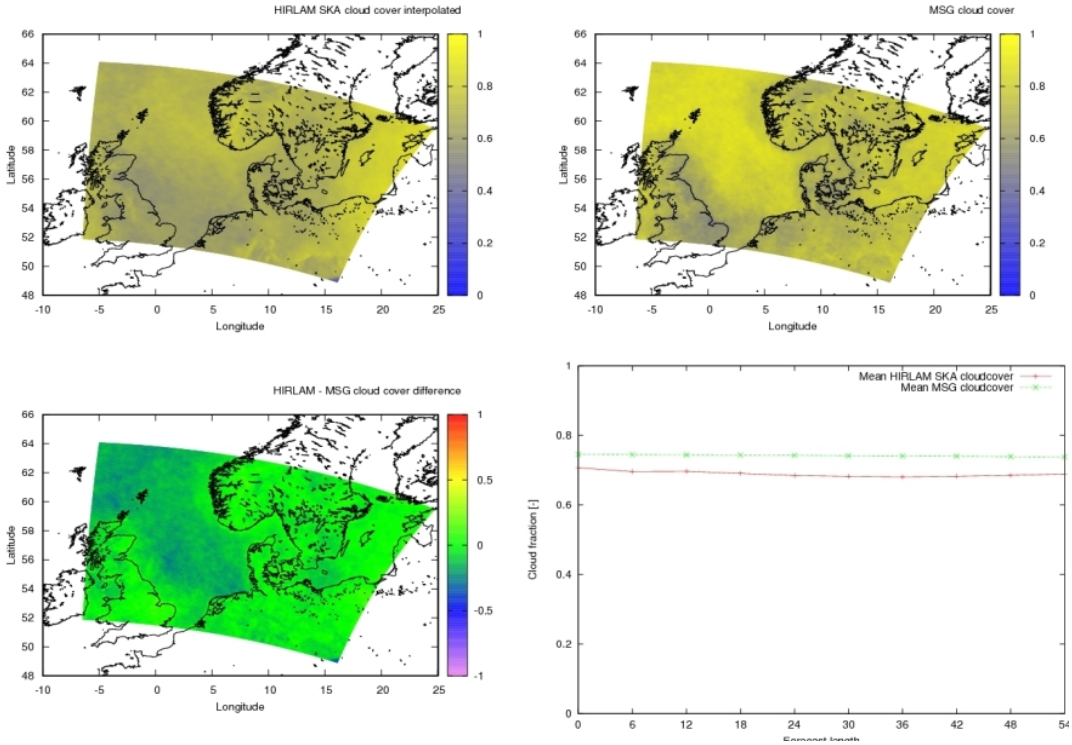

Figure 5: Monthly cloud cover verification of HIRLAM SKA against MSG cloud cover for the month of January 2012. 1 here refers to a cloud cover of 100%. Upper left: Average HIRLAM SKA 24 hour forecasts. Upper right: Averages measured with MSG SEVIRI. Lower left: The average difference between HIRLAM and MSG cloud covers. Lower right: Cloud cover as function of forecast length for HIRLAM SKA (red curve) and MSG (green curve).

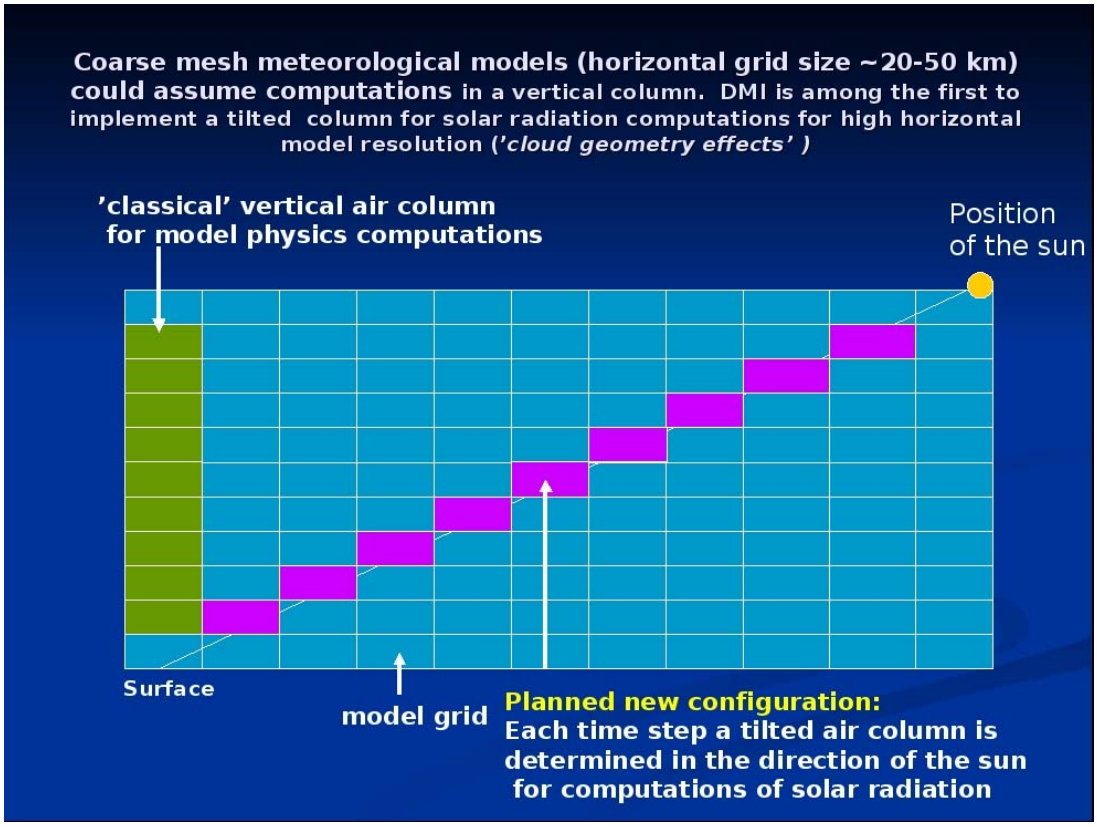

Figure 6. Schematic illustration of modeling direct global radiation in tilted air columns.

4. Smart heat storages

The charging behaviour of smart solar tanks for solar combisystems for one-family houses is investigated with detailed Computational Fluid Dynamics (CFD) modelling and Particle Image Velocimetry (PIV) measurements. The smart solar tank can be charged with a variable auxiliary volume fitted to the expected future energy demand. Therefore the heat loss from the tank is decreased and the thermal performance of the solar heating system is increased compared to a traditional system with a fixed auxiliary volume. The solar tank can be charged either by an electric heating element situated in the tank or by an electric heating element in a side-arm mounted on the side of the tank. Detailed CFD models of the smart tanks are built with different mesh densities in the tank and in the side-arm. The thermal conditions of the tank during charging are calculated with the CFD models. The fluid flow and temperature calculations are compared to PIV (Particle Image Velocimetry) measurements of fluid flows and temperature measurements. The aim is to elucidate the temperature distribution and thermal stratification of the tank during charging. It is elucidated how the calculated temperatures in the tank are influenced by the mesh densities, the distribution of computational cells, the physical model and time steps used in the simulations. The findings of the investigations were used for the design of smart solar tanks.

4.1. Introduction

The two most powerful renewable energy sources are solar and wind energy. It is expected that an increasing part of the electricity consumption in the future will be covered by wind farms. This will result in an increased number of windy periods with a surplus of electricity and thereby a low electricity price. A

concept where individual solar heating systems are optimised for making use of electricity produced by wind turbines in these periods can facilitate the introduction of wind energy on a large scale into the energy system and thereby contribute to increasing the part of the energy consumption covered by renewable energy sources.

The heat of the energy system will be produced by a solar heating system and by electrical heating element(s). The electrical heating element(s) will, if possible, only be in operation in periods where the solar heating system cannot cover the heat demand of the house 100% and where the electricity price is low, for instance due to high electricity generation from wind farms or due to a low electricity consumption. The energy system will need a smart heat storage with a variable water volume heated by low cost electricity and an advanced control system for the electric heating element(s)/heat pump based on prognosis for electricity costs, heat demand and solar heat production and a control system based on weather forecasts. The tank can be charged with a variable volume by internal heating elements installed at different levels in the tank or by a side-arm with a heating element.

Detailed modelling of the auxiliary charging, by means of electric heating element(s), of such a smart solar tank for solar combi systems for a one-family house, will be presented in the following. The focus of the study on the tank with a heating element in the tank is the flow field around the heating element during charging and how the fluid flow influences thermal stratification at the top of the tank. For the tank with a side-arm, the tank is charged by thermosyphon induced circulation through the side-arm. The charging of the tank is influenced by the power of the electric heating element, the position of the electric heating element and the design of the side-arm, for example, diameter of the side-arm pipe and position of the side-arm connection to the tank, etc. The focus of the study on the tank with a side-arm is to investigate how the design of the side-arm and the operating conditions influence charging behaviour of the tank.

4.2. Experimental and Theoretical Investigations

The auxiliary charging behaviour of a tank is investigated theoretically by CFD calculations and experimentally by PIV measurements. To facilitate the PIV measurements, a square glass tank is built with a cross section of 400 mm x 400 mm and a height of 900 mm, see figure 7. The uninsulated tank is made of 12 mm glass with a thermal conductivity of 0.81 W/mK.

Figure 7. The PIV test facility of the smart solar tank with one heating element and a side-arm.

The tank is designed in such a way that it can be charged either by an electric heating element situated in the tank or by an electric heat element in a side-arm mounted on the side of the tank. The internal electric heating element is situated in the tank at a height of 450 mm from the bottom of the tank. One end of the side-arm is mounted on the side of the tank with a distance of 800 mm from the tank bottom while the other end of the side-arm is mounted on the centre of the tank bottom. The side-arm has a built in electric heating element which gives a variable charging power from 1 kW to 3 kW. PIV equipment from Dantec Dynamics is used to determine the fluid flow in the tank, especially in the upper part of the tank where water is heated either by the internal heating element or by the side-arm. Thermal stratification in the tank is measured at different levels by temperature sensors located in one corner of the tank. The accuracy of the temperature measurement is estimated to be 0.5 K. The measured temperatures are compared to temperatures calculated by the CFD models.

The CFD model of the tank with an internal electric heating element is shown in figure 8. The mesh on the vertical cut-plane of the tank is shown in figure 8 (a). A. In order to better resolve the heat transfer and fluid flow in the region adjacent to the electric heating element and in the region adjacent to the tank wall, a boundary layer mesh is applied so that there is a fine and dense mesh in these regions, see figure 8(a) and 8(b). The 3D tank model includes the glass tank wall as a solid region and the hot water volume of the tank as a fluid region. The charging of the electric heating element is modelled as heat flux from the surface of the heating element. The power of the heating element is 500 W which corresponds to a heat flux of 30041 W/m^2. A size function is used to assign denser mesh around the electric heating element where a high temperature gradient is expected. A non-slip wall condition is used for all wall surfaces except the top of the tank where there is free water surface. A zero shear stress wall condition is used for the top inner surface of the tank. The heat loss from the tank is calculated by surface heat transfer coefficients of the tank wall and the temperature differences between the glass tank and the ambient air. The surface heat transfer coefficients of the top, the side and the bottom of the tank are 10 W/m^2K, 7.69 W/m^2K and 5.88 W/m^2K respectively. The Ambient air temperature is constantly 20°C.

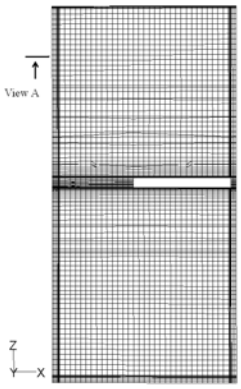

(a). Vertical middle plane of the model

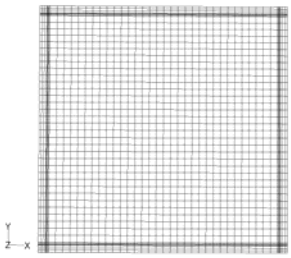

View A

(b). Cross section of the model

Figure 8. CFD model of the tank with an internal electric heating element

The CFD model of the tank charged with a side-arm is shown in figure 9. The vertical cut-plane through the middle of the tank is given in figure 9(a). A boundary layer mesh is applied to the surface of the heating

element, the inner surface of the side-arm and the inner surface of the tank where high temperatures and/or velocity gradients are expected, see figure 9(b). The tank is charged by thermosyphon induced circulation through the side-arm. Modelling of fluid flow and heat transfer in the side-arm is therefore critical. A denser mesh is applied to the side-arm while a coarse mesh is applied to the tank body, see figure 3(c). An interface is used to combine the non-conformal mesh of the upper half and the bottom half of the tank. The side-arm consists of two sections of copper pipes of 28 mm outer diameter and one section steel pipe with an outer diameter of 66 mm with a built in electric heating element. The 3D tank model includes the glass wall of the tank and the copper/steel pipe walls of the side-arm as solid regions, and the hot water volume in the tank and in the side-arm as fluid regions. The charging of the electric heating element is modelled as a heat flux from the surface of the heating element. The power of the heating element is 3 kW which corresponds to a heat flux of 97607 W/m^2. A non-slip wall condition is used for all wall surfaces except the top surface of the tank where a zero shear stress wall condition is applied. Heat loss from the tank is modelled the same way as for the tank with an internal heating element. The side-arm is insulated with a heat transfer coefficient of 2.4 W/m^{2}K between the pipe outer surface and the ambient air.

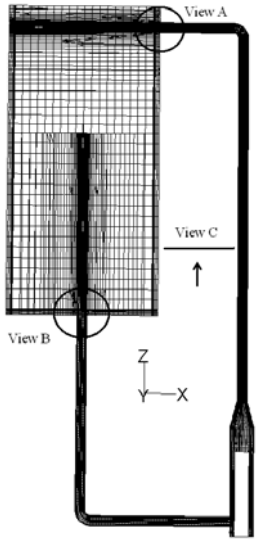

(a) Middle plane of the model

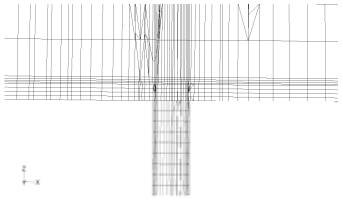

(b) A magnified view of A & B

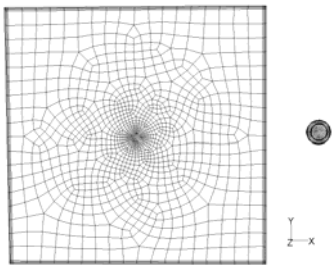

View C

(c) Cross section of the model

Figure 9. CFD model of the tank with electric heating element built in a side-arm

Water is used as the heat storage media. Properties of water and their dependences on temperature are shown as follows:

Dynamic viscosity, [kg/(ms)] $$\mu = 0.0007 * (\frac{T}{315})^{-5.5} \quad (1)$$

Thermal conductivity, [W/(mK)] $$\lambda = 0.375 + 8.84 \times 10^{-4} * T \quad (2)$$

where T is fluid temperature, [K].

The tank wall material, glass, has a thermal conductivity of 0.81 W/mK, while copper and steel has a thermal conductivity of 388 and 60 W/mK, respectively.

The Reynold number of the flow in the side-arm is estimated to be between 3000-4000 which indicates a flow in the transitional region. The flow around the heating element is most likely turbulent due to the high power of the electric heating element. A RNG k-ε turbulence model is therefore used to model the flow.

Transient CFD calculations are carried out with buoyancy driven force modelled by Boussinesq approximation [27]. The PRESTO and second order upwind method is used for the discretization of the pressure and the momentum/energy equations respectively [27]. The SIMPLE algorithm is used to treat the pressure-velocity coupling. The transient simulations start with a tank with a uniform temperature of 20.3˚C and a zero velocity field in the tank. The calculation is considered convergent if the scaled residual for the continuity equation, the momentum equations and the energy equation are less than 10^{-3}, 10^{-3} and 10^{-6}, respectively. The simulation runs with a time step between 1-10 s and a duration of 1 hour. One simulation with a time step size of 3 s takes approx. 12-52 hours for a duo core processor computer with 2 X 3 GHz CPU frequency and 4G memory.

4.3. Results and Discussion

4.3.1. Influence of grid density and time step size

Investigations are carried out to determine the optimal time step and grid density. Time intervals in the range of 1-10 s are investigated. The mesh scheme of the tank with an internal electric heating element is listed in table 1. The minimum mesh interval size is applied to the region adjacent to the surface of the electric heating element. The mesh interval size increases with a ratio of 1.1 further away from the heating element until it reaches the maximum mesh interval size. In the rest of the tank, the maximum mesh interval size is used. A 4-row boundary layer mesh is assigned to the surface of the tank wall and the surface of the heating element. The height of the first row of mesh is listed in table 2 for different mesh schemes. The height of the boundary layer mesh increases with a ratio of 1.2 away from the wall surface. Four mesh schemes are investigated with mesh interval sizes between 0.001 and 0.03 m.

The mesh scheme of the tank with a side-arm is listed in table 3. The mesh size varies between 0.004 m and 0.008 m in the side-arm, while it varies between 0.012 m and 0.03 m in the tank body. Four-row boundary layer mesh is attached to all wall surfaces of the tank and of the side-arm. The first row height of the boundary layer mesh is 0.001 m for the tank wall surfaces while it is either 0.0002 m or 0.0005 m for the wall surfaces of the side-arm.

	Number of cells	**Mesh interval size, [m] Min./Max.**	**Boundary layer mesh, the first row height, [m]**
Grid 1	37,525	0.002/0.03	0.001
Grid 2	193,522	0.002/0.012	0.001
Grid 3	495,936	0.001/0.008	0.001
Grid 4	1,192,380	0.001/0.006	0.0005

Table 2. Mesh schemes of the tank with an internal electric heating element.

	Number of cells	**Mesh interval size, [m]**		**Boundary layer mesh, the first row height, [m]**	
		Tank	**Side-arm**	**Tank**	**Side-arm**
Grid 1	189,698	0.03	0.008	0.001	0.0005
Grid 2	263,768	0.03	0.006	0.001	0.0005

Grid 3	407,314	0.012	0.006	0.001	0.0005
Grid 4	761,465	0.012	0.004	0.001	0.0002

Table 3. Mesh schemes of the tank with a side-arm with built in electric heating elements.

CFD predicted thermal stratification in the tank with a side-arm is shown in figures 10 and 11. The influence of mesh density on prediction of temperatures in the tank is shown in figure 10. At 10 min after the start of the charge, the difference between the temperatures predicted by Grid 2, Grid 3 and Grid 4 is maximum 0.7 K, while the difference between Grid 1 and Grid 4 is up to 2.7 K. The influence of mesh density on predicted temperature becomes less dominant as the test goes on. The difference of temperature predictions between Grid 1 and Grid 4 is decreased to maximum 2.0 K at 60 min after the start. It can be concluded that the mesh scheme Grid 2 is appropriate for modelling the tank with a side-arm. The influence of mesh density and time step size on prediction of temperature distribution in the tank with an internal heating element is investigated as well. The results show that the mesh scheme Grid 2 is appropriate for modelling the tank with an internal heating element. Figure 11 shows the influence of a time step size on temperature predictions in the tank. If a time step size between 1 s and 3 s is used, the difference of temperature prediction is within 0.5 K. With an increase of the time step size to 5 s and 10 s, the variation of temperature calculation increases up to 1.7 K and 5 K. It can be concluded that a model with a time step size between 1 s and 3 s can predict temperatures for most of the tank within an uncertainty of 0.5 K. Due to the dramatic increase of computation time with a decrease of the time step size, a time step of 3 s is used for later calculations.

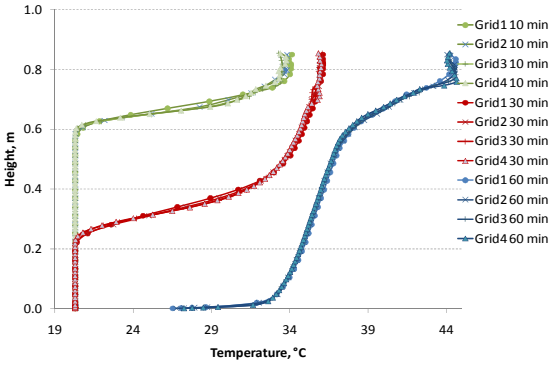

Figure 10. Influence of mesh density on prediction of thermal stratification in the tank with a side-arm

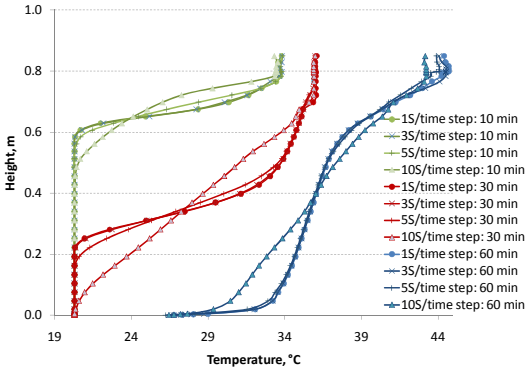

Figure 11. Influence of time step size on prediction of thermal stratification in the tank with a side-arm

4.3.2. Thermal stratification in the tanks

The CFD model with Grid 2 is used with a time step size of 3 s for the calculation of heat transfer and fluid flow in the tanks. The convective heat loss and thermal radiation heat loss from tank surfaces are now considered. The surface convective heat transfer coefficient for the side, the top and the bottom of the tank are respectively $1.49(T-T_a)^{0.33}$, $1.55(T-T_a)^{0.33}$ and $0.68\left(\frac{T-T_a}{l}\right)^{0.25}$ where T is the surface temperature of the tank; T_a is the ambient air temperature of the room; l is the dimension of the tank in m. The thermal radiation heat transfer coefficient is defined as:

$$\frac{\sigma(T+T_a)\left(T^2+T_a{}^2\right)}{\frac{1}{\varepsilon_T}+\frac{1}{\varepsilon_a}-1}$$

where σ is Stefan–Boltzmann constant, 5.67E10-8 W/m^{2}K^4. ε_T is the emittance of the tank surface, 0.8; ε_a is the effective emittance of the surrounding surfaces which is assumed to be 0.8. The ambient air temperature increases as the room is gradually heated up by the heat loss from the tank. A temperature of 20.3°C is used from the start till 30 min after the start, while 22.3°C is used for the rest of the test.

CFD calculated temperatures are compared to the measured temperatures. Figure 12 shows CFD calculated and measured temperatures at different levels in one corner of the tank. The electric heating element with a power of 460 W is installed at a height of 0.45 m. It can be seen in Fig. 12 that after the start of the charging, the water above the level of the element is gradually heated up to almost uniform temperature. There is almost no thermal stratification at the upper part of the tank, which means that the uprising flow from the heating element induced by buoyancy driven force creates mixing in the upper part of the tank. The water at the bottom part of the tank is not heated, indicating that the uprising flow from the element is not large enough to disturb water in the bottom part of the tank. At 58 min after the start, the water temperature in the upper part of the tank increases to 25.0°C, while the water temperature at the bottom part is only slightly higher than 20°C due to heat conduction of water and the glass tank wall. The CFD model predicts well temperatures in the tank with a difference of maximum 0.3 K, especially in the upper part of the tank. The difference is most likely due to the incorrect input of surface heat transfer coefficients and ambient air temperature in the CFD model.

Figure 13 shows thermal stratification in the tank charged by a side-arm with a power of 3 kW. One end of the side-arm is mounted on the side of the tank at a height of 0.8 m, while the other end of the side-arm is mounted on the centre of the tank bottom. The water in the side-arm is heated to a higher temperature than the water in the tank, which generates buoyancy driven flow in the side-arm. The uprising flow in the side-arm creates circulation of water between the side-arm and the tank. Temperatures at different heights in one corner of the tank is measured and compared to CFD calculations in Figure 13. The CFD model predicts well thermal stratification in the tank at 10 min and 30 min after the start of the charging. But it underestimates temperatures in the tank at 60 min after the start, especially at the height of 0.4 m to 0.7 m. The reason could be an overestimated heat loss from the tank.

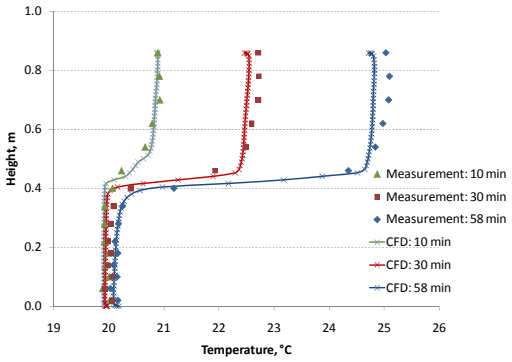

Figure 12. Thermal stratification in the tank with an internal heating element

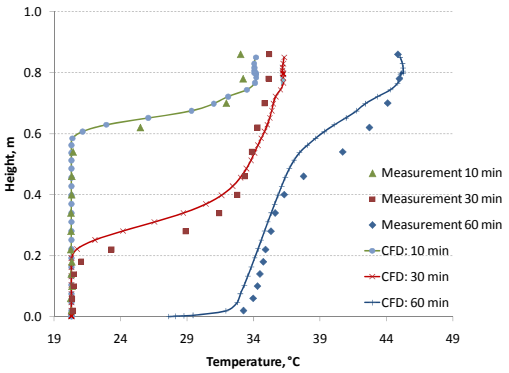

Figure 13. Thermal stratification in the tank with a side-arm

The heat transfer and fluid flow in the side-arm has a significant influence on the charging behaviour of the tank. Figure 14 shows the temperature of the fluid entering into the side-arm. There is a good agreement between measured and calculated temperatures. Figure 15 shows the temperature of the fluid entering into the tank. CFD predicts a flux of hot water entering into the tank 48 s after the electric heating element

is turned on, while it is undetected during the measurement. That could be explained by the fact that the temperature sensor is installed on the outer surface of the copper pipe which makes it difficult to respond to the fast temperature changes of the water in the pipe. There is a difference of maximum 3 K between the measurements and the CFD predictions, which is probably due to a slight underestimation of circulation flow in the side-arm. The calculations show that the volume flow rate through the side-arm varies between 2.6-3.4 l/min during the test.

4.3.3. Fluid flow in the tank with a side-arm

Figure 16 shows PIV measured fluid flow on the middle plane of the upper part of the tank 5 min after the start. The fluid entering into the tank from the side-arm forms a jet flow. The jet flow reaches the other side of the tank and turns back, forming a circulation. Because of the jet flow and the induced circulation, the tank above the side-arm inlet is mixed. That can be verified by the uniform temperature in the tank above 0.78 m, see Figure 13. Figure 17 shows CFD predicted flow field on the middle plane of the upper part of the tank 5 min after the start. The CFD model predicts successfully the flow pattern, although the velocity magnitude of the flow is overestimated. Another reason for the lower fluid flow in the PIV measurement could be the uncertainty of PIV measurement which is influenced by the specification of duration between pulses and the method used for analysis of the particle image. These factors should be further investigated in future work.

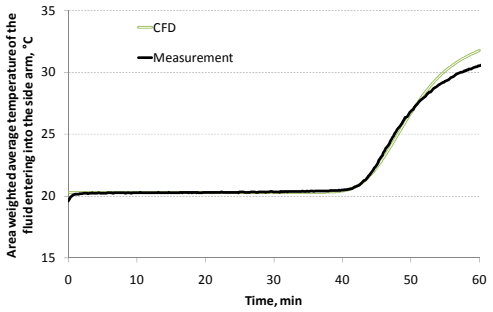

Figure 14. Temperature of the fluid entering into the side-arm.

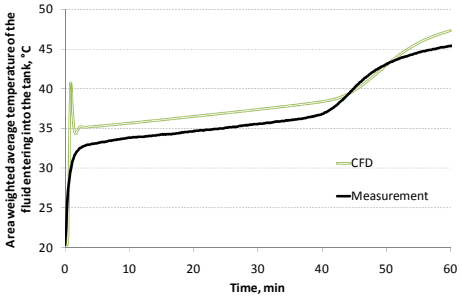

Figure 15. Temperature of the fluid entering into the tank.

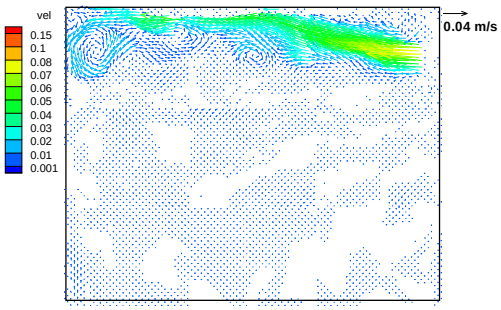

Figure 16. PIV measured flow field on the middle plane of the tank 5 min after the start.

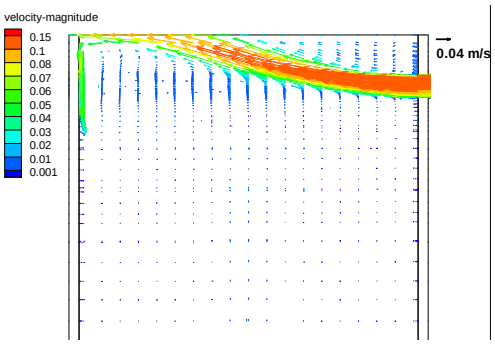

Figure 17. CFD predicted flow field on the middle plane of the tank 5 min after the start.

4.4. Conclusions

The charging behaviour of two smart solar tanks is investigated with detailed CFD modelling and PIV measurements. The solar tank can be charged either by an electric heating element situated in the tank or by an electric heating element in a side-arm mounted on the side of the tank. Thermal stratification can be established in a good way in the tank by both charge methods. The results show that a mesh interval size of 0.03 m and 0.006 m is sufficient for the tank and the side-arm, respectively. The most appropriate time step size is 3 s. The fluid flow and temperature calculations are compared to PIV measurements and temperature measurements. The CFD model predicts well thermal stratifications in the tank, but gives underestimated temperatures due to incorrect heat loss of the tank which should be further investigated. The CFD model predicts successfully the flow pattern in the tank, although the velocity magnitude of the flow is higher than the PIV measurements.

5. Experimental investigations of solar/electric heating systems

Three differently designed heating units including solar collectors, heat storages and auxiliary heat supply were installed at a test facility for solar heating systems at the Technical University of Denmark. The systems were exposed to the actual weather conditions related solar radiation and outdoor climate. The heat storages were installed in a test building. The energy use from the system is applied by an automated discharge system where hot water is taken from the systems and replaced with colder water to imitate actual use. The energy balance for the systems were monitored to evaluate the energy flows and to compare the thermal performance.

5.1 Design of three laboratory test systems

Three systems with differently designed storage tanks and auxiliary heating supply were investigated experimentally.

Each system has a solar collector area of 9 m² and a tank in tank heat storage from Ajva ApS. The inner tank for domestic hot water has a volume of 185 l and the outer tanks for space heating and short term heat storage has a volume of 550 l. The auxiliary heating devices for the three systems are: A large external electrical heating element of 9 kW, three smaller internal electrical heating elements of 3 kW each and a 10 kW heat pump respectively. The three tanks all have a variable auxiliary heated volume.

Solar energy is transferred from the solar collectors to an external heat exchanger by a solar collector loop with a propylene glycol water mixture. The solar heat is transferred from the heat exchanger to the tank by a secondary loop. The water for the secondary loop can be drawn off from the bottom or the middle of the storage tank and is led into the tank through a fabric inlet pipe, which is a stratification device. In this way beneficial thermal stratification is built up during solar collector operation.
Water for space heating is taken from the upper part of the outer tank and the return inlet to the tank is through another fabric inlet pipe. Domestic hot water is drawn from the top of the inner tank and the cold water in led into the bottom of the inner tank.

The tanks are designed as shown in figure 18 and figure 19. In figure 18 the tank is shown with the solar energy supply system, the space heating system and the domestic hot water system.

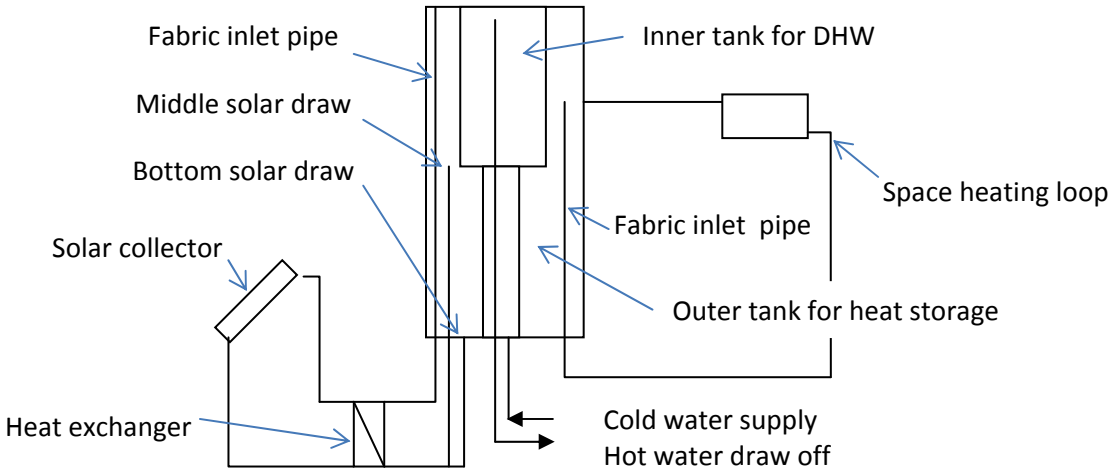

Figure 18. Principal drawing of the heat storage with the solar energy supply system, the space heating system and the domestic hot water system. The auxiliary heating system with the variable auxiliary heated volume is not shown.

In periods where the solar energy cannot cover the heating demand, the tanks are heated by an auxiliary heating device. In figure 19 principle drawings for the auxiliary heating systems are shown. PEX pipes inserted in the tanks to different levels allow for varying the auxiliary volume in system 1 and 2. The three individual 3 kW heating elements in system 3 also allow for controlling how much of the tank that is heated up by the electricity.

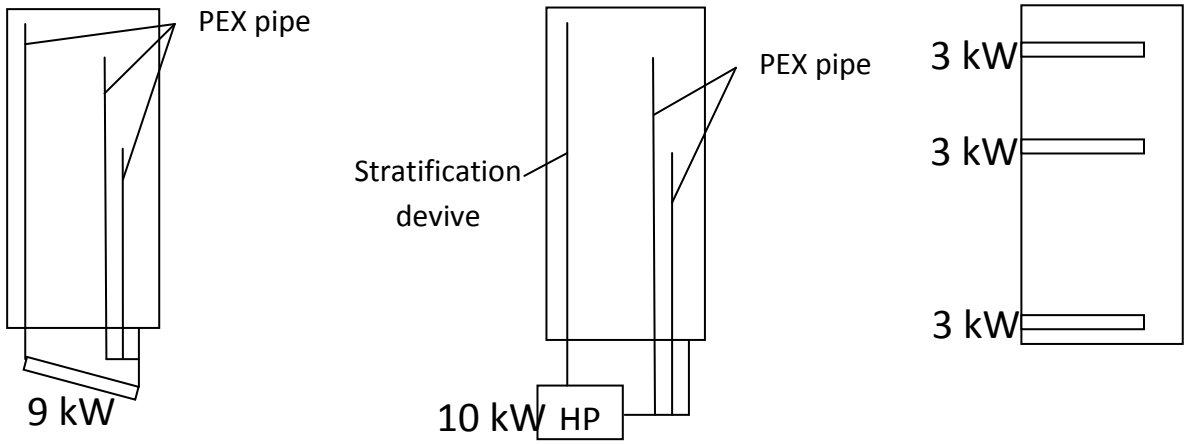

Figure 19. Principal drawings of the auxiliary heating systems for the three heat storages. The solar energy supply system, the space heating system and the domestic hot water system are not shown.

Figure 20 shows the storage tanks installed at the test facility.

Figure 20. The heat storages of the three solar heating systems which are being tested.

The dimensions of the tanks are listed in table 4.

Dimension of the inner tank (upper part/lower part)		**Dimension of the outer tank**	
Diameter [mm]	450/168.3	Diameter [mm]	800
Height [mm]	1102/466	Height [mm]	1568
Volume [l]	175/10	Volume excl. inner tank [l]	550

Table 4. Dimensions of the tanks.

The solar collectors and the solar collector loops

All three systems have the same size and type of solar collectors. The collectors are orientated to the south and the collector tilt is 45°.

The solar collector field is composed of three parallel coupled flat plate solar collectors, type BA 30 from the company Batec Solvarme A/S. Each system has a total solar collector area of 9 m^2. The collector efficiency sheet is available from www.batec.dk. Figure 21 shows a photo of the 3 x 9 m^2 solar collectors mounted in the test facility.

Figure 21. The 3 x 9 m^2 solar collectors from Batec Solvarme A/S and to the right, the pyranometers measuring the total and diffuse irradiance.

The absorber is made of copper with a selective surface and is a so called cu-strip absorber. The liquid flows through the collector via two manifolds, one in the top and one in bottom of the collector and eight parallel cu-strips connect the upper and the lower manifold. In this way, the absorber has four in/out lets and is very well suited for parallel coupling. The flow distribution is usually very good with this absorber design if no more than six collectors are connected in parallel. If the inlet is at the bottom of the parallel coupled collectors and the outlet is at the top, it is important that air escape valves are mounted in such a way that air will not be trapped in the collector preventing the flow from flowing through the area occupied by the air and resulting in a poor thermal performance of the whole solar heating system.

The solar collectors are connected to the three storage tanks via pipes and the lengths of the pipes are listed in table 5. Indoor, the outer diameter of the pipes is 22 mm and the outer diameter of the insulation is 60 mm. Outdoor, the outer diameter of the pipes is 12 mm and the outer diameter of the insulation is 30 mm. The pipes are insulated with armaflex with a thermal conductivity of 0.036 W/(m*K).

	Outdoor: system #1/system #2/system #3	Indoor: system #1/system #2/system #3
Solar collector – Heat exchanger	6.4 m/6.4 m/6.4 m	5.1 m/3.7 m/3.7 m
Heat exchanger – Tank		1.5 m/1.8 m/1.6 m
Tank – Heat exchanger		1.7 m/1.3 m/1.5 m
Heat exchanger – Solar collector	12.6 m/12.6 m/12.6 m	5.9 m/4.1 m/ 4.4 m

Table 5. Pipe lengths in the solar collector loop.

The energy from the solar collector is transferred to the tank via a plate heat exchanger. The solar collector loop between the solar collector and the heat exchanger is referred to as the primary solar collector loop and between the heat exchanger and the tank as the secondary solar collector loop. The inlet to the outer tank from the secondary solar collector loop is through a fabric stratifier with two fabric layers with the diameters of 30 mm and 50 mm. The outlet from the outer tank to the secondary solar collector loop is either from the middle or the bottom of the outer tank, depending on the operation conditions. The outlet to the secondary solar collector loop takes place through pipes made of POM with thick walls in order to reduce the horizontal heat transfer.

A schematic sketch of the solar collector loop inclusive two motor valves is shown in figure 22.

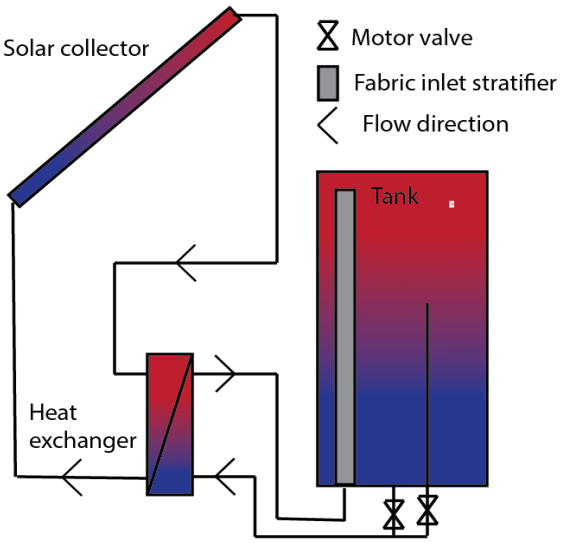

Figure 22. Principle drawing of solar collector loop.

Auxiliary heating system 1

For system 1 the auxiliary volume is heated by an electrical heating element of 9 kW built into a thermo syphoning side arm. The piping in the tank is designed in such a way that the upper 30% or the upper half or the whole tank can be heated by controlling the level of which the water for the thermo syphoning loop is drawn from. The inlet from the side arm to the outer tank is through a rigid POM pipe with a thick wall and the outlet is at the top of the tank. In this way, the tank is heated from the top. The heater has an inner thermostat that allows for operation temperatures up to 85°C. A schematic sketch of the auxiliary heating system is shown in figure 23.

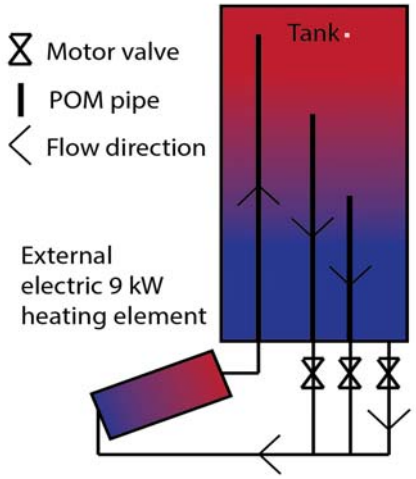

Figure 23. Auxiliary heating for system 1.

Auxiliary heating system 2

The auxiliary volume in system 2 is heated by an air/water heat pump. The tank is designed in such a way that the water for the heat pump loop can be taken from the upper 30% or the upper half or from the

bottom of the tank. The inlet from the heat pump to the outer tank is through a fabric stratifier with two fabric layers with inner/outer diameter of 50/70 mm. The air/water heat pump is type2025 from the company NIBE on 10 kW, see figure 24.

Figure 24. Nibe F2025 – 10 air/water heat pump.

The heat pump is located outside the building of the test systems. The diagrams below show the specified output of the heat pump at different outdoor temperatures. Also the temperature increase of the circulated water at the optimal flow is shown in figure 25 as a function of the outdoor temperature.

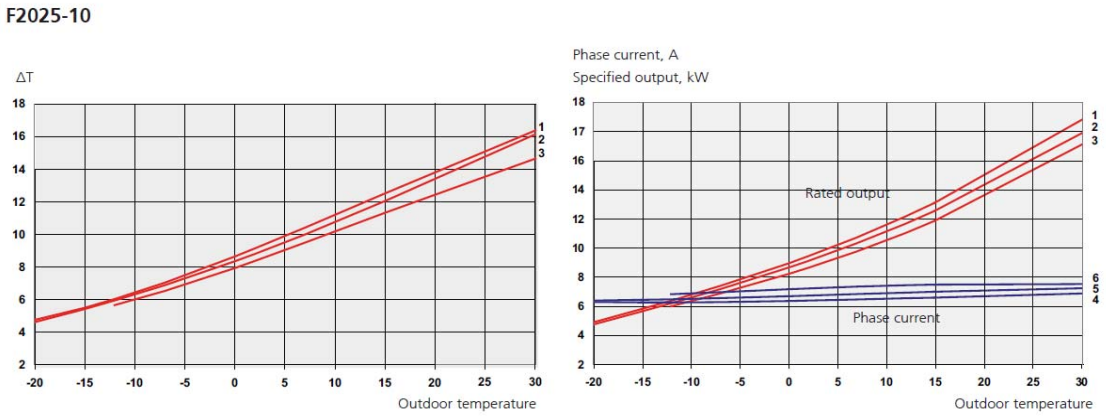

Figure 25. Temperature increase of water and power output as a function of the outdoor temperature for the het pump.

This heat pump has a stop temperature of 50°C for the return flow to the heat pump and of 58°C for the supply from the heat pump as indicated in figure 26. For this type of heat pump the maximum deliverable temperature is therefore 58°C.

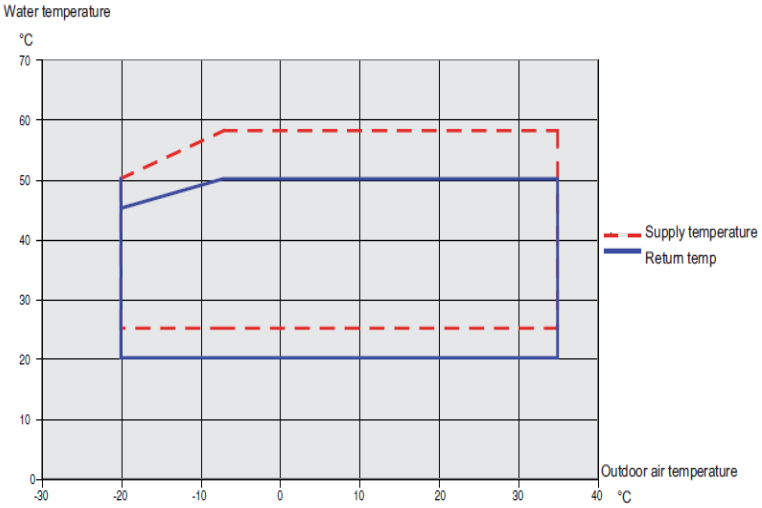

Figure 26. Water temperatures as function of outdoor temperature for the heat pump.

An antifreeze function is initiated at temperatures below +2°C and will run periodically or continuously depending of the outdoor temperature. A principle sketch of the auxiliary heating system for system 2 is shown in figure 27.

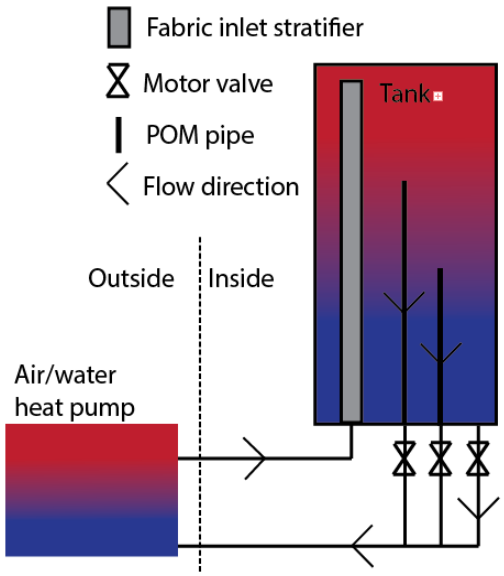

Figure 27. Auxiliary heating for system 2.

Auxiliary heating system 3

The auxiliary volume in system 3 is heated by three internal electrical heating elements. The heating elements are located 30 % down from the top, half way and at the bottom of the tank to allow for the upper 30% or the upper half or the whole tank can be heated. The heating elements are each 3 kW and have a thermostat that allows it to operate up to 85 ^{o}C. The three elements can be in use separately or simultaneously. A schematic sketch of the auxiliary hating system for system 3 is shown in figure 28.

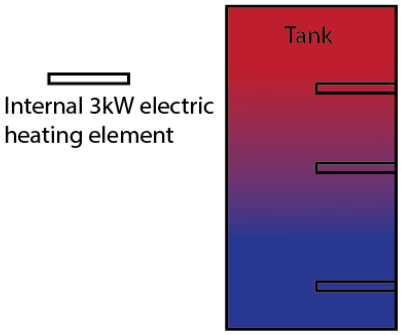

Figure 28. Auxiliary heating for system 3.

Space heating and domestic hot water

The tank is a tank in tank construction with domestic hot water in the inner tank and water for storage and space heating in the outer tank. Domestic hot water is taken from the top of the inner tank and led out through the bottom of the tank via a PEX pipe and cold water is let in at the bottom of the inner tank.

The outlet from the outer tank to the space heating loop is located on the side of the tank in the upper auxiliary volume and the return inlet is through a fabric stratifier with two fabric layers with inner/outer diameter of 50/70 mm. The required power drawn for the space heating loop is set by adjusting the flow and the temperature difference across the inlet and outlet. A thermostatic 3 way valve is used to keep the power steady.

Figure 29 gives an overview of the pipe connections in the tank. The yellow arrows are used for the solar collector loop, the blue arrows for the domestic hot water loop, the red arrows in the auxiliary heating loop and the green arrows in the space heating loop. Only the auxiliary systems differ for the three systems.

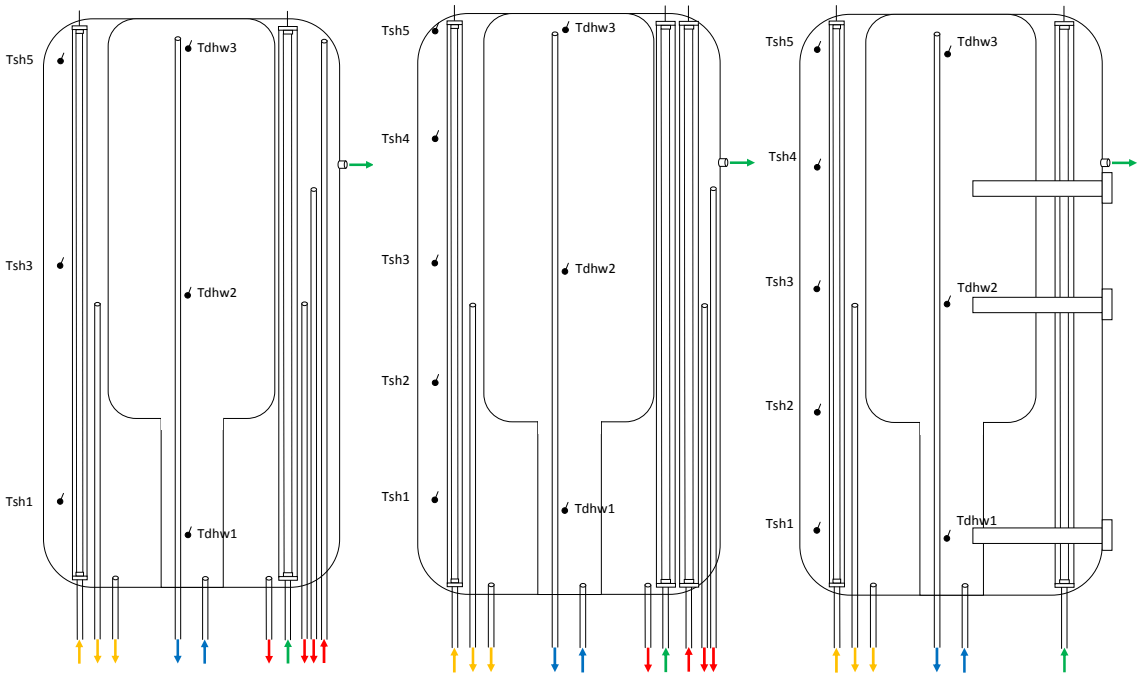

Figure 29. The three different storage tanks and the pipe connections.

5.2 Control system

The control strategy applies to when and how to operate the solar heating system and the auxiliary energy supply system. The aim is to enhance the use of solar energy as much as possible and limit the use and costs of auxiliary energy as much as possible. That is: The control system for the units is developed to reduce the cost of auxiliary energy required to meet the heat demand. The control is based on forecasted heat demands, electricity prices and hourly solar irradiation and outdoor temperature levels. The heat demand is based on a fixed daily demand for domestic hot water and a variable demand for space heating based on the outdoor temperature. The forecasted outdoor temperatures are fed into the control systems from DMI's weather forecasts via an online connection. The forecasted irradiation levels are fed into the control system to estimate the amount of solar heat that will be produced by the collectors and accumulated in the units in the following period. Also the forecasted electricity prices for the following period are supplied to the control system. All this is done to calculate when and how much the auxiliary heating have to be used each hour to meet the coming demand at the lowest cost possible. The strategies for the solar collector loop and for the auxiliary energy system run in parallel to allow for situations where the solar collector loop is running and still additional auxiliary heating is required to meet the demand and maintain the comfort level in the house. The temperatures in the tanks are registered by the control system to determine the energy content of the tank and the operation strategies. Magnetic valves are used to choose from which level of the tank water is drawn from to the external auxiliary heating unit in system 1 and 2 and for the secondary solar loop. Circulation pumps are used to circulate the water and solar collector fluid when required.

Solar collector loop

Figure 30 shows the control system overview. The temperature in the solar collector is measured by a PT 1000 sensor (T1) attached in good thermal contact with the back of the absorber in the solar collector. The temperature stratification in the tank is measured by seven PT 1000 sensors (T2-T8) attached in good thermal contact with the tank wall or in pipes that are inserted into the tank water through the outer tank wall. The reading of temperature sensors T1 – T8 are used to run the control system and the operation of the pumps P1 and P2 and the magnetic valves M1 and M2 in the solar collector loop.

Figure 30 shows the overview screen from the control program at a state where the solar collector loop is running at a "HeatFromBottom" state while the auxiliary is on idle.

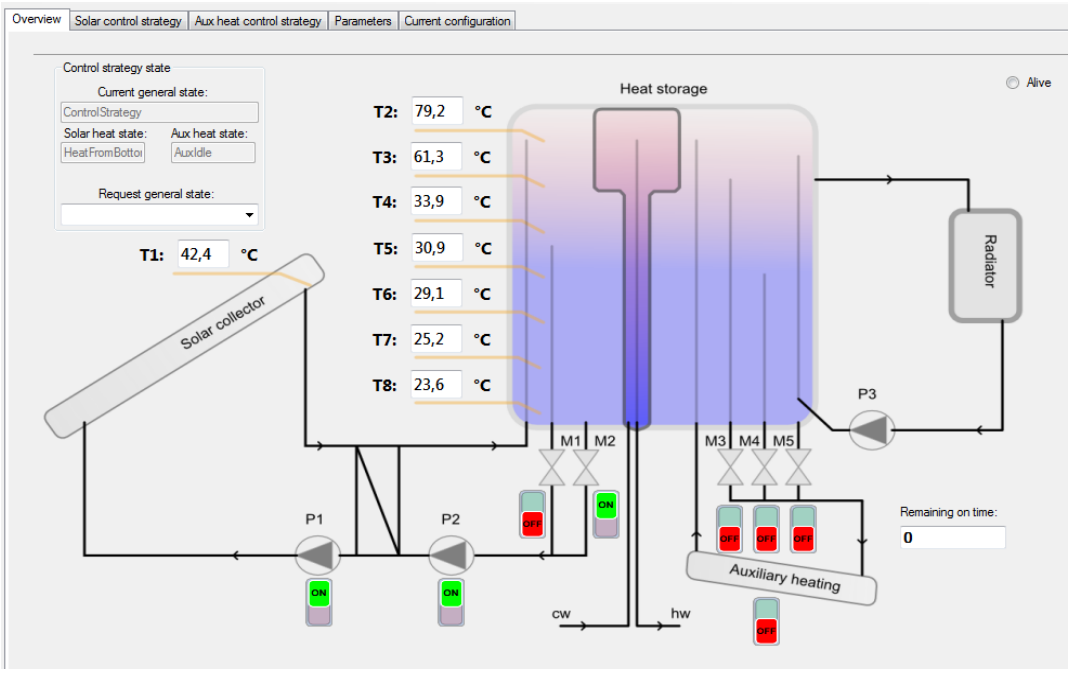

Figure 30. Overview of control system at ”heat from bottom” state.

The overall idea for the solar collector loop is to transfer solar heat from the collector to the tank. Therefore the loops start to run when the temperature in the collector is higher than the bottom of the tank. The control strategy in the solar collector loop is operated by the following algorithm:

Start of collector loop, heat from bottom:

- If T1>T8+10 K and T2 < 95°C -> P1 and P2 ON, M2 open, M1 closed

Start of collector loop, heat from middle:

- If T1>T3+5 K and T3 < 50°C -> P1 and P2 ON, M2 closed, M1 open

Return to collector loop, heat from middle:

- If T1<T3+2 K or T2 > 95°C -> P1 and P2 ON, M2, open M1 closed

Stop of pumps:

- If T1<T8+2 K or T8 > 95°C: P1 and P2 OFF, M1 closed, M2 closed

The solar collector control is graphically displayed on the figure 31 which is a screen shot from the control system.

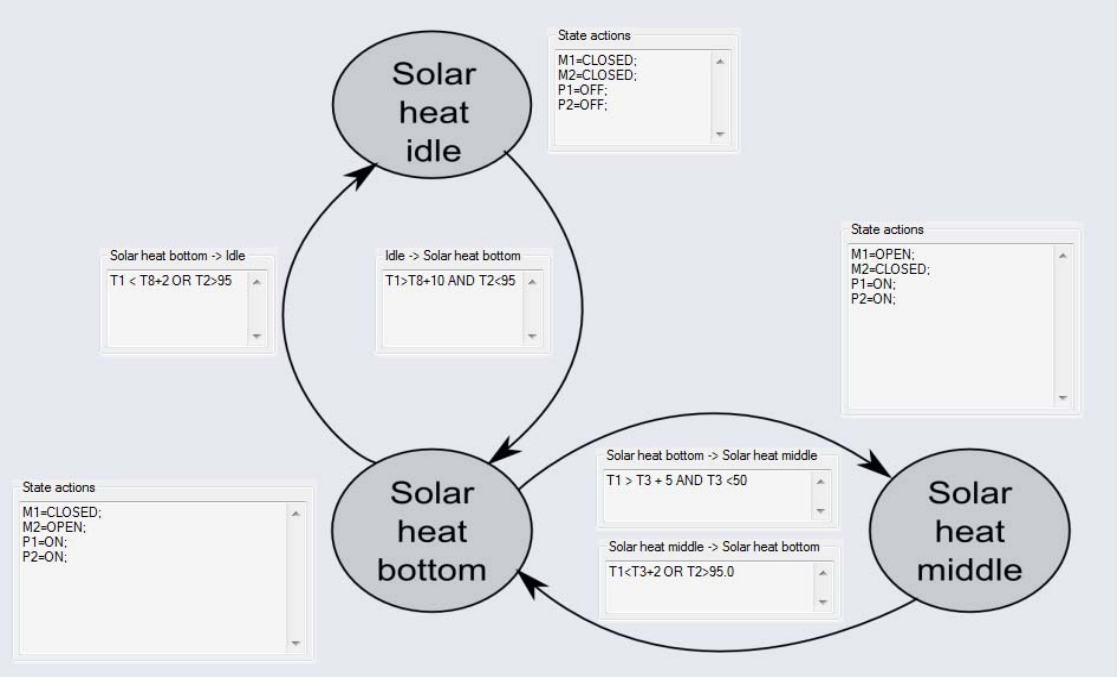

Figure 31. Control strategy.

It is easily possible to change the temperature set points to vary the operating principle for better performance.

Auxiliary energy supply system

Every hour the control system generates a forecast file including the forecasted electricity prices from NORDPOOLSPOT, solar irradiation levels and outdoor temperatures forecasted by DMI for the following 36 hours. The forecast file includes the current temperatures in the tank and the current energy content of the storage is determined. Based on the outdoor temperatures a space heating demand is calculated. A constant demand for domestic hot water is added to this demand. The heating demand of the system is aiming at covering:

- For outdoor temperatures above 15°C: 0.21 [kWh/hour] (only domestic hot water)
- For outdoor temperatures below 15°C: -0.31*OutdoorTemp + 4.84 [kWh/hour] (space heating and domestic hot water)

The forecasted power to the storage from the solar collector array is calculated from the forecasted direct and diffuse radiation level as well as the collector properties. Based on the forecasted heating demand, the forecasted incoming solar heat, the required auxiliary energy demand is calculated. The demand for the auxiliary heating unit is sought to be covered at the lowest cost. The control system therefore chooses the hours with the lowest electricity cost to cover the forecasted heat demand the following period.

As the three auxiliary heating units are different, they require different control strategies to run most efficiently. The temperature level of the systems with electric heating elements can be up to 85°C. This is the limitation for the heating elements. System 2 can due to the limitations of the heat pump loop, operate at temperatures up to 58°C. (Different heat pumps can operate at higher temperatures, by change of

refrigerant to for example CO_2, higher temperatures can be possible in the future). For system 1 and 3 the temperature setting for the control of the auxiliary heaters are set to keep similar thermal stratification for better comparison.

A summary of the auxiliary control strategy is listed in table 6, for states where there is a demand for auxiliary heating. The magnetic valves M3, M4 and M5 are used to control the draw off level for the external auxiliary heating elements. ELP1, ELP2 and ELP3 are the three internal electric heating elements in unit 3.

	System 1, External electric heater	System 2, External heat pump	System 3 Internal electric heaters
Supply power	9 kW	up to 10 kW	3 x 3 kW
Mode: AUX high Applies for heating loads of 0 to 9 kW for system 1 and 2. Applies for heating loads of 6 to 9 kW for system 3	(T2<85.0) HEATER=ON M3= Open M4 = Closed M5 = Closed (T2>=85.0 AND T4<76.0) HEATER=ON M3= Closed M4 = Open M5 = Closed (T2>=85.0 AND T4>=76.0 AND T7<75.0) HEATER=ON; M3= Closed M4 = Closed M5 = Open	(T7>=49.0) HEATER=OFF M3= Closed M4 = Closed M5 = Closed (T3<49.0) HEATER=ON M3= Open M4 = Closed M5 = Closed (T3>=49.0 AND T5<49.0) HEATER=ON M3= Closed M4 = Open M5 = Closed (T3>=49.0 AND T5>=49.0 AND T7<49.0) HEATER=ON; M3= Closed M4 = Closed M5 = Open	(T2<85.0) ELP1= ON ELP2 = ON ELP3 = ON (T2>=85.0 AND T4<80.0) ELP1 = OFF ELP2 = ON ELP3 = ON (T2>=85.0 AND T4>=80.0 AND T7<75.0) ELP1= OFF ELP2= OFF ELP3= ON
Mode: AUX medium Applies for heating loads of 3 to 6 kW for system 3	N/A	N/A	(T2<85.0) ELP1= ON ELP2 = ON ELP3 = OFF (T2>=85.0 AND T4<80.0) ELP1 = OFF ELP2 = ON ELP3 = ON (T2>=85.0 AND T4>=80.0 AND T7<75.0) ELP1= OFF ELP2= OFF ELP3= ON
Mode: AUX Low	N/A	N/A	if (T2<85.0) ELP1= ON ELP2 = OFF

Applies for heating loads of 0 to 3 kW for system 3			ELP3 = OFF (T2>=85.0 AND T4<80.0) ELP1 = OFF ELP2 = ON ELP3 = OFF (T2>=85.0 AND T4>=80.0 AND T7<75.0) ELP1= OFF ELP2= OFF ELP3= ON

Table 6. Summary of auxiliary heating control strategy.

Log files

A log file is generated by the control system. The log file includes values for every minute of the eight measured temperatures, the states of the valves and pumps as well as the active control strategies. Also the points of where the change of running state is recorded. A separate log file is generated for every system every day and is saved with the hourly forecast files on a ftp server. A sample of the log file is shown in figure 32 and explanation of the file is given in table 7.

A	B	C	D	E	F	G
UTC date	UTC time	Algorithm version	General state	Solar heat state	Aux heat state	ONTID
14-03-2013	00:01:41	MARKD 31-01-2013	Strategy	Idle	AuxHigh	60
14-03-2013	00:01:41	MARKD 31-01-2013	Strategy	Idle	AuxHigh	59
14-03-2013	00:02:41	MARKD 31-01-2013	Strategy	Idle	AuxHigh	58
14-03-2013	00:03:41	MARKD 31-01-2013	Strategy	Idle	AuxHigh	57
14-03-2013	00:04:41	MARKD 31-01-2013	Strategy	Idle	AuxHigh	56
14-03-2013	00:05:41	MARKD 31-01-2013	Strategy	Idle	AuxHigh	55
14-03-2013	00:06:41	MARKD 31-01-2013	Strategy	Idle	AuxHigh	54

H	I	J	K	L	M	N	O	P	Q	R	S	T	U	V	W	X
T1	T2	T3	T4	T5	T6	T7	T8	P1	P2	Heater	M1	M2	M3	M4	M5	State shift
-2,1	51,4	51,3	50,8	48,6	46,4	44,8	42,7	0	0	1	0	0	0	1	0	0
-2,1	51,4	51,3	50,8	48,6	46,4	44,8	42,7	0	0	1	0	0	0	1	0	1
-2,1	51,4	51,2	50,7	48,5	46,3	44,6	42,5	0	0	1	0	0	0	1	0	0
-2,1	51,4	51,2	50,5	48,4	46	44,4	42,4	0	0	1	0	0	0	1	0	0
-2,1	51,4	51,2	50,3	48,2	45,8	44,4	42,2	0	0	1	0	0	0	1	0	0
-2,1	51,5	51,2	50,3	48,3	45,9	44,3	42,1	0	0	1	0	0	0	1	0	0
-2,2	51,6	51,2	50,4	48,4	46	44,3	42	0	0	1	0	0	0	1	0	0

Figure 32. Sample of log file.

Column	
A	Date
B	Time
C	Algorithm version
D	General state: Strategy/manuel
E	Solar heat state: idle/heat from middle/heat from Bottom
F	Aux heat state: Auxidle/AuxHigh/AuxMid/AuxLow
G	ONTID: remaining minutes Aux in on this clock hour

H	T1: temperature in solar collector
I-O	T2-T8: temperatures is tank
P,Q	P1,P2: 0/1 (pump on/off)
R	Heater: 0/1 (Aux heater on/off)
S-W	M1-M5: 0/1 (Motor valve open/closed)
X	State Shift: 0/1 (1=shift of state)

Table 7. Log file explanation.

5.3 Monitoring system for the test systems

The systems are monitored in terms of solar radiation, temperatures and flow rates at key points. Also the energy used by the auxiliary units is recorded. The temperatures are measured by thermo couples and PT 1000 sensors. Temperature differences are measured by thermopiles. The flows are measured by Brunata HGQ energy meters and Clorius Combi meters. The energy consumption for the auxiliary energy units are measured by energy meters. Temperatures, flows and energy uses are recorded every minute by data loggers.

In order to measure the temperatures inside the tanks, two glass tubes with temperature sensors are inserted through the top of the tank: One in the inner tank and one in the outer tank. The positions are indicated in figure 33 and tables 8, 9 and 10.

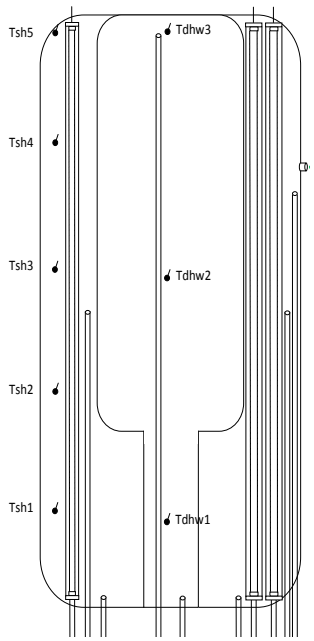

Figure 33. Positions of temperature sensors.

Height of temperature sensor in the inner tank from bottom of tank		**Height of temperature sensor in the outer tank from bottom of tank**	
Tdhw1 [mm]	146	Tsh1 [mm]	238
Tdhw2 [mm]	810	Tsh2 [mm]	not used
Tdhw3 [mm]	1490	Tsh3 [mm]	893
		Tsh4 [mm]	not used

		Tsh5 [mm]	1453

Table 8. Position of temperature sensors in the tank in system #1.

Height of temperature sensor in the inner tank from bottom of tank		**Height of temperature sensor in the outer tank from bottom of tank**	
Tdhw1 [mm]	231	Tsh1 [mm]	258
Tdhw2 [mm]	873	Tsh2 [mm]	577
Tdhw3 [mm]	1528	Tsh3 [mm]	898
		Tsh4 [mm]	1233
		Tsh5 [mm]	1554

Table 9. Position of temperature sensors in the tank in system #2.

Height of temperature sensor in the inner tank from bottom of tank		**Height of temperature sensor in the outer tank from bottom of tank**	
Tdhw1 [mm]	156	Tsh1 [mm]	180
Tdhw2 [mm]	790	Tsh2 [mm]	496
Tdhw3 [mm]	1463	Tsh3 [mm]	828
		Tsh4 [mm]	1158
		Tsh5 [mm]	1478

Table 10. Position of temperature sensors in the tank and dimension of the tank in system #3.

The energy flows for the systems are recorded by logging data at specific points of interest. For the piping the flow rates and temperatures are logged at the locations indicated in figure 34. Also the energy use for the auxiliary heating units is logged.

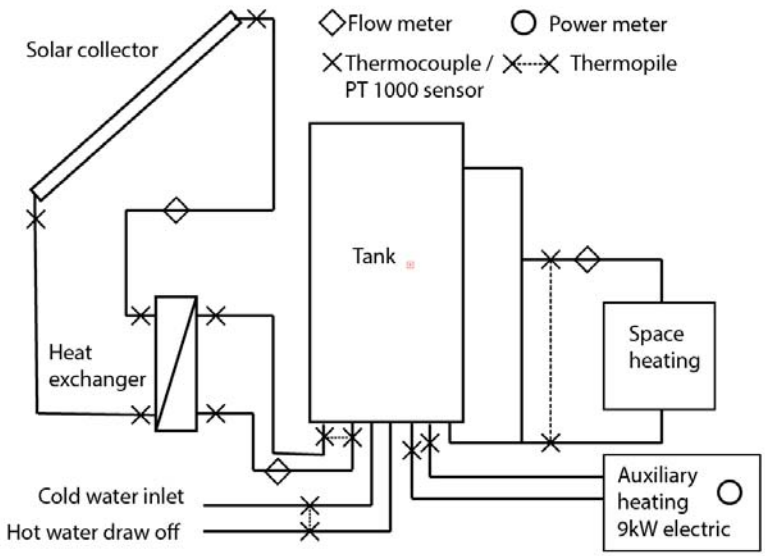

Figure 34. Flow meters and temperature logging for system 1.

As the three systems design vary slightly so does the measuring points of interest. The measured points for system 2 are indicated on figure 35.

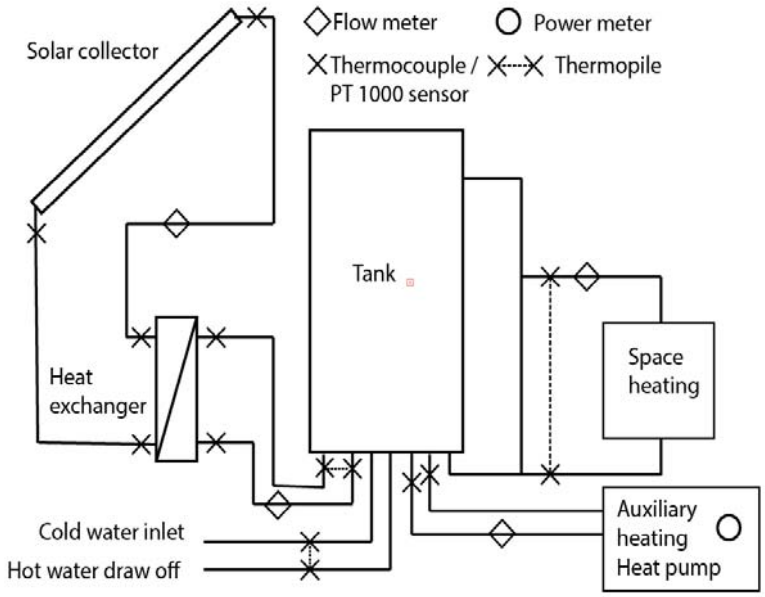

Figure 35. Flow meters and temperature logging for system 2.

The measured points for system 3 are indicated on figure 36.

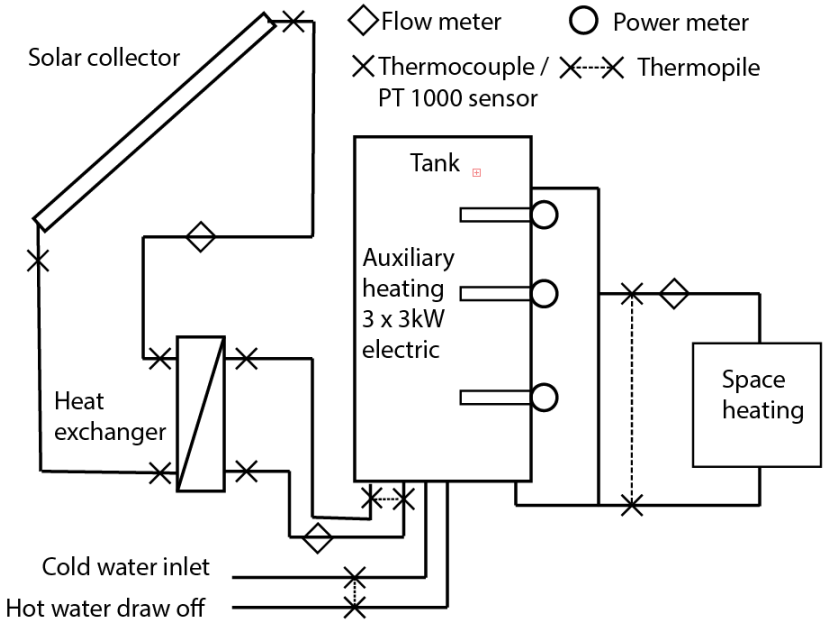

Figure 36. Flow meters and temperature logging for system 3.

5.4 Operation conditions

The measurements of the three systems are carried out over a period from February 20 to April 30, 2013.

The indoor temperature at the test facility where the tanks are located varies around 15°C to 22°C for the period of measurements.

The space heating draw offs are set to a temperature of 30-35 °C with a return temperature of 20 °C which is controlled by a cooling system in the test facility. The flow for the space heating loop resulting in the power drawn from the system is set to balance the demand. For the test period similar loads for space heating for the three systems are applied. The space heating load is set as a stable load throughout the day based on an average outdoor temperature. The load is determined based on the similar relation as for the auxiliary heating requirements of: -0.31*OutdoorTemp + 4.84 kW. The energy requirement for the domestic hot water use is integrated in the draw off for the space heating. As the temperature in the tanks varies throughout the day also the power varies.

5.5 Weather data

The measured weather data are:

- Total irradiance on the collector plane
- Diffuse irradiance on the collector plane measured with a shadow ring (diameter = 0.225 m, width = 0.07 m)

The solar irradiance is measured with pyranometers CM 11 from Kipp & Zonen. The pyranometers are mounted on the roof next to the solar collectors in the same tilted plane and can be seen in figure 21. The diffuse irradiance is measured with a shadow ring screening of the beam and part of the diffuse irradiance and hence corrected by an isotropic correction factor.

5.5.1 Test results

The systems are compared on the basis of:

- energy consumption for the auxiliary heating
- energy cost for the auxiliary heating
- net utilized solar energy of the systems

The energy balances for the systems are shown in table 11.

	System 1 (9 kW elec.)	System 2 (HP)	System 3 (3x3 kW)
Input to the storage			
Auxiliary heating, electricity	5321 kWh	2443 kWh	5722 kWh
Auxiliary heat to storage, heat	5321 kWh	5381 kWh	5722 kWh
Solar heat to storage	809 kWh	790 kWh	668 kWh
Total input	6130 kWh	6171 kWh	6390 kWh
Discharge from the system			
Space heating draw off incl. DHW from storage	5743 kWh	5856 kWh	5947 kWh
Heat losses from storage tanks			
Heat loss (calculated)	387 kWh	315 kWh	443 kWh
Utilized solar energy			
Net utilized solar energy (calculated)	422 kWh	476 kWh	226 kWh

Table 11. Measured energies for period February 20 - April 30, 2013.

The effective COP for the heat pump under these actual operating conditions are from the data above calculated to: COP = 2.2. This value includes the losses in the piping from the heat pump to the storage and the antifreeze function. The heat pump COP could possibly be improved by adjusting the flow in the output pipe for the heat pump to its optimal operating condition.

The heat loss coefficients for the three storages are calculated based on an average storage and ambient temperature and the calculated losses, see table 12.

	System 1 (9 kW elec.)	System 2 (HP)	System 3 (3x3 kW)
Heat loss coefficient UA	9.1 W/K	7.0 W/K	7.8 W/K

Table 12. Heat loss coefficients.

The losses are higher for system 1 and 3 compared to system 2. This is due to the external heating element and the piping in system 1 being included in the calculations for the storage. For system 3 the three electric heating elements inserted in the tank result in thermal bridges. The losses for the piping to and from the heat pump in system 2 are reflected in the calculated COP for the heat pump above.

The way the thermal stratification is built up is highly dependent on the auxiliary heating. The thermal stratification has shown to work best for the system 1 heated by the external electric heating element. The temperatures in the bottom of the tanks in system 2 and system 3 have generally been higher than for system 1. Averaged temperatures for the whole operating period are listed for the top and bottom layer of the tanks as well as for the entire tank in table 13.

Average temperatures	System 1 (9 kW elec.)	System 2 (HP)	System 3 (3x3 kW)
Top layer	69.0°C	52.0°C	71.3°C
All layers	44.8°C	46.5°C	54.6°C
Bottom layer	27.5°C	40.2°C	35.3°C

Table 13 . Average temperatures in storage tank.

This result in a lower operation time for the solar collectors due to a higher required temperature in the solar collector before the solar collector loop starts, see table 14.

	System 1 (9 kW elec.)	System 2 (HP)	System 3 (3x3 kW)
Total system operating time	1495 hours	1495 hours	1495 hours
Operating hours for solar collector loop	375 hours	319 hours	319 hours
Auxiliary operating hours	719 hours	827 hours	184 hours (3 kW) 162 hours (6 kW) 515 hours (9 kW) 861 hours (all)
Standby/defrost time	-	607 hours	-

Table 14. Measured data for solar collector loops.

The cost of the energy for the auxiliary heating is summarized in table 15. The cost in this calculation is based on the hourly prices provided by the Nordpoolspot website without the extra cost of taxes and other additional costs. The costs are compared to an average cost of the electricity for the data.

	System 1 (9 kW elec.)	System 2 (HP)	System 3 (3x3 kW)

Cost for auxiliary heating as operated	1548 DKK	751 DKK	1637 DKK
Cost for auxiliary heating based on an average electricity price	1661 DKK	764 DKK	1783 DKK
Savings due to electricity price variations, DKK	113 DKK	13 DKK	146 DKK
Savings due to electricity price variations, %	6.8 %	1.8 %	8.2 %

Table 15. Costs of auxiliary energy.

The operation costs for system 1 and 3 are almost the same, and the operation costs are lower for system 2 than for system 1 and 3 due to the COP of 2.2 of the heat pump. Under these operating conditions the savings for utilizing the forecasted electricity prices and heat storage for the electric heated system are 7-8 %. For the system with the heat pump the savings are only around 2 %. This is due to the lower heat storage capacity of the system due to the limited maximum temperature in the tank caused by the limited output temperatures of the heat pump.

5.6 Conclusions and discussion

The systems have been tested during a cold winter and spring period of 2013 of about 2 months. The operation costs for the systems based on electric heating element(s) are at the same level and about twice as high as the operation costs for the system based on the heat pump.

System 1 with the external heating element has shown to be marginally cheaper to operate compared to system 3 with the internal heating elements. This is due to better thermal stratification in the tank and therefore more operating hours for the solar collector loop. The heat loss coefficient is on the other hand higher with the external auxiliary heating element.

The tank in system 3 have generally been operating at a higher average temperature which also have caused I higher overall heat loss from that system compared to the two other systems. This is causing a lower net utilized solar energy from that system. The higher average tank temperature in system 3 also indicates that it has worked better as storage therefore also giving a slightly higher cost saving compared to system 1 when the smart control uses forecasted electricity prices.

The COP of 2.2 for the heat pump system gives an operating cost of system 2 of less than half the cost of the other systems.

The cost reduction due to variable electricity prices is about 2-8%.

Most likely the results will be different for other periods.

It must be mentioned that the energy used by the system with the heat pump is relatively high due to the cold outdoor temperature in the test period, since antifreeze operation starts for outdoor temperatures below +2°C. Further, the heat pump has 20 minutes start up periods with low efficiency, the heat pump can only heat the heat storage to 58°C, the volume flow rate in the heat pump loop is not optimal and the output power of the heat pump is relatively low in periods with low outdoor temperatures.

6. Theoretical investigations

6.1 Simplified simulations

In the deregulated electricity market situation in the Nordic countries, the electricity prices can vary dramatically from hour to hour. Therefore a smart control system that can use and adapt to these variations is very desirable, [28], [29]. When a storage tank is available in the system, it can be used for storage of both solar thermal and auxiliary energy.

As more and more renewable energy sources are feeding into the electricity grid, the price variations will most probably be larger during the day. This happens now in Denmark where the wind power fraction in the grid is higher than 20%.

Typically the electricity prices are higher during the day than in the night. This is good for solar heating systems that can reduce the use of backup electricity during peak hours of the day. Especially if the solar heating system inclusive the heat storage is well designed and properly sized. This happens partly automatically in existing solar combi systems with normal thermostatically controlled backup electric heating elements or a heat pump. Also the thermal load of a house has a daily variation matching the price variations quite well, especially if the house has significant passive solar gains during the day. The problem today is that the customer is not given credit to this as variable electricity prices are very uncommon yet on the market. But most likely this will come soon for most customers as this is an important possibility to make it easier to introduce more renewable energy in the electric grid.

A normal control system in a solar combi system does not have information about the weather and prices for the next day. Therefore the auxiliary charge can not be optimized for high solar production by minimizing the auxiliary charge and optimizing the power and timepoint, in the night before. If this was possible it would allow more solar input to the store and less use of backup energy at high electricity prices. In a normal combi system a secure charging level in the store has to be maintained as if the next day will be rainy. Otherwise a lot of high cost electricity will be used during the peak hours of the next day to meet the load.

There are several control options for varying and thereby adapting the auxiliary charge of the storage. Figure 37 shows sketches of the main options. They can be divided into two main principles: Variable temperature and variable volume auxiliary charge. Both ways will open for advanced control of the auxiliary energy charge and thereby adaptation to the conditions of the electricity price variations, load and potential solar energy production the next day. To the left in figure 37, the standard auxiliary charging method with a fixed volume and thermostat control and to the right the most advanced charging option with variable temperature and variable volume simultaneously.

These two extremes, traditional and advanced control, are compared to give a potential for improvement by smart tanks and smart control in a combi system.

In this case a simplified calculation model has been chosen that can be implemented in Excel.

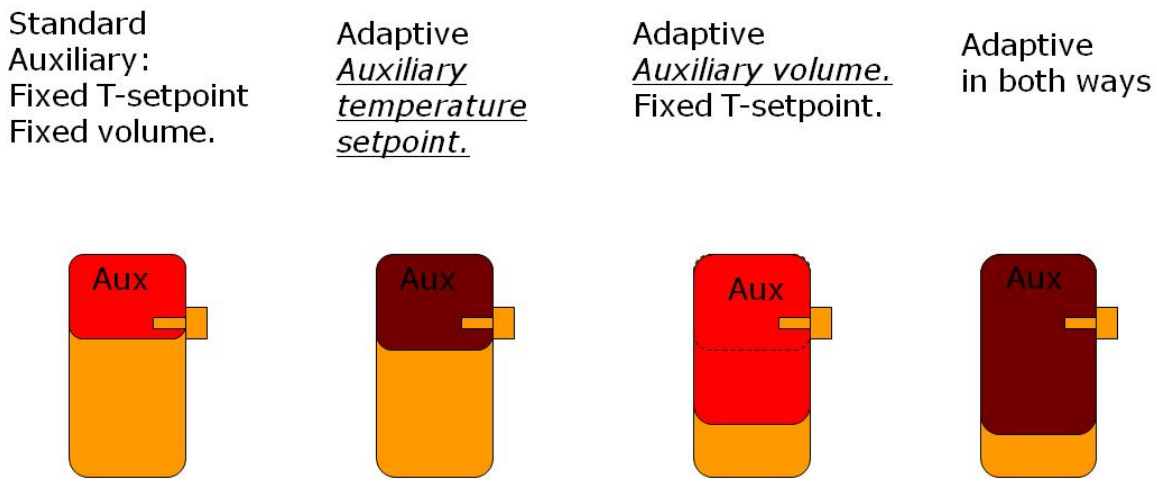

Figure 37. Auxiliary charge control options for the storage in a combisystem. The standard solution to the left with fixed volume and thermostat control and the most advanced to the right with variable volume and temperature and forecast control.

The forecast control is here utilizing the real weather data for the next day in the simulation. This is done to separate and eliminate uncertainties in system modeling and control from inevitable uncertainties in the weather forecasts.

The simplified energy balance model, used here is shown in figure 38.

All relevant energy flows in and out of the tank in the system are present, so no energy is neglected. In the figure also the very simple equation for the auxiliary energy need is shown. To be complete and realistic one also have to check the minimum and maximum charge level Q(t) so that the minimum load temperatures can be delivered and that the tank is not overheated or boiling of course.

The component models are also very much simplified to first order options, to make it easy to implement in Excel without the need for iterative procedures. Still also here the main effects are present. In a next step it can be possible to refine both the system model and component models in Excel, but the accuracy gain is limited for the aim of this study to find out the potential improvement level.

For future design optimization of the components together with manufacturers though, continued work with a TRNSYS model is very interesting and the idea is to validate the TRNSYS model against the tests in the laboratory.

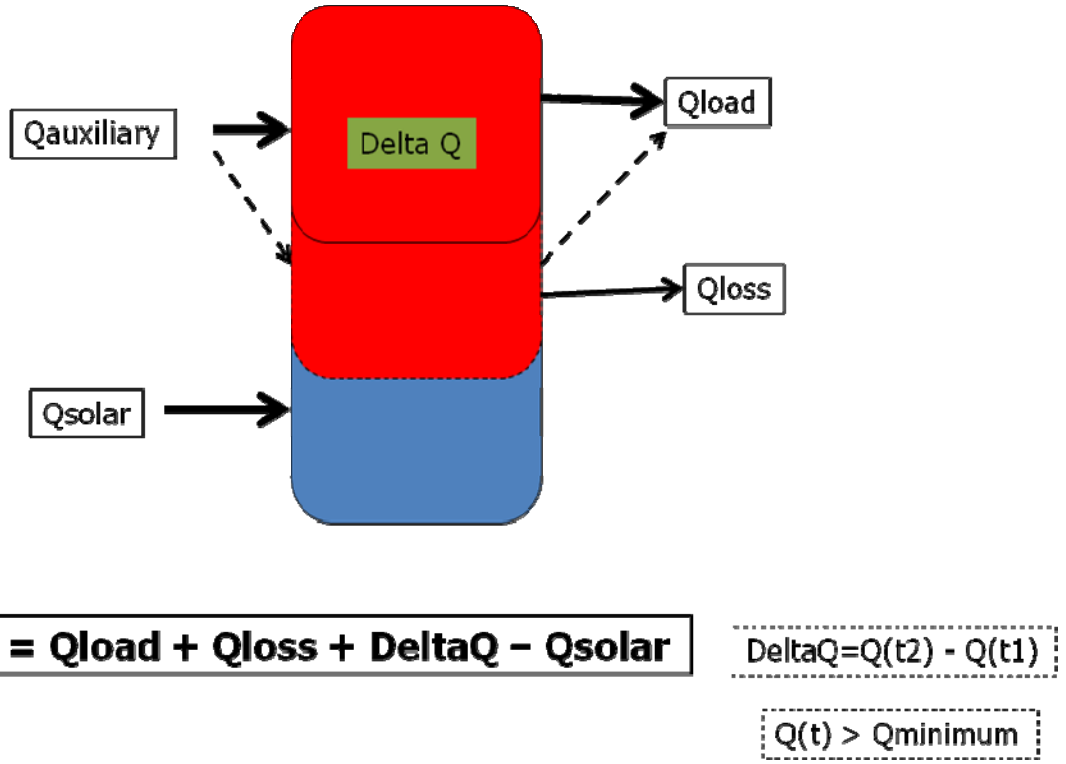

Figure 38. The energy flows considered in the simplified model of the combisystem. The very simple equation for the required auxiliary charge is also given, together with limits for the energy content Q(t) of the store.

Detailed and carefully monitored climate data from the DTU Byg weather station for year 2008 together with hourly electricity price data from Nordpool for year 2008 are used. The forecast calculations are based on known climate data the next day in the climate file.

The system model is extremely simple as shown in figure 33. The aim here is to make a potential study how much ideal forecast control and ideal tank behavior (working as a capacitor for heat) can reduce the annual auxiliary costs in combination with addition of energy from a solar collector.

The component models for solar collector and building are simplified to stationary first order models to avoid iterations in Excel. The storage tank is modeled according to the energy balance given in figure 38.

The collector is tilted 45° and oriented due south. The collector model is an extremely simple first order model with an effective zero loss efficiency of 0.75 and a total heat loss factor of 3.5 W/m²K including pipe losses. The mean operating temperature of the collector is assumed to be constant 50°C. In a real system this temperature is of course varying with many other variables and parameters, in the system but here this is second order parameter and only affects the collector and pipe heat losses.

The tank is modeled as an ideal “themal capacitor” and only the energy flows are studied, with no mixing between the energy flows as solar and auxiliary. The load and heat losses are also just extracted as a change in energy content of the store. The heat losses are assumed to be constant: 100 W total for the tank plus system outside the collector loop. In reality of course the losses are very dependent on the tank design and control. But as the charging and discharging powers are of a magnitude 10-100 times larger, this heat loss variation was neglected in these calculations.

The auxiliary volume and auxiliary temperature of the tank are variable (but not calculated explicitly). The tank size is automatically adapted and set to the worst winter day, when the store has to be able to store the forecasted auxiliary need for one day, with the whole tank used as auxiliary volume. At this time of the year the solar charge is small and this volume need is neglected at this stage.

In the normal reference system the auxiliary part for the store is kept at a constant minimum temperature of 60°C, but occasionally when there is a lot of solar radiation available the tank temperature will increase above this level. If the tank is heated above a max temperature of 95°C the solar and auxiliary charge is stopped.

In the advanced forecast control alternative the auxiliary energy charge is done in the night and in an amount that will exactly meet the total load during the next day including house heating, hot water consumption and heat losses, but minus the predicted solar charge during the next day.

The control timing of the auxiliary charge is simplified to a fixed time period each morning when the prices are at minimum around 3 o'clock very regularly in the Danish grid. This is due to the low load in the grid at the end of the night, when very little activities occur in the society. In the full forecast control also the time for charge should be optimized but this turned out to be too complicated in this simplified potential study. An estimate is therefore given for this case in the results, using the lowest price every day to calculate the annual auxiliary cost.

Figure 39 shows an example of the hourly energy flows and energy content in the store in two control options 1) normal control and 2) forecast control. In the normal control case the auxiliary energy is added all the day instantaneously when needed. In the case of forecast control the auxiliary supply is done in the night to use the lowest possible electricity prices. The absolute level of the energy content curves Qstore=Q(t) (two upper ones) are not representative for the future system design. They are just shown relative to 0 °C here. In a real system the advanced auxiliary control can allow the store to go below the energy content of the normal storage control option, as the forecast information warrants the comfort the next hours. Also extreme stratification measures will work in this direction.

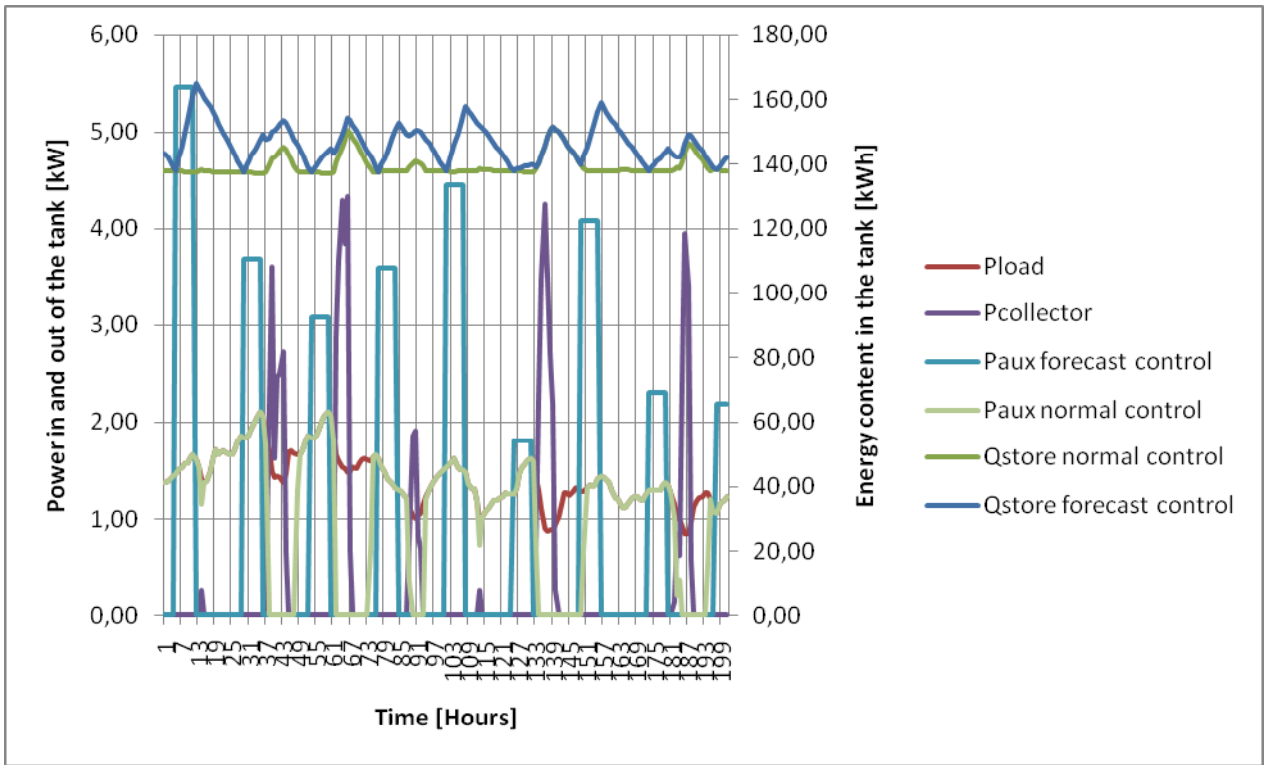

Figure 39. Hourly energy flows in the system in kW, Pload, Pcoll and Paux (four lower curves) and energy content Qstore=Q(t) (the two upper curves) for the two control options. 100W/K house and 10 m² of collectors. The absolute level of the two upper energy content curves are not relevant for the auxiliary cost results, only the variations that reflects smart auxiliary charge at low prices.

The results of the calculations for annual auxiliary costs in DKK (Nordpool cost level), have been summarized in figure 40, 41 and 42.

In figure 40 the costs are given for two different building insulation standards 200 W/K and 100 W/K, five different storage sizes and four different solar collector areas 5-20 m². The hot water load has been the same for all cases 100 l/day.

The cost level is at the NORDPOOL electric stock exchange level http://www.nordpoolspot.com/.

This is much lower than the final customer price level, so the potential savings in absolute numbers, in DKK per year, are much larger than shown in the diagrams.

The tank volume has been adapted to a minimum size needed to store enough energy for the different options. (The leftmost points on all curves represent a traditional tank design and a volume of 750 and 500 l has been set to be appropriate for the two house insulation standards).

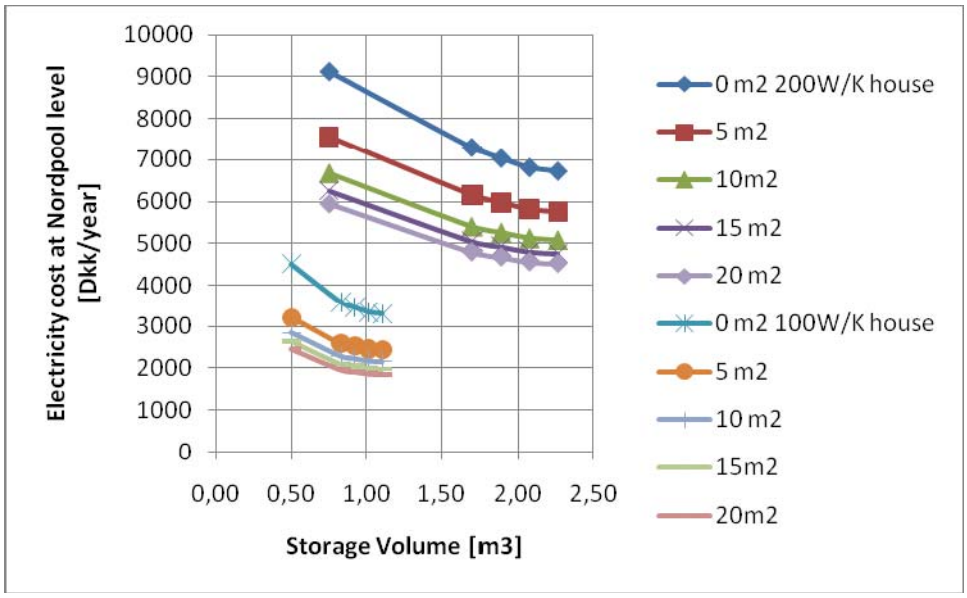

Figure 40. Calculation results for ideal forecast control (the next days weather is known), compared to a standard auxiliary control where the thermostat decides when to use electricity instantaneously. Note in all cases a variable electricity cost is assumed for the system owner. The case of fixed price at the annual average level is only shown in figure 26.

In Figure 41 and 42 the same calculations are shown as a function of collector area. Only the 200W/K house is shown in figure 41 to limit the number of curves. But here also the reference case is shown with constant electricity price all year (uppermost curve) and the extreme case of using the lowest price every day (24 hours) is shown too, as the lower curve giving the extreme improvement potential. In figure 40 all curves are for the same variable electricity price conditions and only the auxiliary charging strategy/principle is changed.

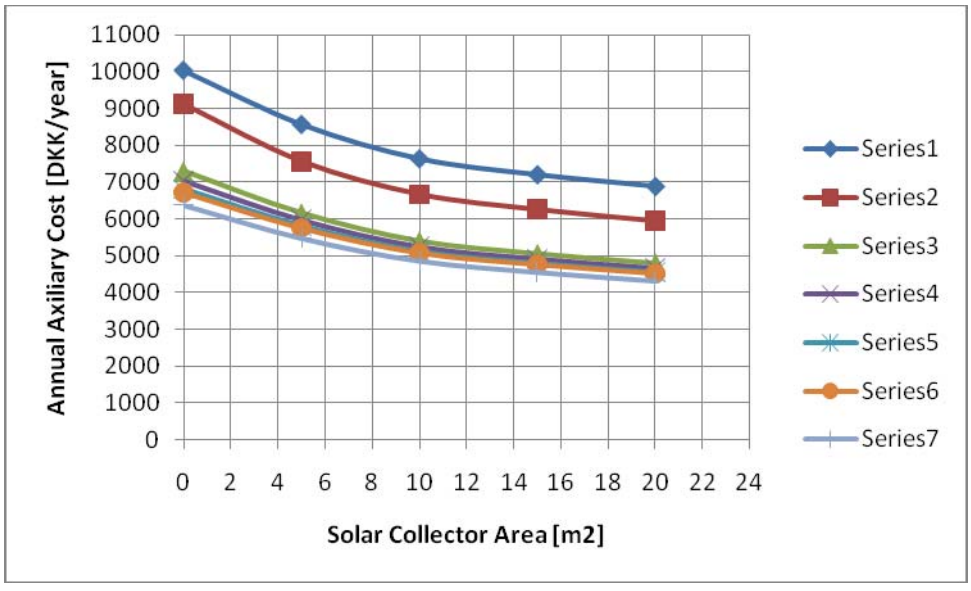

Figure 41. Annual auxiliary cost variation for a 200 W/K house with different collector area and control option/pricing. Series 1 is the reference case with constant electricity price and normal thermostat aux control. Series 2 is the same thermostat control as series 1, but variable electricity price. Series 3 to 6 are shorter and shorter charging period and higher charging power around the minimum price time each day. Series 7 is the extreme case when the lowest electricity price each 24 hours is used.

In figure 42 the same calculations and curves are given for a well insulated house 100 W/K. It can be seen that the optimum collector area is smaller as expected closer to what is needed for the 100 l/day hot water demand. Still the relative cost savings between a traditional system without solar collectors and an advanced system with solar is in the range of 50%.

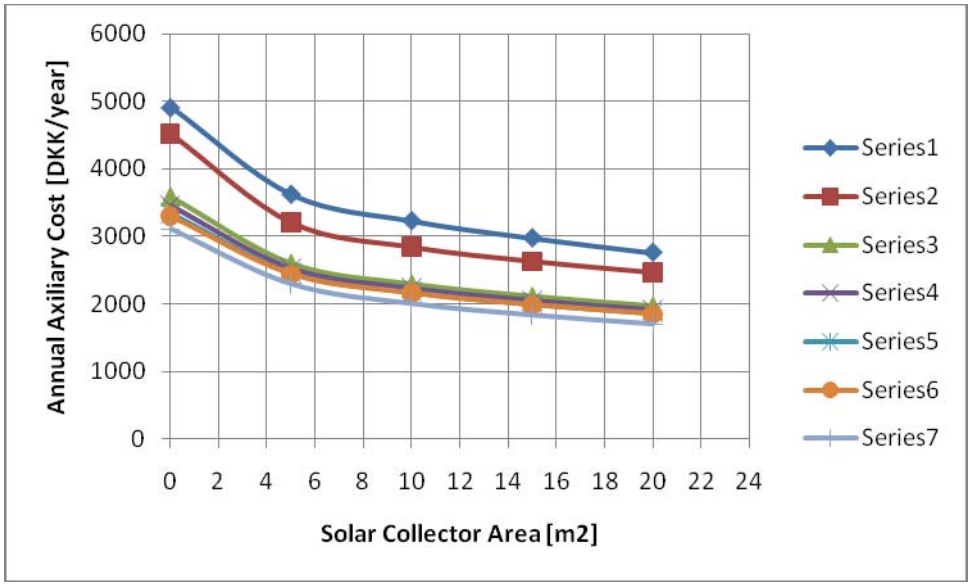

Figure 42. Annual auxiliary cost variation for a 100W/K house. Otherwise the same curves as in Figure 26.

The extra cost of receiving the maximum electric power level (max kW) needed to charge the tank in a short time span, is not included here, but this pricing may be adapted on the market in the future, as there is plenty of power available in the grid when the load is low and the electricity kWh cost is close to minimum. The curve series 3 in figure 36 with power needs of maximum 17 kW can be met by normal domestic electric connections of three phase 400V 25 A for the 200 W/K house. For the 100 W/K house series 3-5 can be covered with 16- 25 A three phase fuses at the final customer. The very lowest curves need special arrangements to meet the maximum load and are more shown as limiting curves with just 1 hour or less charging time per day. In case of a heat pump the electric power need, is at least halved, for normal conditions and the electric power need is no problem.

The combination of smart auxiliary control and addition of 10 m² of solar collectors in a solar combi system can reduce the auxiliary cost for a house by around 50% in an example for Danish conditions and a normal house.

The annual auxiliary cost savings is around 3000-5000 DKK on the Nordpool electricity cost level. The cost savings at the final customer price level is hard to predict, but can be estimated to two to three times larger depending on how the variable price structure will be and how energy and CO_2 tax will change in this case.

For the same collector area in the system a smart forecast auxiliary control has the potential of reducing the auxiliary electricity cost by 30-40% more alone.

From the results one can estimate that for a 200 W/K house with 100 l/day hot water load, 10 m² of collectors is reasonable and for a well insulated 100 W/K house around 5 m² can be recommended.

The very simple system model and forecast control shown here seems to give reasonable results and the principle was used for the controller programming for the three laboratory test systems. Of course, a lot of refinements are possible.

6.2 TRNSYS simulations

Investigations on simplified control strategy.

A simplified control strategy is investigated for three smart (solar) heating systems with storage volumes of 750 litres and solar collector areas of 0 m^2, 9 m^2 and 18 m^2. The auxiliary volume can be 240 litres or 390 litres or 750 litres. Auxiliary heating is restricted to the night time from 2 am until 5 am where the electricity price is low. The size of the auxiliary volume and the set point temperature of the auxiliary volume are determined month by month in such a way that the energy demand is fully covered at the lowest electricity price. The smart (solar) heating systems are referred to as S-0m2, S-9m2 and S-18m2.

Further calculations are made for a semi smart solar heating system with a storage volume of 750 litres and 9 m^2 solar collector area and a fixed auxiliary volume of 750 litres and a fixed set point temperature of 90 °C in such a way that the energy demand is fully covered when the auxiliary heating is restricted to the night time from 2 am until 5 am. The semi smart solar heating system is referred to as SS-9m2.

Finally, calculations are made for three traditional (solar) heating systems with storage volumes of 750 litres and solar collector areas of 0 m^2, 9 m^2 and 18 m^2. The auxiliary volumes and the set point temperatures are fixed to 240 litres and 50 °C, respectively and auxiliary heating can take place during all hours whenever it is needed in order to fully cover the energy demand. The traditional (solar) heating systems are referred to as T-0m2, T-9m2 and T-18m2.

All the calculations are made with a real highly variable electricity price hour by hour and with a fixed electricity price of 1.8 DKK/kWh.

The control strategy is investigated with a TRNSYS model of a solar heating system. The TRNSYS model used is worked out in the solar heating and cooling program Task 32 within the International Energy Agency [30]. Figure 43 shows a schematically illustration of the solar heating system used in the calculation. The variable auxiliary volume is facilitated by varying the position of the outlet for the auxiliary loop.

The weather data used in the calculations are measured at the solar radiation measurement station at the Technical University of Denmark in 2009 [31]. Figure 44 shows the ambient temperature, the beam irradiance on horizontal and the diffuse irradiance on horizontal.

The electricity price used in the calculations is also from 2009. The electricity price is shown in Figure 45 as the variable electricity price hour by hour. It can be seen that there are large variations in the electricity price during the year. Detailed study of the electricity price shows that the price most often is lowest in the night in the hours from 2 am to 5 am.

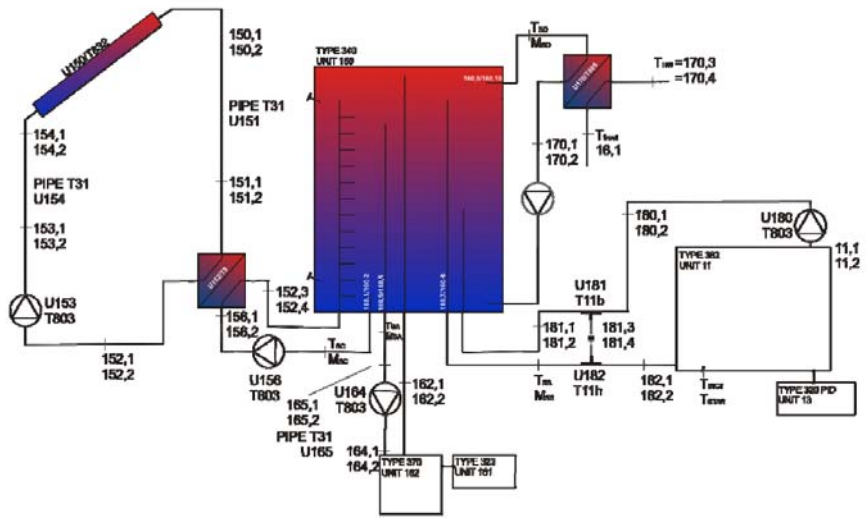

Figure 43. Schematically illustration the solar heating system used in the calculations. Picture from [30].

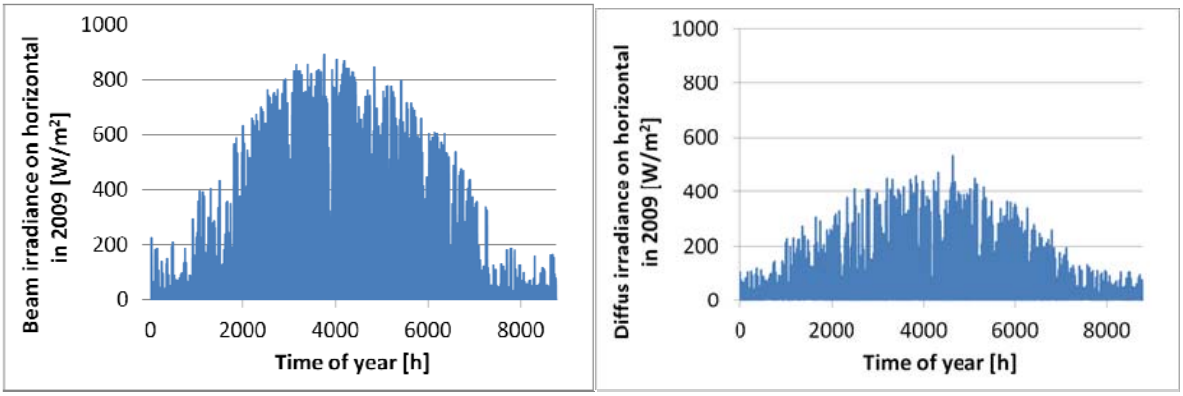

Figure 44. Left: The ambient temperature. Middle: The beam irradiance on horizontal. Right: The diffuse irradiance on horizontal.

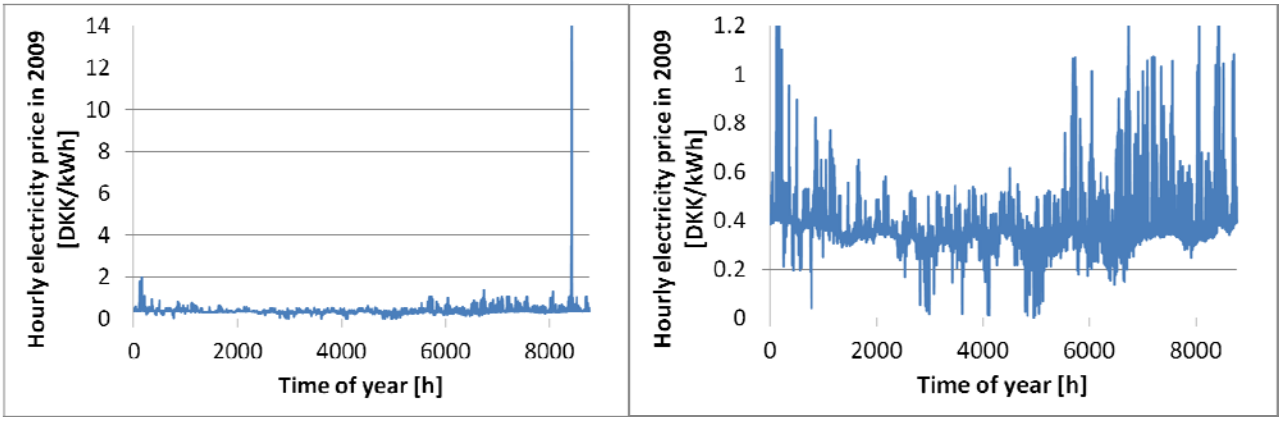

Figure 45. The hourly electricity price during 2009. The two graphs show the same with different resolution on the y-axis.

The calculations are made for a single family house with a yearly energy consumption of about 4700 kWh and a daily hot water consumption of 100 litres heated from a varying cold water temperature to 45 °C, corresponding to a yearly energy consumption of about 1500 kWh. The cold water temperature varies between 3.4 °C and 16.0 °C throughout the year. Hot water for domestic hot water is taken from the top of the tank and lead through an external plate heat exchanger and back to the bottom of the tank. The domestic hot water is heated in the plate heat exchanger. Domestic hot water is tapped three times per day at 7 am, noon and 7 pm in three equal portions with a low volume flow rate.

Figure 46 shows the monthly space heating consumption and domestic hot water consumption, respectively. The data of the solar heating system used in the calculations are listed in Table 16.

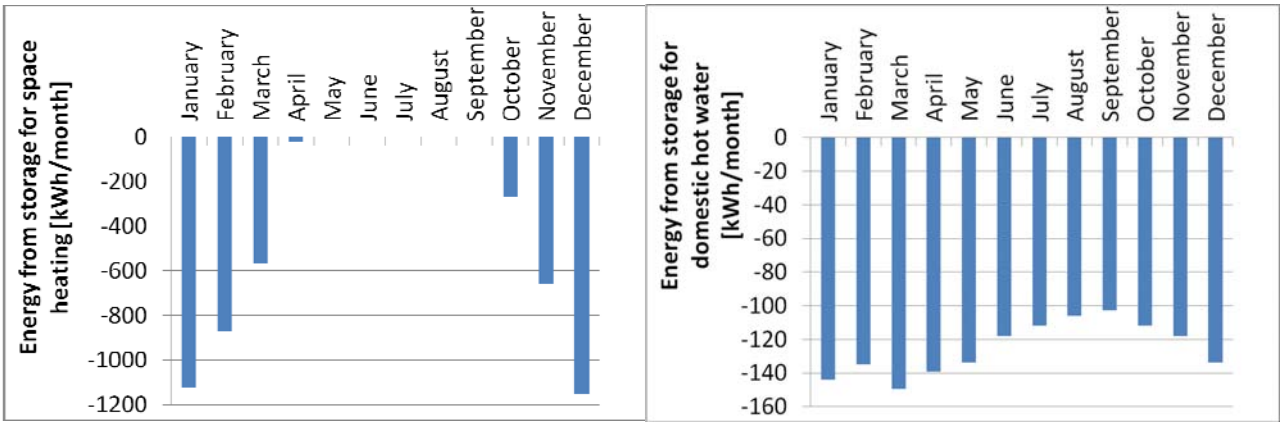

Figure 46. Left: Energy from the storage used for space heating. Right: Energy from the storage used for domestic hot water.

Table 16 shows data of the solar heating system used in the calculations. The heat loss coefficient of the sidearm and the external heat exchanger for domestic hot water preparation are not taken into calculation.

Solar collector area	9 m^2 / 18 m^2
Optical efficiency of incident radiation, η_0	0.756
Heat loss coefficients, a_1 / a_2	4.37 $W/m^2/K$ / 0.01 $W/m^2/K^2$
Efficiency for all incidence angles, η	$\eta_0 \cdot k_\theta - a_1 \cdot (T_m - T_a)/E - a_2 \cdot (T_m - T_a)^2/E$
Incidence angle modifier for beam radiation, k_θ	$1\text{-}\tan^{4.2}(\theta/2)$
Collector tilt / Orientation	45° / South
Solar collector fluid	40% (weight) propylene glycol/water mixture
Volume flow rate in solar collector loop	0.20 l/min/m^2
Storage volume / auxiliary volume	750 l / 240 l, 390 l, 750 l
Height/diameter	1.89 m/ 0.71 m

Tank insulation top / side / bottom	200 mm / 200 mm / 20 mm
Heat transfer coefficient of external heat exchanger in solar collector loop	125 W/K per m^2 collector
Relative inlet/outlet height of domestic hot water loop	0 / 1
Relative outlet height of space heating system	0.84
Relative inlet/outlet height in solar collector loop	Stratifier / 0.06
Auxiliary power	30 kW
Control system – Differential thermostat control with one sensor in the solar collector and one in the tank	
Relative height of temperature sensor in solar collector loop	0.1
Maximum/Minimum temperature differential	7 K / 0.5 K

Table 16. Data used in the calculations.

In figure 47 the solar energy and the auxiliary energy transferred to the storage tanks in the different calculated solar heating systems are shown. It can be seen that the smart solar heating systems and the semi smart solar heating system get less solar energy and more auxiliary energy to the storage tank than the traditional solar heating systems. The reason is that the auxiliary volume in the smart systems often is higher than the auxiliary volume in the traditional systems. As expected, the figure also shows that the difference between the auxiliary energy for solar heating systems with 9 m^2 and 18 m^2 solar collector areas is not very large, because the used storage volume is too small for a solar collector area of 18 m^2.

In figure 48 the electricity price for operating the smart, semi smart and traditional solar heating systems can be seen. The figure shows that the yearly electricity price is lower for the traditional solar heating systems than for the smart solar heating systems when a fixed electricity price is used. If the variable electricity price is used, the yearly electricity price is lowest for the smart solar heating systems and there is no difference in the yearly electricity price between the traditional and the semi smart solar heating system. Consequently, the use of cheap electricity plays a large role for the yearly auxiliary energy price.

The most attractive system for the home owner is a system resulting in the lowest energy costs. Therefore the cost of the system as well as the yearly electricity costs must be considered. In order to elucidate which collector areas and tank volumes will result in the most attractive systems, more calculations are needed. Most likely, the optimal system size will depend on the heat demand of the house.

In figure 49 the needed size of the auxiliary volume and the needed set point temperature of the auxiliary volume in the smart solar heating system with 9 m^2 solar collector area are shown. Also the sensitivity of the monthly electricity price as function of the needed size of the auxiliary volume and the needed set point temperature of the auxiliary volume that can fully cover the energy demand in October is shown. It

can be seen that the electricity price can be reduced further by 5 % by using a stepless auxiliary volume instead of the three auxiliary volume sizes used in this investigation.

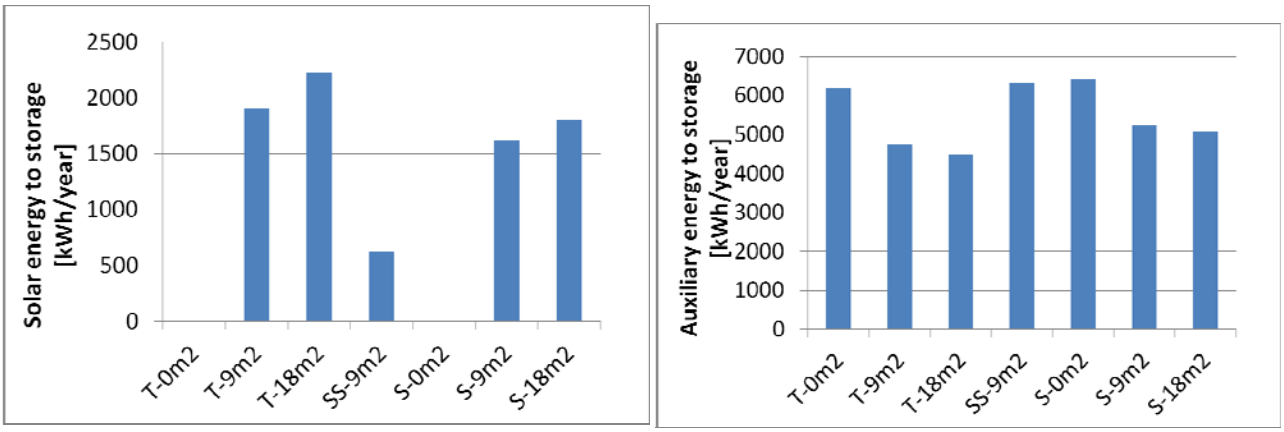

Figure 47. Left: Solar energy to the storage. Right: Auxiliary energy to the storage.

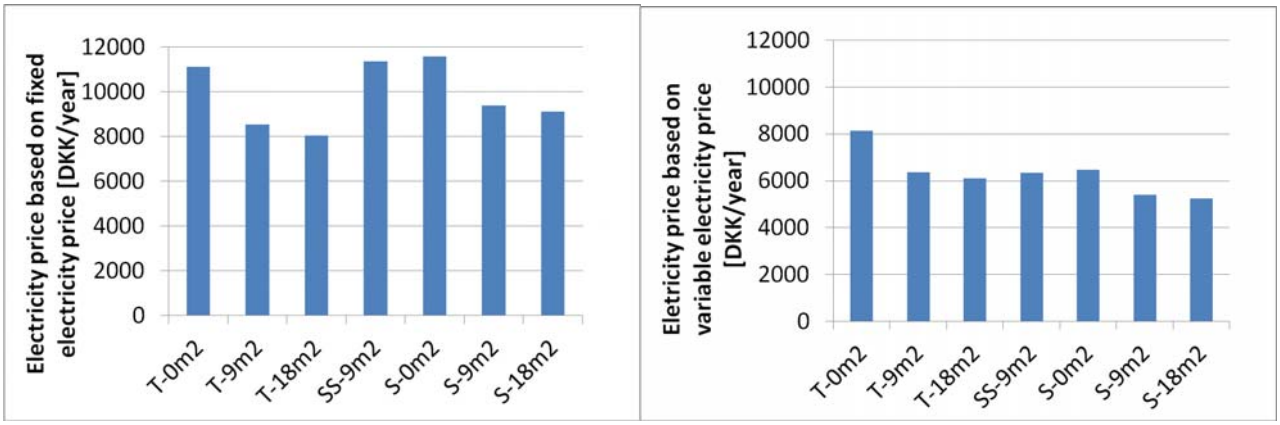

Figure 48. Left: Electricity price based on fixed electricity price of 1.8 DKK/kWh. Right: Electricity price based on variable electricity price.

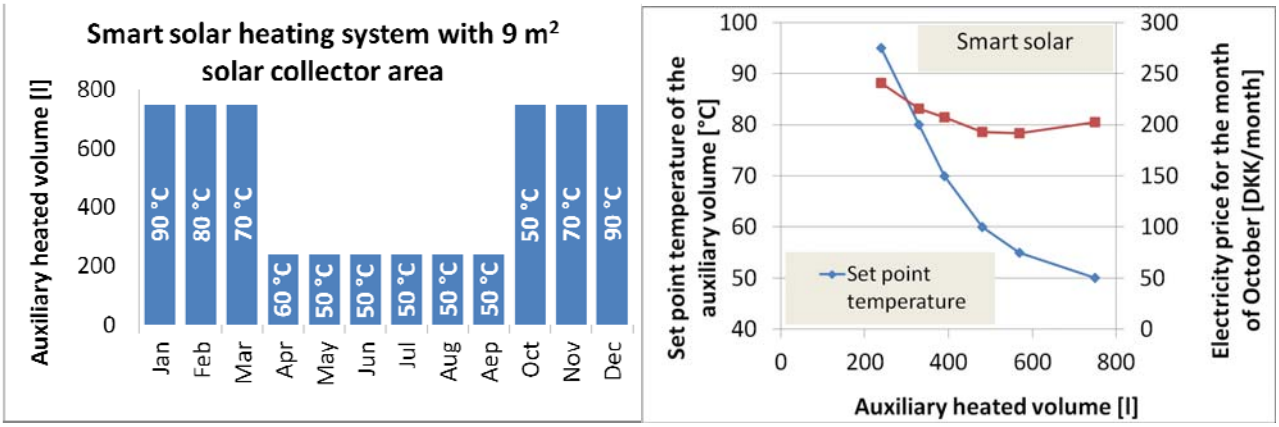

Figure 49. Left: Needed auxiliary heated volume and set point temperature of auxiliary heated volume if auxiliary heating takes place from 2 am to 5 am. Right: Electricity price in October as function of the auxiliary heated volume and the set point temperature of the auxiliary heated volume with variable electricity price.

Discussion and conclusions on the simplified control strategy.

The investigation shows that it is possible to reduce the yearly energy price by 25 % by using a simple control strategy, a smart solar heating system and cheap electricity even if the thermal performance in terms of solar and auxiliary energy transferred to the tank is worse for the smart solar heating system than for the similar traditional solar heating system.

For each month the energy demand is covered by the smart solar heating with one auxiliary volume with a fixed set point temperature resulting in the lowest monthly electricity price. The auxiliary volume and the set point temperature can be different from month to month.

Therefore it is expected that the yearly energy price can be reduced even further by only using the exact needed auxiliary volume size and set point temperature for all periods. This can be achieved by a smart control system that makes use of weather forecast.

The concept can be further improved by making use of a control system which is also based on forecasts of the solar heat production and on prognoses for electricity costs and a larger tank volume.

The power used in the calculations, 30 kW is unrealistic high for a normal electricity installation in a single family house. It is used in order to be able to supply the needed energy during the allowed heating period of 3 hours during the night time with known cheap electricity. The electricity will be cheap in other periods during the day and a real smart control system will be able to utilize all periods with cheap electricity and consequently, lower power consumption is needed. If large power consumption is needed, this can be achieved by a heat pump.

Investigations on advanced control strategy.

The TRNSYS model T-9m2 is used to calculate energy flows for three single family houses with different space heating consumption. The TRNSYS model is described in figure 43 and table 16. The energy flows are: heat loss from the storage tank, domestic hot water consumption, space heating consumption, solar energy transferred to the tank and auxiliary energy transferred to the tank.

The houses have space heating consumption of 30 kWh/m^2/year, 60 kWh/m^2/year and 100 kWh/m^2/year corresponding to 4660 kWh/year, 8940 kWh/year and 14670 kWh/year respectively. The houses are referred to as SH30, SH60 and SH100 corresponding to the respective space heating consumption. The weather data is measured during 2009, see figure 44 and electricity prices are also from 2009, see figure 45.

The energy flows and the auxiliary energy cost for the traditional solar heating systems are shown in table 17. The electricity costs are the raw electricity cost multiplied by 3 in order to include the taxes and distribution costs the consumer also must pay.

	SH30	SH60	SH100
Heat loss from storage tank [kWh/year]	510	485	464
Domestic hot water consumption [kWh/year]	1503	1502	1503
Space heating consumption [kWh/year]	4657	8941	14670
Solar energy to storage tank [kWh/year]	1907	2092	2397
Auxiliary energy to storage tank [kWh/year]	4747	8839	14240
Cost for auxiliary energy for the traditional heating system based on variable electricity prices [DKK/year]	6375	11748	18633
Cost for auxiliary energy for the traditional heating system based on a fixed electricity price of 1.8 DKK/kWh [DKK/year]	8545	15910	25631

Table 17. Energy flows and energy costs.

From table 17 it is seen that the cost for auxiliary energy can be reduced by 25%, 26% and 27% for the houses with space heating consumptions of 30 kWh/m^2/year, 60 kWh/m^2/year and 100 kWh/m^2/year respectively by using variable electricity prices instead of a fixed electricity price.

Now, the costs for electricity in the three single family houses are calculated hour by hour in such a way that the needed energy is always covered with the cheapest electricity price possible. Three forecast periods of 12 hours, 24 hours and 36 hours are used for the calculations. The hour by hour energy flows from the TRNSYS calculations are used, except the calculated auxiliary consumption. Based on an energy balance, the hourly auxiliary energy need is calculated:

Solar energy to tank – tank heat loss – domestic hot water – space heating = auxiliary energy need

If the energy balance shows a surplus of energy, this energy is distributed to the following hours if the energy balance shows an energy demand in the following hours and the storage tank is not fully charged. In the calculations, the storage tank can be charged with maximum 30 kWh.

Based on the length of forecast period, the auxiliary energy need is covered at the cheapest electricity price. Table 18 shows the cost for electricity based on the variable electricity price and how much the price is reduced compared to a traditional control system based on variable electricity prices and a fixed electricity price of 1.8 DKK/kWh.

	SH30	Reduction compared to traditional system with variable / fixed electricity price [%]	SH60	Reduction compared to traditional system with variable / fixed electricity price [%]	SH100	Reduction compared to traditional system with variable / fixed electricity price [%]
Cost for auxiliary energy based on variable electricity prices, 12 hour forecast [DKK/year]	5160	19.1 / 39.6	9564	18.6 / 39.9	15597	16.3 / 39.2
Cost for auxiliary energy based on variable electricity prices, 24 hour forecast [DKK/year]	4929	22.7 / 42.3	9252	21.3 / 41.9	15128	18.8 / 41.0
Cost for auxiliary energy based on variable electricity prices, 36 hour forecast [DKK/year]	4902	23.1 / 42.6	9226	21.5 / 42.0	15075	19.1 / 41.2

Table 18. Costs for auxiliary energy.

6.3 Summary and conclusions

The investigation shows that it is possible to reduce the yearly energy price by around 40% if a smart control system that makes use of the highly variable electricity prices based on weather forecast and electricity price forecast is used.

The investigation also shows that a forecast of 24 hours is sufficient for a solar heating system with a tank of 750 litres and a solar collector area of 9 m^2. In order to utilize longer weather and electricity forecast periods, larger solar heating systems are needed.

7. Socio-economic benefits by implementation of the energy unit in large numbers

7.1 Methodology for analysing socio-economic benefit

The substitution of individual oil and natural gas boilers with the solar/electric heating units will reduce the use of oil and natural gas, but on the other hand, it will increase the demand of electricity. When the solar/electric heating units are operated in an optimal way they will, however, mainly use electricity in hours with low electricity prices. This may

for instance be in hours with large contributions from wind power, and thereby the solar/electric heating units can help on utilising excess generation from wind turbines and contribute to integrating more wind power in the system.

The socio-economic benefit is analysed by use of the Balmorel model, www.balmoral.com, which is a detailed model of the overall electricity and heat system. The model takes into consideration variations in electricity demand, technical and economic data for production units (e.g. power plants), fuel prices, share of wind power in the system etc. The analysis estimates - under given assumptions - the interplay between the solar/electric heating units and the overall system, and based on this it also estimates changes in total fuel consumption, emissions, costs etc. as a consequence of the solar/electric heating units.

The model essentially finds a least-cost solution for electricity and heat taking into account:

- Electricity and heat demand (including time variations)
- Technical and economic characteristics for each kind of production unit, e.g., capacities, fuel efficiencies, operation and maintenance costs, and fuel prices
- Environmental taxes, CO_2-price and regulations
- Transmission capacities between regions and countries

As output, the model derives among others electricity and heat generation at different units, electricity exchange between regions and countries, electricity prices and total costs in the system.

By comparing one model run including the solar/electric heating units with one model run without the solar/electric heating units, it is possible to estimate how the solar/electric heating units influence on the total system in terms of:

- Difference in production at generation units in the system
- Difference in fuel consumption
- Difference in emissions
- Difference in total costs

7.2 General assumptions

The analyses have been carried out for the year 2020. In this section, some of the main general assumptions are listed.

Wind power

The electricity generation in Denmark will be covered by 50 % wind power in 2020.

Geographical scope

The specific model version used contains the electricity and CHP system in the Nordic countries (Denmark, Finland, Norway and Sweden) and Germany.

Fuel prices

The development in prices of fuel is based on the latest forecast from the Danish Energy Agency from September 2012. Fuel prices used for the gas and oil boilers are "an consumer" which means that they include distribution costs. In order to analyse the solar/electric heating units in a consistent way, distribution costs (according to the DEA assumption) are also added to the spot price regarding electricity use in the solar/electric heating units.

CO_2-costs

Similar to the fuel prices, the CO_2-costs are based on the latest forecast from the Danish Energy Agency (from September 2012). The CO_2-price in 2020 is approximately 162 DKK/ton.

Time resolution

The analyses have been carried out by use of an hourly time division, i.e. 8.760 time segments per year.

7.3 Approach to scenario analyses

The analyses are carried out for the following four scenarios (EH means electric heater and HP mean heat pump):

- S/E heating units (HP) replaces gas and oil boilers
- S/E heating units (EH) replaces gas and oil boilers
- S/E heating units (HP) replaces gas and oil boilers - lower heat demand
- S/E heating units (EH) replaces gas and oil boilers - lower heat demand

The scenarios with lower heat demand are relevant because future buildings are expected to have a much lower heat demand than today.

In addition to these scenarios, scenarios with double heat storage capacity were carried out. The calculations showed no change in the results compared to the reference scenarios which means that the capacity of the heat storage in the reference scenario is larger than needed at any time during the year.

7.4 Specific assumptions in the scenario analyses

Heat demand and capacities

According to the Danish Energy Agency there were 2.7 million heat installations in Denmark in 2011. The allocation on natural gas and oil installations are shown in table 19.

Natural gas boilers	Oil boilers	District heating	Others	Total
418	365	1,694	269	2,745

Table 19. Number of heat installations in Denmark in 2011

The distribution of the installations and heat demand between Eastern and Western Denmark is unknown. An assumption is made that the distribution is 45 % and 55 %, respectively.

The heat demand for the households supplied by individual oil and gas boilers is 18 PJ and 27 PJ, respectively, see table 20.

Number of heating units in thousands				Heat demand, GWh			
East		West		East		West	
NG	Oil	NG	Oil	NG	Oil	NG	Oil
188	165	230	201	3,366	2,255	4,113	2,756

Source: "Energistatistik 2011", Danish Energy Agency, September 2012

Table 20. Heat installations and demand in individual oil and gas supplied areas distributed by geographical areas and fuel type

In the analysis, 10 % of the heat installations are considered. The reason for limiting the number of gas and oil installations converted to the solar heating systems is that 100 % is probably not realistic and because the more solar heating systems established the more energy system in Denmark (and the neighbouring countries) will be affected.

The necessary heat capacities in the areas are determined by the respective heat demands. In the reference scenario with only oil and gas boilers, there is not heat storage. This means that the boilers must be able to cover the peak demands.

Figure 50 shows the heat demand for a typical winter week on an hourly basis.

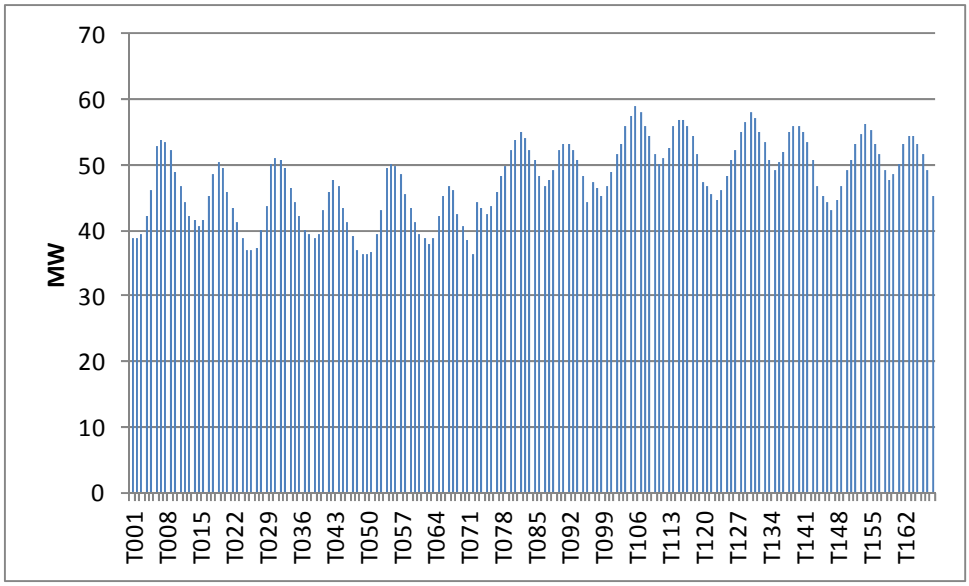

Figure 50. Heat demand for households in Eastern Denmark (week 15, 2020)

Existing oil and gas boilers

The capacity of the individual gas and oil units is assumed to be large enough to cover the total heat demand if the micro CHP unit should be out of operation. Both the oil boiler and the gas boiler have an assumed heat efficiency of 85 %.

Solar/electric heating units

Data for the solar/electric heating units are listed in table 21.

	Per unit	Total
Solar heating		
- area, m2	9	705,000
- capacity, kW	6.3	494,000
COP for heat pump	3.3	-
Efficiency for electric heater	100 %	-
Heat storage		
- volume, m^2	0.750	59,000
- energy content, kWh	33.75	2,645,000
- load and unload, kW	28	2,204,000

Table 21. Technology and economic data for the solar heating systems.

The solar heating units are assumed to produce 500 kWh/m^2/year (corresponding to app.714 full load hours).

7.5 Results of scenario analyses

S/E heating units (HP) replaces gas and oil boilers

The heat generation in the areas with oil and natural gas boilers in the reference scenario is shown in figure 51. The two left columns show the heat generation from the oil and natural gas boilers in the reference scenario. The two right columns show the heat generation in the solar heating scenario with heat pumps. In the solar heating scenario with heat pumps the solar collectors generates 287 GWh or 23 % of the total heat demand of 1.249 GWh. The potential heat generation from the solar collectors is 353 GWh and it is therefore only about 80 % of the potential heat generation from the solar collectors which are generated.

The content of the heat storage is restricted in the model to begin and end the week at the same level. This means that even if the solar collectors generated the potential amount of heat and the heat storage were unlimited then heat could not be moved to another week. This indicates that the 9 m^2 of solar collectors could be too large compared with the demand. This is of course a weighing between costs and CO_2 reduction. It also indicates that the size of the storage meets the storage demand and perhaps exceeds it.

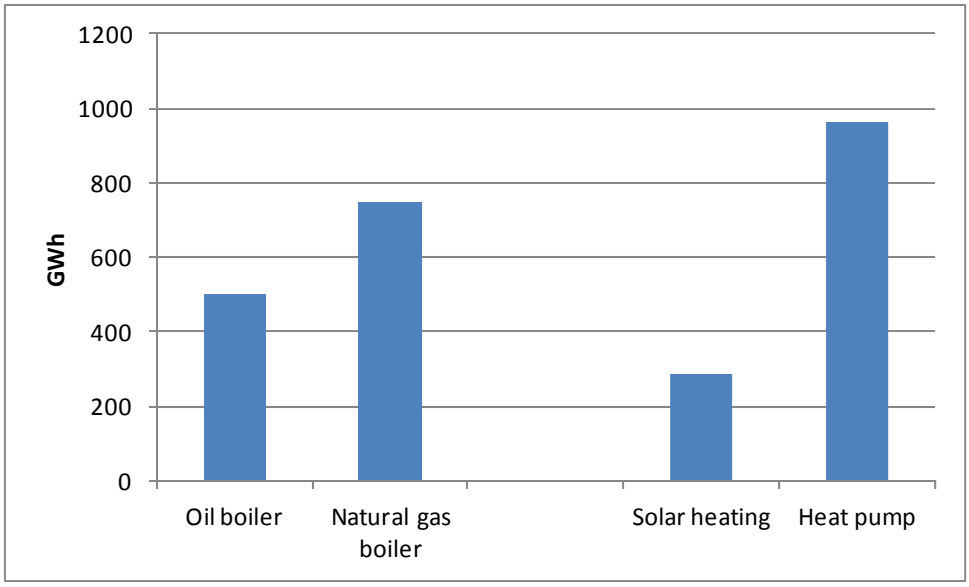

Figure 51. Heat production in areas with oil and natural gas boilers in the reference scenario (left hand side of the figure) and in the solar heating scenario with heat pumps (right hand side of the figure).

Figure 52 illustrates a summer week where the heat demand is covered entirely by the solar collectors - with support of the heat storage. The figure shows that the solar collectors generate heat during the daytime and that the generation exceeds the heat demand. The surplus heat generation from the solar collectors will therefore be loaded into the storage which then will cover the heat demand during the night.

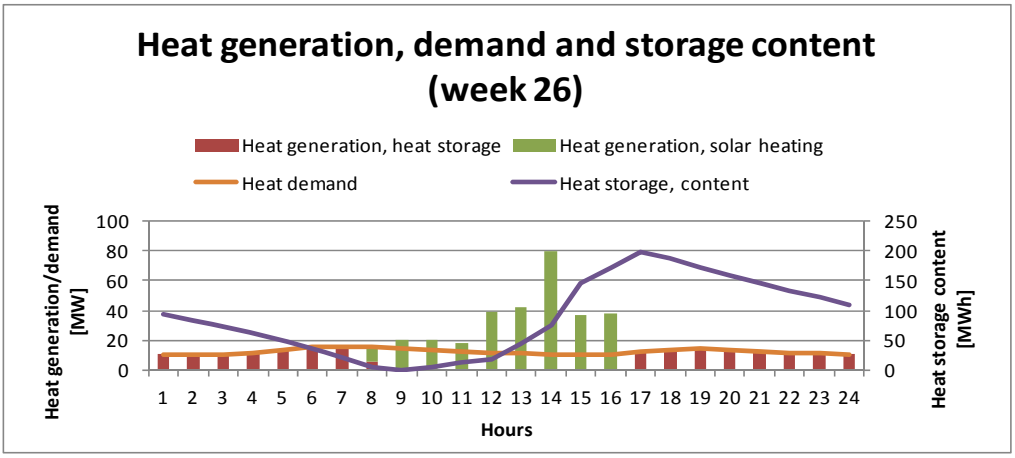

Figure 52. Heat generation (unload from the heat storage), heat demand and heat storage content in the natural gas area in Eastern Denmark (week 26, day 2).

Figure 53 illustrates a winter week with no heat generation from the solar collectors. The heat pumps cover all heat demand during the day. With use of the heat storage the heat pumps can be used only during night time when electricity price is low and surplus heat generation is loaded into the heat storage.

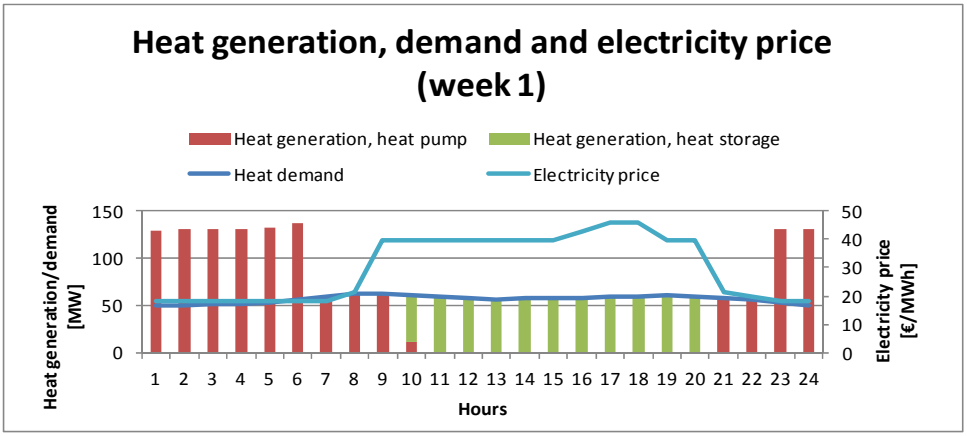

Figure 53. Heat generation (unload from the heat storage) and heat demand in the natural gas area in Eastern Denmark along with the electricity price in Eastern Denmark (week 1, day 3).

Figure 54 illustrates a spring week where both the heat pump and the solar collectors provides the heat. The figure shows the interaction between the heat pump, solar collectors and heat storage. The solar collectors generate heat during nine hours in the middle of the day. The heat demand not met by the solar collectors is supplied by heat from the heat pump stored in the heat storage. Without the heat storage the heat would have been supplied directly from the heat pump. Because of the heat storage the heat - not supplied by the solar collectors - is generated by the heat pumps during the night where the electricity price is low and then stored in the heat storage.

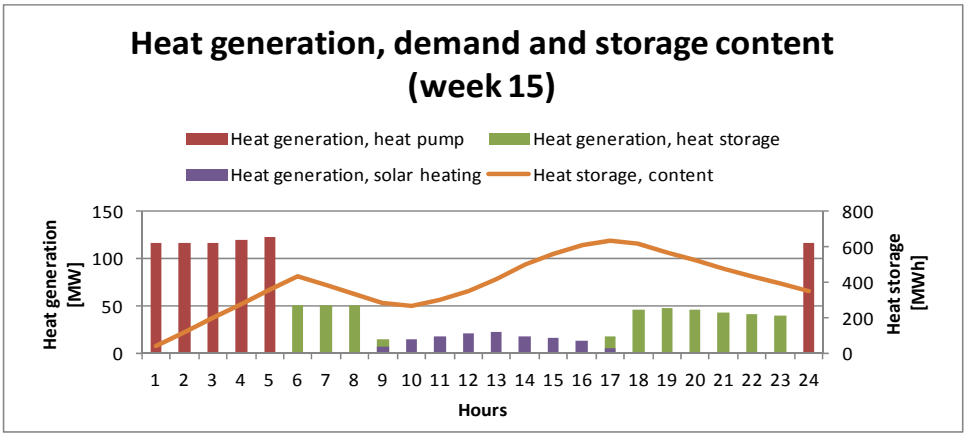

Figure 54. Heat generation (unload from heat storage) and heat storage content in the natural gas area in the Eastern Denmark (week 15, day 2).

The conversion from heat only boilers to electric heat pumps will increase the electricity generation. The change in electricity generation by fuels is shown in figure 55.

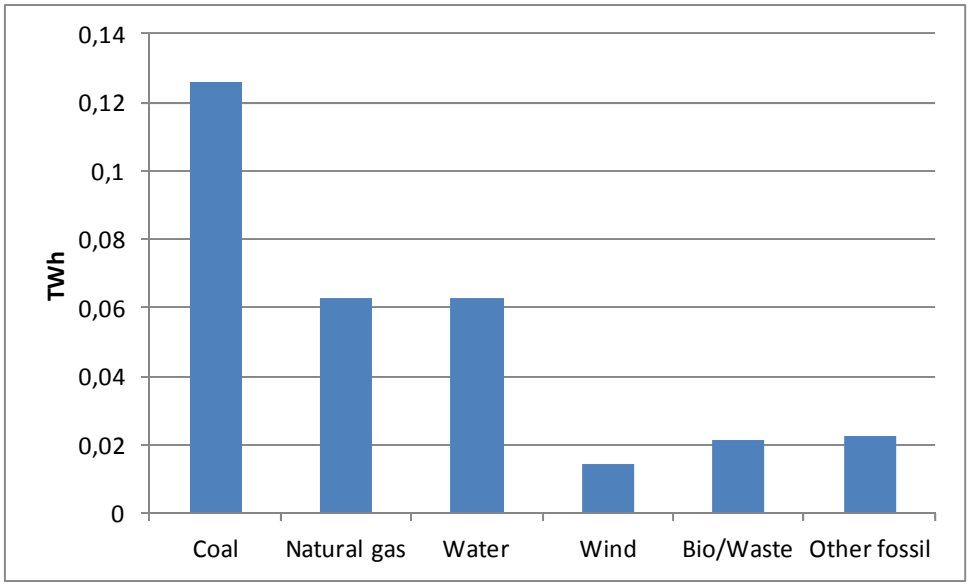

Figure 55. Change in electricity generation by fuels (positive equals increase).

The increase of the electricity generation leads to a large increase in the use of coal and natural gas which is expected. What is more interesting is that the combination of heat pumps and heat storage increases the electricity generation from both water and wind. In the reference scenario this electricity generation didn't occur because generation and demand did not match at the necessary time periods. What would actually happen in the reference scenario was that the hydro power plants without storage would let the water run without generating electricity and some of the wind turbines would be shut down. The increase in electricity generation from water and wind technologies is CO_2 free and almost cost free (no fuel costs).

The increased electricity generation leads to an increase in fuel consumption for electricity generation. But the electricity replaces a lot of oil and natural gas used for individual heating. Figure34 shows the change in total fuel consumption when replacing individual oil and natural gas heat only boilers with a combination of solar collectors, heat pumps and heat storages.

Figure 56 shows a total decrease of fuel consumption in the system. The decrease of fuel consumption is primarily a result of the high COP of the heat pumps and the fuel free heat generation from the solar collectors. In addition to this app. 25 % of the increase in electricity generation is supplied by water and wind technologies which consume no fuels.

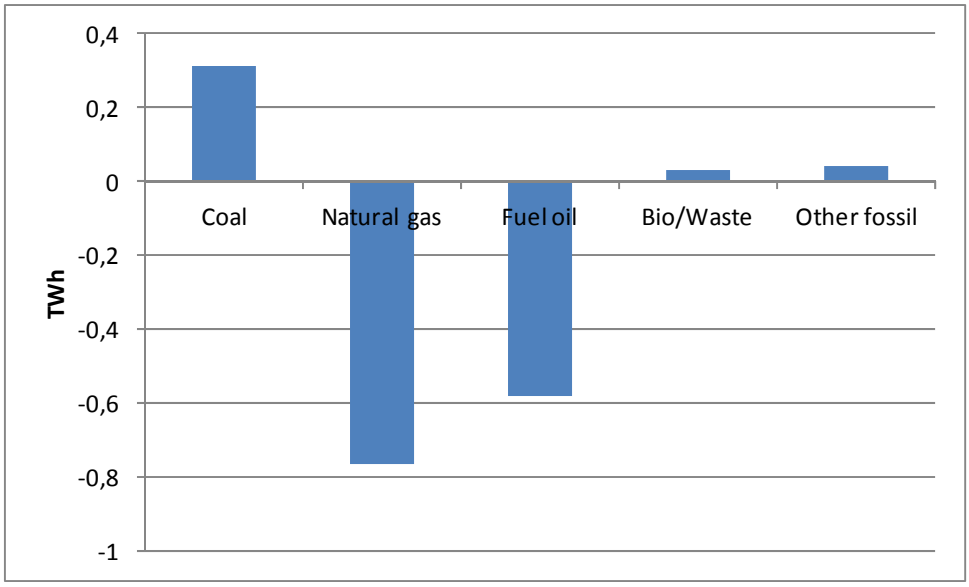

Figure 56. Change in fuel consumption for electricity and heat generation (positive equals increase).

The large decrease of fuels and especially of fossil fuels causes the CO_2 emission to decrease with 200,000 tons per year. The CO_2 emission in the reference and solar heating scenario along with the CO_2 reduction are listed in table 22.

CO_2-emission		
Reference scenario [kTon]	Solar heating scenario [kton]	Reduction [kTon]
364,447	364,247	200

Table 22. CO_2 emission and reduction.

S/E heating units (EH) replaces gas and oil boilers

This solar heating scenario is very similar to the previous described scenario. The only difference is that instead of heat pumps with a COP of 3.3 the solar collectors are backed up by electric heater with an efficiency of 100 %.

The interaction between the electric heater and heat storage is the same as with the heat pump and heat storage. The electric heating units will generate heat when the electricity price is low and the heat generation from the electric heaters in this scenario is the same as the heat generation in the solar heating scenario with heat pumps. The heat generation from the technologies in both the reference and the solar heating scenario with electric heating is illustrated in figure 57.

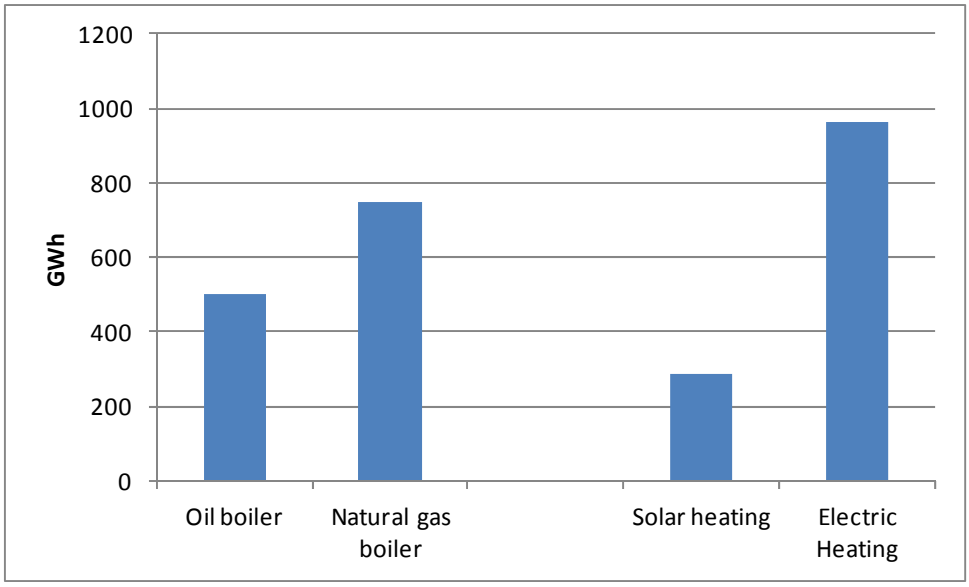

Figure 57. Heat production in areas with oil and natural gas boilers in the reference scenario (left hand side of the figure) and in the solar heating scenario with electric heaters (right hand side of the figure).

As with the heat pumps the electric heating units result in an increase of electricity generation. The increase is higher due to the lower performance of the electric heating units compared with the heat pumps. The fuel consumption increase allocated on fossil and fossil free fuels are app. the same in the two solar heating scenarios. The change in electricity generation by fuels is shown in figure 58.

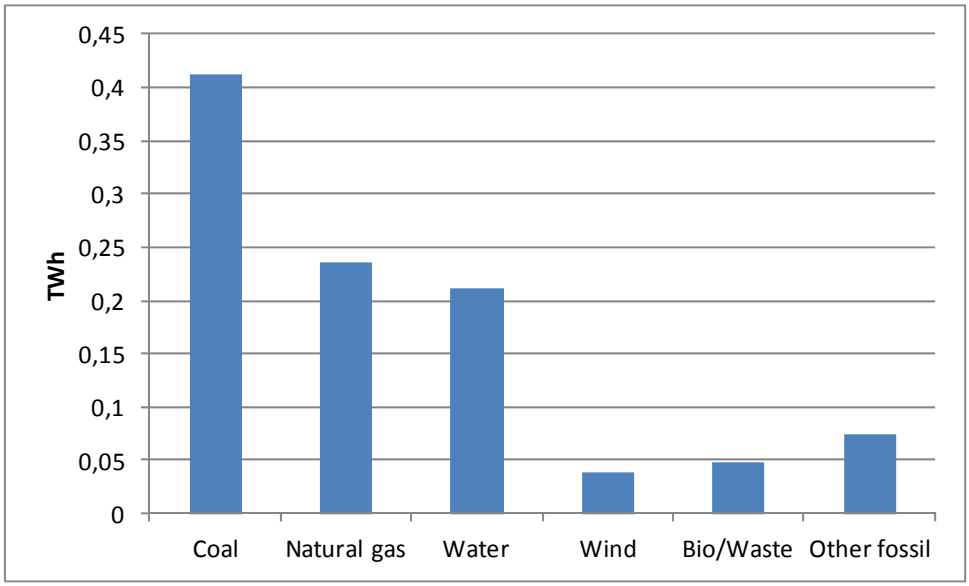

Figure 58. Change in electricity generation by fuels (positive equals increase).

Coal based condensing power plants are often the marginal electricity producer. The electricity efficiency of these types of plants is usually in the area of 35-40 %. Even though the electric heating units have an efficiency of 100 % the efficiency from fuel to generated heat will be 35-40 %. The oil and natural gas boilers had fuel efficiencies of 85 %.

The change in fuel consumption is shown in figure 59. The total fuel consumption increases when converting oil and natural gas boilers to the solar heating systems with electric heater.

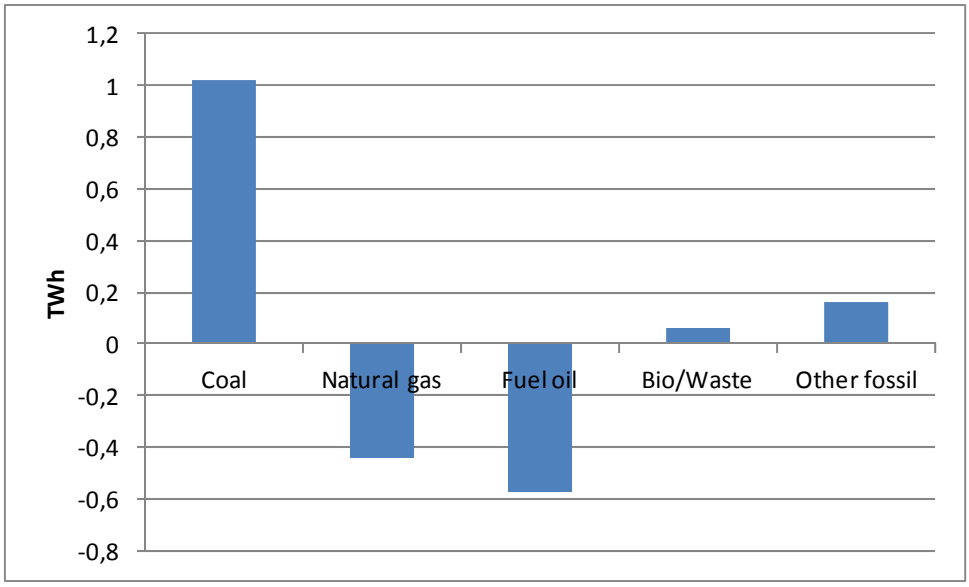

Figure 59. Change in fuel consumption for electricity and heat generation (positive equals increase).

The increase in fossil fuel consumption leads to an increase in CO_2 emission of 155,000 tons. CO_2 emission and reduction are listed in table 23.

CO_2-emission		
Reference scenario [kTon]	Solar heating scenario [kton]	Reduction [kTon]
364,447	364,601	-155

Table 23. CO_2 emission and reduction.

All scenarios

The economic benefit and the CO_2-reductions in all scenarios including the ones with lower heat demand are shown in the table 24. The economic benefit includes the benefit/costs of reduced/increased CO_2.

	Economic benefit (reduction in socio-economic costs)		Reduction in CO2 (which is also included in the economic benefit)	
	Million EUR/year	Euro per installation/year	1,000 ton/year	Ton per installation/year
S/E heating units (HP) replaces gas and oil boilers	64	814	200	2,5
S/E heating units (EH) replaces gas and oil boilers	33	426	-155	-2,0
S/E heating units (HP) replaces gas and oil boilers - lower heat demand	26	329	53	0,7
S/E heating units (EH) replaces gas and oil boilers - lower heat demand	23	292	17	0,2

Table 24. Socio-economic benefit and CO2-reduction by scenarios in 2020

It appears that all scenarios result in a socio-economic benefit compared with the reference scenario with oil and natural gas boilers. The economic results don't take into consideration the investment of neither the solar heating systems nor the oil and gas boilers. The fixed O&M costs are excluded as well.

The CO_2 emission is reduced in all scenarios besides the scenario with electric heating and regular heat demand. The reason is - as mentioned earlier - that the fuel-to-heat efficiency of electric heating units is often below the corresponding efficiency of the oil and gas boilers which increases the total fuel consumption. Besides this the fuel shifts from oil and gas to primarily coal.

The CO_2 emission is reduced in the scenario with electric heating and lower heat demand. In this scenario the solar collectors generates a bit more than 50 % of the yearly heat demand (127 GWh of a total heat demand of 250 GWh). The high CO_2 free heat generation from the solar collectors compensates for the higher fuel use from the electric heating units.

7.6 Summary and conclusions

As part of the project, a number of quantitative analyses have been carried out focusing on the economic benefit of solar heating systems with either electric heating units or heat pumps. This benefit has been estimated by use of the system modelling tool Balmorel, which simulates the electricity and heat generation in electricity and CHP systems.

During the summer where the heat generation from the solar collectors is highest the heat generation from the solar collectors exceeds the heat demand and not all solar heating potential is used. Larger heat storages aren't the solution except if these are seasonal storages.

The heat storage is used to store solar heating from the daytime to be used at night time and to store heat generated by electric heating units or heat pumps when electricity prices is low to periods when electricity prices are high.

Without the heat storages the solar heating generation would be significantly lower than the potential solar heating generation and the price of heat generated by the electric heating units/heat pumps would be higher. Both the reduced solar heating generation and the non-flexible heat generation from the electric heating units/heat pumps would result in a lower CO_2 reduction.

All scenarios result in a socio-economic benefit compared with the reference scenario with oil and gas boilers. The total benefit of 23-64 M€ or 292-813 €, corresponding to 2175 - 6057 DKK per installation per year should be compared to the extra annual costs of establishing the solar heating systems instead of re-establishing the current oil and gas boilers.

The use of electric heating units/heat pumps for heat generation leads to an increase in fuel consumption for electricity generation. When using electric heating units the fuel-to-heat efficiency is below the fuel-to heat efficiency for the oil and gas boilers. This means that the CO_2 emission increases for the part of the heat generated by these units. The heat from the solar collectors has the opposite influence.

In the scenario with electric heating units and regular heat demand the CO_2 reduction from the solar collectors is lower than the CO_2 increase because of the high fuel consumption for electricity for the electric heating units. This means that the total CO_2 emission increases. In the scenario with electric heating units and low heat demand the CO_2 emission decreases due to the relatively large heat generated by the solar collectors. Both scenarios with heat pumps cause the CO_2 emission to fall.

8. Evaluation of different energy unit designs

The yearly energy costs for space heating and domestic hot water supply for a typical house can be reduced by 50-70% by a solar/electric heating system with a collector area of 10 m² and a smart heat storage with a smart control system as long as the auxiliary/existing energy supply system is electric heating elements.

The experimentally investigated solar/electric heating systems based on one or more electric heating elements have almost the same operation costs for the consumer. The operation costs for the investigated solar/electric heating system based on a heat pump as auxiliary energy supply system is about half the operation costs for the solar/electric heating systems based on electric heating element(s).

The costs of a solar/electric heating system with a 10 m² solar collector, a 750 l smart heat storage and a smart control system is about 80,000 DKK, while the costs of the system with the investigated heat pump instead of electric heating element(s) is about 130,000 DKK.

Based on the system costs and the operation costs it seems that the system based on electric heating element(s) is most attractive for house owners with houses with low heat demands, while the system based on the heat pump is most attractive for house owners with houses with large heat demands.

Most likely heat pumps with the ground as heat source will be more attractive for houses with high heat demands than the investigated air/liquid heat pump.

9 Conclusions, recommendations and outlook

Starting from a normal house a solar combi system (for hot water and house heating) can save 20-30% energy cost, alone, depending on sizing of collector area and storage volume.

By replacing the heat storage with a smart tank based on electric heating elements and a smart control based on weather/load forecast and electricity price information 24 hours ahead, another 30-40% can be saved.

That is: A solar heating system with a solar collector area of about 10 m², a smart tank based on electric heating element and a smart control system, can reduce the energy costs of the house by at least 50%.

No increase of heat storage volume is needed to utilize the smart control.

The savings in % are similar for different levels of building insulation.

As expected a heat pump in the system can further reduce the auxiliary electricity cost by 50% of the remaining auxiliary use (COP = 2) but the investment cost for the system will increase significantly. Systems based on electric heating elements are most suitable for houses with a low heat demand, while systems based on a heat pump are most attractive for houses with a high heat demand.

The socio economic benefit for the national energy system is in the range 2175 - 6057 DKK per year for a system.

A non adaptive control system based on weather forecasts, prognoses for electricity prices and simple prognoses for solar heat production of solar collectors and heat demand for a house has been tested in real life in a laboratory test facility for three different solar heating system designs: Two systems were based on electric heating elements and one system was based a heat pump.

More advanced adaptive models for control based on forecasts have been developed by DTU Informatics. Solar contribution from collectors, heat demand of a house and electricity price and weather is treated to improve the efficiency and comfort of this concept in a real system with as little input as possible. Also double check of the forecast results is built in. It is expected that such an advanced control system will further decrease the energy costs somewhat for the consumer.

Comfort is very important for the normal final user. Therefore the control system should be prepared to add energy according to user needs, independently of auxiliary cost for the individual hour. Sometimes the forecast control can fail due to special weather conditions or price situations and too little energy would be available for space heating and hot water. Adaptive control is also a big advantage in this respect as the use behavior can change with time too.

The project has created an excellent basis for development of optimized solar/electric heating systems for the future energy system. Development of a product is the next step. A complete system concept including solar collectors, a smart heat storage, electric heating element(s) or a heat pump and a smart adaptive forecast control is desirable to avoid installation mistakes. Optimization is needed in order to find the most suitable collector area and tank volume for houses with different heat demands.

Full adaptive control should be implemented in the system, to automatically adjust to the building, weather, location and persons living in the house.

Use of the building thermal capacity could be used in the future, in addition to the storage tank capacity.

It is recommended to develop a system which is suitable for a house with a low and for a house with a high heat demand, to test the concepts in the laboratory and to demonstrate the suitability of the systems in practice.

In general, it is recommended to investigate if smart tanks and/or smart controllers are attractive for normal solar heating systems.

Finally, it should be mentioned that cooling is a coming comfort need in modern houses and that cooling can be supplied from a solar heating/heat pump system based on a ground source heat exchanger.

References

[1] P. Bacher, H. Madsen, and H. A. Nielsen. Online short-term solar power forecasting. Solar Energy, 83(10):1772–1783, 2009. ISSN 0038092x.
[2] P. Bacher and H. Madsen. Identifying suitable models for the heat dynamics of buildings. Energy & Buildings, 43(7):1511–1522, 2011. ISSN 03787788. doi: 10.1016/j.enbuild.2011.02.005.
[3] P. Bacher, H. Madsen, H. A. Nielsen, and B. Perers. Short-term heat load forecasting for single family houses. Submitted to Buildings and Energy, April 2012b.
[4] P. Bacher, H. Madsen, B. Perers, and H. A. Nielsen. A non-parametric method for correction of global radiation observations. Solar Energy, 88:13–22, 2013. ISSN 0038092x. doi: 10.1016/j.solener.2012.10.024.
[5] P. Bacher, H. Madsen, and H. Nielsen. Models for efficient integration of solar energy. IMM-PhD-2012. Technical University of Denmark, 2012a.
[6] P. Bacher, H. Madsen, and B. Perers. Short-term solar collector power forecasting. In Proceedings of ISES Solar World Conference 2011, 2011b.
[7] P. Bacher, H. Madsen, and B. Perers. Models of the heat dynamics of solar collectors for performance testing. In Proceedings of ISES Solar World Conference 2011, 2011c.
[8] P. Bacher and B. Perers. Opensource software for mlr-modelling of solar collectors. In Proceedings of ISES Solar World Conference 2011, 2011.
[9] P. Bacher, H. Madsen, and H. A. Nielsen. Online short-term solar power forecasting. In 1st International Workshop on the Integration of Solar Power into Power Systems, 2011a.
[10] W. Kong, Z. Wang, J. Fan, P. Bacher, B. Perers, Z. Chen, and S. Furbo. An improved dynamic test method for solar collectors. Solar Energy, 86(6):1838–1848, 2012. ISSN 0038092x. doi: 10.1016/j.solener.2012.03.002.
[11] C. Lodi, P. Bacher, J. Cipriano, and H. Madsen. Modelling the heat dynamics of a monitored test reference environment for building integrated photovoltaic systems using stochastic differential equations. Energy & Buildings, 50:273–281, 2012. ISSN 03787788. doi: 10.1016/j.enbuild.2012.03.046.
[12] H. A. Nielsen, S. B. Mortensen, P. Bacher, and H. Madsen. Analysis of energy consumption in single family houses. In DYNASTEE, 11-12 October 2010, Brussels, 2010.
[13] P. A. d. Saint-Aubain, P. Bacher, H. A. Nielsen, and H. Madsen. Methods for splitting readings of total energy consumption. iPower report - Work Package 1, DTU Informatics, 2012.
[14] R. Halvgaard, P. Bacher, B. Perers, E. Andersen, S. Furbo, J. B. Jørgensen, N. K. Poulsen, and H. Madsen. Model predictive control for a smart solar tank based on weather and consumption forecasts. Energy Procedia, 30:270–278, 2012a. ISSN18766102. doi: 10.1016/j.egypro.2012.11.032.
[15] R. Halvgaard, N. K. Poulsen, H. Madsen, and J. B. Jørgensen. Economic Model Predictive Control for Building Climate Control in a Smart Grid. In 2012 IEEE PES Innovative Smart Grid Technologies (ISGT), volume 9781457721588, page2012ISGT0195. IEEE, 2012b.
[16] T. Jonsson, P. Pinson, H. A. Nielsen, H. Madsen, and T. Nielsen. Forecasting electricity spot prices accounting for wind power predictions. IEEE Transactions on Sustainable Energy, Submitted: 2012.
[17] DMI. Danish Meteorological Institute, DMI-HIRLAM-S05, 2011. URL http://www.

dmi.dk/eng/index/research_and_development/dmi-hirlam-2009.htm.
[18] N. R. Kristensen, H. Madsen, and S. B. Jørgensen. Parameter estimation in stochastic grey-box models. Automatica, 40(2):225 – 237, 2004. ISSN 0005-1098. doi: DOI:10.1016/j.automatica.2003.10.001.
[19] S. Fischer,W. Heidemann, H.Müller-Steinhagen, B. Perers, P. Bergquist, and B. Hellström. Collector test method under quasi-dynamic conditions according to the european standard en 12975-2. Solar Energy, 76(1-3):117–123, 2004. ISSN 0038092x.doi:10.1016/j.solener.2003.07.021.
[20] B. Perers. An improved dynamic solar collector test method for determination of non-linear optical and thermal characteristics with multiple regression. Solar Energy, 59(4-6):163–178, 1997. ISSN 0038092x.
[21] J. Fan, Z. Chen, S. Furbo, B. Perers, and B. Karlsson. Efficiency and lifetime of solar collectors for solar heating plants. Proceedings of the ISES Solar World Congress

[22] S.C. Lundholm. Verification of Global Radiation Forecasts from the Ensemble Prediction System at DMI. Ph.D. Thesis, Københavns Universitet, 2013.

[23] K.P. Nielsen. Verification cloud physical properties. Poster-presentation, 4th WMO International verification methods workshop, Helsinki, Finland, 2009.

[24] K.P. Nielsen. Verification of HIRLAM cloud forecasts with MSG cloud physical products. Hirlam Newsletter, 2010; 55B: 11-17.

[25] K.P. Nielsen. Testing cloud parametrizations in NWP models against satellite data. Hirlam Newsletter, 2011; 58: 65-70.

[26] K.P. Nielsen, B.H. Sass. Computationally efficient tilted independent column calculations of surface radiation. Hirlam Newsletter, 2011; 58: 94-97.

[27] Fluent Inc., 2006. “Fluent release 6.3”, 10 Cavendish Court, Lebanon, NH 03766-1442 USA.

[28] B. Perers, S.Furbo, E. Anderssen, J.Fan . Solar/electric heating system for the future energy system. ISES Solar World 2009 Congress Proceedings. Johannesburg, South Africa 2009.
[29] B. Perers, S. Furbo, E. Andersen, J. Fan. Solar/electric heating systems using smart solar tanks and variable electricity costs . Eurosun 2010 Conference Proceedings. Graz, Austria 2010.

[30] R. Heimrath, M. Haller. The Reference Heating System, the Template Solar System. Project Report A2 of Subtask A, IEA SHC Task 32 (2007).

[31] L. Skalík, O. Lulkovičová, S. Furbo, B. Perers B, J. Dragsted, K.P. Nielsen, M. Scharling M, T. Carlund. *Evaluation of long-term global radiation measurements in Denmark and Sweden*. European Solar Energy Conference, EuroSun 2012 Proceedings, Rijeka, Croatia (2012).

Appendix

Simon Furbo, Elsa Andersen, Udvikling af fremtidssikret solvarmeanlæg, HVAC Magasinet, 2009, 3, 40-43

Udvikling af fremtidssikret solvarmeanlæg

I perioden 2008-2011 gennemføres forskningsprojektet "Solar/electric heating systems in the future energy system" i et samarbejde mellem DTU Byg, DTU Informatik, DMI, ENFOR A/S, AllSun A/S og COWI A/S. Interesserede beholder- og tekstilfabrikanter inviteres til at deltage som samarbejdspartner i projektet, der beskrives nærmere i denne artikel

Af Simon Furbo og Elsa Andersen, DTU Byg

Forskningsprojektet er finansieret af Forsknings- og Innovationsstyrelsen under Det Strategiske Forskningsråds program for Energi og Miljø. Projektets formål er at klarlægge, hvordan en individuel varmeforsyningsenhed til enfamiliehuse baseret på solvarme, elpatron/varmepumpe samt et avanceret varmelager og styresystem bedst udformes til fremtidens energisystem. Desuden skal det klarlægges, hvor velegnet sådan en varmeforsyningsenhed er for den enkelte forbruger og for vores fremtidige energisystem.
Varmen produceres dels af solfangere, dels af en elpatron/varmepumpe. Elpatronen/varmepumpen skal så vidt muligt kun køre på tidspunkter, hvor solvarme ikke kan klare hele varmebehovet, og hvor elprisen er lav, for eksempel på grund af stor elproduktion fra vindmøller og/eller på særlige tidspunkter af døgnet.
Enheden forsynes med et intelligent varmelager og et intelligent styresystem, hvor styringen af elpatronen/varmepumpen baseres på prognoser for elpris, varmebehov og solvarmeproduktion. Styresystemet baseres på vejrudsigter.
Varmeforsyningsenheden forventes at være et mere attraktivt solvarmeanlæg end traditionelle solvarmeanlæg, og anlægstypen skal bidrage til en forbedret udnyttelse af elproduktionen fra vindmøller i vindrige perioder. Bliver anlægstypen udbredt, kan den bidrage til at lette indpasningen/rentabiliteten af vindmøller i elsystemet og forøge andelen af landets energiforbrug, der dækkes af vedvarende energi.

Fem hovedelementer

Forskningsprojektet består af fem hovedelementer:

1) Solvarmeanlæg baseret på et intelligent varmelager.
   Der gennemføres detaljerede undersøgelser af forskellige udformninger af solvarmeanlægget. Specielt fokuseres undersøgelserne på det intelligente varmelager. Undersøgelserne gennemføres på DTU Byg, forhåbentlig i samarbejde med beholder- og tekstilfabrikanter.
2) Modeller for detaljerede vejrudsigter.
   Varmeforsyningsenheden planlægges styret af et avanceret styresystem, der baseres på forventet varmebehov, solvarmeproduktion og elpris. Derfor er der behov for pålidelige vejrudsigter. Forskellige modeller for detaljerede vejrudsigter undersøges. Der lægges vægt på, hvor nøjagtigt modellerne kan forudsige huses varmebehov og solvarmeanlægs varmeproduktion. Undersøgelserne gennemføres ved DMI, størstedelen i form af et ph.d.-studium.
3) Prognoser for huses varmebehov og for elpris,
   Der udvikles statistiske modeller til at forudsige huses varmebehov, elpriser og solvarmeproduktion. Modellerne benytter sig af input fra vejrudsigterne, som omtalt oven for. Undersøgelserne gennemføres i et samarbejde mellem DTU Informatik og ENFOR A/S, hovedsageligt i form af et ph.d.-studium ved DTU Informatik.
4) Avanceret styresystem baseret på forventet varmebehov, solvarmeproduktion og elpris.
   Det klarlægges, hvordan et styresystem udformes, så det kan benytte DMI's vejrudsigter og DTU Informatik/ENFOR's prognoser for elpriser, solvarmeproduktion og huses varmebehov til at styre elvarmelegemer og solvarmeanlæg bedst muligt. Undersøgelserne gennemføres af AllSun A/S.
5) Analyse af hele energisystemet
   Det undersøges hvordan varmeforsyningsenheden, hvis den benyttes i stort omfang, påvirker energisystemet. Undersøgelserne gennemføres af COWI A/S.

Udvikling af det intelligent varmelager

Varmeforsyningsenhedens vigtigste komponenter er det avancerede styresystem og det intelligente varmelager. Som nævnt skal AllSun A/S klarlægge hvordan styresystemet bedst udformes. Det forventes derfor, at AllSun A/S efter afslutningen af projektet kan færdigudvikle og markedsføre styresystemet.
Undersøgelserne af det intelligente varmelager gennemføres på DTU Byg. Intelligente varmelagre udformes anderledes end de varmelagre, som markedsføres i dag.

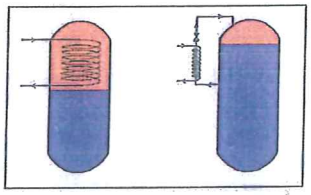

Figur 1. Principskitse af standard (venstre) og intelligent (højre) varmtvandsbeholder. Den nederste del af beholderne opvarmes af solfangerne, den øverste del af en supplerende energikilde.

Figur 1 viser en principskitse af en markedsført standard varmtvandsbeholder (til venstre) og af en intelligent varmtvandsbeholder (til højre) til solvarmeanlæg til brugsvandsopvarmning.
I standard varmtvandsbeholderen holder en supplerende energikilde et konstant volumen i toppen af beholderen opvarmet til en høj temperatur igennem alle årets timer. I den intelligente varmtvandsbeholder kan det vandvolumen, som den supplerende energikilde opvarmer i toppen af beholderen varieres så det tilpasses til det forventede varmtvandsbehov. I perioder med forventet højt varmtvandsbehov er volumenet stort, i perioder med forventet lavt varmtvandsbehov er volumenet lille.
Ydelsen af solvarmeanlæg til brugsvandsopvarmning med intelligente varmtvandsbeholdere kan være op til 35% højere end ydelsen af solvarmeanlæg

med traditionelle varmtvandsbeholdere (1). Det skyldes dels et reduceret varmetab fra varmtvandsbeholderen, dels en øget solfangerydelse forårsaget af et lavere temperaturniveau i solfangerne.

Intelligente varmelagre til sol-/elvarmeanlæg til enfamiliehuse kan, ligesom varmelagre for markedsførte solvarmeanlæg, udformes på mange forskellige måder. Jo større temperaturlagdeling, der opbygges i varmelageret under driften, des højere er solvarmeanlæggets ydelse. Figur 2 viser principskitser af hvordan den øverste del af et intelligent varmelager kan opvarmes af elpatroner.

Der kan benyttes indbyggede elpatroner i forskellige niveauer i beholderen, så en større eller mindre del af toppen af beholderen kan elopvarmes.

Der kan benyttes en elpatron indbygget i en rørkreds, der er koblet til beholderens øverste del på en sådan måde at varme overføres fra elpatronen til toppen af beholderen ved selvcirkulation i rørkredsen/varmelageret i perioder med elpatrondrift. Opvarmningen kan stoppes, så det elopvarmede volumen tilpasses det forventede varmebehov. Der kan benyttes en elpatron, som er indbygget i to eller flere rørkredse på en sådan måde at varme ved selvcirkulation i en rørkreds overføres fra elpatronen til toppen af beholderen, så et ønsket vandvolumen opvarmes til en ønsket temperatur med mindst muligt energiforbrug.

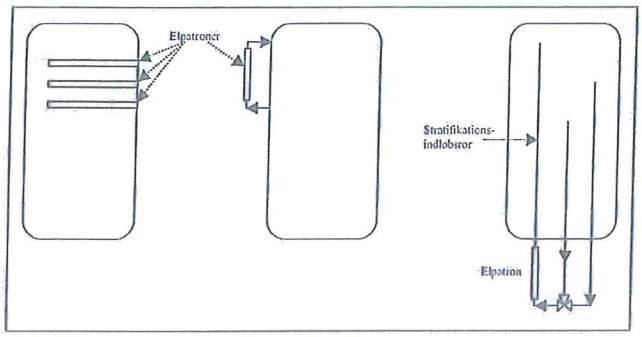

Figur 2. Principskitser af elopvarmning af øverste del af et intelligent varmelager. Elpatroner i forskellige niveauer (venstre). Elpatron i rørkreds med selvcirkulation (midt). Elpatron i rørkredse med selvcirkulation (højre). Styresystemet er baseret på vejrudsigt samt prognoser for varmebehov, elpris og solvarmeproduktion.

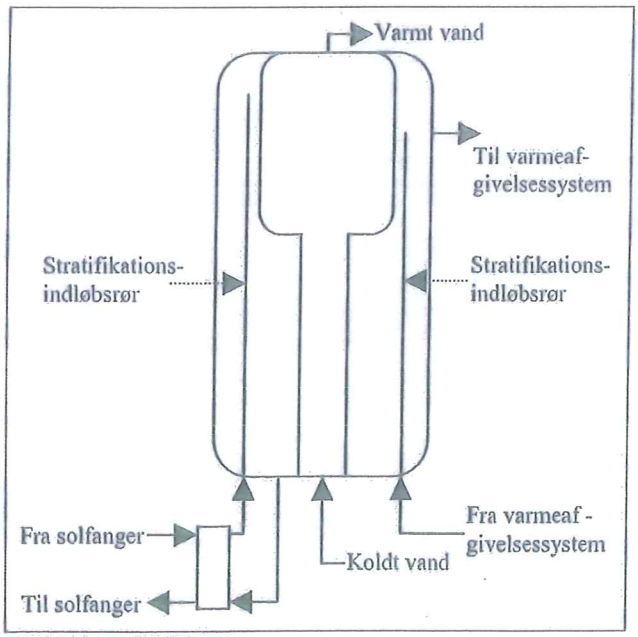

Figur 3. Principskitse af varmelager uden intelligent elopvarmning af øverste del.

Udvikling af fremtids...
Fortsat

Udformning af varmelageret

Det intelligente varmelager, som også kan opvarmes af solfangere, forsyner huset med varmt brugsvand og rumvarme. Eksempelvis kan varmelageret udformes som vist skematisk på figur 3.
Varmelageret er et tank-i-tank-varmelager med en indbygget varmtvandsbeholder til brugsvandsopvarmning.
Solvarmen overføres til varmelageret ved hjælp af en ekstern varmeveksler og cirkulation – enten ved selvcirkulation eller med en cirkulationspumpe – af vand fra bunden af varmelageret gennem den eksterne varmeveksler og retur til varmelageret gennem et stratifikationsindløbsrør. Varme overføres fra den øverste del af varmelageret

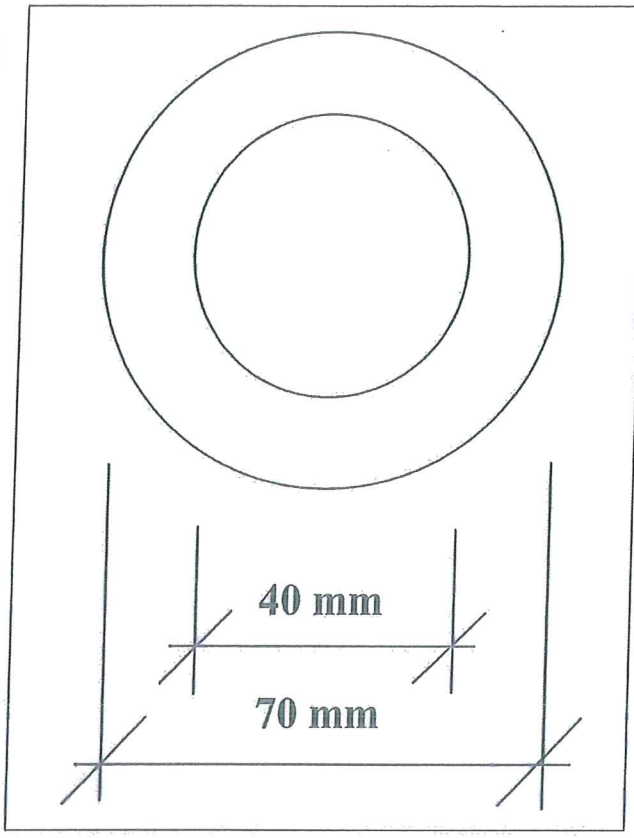

Figur 4. Stofindløbsrør i varmelager.

til varmeafgivelsessystemet og retur til varmelageret gennem et stratifikationsindløbsrør. Stratifikationsindløbsrørene, der indbygges i varmelageret, kan være de på DTU Byg nyudviklede stofindløbsrør. Disse rør kan opbygge en stor fordelagtig temperaturlagdeling i varmelageret. Det skyldes at vandet, som tilføres varmelageret gennem stofrørene løber ud i varmelageret i det niveau, hvor temperaturen er lig med temperaturen af det indkommende vand.
Undersøgelser har vist, at stofindløbsrør fungerer lige så godt som de bedste plaststratifikationsindløbsrør, der markedsføres af europæiske solfangerfabrikanter (2).
Figur 4 viser et stofindløbsrør bestående af to lag stof med diametre på 40 mm og 70 mm.

Stofindløbsrøret installeres lodret i varmelageret fra bunden til toppen af varmelageret. Vandet tilføres varmelageret gennem stofindløbsrørets tilslutning i bunden af varmelageret.
Stofindløbsrørets virkemåde er baseret på, at stofrøret kan trække sig sammen i de niveauer af varmelageret, hvor der er større statisk tryk uden for stofrøret end inde i stofrøret. Det er tilfældet i de niveauer af varmelageret, hvor vandet i stofrøret er varmere end vandet i varmelageret, der omgiver stofrøret.

Invitation til samarbejde med beholder- og tekstilfabrikant

For at fremskynde tidspunktet hvor intelligente varmelagre med stofindløbsrør kan introduceres på markedet, inviteres der til samarbejde med små og mellemstore beholder- og tekstilfabrikanter.
Et samarbejde med beholder- og tekstilfabrikanter om intelligente varmelagre vil muliggøre, at der tages hensyn til produktions- og markedsføringsforhold ved udvælgelsen af de varmelagerudformninger, der udvikles i projektet.
Derudover vil fabrikanternes erfaringer med hensyn til holdbarhed af varmtvandsbeholdere og stoffer være værdifulde i forbindelse med udviklingsarbejdet.

Fordele for fabrikanterne

I dag markedsfører beholderfabrikanter standardbeholdere, der ofte kan produceres billigere af udenlandske fabrikanter. Hvis danske fabrikanter fremover skal have succes inden for solvarmeområdet, har de behov for at udvikle og tilbyde komponenter og anlæg med forbedret ydelse/pris i forhold til standardkomponenter og anlæg.
Grundlaget for udvikling af forbedrede produkter er detaljeret forskning inden for området.
Fabrikanter kan gennem samarbejdet udvikle intelligente varmelagre, der er velegnede til varmeforsyningsenheden, og som resulterer i stærkt forbedrede solvarmeanlæg.
De principper, der benyttes ved udformningen af det intelligente varmelager, kan desuden benyttes i forbindelse med varmelagre til en række forskellige anvendelsesområder. Beholderfabrikanter kan derfor udnytte erfaringerne fra samarbejdet i forbindelse med deres generelle udviklingsarbejde vedrørende varmelagre. Tekstilfabrikanter kan gennem samarbejdet realisere et helt nyt forretningsområde: Anvendelse af tekstiler i avancerede varmelagre.
Forskningsprojektet har mulighed for at finansiere 60% af omkostningerne for en beholder- og tekstilfabrikant i forbindelse med udviklingen af det intelligente varmelager.

Informationsmøde i marts

Der arrangeres mandag den 23. marts kl. 14:00 et informationsmøde for interesserede små/mellemstore beholderfabrikanter og onsdag den 25. marts kl. 14:00 et informationsmøde for interesserede små/mellemstore tekstilfabrikanter.
På møderne, der finder sted på DTU Byg, bygning 119, rum 107, Nordvej, DTU, 2800 Kgs. Lyngby, bliver der informeret om projektet samt samarbejdsmulighederne og -betingelserne.
Information om projektet og samarbejdsmulighederne fås/tilmeldelse til informationsmøderne sker ved henvendelse til: Simon Furbo, email: sf@byg.dtu.dk, tlf.: 45 25 18 57.

Referencer

1. Elsa Andersen, Simon Furbo, Søren Knudsen & Niels Kristian Vejen: Intelligente solvarmeanlæg. Udvikling og afprøvning. BYG.DTU, rapport R-005, 2001. Kan downloades fra http://www.byg.dtu.dk/Forskning/hentned.aspx.
2. Elsa Andersen: Solar Combi Systems, DTU Byg, Ph.D. rapport, rapport nr. R-156, 2007. Kan downloades fra http://www.byg.dtu.dk/Forskning/hentned.aspx.

Bengt Perers, Simon Furbo, Elsa Andersen, Jianhua Fan, Solar/electric heating system for the future energy system, ISES Solar World Congress 2009 proceedings, Johannesburg, South Africa

SOLAR/ELECTRIC HEATING SYSTEM FOR THE FUTURE ENERGY SYSTEM

B. Perers, S.Furbo, E. Anderssen, J.Fan

DTU Civil Engineering, Department of Civil Engineering, Technical University of Denmark, Brovej, Building 118 DK-28000 Kgs. Lyngby, Denmark; email: beper@byg.dtu.dk.

Abstract

Presently 20% of the electricity in Denmark is produced by wind power. It is expected that in the near future this share will be increased to 40%. This will require adapted use of electricity, to the availability and price of electricity in the grid. In the Nordic countries a common electricity stock exchange NORDPOOL exist that creates hourly electricity prices 24 hours ahead for all days of the year. By using this information and also weather forecasts, heat load and solar heat production predictions the price variations and a solar heating system based on a smart controller and a smart storage tank can be used to minimize the energy cost and utilize renewable energy sources in a better way in the future. The electricity can be used both in the form of direct electric heating of the tank or via a heat pump. A TRNSYS model has been further developed to simulate a single family house with a solar combi-system that uses an electric backup system controlled according to the weather and electricity prices. So far the control strategy and tank design is just at a first level. One first result is that even a normal solar heating system without smart control seems to benefit significantly from variable electricity prices compared to a fixed average price. This is mainly caused by the normal load pattern for heating that is largest during off peak hours. Smart control strategies and tank design will further reduce the energy cost for heating and hot water.

1. INTRODUCTION

The two most powerful renewable energy sources are solar and wind energy. It is expected that an increasing part of our electricity consumption in the future will be covered by wind farms. This will result in an increased number of windy periods with a surplus of electricity/low cost electricity. A concept where individual solar heating systems optimised for making use of electricity produced by wind turbines in these periods can facilitate the introduction of wind energy in large scale into the energy system and thereby contribute to increasing the part of our energy consumption covered by renewable energy sources.

The heat is produced by the solar heating system and by the electric heating element(s)/heat pump, which, if possible, only must be in operation in periods where the solar heating system cannot fully cover the heat demand and where the electricity cost is low, e.g. in windy periods with a high electricity production from wind turbines. The unit is equipped with a smart heat storage with a variable auxiliary volume fitted to the expected future heat demand and a smart control system based on prognosis for the electricity price, the heat demand of the house, the solar heat production of the solar heating system and weather forecasts for the next 48 hours.

An ongoing Danish project will elucidate how best to design an individual heating unit for one family houses based on the above mentioned principles. It will also be elucidated how suitable the heating unit is for the home owner and for our future energy system. Different designs of the heating unit and the control system will be investigated and the most promising solutions will be tested experimentally. It is expected that the heating unit is more cost efficient than traditional solar heating systems and that it can be an attractive alternative to oil- and natural gas boilers, both from an economy and environmental point of view.

The project is carried out in a cooperation between Department of Civil Engineering, Technical University of Denmark, Danish Meteorological Institute (DMI), DTU Informatics, Technical University of Denmark, ENFOR A/S, AllSun A/S, Ohmatex ApS and Ajva ApS and COWI A/S,.

At Department of Civil Engineering the above proposed solar heating system will be investigated by means of theoretical calculations and experimental studies.

At DMI simulation models suitable to predict the incoming solar radiation and outdoor temperature for all locations in Denmark will be developed.

At DTU Informatics and ENFOR A/S prognosis for electricity costs, for heat demand and solar heat production will be worked out.

At AllSun A/S an advanced smart controller for the solar heating system based on the above mentioned weather forecast and prognosis for electricity costs, heat demand and solar heat production will be developed.

At Ohmatex ApS durable fabric inlet stratifiers for advanced hot water stores with a high degree of thermal stratification will be developed.

At Ajva ApS smart hot water heat stores with a variable auxiliary volume at the top of the store and with fabric inlet stratifiers to secure a high degree of thermal stratification will be developed.

At COWI A/S the advantage for the energy system by implementing the concept in a large number of one family houses will be elucidated.

This paper describes preliminary results from the project.

The part of the project described in this paper is focused on system simulations of a house with a smart solar combi system and especially on how to design and control the charging of the auxiliary part of the tank.

An advanced TRNSYS solar combi system model from IEA SH&C Task 32 was used as a starting point for this work. Real weather data for Denmark and Nordpool electricity cost data was introduced in the model and also more detailed and flexible control possibilities for the auxiliary energy supply to the tank. The work is in progress and will continue the next two years, and preliminary results will be presented.

2. THE SIMULATION MODEL

The simulation model is based on the advanced TRNSYS deck created for IEA SH&C Task 32 for a single family combisystem. Figure 1 shows the principal system layout. The TRNSYS deck is described in the IEA Task 32 work (Heimrath and Haller 2007).

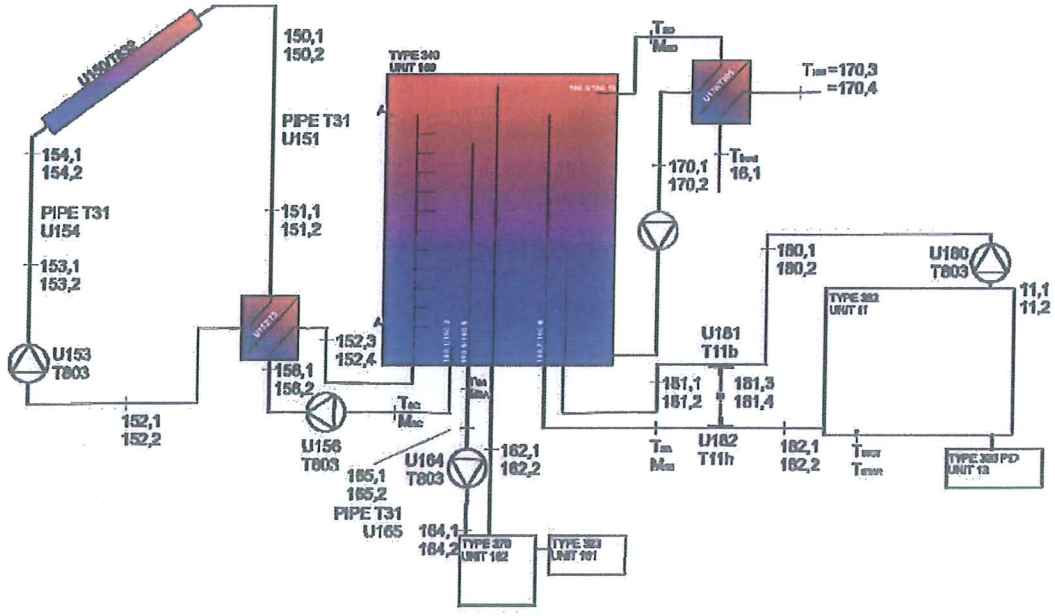

Figure 1. System layout with solar collectors, auxiliary heater, storage tank and hot water and heating loads in the house. The diagram is taken from (Heimrath and Haller 2007)

The complex system simulated has more than 100 parameters to describe, but the major system data are:

- Single family house. Old house 100 kWh/m² yearly heat demand
- Electric auxiliary with different control strategies.
- Solar Collectors 5-15 m², Tilt 45°, south oriented
- Storage 500-2500 l water tank, stratified
- Climate: 2008 weather data from climate station at Department of Civil Engineering, Technical University of Denmark.
- Electricity Prices: Nordpool 2008. Denmark-East (DK2).
- Consumer Electricity Prices assumed to follow Nordpool prices (variable or fixed average).
- Collector type: Standard Single Glassed Selective Flat Plate Collector.
  F'n0=0.8, F'UL1=3.5, F'UL2=0.015 , b0=0.18, Kdiff=0.9

3. NORDPOOL DATA

The electricity price is determined each day at the electric stock exchange NORDPOOL. Historical data some years back has been derived and transformed so that TRNSYS can read and use the data in the simulations. Especially in west Denmark with the highest fraction of wind power the prices vary very much during the day and the year. Figure 2 shows an example of the hourly price variation for one year. The high peaks often occur during the day and the low prices in the early morning. Figure 3 shows the daily average prices for tree years for Denmark West. It can be seen that the prices vary much from year to year too. There is also a day by day pattern that may be used with a larger storage in the solar combi system.

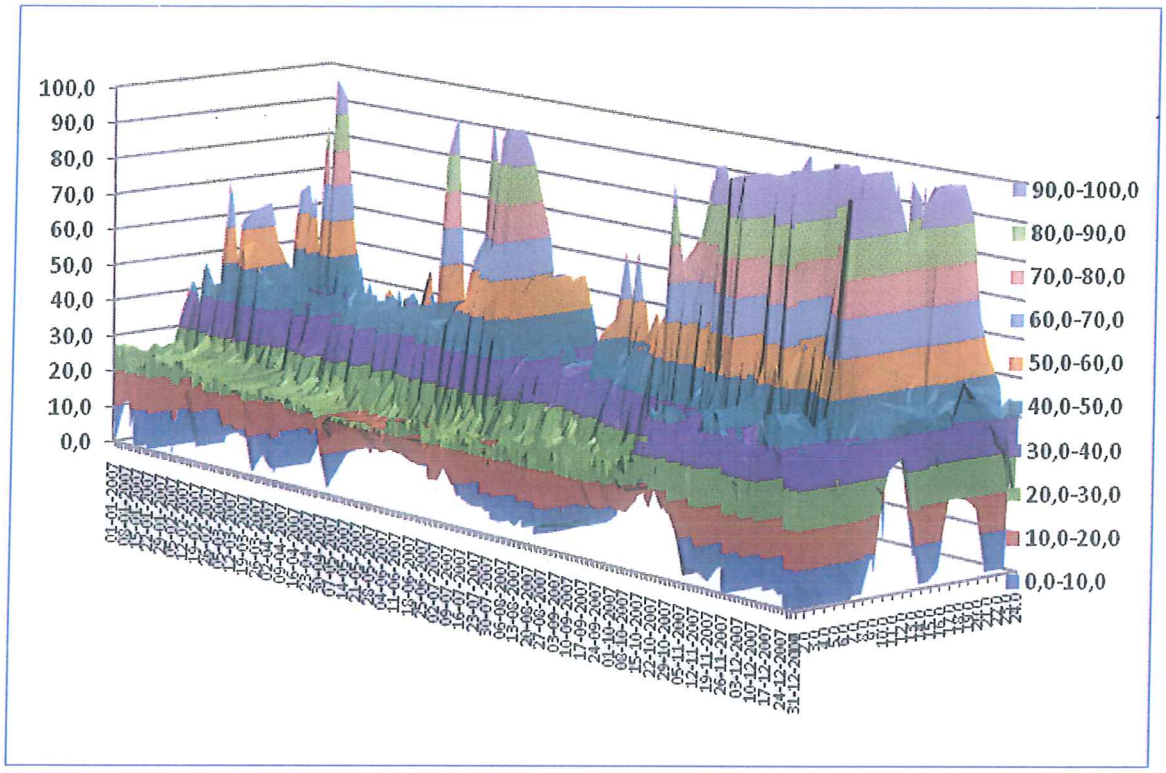

Figure 2. Example of the hourly electricity price variations during one year in western Denmark. Raw data from the NORDPOOL electric stock exchange. The unit on the y-axis is Euro/MWh at the production plant level in the system. Final customer prices are much higher.

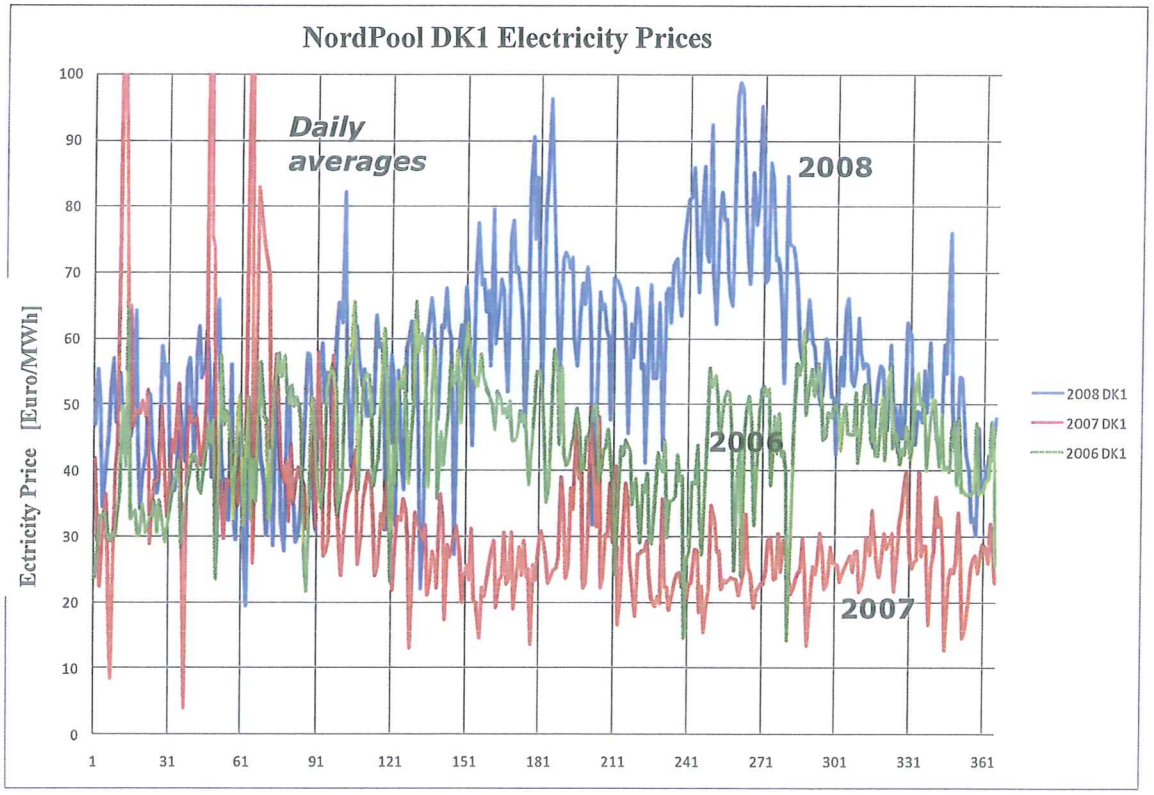

Figure 3. Example of the daily electricity price variations during one year in western Denmark. Raw data from the NORDPOOL electric stock exchange. The unit on the y-axis is Euro/MWh at the production plant level in the system. Final customer prices are much higher.

3. CLIMATE DATA

Climate data from the weather station at Department of Civil Engineering, Technical University of Denmark in Copenhagen has been used together with Nordpool electricity data for the same period (2008) and area (Denmark East) in the TRNSYS simulations. This gives a realistic situation in the simulations and also different control strategies can be evaluated with exactly known prognosis data if desired. Figure 4 gives an example of some of the weather variables that are used in the simulations.

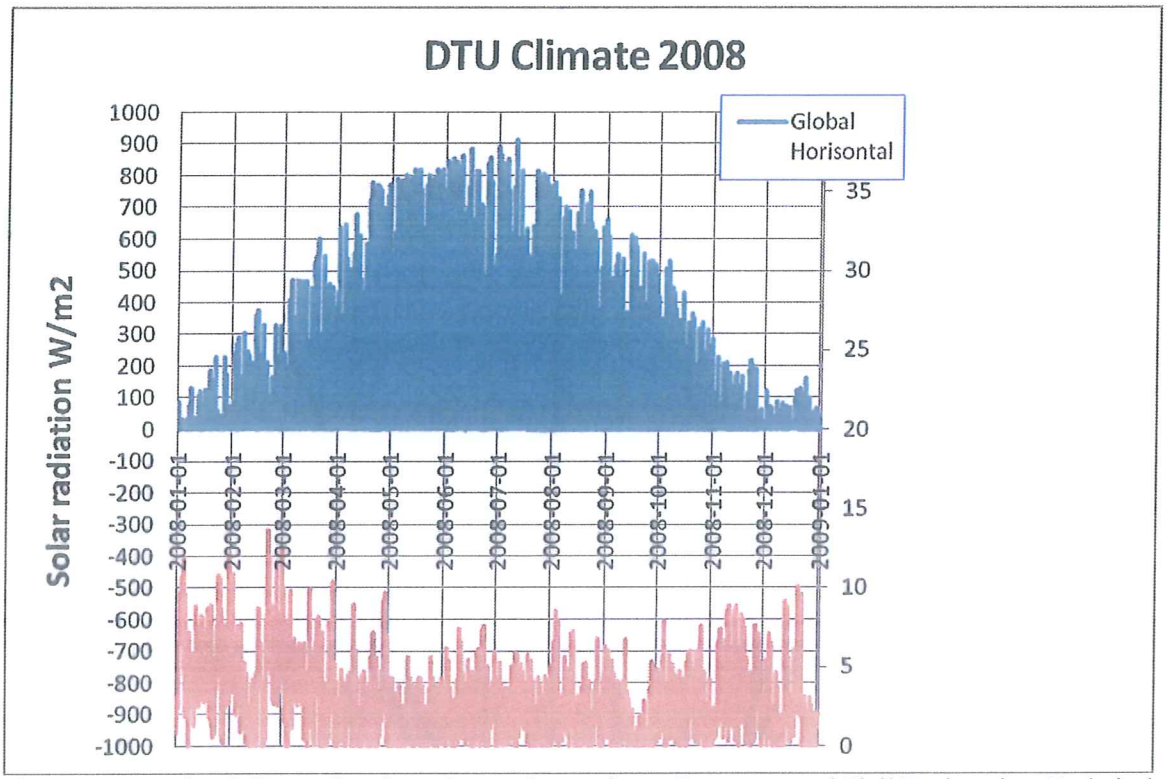

Figure 4. Example of climate data from the weather station at Department of Civil Engineering, Technical University of Denmark for 2008. The lower curve is wind speed with axis to the right.

It can be seen that the wind speed and solar radiation has a positive covariation with higher wind speeds in the winter, when the solar radiation is low. It should also be kept in mind that the wind power is proportional to the cube of the wind speed so the electricity production will match even better if short term mismatch can be evened out by for example hydropower in the regional grid.

3. SIMULATION RESULTS

So far the main work has been spent on adapting the TRNSYS system simulation model, towards this project's requirements for advanced control of the auxiliary, advanced tank design, and input from local weather and NORDPOOL prices. Also careful check of the extended system model has been done.

Figure 5 show monthly costs for bought auxiliary electricity to the house. The house is an old one with typically 100 kWh/m² heating demand per year in the Zürich climate. The backup heater is here a direct electric heater in the tank and no heat pump. No advanced prognosis control is applied here but only an

instantaneous price level check to avoid the highest prices when possible without significant comfort disadvantages. The reference case has only thermostat control of the auxiliary and a fixed electricity price on the yearly average price level. 10 m² collector area and 500 l tank is used in this case. The price is given at raw electricity cost level. By just applying a simple control strategy and variable electricity price the annual auxiliary cost can be reduced by almost 300 Euro.

The lowest curve in figure 6 shows an attempt to use a much larger tank, 2500 l but the economic advantage is surprisingly low. The reason for this is not fully understood and more advanced control and tank design may have a significant potential here. This will be investigated in the next steps in the project.

In this paper the hot water load is reduced to 100l/day that gives a lower solar saving, but this load level is common in Denmark.

The electricity price is at production level but at the final customer the prices are often the double. The future pricing and tax is hard to predict and the known production level at present is assumed. In the future system control the real customer price will be used.

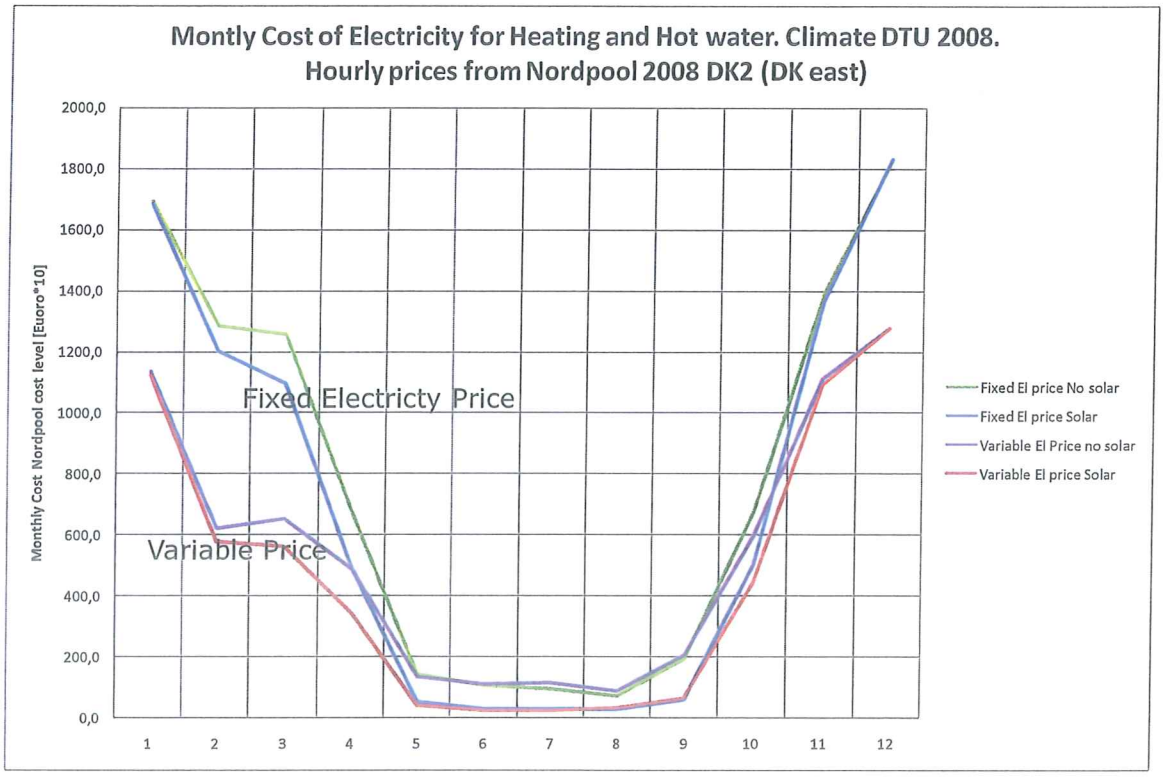

Figure 5. Monthly costs for bought auxiliary electricity to the house. The backup heater is here a direct electric heater in the tank and no heat pump. The reference case has only thermostat control of the auxiliary and a fixed electricity price on the yearly average price level. 10 m² collector and 500 l tank.

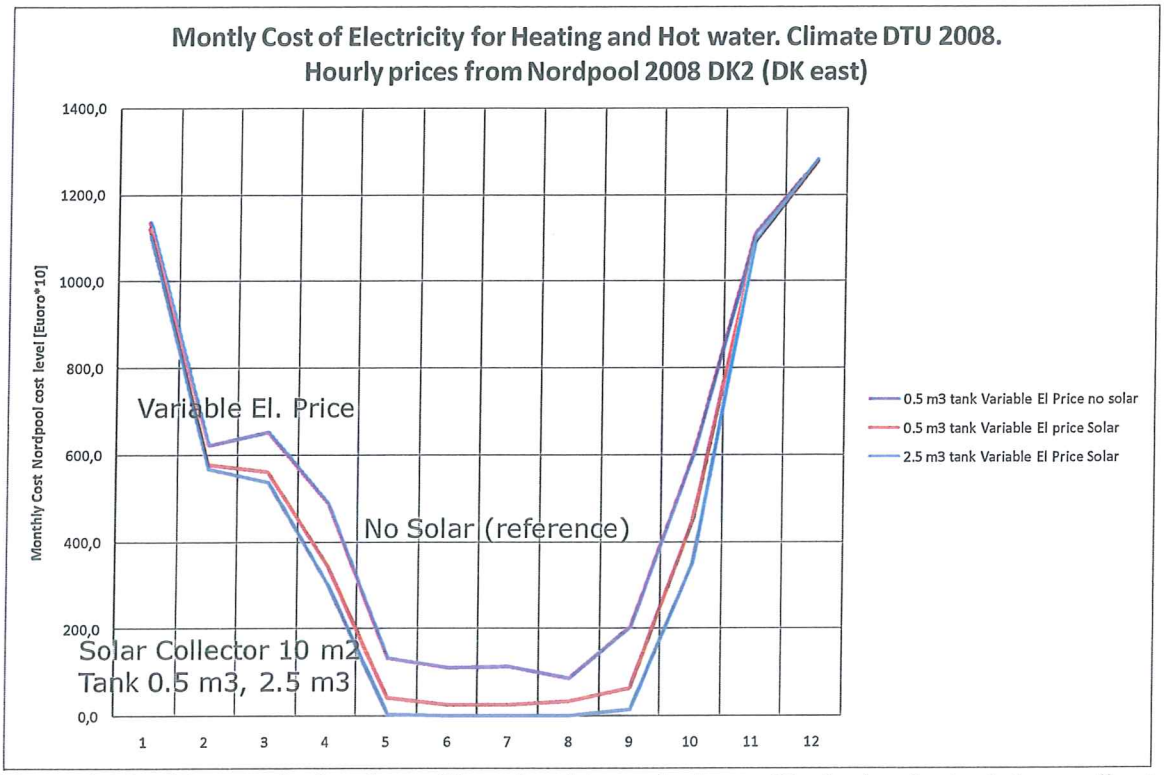

Figure 6. Monthly costs for bought auxiliary electricity to the house. The backup heater is here a direct electric heater in the tank and no heat pump. The reference case has no solar collectors. Variable electricity price is used in all three cases. Collector area: 10 m².

To have a first tank and collector size to start from in the parallel parts of the project the system simulations presented in figure 7 were made. It can be seen that a tank size of 500 l and collector area of 10 m² is reasonable for this load. This does not involve costs more than qualitatively, so later on better estimates of the sizing may be found including more factors.

To give an impression of the level of detail in the simulations figure 8 is presented. It shows the temperature stratification in the tank during charge and discharge for some days. This level is very important for checking the system simulation runs.

To show a more detailed picture of the variability of electricity prices and the timing with the solar radiation figure 9 shows 15 days during the summer half year. It can be seen that the match is very good for this period. The large variation during the day is also evident indicating that a smart solar combi system control could be very interesting, if the final customer will get credit for using auxiliary electricity during low cost hours. In the Danish electricity system with an increasing share of wind power, this means more use of wind power.

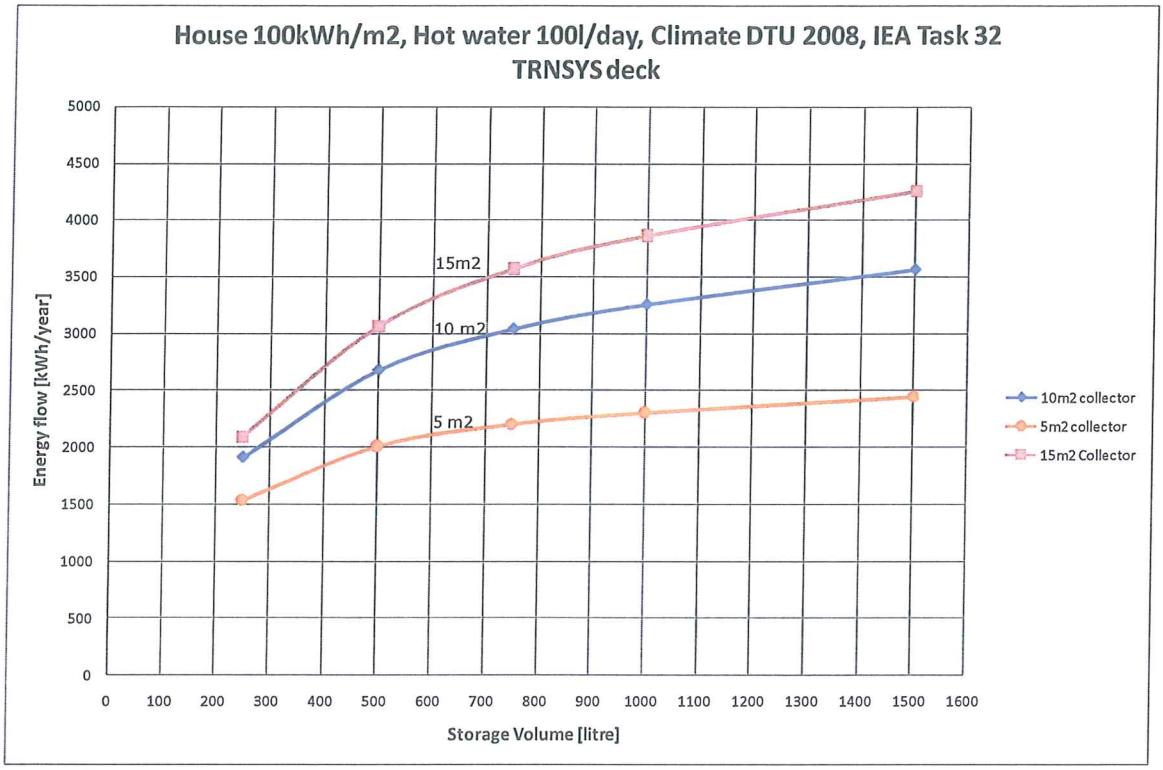

Figure 7. Optimization diagram for tank volume and collector area. A system sizing of 10 m² collector and 500 l storage was chosen as a first estimation of optimum size. Further considerations will probably change this choise somewhat later on.

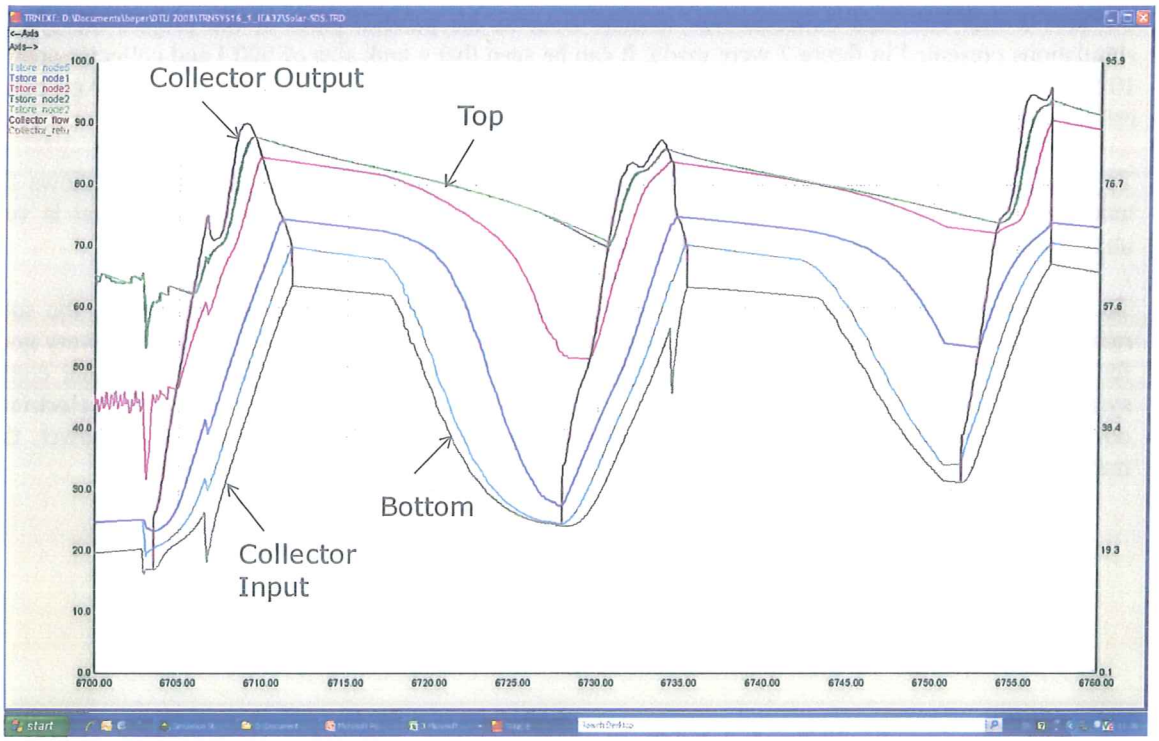

Figure 8. Example of stratification variations during a system simulation. These online plots from TRNSYS are very effective to check the system setup and operation.

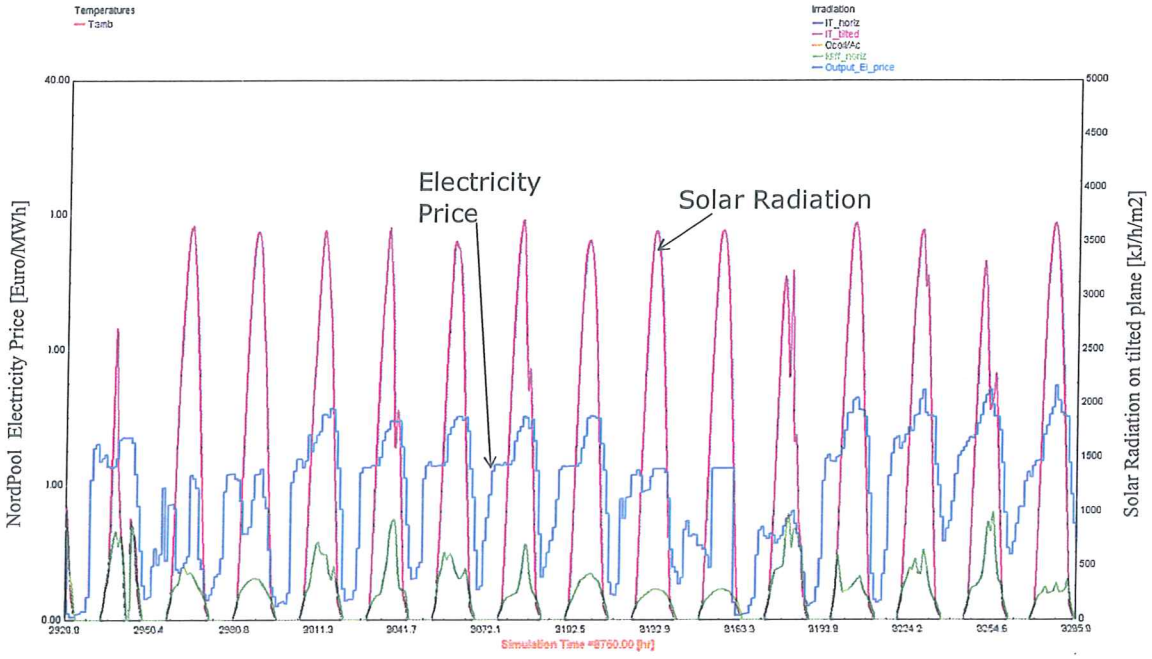

Figure 9. A picture of the covariation of electricity price and solar energy indicating that solar energy (Both PV and Solar Thermal) could be used to releive load from the grid and savee energy cost for the house. A tendensy to a weekly pattern can be seen in the electricity prices with lower values in the weekends when the demand is less for industry and offices. *(Note: the unit for the right axis is TRNSYS units in kJ/h/m2 and therefore 3.6 times higher than W/m2.)*

Many more aspects will be studied in the future. The next steps in simulation studies for this application are:

- Advanced heat storage modeling
- More exact modeling of a side-arm electric heating.
- Modeling of a smart tank design and control where the auxiliary volume is fitted to the expected future heat demand.
- Heat pump modeling and connection to the system.
- More optimization runs for storage size, collector type, size, tilt...
- System control, taking NordPool prices and weather, into account.
- Modeling and optimization of control system for variable electricity prices

4. CONCLUSIONS

A first TRNSYS model is available for the investigation of the interaction of a combi system with direct electric or heat pump backup heating. Historical climate and electricity prices are taken into account.

The normal load pattern of a house already uses a significant part of the energy at lower electricity prices and would benefit from a variable electricity price if implemented all the way to the final customer.

This system type would reduce peak loads in the grid by demand side management and also use more of surplus wind power.

Solar thermal and PV systems deliver energy when the electricity price most often is highest during the day and should be favored for this in some way.

Much work remains in this project to model the system and components more exactly and find optimum heat storage design and control strategy of the system based on weather and electricity price forecasts.

5. REFERENCES

IEA Task 32 homepage: http://www.iea-shc.org/task32/index.html

Heimrath, R and Haller, M. "The Reference Heating system, The Template Solar System. Project Report A2, Subtask A". ITW TU Graz, 2007

Nordpool homepage: www.nordpool.com

Bengt Perers, Simon Furbo, Elsa Andersen, Jianhua Fan, Solar/electric heating systems using smart solar tanks and variable electricity costs, EuroSun 2010 Congress Proceedings, Graz, Austria

SOLAR/ELECTRIC HEATING SYSTEMS USING SMART SOLAR TANKS AND VARIABLE ELECTRICITY COSTS

B. Perers, S.Furbo, E. Andersen, J.Fan

Department of Civil Engineering, Technical University of Denmark, Brovej, Building 118, DK-2800 Kgs. Lyngby, Denmark; Phone: +45 45 25 19 53. E-mail: beper@byg.dtu.dk.

Abstract

By using forecast based system control and a smart tank design in a solar combi system, the excess electric power production, of for example wind power plants, can be used. This can both reduce the auxiliary cost in the solar combi system and increase the use of renewable power sources. The paper will present work, which will be realized to a product. By using the electricity price variations hour by hour to charge the tank, the auxiliary cost can be reduced by 30% compared to a fixed average electricity price and normal thermostat auxiliary control. By introducing forecast based control in combination with a solar thermal combi system with a smart tank with a variable auxiliary volume fitted to the expected coming heat demand it is expected that the auxiliary energy cost can be reduced below 50% compared to the reference situation.

1. Introduction

It is expected that the already large electricity price variations, existing in Denmark, will remain or even increase in the future. The low electricity prices almost down to zero, see figure 1, are often caused by high wind energy production in the winter period

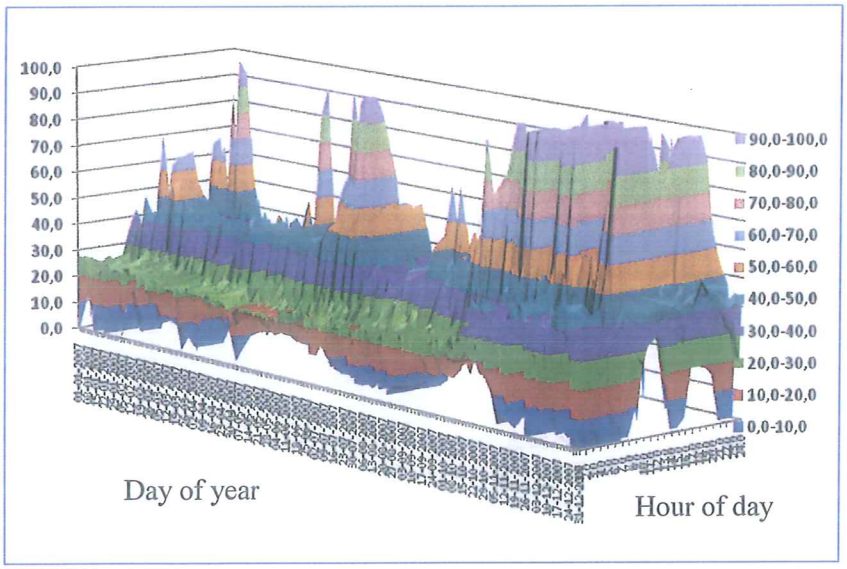

Figure 1. Example of the hourly electricity price variations during 2008 in western Denmark. Data comes from the NORDPOOL electric stock exchange. The unit on the y-axis is Euro/MWh at the production plant level in the system.

Presently 20% of the electricity in Denmark is produced by wind power. It is expected that this share will be increased to 40% in the near future. This will require adapted use of electricity, to the availability and price of electricity in the grid.

These price variations can be used in a solar combi system to charge the auxiliary part of the storage tank in a smart way, when the solar energy production is not large enough to meet the load.

In the high price end, the duration of the peaks in figure 1 are often short, so with a smart control of the storage auxiliary charging, these peaks can be avoided. This also leads to a positive demand side management effect, that is favorable for the electric grid and will give less need for operation of peak power plants, see fig 2.

In the Nordic countries, a common electricity stock exchange NORDPOOL exist, that creates hourly electricity prices 24 hours ahead each afternoon, for all days of the year. By using this information and also forecasts for weather, heat loads and solar heat production, the auxiliary energy cost can be minimized by only using periods with low prices. In this way also renewable energy sources with large variations in power production, can be utilized in a better way in the future.

The low cost electricity can be used both in the form of direct electric heating or via a heat pump system to heat the auxiliary part of the tank. Both variable auxiliary volume and variable auxiliary temperature can be favorable.

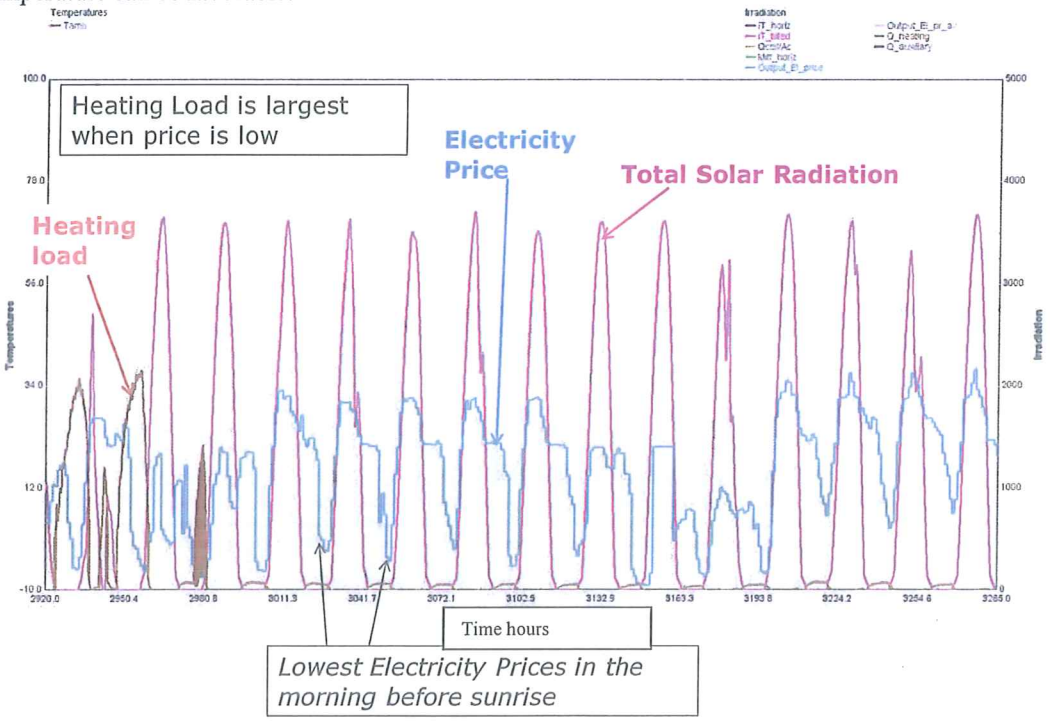

Figure 2. An example of positive covariation between high electricity prices and solar radiation availability. Also a good match between high heating load and low prices can be seen.

A TRNSYS model from IEA SH&C Task 32 (Ref [2] Heimrath and Haller) has been further developed to simulate a single family house with a solar combi system (Ref [1] Perers, Furbo,

Andersen, Fan). The system can use a heat pump or direct electric backup system in combination. The control in the simulations are still according to electricity prices only. But forecasts for weather and price are planned to be used also in the real systems later.

The project is carried out in a cooperation between Department of Civil Engineering, Technical University of Denmark, Danish Meteorological Institute (DMI), DTU Informatics, Technical University of Denmark, ENFOR A/S, AllSun A/S, Ohmatex ApS, Ajva ApS and COWI A/S.

2.1. Description of the TRNSYS system model

The simulation model is based on the advanced TRNSYS deck created for IEA SH&C Task 32 for a single family combi system. Figure 3 shows the principal system layout. The TRNSYS deck is described in the IEA Task 32 work (Heimrath and Haller 2007).

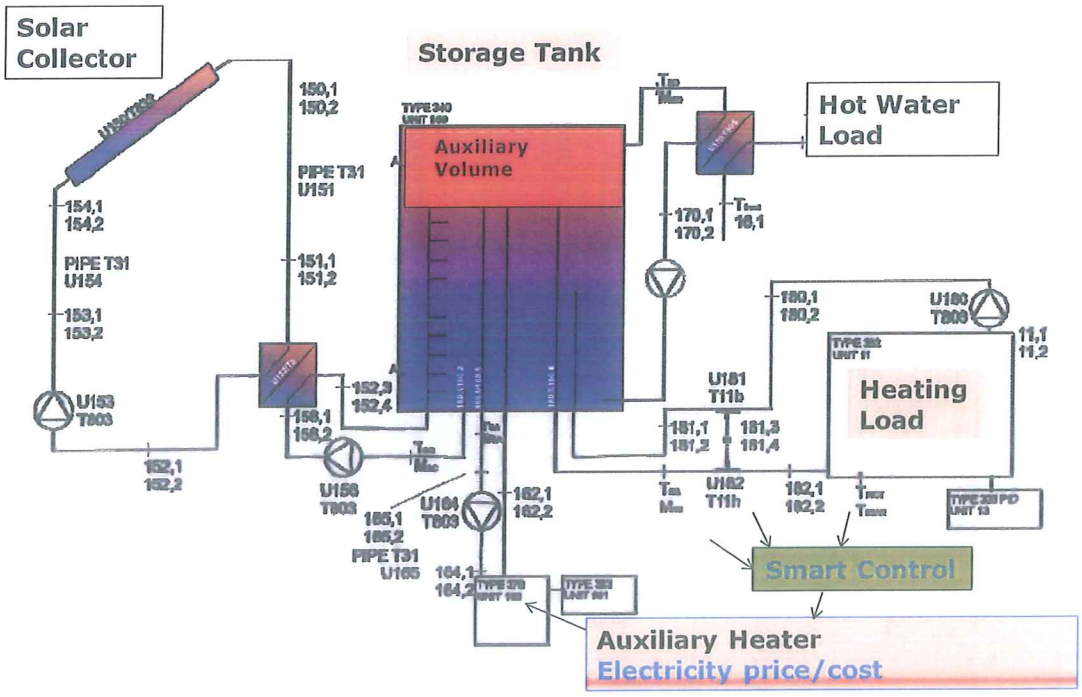

Figure 3. The solar combi system layout with solar collectors, auxiliary heater, storage tank and hot water and heating loads in the house. The diagram is taken from (Ref [2]. Heimrath and Haller 2007)

The system simulated needs more than 100 parameters to describe all details of the components, but the major system data are:

- Single family house. Old house 100 kWh/m² or 30 kWh/m2, yearly heat demand
- Electric auxiliary with different control strategies.
- Solar Collectors 5-15 m², Tilt 45°, south oriented
- Storage 500-5500 l water tank, stratified
- Climate: 2008 weather data from climate station at Department of Civil Engineering, Technical University of Denmark.
- Electricity Prices: Nordpool 2008. Denmark-East (DK2).

- Consumer Electricity Prices assumed to follow Nordpool prices (variable or a fixed average).
- Collector type: Standard Single Glazed Selective Flat Plate Collector.
  F'n0=0.8, F'UL1=3.5, F'UL2=0.015 , b0=0.18, Kdiff=0.9

2.2. Nord Pool data on Electricity price variations

The electricity price is determined each day at the electric stock exchange NORDPOOL. Historical data some years back has been derived and transformed so that TRNSYS can read and use the data in the simulations. Especially in west Denmark with the highest fraction of wind power the prices vary very much during the day and the year. Figure 1 shows an example of the hourly price variation for one year. The high peaks often occur during the day and the low prices in the early morning. Figure 4 shows the daily average prices for three years for Denmark West. It can be seen that the prices vary much from year to year too. There is also a day by day pattern that may be used with a larger storage in the solar combi system.

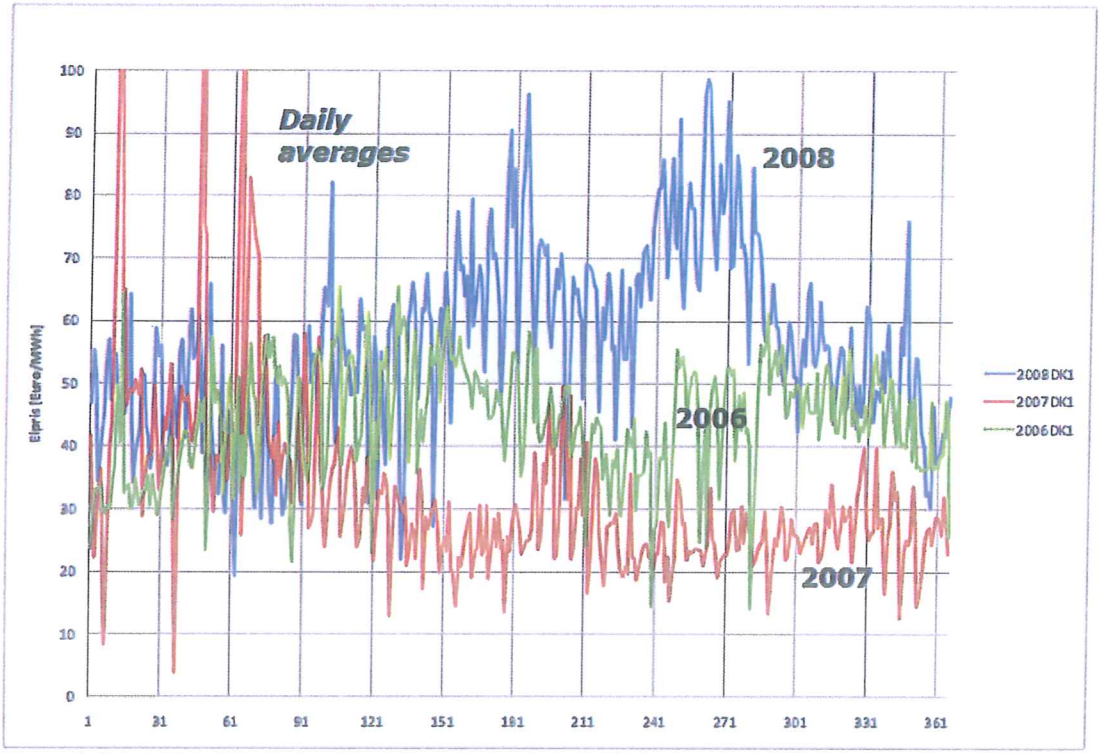

Figure 4. Example of the daily electricity price variations during one year in western Denmark. Raw data from the NORDPOOL electric stock exchange are used. The unit on the y-axis is Euro/MWh at the production plant level (what is paid to the producer) in the system. Final customer prices are much higher.

2.3. Climate Data used in the Simulations

Climate data from the weather station at Department of Civil Engineering, Technical University of Denmark in Copenhagen has been used together with Nordpool electricity data for the same time period (2008) and area (Denmark East) in the TRNSYS simulations. This gives a realistic situation in the simulations and also different control strategies can be evaluated with exactly known prognosis data if desired. Figure 5 gives an example of the annual variation of global solar radiation and wind speed data that are used as input in the simulations.

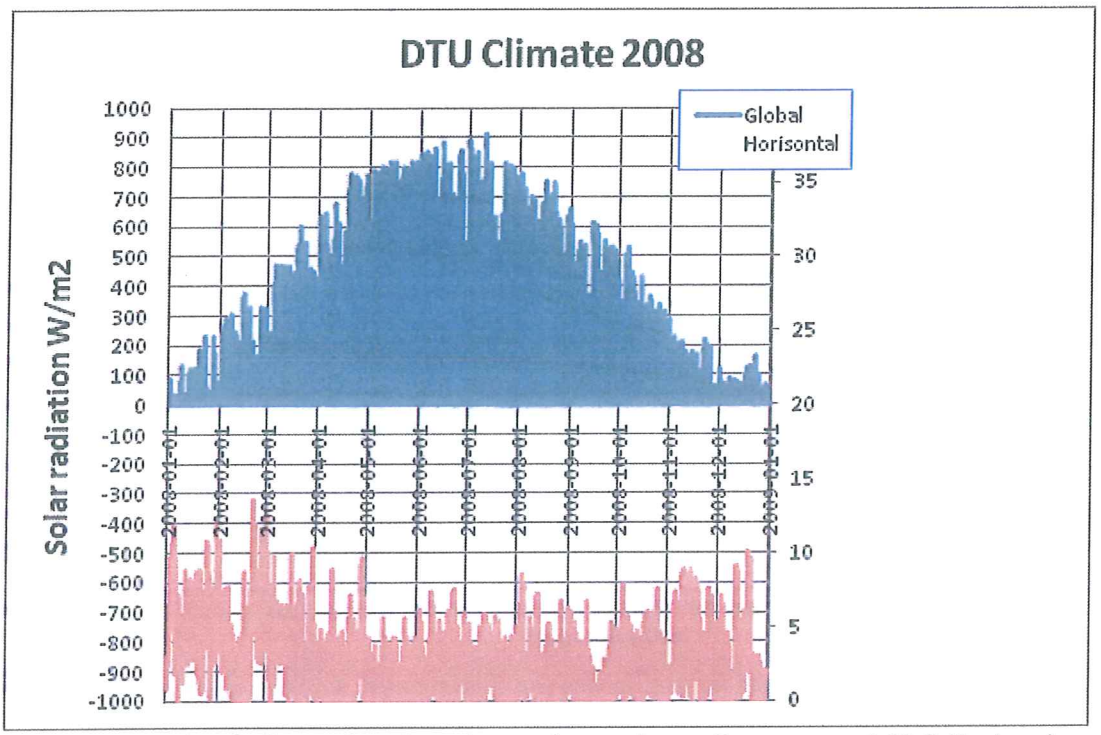

Figure 5. Example of climate data from the weather station at Department of Civil Engineering, Technical University of Denmark for 2008. The lower curve is wind speed with axis to the right.

It can be seen that the wind speed and solar radiation has a positive co-variation with higher wind speeds in the winter, when the solar radiation is low. It should also be kept in mind that the wind power is proportional to the cube of the wind speed so the electricity production will match even better if short term mismatch can be evened out by for example hydropower and a large enough storage in the solar combi system.

2.4. Basic System input data

To have limitation of the range of storage tank and solar collector sizes to start from in the project, the system simulations presented in figure 6 and 7 were made. It can be seen that a tank size of 500-1000 l and collector area of around 10 m² is reasonable for this load (100kWh/m2 house). This does not involve costs more than qualitatively, so later on, better estimates of the sizing may be found including more factors. The reason for the somewhat higher optimum collector loop flow rate, than usual, is that this system on the annual average is dominated by the heating load with higher flow rate in and out of the tank than a pure domestic hot water system. The low flow concept, is actually a matched flow concept and an adaption to the load flow gives the optimum collector output and energy savings.

The optimum volume flow rate in the solar collector loop is a bit higher than for traditional low flow solar heating systems.

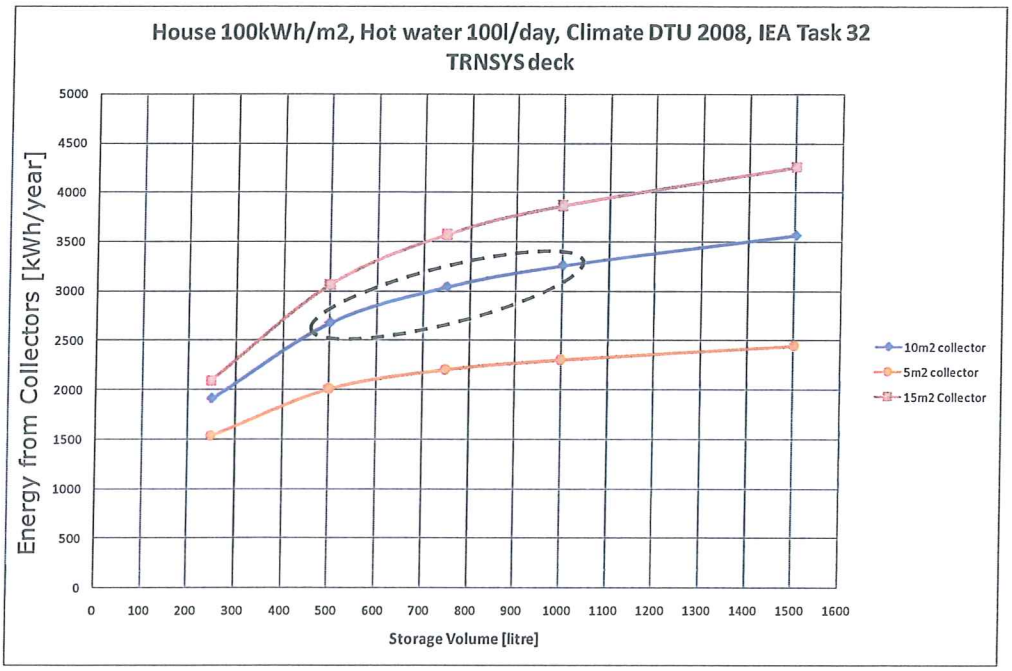

Figure 6. Optimization diagram for tank volume and collector area. A system sizing of 10 m² collector and 500 l storage was chosen as a first estimation of optimum size. Further considerations will probably change this choise somewhat later on.

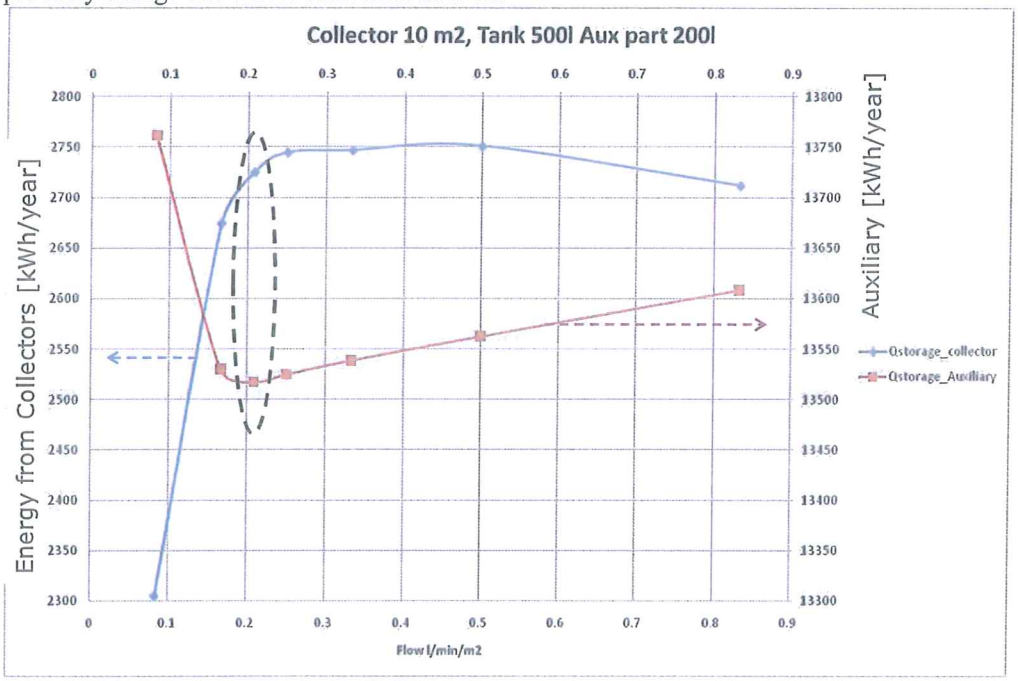

Figure 7. Flow optimization in the collector loop.

3. Simulation Results

This paper presents calculations with the TRNSYS system model to elucidate how best to design solar combi systems with advanced control strategies and smart tank design. The auxiliary energy cost for heating and hot water for different system designs is minimized. Figure 8 shows examples of calculated auxiliary costs for a $10m^2$ solar combi system in a house with a yearly heat demand of 15000 kWh inclusive domestic hot water consumption, (DTU Lyngby 2008 climate) and NordPool 2008 electricity costs. **The red curve** is a reference case with fixed thermostat control (63°C) and fixed electricity price (annual average price). **The blue curve** is added to show the effect of only introducing a variable electricity price, but still normal fixed temperature (63°C) auxiliary control. The annual cost reduction is 17% compared to the reference case. **The green curve** is for a control strategy that use a higher auxiliary temperature set point during hours with low electricity price (the price is below the 24h average price). This means that more auxiliary energy is charged when the price is extra low during the 24h period.

The annual cost reduction with this simple strategy is about 30%. This is just an indication, what may be achieved with more advanced control and a smart storage.

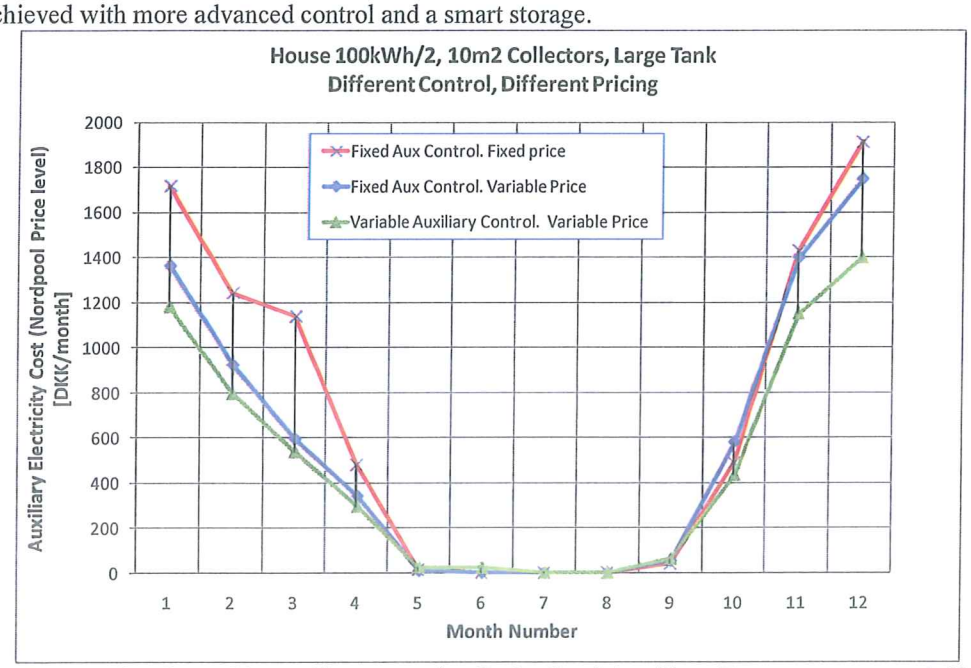

Figure 8. Example of monthly auxiliary costs for: Red - fixed Auxiliary Temperature control 63C and fixed electricity price. Blue - fixed Auxiliary Temperature control 63C butand variable price. Green - variable temperature control and variable price, but without forecast control.

It can be seen that just by introducing variable electricity price at the final customer a saving of about 17% can be achieved. This saving is dependent on the timing between the price and load, both during the day and year. This timing effect can vary from period to period, as can be seen in the figure following the difference between the red and the blue curve. On the average a customer would gain from variable prices, as the house needs most auxiliary heating power in the night when the electricity prices are low. This applies for both direct electric auxiliary heating and heat pump auxiliary heating as the load pattern is the same.

So far the main work has been spent on adapting the TRNSYS system simulation model, towards this project's requirements for advanced control of the auxiliary: Advanced simulation of the tank, input from local weather and NORDPOOL prices to the control system and forecast based control. Also careful check of the output of the extended system model has been done.

The electricity cost results presented are at NordPool electric stock exchange level. At the final customer the prices are often the double or triple. The future pricing and taxes are hard to predict. The known Nordpool cost level are therefore used and presented in the simulations. In the future system control unit the real customer price will be used as input of course.

Many more aspects can be studied in the future. The next steps in simulation studies for this application is the full implementation of forecast control in the TRNSYS model:

4. Conclusions

A TRNSYS model is available for the investigation of the interaction of a solar combi system with direct electric auxiliary heating or heat pump backup heating. Real climate and electricity prices can be taken into account.

The normal load pattern of a house already uses a significant part of the energy at lower electricity prices in the night and would benefit from a variable electricity price if implemented all the way to the final customer.

This system type would reduce peak loads in the grid due to the solar collector energy input to the tank during daytime when the electricity prices and demands are high. This will give an extra demand side management effect. The system will also use more of surplus wind power.

Solar thermal and PV systems deliver energy when the electricity price is high during the day and should be favored for this in some way.

Much work remains in this project to model the system and components more exactly and find optimum heat storage design and control strategy of the system, based on weather and electricity price forecasts.

References

[1] B. Perers, S.Furbo, E. Anderssen, J.Fan . Solar/electric heating system for the future energy system. ISES Solar World 2009 Congress Proceedings. Johannesburg 2009.

[2] R. Heimrath and M. Haller. The Reference Heating System, the Template Solar System. Project Report A2 of Subtask A. A report of IEA SHC- Task 32. April 2007.

IEA Task 32 homepage: http://www.iea-shc.org/task32/index.html
Nordpool homepage: www.nordpool.com

Jianhu Fan, Elsa Andersen, Simon Furbo, Bengt Perers, Detailed modelling of charging behaviour of smart solar tanks, EuroSun 2010 Congress Proceedings, Graz, Austria

DETAILED MODELLING OF CHARGING BEHAVIOUR OF SMART SOLAR TANKS

Jianhua Fan*, Elsa Andersen, Simon Furbo and Bengt Perers

Department of Civil Engineering, Technical University of Denmark,

Brovej, building 118, DK-2800 Kgs. Lyngby., Denmark.

* Corresponding Author, jif@byg.dtu.dk.

Abstract

The charging behaviour of smart solar tanks for solar combisystems for one-family houses is investigated with detailed Computational Fluid Dynamics (CFD) modelling and Particle Image Velocimetry (PIV) measurements. The smart solar tank can be charged with a variable auxiliary volume fitted to the expected future energy demand. Therefore the heat loss from the tank is decreased and the thermal performance of the solar heating system is increased compared to a traditional system with a fixed auxiliary volume. The solar tank can be charged either by an electric heating element situated in the tank or by an electric heating element in a side-arm mounted on the side of the tank. Detailed CFD models of the smart tanks are built with different mesh densities in the tank and in the side-arm. The thermal conditions of the tank during charging are calculated with the CFD models. The fluid flow and temperature calculations are compared to PIV (Particle Image Velocimetry) measurements of fluid flows and temperature measurements. The aim is to elucidate the temperature distribution and thermal stratification of the tank during charging. It is elucidated how the calculated temperatures in the tank are influenced by the mesh densities, the distribution of computational cells, the physical model and time steps used in the simulations. The findings of the investigations will be used as guidance for creation of CFD models for optimal design of smart solar tanks.

1. Introduction

The two most powerful renewable energy sources are solar and wind energy. It is expected that an increasing part of the electricity consumption in the future will be covered by wind farms. This will result in an increased number of windy periods with a surplus of electricity and thereby a low electricity price. A concept where individual solar heating systems are optimised for making use of electricity produced by wind turbines in these periods can facilitate the introduction of wind energy on a large scale into the energy system and thereby contribute to increasing the part of the energy consumption covered by renewable energy sources.

An ongoing research project will elucidate how best to design an individual heating unit for one-family houses based on smart solar tanks [1]. The project will elucidate how suitable the heating unit is for the home owner and for our future energy system. Different designs of the heating unit and the control system will be investigated.

The heat of the energy system will be produced by a solar heating system and by electrical heating element(s). The electrical heating element(s) will, if possible, only be in operation in periods where the

solar heating system cannot cover the heat demand of the house 100% and where the electricity price is low, for instance due to high energy production from wind farms or due to a low electricity consumption. The energy system will need a smart heat storage with a variable water volume heated by low cost electricity and an advanced control system for the electric heating element(s)/heat pump based on prognosis for electricity costs, heat demand and solar heat production and a control system based on weather forecasts. The tank can be charged with a variable volume by internal heating elements installed at different levels in the tank or by a side-arm with a heating element.

This paper focuses on detailed modelling of the auxiliary charging, by means of electric heating element(s), of such a smart solar tank for solar combisystems for a one-family house. The focus of the study on the tank with a heating element in the tank is the flow field around the heating element during charging and how the fluid flow influences thermal stratification at the top of the tank. For the tank with a side-arm, the tank is charged by thermosyphon induced circulation through the side-arm. The charging of the tank is influenced by the power of the electric heating element, the position of the electric heating element and the design of the side-arm, for example, diameter of the side-arm pipe and position of the side-arm connection to the tank, etc. The focus of the study on the tank with a side-arm is to investigate how the design of the side-arm and the operating conditions influence charging behaviour of the tank. The ultimate aim of the study is to validate CFD models of the smart solar tanks and to give recommendations for creation of the CFD models for optimization of smart solar tanks.

2. Experimental and Theoretical Investigations

The auxiliary charging behaviour of a tank is investigated theoretically by CFD calculations and experimentally by PIV measurements. To facilitate the PIV measurements, a square glass tank is built with a cross section of 400 mm x 400 mm and a height of 900 mm, see Fig. 1. The uninsulated tank is made of 12 mm glass with a thermal conductivity of 0.81 W/mK.

Fig. 1. The PIV test facility of the smart solar tank with one heating element and a side-arm.

The tank is designed in such a way that it can be charged either by an electric heating element situated in the tank or by an electric heat element in a side-arm mounted on the side of the tank. The internal electric heating element is situated in the tank at a height of 450 mm from the bottom of the tank. One end of the side-arm is mounted on the side of the tank with a distance of 800 mm from the tank bottom while the other end of the side-arm is mounted on the centre of the tank bottom. The side-arm has a built in electric heating element which gives a variable charging power from 1 kW to 3 kW. PIV equipment from Dantec Dynamics is used to determine the fluid flow in the tank, especially in the

upper part of the tank where water is heated either by the internal heating element or by the side-arm. Thermal stratification in the tank is measured at different levels by temperature sensors located in one corner of the tank. The accuracy of the temperature measurement is estimated to be 0.5 K. The measured temperatures are compared to temperatures calculated by the CFD models.

The CFD model of the tank with an internal electric heating element is shown in Fig. 2. The mesh on the vertical cut-plane of the tank is shown in Fig. 2 (a). A. In order to better resolve the heat transfer and fluid flow in the region adjacent to the electric heating element and in the region adjacent to the tank wall, a boundary layer mesh is applied so that there is a fine and dense mesh in these regions, see Fig. 2(a) and 2(b). The 3D tank model includes the glass tank wall as a solid region and the hot water volume of the tank as a fluid region. The charging of the electric heating element is modelled as heat flux from the surface of the heating element. The power of the heating element is 500 W which corresponds to a heat flux of 30041 W/m^2. A size function is used to assign denser mesh around the electric heating element where a high temperature gradient is expected. A non-slip wall condition is used for all wall surfaces except the top of the tank where there is free water surface. A zero shear stress wall condition is used for the top inner surface of the tank. The heat loss from the tank is calculated by surface heat transfer coefficients of the tank wall and the temperature differences between the glass tank and the ambient air. The surface heat transfer coefficients of the top, the side and the bottom of the tank are 10 W/m^2K, 7.69 W/m^2K and 5.88 W/m^2K respectively. The Ambient air temperature is constantly 20°C.

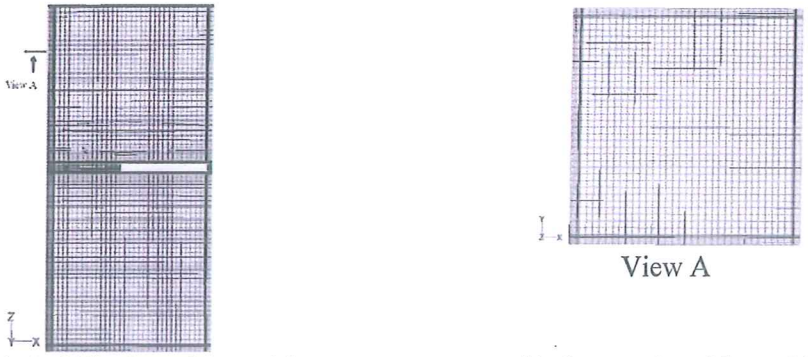

(a). Vertical middle plane of the model (b). Cross section of the model

Fig. 2. CFD model of the tank with an internal electric heating element

The CFD model of the tank charged with a side-arm is shown in Fig. 3. The vertical cut-plane through the middle of the tank is given in Fig. 3(a). A boundary layer mesh is applied to the surface of the heating element, the inner surface of the side-arm and the inner surface of the tank where high temperatures and/or velocity gradients are expected, see Fig. 3(b). The tank is charged by thermosyphon induced circulation through the side-arm. Modelling of fluid flow and heat transfer in the side-arm is therefore critical. A denser mesh is applied to the side-arm while a coarse mesh is applied to the tank body, see Fig. 3(c). An interface is used to combine the non-conformal mesh of the upper half and the bottom half of the tank. The side-arm consists of two sections of copper pipes of 28 mm outer diameter and one section steel pipe with an outer diameter of 66 mm with a built in electric heating element. The 3D tank model includes the glass wall of the tank and the copper/steel pipe walls of the side-arm as solid regions, and the hot water volume in the tank and in the side-arm as fluid regions. The charging of the electric heating element is modelled as a heat flux from the surface of the

heating element. The power of the heating element is 3kW which corresponds to a heat flux of 97607 W/m^2. A non-slip wall condition is used for all wall surfaces except the top surface of the tank where a zero shear stress wall condition is applied. Heat loss from the tank is modelled the same way as for the tank with an internal heating element. The side-arm is insulated with a heat transfer coefficient of 2.4 W/m^2K between the pipe outer surface and the ambient air.

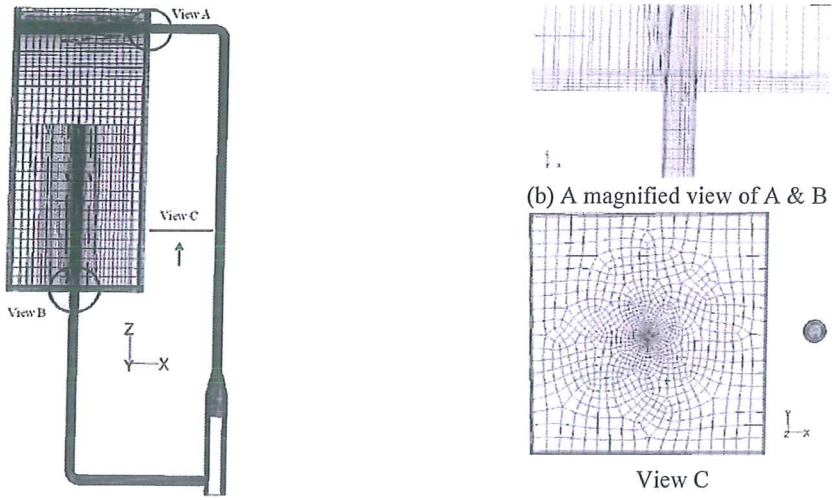

(a) Middle plane of the model

(b) A magnified view of A & B

View C

(c) Cross section of the model

Fig. 3. CFD model of the tank with electric heating element built in a side-arm

Water is used as the heat storage media. Properties of water and their dependences on temperature are shown as follows:

Dynamic viscosity, [kg/(ms)] $$\mu = 0.0007 * (\frac{T}{315})^{-5.5} \quad (1)$$

Thermal conductivity, [W/(mK)] $$\lambda = 0.375 + 8.84 \times 10^{-4} * T \quad (2)$$

where T is fluid temperature, [K].

The tank wall material, glass, has a thermal conductivity of 0.81 W/mK, while copper and steel has a thermal conductivity of 388 and 60 W/mK, respectively.

The Reynold number of the flow in the side-arm is estimated to be between 3000-4000 which indicates a flow in the transitional region. The flow around the heating element is most likely turbulent due to the high power of the electric heating element. A RNG k-ε turbulence model is therefore used to model the flow.

Transient CFD calculations are carried out with buoyancy driven force modelled by Boussinesq approximation [2]. The PRESTO and second order upwind method is used for the discretization of the pressure and the momentum/energy equations respectively [2]. The SIMPLE algorithm is used to treat the pressure-velocity coupling. The transient simulations start with a tank with a uniform temperature of 20.3°C and a zero velocity field in the tank. The calculation is considered convergent if the scaled residual for the continuity equation, the momentum equations and the energy equation are less than 10^{-3}, 10^{-3} and 10^{-6}, respectively. The simulation runs with a time step between 1-10 s and a duration of 1

hour. One simulation with a time step size of 3 s takes approx. 12-52 hours for a duo core processor computer with 2 X 3 GHz CPU frequency and 4G memory.

3. Results and Discussion

3.1. Influence of grid density and time step size

Investigations are carried out to determine the optimal time step and grid density. Time intervals in the range of 1-10 s are investigated. The mesh scheme of the tank with an internal electric heating element is listed in Table 1. The minimum mesh interval size is applied to the region adjacent to the surface of the electric heating element. The mesh interval size increases with a ratio of 1.1 further away from the heating element until it reaches the maximum mesh interval size. In the rest of the tank, the maximum mesh interval size is used. A 4-row boundary layer mesh is assigned to the surface of the tank wall and the surface of the heating element. The height of the first row of mesh is listed in Table 1 for different mesh schemes. The height of the boundary layer mesh increases with a ratio of 1.2 away from the wall surface. Four mesh schemes are investigated with mesh interval sizes between 0.001 and 0.03 m.

The mesh scheme of the tank with a side-arm is listed in Table 2. The mesh size varies between 0.004 m and 0.008 m in the side-arm, while it varies between 0.012 m and 0.03 m in the tank body. Four-row boundary layer mesh is attached to all wall surfaces of the tank and of the side-arm. The first row height of the boundary layer mesh is 0.001 m for the tank wall surfaces while it is either 0.0002 m or 0.0005 m for the wall surfaces of the side-arm.

Table 1. Mesh schemes of the tank with an internal electric heating element.

	Number of cells	**Mesh interval size, [m] Min./Max.**	**Boundary layer mesh, the first row height, [m]**
Grid 1	37,525	0.002/0.03	0.001
Grid 2	193,522	0.002/0.012	0.001
Grid 3	495,936	0.001/0.008	0.001
Grid 4	1,192,380	0.001/0.006	0.0005

Table 2. Mesh schemes of the tank with a side-arm with built in electric heating elements.

	Number of cells	**Mesh interval size, [m]**		**Boundary layer mesh, the first row height, [m]**	
		Tank	**Side-arm**	**Tank**	**Side-arm**
Grid 1	189,698	0.03	0.008	0.001	0.0005
Grid 2	263,768	0.03	0.006	0.001	0.0005
Grid 3	407,314	0.012	0.006	0.001	0.0005
Grid 4	761,465	0.012	0.004	0.001	0.0002

CFD predicted thermal stratification in the tank with a side-arm is shown in Fig. 4 and 5. The influence of mesh density on prediction of temperatures in the tank is shown in Fig. 4. At 10 min after the start of the charge, the difference between the temperatures predicted by Grid 2, Grid 3 and Grid 4 is maximum 0.7 K, while the difference between Grid 1 and Grid 4 is up to 2.7 K. The influence of mesh density on predicted temperature becomes less dominant as the test goes on. The difference of temperature predictions between Grid 1 and Grid 4 is decreased to maximum 2.0 K at 60 min after the start. It can be concluded that the mesh scheme Grid 2 is appropriate for modelling the tank with a side-arm. The influence of mesh density and time step size on prediction of temperature distribution in the tank with an internal heating element is investigated as well. The results show that the mesh

scheme Grid 2 is appropriate for modelling the tank with an internal heating element. Fig. 5 shows the influence of a time step size on temperature predictions in the tank. If a time step size between 1 s and 3 s is used, the difference of temperature prediction is within 0.5 K. With an increase of the time step size to 5 s and 10 s, the variation of temperature calculation increases up to 1.7 K and 5 K. It can be concluded that a model with a time step size between 1 s and 3 s can predict temperatures for most of the tank within an uncertainty of 0.5 K. Due to the dramatic increase of computation time with a decrease of the time step size, a time step of 3 s is used for later calculations.

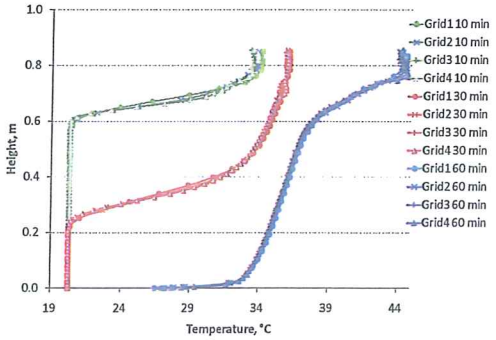

Fig. 4. Influence of mesh density on prediction of thermal stratification in the tank with a side-arm

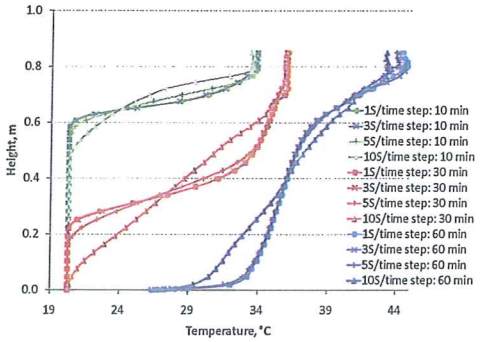

Fig. 5. Influence of time step size on prediction of thermal stratification in the tank with a side-arm

3.2. Thermal stratification in the tanks

The CFD model with Grid 2 is used with a time step size of 3 s for the calculation of heat transfer and fluid flow in the tanks. The convective heat loss and thermal radiation heat loss from tank surfaces are now considered. The surface convective heat transfer coefficient for the side, the top and the bottom of the tank are respectively $1.49(T-T_a)^{0.33}$, $1.55(T-T_a)^{0.33}$ and $0.68\left(\frac{T-T_a}{l}\right)^{0.25}$ where T is the surface temperature of the tank; T_a is the ambient air temperature of the room; l is the dimension of the tank in m. The thermal radiation heat transfer coefficient is defined as:

$$\frac{\sigma(T+T_a)\left(T^2+T_a{}^2\right)}{\frac{1}{\varepsilon_T}+\frac{1}{\varepsilon_a}-1}$$

where σ is Stefan–Boltzmann constant, 5.67E10-8 W/m^{2}K^4. ε_T is the emittance of the tank surface, 0.8; ε_a is the effective emittance of the surrounding surfaces which is assumed to be 0.8. The ambient air temperature increases as the room is gradually heated up by the heat loss from the tank. A temperature of 20.3°C is used from the start till 30 min after the start, while 22.3°C is used for the rest of the test.

CFD calculated temperatures are compared to the measured temperatures. Fig. 6 shows CFD calculated and measured temperatures at different levels in one corner of the tank. The electric heating element with a power of 460 W is installed at a height of 0.45 m. It can be seen in Fig. 6 that after the start of the charging, the water above the level of the element is gradually heated up to almost uniform temperature. There is almost no thermal stratification at the upper part of the tank, which means that the uprising flow from the heating element induced by buoyancy driven force creates mixing in the upper part of the tank. The water at the bottom part of the tank is not heated, indicating that the uprising flow from the element is not large enough to disturb water in the bottom part of the tank. At

58 min after the start, the water temperature in the upper part of the tank increases to 25.0°C, while the water temperature at the bottom part is only slightly higher than 20°C due to heat conduction of water and the glass tank wall. The CFD model predicts well temperatures in the tank with a difference of maximum 0.3 K, especially in the upper part of the tank. The difference is most likely due to the incorrect input of surface heat transfer coefficients and ambient air temperature in the CFD model.

Fig. 7 shows thermal stratification in the tank charged by a side-arm with a power of 3kW. One end of the side-arm is mounted on the side of the tank at a height of 0.8 m, while the other end of the side-arm is mounted on the centre of the tank bottom. The water in the side-arm is heated to a higher temperature than the water in the tank, which generates buoyancy driven flow in the side-arm. The uprising flow in the side-arm creates circulation of water between the side-arm and the tank. Temperatures at different heights in one corner of the tank is measured and compared to CFD calculations in Fig. 7. The CFD model predicts well thermal stratification in the tank at 10 min and 30 min after the start of the charging. But it underestimates temperatures in the tank at 60 min after the start, especially at the height of 0.4 m to 0.7 m. The reason could be an overestimated heat loss from the tank.

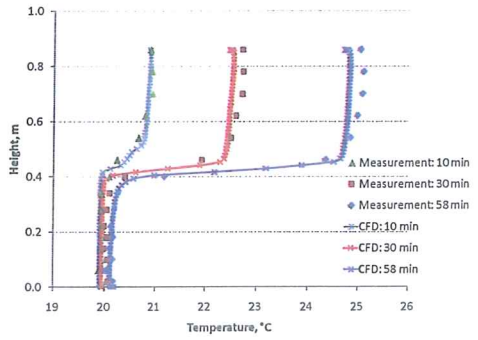

Fig. 6. Thermal stratification in the tank with an internal heating element

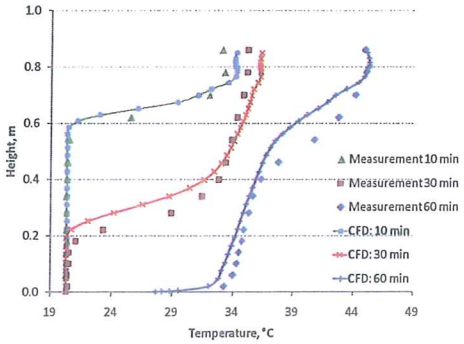

Fig. 7. Thermal stratification in the tank with a side-arm

The heat transfer and fluid flow in the side-arm has a significant influence on the charging behaviour of the tank. Fig. 8 shows the temperature of the fluid entering into the side-arm. There is a good agreement between measured and calculated temperatures. Fig. 9 shows the temperature of the fluid entering into the tank. CFD predicts a flux of hot water entering into the tank 48 s after the electric heating element is turned on, while it is undetected during the measurement. That could be explained by the fact that the temperature sensor is installed on the outer surface of the copper pipe which makes it difficult to respond to the fast temperature changes of the water in the pipe. There is a difference of maximum 3 K between the measurements and the CFD predictions, which is probably due to a slight underestimation of circulation flow in the side-arm. The calculations show that the volume flow rate through the side-arm varies between 2.6-3.4 l/min during the test.

3.3. Fluid flow in the tank with a side-arm

Fig. 10 shows PIV measured fluid flow on the middle plane of the upper part of the tank 5 min after the start. The fluid entering into the tank from the side-arm forms a jet flow. The jet flow reaches the other side of the tank and turns back, forming a circulation. Because of the jet flow and the induced circulation, the tank above the side-arm inlet is mixed. That can be verified by the uniform temperature in the tank above 0.78 m, see Fig. 7. Fig. 11 shows CFD predicted flow field on the middle plane of

the upper part of the tank 5 min after the start. The CFD model predicts successfully the flow pattern, although the velocity magnitude of the flow is overestimated. Another reason for the lower fluid flow in the PIV measurement could be the uncertainty of PIV measurement which is influenced by the specification of duration between pulses and the method used for analysis of the particle image. These factors should be further investigated in future work.

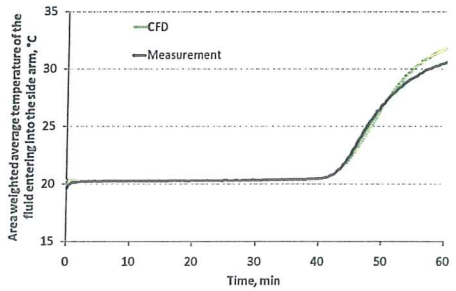

Fig. 8. Temperature of the fluid entering into the side-arm

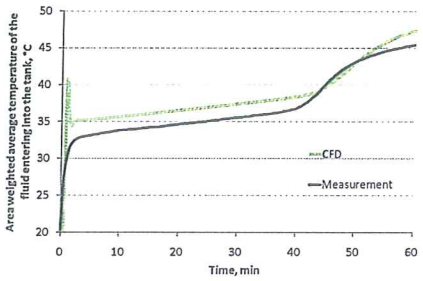

Fig. 9. Temperature of the fluid entering into the tank

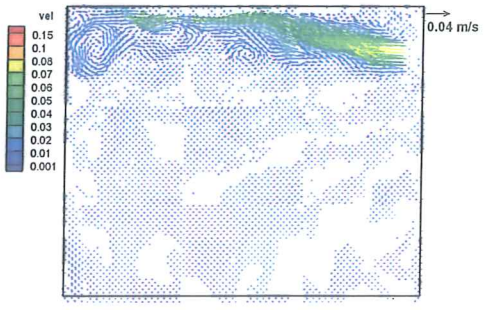

Fig.10. PIV measured flow field on the middle plane of the tank 5 min after the start

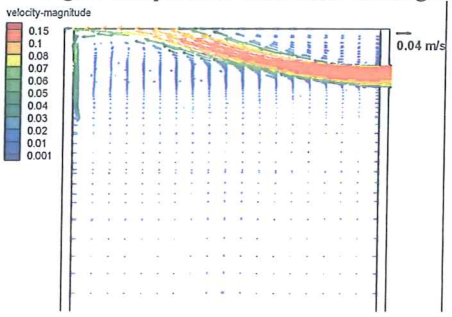

Fig.11. CFD predicted flow field on the middle plane of the tank 5 min after the start

5. Conclusions

The charging behaviour of two smart solar tanks is investigated with detailed CFD modelling and PIV measurements. The solar tank can be charged either by an electric heating element situated in the tank or by an electric heating element in a side-arm mounted on the side of the tank. The results show that a mesh interval size of 0.03 m and 0.006 m is sufficient for the tank and the side-arm, respectively. The most appropriate time step size is 3 s. The fluid flow and temperature calculations are compared to PIV measurements and temperature measurements. The CFD model predicts well thermal stratifications in the tank, but gives underestimated temperatures due to incorrect heat loss of the tank which should be further investigated. The CFD model predicts successfully the flow pattern in the tank, although the velocity magnitude of the flow is higher than the PIV measurements.

References

[1] B. Perers, S. Furbo, E. Andersen, J. Fan. Solar/electric heating system for the future energy system. ISES Solar World 2009 Congress Proceedings. Johannesburg 2009.

[2] Fluent Inc., 2006. "Fluent release 6.3", 10 Cavendish Court, Lebanon, NH 03766-1442 USA.

[3] O. B. Stampe, Glent Ventilation, Glent & CO A/S, 1977.

Bengt Perers, Simon Furbo, Elsa Andersen, Jianhua Fan, The covariation of heating load and solar energy production with the electricity price variations in Denmark, EuroSun 2010 Congress Proceedings, Graz, Austria

THE COVARIATION OF HEATING LOAD AND SOLAR ENERGY PRODUCTION WITH THE ELECTRICITY PRICE VARIATIONS IN DENMARK

B. Perers, S. Furbo, E. Andersen, J. Fan

Department of Civil Engineering, Technical University of Denmark, Brovej, Building 118 DK-2800 Kgs. Lyngby, Denmark; Phone: +45 45 25 19 53. E-mail: beper@byg.dtu.dk.

Abstract

There are large variations of the electricity price from hour to hour in Denmark. This is much dependent on the large fraction of wind power in the electric grid (already about 20% with an expansion to 40% planned). The electricity prices are very low when the wind power production is large. Simple plotting of the electricity price versus heating load and solar radiation, indicate that there can be a positive match when using electricity as a backup source in a solar combi system. The electricity is used to charge the auxiliary part of the storage, in low cost periods. This also gives a demand side management effect for the electric grid. If enough auxiliary storage capacity and smart forecast based control is introduced in the combisystem, this match can be further used to increase the utilization of renewable energy sources, in an economical way. Presently the final customer electricity prices are variable only for a few customers on trail, but it is expected to become more and more common in Denmark.

1. Introduction

Electricity cost data from the Nord Pool electricity stock exchange and climate data from the DTU Byg climate station, has been used to analyse the covariation with climate related energy flows in a solar combisystem.

It is well known that the electricity demand and therefore the electricity price, is higher during the day than during the night. The demand increases during the day when for example offices, shops, schools, hospitals and industry need electricity during working hours. This gives a positive match with available solar radiation, se examples in figure 1. Therefore Solar Photovoltaics (PV) and solar thermal systems can help to reduce the need for daytime peak load electricity production in the grid. This can be created both by injecting PV electricity into the grid and also by reducing the electric load in the grid to auxiliary electric heaters.

Perhaps not so often thought about, is that the heating load of a house also has a positive match with the electricity price. The heating load is largest in the night when the outdoor temperature is low. The house also have a minimum heating load during daytime, when solar radiation heating through the windows of the house, is largest and the outdoor temperature is highest, see figure 2.

It is also well known that the wind power production is larger in the winter period, when the heating load is larger. This should give an extra value for wind and solar energy in combination even if these sources cannot be relied upon hour by hour. By utilizing weather forecasts both for planning of the electricity production and load adaptation in the grid, the fraction of renewables can be increased

without the need for extra electrical storage capacity in the grid. This paper is aiming at describing some of these relations in a more quantitative way on a local level for a house.

The covariations have been analysed for the use of low cost electricity as backup energy in a solar combisystem.

During long periods in the summer half year, the solar heating system will heat the whole tank including the auxiliary part, especially during daytime, when the electricity price is high. No electricity at all, will be used for heating and hot water during this period.

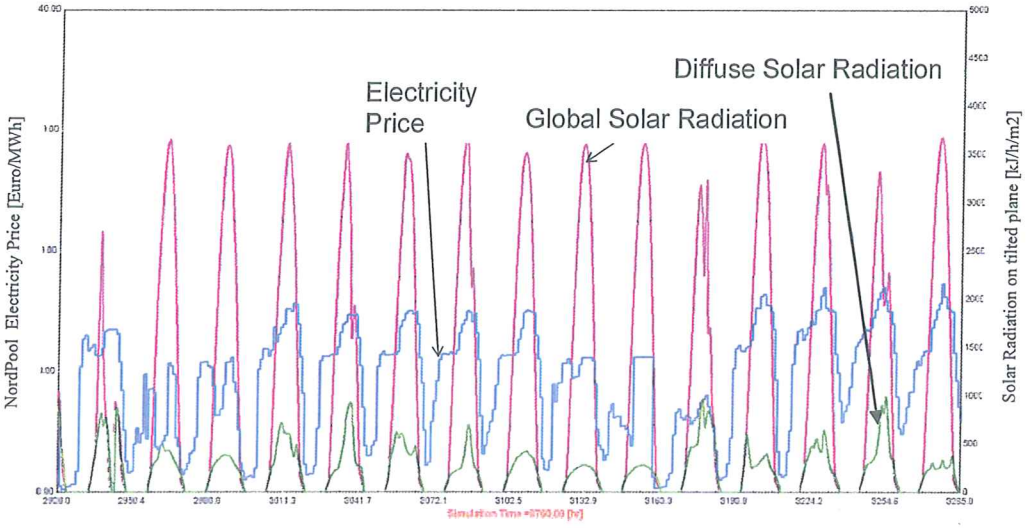

Figure 1. Covariation of electricity price and solar energy, indicating that distributed solar energy (both PV and Solar Thermal) could be used to relieve load from the grid and save energy cost for the house owner. A tendency to a weekly pattern can also be seen in the electricity prices with lower values in the weekends when the demand is lower for industry and offices.

The heating load is lower during daytime than during nights, as the ambient temperature is higher and because solar energy through windows will add to the internal free heating. At the same time the electricity prices are higher during the day. This will give a positive match when using electricity as a backup source.

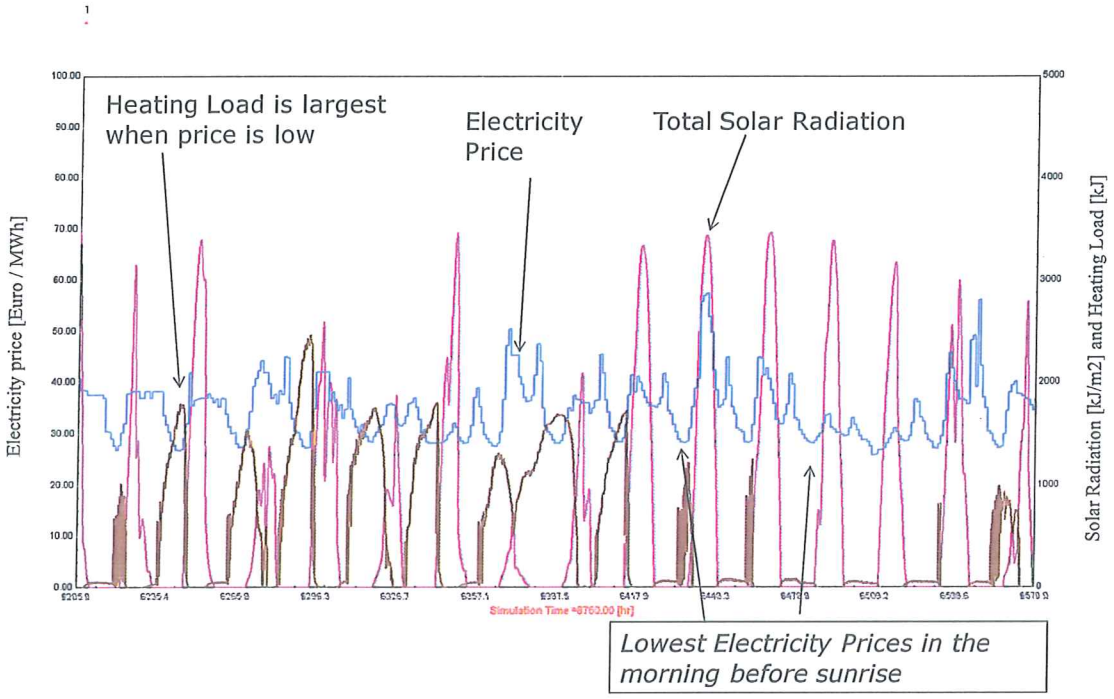

Figure 2. Heating load (brown) and electricity price (blue) for two weeks in the late winter 2008. There is a tendency to a favourable match.

In figure 3 the variation of the hourly electricity price during the day is shown for one year of data (Denmark East 2008). It can be seen that on the average (yellow line) the price is lowest in the late night/early morning and highest during mid day - afternoon. The extreme low prices occur only in the night/morning and the extreme high prices only during the day and evening.

Another way of presenting the variability is shown in figure 4 and 5 where the hourly values are plotted in time and size order (duration line). Both all year- and heating season data are shown in figure 5. It can be seen that the variability is almost independent of the season, so there is a basis for electricity cost reduction by smart system design and control during all seasons of the year.

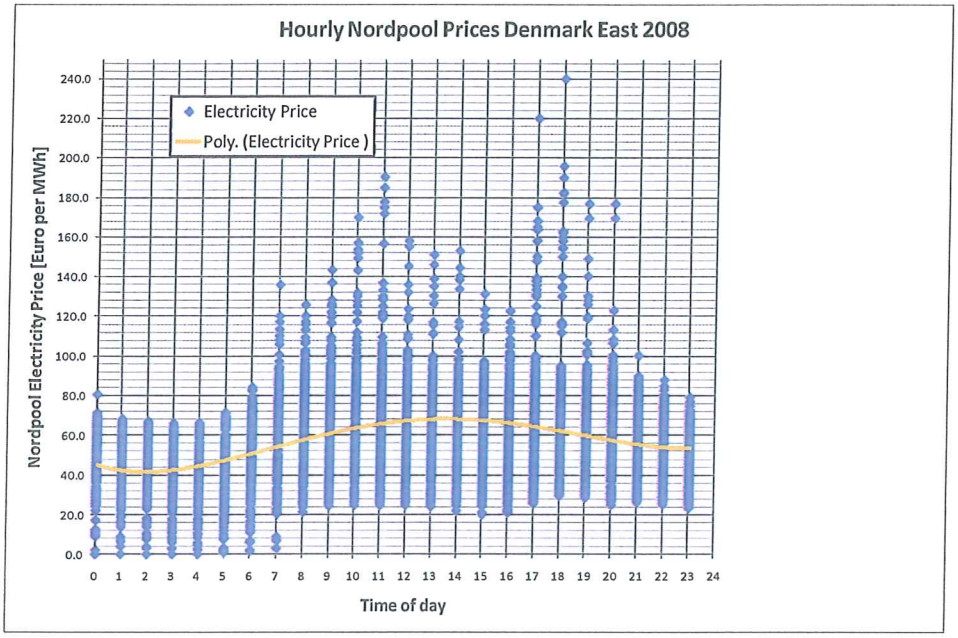

Fig 3. The variation of the hourly electricity price during the day (Denmark East 2008). It can be seen that on the average (yellow curve) the price is lowest in the late night/early morning and highest during mid day - afternoon.

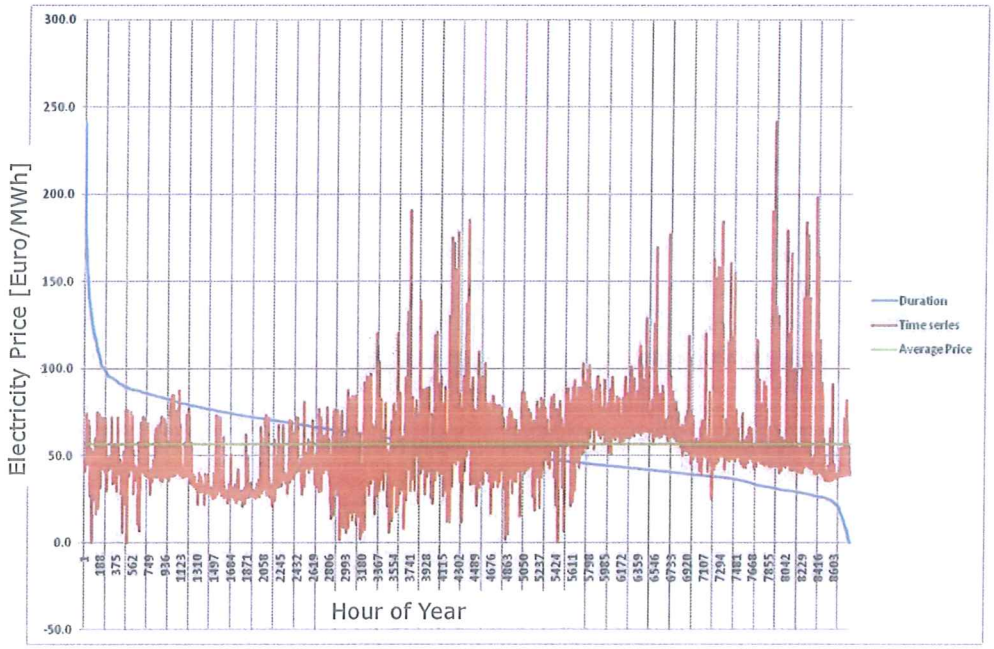

Fig 4. Electricity price variations for one year (2008 Denmark East). The green line is the annual average price level. The red curve is the hourly prices over one full year. The blue curve is the hourly prices sorted in size to create a duration curve.

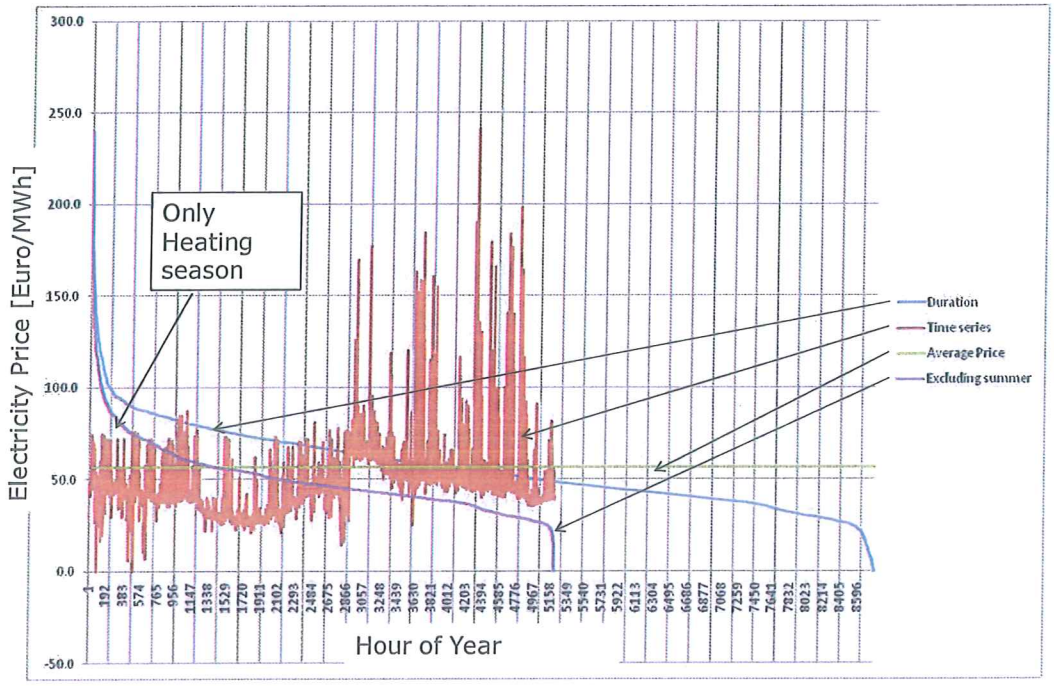

Fig 5. Electricity price variations for the *heating season* versus full year (2008 Denmark East). The green line is the annual average price level. The red curve is the hourly prices only for the *heating season* and the blue curve is the hourly prices sorted in size to create a duration curve over the year. The pink curve is the duration curve of the electricity price for the *heating season* only.

2. Results

To quantify the potential for auxiliary cost reduction in a domestic combi system by using low electricity prices and advanced control, some calculations were made with a hot water plus heating load hour by hour for one year for a single family house.

Three different price levels were used. 1) The traditional fixed price set to the annual average level. 2) The actual price every hour from Nord Pool and 3) The minimum hourly price every 24 hour as an extreme potential if the auxiliary could be charged during only one hour per day at the lowest price.

Figure 6 shows an example of results from January for a house with 200 W/K transmission plus ventilation losses and 400 W of internal heat generation from persons and appliances and 100 l/day hot water load. No solar input.

It can be seen that the option 3 always is cheapest as expected and that the variable price alternative often comes on second place in hourly cost.

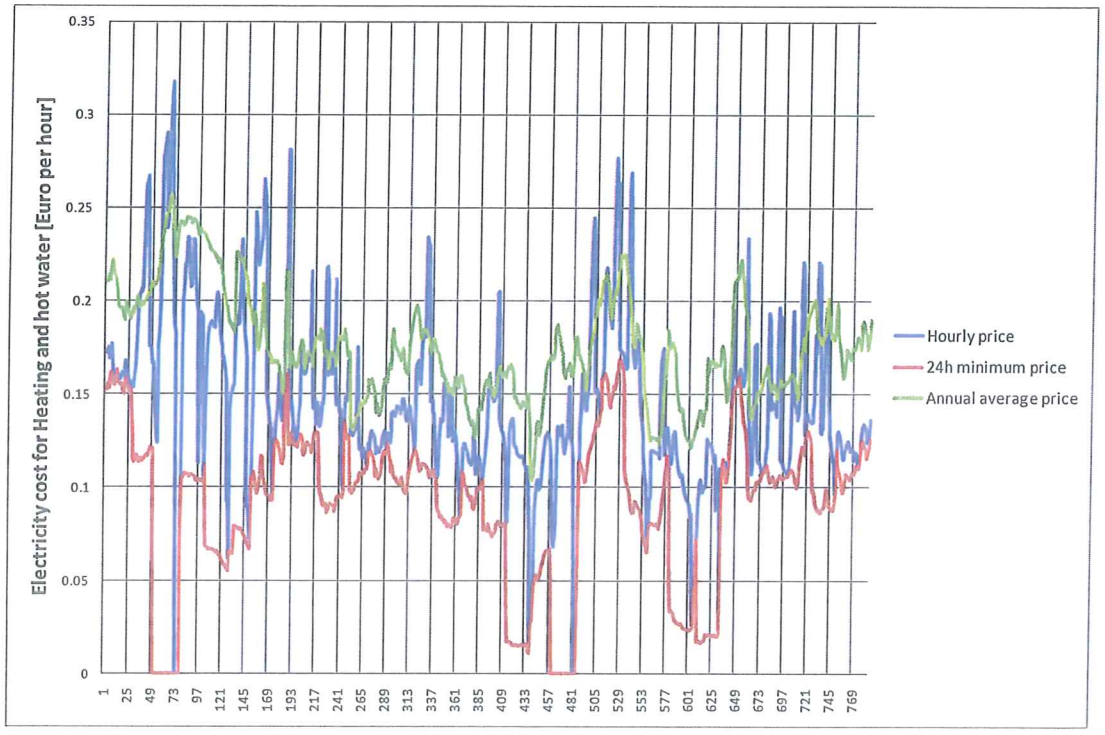

Figure 6. Electricity costs (on Nord Pool price level) for a house with 200W/K transmission + ventilation losses. 400W of internal heat from persons + appliances and 100 l/day hot water load. No solar input.

The annual auxiliary electricity cost for the three different price levels is shown in Fig 7. To the right (right bar) the traditional fixed price level is applied all year. To the left the actual variable price each

hour at Nord pool level is used. In the middle an extreme case, if all auxiliary needed is charged during the cheapest hour every 24 hour.

This last case is the minimum cost that can be achieved with perfect forecasting and a large enough 24 hour storage capacity. This may be achieved in a real system, but then the extra system cost has to be balanced with the extra cost savings, so the optimum savings may be less extreme.

In percentage points the result is 10% lower cost just by introducing variable price but no advanced control or storage technology. By applying extreme forecast control and large enough storage, that use the lowest electricity price every 24 hour, a cost saving of 37% can be achieved.

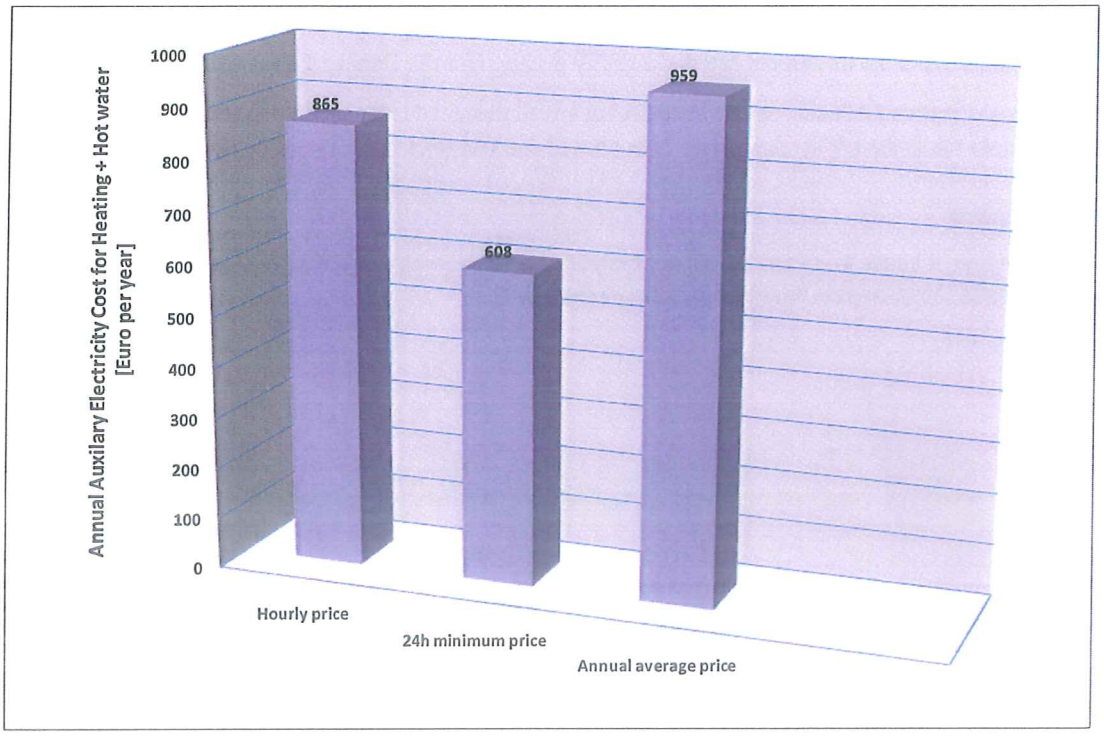

Fig 7 Annual auxiliary electricity cost for three different price levels and different control. To the right the traditional fixed electricity price all year. To the left the variable price each hour at Nord pool level. In the middle an extreme case if all auxiliary needed is charged during the cheapest hour during every 24 hour period.

3. Conclusion

The variations in electricity price hour by hour can be used both to reduce the cost for the final customer and also create a demand side management effect that will reduce the need for peak power plant operation in the grid.

Both solar radiation and heating load has a positive match with the electricity price variations during the day and would reduce the cost for the final customer without advanced forecast control, if only variable prices were introduced at the final customer.

In these simplified calculations an annual electricity cost saving of 10% can be achieved just by introducing variable price at the final customer.

By extreme forecast control and enough thermal storage capacity the cost savings is in the range of 37% compared to the traditional fixed electricity pricing (for the Denmark East area 2008).

Further savings can be achieved by introducing a well designed solar thermal system and of course a PV system when the PV system prices come lower and PV electricity is paid better in the grid.

References

[1] B. Perers, S.Furbo, E. Anderssen, J.Fan . Solar/electric heating system for the future energy system. ISES Solar World 2009 Congress Proceedings. Johannesburg 2009.

Elsa Andersen, Simon Furbo, Ziqian Chen, Thermal stratification in hot water storage tanks with fabric startification inlet pipes, ISES Solar 2011 World Congress Proceedings, Kassel, Germany

THERMAL STRATIFICATION IN HOT WATER STORAGE TANKS WITH FABRIC STRATIFICATION INLET PIPES

Elsa Andersen, Simon Furbo, Ziqian Chen

Department of Civil Engineering, Technical University of Denmark, Kgs. Lyngby, Denmark

1. Abstract

Double walled Fabric inlet stratification pipes made of Teflon and Polyester are investigated experimentally with the aim to study the thermal stratification that is build up in a hot water tank. The fabric pipes are mounted in the centre of a transparent circular acrylic tank from the bottom to the top of the tank. The thermal stratification is investigated during charge and discharge with inlet to the fabric pipes through the top of the tank and through the bottom of the tank. The fabric pipes are closed in the end opposite to the inlet. During charge, the outlet is at the bottom of the tank and during discharge, the outlet is at the top of the tank. The investigations show that the use of fabric inlet stratification pipes significantly improves the thermal stratification compared to the thermal stratification in the tank with no inlet stratification device. This is true both with inlet to the fabric pipes through the bottom and the through top of the tank. The investigations also show that the thermal stratification during charging is build up best with inlet to the fabric stratification pipe through the top of the tank while the thermal stratification during discharge is build up best with inlet to the fabric stratification pipe through the bottom of the tank. Finally, the investigations show that thermal stratification all in all is build up better with inlet to the fabric stratification pipes through the bottom of the tank than with inlet to the pipes through the top of the tank.

2. Introduction

Thermal stratification in hot water storage tanks for solar heating systems can be achieved in different ways. Excellent thermal stratification can be established in the tank when water heated by the solar collectors or water returning from the heating system is lead into fabric stratification inlet pipes through the bottom of the tank. The pipes are made of two concentric mounted fabric pipes with different diameters (Andersen, 2007). With a well performing fabric stratification pipe, the cross section area of the pipe is flexible. The most important function of the fabric stratification pipe is the ability to contract, whereby the cross section area of the pipe is reduced. The contraction is caused by temperature differences and thereby pressure differences between the inside of the fabric stratification pipe and the tank. When the temperature in the fabric stratification pipe is higher than the temperature in the tank, water in the tank flows toward the fabric stratification pipe due to lower pressure in the fabric stratification pipe. Thereby, the cross section area of the fabric stratification pipe is reduced. This leads to a higher velocity inside the fabric stratification pipe and thereby a higher pressure. The fabric stratification pipe contracts until the pressure difference between the inside of the pipe and the tank is eliminated. Consequently, no water from the tank will enter the fabric stratification pipe. Water from the fabric stratification pipe enters the tank at the level, where the tank temperature is the same as the temperature of the entering water. It is very important that the fabric stratification pipe is mounted vertically and that the pipe is closed in the end opposite to the inlet.

However, many tank designs have all the pipe connections in the top of the tank; hence incoming water must enter the fabric stratification pipe through the top of the tank. Fabric stratification pipes made of one fabric layer with inlet to the pipes through the top of the tank have been investigated by Davidson and Adams (1994). They found that the performance was highly dependent on the fabric style and that the performance of fabric pipes over a reasonable range of operation conditions were better that the performance of a rigid porous manifold. The natural forces that make the fabric pipe work with inlet to the pipe through the bottom of the tank are not the same as with inlet to the pipe through the top of the tank. During heating, the incoming water has a low density and will therefore stay at the top of the tank regardless of a fabric stratification pipe or not. During cooling, the pressure in the fabric stratification pipe is higher than the pressure in the tank. Hence natural forces will make the cold water flow towards the tank in all levels. The velocity of the incoming cold water together with the gravity will result in some kind stratification during cooling, but the

quality of the stratification is highly dependent on the incoming velocity. Consequently, a high velocity is an advantage during cooling. Also here it is very important that the fabric stratification pipe is mounted vertically and that the pipe is closed in the end opposite to the inlet.

In this paper it is investigated how thermal stratification is build up in hot water storage tanks with fabric stratification pipes during charging and discharging when heated or cooled water enters the fabric stratification pipes through the top or the bottom of the tank. The investigations are carried out with different two layer fabric stratification pipes made of Teflon and Polyester fibres.

3. Experimental investigations

3.1. Experimental set up

Figure 1 shows a picture of the experimental setup consisting of a transparent circular acrylic tank with a diameter of 388 mm and a height of 1270 mm. The tank is not insulated. The fabric stratification pipes are mounted in the centre of the tank and a forced volume flow can enter the stratification pipe either from the bottom or the top of the tank. The outlet can take place from the bottom or the top of the tank. In this way heated or cooled water can be charged at the top or at the bottom of the tank and water can be discharged from the top or the bottom of the tank. The fabric stratification pipes are closed in the end opposite to the inlet.

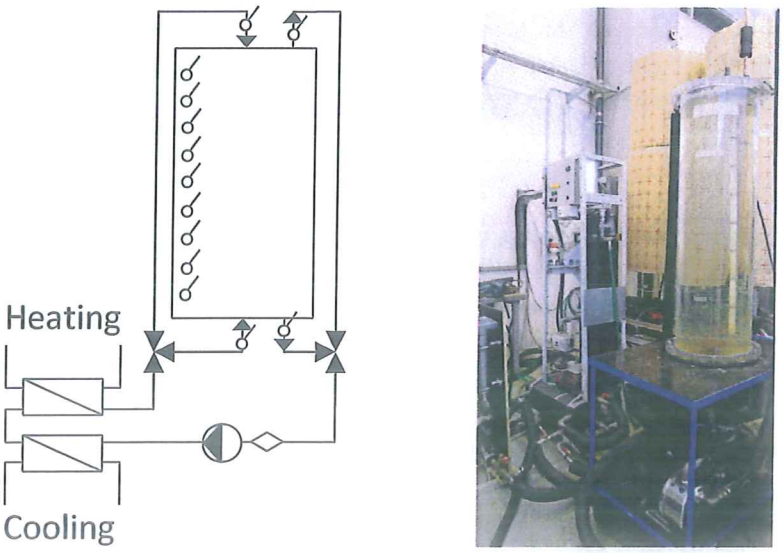

Fig. 1: Experimental set up. Left: A schematic illustration. Right: A photo.

The volume flow rate is measured by Brunata HGQ energy meter. The temperatures are measured with copper-constantan thermocouples type TT. The temperature sensors which are mounted in the tank can be seen in Figure 1 and the sensors are positioned as shown in table 1.

Tab. 1: Sensor positions.

Sensor number	Height from bottom of tank [mm]
1	80
2	220
3	360
4	505
5	645
6	785
7	930
8	1075
9	1210

3.2. Experiments

The thermal behaviour of three different types of fabric inlet stratification pipes made of two concentric fabric pipes with diameters of 30 mm and 50mm is investigated during charging and discharging. The operation conditions are:

- Charging with inlet to the fabric stratification pipe through the bottom of the tank. The start temperature of the tank is around 20°C and the water that enters the fabric stratification pipes is 40°C. The outlet is in the bottom of the tank.
- Discharging with inlet to the fabric stratification pipe through the bottom of the tank. The start temperature of the tank is around 40°C and the water that enters the fabric stratification pipes is 20°C. The outlet is in the top of the tank.
- Charging with inlet to the fabric stratification pipe through the top of the tank. The start temperature of the tank is around 20°C and the water that enters the fabric stratification pipes is 40°C. The outlet is in the bottom of the tank.
- Discharging with inlet to the fabric stratification pipe through the top of the tank. The start temperature of the tank is around 40°C and the water that enters the fabric stratification pipes is 20°C. The outlet is in the top of the tank.

As a reference, the thermal behaviour without inlet stratification pipe is investigated during charging and discharging through the bottom and the top of the tank. The operation conditions are as described above.
The volume flow rate is 4 l/min during charging and discharging. During the experiments, the tank is filled with water to a level of 1225 mm. Hence the water volume is 144.5 litres.

The investigated fabrics are shown in Table 2. The fabrics are obtained from the Danish company Ohmatex ApS during project cooperation (Perers et. al, 2009). The fabrics are knit with yarn made of Teflon and Polyester fibres: Polyvinylidene Fluoride (PVDF) and Polyethersulfone (PES) respectively. These fibres have some excellent qualities, among others high temperature resistance.

Tab. 2: Investigated fabric styles.

Fabric style
440 dtex PVDF
220 dtex*2 PVDF
167/36 PES

3.3. Analysis method

The tank is divided into N horizontal layers with the volume V. The temperature of each volume is measured.

In the analysis of the "momentum of energy", M, the energy of each layer of the tank E_i, is weighted by the vertical distance from the bottom of the tank to the centre of each layer, y_i. The energy of each tank layer and the "momentum of energy" are:

$$E_i = \rho_i \cdot c_i \cdot V \cdot \Delta T_i \qquad \text{(eq. 1)}$$

$$M = \sum_{i=1}^{N} y_i \cdot E_i, \qquad \text{(eq. 2)}$$

During charging, ΔT_i is the temperature difference between layer number i and the start temperature of the tank.
During discharging, ΔT_i is the temperature difference between layer number i and the end temperature of the tank when one tank volume has been exchanged.

A mixing number is derived based on the measured temperature profile and the corresponding ideal stratified and fully mixed temperature profiles.
The mix number is:

$$MIX = \frac{M_{str} - M_{\exp}}{M_{str} - M_{mix}}, \qquad \text{(eq. 3)}$$

M_{str}, $M_{\exp}$ and M_{mix} are the "momentum of energy" of a perfectly stratified tank, of the experiment and of a fully mixed tank respectively. The value of the mix number is between 0 and 1 where 0 corresponds to a perfectly stratified tank and 1 corresponds to a fully mixed tank.

The temperature profiles for the perfectly stratified tank and the fully mixed tank are calculated by means of the measured energy content of the tank. In this way heat losses and the heat capacity of the tank material are accounted for.

In the charging case, the low temperature equals the start temperature of the tank. The lower part of the tank has a volume equal to the total water volume in the tank minus the water volume which has entered the tank during the test. Based on the measured temperatures, the temperature in the upper part of the tank with a volume equal to the water volume which has entered the tank during the test is determined in such a way that the energy of the perfectly stratified tank is equal to the measured energy in the tank.
The temperature of the fully mixed tank is calculated based on the measured energy content of the tank at the time *t*.

In the discharging case, the low temperature equals the end temperature of the tank when the whole volume of the tank has been replaced once. The lower part of the tank has a volume equal to the water volume which has entered the tank during the test. Based on the measured temperatures, the temperature in the upper part of the tank with a volume equal to the total water volume in the tank minus the water volume which has entered the tank during the test is determined in such a way that the energy of the perfectly stratified tank is equal to the measured energy in the tank.
The temperature of the fully mixed tank is calculated based on the measured energy content of the tank at the time *t*.

4. Results

4.1. Experiments

Figure 2 shows the temperature stratification in the tank in different heights after 5 minutes, 15 minutes and 25 minutes during charging test without stratification manifold with inlet through the bottom of the tank (left) and inlet through the top of the tank (right). The outlet is at the bottom of the tank.
Thermal stratification is established in a good way if the inlet is at the top and in a very poor way if inlet is at the bottom.

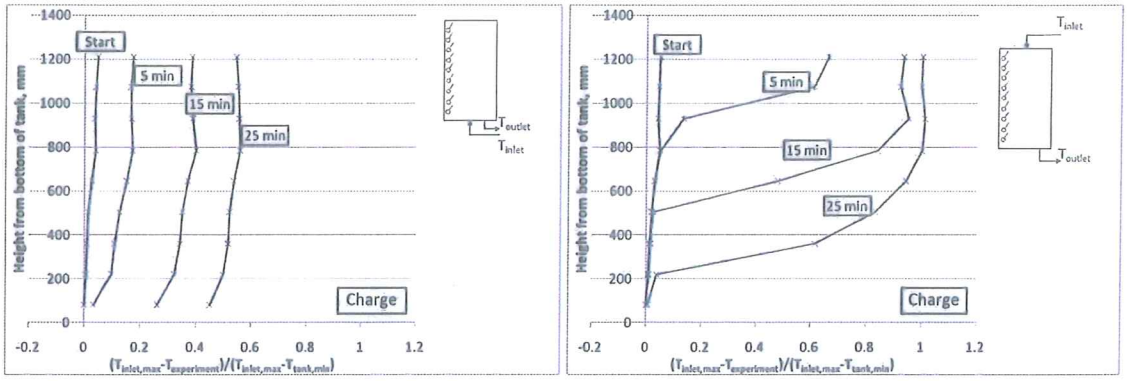

Fig. 2: Temperature profiles during charging tests without stratification inlet manifold. On the left with inlet from the bottom of the tank and on the right with inlet from the top of the tank.

Figure 3 shows how the temperature stratification in the tank is improved when charging is performed through stratification manifolds of two fabric layers. The temperature stratification is significantly improved for the operation conditions with inlet through the bottom of the tank, but an improvement can also be seen for the operation conditions with inlet through the top of the tank. In this case the improved stratification is because the fabric inlet stratifier reduces the inlet velocity and thereby the mixing in the tank.

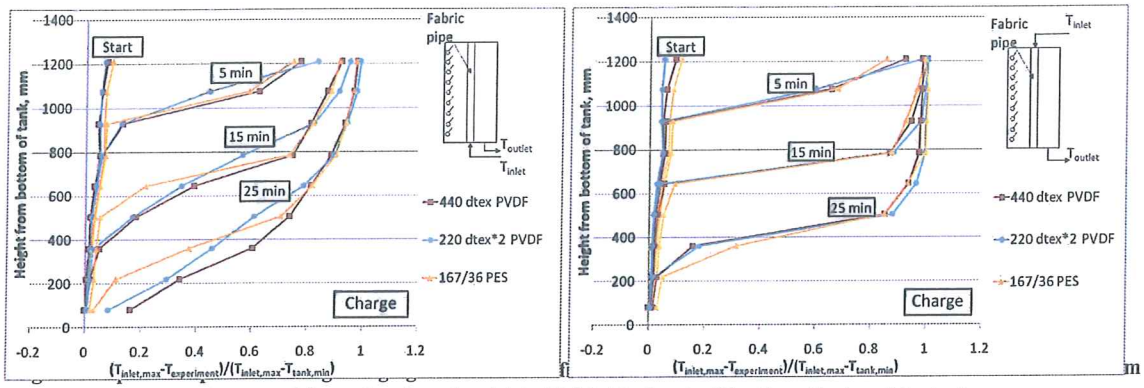

the bottom of the tank and on the right with inlet to the stratifier from the top of the tank.

Figure 4 shows the temperature stratification in the tank in different heights after 5 minutes, 15 minutes and 25 minutes during discharging test without stratification manifold with inlet through the bottom of the tank (left) and inlet through the top of the tank (right). The outlet is at the top of the tank.
Thermal stratification is established in a good way if the inlet is at the bottom and in a very poor way if the inlet is at the top.

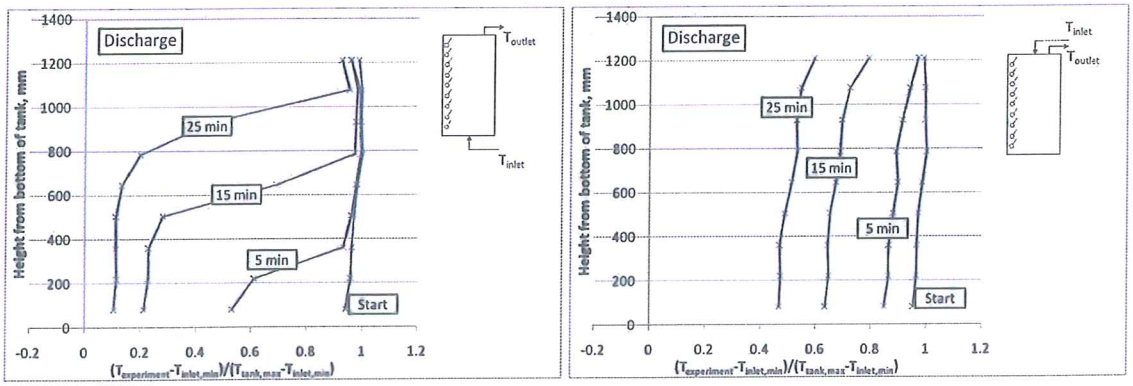

Fig. 4: Temperature profiles during discharging tests without stratification inlet manifold. On the left with inlet from the bottom of the tank and on the right with inlet from the top of the tank.

Figure 5 shows how the temperature stratification in the tank is improved when discharge is performed through stratification manifolds of two fabric layers. The temperature stratification is slightly improved for the operation conditions with inlet through the bottom of the tank and significantly improved with inlet through the top of the tank the tank. The slight improvement of the temperature stratification in the case with discharge through the bottom of the tank is because the two layer fabric pipe reduces the inlet velocity and thereby the mixing in the tank.

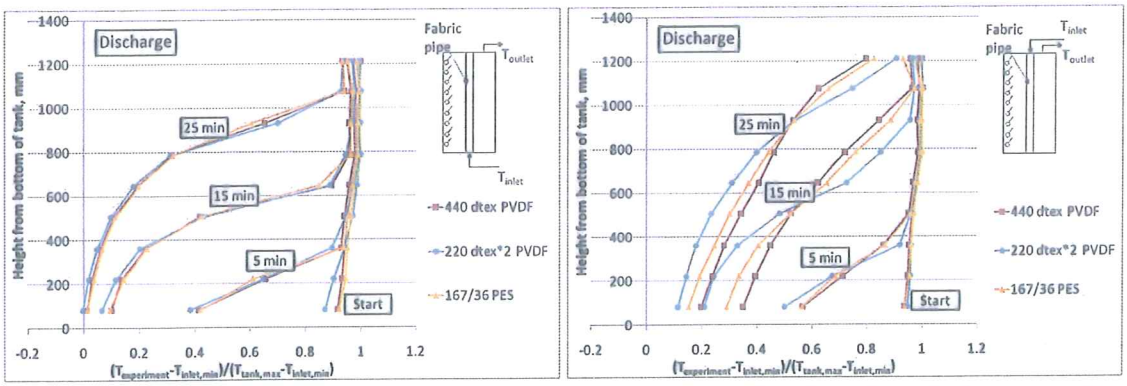

Fig. 5: Temperature profiles during discharging tests with stratification inlet manifold. On the left with inlet to the stratifier from the bottom of the tank and on the right with inlet to the stratifier from the top of the tank.

4.2. Analysis

Figure 6 shows the mix numbers during charge and discharge without inlet stratifiers with inlet from the bottom (left) or the top (right) of the tank. As expected, the mix number is high during charging with inlet from the bottom of the tank and during discharging with inlet from the top of the tank. The mix number is dramatically reduced when charging takes place from the top of the tank and discharging from the bottom of the tank.

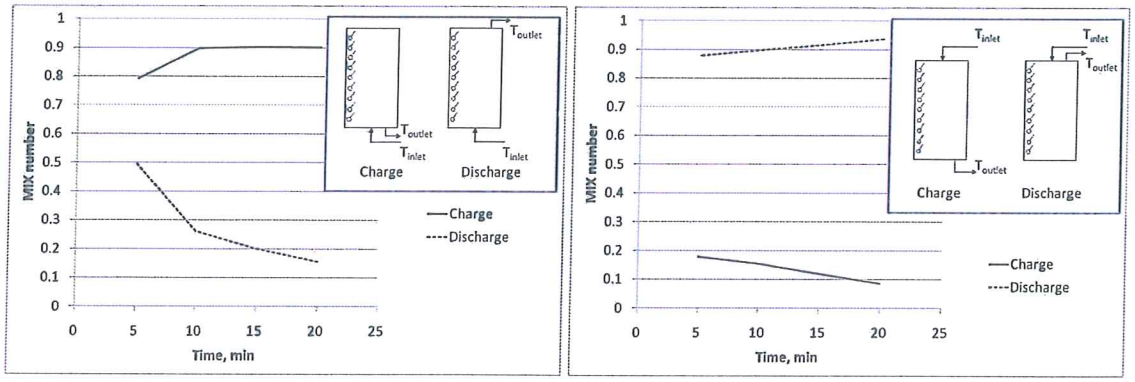

Fig. 6: Temperature profiles during charging tests without stratification inlet manifold. On the left with inlet from the bottom of the tank and on the right with inlet from the top of the tank.

The thermal behaviour of the different fabric pipes with the same operation conditions is very similar and hence only represented by one curve for each applied operation condition.

Figure 7 shows the mix numbers during charge and discharge with inlet stratifiers with inlet from the bottom (left) or the top (right) of the tank. It can be seen that the mix numbers are reduced dramatically when an inlet stratifier is used during charging through the bottom of the tank and during discharging through the top of the tank. It can also be seen that the mix number improves when an inlet stratifier is used during discharging through the bottom of the tank and charging through the top of the tank.

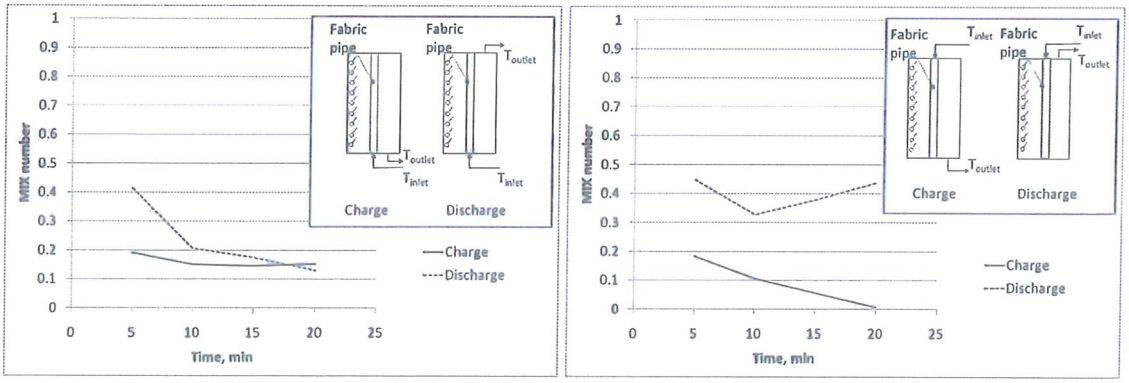

Fig. 7: Mix number during charging tests with stratification inlet manifold. On the left with inlet to the stratifier from the bottom of the tank and on the right with inlet to the stratifier from the top of the tank.

Based on the mix numbers of Figure 7 it is concluded that thermal stratification all in all is established in a better way with the inlet to the stratifier placed at the bottom of the tank than with inlet to the stratifier placed at the top of the tank.

5. Further discussion

Andersen (2007) showed that the theoretical thermal performance of solar heating systems with perfectly stratified tanks is much higher than the thermal performance of similar solar heating systems with non stratified tanks and that the thermal performance improvement was strongly dependent on the solar fraction. The smaller the solar fraction, the higher the thermal performance improvement will be. This conclusion is independent of the system size, the total consumption and the climate.

Figure 8 shows the performance ratio as function of the solar fraction. The performance ratio is calculated as the thermal performance of solar heating systems with perfectly stratified tanks divided with the thermal performance of solar heating systems with non stratified tanks. The dots in the figure represent differently sized solar heating systems under different reference conditions. The solar heating system sizes range from 5 m^2 – 60 m^2 with tank volumes in the range from 0.5 m^3 – 1.5 m^3. The different reference conditions are those used in the International Energy Agency taskforce 32 and Danish climate conditions.

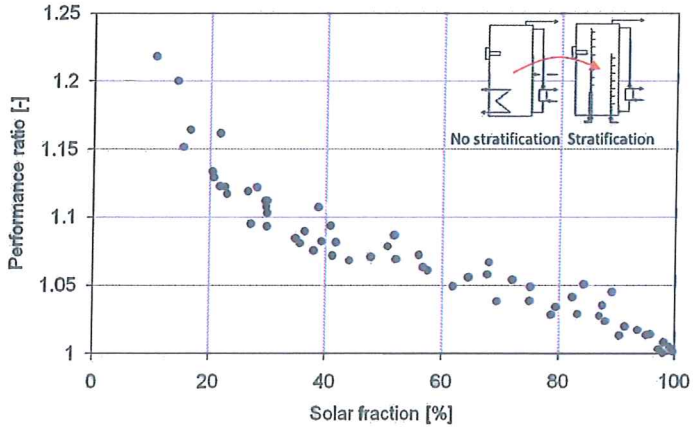

Fig. 8: Performance ratio as function of the solar fraction (Andersen and Furbo, 2008 a).

Further it was shown that the additional solar collector area needed to increase the thermal performance as much as the use of inlet stratifiers would result in, was increasing for increasing solar fraction making fabric inlet stratifiers an attractive solution for increasing the thermal performance.

An inlet at the top of the tank results in perforation of the insulation material encapsulating the hot water tank. This leads to a thermal bridge at the perforation and to a reduction of the thermal performance of solar heating systems. Furbo (1989) showed experimentally that one pipe connection at the top of the tank would increase the heat loss coefficient by 0.3 W/K – 0.5 W/K depending on the design of the pipe and pipe connection. Andersen (2007) showed theoretically that the thermal performance of a small solar heating system with an auxiliary heated volume would decrease by 20 % with a thermal bridge of 0.5 W/K. This makes inlet stratifiers with inlet through the bottom of the tank an attractive solution for increasing the thermal performance.

The weak point of the fabric inlet stratifier is its sensitivity towards correct mounting and the durability. Andersen and Furbo (2008 b) investigated the long time durability of different fabric inlet stratification pipes both in a domestic hot water tank and in a space heating tank. They found that lime in relatively short time destroyed the functionality of the fabric pipes, not by reducing the porosity, but by making the pipes stiff and thereby unable to contract in order to eliminate the pressure difference between the pressure in the pipe and the pressure in the tank. They also found that the amount of deposits in the fabrics was less important than the structure of the deposits.

The fabric styles investigated in this paper have high temperature resistance and are expected to have very high resistance towards lime, dirt and algae deposits. This will be investigated.

6. Conclusion

Three double walled fabric inlet stratification pipes made of Teflon and Polyester fibers are investigated experimentally. The inlet stratification pipes are made of two concentric fabric pipes with diameters of 30 mm and 50 mm. The thermal performance of the pipes is investigated during charging and discharging with a volume flow rate of 4 l/min. Inlet to the stratification pipes is investigated both through the bottom and the top of the tank. During charging, the outlet is at the bottom of the tank and during discharging, the outlet is at the top of the tank. The fabric pipes are closed at the opposite end of the inlet.

The investigations show that thermal stratification is build up in a good way with inlet to the pipe through the bottom of the tank during charging with a high inlet temperature and in a very good way during discharging with a low inlet temperature. When the inlet to the pipes is through the top of the tank, thermal stratification is build up in a very good way during charging with a high inlet temperature and in a poor way during discharging with a low inlet temperature.

All in all, thermal stratification is established in a better way with the inlet to the stratifier placed at the bottom of the tank than with the inlet to the stratifier placed at the top of the tank.

7. Nomenclature

Quantity	Symbol	Unit
Momentum of energy	M	J m
Energy	E	J
Vertical distance	y	m
Volume	V	m^3
Specific heat capacity	c	J kg^{-1} K^{-1}
Density	ρ	Kg m^{-3}
Temperature	T	K
Temperature difference	ΔT	K
Number of tank layers	N	
Mix number	MIX	
Subscripts		
Tank layer	i	
Perfectly stratified tank	str	
Experimental tank	exp, $experiment$	
Fully mixed tank	mix	
Maximum inlet temperature	$inlet,max$	K
Minimum inlet temperature	$inlet,min$	K
Maximum tank temperature	$tank,max$	K
Minimum tank temperature	$tank,min$	K

8. References

Andersen E., 2007. Solar Combi Systems. Report no. R-156, Department of Civil Engineering, Technical University of Denmark, DTU Byg.

Andersen E., Furbo, S., 2008 a. Stratification devices. In proceedings of Conference on Thermal Storage, Prague, Czech Republic.

Andersen E., Furbo, S., 2008 b. Long time durability tests of fabric inlet stratification pipes. In proceedings of EuroSun 2008 Congress, Lisboa, Portugal.

Davidson J.H., Adams D.A, 1994. Fabric Stratification Manifolds for Solar Water Heating. Journal of Solar Energy Engineering, Vol. 116, pp. 130-136.

Furbo, S., 1989. Thermal bridges. EU Solar Storage Testing Group Final Report. Vol. II, Part B, 15, pp. 309-318.

Perers, B., Furbo, S., Anderssen, E., Fan, J., 2009. Solar/electric heating system for the future energy system. ISES conference 2009 Johannesburg, South Africa

Bengt Perers, Simon Furbo, Jianhua Fan, Elsa Andersen, Ziqian Chen, Solar combisystems with forecast control to increase the solar fraction and lower the auxiliary energy consumption, ISES Solar 2011 World Congress Proceedings, Kassel, Germany

SOLAR COMBISYSTEMS WITH FORECAST CONTROL TO INCREASE THE SOLAR FRACTION AND LOWER THE AUXILIARY ENERGY COST

Bengt Perers, Simon Furbo, Jianhua Fan, Elsa Andersen, and Ziqian Chen

Department of Civil Engineering, Technical University of Denmark, Kgs. Lyngby, Denmark

Abstract

Solar Combi systems still need quite a lot of auxiliary energy especially in small systems without seasonal storage possibilities. The control of the auxiliary energy input both in time and power is important to utilize as much as possible of the solar energy available from the collectors and also to use low backup energy prices during the day if electricity is used. The storage function and both stratified charging and extraction of heat, are very important, to separate different temperature zones in the storage. This paper describes a step towards forecast control for electricity based auxiliary energy sources. It can be either direct electric heating elements or a heat pump upgrading ambient energy in the air, ground, solar collector or waste heat from the house.

The paper describes system modeling and simulation results. Advanced laboratory experiments are also starting now with three different combisystems, operating in parallel. These systems will be briefly described too.

1. Introduction

In the deregulated electricity market situation in the Nordic countries, the electricity prices can vary dramatically from hour to hour. Therefore a smart control system that can use and adapt to these variations is very desirable, (Perers 2010, 2009). When a storage tank is available in the system, it can be used for storage of both solar thermal and auxiliary energy.

As more and more renewable energy sources are feeding into the electricity grid, the price variations will most probably be larger during the day. This happens now in Denmark where the wind power fraction in the grid is higher than 20%. This paper will present continued investigations for Danish conditions of climate, load, solar production, and electricity prices.

The work is done within a larger project with several Danish partners and the aim is to give the basis for a combisystem design that can be developed to a product on the market. The term combisystem means a solar heating system, that can deliver both heating and hot water to a house.The project is carried out in cooperation between Department of Civil Engineering, Technical University of Denmark, Danish Meteorological Institute (DMI), DTU Informatics, Technical University of Denmark, ENFOR A/S, AllSun A/S, Ohmatex ApS, Ajva ApS and COWI A/S.

Typically the electricity prices are higher during the day than in the night. This is good for solar heating systems that can reduce the use of backup electricity during peak hours of the day. Especially if the solar heating system inclusive the heat storage is well designed and properly sized. This happens partly automatically in existing combisystem with normal thermostatically controlled backup electric heating elements or a heat pump. Also the thermal load of a house has a daily variation, that match the price variations quite well, especially if the house has significant passive solar gains during the day. The problem toady is that the customer is not given credit to this as variable electricity prices are very uncommon yet on the market. But the project assumes that this will come soon for most customers as this is an important possibility to make it easier to introduce more renewable energy in the electric grid.

A normal control system in a combisystem does not have information about the weather and prices for the next day. Therefore the auxiliary charge can not be optimized for high solar production by minimizing the auxiliary charge and optimizing the power and time point, in the night before. If this was possible it would allow more solar input to the store and less use of backup energy at high electricity prices. In a normal combisystem a secure charging level in the store has to be maintained as if the next day will be rainy. Otherwise a lot of high cost electricity will be used during the peak hours of the next day to meet the load.

The paper describes further steps and progress in this area as well as describing the basic concept. The three test systems will also be described. The results can also be applicable to minimize the use of other backup energy sources and increase the solar fraction of a combisystem.

There are several control options for varying and thereby adapting the auxiliary charge of the storage. Figure 1 shows sketches of the main options. They can be divided into two main principles: Variable temperature and variable volume auxiliary charge. Both ways will open for advanced control of the auxiliary energy charge and thereby adaptation to the conditions of the electricity price variations, load and potential solar energy production the next day. To the left in figure 1 is the standard auxiliary charging method with a fixed volume and thermostat control and to the right the most advanced charging option with variable temperature and variable volume simultaneously.

In this paper these two extremes, traditional and advanced control, are compared to give a potential for improvement by smart tanks and smart control in a combisystem.

In this case a simplified calculation model has been chosen that can be implemented in Excel. The detailed TRNSYS system model described in previous papers (Perers 2010 and 2009) turned out to be problematic to use for the most advanced forecast control, with a combination of variable temperature and variable volume options. Therefore to be able to proceed and to find the maximum potential improvement level, a simplified model option was chosen as an intermediate step.

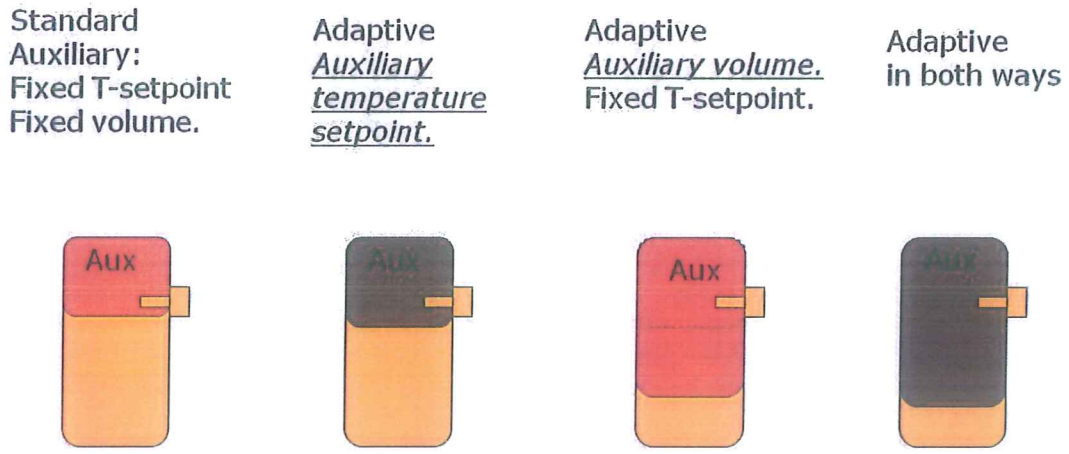

Fig. 1: Auxiliary charge control options for the storage in a combisystem. The standard solution to the left with fixed volume and thermostat control and the most advanced to the right with variable volume and temperature and forecast control.

In this study the forecast control is utilizing the known weather data for the next day in the measured weather data file that is available in the simulation. This was done to separate and eliminate, uncertainties in system modeling and control from inevitable uncertainties in the weather forecasts. DTU Informatics are working with the next step how to utilize real forecast data from DMI for smart control and handle these added uncertainties and still maintain an acceptable energy comfort in the house (Bacher 2011)

Experimental investigations are also an important part of this project. In figure 2 a description is given of the three laboratory combisystems and the three different tank designs, under monitoring at DTU Byg. These combisystems will be investigated to find an optimal tank configuration for this application. Tests of variable temperature and variable volume auxiliary charge and with extreme stratification measures, both during charge and discharge, in combined solar and auxiliary operation, are the main aims of the tests.

Fabric stratifiers will also be tested in the systems to keep the high temperatures in the top of the tank to meet the load and to have as low inlet temperature as possible in the bottom for the solar collectors and a possible heat pump as auxiliary source. The stratifiers are applied both in the load loops and in the collector loop.

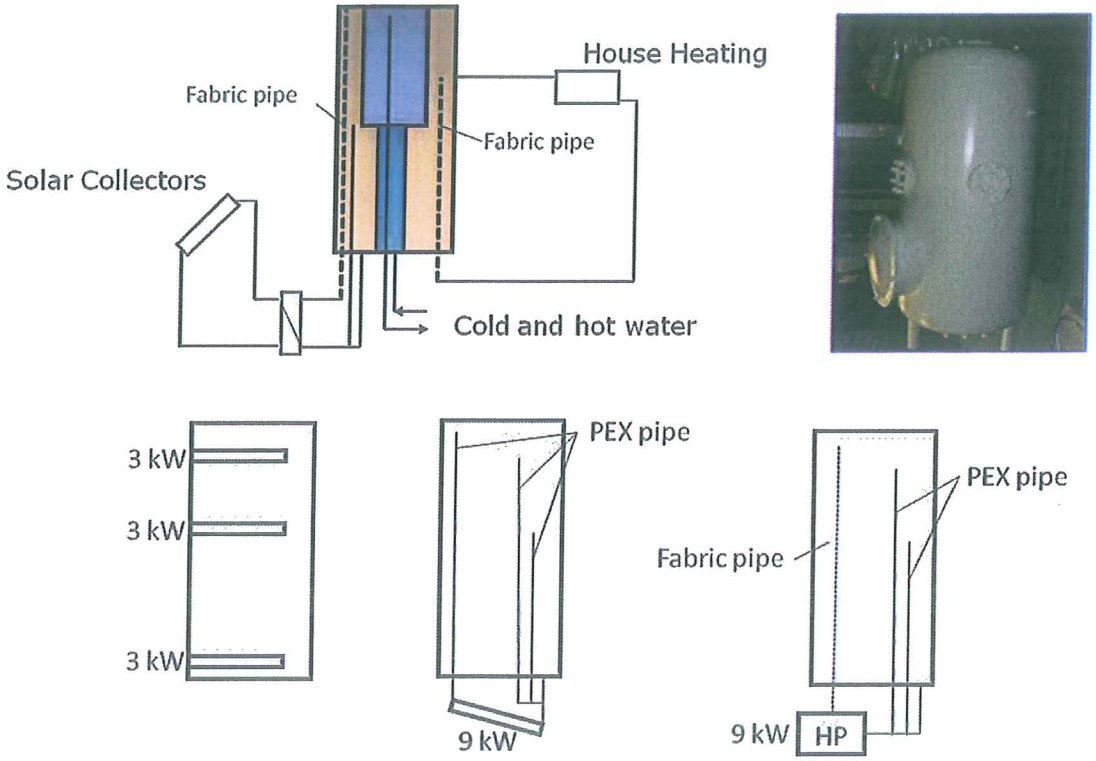

Fig. 2: Description of the system and the three tank designs in the system tests at DTU Byg. The combisystems will be investigated to find an optimal tank configuration for this application. Tests of variable auxiliary temperature and variable volume auxiliary charge and extreme stratification measures both during charge and discharge, are the main aims of the tests. Also a heat pump auxiliary solution is tested.

2. The simplified energy balance model

The simplified energy balance model, used here is shown in figure 3. This is also closer to the simplified system model that probably will be used in the controller. The full TRNSYS model in previously presented research work in this project Perers (2009, 2010) is probably too complicated with hundreds of parameters to be set for each system, to be implemented in a commercial controller.

Still all relevant energy flows in and out of the tank in the system are present, so no energy is neglected. In the figure also the very simple equation for the auxiliary energy need is shown. To be complete and realistic one also have to check the minimum and maximum charge level Q(t) so that the minimum load temperatures can be delivered and that the tank is not overheated or boiling of course.

The component models are also very much simplified to first order options, to make it easy to implement in Excel without the need for iterative procedures. Still also here the main effects are present. In a next step it can be possible to refine both the system model and component models in Excel, but the accuracy gain is limited for the aim of this study to find out the potential improvement level.

For future design optimization of the components together with manufacturers though, continued work with the full TRNSYS model can be very interesting and the idea is to validate the full TRNSYS model against the tests in the laboratory.

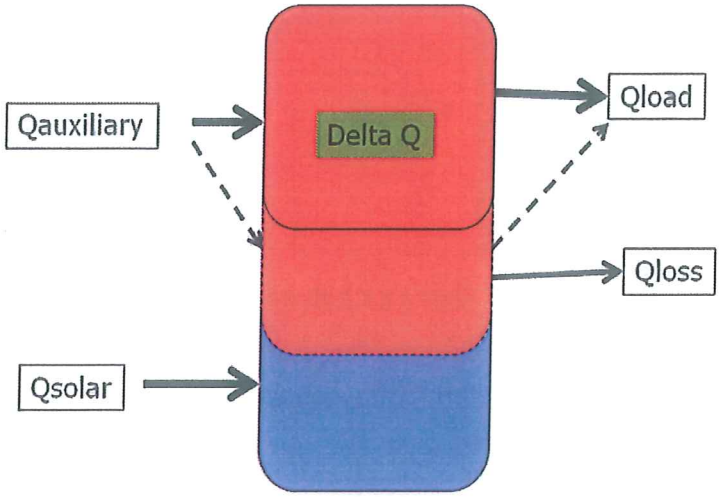

Qaux = Qload + Qloss + DeltaQ – Qsolar

DeltaQ=Q(t2) - Q(t1)

Q(t) > Qminimum

Fig. 3: The energy flows considered in the simplified model of the combisystem. The very simple equation for the required auxiliary charge is also given, together with limits for the energy content Q(t) of the store.

3. Input data and calculations

The same detailed and carefully monitored climate data from the DTU Byg weather station for year 2008 are used here as in the previous detailed TRNSYS simulation studies. Also the same hourly electricity price data from Nordpool for year 2008 are used. The forecast calculations are based on known climate data the next day in the climate file and not forecast data from DMI to be able to separate different effects and uncertainties from each other.

The system model is extremely simple as shown in figure 3. The aim here is to make a potential study how much ideal forecast control and ideal tank behavior (working as a capacitor for heat) can reduce the annual auxiliary costs in combination with addition of energy from a solar collector.

The component models for solar collector and building are simplified to stationary first order models to avoid iterations in Excel. The storage tank is modeled according to the energy balance given in figure 3.

The collector is tilted 45 deg and oriented due south. The collector model is an extremely simple first order model with an effective zero loss efficiency of 0.75 and a total heat loss factor of 3.5 W/m²K including pipe losses. The mean operating temperature of the collector is assumed to be constant (set to 50C in the presented calculations). In a real system this temperature is of course varying with many other variables and parameters, in the system but here this is second order parameter and only affects the collector and pipe heat losses.

The tank is modeled as an ideal "themal capacitor" and only the energy flows are studied, with no mixing between the energy flows as solar and auxiliary. The load and heat losses are also just extracted as a change in energy content of the store. The heat losses are assumed to be constant (in this case set to 100 W total for the tank plus system outside the collector loop). In reality of course the losses are very dependent on the tank design and control. But as the charging and discharging powers are of a magnitude 10-100 times larger, this heat loss variation was neglected in the presented calculations. But of course to optimize the system and for component design this should be variable and determined by full system simulation like in the TRNSYS model. Low heat losses are really essential for a well performing combisystem.

The auxiliary volume and auxiliary temperature of the tank are variable (but not calculated explicitly). The tank size is automatically adapted and set to the worst winter day, when the store has to be able to store the forecasted auxiliary need for one day, with the whole tank used as auxiliary volume. At this time of the year the solar charge is small and this volume need is neglected at this stage.

In the normal reference system the auxiliary part for the store is kept at a constant minimum temperature of 60°C, but occasionally when there is a lot of solar radiation available the tank temperature will increase above this level. If the tank is heated above a max temperature of 95°C the solar and auxiliary charge is stopped.

In the advanced forecast control alternative the auxiliary energy charge is done in the night and in an amount that will exactly meet the total load during the next day including house heating, hot water consumption and heat losses, but minus the predicted solar charge during the next day.

The control timing of the auxiliary charge is simplified to a fixed time period each morning when the prices are at minimum around 3 o'clock very regularly in the Danish grid. This is due to the low load in the grid at the end of the night, when very little activities occur in the society. In the full forecast control also the time for charge should be optimized but this turned out to be too complicated in this simplified potential study. An estimate is therefore given for this case in the results, using the lowest price every day to calculate the annual auxiliary cost.

Figure 4 shows an example of the hourly energy flows and energy content in the store in two control options: 1) normal control and 2) forecast control. In the normal control case (1) the auxiliary energy is added all the day instantaneously when needed. In the case of forecast control (2) the auxiliary supply is done in the night to use the lowest possible electricity prices. The absolute level of the energy content curves Qstore=Q(t) (two upper ones) are not representative for the future system design. Then the tank with forecast control should be possible to discharge deeper each day. Here the energy content is shown relative to 0 °C with a minimum allowable temperature of 60°C in the store. In a real system the advanced auxiliary control can allow the store to go below the energy content of the normal storage, as the forecast information warrants the comfort for the next day. Also extreme stratification measures will work in this direction to allow a lower minimum charging level of the tank.

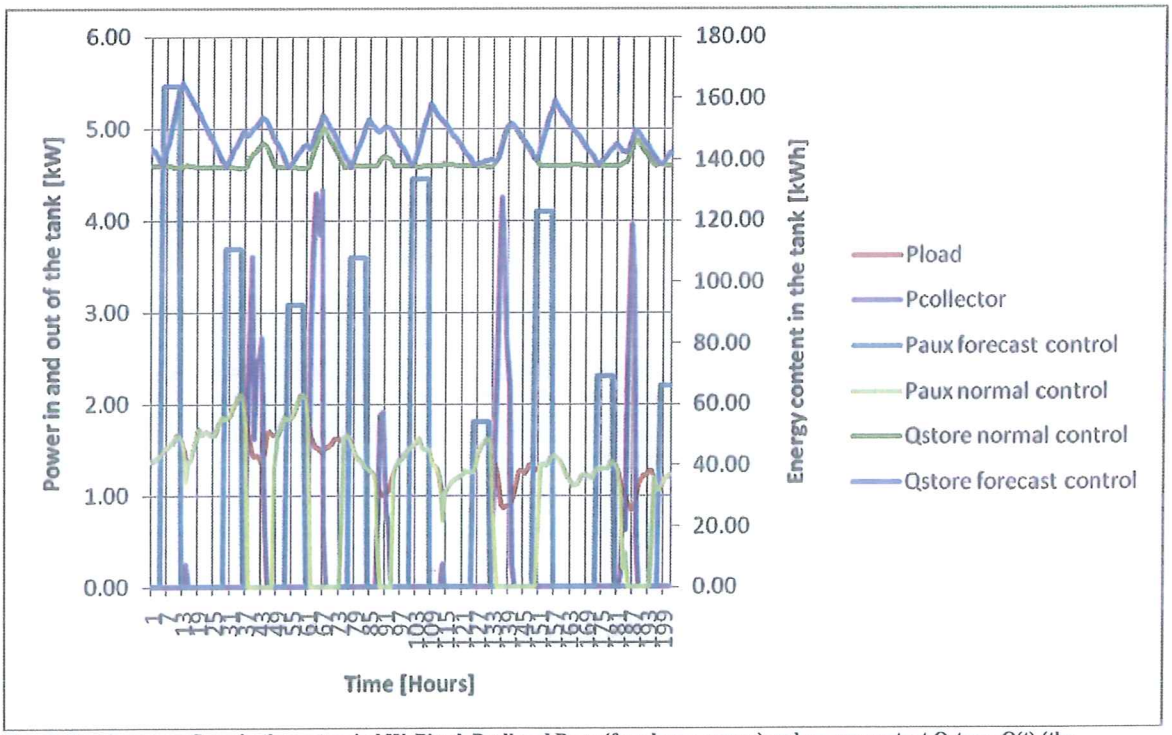

Fig. 4: Hourly energy flows in the system in kW, Pload, Pcoll and Paux (four lower curves) and energy content Qstore=Q(t) (the two upper curves) for the two control options. 100W/K house and 10 m² of collectors. The absolute level of the two upper energy content curves are not relevant for the auxiliary cost results, only the variations that reflect smart auxiliary charge at low prices.

4. Results

The results of the calculations for annual auxiliary costs in DKK (Nordpool cost level), have been summarized in figure 5, 6 and 7.

In figure 5 the costs are given for two different building insulation standards 200W/K and 100W/K, five different storage sizes and four different solar collector areas 5-20 m². The hot water load has been the same for all cases 100 litres/day.

The cost level is at the NORDPOOL electric stock exchange level http://www.nordpoolspot.com/
This is much lower than the final customer price level, so the potential savings in absolute numbers, in DKK per year, are much larger than shown in the diagrams.

The tank volume has been adapted to a minimum size needed to store enough energy for the different options. (The leftmost points on all curves represents a traditional tank design and a volume of 750 and 500 l has been set to be appropriate for the two house insulation standards).

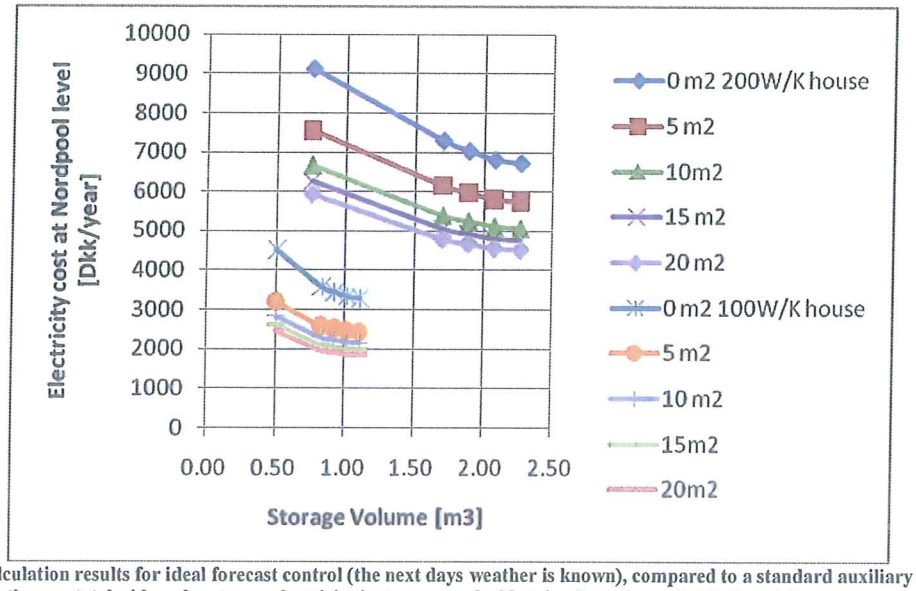

Fig. 5: Calculation results for ideal forecast control (the next days weather is known), compared to a standard auxiliary control where the thermostat decides when to use electricity instantaneously. Note in all cases a variable electricity cost is assumed for the system owner. The case of fixed price at the annual average level is only shown in figure 6.

In Figure 6 and 7 the same calculations are shown as a function of collector area. The tank volumes are also the same as in figure 5. Only the 200W/K house is shown in figure 6 to limit the number of curves. But here also the reference case is shown with constant electricity price all year (uppermost curve) and the extreme case of using the lowest price every day (24 hours) is shown too, as the lower curve giving the extreme improvement potential. (In figure 5 all curves are for the same variable electricity price conditions and only the auxiliary charging strategy/principle is changed.).

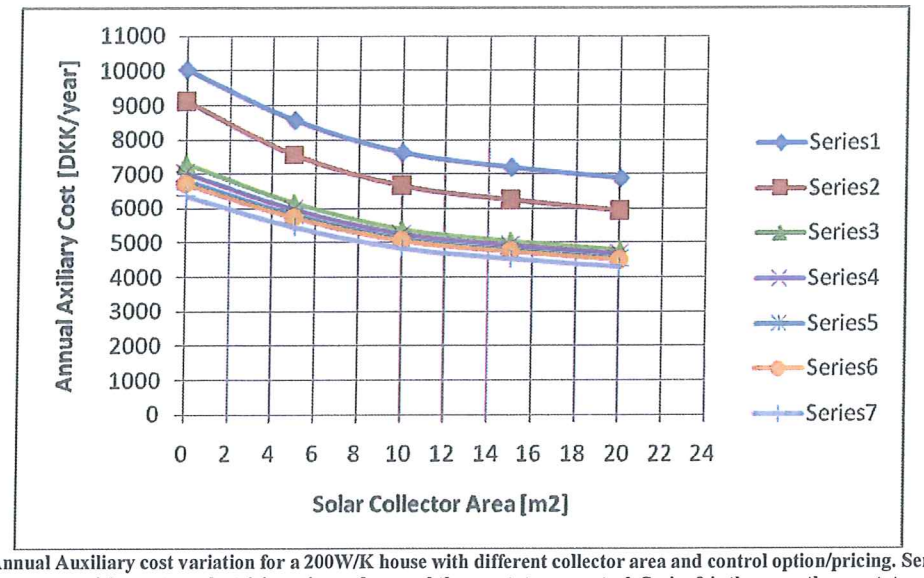

Fig. 6: Annual Auxiliary cost variation for a 200W/K house with different collector area and control option/pricing. Series 1 is the reference case with constant electricity price and normal thermostat aux control. Series 2 is the same thermostat control as series 1, but variable electricity price. Series 3 to 6 are shorter and shorter charging period and higher charging power around the minimum price time each day. Series 7 is the extreme case when the lowest electricity price each 24 hours is used.

In figure 7 below the same calculations and curves are given for a well insulated house 100W/K. It can be seen that the optimum collector area is smaller as expected closer to what is needed for the 100 l/day hotwater demand. Still the relative cost savings between a traditional system without solar collectors and an advanced system with solar is in the range of 50%.

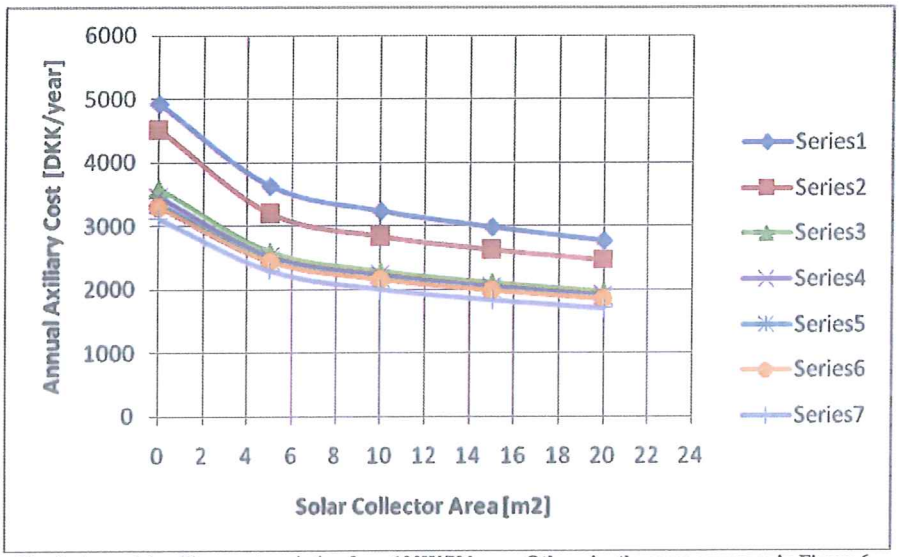

Fig. 7: Annual Auxiliary cost variation for a 100W/K house. Otherwise the same curves as in Figure 6.

The extra cost of receiving the maximum electric power level (max kW) needed to charge the tank in a short time span, is not included here, but this pricing may be adapted on the market in the future, as there is plenty of power available in the grid when the load is low and the electricity kWh cost is close to minimum. The curve series 3 in fig 6 with power needs of maximum 17 kW can be met by normal domestic electric connections of three phase 400V 25 A for the 200W/K house. For the 100W/K house series 3-5 can be covered with 16- 25 A three phase fuses at the final customer. The very lowest curves need special arrangements to meet the maximum load and are more shown as limiting curves with just 1 hour or less charging time per day. In case of a heat pump the electric power need, is at least halved, for normal conditions and the electric power need is no problem.

5. Conclusions

The combination of smart auxiliary control and addition of 10m² of solar collectors in a combisystem can reduce the auxiliary cost for a house by around 50% in an example for Danish conditions and a normal house.

The annual auxiliary cost savings is around 3000-5000 DKK on the Nordpool electricity cost level. The cost savings at the final customer price level is hard to predict, but can be estimated to two to three times larger depending on how the variable price structure will be and how energy and CO_2 tax will change in this case.

For the same collector area in the system a smart forecast auxiliary control has the potential of reducing the auxiliary electricity cost by 30-40% more alone.

From the results one can estimate that for a 200W/K house with 100l/day hot water load, 10m² of collectors is reasonable and for a well insulated house (100W/K) around 5m² can be recommended.

The very simple system model and forecast control shown here seems to give reasonable results and may be used as a template for commercial controller programming. Though a lot of refinements are possible.

This first order system modeling can give reasonable values for the potential value of smart forecast control and solar contribution in a solar combisystem. No energy flows are forgotten, but the exact levels are approximative in time and size. Compared to a full TRNSYS simulation the complexity and number of parameters needed are one or two orders of magnitude lower. For component design optimization and detailed control research the full TRNSYS model is needed and will be validated against measured data in the next step of the project.

6. References

Perers, B., Furbo, S., Andersen, E., Fan, J., (2010). Solar/electric heating systems using smart solar tanks and variable electricity costs . Eurosun Conference 2010 Graz Austria.

B. Perers, S.Furbo, E. Anderssen, J.Fan., (2009). Solar/electric heating system for the future energy system. ISES conference 2009 Johannesburg, South Africa

P. Bacher, H.Madsen, B.Perers. (2011). Short term Solar Collector Power Forecasting. ISES Solar World Congress 2011, Kassel, Germany.

Simon Furbo, Elsa Andersen, Udvikling af intelligent styresystem til fremtidens solvarmeanlæg, HVAC magasinet, 2012, 1, 22-28

Dit branchemagasin fra TechMedia

MAGASIN FOR KLIMA- & ENERGITEKNIK, MILJØ, BYGNINGSINSTALLATIONER & - NETVÆRK

HVAC Magasinet

1
Januar 2012
Årgang 48

Styring af solvarme

VA-møde • Energiforsyning • Passivhusvarme

Se pigen med ballonerne på side 9

Udvikling af intelligent styresystem til

Forskningsprojekt skal klarlægge hvorledes en individuel varmeforsyningsenhed til enfamiliehuse baseret på solvarme, elpatron/varmepumpe samt et avanceret varmelager og styresystem bedst udformes til fremtidens energisystem

Af lektor Simon Furbo og seniorforsker Elsa Andersen, DTU Byg

I perioden 2008-2012 gennemføres forskningsprojektet "Solar/electric heating systems in the future energy system" i et samarbejde mellem DTU Byg, DTU Informatik, DMI, ENFOR A/S, COWI A/S, Ajva ApS og Ohmatex ApS. Interesserede styresystem- og solfangerfabrikanter inviteres til at deltage i den sidste del af projektet i forbindelse med udvikling af et intelligent styresystem. Projektet beskrives i denne artikel. Forskningsprojektet er finansieret af Styrelsen for Forskning og Innovation under Det Strategiske Forskningsråds program for Energi og Miljø.

Projektets formål er at klarlægge hvorledes en individuel varmeforsyningsenhed til enfamiliehuse baseret på solvarme, elpatron/varmepumpe samt et avanceret varmelager og styresystem bedst udformes til fremtidens energisystem. Desuden skal det klarlægges hvor velegnet sådan en varmeforsyningsenhed er for den enkelte forbruger og for vores fremtidige energisystem.

Lav elpris

Varmen produceres dels af solfangere, dels af en elpatron/varmepumpe. Elpatronen/varmepumpen skal så vidt muligt kun køre på tidspunkter hvor solvarme ikke kan klare hele varmebehovet og hvor elprisen er lav, for eksempel på grund af stor elproduktion fra vindmøller og/eller på særlige tidspunkter af døgnet. Enheden forsynes med et intelligent varmelager og et intelligent styresystem hvor styringen af elpatronen/varmepumpen baseres på prognoser for elpris, varmebehov og solvarmeproduktion. Styresystemet baseres på vejrudsigter.

Varmeforsyningsenheden forventes at være et mere attraktivt solvarmeanlæg end traditionelle solvarmeanlæg og anlægstypen kan bidrage til en forbedret udnyttelse af elproduktionen fra vindmøller i vindrige perioder. Bliver anlægstypen udbredt kan den bidrage til at lette indpasningen/rentabiliteten af vindmøller i elsystemet og forøge andelen af landets energiforbrug, der dækkes af vedvarende energi.

Fem hovedelementer

Forskningsprojektet består af fem hovedelementer: 1) Solvarmeanlæg baseret på et intelligent varmelager, 2) Modeller for detaljerede vejrudsigter, 3) Prognoser for huses varmebehov og for elpris, 4) Avanceret styresystem baseret på forven-

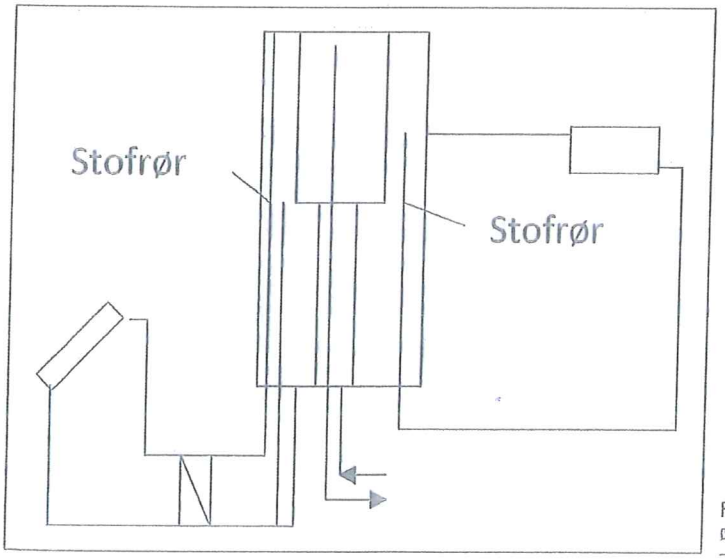

Figur 1. Principskitse af varmelager uden intelligent elopvarmning af øverste del.

tet varmebehov, solvarmeproduktion og elpris og 5) Analyse af hvorledes varmeforsyningsenheden påvirker hele energisystemet hvis den benyttes i stort omfang. Korte beskrivelser af de enkelte hovedelementer:

1. Solvarmeanlæg baseret på et intelligent varmelager: Der gennemføres detaljerede undersøgelser af forskellige udformninger af solvarmeanlægget. Specielt fokuseres undersøgelserne om det intelligente varmelager. Undersøgelserne gennemføres på DTU Byg i samarbejde med Ajva ApS og Ohmatex ApS.

2. Modeller for detaljerede vejrudsigter: Varmeforsyningsenheden planlægges styret af et avanceret styresystem baseret på forventet varmebehov, solvarmeproduktion og elpris. Derfor er der behov for pålidelige vejrudsigter. Forskellige modeller for detaljerede vejrudsigter vil blive undersøgt. Der lægges vægt på hvor nøjagtigt modellerne kan forudsige huses varmebehov og solvarmeanlægs varmeproduktion. Undersøgelserne gennemføres ved DMI, størstedelen i form af et Ph.D. studium.

3. Prognoser for huses varmebehov og for elpris: Der udvikles statistiske modeller til forudsigelse af huses varmebehov, af elpriser og af solvarmeproduktion. Modellerne benytter sig af input fra vejrudsigterne, som er omtalt oven for. Undersøgelserne gennemføres i et samarbejde mellem DTU Informatik og ENFOR A/S, hovedsageligt i form af et Ph.D. studium ved DTU Informatik.

4. Avanceret styresystem baseret på forventet varmebehov,

Figur 2. Her vises to af de tre varmelagre, som er under afprøvning i solvarmeanlæg. Den øverste del af de tre intelligente varmelagre opvarmes af en elpatron, af tre elpatroner og af en varmepumpe, som vist skematisk på figur 3.

solvarmeproduktion og elpris: Det klarlægges hvorledes et styresystem udformes så det kan benytte DMI's vejrudsigter og DTU Informatik/ENFOR's prognoser for elpriser, solvarmeproduktion og huses varmebehov til at styre elvarmelegemer/varmepumpe og solvarmeanlæg bedst muligt. Undersøgelserne gennemføres af projektets deltagere forhåbentlig i samarbejde med en styresystem- eller solfangerfabrikant.

5. Analyse for hele energisystemet: Det undersøges hvorle-

Informationsmøde

Der arrangeres onsdag den 28. marts kl. 14:00 et informationsmøde for interesserede små/mellemstore fabrikanter. På mødet, der finder sted på DTU Byg, bygning 119, rum 107, Nordvej, DTU, 2800 Kgs. Lyngby, vil der blive informeret om projektet samt samarbejdsmulighederne og -betingelserne. Information om projektet og samarbejdsmulighederne fås/tilmeldelse til informationsmødet sker ved henvendelse til: Simon Furbo, email: sf@byg.dtu.dk, tlf.: 45 25 18 57.

Tre solvarmeanlæg med forskelligt udformede intelligente varmelagre er for tiden under afprøvning i DTU Bygs prøvestand for solvarmeanlæg. Hvert anlæg, som har et solfangerareal på 9 m², er baseret på et 725 l varmelager fra Ajva.

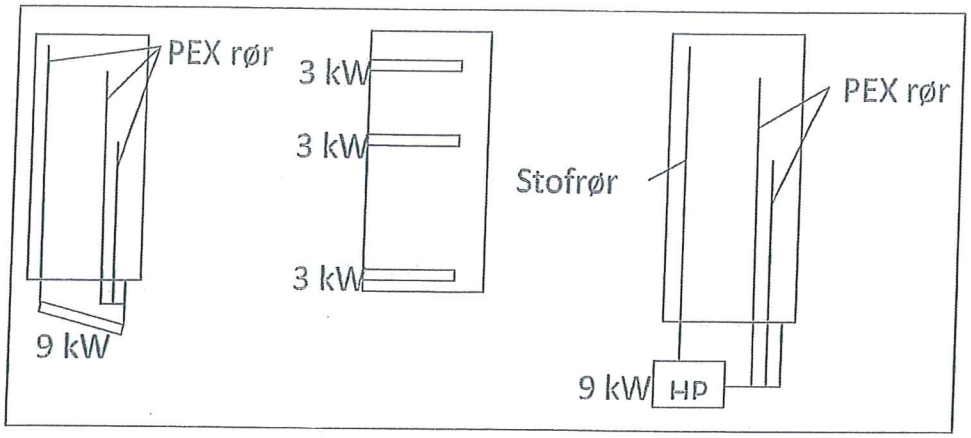

Figur 3. Principskitse af opvarmning af øverste del af de tre intelligente varmelagre.

des varmeforsyningsenheden, hvis den benyttes i stort omfang, påvirker hele energisystemet. Undersøgelserne gennemføres af COWI A/S.

Solvarmeanlæg under afprøvning

Tre solvarmeanlæg med forskelligt udformede intelligente varmelagre er for tiden under afprøvning i DTU Bygs prøvestand for solvarmeanlæg. Hvert anlæg, som har et solfangerareal på 9 m², er baseret på et 725 l varmelager fra Ajva ApS. Varmelagrene kan opvarmes af solfangerne og i perioder, hvor solfangerne ikke kan klare hele opvarmningen, opvarmes de tre varmelagre henholdsvis af en elpatron, af tre elpatroner og af en varmepumpe. Varmelagrene er udformet som vist skematisk på figur 1. Varmelageret er et tank i tank varmelager med en indbygget varmtvandsbeholder til brugsvandsopvarmning. Solvarmen overføres til varmelageret ved at vand cirkuleres fra varmelageret gennem en ekstern varmeveksler og retur til varmelageret gennem et stofstratifikationsindløbsrør. På denne måde opbygges der en fordelagtig temperaturlagdeling i varmelageret når solfangerne producerer varme. Varme overføres fra den øverste del af varmelageret til varmeafgivelsessystemet og retur til varmelageret gennem et andet stofstratifikationsindløbsrør.

Det ene varmelager er forsynet med en elpatron indbygget i tre rørkredse, der er koblet til varmelagerets øverste del på en sådan måde at varme overføres fra elpatronen til toppen af varmelageret ved selvcirkulation i rørkreds/varmelager i perioder med elpatrondrift. Opvarmningen kan stoppes så det elopvarmede volumen tilpasses det forventede varmebehov og så det elopvarmede volumen opvarmes til en ønsket temperatur med mindst muligt energiforbrug.

Det andet varmelager er forsynet med tre elpatroner i varmelageret i forskellige niveauer. Elpatronerne kan opvarme forskellige vandvolumener til ønskede temperaturer.

Den øverste del af det tredje varmelager, hvis volumen kan tilpasses det forventede varmebehov, kan opvarmes af en varmepumpe.

Intelligent styresystem

De tre solvarmeanlæg afprøves parallelt under ensartede driftsbetingelser. På den måde kan det klargøres hvordan varmelageret udformes, så forbrugerens energipris bliver så lav som mulig. Forskellige styringsstrategier undersøges med hensyn til de termiske og energimæssige forhold for varmelageret, solvarmeanlæggets pålidelighed, forbrugerens energipris samt pris-, produktions- og markedsføringsmæssige forhold for styresystemet.

Undersøgelserne vil klarlægge den bedst egnede styringsstrategi. Styringsstrategierne baseres på varmelagerets energiindhold, DMI's vejrudsigter og prognoser for elpriser, solvarmeproduktion og husets varmebehov, så elvarmelegemer/varmepumpe og solvarmeanlæg styres på en sådan måde, at varmebehovene dækkes billigst muligt. Styringsstrategier undersøges teoretisk ved hjælp af simuleringsmodeller for forskelligt udformede solvarmeanlæg.

På basis af undersøgelserne udvælges den bedste styringsstrategi, som implementeres i et styresystem, som benyttes i det bedste forsøgssolvarmeanlæg, som afprøves i DTU Bygs prøvestand for solvarmeanlæg. Målinger fra forsøgssolvarmeanlægget vil vise hvorledes solvarmeanlægget inklusive det intelligente styresystem bedst udformes.

Invitation til samarbejde

For at fremskynde tidspunktet hvor intelligente styresystemer kan introduceres på markedet inviteres der til samarbejde med små og mellemstore styresystem- og solfangerfabrikanter. Et samarbejde med en styresystem-/solfangerfabrikant om intelligente styresystemer vil muliggøre at der tages hensyn til produktions- og markedsføringsforhold for styresystemet, som udvikles i projektet. Derudover vil fabrikantens erfaringer med hensyn til pålidelighed af styresystemer være værdifulde i forbindelse med udviklingsarbejdet.

I dag markedsfører styresystem-/solfangerfabrikanter standard styresystemer, som ofte kan produceres billigere af udenlandske fabrikanter. Hvis danske fabrikanter fremover skal have succes inden for solvarmeområdet har de behov for at udvikle og tilbyde komponenter og anlæg med forbedret ydelse/pris forhold i forhold til standardkomponenter og anlæg. Derfor kan den deltagende fabrikant, som udvikler et intelligent styresystem til solvarmeanlæg, få en fordel på det store internationale solvarmemarked.

Desuden kan de principper, som styringsstrategien benytter, anvendes til andre avancerede styresystemer. Fabrikanten kan derfor udnytte erfaringerne fra samarbejdet i forbindelse med firmaets generelle udviklingsarbejde vedrørende styresystemer.

Forskningsprojektet har mulighed for at finansiere 60 pct. af omkostningerne for en styresystem-/solfangerfabrikant i forbindelse med udviklingen af det intelligente styresystem.

Peder Bacher, Henrik Madsen, Bengt Perers, Henrik Aalborg Nielsen, A non-parametric method for correction of global radiation observations, Solar Energy 88, p. 13-22, 2013

Available online at www.sciencedirect.com

SciVerse ScienceDirect

Solar Energy 88 (2013) 13–22

SOLAR ENERGY

www.elsevier.com/locate/solener

A non-parametric method for correction of global radiation observations

Peder Bacher [a,*], Henrik Madsen [a], Bengt Perers [b], Henrik Aalborg Nielsen [c]

[a] DTU Informatics, Technical University of Denmark, DK-2800 Lyngby, Denmark
[b] DTU Civil Engineering, Technical University of Denmark, DK-2800 Lyngby, Denmark
[c] ENFOR A/S, DK-2970 Hørsholm, Denmark

Received 12 April 2012; received in revised form 1 October 2012; accepted 30 October 2012
Available online 23 December 2012

Communicated by: Associate Editor David Renne

Abstract

This paper presents a method for correction and alignment of global radiation observations based on information obtained from calculated global radiation, in the present study one-hour forecast of global radiation from a numerical weather prediction (NWP) model is used. Systematical errors detected in the observations are corrected. These are errors such as: tilt in the leveling of the sensor, shadowing from surrounding objects, clipping and saturation in the signal processing, and errors from dirt and wear. The method is based on a statistical non-parametric clear-sky model which is applied to both the observed and the calculated radiation in order to find systematic deviations between them. The method is applied to correct global radiation observations from a climate station located at a district heating plant in Denmark. The results are compared to observations recorded at the Danish Technical University. The method can be useful for optimized use of solar radiation observations for forecasting, monitoring, and modeling of energy production and load which are affected by solar radiation.

Keywords: Global solar radiation; Solar energy; Observations; Correction; Quality control; Statistical clear-sky model

1. Introduction

The transition to a reliable and secure energy system based on weather dependent production technologies, especially wind and solar, will require new methods for automated handling of climate data recorded at, in most cases, unsupervised and uncalibrated stations. Reliable observations of solar radiation are an important source of information for operation of the energy system, especially for the energy production and load which are dependent on the solar radiation, for example production from photovoltaics and solar collectors, and load from heating and cooling of buildings.

Observations of solar radiation are exposed to many sources of errors. Younes et al. (2005) list the most important types of errors and divide the errors into two major categories: equipment errors and operation related errors. The present solar radiation sensor technology makes it easy and cheap to install and connect sensors to the Internet, both for professional and amateur applications. Web sites already provide on-line data (DMI, 2012), which can become an important source of information for operation of energy systems. Such, mostly unsupervised and unvalidated installations, will be highly exposed to different error sources.

In the present study observations of global radiation from a station at a district heating plant in Sønderborg, Denmark, are used. Three types of errors are found in

* Corresponding author. Tel.: +45 60774725.
E-mail address: pb@imm.dtu.dk (P. Bacher).
URLs: http://www.imm.dtu.dk/~hm (H. Madsen), http://www.enfor.eu (H.A. Nielsen).

0038-092X/$ - see front matter © 2012 Elsevier Ltd. All rights reserved.
http://dx.doi.org/10.1016/j.solener.2012.10.024

Nomenclature

G_t	observed global radiation (W/m^2)
G_t^{nwp}	numerical weather predictions (NWPs) of global radiation (W/m^2)
G_{cs}	clear-sky global radiation (W/m^2)
B_{cs}	direct clear-sky global radiation (W/m^2)
D_{cs}	diffuse clear-sky global radiation (W/m^2)
G	global radiation (W/m^2)
I_{ext}	extraterrestrial radiation (W/m^2)
G_t^{pr}	projection of global radiation to the plane normal to the direct solar radiation (W/m^2)
$\widehat{G}_t^{\text{pr,cs}}$	estimated clear-sky radiation on a plane normal to the direct solarradiation (W/m^2)
$\widehat{G}_t^{\text{cs}}$	estimated clear-sky global radiation (modeled based on observations) (W/m^2)
$\widehat{G}_t^{\text{nwp,cs}}t$	clear-sky global radiation for numerical weather predictions (NWPs) (W/m^2)
$\widehat{G}_t^{\text{co}}$	corrected global radiation (W/m^2)
θ_t^{zenith}	solar zenith angle (rad)
$\tau_{\text{a,B}}$	transmittance function of the atmosphere for direct radiation under clear-sky conditions
τ_{c}	transmittance function of clouds in the atmosphere
β_t	parameter vector for the local quantile regression
$\rho_q(u)$	the quantile regression objective function
q	sample quantile to be estimated in the local quantile regression
i	counter of days (days)
j	counter in samples
t	time (h)
t_{sp}	sample period (h)
h_{doy}	bandwidth of kernel function in the *day of year* dimension (days)
h_{tod}	bandwidth of kernel function in the *time of day* dimension (h)

the observations: tilt in the leveling of the sensor, shadowing from surrounding objects, and clipping at a maximum level. A method is presented for correction of the observations on the basis of information extracted from global radiation calculated using a model based on physical principles. The method is based on a non-parametric statistical clear-sky model and requires no further information about the installation and sensor than the observed values and the location of the station. With the statistical clear-sky model the sensor output level under clear-sky conditions is modeled directly from the observations. This is compared to solar radiation calculated with a clear-sky model based on physical modeling of the optical effects through the atmosphere, such as the models described by Davies and McKay (1982), Bird (1984), Rigollier et al. (2000), Mueller et al. (2004), and Ineichen (2006). In the preset study forecasts from a numerical weather prediction (NWP) model is used. The result after correction of the observations is compared to high quality measurements recorded at the Danish Technical University.

Studies on quality control of measured solar radiation data can be found in the literature. The procedures are semi-automatic and are mostly based on comparison to physical models for detection of erroneous measurements (Geiger et al., 2002; Younes et al., 2005; Isaac and Moradi, 2009; Journée and Bertrand, 2011).

The paper is organized as follows: the data used in the study is presented in the next section. This is followed by a section in which the statistical clear-sky model is described and a section where the correction is presented. The paper ends with a discussion of the method and a conclusion.

2. Data: observations and numerical weather predictions of global radiation

The data used in this study consists of time series of global radiation observed at two weather stations: one located in Sønderborg (54.91°N and 9.80°E) and one located at DTU Byg in Lyngby (55.79°N and 12.52°E), both in Denmark. In addition NWPs of global radiation for the same locations are used. All values are hourly averages. All times are in UTC and the time points are set to the end of the hour.

2.1. Observations

The observations from Sønderborg are recorded with a weather station, which is located at a district heating plant. The weather station is mounted on a pole on a single-storey building as seen on the image in Fig. 1. No information about the type of the solar radiation sensor was available. The time series from Sønderborg is

$$\{G_t; \quad t = 1, \ldots, N\} \tag{1}$$

where $N = 17520$ and G_t is the observed average global radiation between time t and $t-1$. The upper plot in Fig. 2 shows the series which spans from 2009-01-01 to 2011-01-01. From this plot it is readily seen that the observations are not without systematic errors, for example it can be seen that the values are clipped at a maximum level. This and other types of systematic errors are corrected for the Sønderborg observations using the method described in this paper.

Fig. 1. The weather station in Sønderborg, which is mounted on a pole on the roof of a single-storey district heating plant building (in the image it is on the left side of the building).

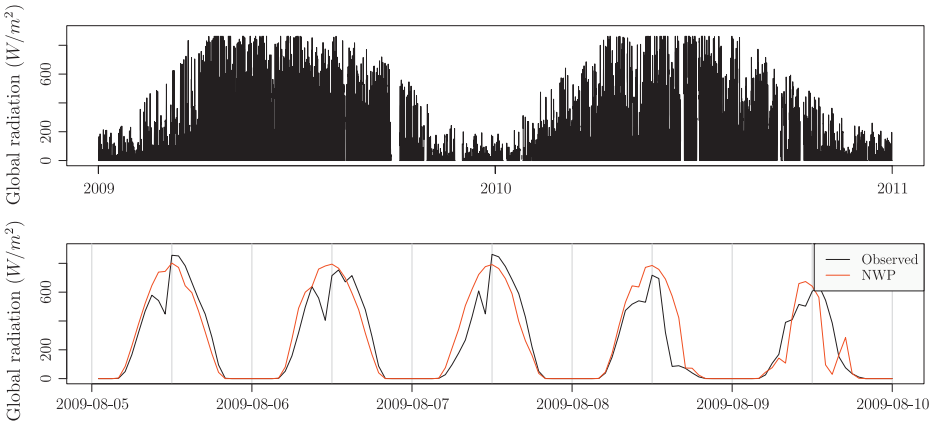

Fig. 2. The upper plot shows the time series of observed global radiation in Sønderborg. In the lower plot the observations and NWPs of global radiation in Sønderborg are shown for 5 days in August 2009.

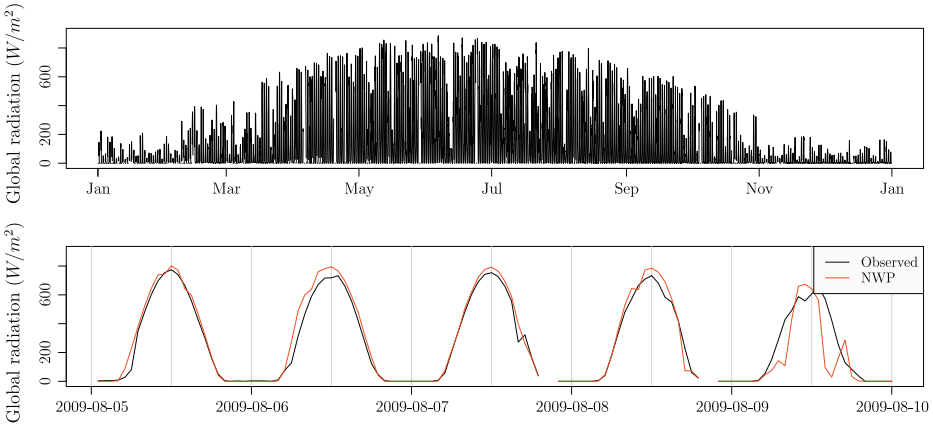

Fig. 3. The upper plot shows the time series of observed global radiation at DTU Byg covering the entire year 2009. In the lower plot the observations and NWPs of global radiation at DTU Byg are shown for five days in August 2009.

The second series of observed global radiation is from a weather station at DTU Byg in Lyngby and is used as a reference to check the corrected data. The upper plot in Fig. 3 shows the series which spans from 2009-01-01 to 2010-01-01. It was measured with a Kipp and Zohnen CM10 pyranometer and the weather station was regularly supervised in the measuring period. The measurement error is in the range of maximum ±3% from the world standard and high class calibrated sensor inter-comparisons indicate an error within the range of ±1%. The lower plot in Fig. 3 shows the observations together with the NWPs of global radiation (defined in the next section) for five days in August 2009.

It is seen that the level of the observed global radiation is generally lower than the level of the NWPs, but that this there is no systematic difference between the deviation in the morning and in the afternoon. The lower level is most likely due to a bias in the NWPs. Since the accuracy of the DTU observations is high and no systematic errors, apart from the generally lower level, is seen, then it is found valid to assume that the DTU observations can used be as a reference to verify the NWPs and the results of the correction.

2.2. Numerical weather predictions

The numerical weather predictions (NWPs) used in the study are provided by the Danish Meteorological Institute (DMI). The NWP model used is DMI-HIRLAM-S05, which has a 5 km grid and 40 vertical layers, see (DMI, 2011; Hansen Sass et al., 2002) for more details. The forecasts are updated four times per day and have a calculation delay of 4 h (e.g. the forecast starting at 00:00 is available at 04:00). Two time series, consisting of the latest available forecast (lead times are 5–11 h) of global radiation, are used: one for the location in Sønderborg and one for the location of DTU in Lyngby. The time series of NWPs for the Sønderborg location is used for the correction. It is denoted with

$$\left\{G_t^{\mathrm{nwp}};\quad t=1,\ldots,N\right\} \tag{2}$$

The time series for DTU Byg in Lyngby is shown, together with the observations, in the lower plot of Fig. 3 for five days in August.

2.3. Systematic errors in Sønderborg observations

The lower plot in Fig. 2 shows the Sønderborg observations and the NWPs of global radiation for five days in August 2009. From the first day, which is a clear-sky day, at least two types of errors can be seen in the observations: compared to the NWPs the observed level is too low in the morning and too high in the afternoon, which is most likely due to the sensor being tilted. It could also be due to a shift in time of the sensor, however it was thoroughly checked that the night hours, where the radiation was zero (or very close to zero), are with only a few exceptions the same hours for both the observed and the NWPs, indicating that they are well synchronized. The second type of error is seen just before noon, where the observations have a drop, which is repeated at the same *time of day* on following clear-sky day. The drop is caused by shading from the chimney, which is located close to the weather station, as seen on the image in Fig. 1.

The scatter plot in Fig. 4 shows the observed values versus the NWPs, together with two lines indicating the relation between the variables in the morning and in the afternoon. The lines are calculated using locally weighted least squares regression between the observations and the NWPs, using the function `loess()` in R (R Development Core Team, 2011) with a bandwidth: `span` = 0.9. A similar plot for the DTU observations is found in Fig. 5. The following three distinct systematic errors can be seen from the scatter plot for the Sønderborg observations:

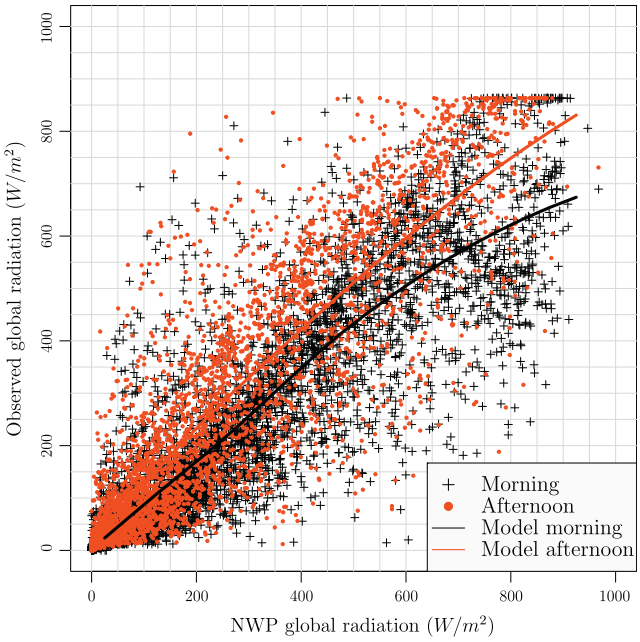

Fig. 4. The values of the Sønderborg observations versus the NWPs covering the entire year 2009. The morning values and the afternoon values are indicated by different symbols and colors. The two lines show a locally weighted least squares regression estimate of the relation between the variables in the morning and the afternoon. (For interpretation of the references to colour in this figure legend, the reader is referred to the web version of this article.)

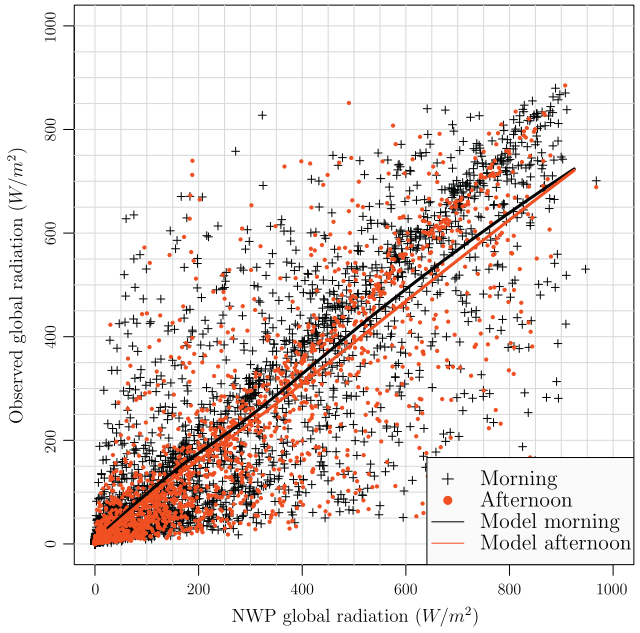

Fig. 5. The values of observed versus NWP global radiation at DTU Byg in Lyngby, Denmark. The morning values and the afternoon values are plotted with different symbols and colors. The two lines are indicating the relation between the variables: one for the morning and one for the afternoon. (For interpretation of the references to colour in this figure legend, the reader is referred to the web version of this article.)

1. Firstly, the observations are clipped at a maximum level around 860 W/m^2.
2. Secondly, the level of the morning observations is generally lower than the level of the afternoon observations. This is confirmed by the fitted regression lines, which mostly have a difference of at least 50–75 W/m^2. This is clearly a larger difference than seen for the two fitted lines for the DTU observations in Fig. 5.
3. Finally, the morning values are significantly lower in the NWP range of 700–900 W/m^2. These values are the observations in the drop before noon, which, as described earlier, is caused by shadowing from the chimney right next to the weather station.

Considering the scatter plot for the DTU observations in Fig. 5 it is seen that these systematic errors are not found in the DTU observations. As noted before the level of the DTU observations is generally a bit lower than the level of NWPs, which is most likely due to a bias of the NWPs, since the accuracy of the DTU observations is verified to be in the range of ±3%. For correction of the systematical errors, as the listed above, a statistical clear-sky model fitted to the observations can be used, as outlined in the following sections.

3. Statistical clear-sky model

In this section it is described how the clear-sky global radiation is modeled using a statistical model. With the statistical clear-sky model the level under clear-sky conditions at time t is estimated for the particular series of observations. It is the output of the sensor under clear-sky conditions which is estimated. This implies that if an observation is affected by a systematical error, for example shadowing from an object in the surroundings, the estimated clear-sky output will be lowered. It is this feature which enables the model to be used for correction. The statistical clear-sky model is a non-parametric model based on local polynomial quantile regression (Koenker, 2005) similar to the clear-sky model presented in (Bacher et al., 2009).

Usually, clear-sky models are models with which the global radiation in clear (non-overcast) sky at any given time can be calculated based on physical modeling of the atmosphere. Usually the clear-sky global radiation G_{cs} is separated into a direct (or beam) B_{cs} and diffuse D_{cs} component

$$G_{cs} = B_{cs} + D_{cs} \tag{3}$$

which are then modeled separately. The direct component by

$$B_{cs} = I_{ext} \cos(\theta_{zenith})\ \tau_{a,B} \tag{4}$$

where I_{ext} is the extraterrestrial radiation, θ_{zenith} is the solar zenith angle and $\tau_{a,B}$ is a transmittance function of the atmosphere for direct radiation under clear-sky conditions, which for example can be modeled taking Rayleigh scattering, aerosol extinction, and ozone, water and uniformly mixed gas absorption into account Bird and Riordan (1984).

The diffuse component can be modeled by adding several contributions from reflections and scattering through the atmosphere.

The global radiation (at the surface of the earth) can be modeled by

$$G = G_{cs}\ \tau_c \tag{5}$$

where τ_c is a transmittance function of clouds in the atmosphere, which can be modeled with "layer models" (Davies and McKay, 1982) where cloud layer transmittance and reflections are taken into account.

A clear-sky model, similar to the one proposed by Bacher et al. (2009) for observations of solar power, is here proposed for observations of global radiation. The proposed clear-sky model does not include any prior physical knowledge, it is based solely on the information obtained from the observations. It is denoted as a statistical clear-sky model, since it is based on a non-parametric statistical model of clear-sky radiation. Information embedded in the observations, which is particular for the sensor and its location, can be modeled with the statistical clear-sky model, for example shadowing and non-horizontal leveling of the sensor. This is a fundamental difference to the clear-sky models based on prior physical knowledge, which implies that the statistical clear-sky model can be used for different applications.

The statistical clear-sky model is based on time series of global radiation observations (or simulated values) and is defined by

$$G_t = \widehat{G}_t^{cs}\ \tau_t \tag{6}$$

where the t is used to indicate that the variables the time series of actual observations, G_t is observed global radiation, $\widehat{G}_t^{cs}$ is estimated clear-sky global radiation and τ_t is a factor, which is much to alike τ_c, but different due to the fact that it is estimated based on information from observations and not calculated based on prior physical knowledge. It is noted here that the clear-sky model could be defined for the direct component solely, which would be obvious since nearly all local systematic effects have a much higher impact on the direct component compared to the diffuse component. However, since the application of the clear-sky model in the present study is for observations of global radiation and since the systematic errors would propagate into both the direct and diffuse component calculated with a splitting scheme, such as suggested by Ruiz-Arias et al. (2010), the clear-sky model is applied to the global radiation directly.

Considering the observed global radiation as samples of a random variable with a probability distribution function, which is a function of the *day of year* x_t and the *time of day* y_t, the observed clear-sky global radiation can be estimated as a quantile

$$\widehat{G}_t^{cs} = Q_q(x_t, y_t) \tag{7}$$

of this distribution function, where the quantile $q \in [0, \ldots, 1]$ must be close to one

$$q \lesssim 1 \tag{8}$$

Assuming that the quantile function is a smooth function it can be approximated with local quantile regression Koenker (2005). The result in the three-dimensional space formed by global radiation, *day of year* and *time of day*, can be seen as a surface which follows the observed global radiation under clear-sky conditions and is located "on top" of the point cloud of observed global radiation.

In order to decrease the gradient and curvature of the estimated clear-sky radiation surface a projection is carried out. The projection is from the horizontal plane to the plane which is normal to the direct solar radiation (i.e. the plane tracking the sun position)

$$G_t^{\mathrm{pr}} = \frac{G_t}{\cos\left(\theta_t^{\mathrm{zenith}}\right)} \tag{9}$$

where $\theta_t^{\mathrm{zenith}}$ is the average solar zenith angle in the sample period between $t-1$ and t. Values where $\cos\left(\theta_t^{\mathrm{zenith}}\right) < 0.01$ are removed: this corresponds to sun elevation below 0.5°. The quantile close to one is then estimated for the projected values. A general form of the proposed statistical clear-sky model is formulated in Appendix A, which is based on a local quantile regression model with second order polynomials and a two-dimensional kernel in both the *day of year* and *time of day* dimensions.

For correction of hourly values a local quantile regression model based only on a one-dimensional kernel, where on the *day of year* dimension is used, was found most suitable. The reason for using only a one-dimensional kernel, and not including the *time of day* dimension in the local weighting, is that the model becomes too biased and the estimated clear-sky global radiation does not follow the drop before noon caused by shadowing (the systematic error described on page 7) very well. Hence only values lagged in steps of 24 h from t are used as input, which is a similar approach as in classical decomposition of seasonal time series (Cleveland and Tiao, 1976). Furthermore, it is noted that this is equivalent to using a bandwidth in the *time of day* dimension below 1 h (i.e. below the sample period) for the two-dimensional model presented in Appendix A, hence for time series with a shorter sample period a two-dimensional model should be considered. The applied local quantile regression model based on a third order polynomial is

$$\hat{\beta}_t = \mathrm{argmin}_{\beta\in\mathbb{R}^4} \sum_{i=-\infty}^{\infty} \rho_q\left(G_{t+24i}^{\mathrm{tr}} - (\beta_{0,t} + \beta_{1,t} i + \beta_{2,t} i^2 + \beta_{3,t} i^3)\right) K(i) \tag{10}$$

where $\rho_q(u) = u(q - I(u<0))$ is the quantile regression objective function (see (Koenker, 2005, 2011)), $q \in [0, \ldots, 1]$ is the sample quantile to be estimated, $i \in \mathbb{N}$ is a counter of days, and $K(i)$ is a kernel function. The estimated projected clear-sky radiation is then found as the local intercept

$$\widehat{G}_t^{\mathrm{pr,cs}} = \hat{\beta}_{0,t} \tag{11}$$

The weights are calculated with the Epanechnikov kernel function

$$K(i) = \begin{cases} \frac{3}{4}\left(1 - \left[\frac{|i|}{h_{\mathrm{doy}}}\right]^2\right) & \text{for } \frac{|i|}{h_{\mathrm{doy}}} \geqslant 1 \\ 0 & \text{for } \frac{|i|}{h_{\mathrm{doy}}} < 1 \end{cases} \tag{12}$$

where h_{doy} is the bandwidth.

The R package `quantreg` implementation of quantile regression was used for the estimation (Koenker, 2011). Finally, the estimated projected clear-sky radiation on the projected plane is projected back to the horizontal plane by

$$\widehat{G}_t^{\mathrm{cs}} = \widehat{G}_t^{\mathrm{pr,cs}} \cos\left(\theta_t^{\mathrm{zenith}}\right) \tag{13}$$

Finally, in order to take the clipping at a maximum level into account, the estimated clear-sky radiation is limited to the maximum value of the observations

$$\widehat{G}_t^{\mathrm{cs}} = \begin{cases} \widehat{G}_t^{\mathrm{cs}} & \text{for } \widehat{G}_t^{\mathrm{cs}} \leqslant G_t^{\max} \\ G_t^{\max} & \text{for } \widehat{G}_t^{\mathrm{cs}} > G_t^{\max} \end{cases} \tag{14}$$

where $G_t^{\max}$ is the maximum value of global radiation observations.

The selection of suitable values for the parameters (here the quantile and the kernel bandwidth) for the fitting of the local quantile regression model, would preferably be based on a measure of performance for estimation clear-sky global radiation. Then the parameters could be optimized in order to achieve the best performance. However thorough studies are required in order to define such a measure. Therefore the parameter values are selected based on visual inspection of the estimated clear-sky global radiation for days with only clear-sky. These days are chosen such that they are distributed evenly over the entire period. The selected values are

$$q = 0.97, \; h_{\mathrm{doy}} = 125 \tag{15}$$

which gives the estimate of the clear-sky global radiation for the observations $\widehat{G}_t^{\mathrm{cs}}$ shown in Fig. 6 and for the NWPs $\widehat{G}_t^{\mathrm{nwp,cs}}$ shown in Fig. 7. Note, that the estimated surface for the observations is clipped at the maximum value of the observations, which gives the "flat" top. Furthermore, notice that the drop due to shadowing is clearly seen in the estimated clear-sky radiation for the observations.

4. Correction of observations

The correction of the observations is carried out by multiplying the observations with the ratio between the estimated clear-sky radiation for the NWPs and the observations

$$\widehat{G}_t^{\mathrm{co}} = \frac{\widehat{G}_t^{\mathrm{nwp,cs}}}{\widehat{G}_t^{\mathrm{cs}}} \; G_t \tag{16}$$

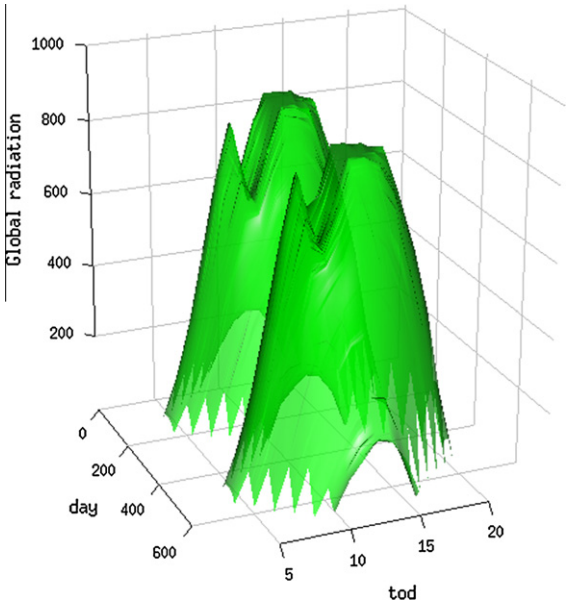

Fig. 6. The clear-sky global radiation estimated for the Sønderborg observations. Shown as a surface parametrized in the two dimensions: day (days since 2009-01-01) and tod (*time of day*).

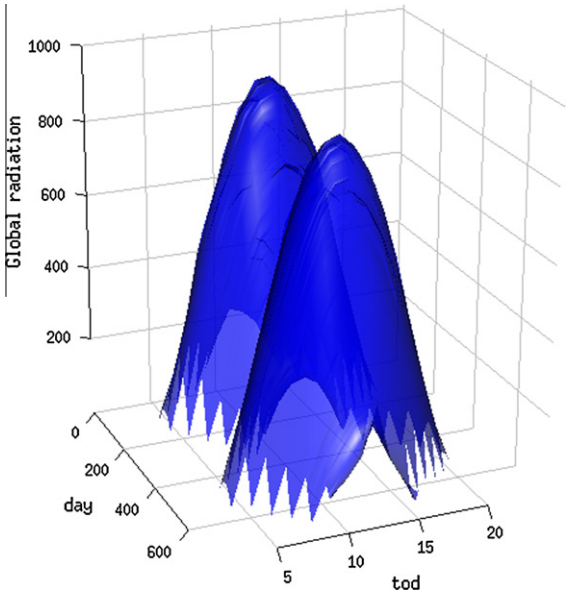

Fig. 7. The clear-sky global radiation estimated for the NWPs for Sønderborg. Shown as a surface parametrized in the two dimensions: day (days since 2009-01-01) and tod (*time of day*).

The level of the correction applied, i.e. $\widehat{G}_t^{\mathrm{nwp,cs}}/\widehat{G}_t^{\mathrm{cs}}$, is shown as function of days since 2009-01-01 and the *time of day* in Fig. 8. The systematical error caused by a tilt of the sensor, resulting in a too low level of the observations in the morning and too high level in the afternoon, can be directly seen in the correction, since in the morning the correction is generally above one and the afternoon level below one. Also apparent is the drop in the observed level due to shadowing objects, especially seen between 9 and 10 am.

The corrected observations are plotted versus the NWPs in Fig. 9, including the local least squares estimate of the relation in the morning and in the afternoon. This plot is similar to the plot in Fig. 4. By comparison of the two plots it is seen that the difference between the estimated relation in the morning and the estimated relation in the afternoon has been decreased significantly. A visual comparison to the similar plot of the high quality DTU observations in Fig. 5 verifies that the pattern of the scatter after the correction is much closer to the pattern found there. It can also be seen that the clipping at a maximum level has been corrected. Finally, it is found that the overall scattering has been reduced. This is confirmed by a comparison of the errors for an estimated relation similar to the ones in Figs. 4 and 9, but using all data points (except nighttime values), i.e. no distinction between morning and afternoon. Note here that the this measure is only used to give a rough indication of the performance of the correction. The root mean square error (RMSE) and mean absolute error (MAE) before the correction are

$$\mathrm{RMSE}_{\mathrm{before}} = 114\ \mathrm{W/m^2},\ \mathrm{MAE}_{\mathrm{before}} = 79\ \mathrm{W/m^2} \tag{17}$$

and after the correction

$$\mathrm{RMSE}_{\mathrm{after}} = 101\ \mathrm{W/m^2},\ \mathrm{MAE}_{\mathrm{after}} = 67\ \mathrm{W/m^2} \tag{18}$$

Hence a notably reduction in RMSE and MAE is achieved by applying the correction.

4.1. On-line operation

For on-line operation the model has to be applied causally, such that only past values can be used for the correction. A causal correction was calculated with slightly different parameter values for the clear-sky model, again selecting the parameters from visual inspection. The estimated quantile q was decreased and the kernel bandwidth h_{doy} increased slightly to

$$q = 0.95,\ h_{\mathrm{doy}} = 150 \tag{19}$$

Using a one-sided kernel will increase the bias of the estimates, which is also reflected by a slightly increased RMSE and MAE of the `loess` fit for the corrected observations to

$$\mathrm{RMSE}_{\mathrm{after}} = 103\ \mathrm{W/m^2},\ \mathrm{MAE}_{\mathrm{after}} = 67\ \mathrm{W/m^2} \tag{20}$$

Considering the similar plots as presented for the causal correction showed only a small visual difference. Hence it is found that the method works well for on-line operation.

5. Discussion

In this section the correction method and results are discussed together with considerations on how to improve the method.

Considering the fitting of the clear-sky model it is noted that the model which should be applied, is dependent on the time resolution of the data. For resolutions higher than

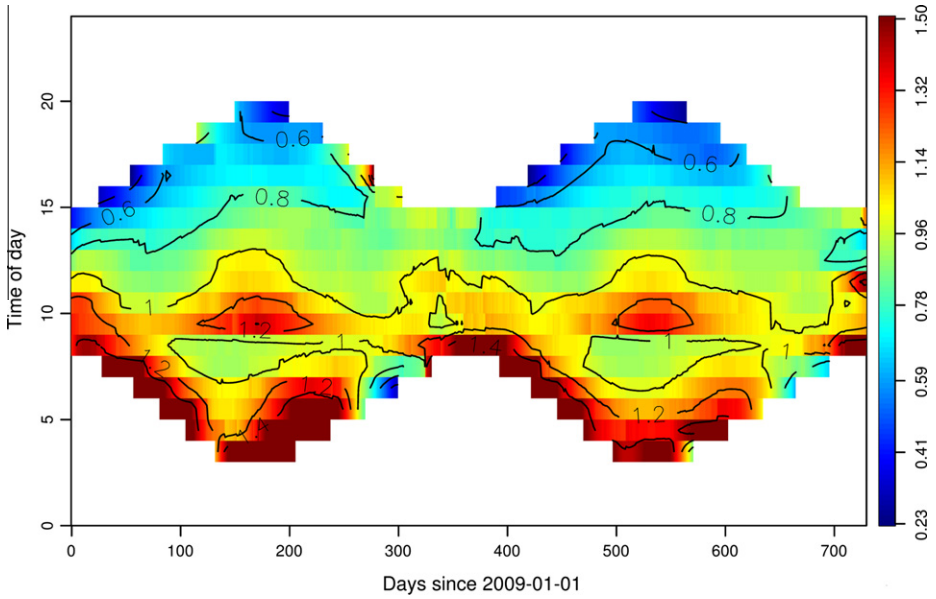

Fig. 8. The applied correction, which is the ratio between the estimated clear-sky radiation of the observations and the NWPs, as a function of days and *time of day*.

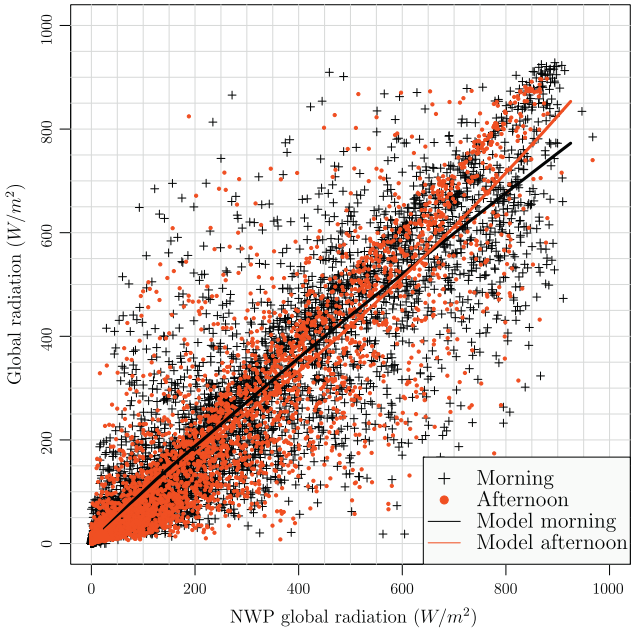

Fig. 9. The values of the corrected observations versus NWPs of global radiation. The morning values and the afternoon values are indicated by different symbols and colors. The two lines show a locally weighted least squares regression estimate of the relation between the variables in the morning and the afternoon. (For interpretation of the references to colour in this figure legend, the reader is referred to the web version of this article.)

hourly a two-dimensional kernel, which also includes the *time of day* dimension, should be used, as in (Bacher et al., 2009) where a similar clear-sky model was applied to 15 min values. Regarding the parameters needed to be tuned in the clear-sky model – the quantile, kernel bandwidth, and order of the polynomial – some manual interaction is required. However the method could be based on a parameter optimization criteria, hence an objective measure to evaluate the performance of the correction, possibly based on cross validation (Friedman et al., 2001), and applied automatically for the general case. Hence it can also be used for monitoring and data quality classification for sub-daily solar data. Clearly, an objective measure of performance of the correction is needed in order to further develop and improve the correction method.

Improvements of the method could be formed by combining it with a prior step in which a parametric model is fitted to correct for drift in time and tilt in the leveling of the sensor. Another possibility for improvement is to treat the direct and diffuse radiation separately, since most of the systematic errors, for example tilt and shadowing, will have a different impact on direct and diffuse radiation. This will require, if the direct and diffuse are not measured separately, a splitting into a diffuse and direct component, which could be carried out with a scheme such as suggested by Ruiz-Arias et al. (2010) and Duffie and Beckman (2006, pp. 75–77). However applying such a scheme will cause the effect of the systematic errors to propagate into both the direct and the diffuse components. Another approach would be to enhance the correction method by using more than one quantile, in the presented approach only a single quantile close to one is used. Several quantiles can be estimated for both the observed and calculated radiation, which, together with an interpolation scheme, will form a more extensive correction. Clearly this also requires that the calculated global radiation, i.e. here the NWPs, describes the distribution well over the entire range of global radiation. Finally, it is mentioned that for on-line operation the method can be implemented computationally

very efficient using time-adaptive quantile regression (Møller et al., 2008).

6. Conclusion

A correction method based on statistical non-parametric modeling techniques is presented and applied on hourly observations of global radiation. Several typical errors in the observations can be corrected with the method, including: tilt in the leveling of the sensor, shadowing from objects in the surroundings and clipping of the observations at a maximum level. The method works semi-automatically and no prior information about the sensor and its surroundings, besides the observations and location, is required. Furthermore only a few parameters needs to be tuned. Information embedded in NWPs of global radiation is used for the correction, but this could be replaced with any calculated clear-sky global radiation model. The method is well suited as part of monitoring and operation applications for which local solar radiation observations provide valuable information, e.g. for forecasting of climate dependent renewables such as solar thermal, PV and heating systems. Finally, it is briefly discussed how the method can be improved or extended in several ways.

Acknowledgments

The observations of global radiation was very kindly provided by Sønderborg Fjernvarme and we also thank the Danish Meteorological Institute for making their numerical weather predictions available. Finally, acknowledgments are given to the The Danish Council for Strategic Research, which have provided the financial support for the project "Solar/electric heating systems in the future energy system" under which the work was carried out.

Appendix A. Two-dimensional local statistical clear-sky model

The proposed statistical clear-sky model in a general form is described in this section. It is based on a two-dimensional second-order polynomial local quantile regression model. In this form the local weighting is carried out with a two-dimensional multiplicative kernel function in the *day of year* and *time of day* dimensions.

The model

$$\hat{\beta}_t = \operatorname{argmin}_{\beta\in\mathbb{R}^5} \sum_{i=-\infty}^{\infty}\sum_{j=-\infty}^{\infty} \rho_q\left(G^{\mathrm{tr}}_{t+\frac{24}{t_{\mathrm{sp}}}i+j} - (\beta_{0,t}+\beta_{1,t}i+\beta_{2,t}i^2+\beta_{3,t}j+\beta_{4,t}j^2)\right)K(i,j) \tag{A.1}$$

where t_{sp} is the sample period of the time series in hours, $\rho_q(u) = u(q - I(u<0))$ is the quantile regression objective function (see Koenker, 2005; Koenker, 2011), $q \in [0,\ldots,1]$ is the sample quantile to be estimated, $i \in \mathbb{N}$ is a counter of days, $j \in \mathbb{N}$ is a counter in steps of the sample period, and $K(i,j)$ is a kernel function. The model could easily be reduced or expanded to polynomials of different orders. The estimated projected clear-sky radiation is then found as the local intercept

$$\widehat{G}^{\mathrm{pr,cs}}_t = \hat{\beta}_{0,t} \tag{A.2}$$

The weights are calculated with the Epanechnikov kernel function

$$K(i,j) = \begin{cases} \frac{9}{16}\left(1-\left[\frac{|i|}{h_{\mathrm{doy}}}\right]^2\right)\left(1-\left[\frac{|j|t_{\mathrm{sp}}}{h_{\mathrm{tod}}}\right]^2\right) & \text{for } \frac{|i|}{h_{\mathrm{doy}}}<1 \wedge \frac{|j|}{h_{\mathrm{tod}}}<1 \\ 0 & \text{for } \frac{|i|}{h_{\mathrm{doy}}}\geqslant 1 \vee \frac{|j|}{h_{\mathrm{tod}}}\geqslant 1 \end{cases} \tag{A.3}$$

where h_{doy} is the bandwidth in the *day of year* dimension (in days) and h_{tod} is the bandwidth in the *time of day* dimension (in hours).

References

Bacher, P., Madsen, H., Nielsen, H.A., 2009. Online short-term solar power forecasting. Solar Energy 83 (10), 1772–1783.

Bird, R.E., 1984. A simple, solar spectral model for direct-normal and diffuse horizontal irradiance. Solar Energy 32 (4), 461–471, <http://www.sciencedirect.com/science/article/pii/0038092X84902603>.

Bird, R., Riordan, C., 1984. Simple solar spectral model for direct and diffuse irradiance on horizontal and tilted planes at the earth's surface for cloudless atmospheres. Tech. rep., Solar Energy Research Inst., Golden, CO, USA.

Cleveland, W., Tiao, G., 1976. Decomposition of seasonal time series: a model for the census x-11 program. Journal of the American statistical Association, 581–587.

Davies, J.A., McKay, D.C., 1982. Estimating solar irradiance and components. Solar Energy 29 (1), 55–64, <http://www.sciencedirect.com/science/article/pii/0038092X82902808>.

DMI, 2011. Danish Meteorological Institute, DMI-HIRLAM-S05. <http://www.dmi.dk/eng/index/research_and_development/dmi-hirlam-2009.htm>

DMI, Feb. 2012. Danish Meteorological Institute, Borgervejr. <http://www.borgervejr.dk>.

Duffie, J.A., Beckman, W.A., 2006. Solar Engineering of Thermal Processes, third ed. Wiley.

Friedman, J., Hastie, T., Tibshirani, R., 2001. The elements of statistical learning. vol. 1. Springer Series in Statistics.

Geiger, M., Diabaté, L., Ménard, L., Wald, L., 2002. A web service for controlling the quality of measurements of global solar irradiation. Solar Energy 73 (6), 475–480.

Hansen Sass, B., Woetmann Nielsen, N., Jørgensen, J.U., Amstrup, B., Kmit, M., Mogensen, K.S., 2002. The operational DMI-HIRLAM system 2002-version. DMI.

Ineichen, P., 2006. Comparison of eight clear sky broadband models against 16 independent data banks. Solar Energy 80 (4), 468–478.

Isaac, Moradi, 2009. Quality control of global solar radiation using sunshine duration hours. Energy 34 (1), 1–6.

Journée, M., Bertrand, C., 2011. Quality control of solar radiation data within the RMIB solar measurements network. Solar Energy 85 (1), 72–86.

Koenker, R., 2005. Quantile Regression. Cambridge University Press.

Koenker, R., 2011. Quantreg: Quantile Regression. R Package Version 4.76. <http://CRAN.R-project.org/package=quantreg>

Møller, J.J.K., Nielsen, H.A., Madsen, H., 2008. Time-adaptive quantile regression. Computational Statistics and Data Analysis 52 (3), 1292–1303.

Mueller, R., Dagestad, K., Ineichen, P., Schroedter-Homscheidt, M., Cros, S., Dumortier, D., Kuhlemann, R., Olseth, J., Piernavieja, G.,

Reise, Wald, L., Heinemann, D., 2005. Rethinking satellite-based solar irradiance modelling: the solis clear-sky module. Remote Sensing of Environment 91 (2), 160–174.

R Development Core Team, 2011. R: A Language and Environment for Statistical Computing. R Foundation for Statistical Computing, Vienna, Austria, ISBN:3-900051-07-0. <http://www.R-project.org/>

Rigollier, C., Bauer, O., Wald, L., 2000. On the clear sky model of the esra – European solar radiation atlas – with respect to the heliosat method. Solar Energy 68 (1), 33–48.

Ruiz-Arias, J., Alsamamra, H., Tovar-Pescador, J., Pozo-Vázquez, D., 2010. Proposal of a regressive model for the hourly diffuse solar radiation under all sky conditions. Energy Conversion and Management 51 (5), 881–893.

Younes, S., Claywell, R., Muneer, T., 2005. Quality control of solar radiation data: present status and proposed new approaches. Energy 30 (9), 1533–1549 (measurement and modelling of solar radiation and daylight – challenges for the 21st century).

Rasmus Halvgaard, Niels Kjølstad Poulsen, Henrik Madsen, John Bagterp Jørgensen, Economic model predictive control for building climate control in a smart grid, 978-1-4577-2159-5/12/$31.00 ©2011 IEEE

Economic Model Predictive Control for Building Climate Control in a Smart Grid

Rasmus Halvgaard, Niels Kjølstad Poulsen, Henrik Madsen and John Bagterp Jørgensen

***Abstract*—Model Predictive Control (MPC) can be used to control a system of energy producers and consumers in a Smart Grid. In this paper, we use heat pumps for heating residential buildings with a floor heating system. We use the thermal capacity of the building to shift the energy consumption to periods with low electricity prices. In this way the heating system of the house becomes a flexible power consumer in the Smart Grid. This scenario is relevant for systems with a significant share of stochastic energy producers, e.g. wind turbines, where the ability to shift power consumption according to production is crucial. We present a model for a house with a ground source based heat pump used for supplying thermal energy to a water based floor heating system. The model is a linear state space model and the resulting controller is an Economic MPC formulated as a linear program. The model includes forecasts of both weather and electricity price. Simulation studies demonstrate the capabilities of the proposed model and algorithm. Compared to traditional operation of heat pumps with constant electricity prices, the optimized operating strategy saves 25-35% of the electricity cost.**

I. Introduction

The energy policies in the Nordic countries stipulate that 50% of the energy consumed by 2025 should come from renewable and CO_2-free energy sources. By 2050 the aim is to be independent of fossil fuels. This transformation of the energy system is needed to reduce CO_2 emissions and global warming as well as to protect the Nordic economies from the consequences of sharply rising prices of fossil fuels due to an increasing world population and depletion of fossil fuel resources. Not only the Nordic countries but the entire world and industrialized world in particular are facing this grand challenge. Reducing the fossil fuel consumption from 80% of the energy consumption to 0% in 40 years, requires introduction of a significant amount of renewable energy sources and an efficient utilization of energy in buildings, the process industries, and transportation. In the Nordic countries, a major part of the renewable energy will be produced by hydro power and offshore wind turbines. On the consumption side, residential and commercial buildings will use heat pumps for heating and electrical vehicles will replace vehicles based on combustion engines.

Accordingly, electricity will be the main energy carrier in such an energy system independent of fossil fuels. Depending on the rate of adoption of electrified vehicles, 40-70% of the energy consumption will originate from electricity in 2050. Currently, 20% of the energy consumption is electricity. As it is more difficult to store electricity than fossil fuels, such a large share of stochastic electricity production requires an intelligent power system - also referred to as a Smart Grid - that continuously balances the power consumption and the power production. This balancing requires control of the power consumption from heat pumps and electrical vehicles such that surplus of cheap wind energy is used as it is produced. Heat tanks in residential homes as well as in district heating plants must be established such that heat pumps can store electricity as heat in periods with low electricity prices. The power consumption by the process industries and retail industry, e.g. refrigeration in supermarkets and large cooling houses, must also be made flexible. Such a system is a large-scale complex system that must be coordinated to balance consumption and production of electricity.

Buildings account for approximately 40% of the total energy use in Europe. Therefore, intelligent control of the energy use in buildings is a necessity for the future smart energy system. In the Nordic countries, the energy is mainly used for heating, lighting, and electrical appliances. Heat pumps combined with water based floor heating systems will be one of the main sources for heating of buildings [1]–[4]. By themselves, these heat pumps are very energy efficient as their coefficient of performance is typically 3 or larger, i.e. for each kWh electricity supplied, they deliver more than 3 kWh heat. As heat pumps are driven by electricity and can be connected to floors with large thermal capacity, they have a large potential to shift the electricity consumption and adapt to the stochastic electricity production from wind turbines. The adoption of heat pumps could very well accelerate in the coming years. Especially for buildings situated outside district heating areas. They can benefit from heating using electric heat pumps instead of the current oil and natural gas. Heat pumps connected to the district heating system can benefit from a large store of heat and can be used to shift electricity consumption on a 24-hour or weekly basis. Furthermore, large electric heat pumps can be installed at a number of district heating plants. The large heat pumps can better exploit heat from the sea, lakes or waste heat, while small heat pumps can exploit geothermal heat.

The use of Model Predictive Control to provide indoor thermal comfort in heating systems of buildings has been reported in [5]–[7]. In the future energy systems with a large share of stochastic power producers such as wind turbines, the ability to shift the load of electricity is just as important as providing indoor thermal comfort in a heating system based on heat pumps. Different control strategies have been suggested for load balancing and load shifting in electrical grids [8]. For

R. Halvgaard, N. K. Poulsen, H. Madsen and J. B. Jørgensen are with DTU Informatics, Technical University of Denmark, Richard Petersens Plads, Building 321, DK-2800 Kgs. Lyngby, Denmark {rhal,nkp,hm,jbj}@imm.dtu.dk

978-1-4577-2159-5/12/$31.00 ©2011 IEEE

heat pumps, these strategies can be summarized as

1) **Frequency based control**. The heat pump senses the grid frequency, which in Europe has the nominal value of 50 Hz. When demand exceeds supply, the frequency falls. When supply exceeds demand, the frequency increases. Depending on a measured difference from the nominal value of the frequency, the heat pump can decide to pre-heat by starting the compressor or to delay the activation of the compressor for a short time. The advantage of this type of control is the low price of the controller, because no additional communication between the utility and the heat pump is necessary. However, there is no way to integrate the device into an intended schedule as it responds completely autonomously.
2) **Price based control**. The heat pump controller computes a schedule for the compressor based on dynamic price information given by the utility. This enables the heat pump to shift its load to times with low electricity price. It requires a communication infrastructure between utilities and households. The drawback of this control strategy is that it is relatively complex and the fact that effects of sent tariff information to affect the load are not completely sure for the utility.
3) **Direct control**. Given the communication infrastructure required for the price based control, utilities can send control signals to the heat pump to raise or reduce the demand. This allows the utility a more direct control of the demand. Furthermore, it allows the controller in the heat pump to be quite simple as it only sends information and receives commands from the utility. The drawback of course is that the utility must solve large-scale optimization problems to coordinate a large number of heat pumps.

[9] use Economic Model Predictive Control (MPC) in a direct control case to shift the electricity load of refrigeration systems. In this paper, we use Economic MPC based on price signals to control a heat pump such that certain temperature limits in a building with a floor heating system are respected. By using price signals, both current and future prices, the optimization of the energy consumption of each individual residential building decouples from the energy consumption of all other agents in the system. However, we do not specify how to determine this price but assume that it is given based on market principles of supply and demand. Consequently, each individual house is a price taker.

Simple weather conditions such as outdoor temperature and solar radiation are included in the model. By adding forecasts of prices and weather conditions to the heat pump control problem, the energy consumption is made flexible. It is thus possible to predict where to place the heat pump energy consumption and minimize the electricity cost of operating the heat pump to meet a certain indoor thermal comfort, i.e. a desired temperature interval. The temperature interval can be time varying. We exploit that the dynamics of the temperatures in the house floor heating system and indoor air are slow while the power consumption can be changed rapidly. The thermal capacity of the residential building determines how much of the electricity consumption that can be shifted to times with cheap electricity.

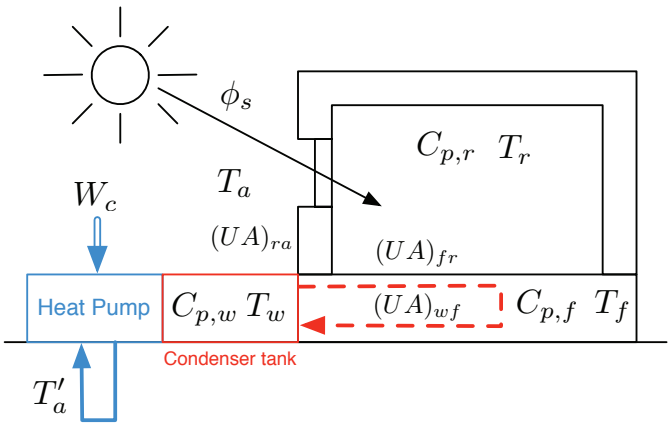

Fig. 1. House and heat pump floor heating system and its thermal properties. The dashed line represents the floor heating pipes.

MPC is increasingly being considered for building climate control [10]–[12]. Traditionally, MPC is designed using objective functions penalizing deviations from a given setpoint. Recently Economic MPC has emerged as a general methodology with efficient numerical implementations and provable stability properties [13], [14].

This paper is organized as follows. In Section II, we develop and discuss a model for a heat pump connected to a floor heating system of a building. Section III states and discusses the Economic MPC. Simulation results for the Economic MPC applied to the model are described in Section IV. Section V provides conclusions.

II. Model

In this section, we develop a model of the heat dynamics of a house floor heating system connected to a ground source based heat pump. The system is illustrated in Fig. 1. The model is a linear third order model. Table I lists the variables and parameters of the model.

TABLE I
Description of Variables

Variable	Unit	Description
T_r	°C	Room air temperature
T_f	°C	Floor temperature
T_w	°C	Water temperature in floor heating pipes
T_a	°C	Ambient temperature
T'_a	°C	Ground temperature
W_c	W	Heat pump compressor input power
ϕ_s	W	Solar radiation power

A. Energy Balances and Heat Conduction

In this subsection we develop energy balances for the air in the room, the floor and the water in the floor heating pipes

and condenser water tank. In the simple model developed in this paper, the house is considered to be one big room. Furthermore, we make the following simplifying assumptions: 1) One uniform air temperature, 2) no ventilation, 3) no influence from humidity of the air, 4) no influence from the heat released from people in the room, 5) no influence from wind.

In [15] a model of the indoor temperature in buildings is identified and suggests at least two dominating heat accumulating media in order to capture the short-term and long-term variations of the heat dynamics. In our model two heat accumulating media are thus included, namely the room air and the floor. The resulting energy balances are

$$C_{p,r}\dot{T}_r = Q_{fr} - Q_{ra} + (1-p)\phi_s \tag{1}$$
$$C_{p,f}\dot{T}_f = Q_{wf} - Q_{fr} + p\,\phi_s \tag{2}$$

The disturbances are the ambient temperature and the solar radiation through a window. These disturbances are also illustrated in Fig. 1.

The energy balance for the water circulating in the floor heating pipes can be stated as

$$C_{p,w}\dot{T}_w = Q_c - Q_{wf} \tag{3}$$

in which Q_c is the heat transferred to the water from the condenser in the heat pump. Q_{wf} is the heat transferred from the water to the floor.

The conductive heat transfer rates are

$$Q_{ra} = (UA)_{ra}(T_r - T_a) \tag{4a}$$
$$Q_{fr} = (UA)_{fr}(T_f - T_r) \tag{4b}$$
$$Q_{wf} = (UA)_{wf}(T_w - T_f) \tag{4c}$$

Q_{ra} is the heat transferred from the air in the room to the surroundings, Q_{fr} is the heat transferred from the floor to the air in the room, and Q_{wf} is the heat transferred from the water in the floor heating pipes to the floor. The term $U \cdot A$ is a product of the heat conductivity and the surface area of the layer between two heat exchanging media. Its reciprocal value $R = 1/(UA)$ is often used since it can be interpreted as a resistance against heat flow [16].

B. Heat Pump

A heat pump is a device that transfers heat from a low temperature zone to a higher temperature zone using mechanical work. A heat pump can provide both heating or cooling, but in cooler climates heating is of course more common. Heat pumps normally draw heat from the air or from the ground and uses a vapor compression refrigeration cycle. This cycle requires the four basic components as sketched in Fig. 2. The components are a compressor, an expansion valve, a condenser converting the working fluid from its gaseous state to its liquid state, and an evaporator converting the working fluid from its liquid state to its gaseous state [17], [18].

As the heat pump dynamics is much faster than the thermodynamics of the building, we can assume a static model for the heat pump. The amount of heat transferred from the condenser

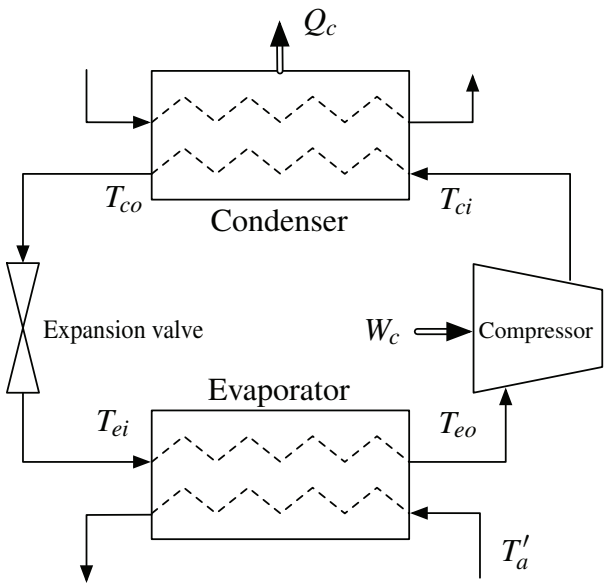

Fig. 2. Heat pump vapor compression refrigeration cycle. The temperatures are denoted T with subscript c or e for condenser or evaporator, respectively, while i or o denotes input or output.

to the water, Q_c, is related to the work of the compressor, W_c, using the coefficient of performance

$$Q_c = \eta W_c \tag{5}$$

The coefficient of performance η for heat pumps varies with type, outdoor ground temperature, and the condenser temperature. As the outdoor ground temperature and the condenser temperature are approximately constant, we can assume that the coefficient of performance is constant. For ground source based heat pumps η is typically around 3 in the specified operating range.

The model consists of (1)-(5). Consequently, a third order linear model can be stated as

$$\begin{aligned} C_{p,r}\dot{T}_r = {} & (UA)_{fr}(T_f - T_r)\ldots \\ & -(UA)_{ra}(T_r - T_a) + (1-p)\phi_s \end{aligned} \tag{6a}$$
$$\begin{aligned} C_{p,f}\dot{T}_f = {} & (UA)_{wf}(T_w - T_f)\ldots \\ & -(UA)_{fr}(T_f - T_r) + p\phi_s \end{aligned} \tag{6b}$$
$$C_{p,w}\dot{T}_w = \eta W_c - (UA)_{wf}(T_w - T_f) \tag{6c}$$

C. State space model

The model (6) can be expressed as a continuous-time state space model

$$\dot{x} = Ax + Bu + Ed \tag{7a}$$
$$y = Cx \tag{7b}$$

x is the states, u is the manipulated variables, d is the disturbances, and y is the controlled variable. In the case studied, the states are $x = \begin{bmatrix} T_r & T_f & T_w \end{bmatrix}^T$; the manipulate variable is the power used by the compressor in the heat pump, $u = W_c$; the disturbances are the ambient temperature and the sun radiation such that $d = \begin{bmatrix} T_a & \phi_s \end{bmatrix}^T$; and the controlled

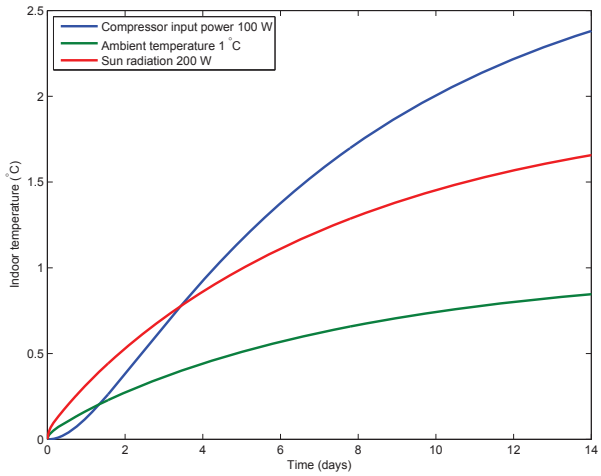

Fig. 3. Step responses from inputs and disturbances to indoor temperature T_r. Step size is noted in the plot legend.

variable is the indoor temperature $y = T_r$. The matrices in the state space model (7) are

$$A = \begin{bmatrix} a_{11} & a_{12} & 0 \\ a_{21} & a_{22} & a_{23} \\ 0 & a_{32} & a_{33} \end{bmatrix} \quad E = \begin{bmatrix} \frac{(UA)_{ra}}{C_{p,r}} & \frac{1-p}{C_{p,r}} \\ 0 & \frac{p}{C_{p,f}} \\ 0 & 0 \end{bmatrix}$$

$$C = \begin{bmatrix} 1 & 0 & 0 \end{bmatrix} \quad B = \begin{bmatrix} 0 & 0 & \frac{\eta}{C_{p,w}} \end{bmatrix}^T$$

with the coefficients

$$a_{11} = (-(UA)_{fr} - (UA)_{ra})/C_{p,r}$$
$$a_{22} = (-(UA)_{wf} - (UA)_{fr})/C_{p,f} \qquad a_{33} = -(UA)_{wf}/C_{p,w}$$
$$a_{12} = (UA)_{fr}/C_{p,r} \qquad a_{23} = (UA)_{wf}/C_{p,f}$$
$$a_{21} = (UA)_{fr}/C_{p,f} \qquad a_{32} = (UA)_{wf}/C_{p,w}$$

[19] provides values for building heat capacities and thermal conductivities obtained from system identification methods. The values of these parameters for a representative building are listed in Table II. The water tank heat capacity is estimated as $C_{p,w} = m_w c_w$ for a 200 liter tank filled with water having the specific heat capacity c_w and mass m_w. The resulting time constants of the third order model are 1, 24, and 186 hours for the room air, water condenser tank, and the floor, respectively. This is also observed from the step responses seen in Fig. 3.

III. Economic MPC

The state space model (7) is converted to a discrete-time state space model using zero-order-hold sampling of the input signals

$$x_{k+1} = A_d x_k + B_d u_k + E_d d_k \tag{8a}$$
$$y_k = C_d x_k \tag{8b}$$

Using this discrete-time linear state space formulation to predict the future outputs, we may formulate a linear program that minimizes the electricity cost for operating the heat pump while keeping the indoor room temperature in prespecified intervals

$$\min_{\{x,u,y\}} \quad \phi = \sum_{k\in\mathcal{N}} c_{u,k} u_k + \rho_v v_k \tag{9a}$$
$$s.t. \quad x_{k+1} = A_d x_k + B_d u_k + E_d d_k \quad k \in \mathcal{N} \tag{9b}$$
$$y_k = C_d x_k \quad k \in \mathcal{N} \tag{9c}$$
$$u_{\min} \le u_k \le u_{\max} \quad k \in \mathcal{N} \tag{9d}$$
$$\Delta u_{\min} \le \Delta u_k \le \Delta u_{\max} \quad k \in \mathcal{N} \tag{9e}$$
$$y_{k,\min} \le y_k + v_k \quad k \in \mathcal{N} \tag{9f}$$
$$y_{k,\max} \ge y_k - v_k \quad k \in \mathcal{N} \tag{9g}$$
$$v_k \ge 0 \quad k \in \mathcal{N} \tag{9h}$$

$\mathcal{N} \in \{0, 1, \ldots, N\}$ and N is the prediction horizon. The electricity prices enter the optimization problem as the cost coefficients $c_{u,k}$. It may not always be possible to meet the temperature demand. Therefore, the MPC problem is relaxed by introduction of slack variable v_k and the associated penalty cost ρ_v. The penalties can be set sufficiently large, such that the output constraints are met whenever possible. The Economic MPC also contains bound constraints and rate-of-movement constraints on the manipulated variables. The rate-of-movement is defined in discrete time as $\Delta u_k = u_{k+1} - u_k$ and adds to robustness of the numerical optimization routine.

The prediction horizon, N, is normally selected large to avoid discrepancies between open-loop and closed-loop profiles. However, long horizons increases computation speed rapidly and uncertainties in the forecasts grow larger and larger with time. At each sampling time, we solve the linear program (9) to obtain $\{u_k^*\}_{k=0}^{N-1}$. We implement u_0^* on the process. As new information becomes available at the next sampling time, we redo the process of solving the linear program using a moving horizon and implementing the first part, u_0^*, of the solution.

The electricity prices, $\{c_{u,k}\}_{k=0}^{N-1}$, as well as the ambient temperature and sun radiation, $\{d_k\}_{k=0}^{N-1}$, must be forecasted. In this paper we assume that we have perfect forecasts.

IV. Results

The Economic MPC has been implemented in Matlab calling a primal active set solver. To illustrate the potential of the Economic MPC for controlling heat pumps, we simulate scenarios using day-ahead electricity prices from Nordpool, the Nordic power exchange market. These electricity prices are available in one hour intervals. We also discretize the system using a sample time of 30 minutes, i.e. $T_s = 0.5$ hour. Both the outdoor temperature, T_a, and solar radiation ϕ_s are modeled as diurnal cycles with added noise [10]. We aim to minimize the total electricity cost in a given period while keeping the indoor temperature, T_r, in predefined intervals. In the case studied, we assume that the forecasts are perfect, i.e. that the forecasts are without uncertainty. We simulate a five day period using a prediction horizon $N = 96$ (= 48 hours). The optimal control signal is calculated at every time step over the prediction horizon to obtain a closed loop profile.

Fig. 4 illustrates the optimal compressor schedule and the predicted indoor temperature for a five day horizon. The lower

TABLE II
ESTIMATED MODEL PARAMETERS

	Value	Unit	Description
$C_{p,r}$	810	kJ/°C	Heat capacity of room air
$C_{p,f}$	3315	kJ/°C	Heat capacity of floor
$C_{p,w}$	836	kJ/°C	Heat capacity of water in floor heating pipes
$(UA)_{ra}$	28	kJ/(°C h)	Heat transfer coefficient between room air and ambient
$(UA)_{fr}$	624	kJ/(°C h)	Heat transfer coefficient between floor and room air
$(UA)_{wf}$	28	kJ/(°C h)	Heat transfer coefficient between water and floor
c_w	4.181	kJ/(°C kg)	Specific heat capacity of water
m_w	200	kg	Mass of water in floor heating system
p	0.1		Fraction of incident solar radiation on floor
η	3		Compressor coefficient of performance (COP)
ρ_v	10^4		Slack variable penalty

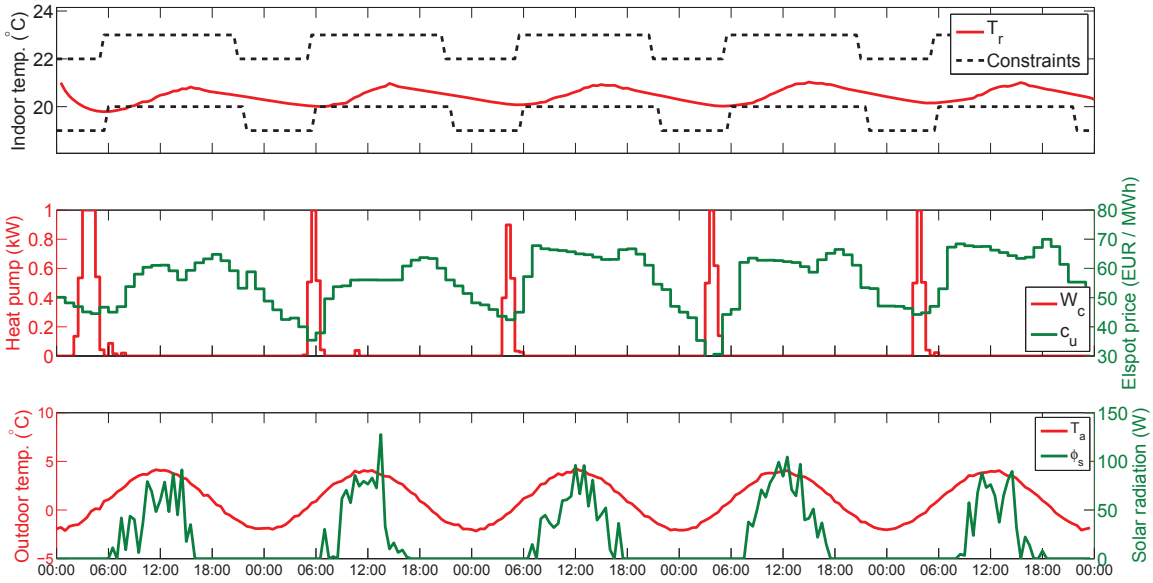

Fig. 4. Temperature in a house with time varying soft constraints, time varying electricity prices, and time varying outdoor temperatures. The simulation time is five days starting 20 JAN 2011 00:00. The upper figure shows the indoor temperature, the middle figure contains the electricity spot price and the optimal schedule for the heat pump, and the lower figure contains the ambient temperature and solar radiation. The compressor is on when the electricity spot price is low.

plot shows the outdoor temperature, T_a, and the solar radiation, ϕ_s. The outdoor temperature reflects a cold climate, i.e. the outdoor temperature is lower than the indoor temperature. The solar radiation has a peak around noon contributing to heating the building. The middle plot shows the actual electricity prices in Western Denmark. The middle plot also contains the computed optimal heat pump power input, W_c. The upper plot shows the predicted indoor temperature along with the predefined time varying constraints. The constraints indicate that during night time the temperature is allowed to be lower than at day time. The figure reveals clearly that the power consumption is moved to periods with cheap electricity and that the thermal capacity of the house floor is able to store enough energy such that the heat pump can be left off during day time. This demonstrates that the slow heat dynamics of the floor can be used to shift the energy consumption to periods with low electricity prices and still maintain acceptable indoor temperatures. Notice that the soft constraints are violated in the beginning due to the initial conditions. We allow for such violations by using reasonable moderate penalty costs for violation of the soft constraints. Consequently, the controller will find cheaper optimal solutions while the comfort level is compromized very little.

We also conducted a simulation with constant electricity prices. In this case, the heat pump now is turned on to just keep the indoor temperature at its lower limit. This implies that there is no load shifting from the heat pump in this case. By comparing the case with varying electricity price, $\{u_k^*\}_{k=0}^{N-1}$, to the case with constant electricity price, $\{u_{k,cst}^*\}_{k=0}^{N-1}$, we observe economic savings around 35%. We obtained this figure

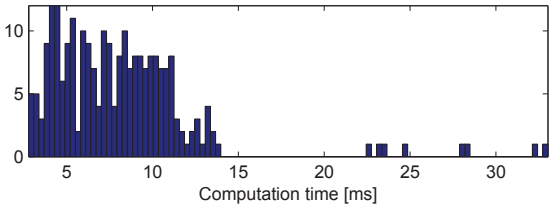

Fig. 5. Computation time distribution for all open loop profiles calculated in the five days closed loop simulation with prediction horizon 48 hours.

by comparing the total electricity expenses using the true time varying electricity prices $\{c_{u,k}\}_{k=0}^{N-1}$ such that the savings S are calculated as

$$S = -\frac{c_u^T u_{cst}^* - c_u^T u^*}{c_u^T u_{cst}^*} \tag{10}$$

Using a simulation study with hard constraints on the indoor temperature, the saving by load shifting was 25%.

Figure 5 shows the computation times of solving the open loop optimization problems for the given simulation using a PC with Intel Core i7 2.67 GHz. The average computation time is seen to be around 8 ms. Using hard constraints the average computation time reduces to 1 ms.

V. Conclusions

In this paper, we have presented a model for the temperature in a residential building with a floor heating system and a heat pump. We used an Economic Model Predictive Controller (Economic MPC) to manipulate the compressor in the heat pump such that the total electricity cost is minimized, while keeping the indoor temperature in a predefined interval. Using actual electricity prices and weather conditions, we demonstrated that the Economic MPC is able to shift the power consumption load to periods with low electricity prices. As the Nordic Electricity spot prices reflect the amount of wind power in the system, the large thermal capacity of the house floor can essentially be used to store cheap electricity from renewable energy sources such as wind turbines. We also observed that the load shifting ability of the Economic MPC can exploit weather forecasts to reduce the total cost of operating a heat pump.

The Economic MPC concept was proofed using perfect forecasts. In the future, we will use real forecast to investigate cases with uncertainty.

References

[1] A. Hepbasli and Y. Kalinci, "A review of heat pump water heating systems," *Renewable and Sustainable Energy Reviews*, vol. 13, pp. 1211–1229, 2009.

[2] F. Karlsson and P. Fahlén, "Impact of design and thermal intertia on the energy saving potential of capacity controlled heat pump heating systems," *International Journal of Refrigeration*, vol. 31, pp. 1094–1103, 2008.

[3] Z. Han, M. Zheng, F. Kong, F. Wang, Z. Li, and T. Bai, "Numerical simulation of solar assisted ground-source heat pump heating system with latent heat energy storage in severly cold area," *Applied Thermal Engineering*, vol. 28, pp. 1427–1436, 2008.

[4] A. Molyneaux, G. Leyland, and D. Favrat, "Environomic multi-objective optimisation of a district heating network considering centralized and decentralized heat pumps," *Energy*, vol. 35, pp. 751–758, 2010.

[5] T. Y. Chen, "Application of adaptive predictive control to a floor heating system with a large thermal lag," *Energy and Buildings*, vol. 34, pp. 45–51, 2001.

[6] H. Karlsson and C.-E. Hagentoft, "Application of model based predictive control for water-based floor heating in low energy residential buildings," *Building and Environment*, vol. 46, pp. 556–569, 2011.

[7] S. Privara, J. Siroky, L. Ferkl, and J. Cigler, "Model predictive control of a building heating system: The first experience," *Energy and Buildings*, vol. 43, pp. 564–572, 2011.

[8] M. Stadler, W. Krause, M. Sonnenschein, and U. Vogel, "Modelling and evaluation of control schemes for enhancing load shift of electricity demand for cooling devices," *Environmental Modelling & Software*, vol. 24, pp. 285–295, 2009.

[9] T. G. Hovgaard, K. Edlund, and J. B. Jørgensen, "The potential of economic MPC for power management," in *49th IEEE Conference on Decision and Control*, 2010, pp. 7533–7538.

[10] F. Oldewurtel, A. Ulbig, A. Parisio, G. Andersson, and M. Morari, "Reducing peak electricity demand in building climate control using real-time pricing and model predictive control," *IEEE Conference on Decision and Control*, 2010.

[11] F. Oldewurtel, A. Parisio, C. N. Jones, M. Morari, D. Gyalistras, M. Gwerder, V. Stauch, B. Lehmann, and K. Wirth, "Energy efficient building climate control using stochastic model predictive control and weather predictions," *Proceedings of ACC*, 2010.

[12] V. M. Zavala, E. M. Constantinescu, and T. K. amd Mihai Anitescu, "On-line economic optimization of energy systems using weather forecast information," *Journal of Process Control*, no. 19, pp. 1725–1736, 2009.

[13] J. B. Rawlings and R. Amrit, "Optimizing process economic performance using model predictive control," in *Nonlinear Model Predictive Control: Towards New Challenging Applications*. Springer, 2009, pp. 119–138.

[14] M. Diehl, R. Amrit, and J. B. Rawlings, "A lyapunov function for economic optimizing model predictive control," *IEEE Transactions on Automatic Control*, 2009.

[15] H. Madsen and J. Holst, "Estimation of continuous-time models for the heat dynamics of a building," *Energy and Buildings*, vol. 22, no. 1, pp. 67–79, 1995.

[16] A. Thavlov, "Dynamic optimization of power consumption," Master's thesis, Dept. of Informatics and Mathematical Modelling, Technical University of Denmark, 2008.

[17] A. Schijndel and M. de Wit, "Advanced simulation of building systems and control with simulink," *Building Simulation*, pp. 1185–1192, 2003.

[18] B. P. Rasmussen, "Dynamic modeling and advanced control of air conditioning and refrigeration systems," Ph.D. dissertation, University of Illinois, 2000.

[19] K. K. Andersen, H. Madsen, and L. H. Hansen, "Modelling the heat dynamics of a building using stochastic differential equations," *Energy and Buildings*, vol. 13, pp. 13–24, 2000.

Peder Bacher, Henrik Madsen, Identifying suitable models for the heat dynamics of buildings, Energy and Buildings 43, p. 1511-1522, 2011

Energy and Buildings 43 (2011) 1511–1522

Contents lists available at ScienceDirect

Energy and Buildings

journal homepage: www.elsevier.com/locate/enbuild

Identifying suitable models for the heat dynamics of buildings

Peder Bacher*, Henrik Madsen

Informatics and Mathematical Modelling, Richard Pedersens Plads, Technical University of Denmark, Building 321, DK-2800 Lyngby, Denmark

ARTICLE INFO

Article history:
Received 25 November 2010
Accepted 16 February 2011

Keywords:
Continuous time modelling
Likelihood ratio tests
Grey-box models
Heat dynamics
Thermal dynamics
Buildings
Model selection
Lumped models
Parameter estimation

ABSTRACT

The present paper suggests a procedure for identification of suitable models for the heat dynamics of a building. Such a procedure for model identification is essential for better usage of readings from smart meters, which is expected to be installed in almost all buildings in the coming years. The models can be used for different purposes, e.g. control of the indoor climate, forecasting of energy consumption, and for accurate description of energy performance of the building. Grey-box models based on prior physical knowledge and data-driven modelling are applied. This facilitates insight into otherwise hidden information about the physical properties of the building. A hierarchy of models of increasing complexity is formulated based on prior physical knowledge and a forward selection strategy is suggested enabling the modeller to iteratively select suitable models of increasing complexity. The performance of the models is compared using likelihood ratio tests, and they are validated using a combination of appropriate statistics and physical interpretation of the results. A case study is described in which a suitable model is sought after for a single storey 120 m^2 building. The result is a set of different models of increasing complexity, with which building characteristics, such as: thermal conductivity, heat capacity of different parts, and window area, are estimated.

1. Introduction

This paper describes a new method for obtaining detailed information about the heat dynamics of a building based frequent readings of the heat consumption, indoor temperature, ambient air temperature, and other climate variables. Such a method is considered to be of uttermost importance as a key procedure for better usage of readings from smart meters, which is expected to be installed in almost all buildings in the coming years. The method is based on a procedure for selecting a suitable model of the heat dynamics for a building. Rabl [12] gives an overview of techniques for steady state and for dynamic analysis of energy use in a building, the latter implicate modelling of the heat dynamics of the building. Such dynamic models can be realized with a set of differential equations, as carried out by Sonderegger [13] and Boyer et al. [4]. Parameter estimation in dynamical models is known as system identification and a survey of different approaches for buildings is found in Ref. [3]. The applied models in the present method are grey-box models, which consist of a set of continuous time stochastic differential equations coupled with a set of discrete time measurement equations. Grey-box modelling is well proven as a comprehensive and accurate method to model dynamical systems and thereby obtain knowledge of the thermal properties of a building (see [8,1,5]). The problem of identifying a suitable model is both finding a model that is in agreement with the physical reality and finding a model, which has a complexity that is in agreement with the level of information embedded in data, which means that the model should neither be under-fitted nor over-fitted. The most suitable model is identified from a set of models of increasing complexity. A forward selection strategy is used, in which the modeller starts out with the simplest feasible model and iteratively selects models of increasing complexity. In each iteration the models are compared using likelihood-ratio tests and the models performances are evaluated. The selection procedure runs until no significant improvement of the model is found. See Refs. [11,10] for an in-depth assessment of likelihood theory and model selection. The procedure is demonstrated by identifying a suitable model for a single storey 120 m^2 building. The building is part of the experimental distributed energy system, Syslab, at Risø DTU in Denmark. It is constructed of wood on the outside and plaster boards on the inside, with a layer of insulation wool in between. The data used spans 6 days and stems from a set of experiments for building energy performance, which was carried out in the winter period of 2009. It is thoroughly described in Ref. [2].

The remaining of the article is organized as follows. The applied grey-box modelling technique is described in Section 2, and in Section 3 the statistical test used for model selection is described. Then the suggested procedure for identifying a suitable model is outlined in Section 4. The following section is devoted to a case-study,

* Corresponding author. Tel.: +45 60774725.
E-mail address: pb@imm.dtu.dk (P. Bacher).
URL: http://www.imm.dtu.dk/~hm (H. Madsen).

0378-7788/$ – see front matter © 2011 Elsevier B.V. All rights reserved.
doi:10.1016/j.enbuild.2011.02.005

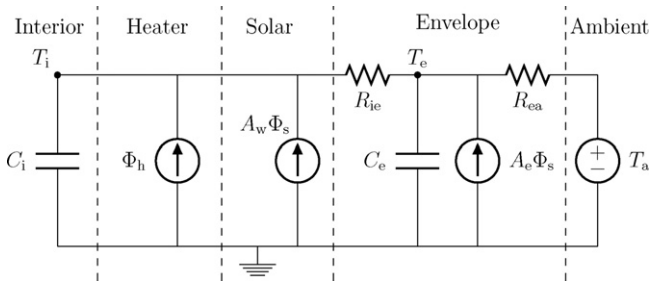

Fig. 1. RC-network of the model described by Eqs. (1) and (2). The model is divided into different parts indicating the corresponding part of the building.

where the procedure is applied. It starts with a description of the building and the data, followed by an outline of the applied models and the selection, and ends with a discussion of the results. Finally a perspective of the applications are given in Section 6 and the conclusions are drawn in Section 7.

2. Grey-box models of a dynamic system

A grey-box model is established using a combination of prior physical knowledge and statistics, i.e. information embedded in data. The prior physical knowledge is formulated by a set of first-order stochastic differential equations, also called a stochastic linear state-space model in continuous time. The equations describe a lumped model of the heat dynamics of the building. It is emphasized that the physical interpretation of the parameters is dependent on how the building is divided into entities in the model.

An example of a feasible model is given here. It has two state variables, one describing the interior temperature T_i and one representing the temperature of the building envelope T_e. The first-order dynamics are represented by the stochastic differential equations

$$dT_i = \frac{1}{R_{ie}C_i}(T_e - T_i)dt + \frac{1}{C_i}\Phi_h dt + \frac{1}{C_i}A_w\Phi_s dt + \sigma_i d\omega_i \quad (1)$$

$$dT_e = \frac{1}{R_{ie}C_e}(T_i - T_e)dt + \frac{1}{R_{ea}C_e}(T_a - T_e)dt + \sigma_e d\omega_e \quad (2)$$

where t is the time, R_{ie} is the thermal resistance between the interior and the building envelope, R_{ea} is the thermal resistance between the building envelope and the ambient air, C_i is the heat capacity of the interior, C_e is the heat capacity of the building envelope, Φ_h is the energy flux from the heating system, A_w is the effective window area, Φ_s is the energy flux from solar radiation, T_a is the ambient air temperature, $\{\omega_{i,t}\}$ and $\{\omega_{e,t}\}$ are standard Wiener processes, and σ_i^2 and σ_e^2 are the incremental variances of the Wiener processes. The model can be represented with the RC-network depicted in Fig. 1, where the model is divided into different parts to show the corresponding parts of the building.

The physical model part is coupled with the data-driven model part with which the information embedded in observed data is used for parameter estimation. The data-driven part in the considered example is represented by the discrete time measurement equation

$$Y_k = T_{ik} + e_k \quad (3)$$

where k is the point in time t_k of a measurement, Y_k is the measured interior temperature and e_k is the measurement error, which is assumed to be a Gaussian white noise process with variance σ^2. This assumption enables evaluation and tests of the performance of the model, since if it is met, this indicates that the physical model is consistent with the observed heat dynamics of the building.

2.1. Maximum likelihood estimation of parameters

Given a grey-box model, as described above, maximum likelihood estimates of the parameters can be obtained. Let the observations be represented by

$$\mathcal{Y}_N = [Y_N, Y_{N-1}, \ldots, Y_1, Y_0] \quad (4)$$

then the likelihood function is the joint probability density

$$L(\theta; \mathcal{Y}_N) = \left(\prod_{k=1}^{N} p(Y_k|\mathcal{Y}_{k-1}, \theta)\right) p(Y_0|\theta) \quad (5)$$

where $p(Y_k|\mathcal{Y}_{k-1}, \theta)$ is a conditional density denoting the probability of observing Y_k given the previous observations and the parameters θ, and where $p(Y_0|\theta)$ is a parameterization of the starting conditions. The maximum likelihood estimates of the parameters are then found by

$$\hat{\theta} = \arg\max_{\theta}\{L(\theta; Y_N)\} \quad (6)$$

Due to the previously mentioned assumptions about the noise process and the fact that the model is linear, it follows that the conditional densities in Eq. (6) are Gaussian densities. Since the conditional densities are Gaussian a Kalman filter can be used to calculate the likelihood function, and an optimization algorithm can be applied to maximize it, thereby calculating the maximum likelihood estimates (see [7] for a detailed discussion). This is implemented in the computer software CTSM, which has been used for carrying out the parameter estimation (see more about the software at[1] and in Ref. [6]).

3. A statistical test for model selection

Statistical tests can be utilized in the search for the most suitable model. If a model is a sub-model of larger model, then a likelihood ratio test can determine if the larger model performs significantly better than the sub-model. Using a sequence of such tests a strategy for selection of the best model can be evolved.

3.1. Likelihood ratio tests

Let a model have parameters $\theta \in \Omega_0$ where $\Omega_0 \in \mathbb{R}^r$ is the parameter space and $r = \dim(\Omega_0)$ is the number of parameters in the model. Let a larger model have parameters $\theta \in \Omega$ where $\Omega \in \mathbb{R}^m$ and $\dim(\Omega) = m$, and assume that

$$\Omega_0 \subset \Omega \quad (7)$$

i.e. the first model is a sub-model of the second model and $r < m$.

The likelihood ratio test

$$\lambda(\mathcal{Y}_N) = \frac{\sup_{\theta \in \Omega_0} L(\theta; \mathcal{Y}_N)}{\sup_{\theta \in \Omega} L(\theta; \mathcal{Y}_N)} \quad (8)$$

where $\mathcal{Y}_N$ is the observed values, can then be used to test the hypothesis

$$H_0 : \theta \in \Omega_0 \quad \text{vs.} \quad H_a : \theta \in \Omega \backslash \Omega_0 \quad (9)$$

since under H_0 the test statistic $-2\log(\lambda(\mathcal{Y}_N))$ converges to a χ^2 distributed random variable with $(m - r)$ degrees of freedom as the number of samples in $\mathcal{Y}_N$ goes to infinity. If H_0 is rejected then the likelihood of the larger model is significantly higher than the likelihood of the sub-model, and it is concluded that $\mathcal{Y}_N$ is more likely to be observed with the larger model. Hence the larger model is

[1] http://www.imm.dtu.dk/ctsm.

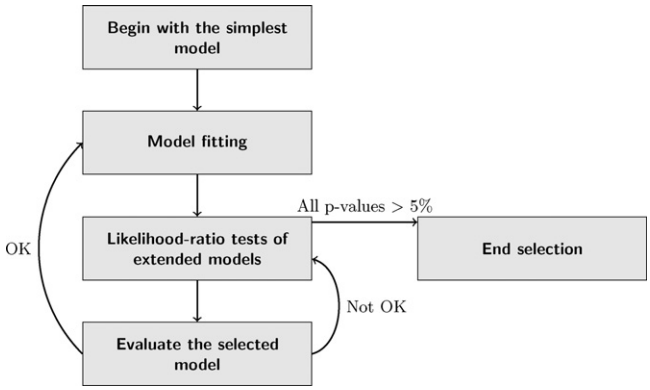

Fig. 2. Illustration of the model selection procedure.

needed over the sub-model to describe the information embedded in data. For more details see Ref. [10].

3.2. Forward selection

In a forward selection procedure the modeller starts with the smallest feasible model and then in each step extends the model with the part that gives the lowest p-value, i.e. the most significant improvement. The possible candidates for improvement that are selected in each iteration are the smallest possible extensions to the current model. The procedure stops when no extensions to the model yields a p-value below a pre-specified limit, usually set to 5%.

4. Model selection procedure

Different strategies for identifying a suitable model is proposed in the literature and finding an appropriate strategy depends on the specific modelling setup. An purely algorithmic and exhaustive selection procedure is seldomly feasible, hence iterative methods, in which the modeller is partly involved in the selection, are commonly applied. Here, a forward selection procedure is suggested for identification of a suitable model for the heat dynamics. It is based on likelihood ratio testing, which is described in Section 3.1.

4.1. Model selection

The procedure starts by a formulation of the simplest feasible model having parameter space Ω_m and a full model with parameter space Ω_{full}, such that

$$\Omega_m \subset \Omega_{full}. \tag{10}$$

Within this range a set of models can be formed, in which a suitable model is to be identified. A suitable model is a sufficient model, which is the smallest model that describes all information embedded in the data [10]. The selection is initiated with the simplest model and then extensions of the model are iteratively added. The selection stops when all of the extensions to the selected model, gives a likelihood-ratio test p-value above the pre-specified limit. Hence the procedure will stop with a model from which no larger model can be found, with which it is significantly more likely to observe the data. As mentioned above a purely algorithmic procedure is not possible, hence the modeller must be involved to evaluate the models estimated in each iteration. The evaluation is carried out by analyzing the properties of residuals and parameter estimates, and if some of the properties are not in line with the assumptions and physical reality, then the modeller may have to influence the choice of model. The procedure is illustrated in Fig. 2 and the steps are

Model fitting: The models which are extended from the current model are fitted to the data by maximum likelihood estimation of the parameters.
Likelihood-ratio tests: Calculate the likelihood-ratio test statistic for the current model versus each of the extended models. Stop if none of the tests have a p-value below 5% and use the current model as the final model, else then select the extended model which yield the lowest p-value.
Evaluate: The modeller evaluates the selected extended model. If the result is satisfactory the model is kept and next iteration can be started; if not, the previous step should be repeated to select another extension.

If two extensions show an almost identical improvement, i.e. the p-values of the tests are nearly equal, the selection can be branched and extensions with different parts examined separately. The procedure will then end with several models, which cannot be tested directly against each other, and it is then up to the modeller to decide which should be preferred. This should be done by comparing the likelihoods, where if two models have almost equal likelihoods the smaller model should be preferred, and furthermore by an evaluation of the residuals and parameter estimates. It can also happen that several models have only marginal difference in performance and that each of them can be considered to be a sufficient model.

4.2. Model evaluation

In each step the selected model must be evaluated. This serves both to check if the model meet the assumptions and if it gives reasonable estimates from a physical point of view. Furthermore the evaluation can reveal model deficiencies from which it can be learned which parts of the model should be further elaborated. The evaluation should consist of the following:

- The assumption of white noise residuals should be inferred upon using the auto-correlation function (ACF) and the cumulated periodogram (CP), which can also reveal how well dynamics on different timescales are modelled.
- Plots of the inputs, outputs, and residuals. These plots can be used to understand which effects are not described properly by the model.
- Evaluation of the estimated physical parameters. Clearly the results should be consistent among different models, e.g. estimate of the thermal resistance of the building envelope should not change significantly among the models. Furthermore the modeller have to judge if the results are consistent with reality.

5. Case study: model identification for a building

The method is demonstrated by applying it to identify a suitable model for a building. The building, named FlexHouse, is part of the experimental energy system Syslab, at Risø DTU in Denmark. It is well suited for such experiments since it has a controllable electrical heating system. Measurements consisting of five minute values over a period of six days are used (for further details see Ref. [2]) in which a thorough description of the experiments and data is given. This section starts with a description of the building and measurement equipment, then the data is presented, followed by an outline of the considered models, and finally the model identification and evaluation is given.

5.1. Description of the building and measurement equipment

The outer walls of the building are constructed of wood on the outside and plaster boards on the inside, with a layer of insulation

Fig. 3. (a) The north facade and (b) is the south facade of the building.

wool in between. An image of the north facade and an image of the south facade of the building can be seen in Fig. 3. The building rests on piles, leaving an air gab between the ground and the building. The roof is flat and covered with roofing felt. The dimensions of the floor plan are approximately 7.5 times 16 m. In Fig. 4 the floor plan of the building is shown. A server system is installed in the building, which can control the electrical heaters located as indicated on the floor plan. To measure the indoor temperature Hobo U12-012 Temp/RH/Light/Ext sensors mounted on a small piece of wood was hanged freely in the middle of each each room. A small climate station is located two meters east of the building, the position relative to the building is indicated in Fig. 4.

5.2. Data

The present study is based on data collected during a series of experiments carried out in February to April 2009. The following time series consisting of five minute average values are used:

y (°C) A single signal representing the indoor temperature. It is formed as the first principal component of the measurements of the indoor temperature from the Hobo sensors.
T_a (°C) Observed ambient air temperature at the climate station.
Φ_h (kW) Total heat input from the electrical heaters in the building.
Φ_s (kW/m^2) The global irradiance measured at the climate station.

Plots of the time series can be found in Fig. 5. The controlled heat input is a pseudo-random binary sequence (PRBS), which has white noise properties and no correlation with the other inputs. It is designed to excite the heat dynamics at several ranges of frequencies in which the time constants of the building is expected to be, such that the information embedded in data is optimized for estimation of the heat dynamic properties of the building (see Ref. [9]).

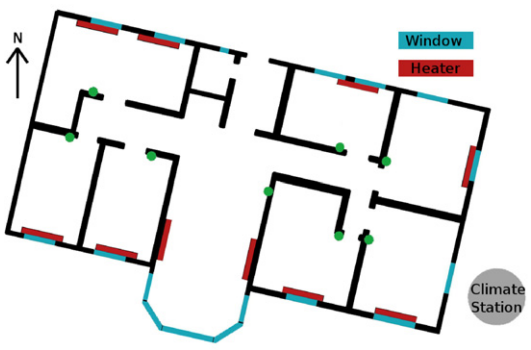

Fig. 4. The floor plan of the building.

5.3. Applied models

The proposed procedure is such, that the modeller starts with the simplest model and iteratively selects more complex models. This implies fitting a set of models from the simplest model to the most feasible complex model, denoted the full model. In this section the set of applied models and the result of the iterative selection procedure is described. All the models are grey-box models, in which the physical part is stochastic linear state-space model (as presented in Section 2) and where the dynamics of the states can be written

$$d\mathbf{T} = \mathbf{AT}dt + \mathbf{BU}dt + d\omega \tag{11}$$

where $\mathbf{T}$ is the state vector and $\mathbf{U}$ is the input vector, and none of the state variables or input variables are in $\mathbf{A}$ or $\mathbf{B}$ which only consist of parameters. All the considered models have an input vector with three inputs

$$\mathbf{U} = [T_a, \Phi_s, \Phi_h]^T \tag{12}$$

All the models are lumped, but with a different structure, which implies that a given parameter does not necessarily represent the same physical entity in each model. For example the parameter C_i is representing the heat capacity of the entire building in the simplest model, whereas this heat capacity is divided into five heat capacities in the full model, in which the parameter C_i represents the heat capacity of the indoor air. This is elaborated further in Section 5.5.2, where the parameter estimates for the models are presented. Furthermore it should be kept in mind that these models are linear approximations to the real system.

In the following sections the full and the simplest model are described, since they represent the range of applied models. First the full model is outlined to give a complete overview of all the individual parts, which is included in the models. Then the simplest model is presented, since it is the first model applied in the selection procedure and furthermore it illustrates how the models are lumped. Each model is named from its state vector and where needed a few parameter names. See Appendix A for a list of RC-networks corresponding to all applied models.

5.3.1. The full model TiTmTeThTsAeRia

The RC-network of the full model, which is the most complex model applied, is illustrated in Fig. 6. This model includes all the individual parts of the building, which it is found feasible to include in linear models, with the current available data. The individual model parts are indicated on the figure. The model parts are:

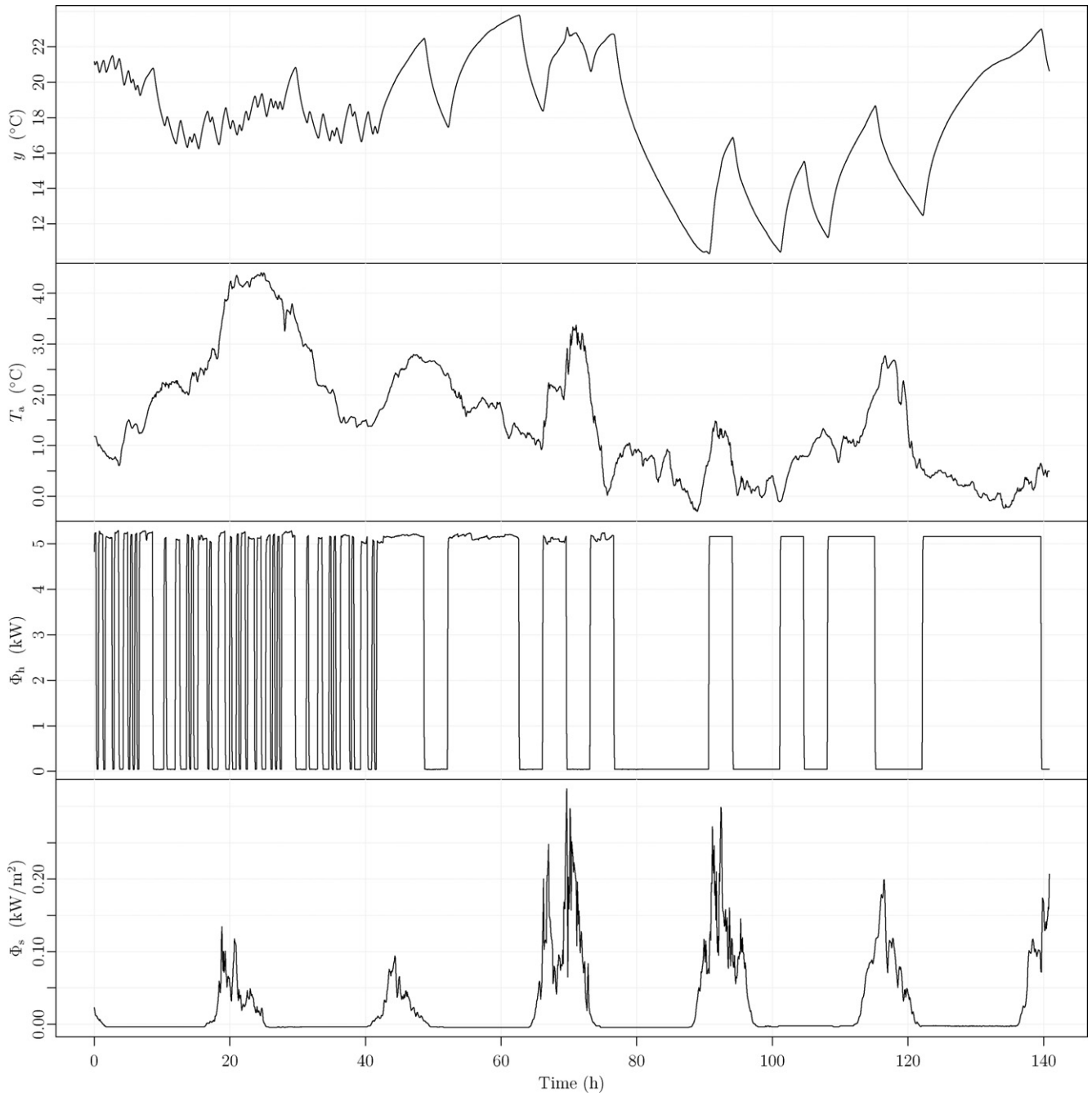

Fig. 5. The data set. From the top, the first plot shows the observed indoor temperature y, the second shows the ambient air temperature T_a, followed by a plot of the heat input Φ_h, and finally the lower plot shows the global irradiance Φ_s.

Sensor: The temperature sensors are modelled with a heat capacity and a thermal resistance to the interior.
Interior: In the full model the interior is considered to be the indoor air (again remember that, since the models are lumped models, the building part represented by "Interior" is mostly different for each model) and it is modelled as a heat capacity connected to other parts by thermal resistances.
Medium: A thermal medium inside the building is the interior walls and furniture, which is modelled with a heat capacity and a thermal resistance to the interior.
Heater: The heaters are modelled by a heat capacity and a thermal resistance to the interior.
Solar: The heat input from solar radiation is modelled by the global irradiance multiplied with the effective window area.
Envelope: The building envelope is modelled with a heat capacity and thermal resistances to both the interior and the ambient. A thermal resistance directly coupled to the ambient is also included.
Ambient: The ambient is represented by the observed ambient air temperature.

The full model includes five state variables, that each represents the temperature in a part of the building, and they are:

T_s: The temperature of the sensor, which for the full model is used as the model output, i.e. Y_k in the measurement equation (Eq. (19)).
T_i: The temperature of the interior, i.e. the indoor air.

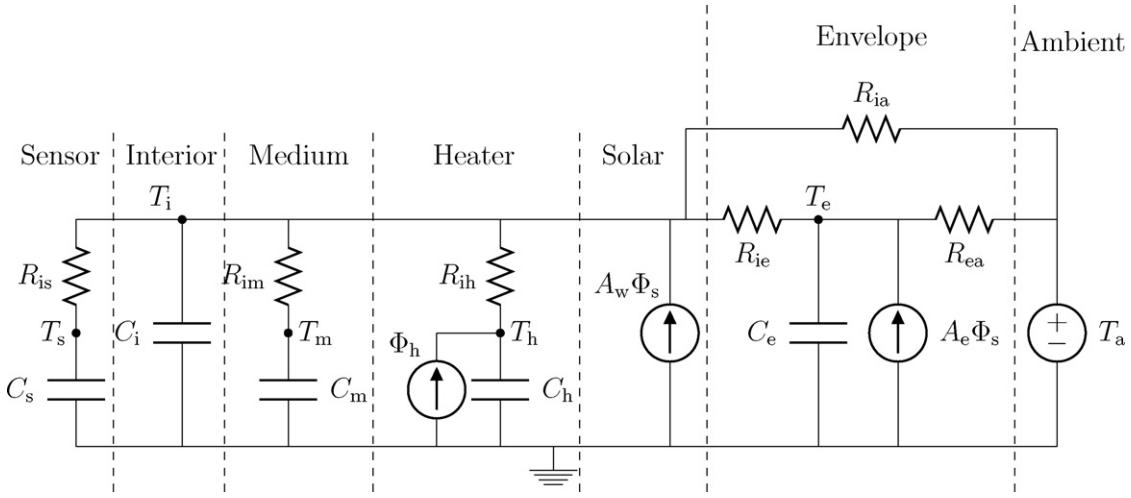

Fig. 6. The full model *TiTmTeThTsAeRia* with the individual model parts indicated. This model includes all parts which is included in any of the applied models.

T_m: The temperature of an interior thermal medium, i.e. interior walls and furniture.
T_h: The temperature of the heaters.
T_e: The temperature of the building envelope.

The parameters of the model represent different thermal properties of the building. This includes thermal resistances:

R_{is}: between the interior and the sensor,
R_{im}: between the interior and the interior thermal medium,
R_{ih}: between the heaters and the interior,
R_{ia}: between the interior and the ambient,
R_{ie}: between from the interior and the building envelope,
R_{ea}: between the building envelope and the ambient.

The heat capacities of different parts of the building are represented by:

C_s: for the temperature sensor,
C_i: for the interior,
C_m: for the interior walls and furniture,
C_h: for the electrical heaters,
C_e: for the building envelope.

Finally two coefficients are included, each representing an estimate of an effective area in which the energy from solar radiation enters the building. They are:

A_w: The effective window area of the building.
A_e: The effective area in which the solar radiation enters the building envelope.

The set of stochastic differential equations describing the heat flows in the full model are

$$dT_s = \frac{1}{R_{is}C_s}(T_i - T_s)dt + \sigma_s d\omega_s \tag{13}$$

$$dT_i = \frac{1}{R_{is}C_i}(T_s - T_i)dt + \frac{1}{R_{im}C_i}(T_m - T_i)dt + \frac{1}{R_{ih}C_i}(T_h - T_i) \tag{14}$$

$$\frac{1}{R_{ie}C_i}(T_e - T_i)dt + \frac{1}{R_{ia}C_i}(T_a - T_i)dt + \frac{1}{C_i}A_w\Phi_s dt + \sigma_i d\omega_i \tag{15}$$

$$dT_m = \frac{1}{R_{im}C_m}(T_i - T_m)dt + \sigma_m d\omega_m \tag{16}$$

$$dT_h = \frac{1}{R_{ih}C_h}(T_i - T_h)dt + \frac{1}{C_h}\Phi_h dt + \sigma_h d\omega_h \tag{17}$$

$$dT_e = \frac{1}{R_{ie}C_e}(T_i - T_e)dt + \frac{1}{R_{ea}C_e}(T_a - T_e)dt + \frac{1}{C_e}A_e\Phi_s dt + \sigma_e d\omega_e \tag{18}$$

and the measurement equation is

$$Y_k = T_{s,k} + e_k \tag{19}$$

since the observed temperature is encumbered with some measurement error.

5.3.2. The simplest model Ti

The simplest model considered is illustrated by the RC-network in Fig. 7. The model has one state variable T_i and the following parameters:

R_{ia}: The thermal resistance from the interior to the ambient.
C_i: The heat capacity of the entire building, including the indoor air, interior walls, furniture etc., and the building envelope.
A_w: The effective window area of the building.

The stochastic differential equation describing the heat flow is

$$\frac{dT_i}{dt} = \frac{1}{R_{ia}C_i}(T_a - T_i) + \frac{1}{C_i}A_w\Phi_s + \frac{1}{C_i}\Phi_h + \sigma_i\frac{d\omega_i}{dt} \tag{20}$$

and the measurement equation is

$$Y_k = T_{i,k} + e_k \tag{21}$$

Note the differences in representation of the building parts between the simplest and full model, e.g. R_{ia} represent the thermal

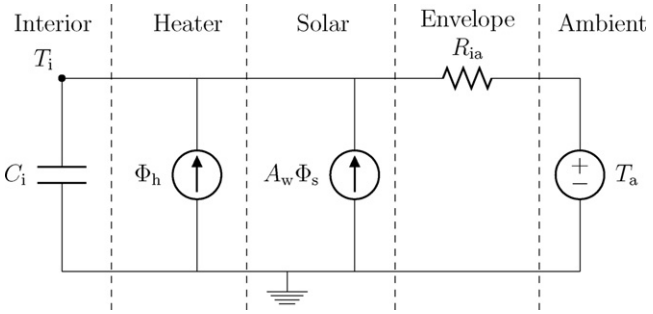

Fig. 7. RC-network of the model *Ti*, which is the simplest feasible model.

Table 1
Log-likelihood $l(\theta; y_N)$ for the fitted models ordered by iterations of the model selection procedure and in each row by log-likelihood. In each iteration the extended model with highest log-likelihood is selected, which is the rightmost models in the table. The number of estimated parameters for each model is indicated by m.

Iteration	Models			
Start	*Ti*			
$l(\theta; y_N)$	2482.6			
m	6			
1	*TiTe*	*TiTm*	*TiTs*	*TiTh*
	3628.0	3639.4	3884.4	3911.1
	10	10	10	10
2	*TiThTs*	*TiTmTh*	*TiTeTh*	
	4017.0	5513.1	5517.1	
	14	14	14	
3	*TiTeThRia*	*TiTeThAe*	*TiTmTeTh*	*TiTeThTs*
	5517.3	5520.5	5534.5	5612.4
	15	15	18	18
4	*TiTeThTsRia*	*TiTmTeThTs*	*TiTeThTsAe*	
	5612.5	5612.9	5614.6	
	19	22	19	
5	*TiTmTeThTsAe*	*TiTeThTsAeRia*		
	5614.6	5614.7		
	23	20		

resistance of the building envelope in the simplest model, whereas this is represented by a coupling of R_{ia}, R_{ie}, and R_{ea} in the full model.

5.4. Model identification

The identification procedure is applied to find a sufficient model in the set of models ranging from *Ti* to *TiTmTeThTsAeRia*. The log-likelihood of each model, which is fitted, is listed in Table 1 ordered by the iterations of the model selection. The procedure begins with the simplest model. Then in the first iteration four extended models are fitted and *TiTh* is selected since it has the highest log-likelihood, hence the lowest p-value of the likelihood-ratio tests (the four models have the same number of parameters). The selection procedure is carried out until no significant extension can be found, which occurs in iteration number five. During each iteration the current selected model is evaluated (see Section 5.5). It is found that the models selected in each iteration are all satisfying the evaluation with respect to improvement of the results, etc. In Table 2 the result of likelihood-ratio tests for model expansion in each iteration is listed. Clearly, the expansions carried out in the first three iterations indicate very significant improvements of the model. In iteration four, the improvement is still below 5%, whereas no improvement is found in iteration five. The procedure thus ends with *TiTeThTsAe* as a sufficient model, which is illustrated by the RC-network in Fig. 8.

5.5. Model evaluation

In the following the selected models are evaluated as outlined in Section 4.2.

Table 2
Tests carried out in the model selection procedure.

Iteration	Sub-model	Model	$m-r$	$-2\log(\lambda)(y)$	p-Value
1	*Ti*	*TiTh*	4	4121	$<10^{-16}$
2	*TiTh*	*TiTeTh*	4	4634	$<10^{-16}$
3	*TiTeTh*	*TiTeThTs*	4	274	$<10^{-16}$
4	*TiTeThTs*	*TiTeThTsAe*	1	6.4	0.011
5	*TiTeThTsAe*	*TiTeThTsAeRia*	1	0.17	0.68

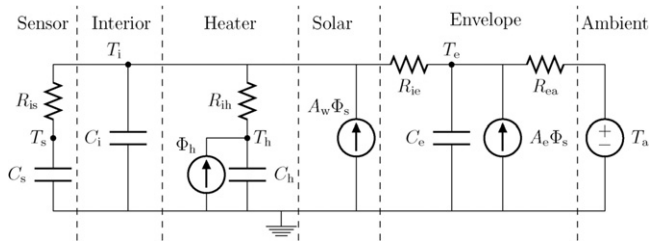

Fig. 8. The final selected model *TiTeThTsAe* with the individual model parts indicated.

Table 3
The estimated parameters. The heat capacities, C_x, are in [kWh/°C]. The thermal resistances, R_{xx}, are in [°C/kW]. The areas, A_x, are in [m^2]. The time constants, τ_x, are in (h). Note that the physical interpretation for many of the parameters is different for each model.

	Model				
	Ti	*TiTh*	*TiTeTh*	*TiTeThTs*	*TiTeThTsWithAe*
C_i	2.07	1.36	1.07	0.143	0.0928
C_e	–	–	2.92	3.24	3.32
C_h	–	0.309	0.00139	0.321	0.889
C_s	–	–	–	0.619	0.0549
R_{ia}	5.29	5.31	–	–	–
R_{ie}	–	–	0.863	0.909	0.897
R_{ea}	–	–	4.54	4.47	4.38
R_{ih}	–	0.639	93.4	0.383	0.146
R_{is}	–	–	–	0.115	1.89
A_w	7.89	6.22	5.64	6.03	5.75
A_e	–	–	–	–	3.87
τ_1	10.9	0.16	0.129	0.0102	0.0102
τ_2	–	8.9	0.668	0.105	0.105
τ_3	–	–	18.4	0.786	0.788
τ_4	–	–	–	19.6	19.3

5.5.1. Residuals

Plots of output, inputs, and residuals for each model can be seen in Fig. 9. For each model the auto-correlation function (ACF) of the residuals is plotted in Fig. 10 and the cumulated periodogram (CP) in Fig. 11. It is seen directly from the plot of the residuals from the simplest model T_i, that they do not have white noise properties and that they are not independent of the inputs. The ACF of the residuals also clearly show a high lag dependency, and the CP reveals that the model is not detailed enough to describe the dynamics. Examining the plot of the residuals for the model selected in the first iteration, *TiTh*, it is seen that the level of the residuals is reduced compared to the residuals for *Ti*. The ACF and CP indicate that the assumption of white noise residuals is not fulfilled. From the plot of the residuals for the model selected in the second iteration, *TiTeTh*, it is seen that the level of the residuals is reduced dramatically, but that some dependency of the inputs is still seen, mostly from the solar irradiance. The ACF reveals that the characteristics of the residuals are much closer to white noise, which is also seen from the CP, indicating that the model now describes the heat dynamics of the building quite well. The plot of the residuals, ACF, and CP for the model selected in the third iteration *TiTeThTs*, reveals only slight improvements compared to the previous model. Finally the plots for the final selected model *TiTeThTsAe*, show that almost no differences can be observed from the previous model. The highest level of error can be observed where the solar irradiance is high, hence it is found that further improvement of the model should be focused on the part in which the solar radiation enters the building, or alternatively in letting the incremental variance of the Wiener process depend on the solar radiation.

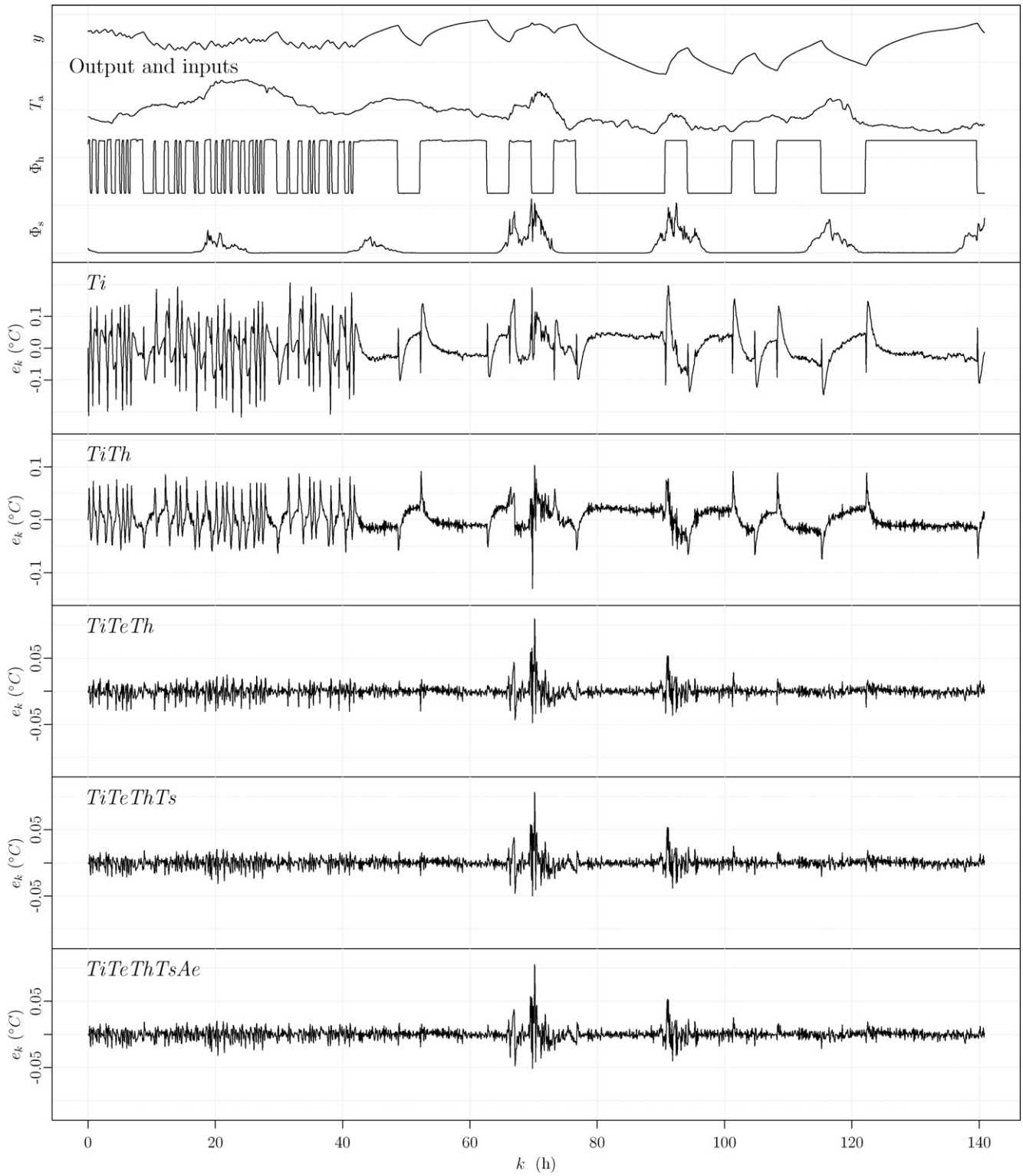

Fig. 9. The upper plot is of the output and inputs, and the following plots are of the residuals for each of the selected models. On each plot of the residuals the model name is indicated.

5.5.2. Parameter estimates

The parameter estimates of the selected models are evaluated in the following. The estimates are presented in Table 3 together with the time constants calculated for each of the selected models. The total heat capacity and thermal resistance of the building envelope estimated by the selected models are presented in Table 4. As found by evaluating the residuals (see previous section) the models *Ti* and *TiTh* do not describe the dynamics of the system very well, which implies that the estimates of the heat capacities are not reliable. Estimates of the heat capacities found by the tree larger models are more credible, especially it is seen that the time constants are almost equal, indicating that the models comprise the same dynamics. The exact physical interpretation of the smaller heat capacities C_i, C_h, and C_s cannot be given, but it is noted that their sum, for

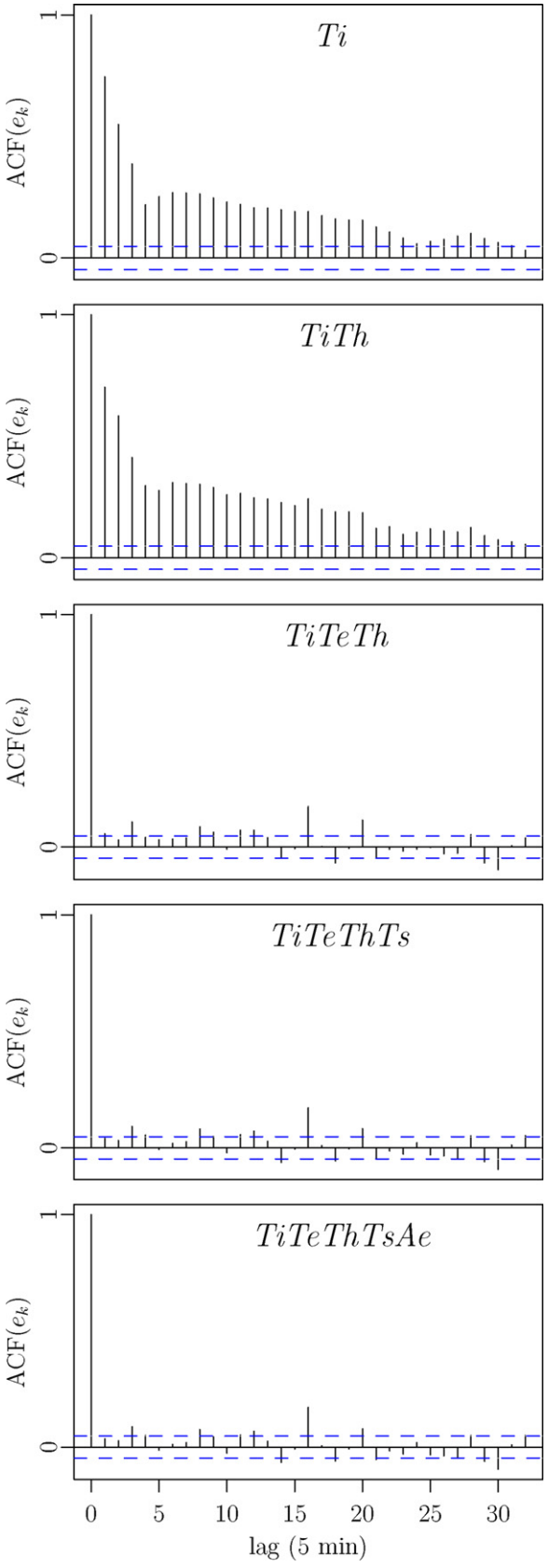

Fig. 10. The auto-correlation function of the residuals for each of the selected models.

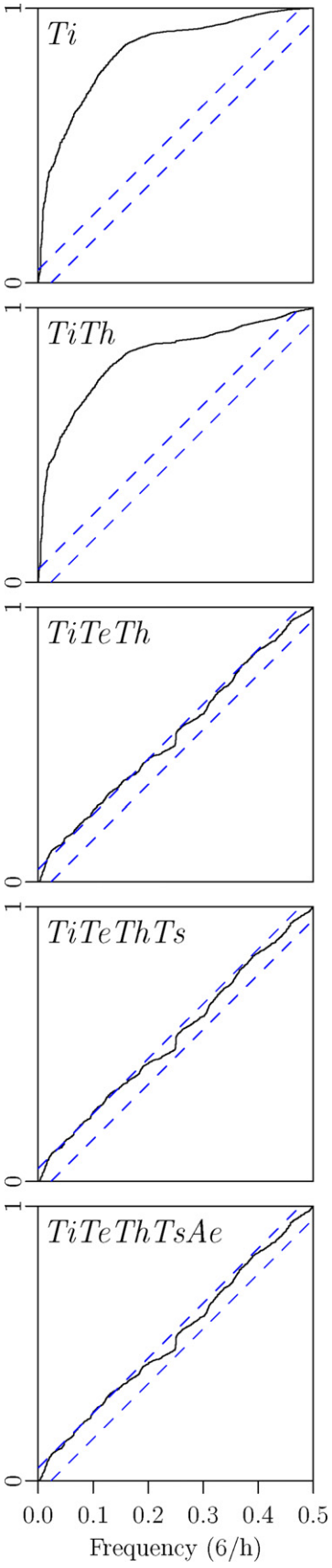

Fig. 11. The cumulated periodogram of the residuals for each of the selected models.

Table 4
The total heat capacity [kWh/°C] and thermal resistance [°C/kW] of the building envelope estimated by the selected models. The *UA*-values α_{UA} are in [W/°C m^2].

	Model				
	Ti	*TiTh*	*TiTeTh*	*TiTeThTs*	*TiTeThTsAe*
C_{total}	2.07	1.67	3.99	4.32	4.36
$R_{envelope}$	5.29	5.31	5.40	5.38	5.28
α_{UA}	1.55	1.55	1.52	1.53	1.55

each of the three larger models, is quite close ranging from 1.03 to 1.08 kWh/°C.

The estimated total thermal resistance of the building envelope and thereby the *UA*-values is quite similar for all models, as seen in Table 4.

6. Applications

Identification of a suitable model of the heat dynamics of a building based on frequent readings of heat consumption, indoor temperature, ambient air temperature, and climate variables, will be very useful for different purposes. Important fields of application are:

Accurate description of energy performance of the building: An energy signature of buildings can provide important information for energy- and cost effective improvements of the building. The most effective actions to be taken for an individual building can be identified. Furthermore the heat consumption due to physical effects, such as a poor isolated building envelope, can be separated from behavioral effects, e.g. a high indoor temperature.
Forecasting of energy consumption for heating: Forecasting of energy consumption for heating can be used for integration of large amounts of renewable energy, such as wind- and solar energy. Implementation of electrical heating with hot water tanks for heat storage in individual houses can be profitable in the near future. Knowledge of the heat dynamics of buildings is essential to forecasting and control of such systems.
Indoor climate control: Control of the indoor temperature, ventilation, etc. to provide a good indoor climate conditions can be carried out with methods which include models of the heat dynamics. The models can also be extended to include the effect of wind and thereby provide information of the air tightness of buildings.

7. Conclusion

A procedure for identification of the most suitable models for the heat dynamics of a building has been described and applied on the basis of data from an experiment carried out in February 2009. The procedure is based on likelihood-ratio testing combined with a forward selection strategy. The proposed models are grey-box models, where a combination of prior physical knowledge and data-driven modelling is utilized. The data used for the modelling consist of: climate data measured at the location, measurements of the indoor temperature, and a PRBS controlled heat input.

The results of the identification procedure are evaluated and discussed, both in a statistical and physical context. The evaluation reveal that the selected model meet the assumptions of white noise residuals, hence it can be applied to give reliable estimates consistent with reality and the results are statistically validated. Furthermore model deficiencies are pointed out, from which further advancement of the model should be pursued. For the considered building this is primarily on the model part where the solar radiation input enters the building.

It has been shown that the method is able to provide rather detailed knowledge of the heat dynamics of the building. This includes for instance the thermal resistance of the envelope and thereby the *UA*-value, parameters describing the capabilities for storing heat, and the time constants of the building.

Appendix A. RC-networks of applied models

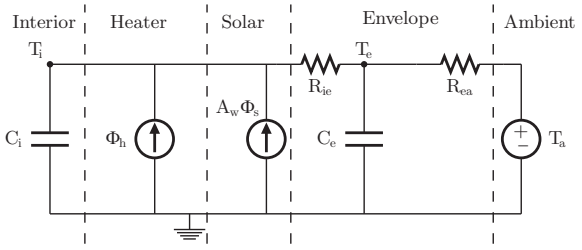

(a) RC-network network of *TiTe*.

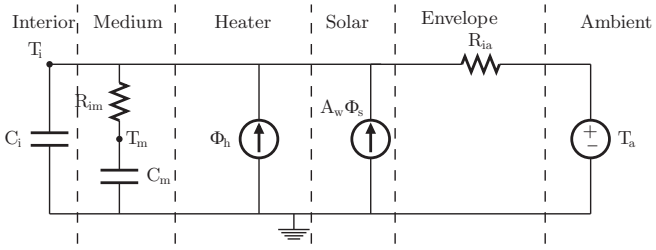

(b) RC-network network of *TiTm*.

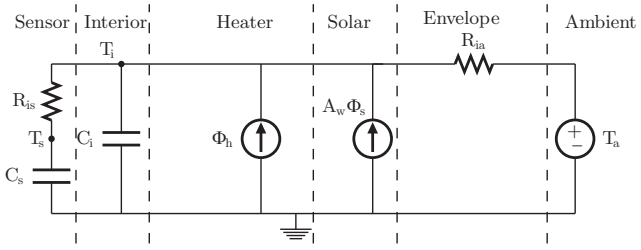

(c) RC-network network of *TiTs*.

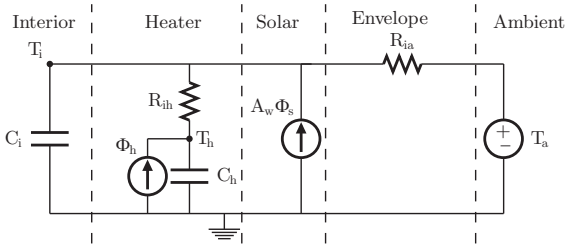

(d) RC-network network of *TiTh*.

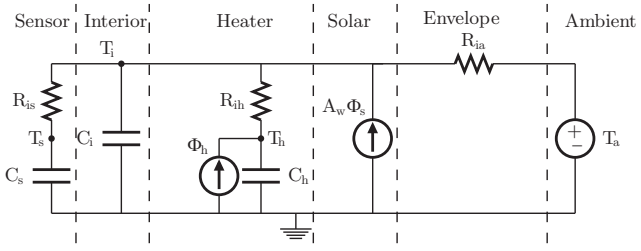

(e) RC-network network of *TiThTs*.

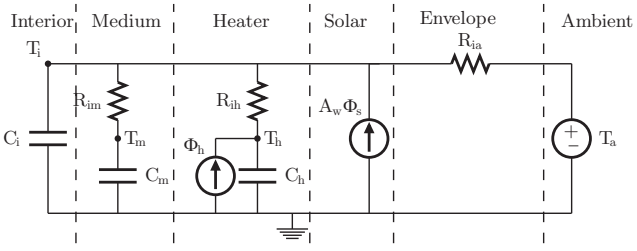

(f) RC-network network of *TiTmTh*.

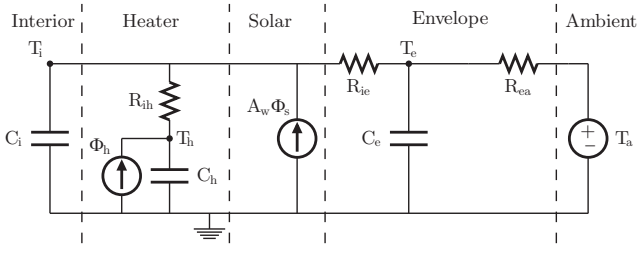

(g) RC-network network of *TiTeTh*.

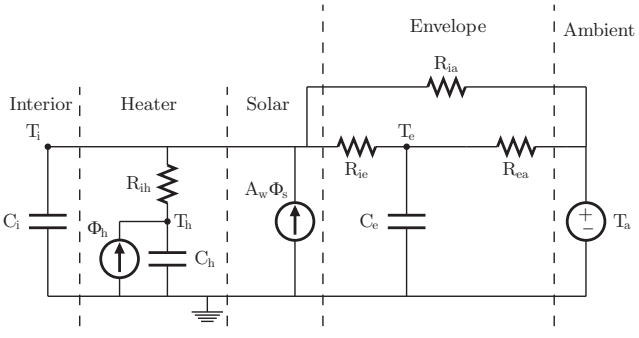

(h) RC-network network of *TiTeThRia*.

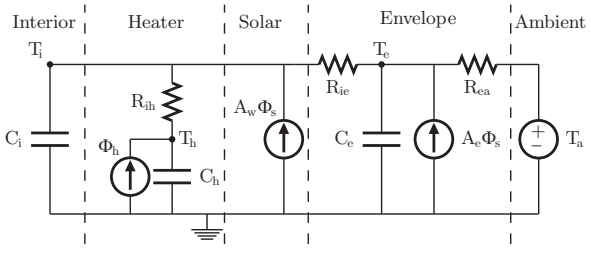

(i) RC-network network of *TiTeThAe*.

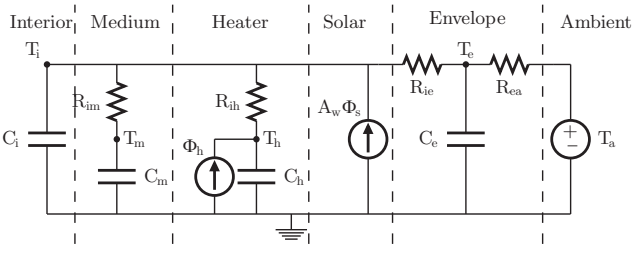

(j) RC-network network of *TiTmTeTh*.

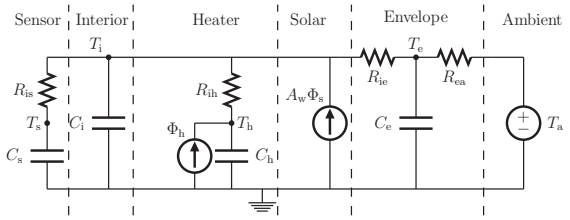

(k) RC-network network of $TiTeThTs$.

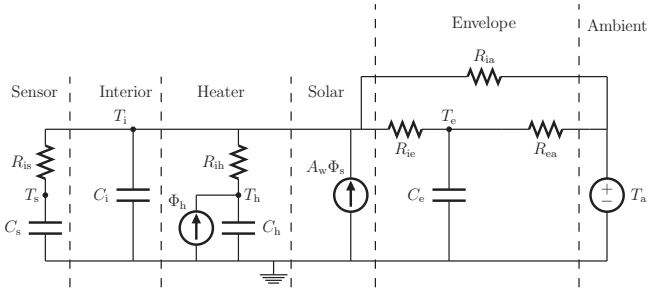

(l) RC-network network of $TiTeThTsRia$.

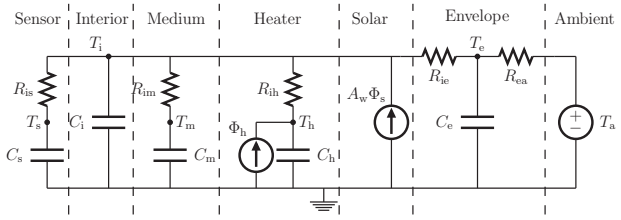

(m) RC-network network of $TiTmTeThTs$.

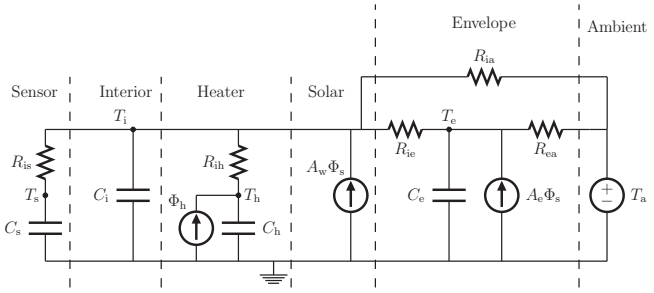

(n) RC-network network of $TiTeThTsAeRia$.

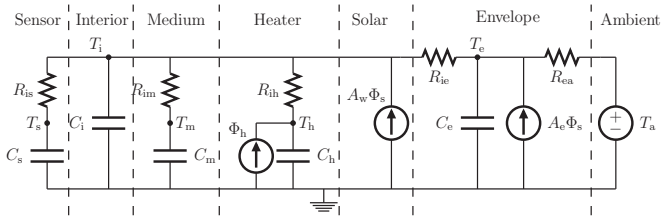

(o) RC-network network of $TiTmTeThTsAe$.

References

[1] K.K. Andersen, H. Madsen, L.H. Hansen, Modelling the heat dynamics of a building using stochastic differential equations, Energy and Buildings 31 (1) (2000) 13–24.

[2] P. Bacher, H. Madsen, Experiments and data for building energy performance analysis: financed by the Danish electricity saving trust, in: Tech. Rep., DTU Informatics, Building 321, Kgs. Lyngby, 2010.

[3] J.J. Bloem (Ed.), System Identification Applied to Building Performance Data. CEC-EUR 15885 EN, 1994.

[4] H. Boyer, J. Chabriat, B. GrondinPerez, C. Tourrand, J. Brau, Thermal building simulation and computer generation of nodal models, Building and Environment 31 (May (3)) (1996) 207–214.

[5] M. Jiménez, H. Madsen, J. Bloem, B. Dammann, Estimation of non-linear continuous time models for the heat exchange dynamics of building integrated photovoltaic modules, Energy and Buildings 40 (2) (2008) 157–167.

[6] N.R. Kristensen, H. Madsen, Continuous Time Stochastic Modelling, CTSM 2.3—Mathematics Guide. Tech. Rep., DTU, 2003.

[7] N.R. Kristensen, H. Madsen, S.B. Jørgensen, Parameter estimation in stochastic grey-box models, Automatica 40 (2) (2004) 225–237.

[8] H. Madsen, J. Holst, Estimation of continuous-time models for the heat dynamics of a building, Energy and Buildings 22 (1) (1995) 67–79.

[9] H. Madsen, J. Schultz, Short Time Determination of the Heat Dynamics of Buildings. Tech. Rep., DTU, 1993.

[10] H. Madsen, P. Thyregod, Introduction to General and Generalized Linear Models, CRC Press, 2010.

[11] Y. Pawitan, In All Likelihood: Statistical Modelling and Inference Using Likelihood, Oxford University Press, 2001.

[12] A. Rabl, Parameter-estimation in buildings—methods for dynamic analysis of measured energy use, Journal of Solar Energy Engineering—Transactions of the ASME 110 (1) (1988) 52–66.

[13] R.C. Sonderegger, Dynamic models of house heating based on equivalent thermal parameters, Ph.D. Thesis, Princeton Univ., NJ, 1978.

Rasmus Halvgaard, Peder Bacher, Bengt Perers, Elsa Andersen, Simon Furbo, John B. Jørgensen, Niels K. Poulsen, Henrik Madsen, Model predictive control for a smart solar tank based on weather and consumption forecasts, Energy Procedia 30, p. 270-278, 2012

Available online at www.sciencedirect.com

SciVerse ScienceDirect

Energy Procedia 30 (2012) 270 – 278

Energy Procedia

SHC 2012

Model predictive control for a smart solar tank based on weather and consumption forecasts

Rasmus Halvgaard[a*], Peder Bacher[a], Bengt Perers[b], Elsa Andersen[b], Simon Furbo[b], John B. Jørgensen[a], Niels K. Poulsen[a], Henrik Madsen[a]

[a]*Technical University of Denmark, Department of Informatics, Richard Petersens Plads, Kgs. Lyngby 2800, Denmark*
[b]*Technical University of Denmark, Department of Civil Engineering, Brovej, Kgs. Lyngby 2800, Denmark*

Abstract

In this work the heat dynamics of a storage tank were modelled on the basis of data and maximum likelihood methods. The resulting grey-box model was used for Economic Model Predictive Control (MPC) of the energy in the tank. The control objective was to balance the energy from a solar collector and the heat consumption in a residential house. The storage tank provides heat in periods where there is low solar radiation and stores heat when there is surplus solar heat. The forecasts of consumption patterns were based on data obtained from meters in a group of single-family houses in Denmark. The tank can also be heated by electric heating elements if necessary, but the electricity costs of operating these heating elements should be minimized. Consequently, the heating elements should be used in periods with cheap electricity. It is proposed to integrate a price-sensitive control to enable the storage tank to serve a smart energy system in which flexible consumers are expected to help balance fluctuating renewable energy sources like wind and solar. Through simulations, the impact of applying Economic MPC shows annual electricity cost savings up to 25-30%.

Keywords: Model predictive control; solar heating; smart solar tank; smart energy systems

1. Introduction

Economic Model Predictive Control (MPC) has previously been used to reduce the electricity costs of heating and cooling in buildings [1,2,3]. For a smart solar tank [4] the same MPC framework can be

* Rasmus Halvgaard. Tel.: +45 45255281; fax: +45 45882673.
E-mail address: rhal@imm.dtu.dk

1876-6102 © 2012 The Authors. Published by Elsevier Ltd.
Selection and peer-review under responsibility of the PSE AG
doi:10.1016/j.egypro.2012.11.032

applied in order to save energy and reduce electricity costs. For the system considered in this paper, the electricity consumption of the auxiliary heating elements in a storage tank must be controlled. The heating elements can be turned on in periods when the amount of solar energy alone cannot meet the heat demand, e.g. hot water and space heating in a residential house.

The MPC exploits knowledge about the future inputs, so to minimize electricity costs a good tank model is required, along with excellent forecasts of both solar radiation and consumption patterns. In this paper we estimate the parameters in a storage tank model from measured data with a maximum likelihood method. With this model we design an Economic MPC to control the power consumption of the heating elements according to a price. By adding a price signal to the objective of the controller, the MPC will minimize the electricity costs for the individual tank by shifting power consumption to periods with cheap electricity. As the electricity costs are reduced the trade-off of considering prices and not power consumption alone is to use more power, but at the right time.

The performance of the MPC in terms of power consumption and electricity costs is investigated for different consumption patterns in a one-year simulation period. The influence of uncertainty in the forecasts of both solar radiation and consumption is also examined. We assume that electricity prices are known each hour at least 12 hours ahead, which is true for the day-ahead Elspot market in Denmark [5]. These prices reflect the power demand of the overall energy system and also indicate the amount of cheap renewable energy sources available, such as wind power.

2. Solar thermal collector and storage tank

The smart solar tank consists of a solar collector with area of 9 m^2, and a storage tank with a total volume of 788 l. The tank itself contains an inner tank for domestic hot water and a pressureless outer tank for space heating. The tank can be heated by the solar collectors. To help cover the remaining heat demand, three smaller electric heating elements of 3 kW each are installed in the tank, as shown in Figure 1b.

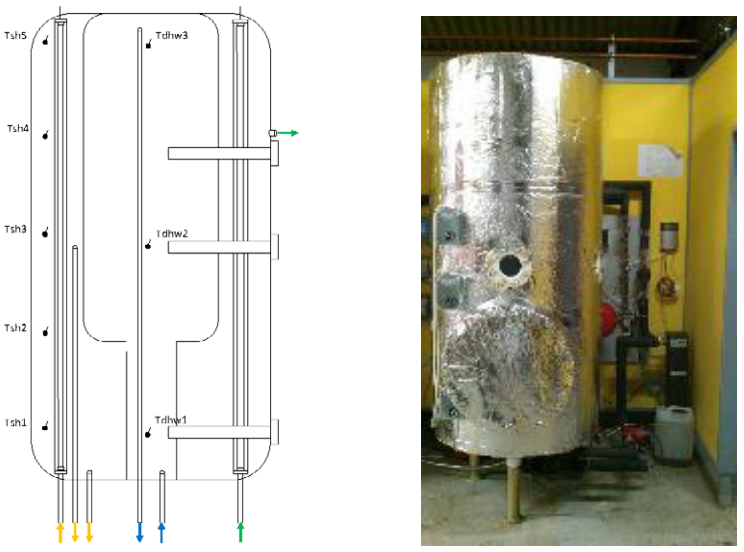

Fig. 1. (a) Sketch of the tank with inlets, outlets and eight temperature measurement points. (b) Photo of storage tank in lab

Solar energy is transferred to the tank by feeding water into the tank through a stratification device. In this way, beneficial thermal stratification is built up during solar collector operation [4,6]. Space heating is transferred from the upper part of the tank and the return inlet to the tank goes through another stratification device.

2.1. Tank model

We model the storage tank separated from the solar collector such that the energy balance is

$$Q_{\text{tank}} = Q_{heater} + Q_{solar} - Q_{consumption} - Q_{loss} \quad (1)$$

The contribution from the solar collector Q_{solar} and heat consumption $Q_{\text{consumption}}$ are forecasted inputs. The heating element input power consumption Q_{heater} is controllable. The loss is modelled as proportional to the temperature difference between the internal tank temperature and the ambient room temperature. The actual energy in the tank Q_{tank} cannot be physically measured, but is assumed to be dependent on the measured tank temperatures. Eight temperature measurements from different layers of the tank are combined to represent an overall tank temperature (T_t) proportional to the stored energy. Using an average from the eight sensors (n = 8) we get the tank temperature

$$T_t = \frac{1}{n}\sum_{j=1}^{n} T_j \quad (2)$$

Based on (1), the heat dynamics of the tank can be described as a simple first order differential equation

$$C_t \cdot \dot{T}_t = Q_h + \hat{Q}_s - \hat{Q}_c - UA \cdot (T_t - \hat{T}_i) \quad (3)$$

Q_h is the controllable power consumption for the electric heating elements with efficiency η. C_t is the specific heat capacity of the tank, while the energy contribution from the solar collector Q_s and the house consumption Q_c are both forecasted inputs. We use the forecasts computed from measurements in domestic households in southern Denmark based on [7,8]. The ambient temperature T_i should also be forecast, but is assumed to be a constant 20°C in further simulations.

The model data to be used for model estimation was based on a storage tank that uses stratification pipes for optimal injection of the return water. Therefore a layered model with more than one temperature state should possibly be considered. However, for the given data set and a time scale of minutes, a first order model with only one layer was found sufficient for describing the heat dynamics of the tank.

The solar thermal power is simulated from measured climate data recorded at the local district heating plant in Sønderborg. A standard flat-plate collector is used as the simulation model, as described in [9]. The solar thermal power is forecast with the method described in [7], where a conditional parametric model is applied for forecasting the hourly solar thermal power up to 36 hours ahead. The forecasting model takes numerical weather predictions of global radiation as input. Based on past data, the collector thermal performance is modelled and takes local effects into account, such as the orientation of the collector and shading from objects in the surroundings.

2.2. Model parameter estimation

CTSM was used to estimate the unknown parameters of a continuous discrete stochastic state space model. The model consists of a set of stochastic differential equations describing the dynamics of a

system in continuous time and a set of algebraic equations describing how measurements are obtained at discrete time instants.

$$\begin{aligned} \mathrm{d}x &= (A(\theta)x + B(\theta)u + E(\theta)d)\mathrm{d}t + \sigma \mathrm{d}w \\ \mathrm{y} &= C(\theta)x + e \end{aligned} \qquad (4)$$

The model includes a diffusion term to account for random effects, but otherwise it is structurally similar to ordinary differential equations. Therefore conventional modelling principles can be applied to set up the model structure. Given the model structure, any unknown model parameters can be estimated from data, including the parameters of the diffusion term. The parameter estimation method is a *maximum likelihood* (ML) method and a *maximum a posteriori* (MAP) method [10,11,12,13].

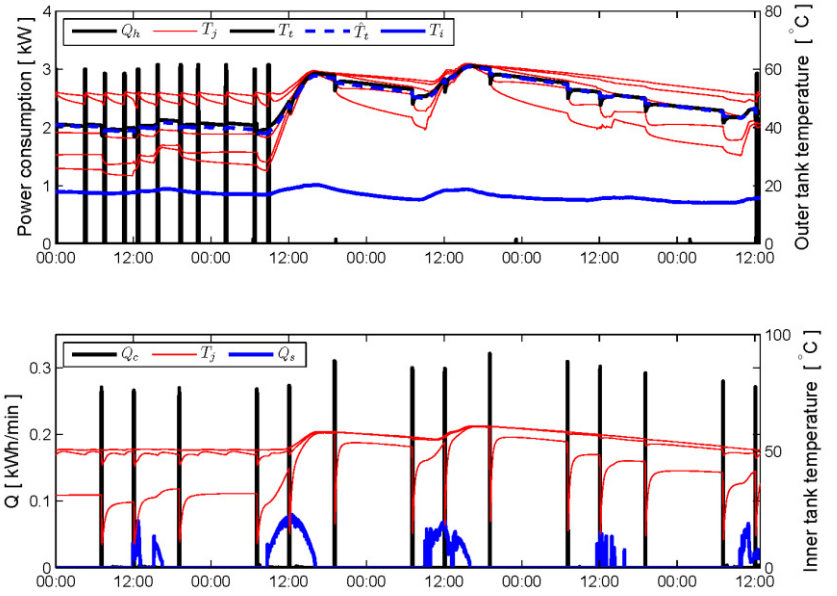

Fig. 2. Data measurements from real storage tank used for parameter estimation. The estimated tank temperature has been also been plotted

The model parameters $\theta = [C_t \quad UA \quad \eta]$ were estimated in the continuous time stochastic state space model (4) with $x = y = T_t$ and $d = [Q_s \quad Q_c \quad T_i]$ that contains the forecast disturbances from (3). It is assumed that the measurement error is normal-distributed. with a variance of 1°C such that $e \in N(0,1)$. The process noise was assumed to have standard deviation $\sigma = 0.001$.

The parameter estimation was based on the data shown in Fig. 2. The estimated parameters of (3) were found to be:

$$UA = 8.29\ (\pm\ 0.0278)\ \mathrm{W/K} \qquad C_t = 3881.3\ (\pm\ 0.00167)\ \mathrm{kJ/K} \qquad (5)$$

It should be noted that the heating element efficiency was fixed at $\eta = 1$ and the tank temperature representing the stored energy was assumed to be an average of all eight temperature measurements. The fit of the resulting estimated tank temperature $\hat{T}_t$ is also compared to the average tank temperature T_t in

Fig. 2, and reveals a nice match. Note that the consumption pattern Q_c in this data set is deterministic and the same amount of energy is deliberately drawn from the tank at 7 am, 12 pm, and 7 pm.

3. Economic MPC

Traditionally the heating elements in a storage tank are controlled by a thermostat that is either on or off and keeps the temperature close to a temperature set point in a hysteresis loop. Instead of specifying a temperature set point for the tank, a set of constraints on the tank temperature and on power consumption is specified. For the MPC strategy, as long as the temperature is within some bounds, there is no need to force it to a certain temperature. In this way knowledge about the future weather and heat consumption can help to minimize the power consumption of the heating elements. Adding a price signal to the objective will then not only try to minimize the power consumption, but also the electricity costs. So the finite static MPC optimization problem to be solved at every sampling time t is

$$\begin{aligned} \text{minimize} \quad & \sum_{k=t}^{t+N-1} p_k u_k \\ \text{s.t.} \quad & x_{k+1} = Ax_k + Bu_k + Ed_k \\ & y_k = Cx_k \\ & 0\text{kW} \le u_k \le 9\,\text{kW} \\ & 50°\text{C} \le y_k \le 95°\text{C} \end{aligned} \tag{6}$$

At each sampling time, t, we minimize the electricity costs over the prediction horizon N, given the forecasts available at time t. The first control action u_0 of the solution is implemented on the process and the procedure is repeated at the next sampling instant. This is usually referred to as receding horizon control. The model (3) is discretized into a discrete time state space model defined by the matrices (A,B,E,C) with the estimated parameters (5). The constraints on temperature and power consumption must also be satisfied.

4. Simulation

Fig. 3 shows a simulation of the resulting MPC with the estimated tank model. The scenario is based on real measured solar radiation and consumption patterns from residential houses in southern Denmark during a whole year from May 17 2010. The simulation is a closed loop simulation with a 24-hour prediction horizon based on forecasts subject to uncertainty and actual electricity prices from the Nordic Elspot market [5].

In Fig. 4, one week in March 2011 of the simulation from Fig. 3 has been extracted. During the first few days the heating elements mostly use power during night-time when the prices are low. In the remaining period a lot of solar radiation heats up the tank and the heating elements are practically not used. The temperature stays within the predefined interval that defines the storage capability.

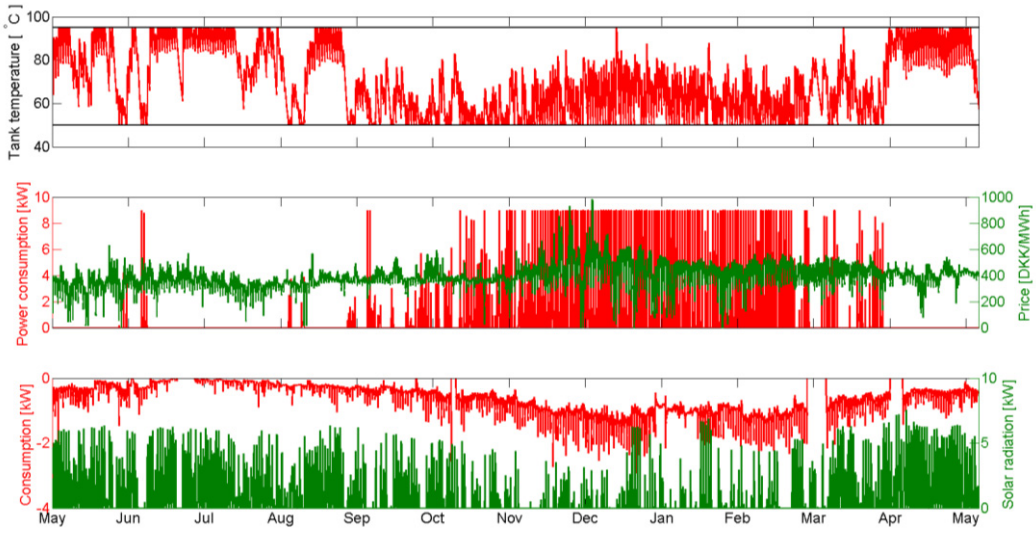

Fig. 3. A one-year simulation starting May 17 2010 with 24 h prediction horizon using uncertain forecasts. The upper plot shows the tank temperature, the middle plot contains the electricity price and the optimal power consumption for the heating element, and the lower plot contains the solar heat input and the house consumption demand. The heating element is turned on when the electricity price is low.

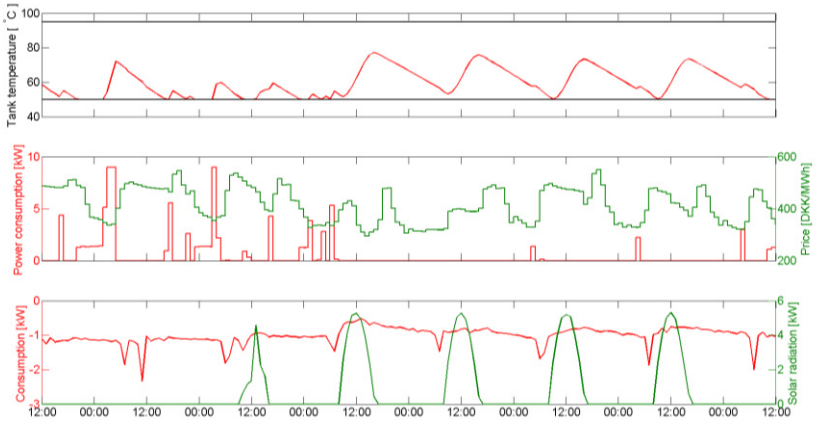

Fig. 4. Shows the same as Fig. 3. but contains only one week in March 2011 to make it easier to read the details.

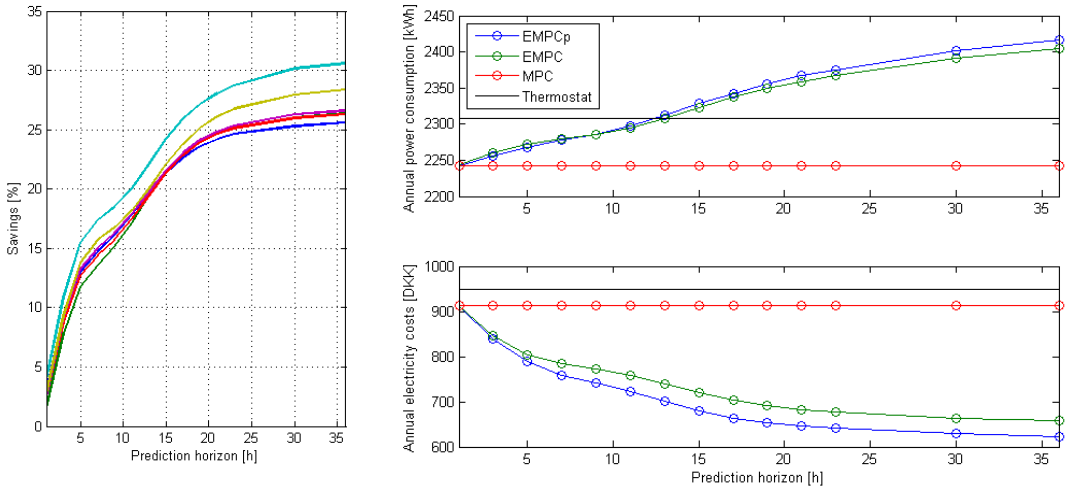

Fig. 5. (a) Annual savings in percent compared to conventional thermostat control for the six different houses. (b) Annual power consumption (upper) and electricity costs (lower) for house #2 as a function of the prediction horizon N for four different control strategies. Closed loop Economic MPC with perfect forecasts (EMPCp), with real forecasts subject to uncertainty (EMPC), a constant electricity price of 1 (MPC) and a Thermostat control keeping the temperature at 60°C.

5. Results and discussion

For a whole year the annual power consumption and electricity costs were found from closed loop MPC simulations for four different control strategies. The results can be found in Fig. 5a, while a simulation for one of the houses is shown in Fig. 5b. For a prediction horizon N larger than 24 hours, the cost savings do not increase by much as the prediction horizon increases further. This is mainly due to the maximum input power and the storage capacity of the system. Information about the solar radiation or the consumption next week will not change the optimal power consumption due to these system constraints. Furthermore, using perfect forecasts, i.e. knowing the future inputs exactly, does not increase the savings significantly. The annual savings of considering the price with an Economic MPC are 25-30% for the given simulation scenarios for six different houses.

Note that the power consumption for the Economic MPC grows larger than for the ordinary thermostat control as the prediction horizon increases. However the costs go down. Consequently, to save more money, more electricity must be used for control. However, the increased power consumption can be justified when the electricity price reflects the amount of renewable energy in the power system.

Another result of the investigations is that in the MPC strategy in which only power consumption is minimized and where prices are not considered, the annual power consumption is constant regardless of the prediction horizon. Since the sampling period is so high (1 h) compared to the dynamics (< 5 min), the amount of power (9 kW) that can be delivered instantaneously in every one-hour sampling period is higher than the instantaneous demand at any time. So the control signal matches the consumption at every sampling time even for a one-hour prediction horizon. Also the control is only active at the lower temperature bound, because it is not possible to actively cool the tank.

Similar results were obtained for the five other houses, with the same conclusions.

Any missing data in the forecasts was ignored by setting it to zero. This means that some periods in the annual simulation have no solar input or no consumption at all. For the six different houses the total missing number of samples in the consumption data sets was around 510 (~21 days) for all houses except

house 1, where 1800 samples were missing (~78 days). For the solar data that were used for every house, 351 samples were missing (~14 days). An example of the missing data in the consumption forecast can easily be seen in Fig. 3.

Computation times for solving the individual open loop MPC problem are in the millisecond range. Simulating a whole year takes around 5-10 seconds for a prediction horizon of 24 hours running Matlab on an Intel i7 2.67 GHz laptop.

6. Conclusion

The heat dynamics of a smart solar storage tank were modelled and its parameters were found from maximum likelihood estimation procedures. An Economic MPC was designed to control the power consumption of the auxiliary heating elements in the storage tank. The MPC minimizes electricity costs given the price and forecasts of the solar radiation and consumption. Electricity cost savings of 25-30% compared to current thermostat control strategy were found for six different houses.

Acknowledgements

Acknowledgements are given to the The Danish Council for Strategic Research, which have provided the financial support for the project ”Solar/electric heating systems in the future energy system” (2104-07-0021) under which the work was carried out. The heat load and climate data was very kindly provided by Sønderborg Fjernvarme and the Danish Meteorological Institute is thanked for making their numerical weather predictions available.

References

[1] R. Halvgaard, N. K. Poulsen, H. Madsen and J. B. Jørgensen, “Economic Model Predictive Control for Building Climate Control in a Smart Grid”, *IEEE PES Innovative Smart Grid Technologies,* 2012.

[2] F. Oldewurtel, A. Ulbig, A. Parisio, G. Andersson and M. Morari “*Reducing Peak Electricity Demand in Building Climate Control using Real-Time Pricing and Model Predictive Control”, IEEE Conference on Decision and Control*, 2010

[3] T.G. Hovgaard, L. F.S. Larsen, K. Edlund, J. B. Jørgensen, “*Model predictive control technologies for efficient and flexible power consumption in refrigeration systems”,* Energy*,* 2012

[4] J. Fan, E. Andersen, S. Furbo and B. Perers, 2010, “Detailed Modelling of Charging Behaviour of Smart Solar Tanks”, *Proceedings of EuroSun 2010: International Conference on Solar Heating, Coolings and Buildings*.

[5] http://www.nordpoolspot.com/Market-data1/Elspot/Area-Prices/ALL1/Hourly/

[6] Elsa Andersen, Simon Furbo, Bengt Perers, Jianhua Fan, Ziqian Chen, “Experimental investigations of intelligent solar heating systems for single family houses”, SHC Conference, San Francisco, USA, July 2012

[7] P. Bacher, H. Madsen, and B. Perers, “Short-term solar collector power forecasting”, in proceedings of *ISES Solar World Conference*, 2011.

[8] P. Bacher, H. Madsen, H. Aalborg and B. Perers, “Short-term heat load forecasting for single family houses”, Submitted to Buildings and Energy, 2012.

[9] B. Perers, S. Furbo, E. Andersen, J. Fan, “Solar/electric heating systems using smart solar tanks and variable electricity costs”, *Eurosun Conference 2010 Graz Austria*, 2010.

[10] Continous Time Stochastic Modeling www2.imm.dtu.dk/~ctsm/

[11] Niels Rode Kristensen and Henrik Madsen and Sten Bay Jørgensen, ”Parameter estimation in stochastic grey-box models”, Automatica, volume 40, p.225-237, 2004.

[12] Niels Rode Kristensen and Henrik Madsen and Sten Bay Jørgensen, ”A method for systematic improvement of stochastic grey-box models”, Computers & Chemical Engineering, volume 28, p. 1431-1449, 2004.

[13] John B. Jørgensen and Sten B. Jørgensen, “MPC-Relevant Prediction-Error Identification”, *Proceedings of the 2007 American Control Conference*, p.128-133, 2007.

Peder Bacher, Models for efficient integration of solar energy, Ph.D. report, DTU Informatics, IMM-PhD-2012-272, 2012

Models for efficient integration of solar energy

Peder Bacher

Kongens Lyngby 2012
IMM-PhD-2012-272

Technical University of Denmark
Informatics and Mathematical Modelling
Building 321, DK-2800 Kongens Lyngby, Denmark
Phone +45 45253351, Fax +45 45882673
reception@imm.dtu.dk
www.imm.dtu.dk IMM-PhD-2012-272

Summary (English)

Efficient operation of energy systems with substantial amount of renewable energy production is becoming increasingly important. Most renewables are dependent on the weather conditions and are therefore by nature volatile and uncontrollable, opposed to traditional energy production based on combustion. The "smart grid" is a broad term for the technology for addressing the challenge of operating an energy system, especially the electrical grid, with a large share of renewables. The "smart" part is formed by technologies, which model the properties of the systems and efficiently adapt the load to the volatile energy production using the available flexibility in the system.

In the present thesis methods related to operation of solar energy systems and for optimal energy use in buildings are presented. Two approaches to forecasting of solar power based on numerical weather predictions (NWPs) are presented. They are applied to forecast the power output from PV and solar thermal collector systems. The first approach is based on a developed statistical clear-sky model, which is used for estimating the clear-sky output solely based on observations of the output. This enables local effects such as shading from trees to be taken into account. The second approach to solar power forecasting is based on conditional parametric modelling. It is well suited for forecasting of solar thermal power, since is it can be made non-linear in the inputs. The approach is also extended to a probabilistic solar power forecasting model.

The statistical clear-sky model is furthermore used as basis for a method for correction of global radiation observations. This method can used for correction of typical errors, for example from shading trees or buildings.

Two methods for flexible heat use in buildings are presented in the last part of the thesis. First a method for forecasting of the heat load in single-family houses based on weather forecasts is presented. A model is identified for forecasting the heat load for sixteen single-family houses. The model adapts to the individual houses and needs no specific information about the buildings. Finally, a procedure for identification of a suitable model for the heat dynamics of a building is presented. The applied models are grey-box model based on stochastic differential equations and model identification is carried out with likelihood ratio tests. The models can be used for providing detailed information of the thermal characteristics of buildings and as basis for optimal control for flexible heating of buildings.

Summary (Danish)

Energiproduktion med vindmøller og solceller kan af naturlige årsager ikke styres som energiproduktion baseret på forbrænding. Derfor kræves en udvikling af nye teknologier til styring af energisystemer med en betydelig andel vind- og solenergi. Elnettet skal udbygges med it-teknologi og blive til et "smart grid". Dette betyder at styringen skal udføres automatisk baseret på computermodeller, der "lærer" –at tilpasse sig systemets egenskaber udfra data opsamlet af sensorer. I afhandlingen præsenteres en række af sådanne modeller og metoder relateret til solenergi og opvarmning i bygninger.

Først præsenteres to metoder til forudsigelse af solenergiproduktionen udfra meteorologiske vejrprognoser. De kan bruges til forudsigelse af energiproduktionen fra både solceller og solfangere, og kræver ikke nogen specifik information om anlæggene udover målinger af energiproduktionen. Den ene metode er baseret på en udviklet statistisk model, der kan estimere solenergiproduktionen ved klar himmel, udelukkende ud fra målinger af produktionen. Dette gør modellen i stand til at inkludere lokale effekter, som for eksempel solenergi-anlæggets vinkling og skygger fra objekter i de lokale omgivelser, f.eks. fra træer. Den anden metode er baseret på en betinget parametrisk model, hvilket giver en effektiv modellering med ikke-lineære funktioner. Denne metode er desuden velegnet til solvarme forudsigelser. Endeligt beskrives en metode til probabilistisk forudsigelse af solenergiproduktion.

En metode til korrektion af fejl i målinger af global stråling præsenteres. Den statistiske model for klar himmel benyttes her på målinger af global stråling og systematiske fejl korrigeres, som for eksempel skyldes skygger fra træer eller bygninger.

En række modeller af solfangeres varmedynamik præsenteres. Modellerne er baseret på stokastiske differentialligninger og kan benyttes til estimation af vigtige fysiske parametre udfra målinger fra en enkelt dag. Dette gør dem oplagte til brug i tests af ydeevne.

To metoder der kan bruges i styringen af fleksibelt varmeforbrug i bygninger præsenteres i sidste del af afhandlingen. Først identificeres en model til forudsigelse af varmeforbrug baseret på meterologiske forudsigelser, og den afprøves på seksten typiske parcelhuse op til 42 timer frem i tiden. Modellen tilpasser sig automatisk de enkelte huses varmeforbrug og kræver ingen specifik information om de enkelte huse.

Tilsidst præsenteres en metode til identificering af en velegnet model af bygningers varmedynamik. Modellerne er baseret på stokastiske differentialligninger og kan bruges til at estimere vigtige fysiske parametre, for eksempel bygningens UA-værdi og varmekapacitet. De kan for eksempel benyttes til at bestemme potentialet for energirenovering og som basis for styring af fleksibelt varmeforbrug.

Preface

This thesis was prepared at the department of Informatics and Mathematical Modelling (Informatics), the Technical University of Denmark (DTU) in partial fulfilment of the requirements for acquiring the Ph.D. degree in engineering. The Ph.D. project was carried as part of the project "Solar/electric heating systems in the future energy system" which is funded by The Danish Council for Strategic Research.

The thesis deals with modelling for operation of energy systems depending on solar radiation and for flexible heating of buildings. Methods for forecasting of solar power and for correction of observations are presented, together with models for forecasting of heat load in buildings and models for the heat dynamics of buildings.

The thesis consists of a summary report and seven research papers. Two of the papers are published in, and two are submitted to, international peer reviewed scientific journals. The last three appear in conference proceedings.

Lyngby, 2012

Peder Bacher

Acknowledgements

My thanks first of all goes to my supervisors Henrik Madsen and Henrik Aalborg Nielsen for being visionary and inventive, and to inspire through a sincere devotion to research and new ideas. Thanks to Bengt Perers for that heartfelt sense of dedication to solar energy research and many eye-opening discussions.

Thanks to all my colleagues at IMM, especially you lovely fellow students for creating an inspiring and really "we get further if we help each other and have fun while doing it"-atmosphere. Very special thanks my office fellows Pierre-Julien and Philip for being so good and meaningful friends. And Janne, thanks for keeping track of things, without you we would not get far before chaos rises to above our ears.

Thanks to all the project participants from DTU Byg and DMI for the fruitful sharing of insights and competencies, especially Simon Furbo for leading the project and bringing it all together. Special thanks to Rasmus Halvgaard for using the forecasts as basis for his work on optimized control of solar and electric heating systems.

All my remaining thanks goes to Christina and our two boys Carl and Vilfred for all the love and support you have given me.

List of publications

Papers included in the thesis:

A Peder Bacher, Henrik Madsen, Bengt Perers, and Henrik Aalborg Nielsen. A non-parametric method for correction of global radiation observations. Submitted to: *Solar Energy*, (April 2012).

B Peder Bacher, Henrik Madsen, and Henrik Aalborg Nielsen. Online Short-term Solar Power Forecasting. *Solar Energy*, 2009, 83(10), pp. 1772-1783.

C Peder Bacher, Henrik Madsen, and Henrik Aalborg Nielsen. Online Short-term Solar Power Forecasting. *1st International Workshop on the Integration of Solar Power into Power Systems. Aarhus, 2011.*

D Peder Bacher, Henrik Madsen, and Bengt Perers. Short-term solar collector power forecasting. *ISES Solar World Congress 2011.*

E Peder Bacher, Henrik Madsen, and Bengt Perers. Models of the heat dynamics of solar collectors for performance testing. *ISES Solar World Congress 2011.*

F Peder Bacher, Henrik Madsen, Henrik Aalborg Nielsen, and Bengt Perers. Short-term heat load forecasting for single family houses. Submitted to: *Buildings and Energy*, (April 2012).

G Peder Bacher and Henrik Madsen. Identifying suitable models for the heat dynamics of buildings. *Energy and Buildings*, 2011, 43(7), pp. 1511-1522.

Contents

Chapter 1

Introduction

The foreseen negative impact on human life conditions due to climate changes caused by the increasing level of greenhouse gases in the atmosphere, is driving a transformation of the energy system: away from the current system based on fossil fuels and over to a future system based on sustainable and climate neutral energy production. Many plans for this transformation have been presented during the last decades and the visions are manifold. They range from focusing on yet not operational technologies, such as nuclear fusion energy, and over to focusing on existing technologies, such as nuclear fission energy, and wind and solar energy. Reality is however, that no single sustainable energy technology, which can cheaply replace coal and oil, and cover the entire demand for energy, has been invented. Currently, it seems like a very realistic scenario is a system composed of wind, solar, bio, and hydro power. See for example the scenarios suggested by Fthenakis et al. (2009), Jacobson and Delucchi (2011), and Mathiesen et al. (2011). The transition should be carried out with the socio-economically most optimal solutions and is highly dependent on the current energy infrastructure and locally available resources. Due to the spacial requirements and intermittent nature of wind and solar energy technologies, two very important aspects have to be considered: energy storage and energy mobility. In one end of the renewable energy scenarios, all energy is produced with large scale plants at locations where the resource is plentiful: solar energy in the desert and wind energy off-shore at sea. This requires strong interconnections over very long distances for transportation of energy to where it is

needed. In the other end, scenarios are suggested where the energy is produced on distributed small scale systems as close as possible to where it is needed. For the Danish energy system several plans for a system based on 100% renewables in 2050 have been put forward. The currently most established plan is put forward by the Danish Commission on Climate Change Policy (2010), who suggest a profound change of the structure of energy system. Away from the current centralized system, which is based on non-volatile power generation technologies and where the power generation is controlled to match the demand, and over to a distributed system, which can handle a much more volatile power generation and where the demand is shifted to match the power generation. The change involves engineering challenges in many fields, where especially the "smart grid" is pointed out as an essential component which must be developed.

The "smart grid" is a term covering a range of technologies for enabling an efficient and flexible operation of a renewable based energy system, in particular with the use of information and communication technology for providing the needs for communication between the units in the system. This forms the basis for the "smart" part, namely the operation of the energy system with computer models, which can "learn" the characteristics of the system and enable an optimized use of the vast amounts of data from sensors in the system. In the present thesis such methods based on such data-driven statistical models are presented. They are centered around the use of real-time energy and climate data for modelling, with focus on solar energy applications and optimal energy use in buildings. This type of methods will be vital for operation of energy systems with a substantial amount of solar energy production, and - especially for the methods related to buildings - also for efficient integration of other renewables, in particular wind energy. Methods for the following applications are presented in the thesis:

- Solar power forecasting, both for PV systems and solar thermal systems.
- Processing and correction of solar radiation measurements.
- Dynamical models for solar thermal collectors.
- Forecasting of heat load for buildings.
- Identification of suitable models for the heat dynamics of buildings.

The methods are based on statistical modelling techniques, which, where it is appropriately, are combined with prior physical knowledge. The models deal with both non-linear and dynamic relations, and thorough statistical analysis for evaluation of the results are carried out. An objective is to provide a solid foundation for operational applications, as well as expanding current state of the art in the addressed fields. Data from both experimental setups and systems

in operation is used, for example data consisting of measurements from test buildings, inhabited buildings, weather stations, and meteorological forecasts.

The PhD-study is carried out under the project "Solar/electric heating systems in the future energy system", in which a heating system scaled for a single-family house is designed, see (Perers et al., 2011) for a detailed description. The core of the system is a hot-water tank, which is connected to both an electrical heater and a solar thermal collector. The system provides both space heating and hot water heating. By heating in advance with electricity, and storing thermal energy in the tank, the system can be used for load-shifting, and thus become valuable also for the integration of wind power (Meibom et al., 2007). An objective of the PhD-study is to provide the forecasting models needed for optimal operation of the system in a Danish context, where the electricity is bought at a variable price on the Nord Pool Spot day-ahead market. The optimal operation is carried out by shifting the load to hours with cheap energy in order to minimize the costs of running the system. The presented methods for forecasting of the hourly solar thermal production and forecasting of heat load, are used to provide the necessary basis for the economic model predictive control (MPC) scheme presented by Halvgaard et al. (2012) for optimal operation of solar-electric combisystems. Furthermore price forecasts are used, which are provided using the models described by Jónsson et al. (2012).

1.1 Solar energy

Energy from solar radiation drives the processes that makes life on earth possible. It has the potential to cover all human energy needs: the energy from solar radiation striking the surface of the earth in 90 minutes (appr. $6.4 \cdot 10^{20}$ J) is well over the current global energy consumption per year (appr. $5.1 \cdot 10^{20}$ J in 2009 (IEA, International Energy Agency, 2011b)). Several plans exist for a renewable based energy system relying heavily on solar energy. For example: Zweibel et al. (2008) plan 35% of the total energy to come from solar, Heide et al. (2010) finds that an optimal balance is 55% wind and 45% solar energy for Europe, and IEA, International Energy Agency (2011a) discuss the IEA High-Renewable Scenario where 25% of global electricity is covered by solar power. A vast palette of technologies exist for using solar radiation as an direct source of energy: from agriculture over architecture and over to conversion of solar radiation directly to electrical power. Many other renewable energy sources are indirectly driven by solar radiation, for example wind and hydro power. The most used technologies, which convert solar radiation directly into heat or electricity, can be divided into following categories:

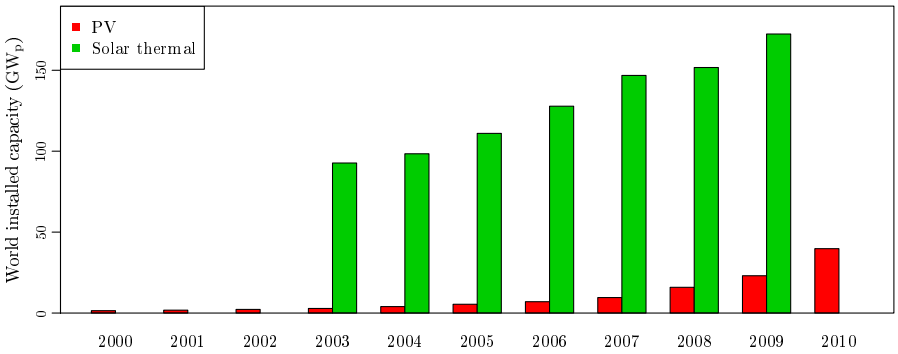

Figure 1.1: Total worldwide installed solar PV and thermal capacity

- Heating, cooling and ventilation in buildings, for example there is a long tradition for buildings to have windows for providing indoor light and heating.
- Water heaters. Different types of solar thermal collectors exist, the most widespread type is flat-plate collectors.
- Photovoltaic (PV) panels, which are either distributed on roof-tops or installed in large power plants, currently the largest is Golmud Solar Park (200 MW_p), which is to be built in China.
- Concentrated solar power. Installed in large plants, where sun beams are concentrated with mirrors to heat fluid for driving steam turbines. This technology has a huge potential in sunny regions, currently the largest is Brightsource's Ivanpah plant in the US, which is planned to reach 392 MW_p when completed. The use of a heated fluid in the process has the advantage that thermal storage can be used to shift the electricity production.

The plot in Figure 1.1 shows the total worldwide installed capacity over the last years of PV (BP, 2011) and solar thermal (appr. 85% from flat-plate and evacuated tube collectors and 15% from unglazed collectors) (IEA - The Solar Heating and Cooling Programme, 2010). Clearly the installed capacity is rapidly increasing and especially the installed PV capacity has been rapidly increasing the last few years. Currently Germany has the highest level of solar power penetration at around 3% of the electricity production, which already has a considerable impact on the power price on sunny days (Nicolosi and Nabe, 2011). The currently installed capacity in Denmark is around 22.5 MW_p, which corresponds to 0.06 % of the electricity production. This is quite little, but in 2011 nearly 8.5 kW_p was installed and the trend seems to be continuing upwards, as seen from the

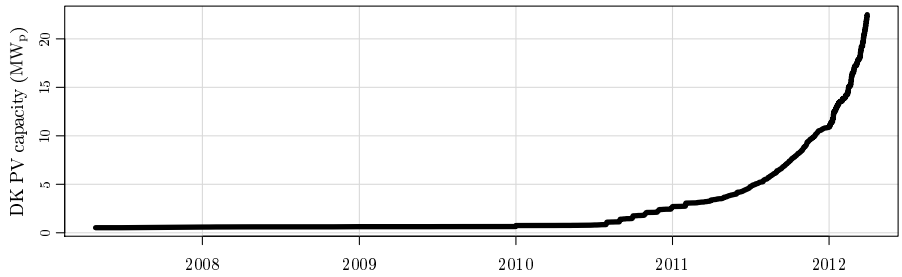

Figure 1.2: Total installed solar PV peak power capacity in Denmark (source: Energinet.dk)

plot in Figure 1.2 of the total installed PV capacity in Denmark. During the large scale smart grid research project Ecogrid, the Danish island of Bornholm (population around 42000) will be equipped with 5MW_p solar power, which will be around 9% peak power penetration (Yang et al., 2011). Hence there is a growing need for methods for an efficient integration of PV solar power.

As seen in Figure 1.1 the globally installed solar thermal capacity is much higher than the installed capacity of PV. The by far largest part of solar thermal is used for water heating and works independently of the surrounding energy system. However there is an increasing trend in application of solar heating for other purposes, such as space heating and industrial heating. As an example is the solar heating system from Innogie[1], where the entire roof is turned into a solar thermal collector. It is coupled to a hot water tank and a geothermal heat pump. In the summertime an HP/ORC module is used for conversion of the solar thermal energy to electricity. Apart from efficient use of solar and electrical energy for heating, the system can also provide flexible electrical load and production.

In order to operate systems with solar power optimally, it is essential to have forecasts of solar power available (Lew et al., 2010). They are required for periods ranging from days ahead down to hours and ten-of minutes ahead (Sayeef et al., 2011). Quite a lot of research in solar forecasting has been carried out the last years and two main approaches, depending on the forecast horizon, have had most attention: for short horizons within a couple of hours, the forecasts are based on satellite images and total sky imagery, and for longer horizons up to a several days, the forecasts are based on numerical weather predictions (NWPs).

The following is a small overview of the recently presented methods for forecasting based on NWPs. Ji and Chee (2011) do a detrending of solar power

[1] `www.innogie.dk`

by fitting a high order polynomial model based on a monthly average of the diurnal curve to account for non-stationarity of the observed process. Then the detrended series is forecasted with an ARMA and TDNN hybrid model. Lorenz et al. (2011) use several steps in a post-processing procedure of NWPs to derive optimized site-specific irradiance forecasts. First a spatial averaging of the NWPs is carried out and thereafter a bias-removal procedure, which is based on a physical clear-sky model, is applied. Finally, a physical model is used to convert the irradiance forecasts to PV power forecasts. An up-scaling method for regional solar power forecasting is also presented. Schmelter et al. (2011) presents a continuous weather classification for combining NWPs, which improves forecasting performance especially for difficult weather conditions such as fog and snow. Pelland et al. (2011) do post processing of NWPs for forecasting global radiation and PV output. First a spacial averaging of the NWPs is applied and a Kalman filter is used for bias removal. Fonseca Júnior et al. (2011) compare neural networks and support vector regression for forecasting 24 hours ahead. It is found that RMSE performance is quite equivalent, while MAE performance is better for support vector regression.

In the present thesis two approaches to solar power forecasting based on NWPs are presented. The first approach is based on a developed statistical clear-sky model, which is used for normalization of the solar power to a stationary process, such that classical linear time series models, here ARX models, can be efficiently applied. The second approach is to forecast the solar power directly with a conditional parametric model. This provides a simple and efficient approach to solar power forecasting. Furthermore an outline of an approach to probabilistic solar power forecasting is given.

In addition to the forecasting methods two other solar energy related studies are presented in the thesis. First a method for correction of global radiation observations based on the statistical clear-sky model is presented. The method can especially be useful for correction of observations from partly unsupervised solar radiation sensors, which will be exposed to many types of errors, for example shading from surrounding objects. Finally, a study, in which grey-box models for the heat dynamics of solar thermal collectors are applied, is presented. The models can be used for obtaining detailed knowledge of the heat dynamics of a collector, including the physical parameters related to the performance of the collector.

1.2 Buildings and energy

An essential key to a successful integration of the volatile energy production from renewables is the development of cheap and operational energy storage. Today many different energy storage technologies exists. They are different with regards to several aspects such as: efficiency, temporal characteristics, and geographic requirements. For example pumped hydro, which can provide seasonal storage with a round-trip efficiency up to 85%, has a limited potential due to the geographic requirements. Another very promising technology is renewable power methane (RPM) storage, which is based on conversion of electricity to methane gas. The gas is stored and can be used later in the existing natural gas energy infrastructure. The draw-back of RPM is that the round-trip efficiency is only in the range of 30% to 37% (Breyer et al., 2011), which makes it expensive and feasible mostly for seasonal storage. Hence cheap and efficient short-term energy storage is really valuable, in Denmark especially for matching the fluctuations in wind power (Meibom et al., 2007), but also for shifting the load away from peak hours within the day. Due to the generally increasing electricity load, even very short time flexibility can be very valuable in order to avoid overload of the transmission system and thereby minimize the needed investments in the transmission system (Danish Commission on Climate Change Policy, 2010). The use of electric vehicle (EV) batteries for short-term load-shifting is possible, but the large scale transition to EVs is yet to come. It is to cover this need that thermal storage in buildings can prove to be the a key solution. As heating become more electricity based, a huge potential for energy buffering and flexible load can be released (Palensky and Dietrich, 2011). Approximately 40% of the total energy consumption is related to buildings, either used for heating or consumed by electrical appliances. Thermal energy can either be stored in the building structures, making it possible to possible to shift load while keeping the indoor temperature within some limits (e.g. 19 to 21 °C), or stored in a thermal storage system, for example a hot water tank. This applies both to heating and cooling, or both at the same time as suggested by Blarke et al. (2012), who finds that thermal storage is a very cheap compared to electro-chemical or mechanical storage.

Apart from the hardware for enabling the use of buildings for energy storage, the methods for optimal operation are necessary to have. Modelling and forecasting of the energy flows in the building are needed, together with methods for modelling the energy systems related locally to the building. For example for forecasting of solar thermal power, if a solar collector is connected to the heating system. Finally, the operation of the heating system must be coupled to the operation surrounding energy system. This will most likely be carried out with energy markets, where a variable energy price will reward a flexible load. Today smart meters are being installed in many buildings and the high

resolution readings (10 to 15 minute values) of heat load will - combined with climate data - form the basis for modelling the building energy characteristics. Especially a proper modelling of the heat dynamics is crucial for this time resolution and provides the key for optimal use of the buildings for load-shifting. Here it is also emphasized, that another very important use of data from smart meters is for determination of the energy performance of buildings, as carried out by ENFOR (2010) and as with the methods presented in below. This will be very valuable for efficient energy refurbishment of buildings, which has a very important feature that must not be overseen: energy savings are far less volatile and to a large extend cheaper, compared to an equivalently increased renewable energy production.

In the thesis two methods for modelling related to building energy use are presented: First a method for forecasting the heat load of single-family houses and secondly a method for obtaining a detailed description of the heat dynamics of a building.

The method for forecasting of heat load is very well suited for optimized operation of a heating system, which include thermal storage in some dedicated medium, for example a hot water tank. As described previously, the objective of the PhD-project is to make methods to be used for optimal operation of a solar-electric combisystem for space and hot water heating in single family houses. The idea is to couple forecasts of: the electricity price, the energy production from the solar thermal collector, and the heat load of the building. The forecasts are then used as input to economic model predictive control scheme (MPC), which then provides an optimal operation plan for the system, i.e. how much electricity should be bought for heating at a given time. If the electricity can be bought at a variable price, then the storage capacity of the hot water tank can be used for lowering the running costs, by shifting the load to hours with cheap electricity. Hence the system can provide services to the grid, and thereby the short-term energy storage for an efficient integration of the large amount of wind power planned in Denmark. It is planned to have around 50% of electricity production in 2020.

The method, which can be used to obtain a detailed and accurate description of the heat dynamics of a building from data, is based on grey-box modelling. The models are formed by stochastic differential equations, which enables a combination of physical and data-driven modelling. The physical part for the model is formed by a description of the heat dynamics with differential equations, which includes the physical thermal properties and a model of how the significant heat transfers occur in the building. This allows for the estimation of parameters, which are directly physically interpretable. The identified model can be used for several purposes. Firstly, thermal properties, such as the UA-value of the building, provide valuable information, which can be used to identify buildings with

high potentials for energy refurbishment. Secondly, the knowledge of the heat dynamics can be used to optimize the operation of the heating system, while keeping the indoor temperature within some limits, as mentioned above, and for example minimize the operation costs, when the electricity can be bought at a variable price. Model predictive control can be used for carrying out the optimization using the model of the dynamics, as described by Široký et al. (2011) and Zong et al. (2011). This will enable the thermal mass of buildings to be used for load-shifting

In the following chapters the methods, which are presented in the included papers, are outlined and discussed. In Chapter 2 an overview is given of the methods relating to solar energy applications, which are presented in Paper A to E. In Chapter 3 an overview is given of the methods related to energy use in buildings, which are presented in Paper F to G. Chapter 4 finalizes the thesis with a general discussion and conclusion.

Chapter 2

Methods for solar energy applications

An overview of the presented methods, which can be used for the different purposes related to solar energy, is given in this chapter. First a statistical clear-sky model, which is used in several different contexts, is presented. For example in the method for correction of systematic errors in global radiation observations, which is outlined subsequently. This is followed by a section in which two methods for point forecasting and an approach for probabilistic forecasting of solar power are described. The chapter ends with a section on grey-box modelling of solar thermal collectors and finally a discussion is given.

2.1 Statistical clear-sky model

Clear-sky models, as described by Bird and Riordan (1984) and Rigollier et al. (2000), are primarily used for calculation of the global radiation under clear sky at some point in time and some location on the surface the earth. They are based on physical modelling of the radiative transfer of solar radiation through the atmosphere. One application of clear-sky models is for making a normalization of observations from sensors, which outputs are directly related to the solar radiation, for example the output of a pyranometer or a PV system. By normalization of the output it becomes evenly distributed throughout the day and thus

becomes a stationary process. The physical based clear-sky models take many effects into account, however they cannot account for effects related locally to the sensor, such as: bias in the sensor, shadows from trees, or reflections from a nearby water surface. In this thesis a statistical clear-sky model is presented, which can account for such effects. This is achieved by modelling the clear-sky output with a statistical model based solely on the data from the sensor. The models provide an estimate of the sensor output at clear-sky conditions for a given time. The estimated clear-sky output for the sensor is very well suited for the normalization and can be used for several purposes - in the thesis it is used for solar power forecasting and, together with a physical clear-sky model, for correction of typical errors in global radiation observations. The principles behind the statistical clear-sky model is the use of a locally weighted quantile regression model, where a quantile close to one is estimated for the given solar output. Depending on the application the statistical clear-sky model can be composed differently. The most generel definition is with second order polynomial quantile regression

$$\hat{\beta}_t = \underset{\beta \in \mathbb{R}^5}{\operatorname{argmin}} \sum_{i=-\infty}^{\infty} \sum_{j=-\infty}^{\infty} \rho_\tau \big(G_{t+24i+j} - (\beta_{0,t} + \beta_{1,t} i + \beta_{2,t} i^2 + \beta_{3,t} j + \beta_{4,t} j^2) \big) K(i,j) \tag{2.1}$$

where $\{G_t, t = 1, \ldots, N\}$ is a time series with hourly values (e.g. global radiation observations), $\rho_\tau(u) = u\big(\tau - I(u < 0)\big)$ (see (Koenker, 2005) and (Koenker, 2011)), $\tau \in [0, \ldots, 1]$ is the sample quantile to be estimated (which should be close to 1), $i \in \mathbb{N}$ is a counter of days, $j \in \mathbb{N}$ is a counter of hours, and $K(i,j)$ is a kernel function. The estimated clear-sky value at time t is then found as the intercept

$$G_t^{\text{cs}} = \beta_{0,t} \tag{2.2}$$

The weights are calculated with the two dimensional multiplicative Epanechnikov kernel function

$$K(i,j) = \begin{cases} \frac{3^2}{4^2} \left(1 - \left[\frac{|i|}{h_{\text{day}}} \right]^2 \right) \left(1 - \left[\frac{|j|}{h_{\text{tod}}} \right]^2 \right) & \text{for } \frac{|i|}{h_{\text{day}}} \geq 1 \wedge \frac{|j|}{h_{\text{tod}}} \geq 1 \\ 0 & \text{for } \frac{|i|}{h_{\text{day}}} < 1 \vee \frac{|j|}{h_{\text{tod}}} < 1 \end{cases} \tag{2.3}$$

where h_{day} is the bandwidth in the *day of year* dimension and h_{tod} is the bandwidth in the *time of day dimension*. The local weighting is thus carried out in the *day of year* and *time of day* dimensions, such that observations which are close in these two dimensions are given a higher weight in the estimation. The strong feature of using these dimensions is that they are directly related to both: the position of the sun and changing conditions over time. In Section A.3 (page 51) and Section B.3 (page 71) more detailed descriptions of the statistical clear-sky model are found, and in the following it is presented together with its applications.

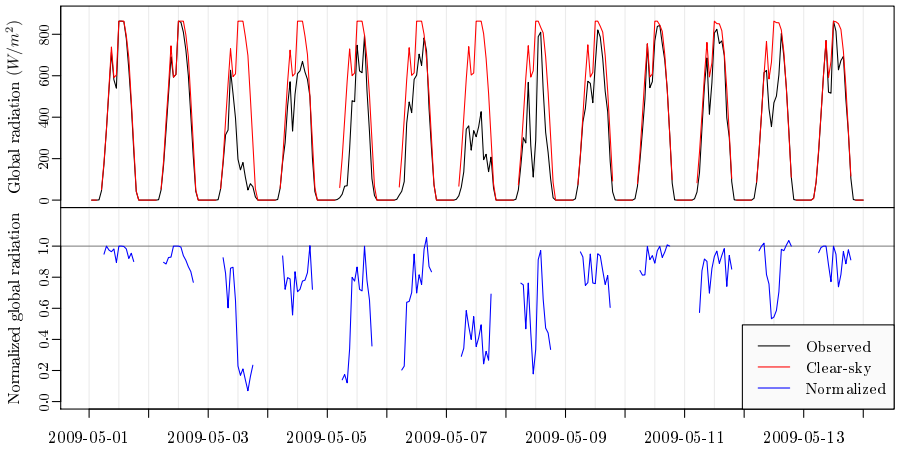

Figure 2.1: The upper plot is of the observed radiation and the estimated clear-sky radiation. The lower plot is of the normalized global radiation.

2.1.1 Correction of global radiation observations

Observations of global radiation is an important source of information, especially for solar energy applications. The observations are typically exposed to several types of systematic errors, for example: shadows from objects in the surrounding, tilt in levelling of the sensor, and processing errors (Younes et al., 2005). In Paper A a method for correction of such errors is presented. The correction is carried out using the statistical clear-sky model, for both the observations G_t and NWPs of global radiation G_t^{nwp} in order to find the systematic deviance between them. The time series consist of hourly average values. Instead of the NWPs, a clear-sky model based on atmospheric physics can be used, e.g. (Bird and Riordan, 1984). The upper plot in Figure 2.1 shows the observed global radiation together with the estimated clear-sky radiation. It can be seen how the estimated clear-sky radiation follows the observed radiation on clear-sky days. Two types of errors are readily seen: there is a drop before noon and the observations are clipped at a maximum level. It can be seen that the errors are apparent in the observations and also described by the clear-sky model. The weather station, at which the observations were recorded, is located at a district heating plant. It is the plant chimney which shades and cause the drop, see the image on page 47. The lower plot in Figure 2.1 shows the normalized solar power, which is obtained by simple division of the observed radiation with the

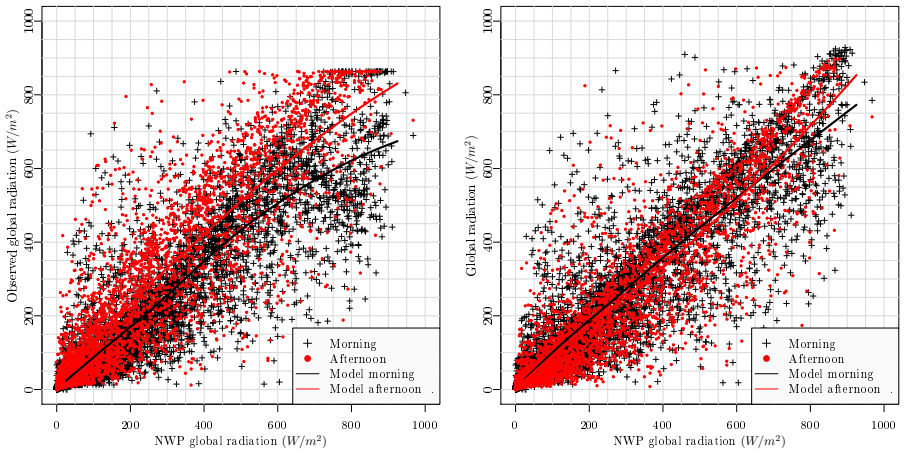

(a) Before the correction. **(b)** After the correction.

Figure 2.2: The values of the observations versus the NWPs before and after the correction. The morning values and the afternoon values are indicated by different symbols and colors. The two lines show a locally weighted least squares regression estimate of the relation between the variables in the morning and the afternoon.

estimated clear-sky radiation

$$\tau_t = \frac{G_t}{G_t^{\mathrm{cs}}} \tag{2.4}$$

This process is clearly much less dependent on the time of day, hence it is a more stationary process, and are much less affected by shadow-drop before noon and saturation. The normalized process is multiplied with the estimated clear-sky radiation for the NWPs and thereby the corrected observations

$$G_t^{\mathrm{co}} = G_t^{\mathrm{nwp,cs}} \frac{G_t}{G_t^{\mathrm{cs}}} \tag{2.5}$$

are obtained. It is furthermore noted that a tilt in the levelling of the sensor cause the observed level to be generally lower in the morning compared to the afternoon. The result of the correction can be seen by comparing the two scatter plots in Figure 2.2. The left scatter plot is of observations versus the NWPs before the correction, where both the shading and the tilt error can be seen. The right plot is a similar plot after the correction. It can be seen that the errors are mostly removed.

2.2 Solar power forecasting

In the following sections an overview of the solar power forecasting methods presented in the papers is given. The methods are based on modelling the power output past data consisting of past measurements and NWPs. The forecast horizons are as long as provided by the NWPs, in presented applications they are complete up to 42 hours ahead at any time of day. Two basic approaches are presented: A two-stage method based on the statistical clear-sky model combined with a linear model, and a one-stage method based on a conditional parametric model. The two-stage approach is applied to forecasting of the total output of 21 PV-systems located in a small village in Denmark, it is described in Paper B. The one-stage approach is applied to forecasting of the output of both: a PV-system, as described Paper C, and to forecast the output of a solar thermal collector, as described in Paper D. Finally, an approach to probabilistic solar power forecasting is outlined in Section 2.2.3.

The obtained results from application of the forecasting methods are based on the data described in the papers, together with NWPs from the Hirlam-S05 (DMI, 2011), which are provided by the Danish Meteorological Institute.

2.2.1 Two-stage method based on the statistical clear-sky model

In paper B a forecasting method is described, where first the statistical clear-sky model is used to normalize the solar power

$$\tau_t = \frac{P_t}{\hat{P}_{\mathrm{cs,t}}} \tag{2.6}$$

where P_t is the solar power, $\hat{P}_{\mathrm{cs,t}}$ is the estimated clear sky solar power and tay_t is the normalized solar power. The NWPs of global radiation are similarly normalized to $\hat{\tau}^{\mathrm{nwp}}_{t+k|t}$. This is carried out to obtain more stationary processes, such that the distribution is much less dependent on the day of year and to the time of day. The normalized processes is in the range of 0 to 1 and have approximately the same distribution at any time t. This is similar to the normalization of global radiation described in the previous section and illustrated in Figure 2.1, where the lower plot shows the normalized process. The normalization allows for of classical linear time series models (Box et al., 1976) to be used for forecasting. The best performing model is identified to the ARX model

$$\tau_{t+k} = m + a_1\tau_t + a_2\tau_{t-s(k)} + b_1\hat{\tau}^{\mathrm{nwp}}_{t+k|t} + e_{t+k} \tag{2.7}$$

where $s(k)$ ensures that the latest diurnal component is used (see page 85). The same ARX model is fitted for each horizon, using a recursive least squares with forgetting scheme to achieve time adaptivity. Finally, the forecasts are transformed back again with the clear-sky model. The results show a root mean square error (RMSE) improvement of around 35 % over a persistence reference model.

2.2.2 Solar power forecasting with a conditional parametric model

An alternative to the statistical clear-sky model for compensating for the non-stationarity of the solar power is to use conditional parametric models, see (Nielsen et al., 2000) for more details about conditional parametric models. The same basic approach, as for the statistical clear-sky model, is taken by using a model, which is fitted locally in the *day of year* and *time of day* dimensions. Furthermore the conditional parametric models allows for the model to be non-linear in the inputs, for example as a non-linear function of the NWPs of global radiation. For improving the forecasting performance for short horizons (up to three hours) the latest available observation is also added as input and the best model is obtained as

$$\begin{aligned} P_{t+k} = m &+ a\big(t_{\text{day}}, t_{\text{tod}}, P_t\big) P_t \\ &+ b\Big(t_{\text{day}}, t_{\text{tod}}, G^{\text{nwp}}_{t+k|t}\Big) G^{\text{nwp}}_{t+k|t} + e_{t+k} \end{aligned} \tag{2.8}$$

where the coefficient function $a\big(t_{\text{day}}, t_{\text{tod}}, P_t\big)$ and $b\Big(t_{\text{day}}, t_{\text{tod}}, G^{\text{nwp}}_{t+k|t}\Big)$ are non-linear functions, see Paper C for more details. For illustration of this, the plot in Figure 2.3 is used. It illustrates the 24 hour ahead forecasts of hourly solar power as a function of the NWPs of global radiation for five days over the year. From these plots it can be seen how the forecasting function can be non-linear and how it changes conditional on the *day of year*. The results for forecasting of the power output from a PV system, as presented in the paper, shows a slight RMSE performance improvement compared to the two-stage method. The approach is also very well suited for forecasting of thermal power output from a solar collector, as presented in Paper D, where it is found that especially the possibilities for modelling non-linearity in the inputs are important.

2.2.3 Probabilistic solar power forecasting

Probabilistic forecasting is not presented in any of the papers in this thesis, however it is found that a natural next step forward is to expand the current

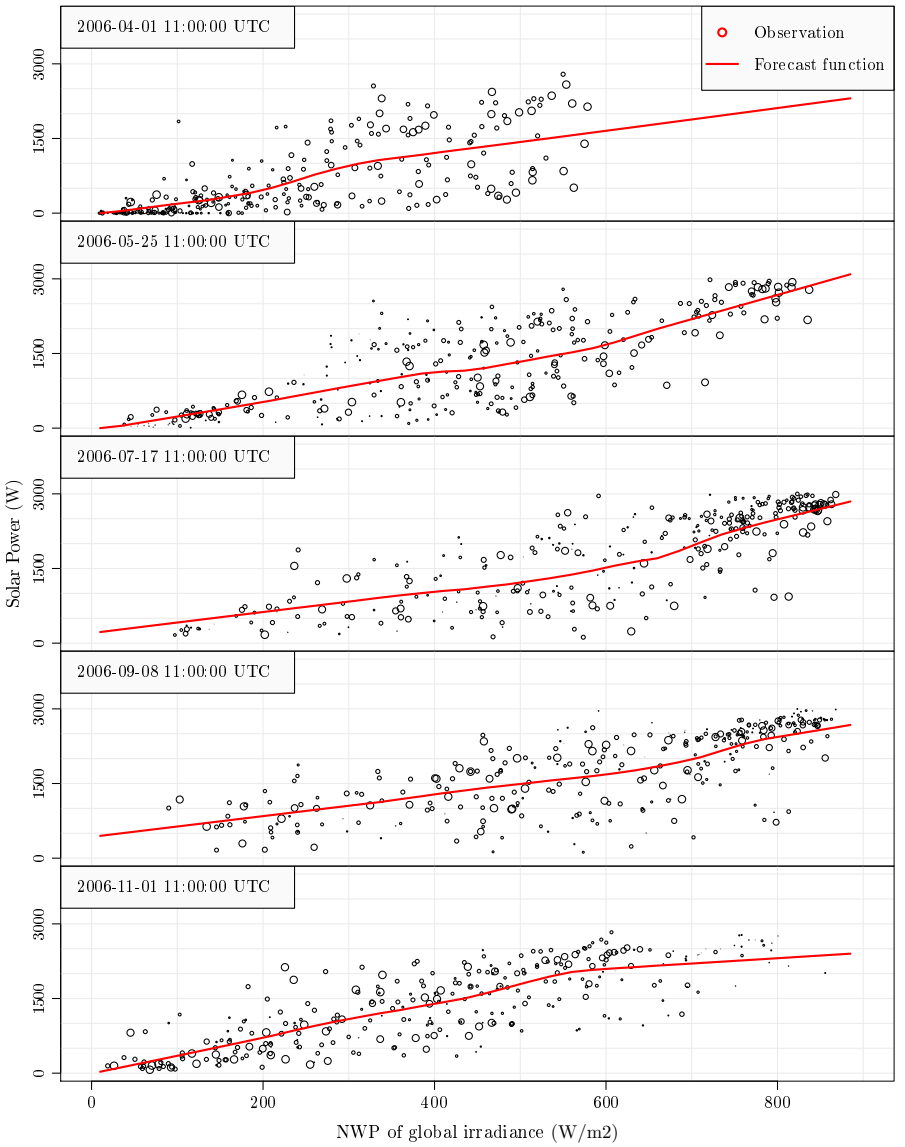

Figure 2.3: Example of the 24 hour ahead forecasted hourly solar power as a function of the NWP of global radiation for five days over the year. The data is presented in Paper C. The weighting of a point (only by $day(t, i)$ and $tod(t, i)$) is indicated by the size of its circle in the plot. A nearest neighbor weighting scheme is used.

point forecasts to probabilistic forecasts. Probabilistic solar power forecasting - which will be valuable for energy system operation, as described for wind power Pinson et al. (2007a) - means that at a given time ahead the probability distribution of solar power is forecasted instead of the single value. Many approaches to probabilistic forecasting exist, here an approach using quantile regression is used for illustration of some important aspects. One aspect is the relation between the normalized solar power - which can be considered equivalent to the clearness index - and the uncertainty on the forecast becomes apparent by considering normalized NWPs plotted versus normalized solar power, as described in Section B.5 (page 82). It is found that the uncertainty of the forecasts is dependent on the cloud cover, which is described with the clearness index, in such a way that forecasts for overcast or cloudless conditions have lower uncertainty, than forecasts of partly cloudy conditions. This is consistent with findings in other studies (Lorenz et al., 2007).

Probabilistic forecasting with quantile regression has been successfully applied for wind power forecasting by Bremnes (2004) and Nielsen et al. (2006). The suggested approach here for solar power is based on the same basic principles as the forecasting with a conditional parametric model, as presented in the previous section and in Paper C. The same data, consisting of observed solar power P_t and NWPs of global radiation $G^{\mathrm{nwp}}_{t+k|t}$, is used, and the forecasting function is simply replaced with the local quantile regression model

$$\hat{\beta}_t = \underset{\beta\in\mathbb{R}^2}{\operatorname{argmin}} \sum_{i=1}^{t} \rho_\tau\Big(P_i - \big(\beta_{0,t} + \beta_{1,t} G^{\mathrm{nwp}}_{i|i-k}\big)\Big)\, K_{3\mathrm{d}}(t,i) \tag{2.9}$$

where i and t are denoting time, $\rho_\tau(u) = u\big(\tau - I_{\{u<0\}}\big)$ is the quantile regression objective function (see (Koenker, 2005)), and the 3-dimensional multiplicative kernel function

$$K_{3\mathrm{d}}(t,i) = K\big(day(t,i)\big) \cdot K\big(tod(t,i)\big) \cdot K\big(G^{\mathrm{nwp}}_{t|t-k} - G^{\mathrm{nwp}}_{i|i-k}\big) \tag{2.10}$$

where $day(t,i)$ is the distance from t to i in days, $tod(t,i)$ is the time of day distance, and the Epanechnikov kernel function

$$K(\Delta) = \begin{cases} \frac{3}{4}\Big(1 - \Big[\frac{|\Delta|}{h}\Big]^2\Big) & \text{for } \frac{|\Delta|}{h} \geq 1 \\ 0 & \text{for } \frac{|\Delta|}{h} < 1 \end{cases} \tag{2.11}$$

with bandwidth h is used for calculating the weights in each dimension. The following bandwidths, which was set from visual inspection of the results, are used in the three weighting dimensions:

- $h_{\mathrm{day}} = 150$ is bandwidth in days

- $h_{\text{tod}} = 2$ is bandwidth in hours
- $h_{G_{\text{nwp}}} = nn(t, i, 300)$ is bandwidth in W/m^2 calculated as the smallest bandwidth where the 300 nearest neighbors are included.

The quantile regression implementation in the **R** (R Development Core Team, 2011) package `'quantreg'` is used for carrying out the calculations.

The plots shown in Figure 2.4 is of the estimated quantiles conditioned on the NWP of global radiation, for a 24 hour horizon. It is the $5\%, 10\%, \ldots, 90\%, 95\%$ τ quantiles. A clear dependency on the level of the global radiation NWPs is seen and the same pattern as described above is found: the uncertainty is higher for values in the middle of the range of forecasted global radiation.

It is evident that more research in probabilistic forecasting of solar power is needed, for example a proper evaluation should be carried out and an optimization of the bandwidths. From the very coarse outline of the presented approach a few conclusions are drawn:

- Evaluation of probabilistic solar power forecasts is needed for assessment of the forecast quality. Solar forecasting is highly related to wind power forecasting and the evaluation can be based on methods for evaluation of probabilistic wind power forecasts, for example the framework proposed by Pinson et al. (2007b).
- It is clearly seen that the distribution of solar power conditional on the NWPs of global radiation is highly skewed for low and high levels of the NWPs. Hence it can be questioned how a proper evaluation of point forecasts should be carried out, since the optimality of the least squares criteria is mostly based on an assumption of normal distributed errors.
- The value of energy forecasts for operation increase as more useful information for system operators is available. In that respect probabilistic solar power forecasting can prove to be very valuable, since the distribution of the error is highly dependent on the inputs and thus contain quite a lot non-trivial information.
- Studies have shown that valuable information about the uncertainty on wind power forecasts can be gained from ensemble forecasting. Ensemble forecasts calculated by the meteorologists can be used as input to model the uncertainty in energy forecasts, for example as described by Nielsen et al. (2006) for probabilistic wind power forecasting. The same approach can be applied for solar power forecasting.

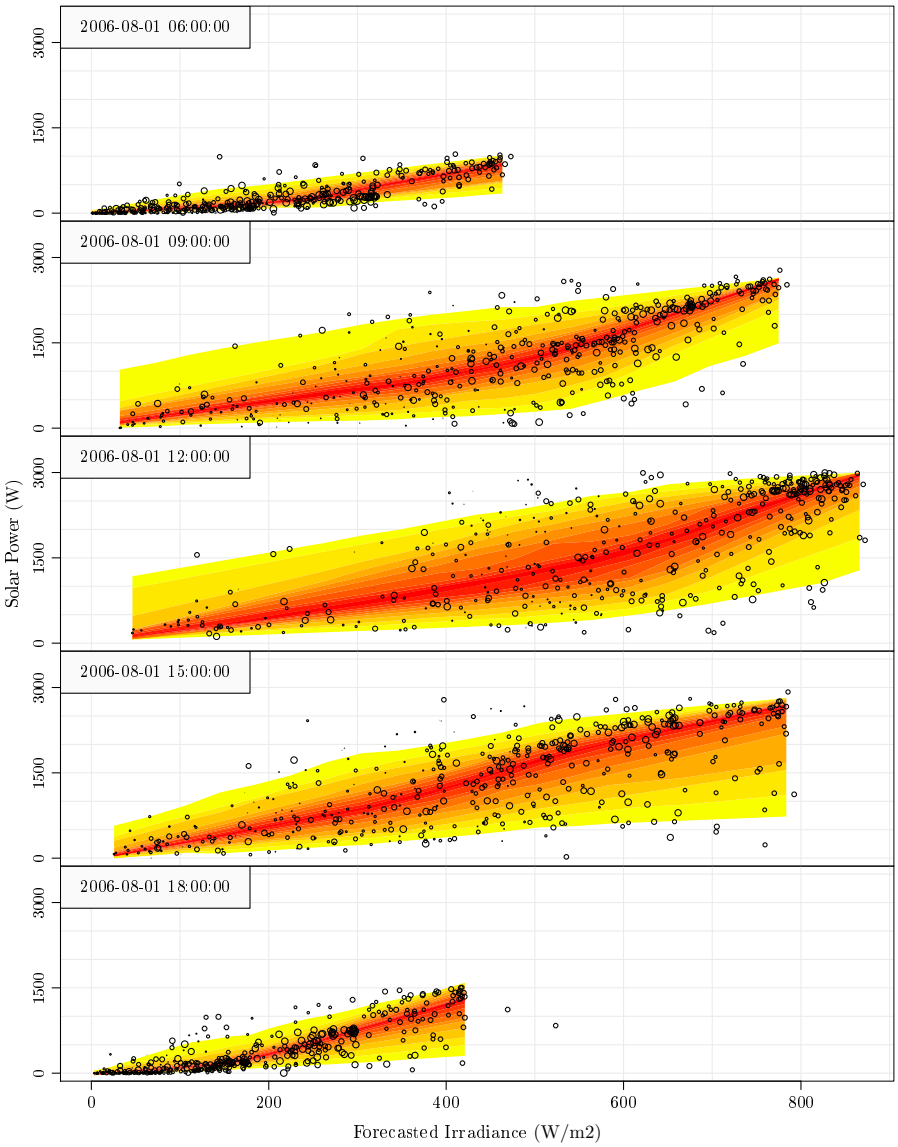

Figure 2.4: Example of probabilistic solar power forecasts for a $k = 24$ hour horizon at five different hours over the day. Local quantile regression is applied to estimate the $5\%, 10\%, \ldots, 90\%, 95\%$ τ quantiles. The weighting of a point (only by $day(t, i)$ and $tod(t, i)$) is indicated by the size of its circle in the plot.

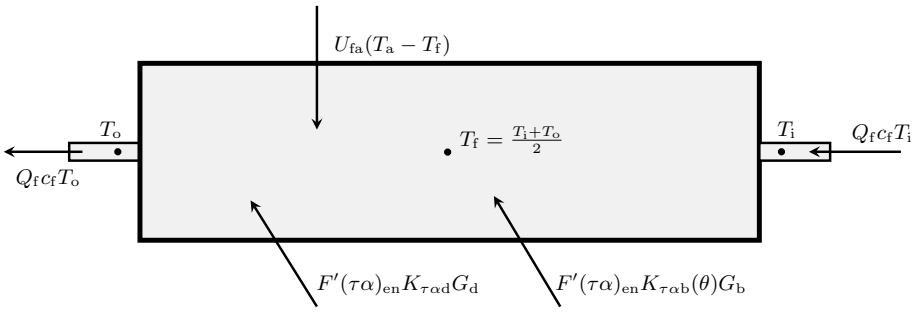

Figure 2.5: Diagram of the single state grey-box model illustrating all the energy flows included in the model.

2.3 Modelling the heat dynamics of solar thermal collectors

In Paper E models for the heat dynamics of solar thermal collectors are presented. The heat dynamics are described with grey-box models. A grey-box model is established using a combination of prior physical knowledge and statistics Kristensen et al. (2004). The prior physical knowledge is formulated by a set of non-linear stochastic differential equations (SDEs). The equations describe a lumped model of the heat dynamics of the system. Models from Perers (1997) of solar thermal collectors based on prior physical knowledge are used to derive the SDE which forms the system equation

$$\begin{aligned} dT_{\mathrm{o}} = \Big(& F'U_0(T_{\mathrm{a}} - T_{\mathrm{f}}) + c_{\mathrm{f}}Q_{\mathrm{f}}(T_{\mathrm{i}} - T_{\mathrm{o}}) \\ & + F'(\tau\alpha)_{\mathrm{en}}K_{\tau\alpha\mathrm{b}}(\theta)G_{\mathrm{b}} + F'(\tau\alpha)_{\mathrm{en}}K_{\tau\alpha\mathrm{d}}G_{\mathrm{d}} \Big) \frac{2}{(mC)_{\mathrm{e}}} dt + \sigma d\omega \end{aligned} \tag{2.12}$$

of the simplest applied grey-box model and it consists of a single state T_{o} which is the outlet temperature of the collector, [°C]. In the diagram in Figure 2.5 the energy flows are illustrated.

The following are parameters in the model

$F'U_0$	Heat loss coefficient at $(T_a - T_f) = 0$, $[W/(m^2K)]$.
$F'(\tau\alpha)_{en}$	Zero loss efficiency for direct radiation at normal incidence
$K_{\tau\alpha b}(\theta)$	Incidence angle modifier for direct radiation. It has a single parameter b_0 which is estimated
$K_{\tau\alpha d}$	Incidence angle modifier for diffuse radiation
$(mC)_e$	Effective thermal capacitance including piping for the collector, $[J/(m^2K)]$.
σ^2	is the incremental variance of the Wiener process $\{\omega\}$

The following are inputs which are measured (or derived directly from measurements)

T_a	Ambient temperature , [°C].
T_f	Average temperature of the collector fluid, [°C].
Q_f	Flow of the fluid per square meter of collector, $[l/(sm^2)]$.
T_i	Temperature of the inlet to the collector, [°C].
G_b	Direct radiation onto the collector plane, $[W/m^2]$.
G_d	Diffuse radiation onto the collector plane, $[W/m^2]$.

and finally c_f which is the specific heat capacity of the fluid, [J/(l K)].

The data-driven part of the grey-box model is formed by the discrete time observation equation

$$Y_k = T_{ok} + e_k \tag{2.13}$$

where k is the point in time t_k of a measurement, Y_k is the measured outlet temperature, and e_k is the measurement error, which is assumed to be a Gaussian white noise process with variance σ^2. The parameters are estimated with maximum likelihood techniques as described in Section E.2.1 on page 130.

A suitable model is identified for a flat plate collector using 30 second average values measured at a test setup at the building department of DTU. It is shown how the models can provide detailed knowledge about the performance of the collector with data from a single day. A forward model selection approach is used, where first a simple model is applied and stepwise expanded. The final model includes two lumped parts: one representing the fluid and one representing the metal and frame of the collector. Each of the two parts are lumped further into three compartments, resulting in the final model having six state variables, see Section E.5.2 on page 136.

A strong feature of using the applied grey-box modelling, is that accurate physical knowledge can be obtained with a minimum of testing time. The results are evaluated and discussed both from a statistical and physical perspective. As a reference the equivalent parameter estimates found with current ISO-standardized multiple linear regression models are used. The results show that parameters can be estimated very accurately with 30 second average values from a single day. It is an prerequisite that the input, especially the ambient temperature and the global radiation is uncorrelated. For the presented study this was achieved by using data from a day, where clouds modulated the radiation with an "on-off" sequence. This should be replaced with a shading device - simply a foil that can be automatically rolled up and down - for enabling an "on-off" testing sequence for the radiation onto the collector. The models can be used in several contexts, both for performance testing and for operational applications.

2.4 Discussion

Two methods for solar power forecasting based on NWPs have been presented, together with a method for correction of measured global radiation, and an outline of a probabilistic solar power forecasting method. The recurrent principle, on which all of the methods is based, is the use of non-parametric local regression techniques to model measured solar output, by using a kernel weighting function in dimensions of *day of year* and *time of day*. The advantage of using such models is that all types of systematic effects embedded in the solar output are included in model, especially effects which are local to the sensor and therefore very complex to model with a physical model, e.g. shadowing from trees. Regarding the statistical clear-sky model, a local fitting in the dimensions of the *sun azimuth* and *sun elevation* has been considered in (Bacher, 2008), where it was found that it leads to decreased accuracy for the considered applications. This is due to the importance of the model being local in time, for example at the positions of the sun where trees are shading, then it makes a huge difference if there are leaves on the trees or not.

Regarding the solar forecasting methods presented it is clear that further work should be addressed to enhance the models. For example regime switching for using different models depending on the weather type and using multiple NWPs as inputs. This has proved to increase performance both for wind power forecasts and solar forecasts. For example Schmelter et al. (2011) presents a method for combining forecasts depending on a weather classification for improving solar power forecast performance, especially for handling special weather conditions like fog and snow.

Chapter 3

Methods for building energy applications

The methods outlined in this chapter can be used to deal with important aspects for optimized energy use in buildings, especially for enabling buildings as a key player in smart grids and for energy performance improvement of the building stock. The method for forecasting of the heat load presented in Paper F is outlined, together with the procedure for identification of a suitable model for the heat dynamics of buildings presented in Paper G. The data used consist of a combination of: measurements and NWPs of climate variables, heat load, and indoor temperature.

3.1 Heat load forecasting

A method for forecasting the heat load in single family houses is presented in Paper F. Adaptive linear time series models are applied to forecast the heat load

$$Q_{t+k} = Q^{\text{ambient}}_{t+k|t} + Q^{\text{diurnal}}_{t+k|t} + Q^{\text{sun}}_{t+k|t} + Q^{\text{wind}}_{t+k|t} + e_{t+k} \tag{3.1}$$

where the terms on the right side represent heat gains caused by several mechanisms together with an error. The inputs to the model are formed from mea-

surements from a local weather station and numerical weather predictions. The following three signals are available

- $\hat{T}^{\mathrm{a}}_{t+k|t}$ the ambient temperature
- $\hat{G}_{t+k|t}$ the global radiation
- $\hat{W}^{\mathrm{s}}_{t+k|t}$ the wind speed

The heat dynamics of the building are described with linear rational transfer functions from the climate variables to the heat load. The heat gain to the ambient (i.e. negative in the winter period) is described by

$$Q^{\mathrm{ambient}}_{t+k|t} = \alpha_{\mathrm{ia}} + \alpha_{\mathrm{a}} H_{\mathrm{a}}(q) \hat{T}^{\mathrm{a}}_{t+k|t} \tag{3.2}$$

where α_{ia} is representing a constant indoor temperature (which is not available and therefore modelled as an intercept) and the first order low-pass filter with unity DC-gain

$$H_{\mathrm{a}}(q) = \frac{1 - a_{T_{\mathrm{a}}}}{1 - a_{T_{\mathrm{a}}} q^{-1}} \tag{3.3}$$

is applied and where q^{-1} is the backward shift operator ($q^{-1} x_t = x_{t-1}$) (see (Madsen, 2007)) and $a_{T_{\mathrm{a}}} \in [0, 1]$ is a coefficient, which is equivalent to the time constant for the part of the building affected by changes in ambient temperature. This is equivalent to describing the heat dynamics of the building with a lumped RC-model having a single heat capacity for the interior of the building and a single thermal resistance through the building envelope. The diurnal curve heat gain describes diurnal patterns caused by systematic user behavior, for example a nightly setback. It is modelled as a harmonic function using a Fourier series

$$\mu(t_{\mathrm{tod}}, \alpha_{\mathrm{diu}}) = \sum_{i=1}^{n_{\mathrm{har}}} \alpha^{\mathrm{diu}}_{i,1} \sin\left(\frac{t_{\mathrm{tod}} i \pi}{12}\right) + \alpha^{\mathrm{diu}}_{i,2} \cos\left(\frac{t_{\mathrm{tod}} i \pi}{12}\right) \tag{3.4}$$

where t_{tod} is the time of day in hours at time t and n_{har} is the number of harmonics included in the Fourier series. The heat gains from solar radiation and wind are modelled as

$$Q^{\mathrm{ambient}}_{t+k|t} = \alpha_{\mathrm{g}} H_{\mathrm{g}}(q) \hat{G}_{t+k|t} \tag{3.5}$$

and

$$Q^{\mathrm{wind}}_{t+k|t} = \alpha_{\mathrm{w}} H_{\mathrm{w}}(q) \hat{W}^{\mathrm{s}}_{t+k|t} \tag{3.6}$$

where the low-pass filters $H_{\mathrm{g}}(q)$ is similar to the filter for ambient temperature (Equation (3.3)), but fitted independently such that the coefficient describing

the dynamic response of the building is different for each of the inputs. Several extensions to this model is also applied as described in the paper. In order to achieve time adaptivity of the model, it is fitted with a recursive least squares scheme, where the past data is down-weighted depending on a forgetting factor. Note that each of the coefficients could have been denoted with a t to indicate that they change as a function of time. Finally, in a second stage a simple AR(1) model is applied to remove the last correlation in the residuals.

To identify a suitable forecasting model measurements of the hourly heat load for sixteen houses, which are typical Danish single family houses, are used. The houses are connected to district heating with a heat exchanger and have radiator heating. In order to lower the signal-to-noise ratio for effects related to the climate conditions, the heat load signals are preprocessed by filtering out the peaks from water heating. Thereafter a thorough model identification is carried out to find a forecasting model, which is suitable for all the houses. The following parameters are tuned for each house separately: transfer function coefficients (they are equivalent to time constants in the building and describe how fast the building respond to changes in the climate variables), harmonics in the diurnal curve, and the optimal time adaptivity. The first step in the model identification is to fit a simple model consisting only of a constant heat gain and a diurnal curve - i.e. this model does not include any climate variables, however it can follow the slow changes in climate due to the adaptive modelling scheme. This model is then expanded in steps, where inputs are included in different ways in a forward selection approach. The final result is a model, which is suitable for forecasting the heat load for each house, without requiring any specific knowledge about the building, apart from the heat load measurements. It can be used solely with NWPs as input, but the addition of local measurements improves forecasting performance for short horizons. It is shown that the forecasting residuals are close to white-noise and thereby that the information embedded in the inputs are very well utilized.

The forecasting performance measured with the mean absolute error as a function of the forecasting horizon is plotted for each of the sixteen houses in Figure 3.1. Clearly, a quite large difference is found between the houses, especially the forecasting performance is poor for House 8. Analysing the forecasts for House 8 it is found that the heat load signal has some oscillations with a period around 6 hours, which are not possible to forecast and which are most likely caused by a poorly tuned thermostatic control. A futher thorough analysis of the forecast for all the houses indicates that the solar radiation part of the model pose a challenge. Improvements could possibly be achieved by using some information about the buildings, such as the azimuth angles of the building walls etc., or by using an off-line model for learning how the solar energy gain of the building depends on the position of the sun, possibly as a function of *day of year* and *time of day*. Furthermore is seen how the error in the global radiation NWPs

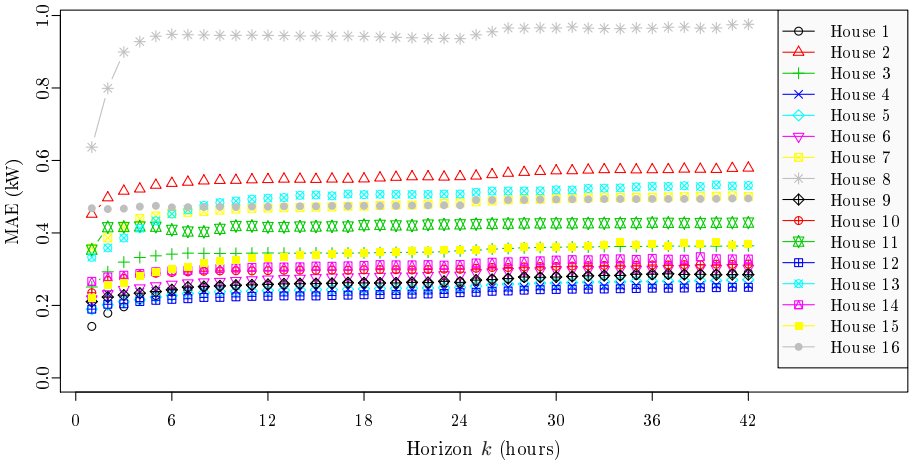

Figure 3.1: Mean absolute error for the hourly forecasted average values as a function of the forecasting horizon for each of the sixteen houses.

for longer horizons, i.e. an error in the input to the model, result in errors in the heat load forecasts. Furthermore, it is seen how effects related to unpredictable behavior of the residents, for example ventilation from opening of windows, appear in the heat loads.

3.2 Models for the heat dynamics of buildings

In Paper G models are presented, which can provide detailed knowledge of the heat dynamics of a building from measurements of: heat load, indoor temperature, ambient temperature, and global radiation. The focus of the paper is a procedure for selection of the most suitable model. The models are grey-box models, which are based on a combination of physical and data-driven modelling. They are based on stochastic differential equations, which allows for extensive modelling of dynamical systems and estimation of parameters which are directly physically interpretable, for example the heat capacity of the building and the UA-value of the building envelope. A description of heat transfer mechanisms which forms the basis for the physical part of the grey-box models can be found in (Bacher et al., 2010, Chapter 3).

The applied grey-box models are stochastic linear state space models, which are formed by a continuous time system equation and a discrete time measurement

equation. The system equation can be formulated in matrix form

$$d\mathbf{T} = \mathbf{A}\mathbf{T}dt + \mathbf{B}\mathbf{U}dt + \boldsymbol{\sigma}d\boldsymbol{\omega}(t) \tag{3.7}$$

where $\mathbf{T}$ is a vector of state variables (typically both measured and unmeasured temperatures), $\mathbf{U}$ is a vector of inputs, and $\boldsymbol{\omega}(t)$ is a Wiener process, which is a stochastic process with independent normal distributed increments. The matrices $\mathbf{A}$ defines how the current state affects the dynamics and $\mathbf{B}$ defines how input enters the system, and $\boldsymbol{\sigma}^2$ is the scaling of the linear in time growing variance of the increments of the Wiener process. The discrete measurement equation can be formulated as

$$\mathbf{Y}_{t_k} = \mathbf{C}\mathbf{T}_{t_k} + \mathbf{D}\mathbf{U}_{t_k} + \mathbf{e}_{t_k} \tag{3.8}$$

where t_k are the equidistant time points on which the output and inputs are measured, $\mathbf{Y}_{t_k}$ is the measured output (typically temperatures and/or heat flows, for example the interior temperature), $\mathbf{e}_{t_k}$ is the measurement error. It is assumed that $\mathbf{e}_{t_k}$ is normal distributed white noise with zero mean and variance $\mathbf{R}_\mathrm{e}$. Furthermore it is assumed that $\mathbf{e}_{t_k}$ and $\boldsymbol{\omega}(t)$ are mutually uncorrelated. $\mathbf{C}$ and $\mathbf{D}$ defines how the measured states are influenced by the state and input respectively.

A lumped parameter model is used to describe the heat dynamics of the building as examplified in the following, where a two state model is defined. One state variable is describing the interior temperature T_i and one is representing the temperature of the building envelope T_e. The first-order dynamics are represented by the stochastic differential equations

$$dT_\mathrm{i} = \frac{1}{R_\mathrm{ie}C_\mathrm{i}}(T_\mathrm{e} - T_\mathrm{i})dt + \frac{1}{C_\mathrm{i}}\Phi_\mathrm{h}dt + \frac{1}{C_\mathrm{i}}A_\mathrm{w}\Phi_\mathrm{s}dt + \sigma_\mathrm{i}d\omega_\mathrm{i} \tag{3.9}$$

$$dT_\mathrm{e} = \frac{1}{R_\mathrm{ie}C_\mathrm{e}}(T_\mathrm{i} - T_\mathrm{e})dt + \frac{1}{R_\mathrm{ea}C_\mathrm{e}}(T_\mathrm{a} - T_\mathrm{e})dt + \sigma_\mathrm{e}d\omega_\mathrm{e} \tag{3.10}$$

where t is the time, R_ie is the thermal resistance between the interior and the building envelope, R_ea is the thermal resistance between the building envelope and the ambient air, C_i is the heat capacity of the interior, C_e is the heat capacity of the building envelope, Φ_h is the energy flux from the heating system, A_w is the effective window area, Φ_s is the energy flux from solar radiation, T_a is the ambient air temperature, $\{\omega_{\mathrm{i},t}\}$ and $\{\omega_{\mathrm{e},t}\}$ are standard Wiener processes, and σ_i^2 and σ_e^2 are the scaling of the linear in time growing incremental variances of the Wiener processes. Note that the equations can easily be written into the matrix form defined in Equation (3.7). The model can be represented with the RC-network depicted in Figure 3.2, where the model is divided into different parts to show the corresponding parts of the building.

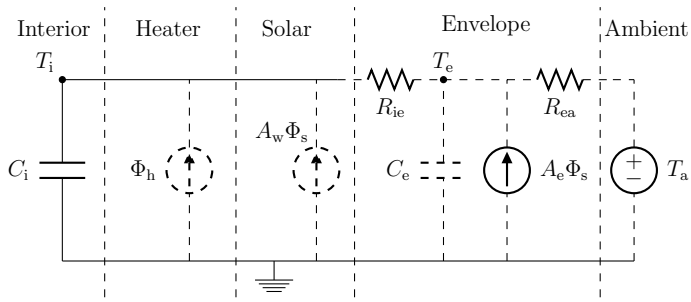

Figure 3.2: RC-network of the model described by Equation (3.9) and (3.10). The model is divided into different parts indicating the corresponding part of the building.

The interior temperature is measured and the discrete time measurement equation is

$$Y_{t_k} = T_{i,t_k} + e_{t_k} \tag{3.11}$$

where t_k is the time point of a measurement, Y_{t_k} is the measured interior temperature and e_{t_k} is the measurement error, which is assumed to be a Gaussian white noise process with variance σ^2.

The presented procedure for identification is based on a forward model selection approach, where likelihood ratio-tests are used for selection of a grey-box model with a suitable complexity. This is important since, on the one hand, a too simple model will be biased and not model the dynamics with the required level of detail, and on the other hand, a too complex model will be over-parametrized leading to degraded performance and incorrect parameter estimates. The procedure is based on a forward selection approach, where a simple model is extended until no significant increase in likelihood is found.

In the paper the procedure is applied to identify a model for the heat dynamics of a single-storey 120 m^2 building. The building is heated with a 6 days test sequence and five minutes average values are used for the modelling. An image and floor plan of the building can be seen in the paper (page 184). First the very simple model illustrated with its RC-diagram in Figure G.7 (page 191) is fitted. Then an expansion of this is seeked by adding different model parts, one at a time, and the expanded model with the highest increase in likelihood is selected. The expansion step is repeated iteratively until likelihood-ratio tests shows that no more significant increase in likelihood is achieved by any expansion. The final selected model is illustrated by its RC-diagram in Figure G.8 (page 193). The one-step prediction residuals for the models selected in each step are analysed with time series plots, the auto-correlation function and the cumulated periodogram. These can be seen in Figures G.9, G.10 and G.11. The

identified model can be applied for several purposes. The estimated parameters gives important information of the thermal performance of the building. The values can be found in Table G.3. The UA-value of the building envelope, which can be calculated directly from the parameters, indicates how well the building is insulated, see Table G.4. Furthermore accurate knowledge of the heat capacity of the building is obtained and thereby the nessesary knowledge for using the model as basis for control is provided.

Due to the rather uncomfortable course of the indoor temperature the modelling method using the used test sequence is not directly applicable in residential buildings. However it can be applied in periods, where the residents are away from the house in some days or for example at night time and during the day. In office buildings it can be run during the weekends. More work is needed for applying the procedure with other buildings in order to determine the minimum requirements for a desired level of estimation accuracy. For MPC methods for optimal load-shifting control of heating systems, in which the models are used, for example Pedersen et al. (2011) and Zong et al. (2011) both suggest that the indoor temperature is to be kept within a given range, for example between 19 to 21 °C in some periods and within 18 to 22 °C in others. Identifying a model for control allowing a indoor temperature variation in this range is probably a feasible task.

A strong feature is the capabilities of modelling the uncertainty in SDE models, which can be important for including residents behavior in the models. For example it can be modelled such that it depends of the time of day, in order to describe an increased uncertainty when the residents are home.

Finally, it is mentioned that the presented grey-box modelling procedure is very well suited for effective modelling in relation to effective performance testing of building components, e.g. in a test cell, as described in (Madsen and Holst, 1995).

3.3 Discussion

Considering the variety in the building stock and the highly diversified use of buildings, it is clear that much more research in modelling of heat use in buildings, based on data from smart meters, is needed. As seen in the data used in Paper F even for the sixteen single-family houses the characteristics of the heat load signals are very different, see for example the plot on page 171. However, even if the models as presented in the two papers are applied for a relatively specific type of buildings, the underlying principles can be applied for

modelling dynamic systems in many respects, including many types of buildings.

The need for details and accuracy for efficient operation of energy systems related to buildings depends on the application and the availability of data. A statistical approach, which eventually enables nearly all available information in data to be modelled, can save costs for hardware, e.g. sensors. The level of forecast uncertainty will naturally be related to the operational performance of the energy system, but it is a (economical) trade-off between the need for information from sensors (how many sensors etc. that are needed) and the performance gain, which finally also maps to an economical value of operating the total energy system, since more expensive energy backup capacity is needed as the forecasting accuracy decrease. Determining the cost-optimal need for sensors and accuracy is a non-trivial task, but a very valuable question to be able to answer.

Modelling the uncertainty for probabilistic forecasting presents another challenge, since the dynamics of the system needs to be included. For example the errors from the NWP forecasts of solar radiation can have a significant and one-sided effect on the forecast uncertainty, and thus the dynamics needs to be taken into account for a proper modelling.

Chapter 4

Discussion and conclusion

The presented methods have been discussed separately, hence in this section a general discussion of the presented work is given.

4.1 General discussion

The methods are closely related by the data-driven approach using statistical times analysis techniques for modelling. They form a basis for a range of operational applications, which are needed as the amount of data acquired from the energy system is increasing rapidly, for example with the widespread installation of smart meters in buildings. The data will be used for providing the needed on-line modelling of the system, where knowledge of the state and the dynamics in different part of the system is vital for an efficient operation. It is widely recognized that the operation of the power grid will be carried with markets, where a variable electricity price is available on different timescales. This will reward consumers which can provide a flexible load. Both for the operator of such markets and the participants, e.g. a consumer offering flexible heat load services in buildings, forecasting and methods for optimal operation are prerequisites for enabling the needed flexible load. Furthermore it is noted that it is very important to avoid sub-optimization of interdependent energy systems, for example as for operation of the considered solar/electric heating system, where

it is very important that the operation of the solar heating and the electrical heating is jointly optimized. Hence the forecasting and modelling methods, as the ones presented, should be combined in order to achieve an efficient operation of smart grid enabling technologies.

The required accuracy for the methods is a very relevant, but non-trivial question, to consider. It is know from statistical modelling theory that performance of a model is decreased if it is too simple or too complex. Therefore models should only comprise the needed complexity and here the statistical techniques for optimization of model complexity are vital. They are for example demonstrated in Paper G with the procedure for model identification based on likelihood-ratio tests. A forward selection approach for model identification is used for most of the presented modelling, in order to optimize the model complexity. Roughly said this simply implies starting with a simple model and trying different expansions until no performance improvement is found. To some extend this will require some manual interaction, but most likely the methods can be applied automatically for the majority of cases, in a combination with an automatic selection of cases which require further manual interaction. Certainly the computational resources needed is also an issue when considering operation of many thousand units. The presented methods are very suited for on-line operation, especially the recursive schemes for forecasting are very computational efficient. Generally it is suggested to run the computations on a central server. This will allow for easier management and more efficient computation, for example some calculations can be carried only once, opposed to stand-alone implementation.

Modelling of the forecast uncertainties is a really important step for power grid operation, as the share of renewables in the power mix is increasing, the forecasting errors will have a greater impact on the operation of the power system. Hence the value of modelling the uncertainties, and have probabilistic forecasting for all different types of power generation and load in the system, will increase. Considering the sources of errors there is a distinction between modelling errors, e.g. errors in the meteorological forecasts, and errors caused by for example user behavior. Errors from meteorological forecasts will mostly be affecting forecasts of wind and solar power generation, but also for the load, as especially the thermal part is included. Errors from user behavior will be affecting the load, but will, when considering the total load be smoothed out due to averaging over many individuals. However for operation of for example the heating system for a single house, the user behavior is very important to take into account.

4.2 Conclusion

Methods for optimized operation of energy systems with substantial amounts of renewable and volatile energy production are presented in the thesis. The methods are very well suited for smart grid applications. The focus is on electrical and thermal solar energy, and on heating in buildings.

The methods are mainly based on data-driven statistical models, which are combined with prior-physical knowledge where appropriate. The modelling carried out takes important aspects into account, such as: dynamical effects, non-stationarity, time adaptivity, non-linearity, user behavior, physical relations, and computationally efficient implementation. In the presentation of the methods, focus is on model identification and performance evaluation, which are carried out with statistical time series analysis techniques. The presented methods are almost directly applicable for operational use without much further development. Many perspectives and ideas for further work on the methods and in the respective fields are given.

A statistical clear-sky model is presented. It can be used to estimate the clear-sky output of a system, where the output is directly dependent on solar radiation at the surface of the earth. It is based solely on observations of the output and is very useful for removing non-stationarity in the observations. It also includes the effects occurring in the system and caused by the local surrondings, for example tilt in the levelling of the sensor (e.g. a pyranometer or a PV panel) or shading from objects in the surroundings. Two applications, where the statistical clear-sky model is used, are presented in the thesis: a two-stage method for solar power forecasting for PV-systems and a method for correction of errors in global radiation observations.

A second approach to solar power forecasting is presented. It is based on a conditional parametric model, which is conditional on the *day of year* and on the *time of day*. It is demonstrated how the method is well suited for forecasting solar power both for PV and solar thermal systems, and furthermore it is outlined how the approach can be used for probabilistic solar power forecasting.

Grey-box models for the heat dynamics of solar thermal collectors are presented. The models can for example be used to obtain accurate estimates of the energy performance parameters based on a very short testing period.

A method for forecasting the heat load for single family houses is presented. A forecasting model is found on the basis of heat load measurements from sixteen houses and local climate measurements combined with weather forecasts. The model is tuned to describe the heat dynamics of the building and the resident

behavior for each individual house. It is shown that practically all information embedded in the inputs are modelled.

Finally, a procedure for identification of a suitable model of the heat dynamics of a building is presented. The applied grey-box models are based on stochastic differential equations, which provide a detailed description of the heat dynamics based on prior physical knowledge combined with data-driven modelling. The models can be used as basis for model predictive control to enable shifting of the heat load, and for obtaining detailed knowledge of the energy performance of buildings.

Bibliography

P. Bacher. Short-term solar power forecasting. Master's thesis, Technical University of Denmark, 2008. IMM-M.Sc.-2008-13.

P. Bacher, A. Thavlov, and H. Madsen. Models for energy performance analysis : Financed by the danish electricity saving trust. Technical report, DTU Informatics, Building 321, Kgs. Lyngby, 2010.

R. Bird and C. Riordan. Simple solar spectral model for direct and diffuse irradiance on horizontal and tilted planes at the earth's surface for cloudless atmospheres. Technical report, Solar Energy Research Inst., Golden, CO (USA), 1984.

M. B. Blarke, K. Yazawa, A. Shakouri, and C. Carmo. Thermal battery with co2 compression heat pump: Techno-economic optimization of a high-efficiency smart grid option for buildings. *Energy and Buildings*, pages –, 2012. ISSN 0378-7788. doi: 10.1016/j.enbuild.2012.03.029.

G. Box, G. Jenkins, and G. Reinsel. *Time series analysis*. Holden-day San Francisco, 1976.

BP. Statistical review of world energy 2011, 2011. URL `www.bp.com/statisticalreview`.

J. B. Bremnes. Probabilistic wind power forecasts using local quantile regression. *Wind Energy*, 7(1):47–54, 2004. ISSN 1099-1824. doi: 10.1002/we.107.

C. Breyer, S. Rieke, M. Sterner, and J. Schmid. Hybrid pv-wind-renewable methane power plants - a potential cornerstone of global energy supply. In *Proceedings of ISES Solar World Conference 2011*, 2011.

Danish Commission on Climate Change Policy. Green energy – the road to a danish energy system without fossil fuels, September 2010.

DMI. Danish Meteorological Institute, DMI-HIRLAM-S05, 2011. URL http://www.dmi.dk/eng/index/research_and_development/dmi-hirlam-2009.htm.

ENFOR. Analysis of energy consumption in single family houses. Technical report, , 2010. URL http://www.enfor.dk/pub/03EKS0009A002-A.pdf.

J. Fonseca Júnior, T. Oozeki, T. Takashima, and K. Ogimoto. Analysis of the use of support vector regression and neural networks to forecast insolation for 25 locations in japan. In *Proceedings of ISES Solar World Conference 2011*, 2011.

V. Fthenakis, J. E. Mason, and K. Zweibel. The technical, geographical, and economic feasibility for solar energy to supply the energy needs of the us. *Energy Policy*, 37(2):387 – 399, 2009. ISSN 0301-4215. doi: 10.1016/j.enpol.2008.08.011.

R. Halvgaard, N. K. Poulsen, H. Madsen, and J. B. Jørgensen. Economic Model Predictive Control for Building Climate Control in a Smart Grid. In *2012 IEEE PES Innovative Smart Grid Technologies (ISGT)*, volume 9781457721588, page 2012ISGT0195. IEEE, 2012.

D. Heide, L. von Bremen, M. Greiner, C. Hoffmann, M. Speckmann, and S. Bofinger. Seasonal optimal mix of wind and solar power in a future, highly renewable europe. *Renewable Energy*, 35(11):2483 – 2489, 2010. ISSN 0960-1481. doi: 10.1016/j.renene.2010.03.012.

IEA - The Solar Heating and Cooling Programme. Solar heat worldwide, 2010. URL http://www.iea-shc.org.

IEA, International Energy Agency. *Solar Energy Perspectives - Executive Summary*. OECD Publishing, 2011a. doi: http://dx.doi.org/10.1787/9789264124585-en.

IEA, International Energy Agency. World energy statistics. Technical report, ESDS International, University of Manchester, 2011b.

M. Z. Jacobson and M. A. Delucchi. Providing all global energy with wind, water, and solar power, part i: Technologies, energy resources, quantities and areas of infrastructure, and materials. *Energy Policy*, 39(3):1154 – 1169, 2011. ISSN 0301-4215. doi: 10.1016/j.enpol.2010.11.040.

W. Ji and K. C. Chee. Prediction of hourly solar radiation using a novel hybrid model of arma and tdnn. *Solar Energy*, 85(5):808–817, 2011. ISSN 0038092x. doi: 10.1016/j.solener.2011.01.013.

T. Jónsson, P. Pinson, H. A. Nielsen, H. Madsen, and T. Nielsen. Forecasting electricity spot prices accounting for wind power predictions. *IEEE Transactions on Sustainable Energy*, Submitted:, 2012.

R. Koenker. *Quantile Regression*. Cambridge University Press, 2005.

R. Koenker. *quantreg: Quantile Regression*, 2011. URL `http://CRAN.R-project.org/package=quantreg`. R package version 4.76.

N. R. Kristensen, H. Madsen, and S. B. Jørgensen. Parameter estimation in stochastic grey-box models. *Automatica*, 40(2):225 – 237, 2004. ISSN 0005-1098. doi: DOI:10.1016/j.automatica.2003.10.001.

D. Lew, N. Miller, K. Clark, G. Jordan, and Z. Gao. Impact of high solar penetration in the western interconnection. *Contract*, 303:275–3000, 2010.

E. Lorenz, D. Heinemann, H. Wickramarathne, H. Beyer, and S. Bofinger. Forecast of ensemble power production by grid-connected pv systems. In *Proc. 20th European PV Conference, September 3-7, 2007, Milano*, 2007.

E. Lorenz, T. Scheidsteger, J. Hurka, D. Heinemann, and C. Kurz. Regional pv power prediction for improved grid integration. *Progress in Photovoltaics: Research and Applications*, 19(7):757–771, 2011. ISSN 1099-159X.

H. Madsen. *Time Series Analysis*. Chapman & Hall, 2007.

H. Madsen and J. Holst. Estimation of continuous-time models for the heat dynamics of a building. *Energy and Buildings*, 22(1):67–79, 1995. ISSN 03787788.

B. V. Mathiesen, H. Lund, and K. Karlsson. 100growth. *Applied Energy*, 88(2): 488 – 501, 2011. ISSN 0306-2619. doi: 10.1016/j.apenergy.2010.03.001.

P. Meibom, J. Kiviluoma, R. Barth, H. Brand, C. Weber, and H. V. Larsen. Value of electric heat boilers and heat pumps for wind power integration. *Wind Energy*, 10(4):321–337, 2007. ISSN 1099-1824. doi: 10.1002/we.224.

M. Nicolosi and C. Nabe. The long-term effects of high shares of pv in the power system–an analysis of the german power market. In *1st International Workshop on the Integration of Solar Power into Power Systems*, 2011.

H. Nielsen, T. Nielsen, A. Joensen, H. Madsen, and J. Holst. Tracking time-varying-coefficient functions. *International Journal of Adaptive Control and Signal Processing*, 14(8):813–828, 2000.

H. A. Nielsen, H. Madsen, and T. S. Nielsen. Using quantile regression to extend an existing wind power forecasting system with probabilistic forecasts. *Wind Energy*, 9(1-2):95–108, 2006. ISSN 1099-1824. doi: 10.1002/we.180.

P. Palensky and D. Dietrich. Demand side management: Demand response, intelligent energy systems, and smart loads. *Industrial Informatics, IEEE Transactions on*, 7(3):381 –388, aug. 2011. ISSN 1551-3203. doi: 10.1109/TII.2011.2158841.

T. Pedersen, P. Andersen, K. Nielsen, H. Starmose, and P. Pedersen. Using heat pump energy storages in the power grid. In *Control Applications (CCA), 2011 IEEE International Conference on*, pages 1106 –1111, sept. 2011. doi: 10.1109/CCA.2011.6044504.

S. Pelland, G. Galanis, and G. Kallos. Solar and photovoltaic forecasting through post-processing of the global environmental multiscale numerical weather prediction model. *Progress in Photovoltaics: Research and Applications*, pages n/a–n/a, 2011. ISSN 1099-159X. doi: 10.1002/pip.1180.

B. Perers. An improved dynamic solar collector test method for determination of non-linear optical and thermal characteristics with multiple regression. *Solar Energy*, 59(4-6):163–178, 1997. ISSN 0038092x.

B. Perers, S. Furbo, J. Fan, E. Andersen, and Z. Chen. Solar combisystems with forecast control to increase the solar fraction and lower the auxiliary energy cost. In *ISES Solar World Congress 2011 Proceedings*, page , 2011. ISBN 978-3-9814659-0-7. Presented at: ISES Solar World Congress, SWC ; 30 : Kassel, Germany, 2011.

P. Pinson, C. Chevallier, and G. Kariniotakis. Trading wind generation from short-term probabilistic forecasts of wind power. *Power Systems, IEEE Transactions on*, 22(3):1148 –1156, aug. 2007a. ISSN 0885-8950. doi: 10.1109/TPWRS.2007.901117.

P. Pinson, H. A. Nielsen, J. K. Møller, H. Madsen, and G. N. Kariniotakis. Non-parametric probabilistic forecasts of wind power: required properties and evaluation. *Wind Energy*, 10(6):497–516, 2007b. ISSN 1099-1824. doi: 10.1002/we.230. URL `http://dx.doi.org/10.1002/we.230`.

R Development Core Team. *R: A Language and Environment for Statistical Computing*. R Foundation for Statistical Computing, Vienna, Austria, 2011. URL `http://www.R-project.org/`. ISBN 3-900051-07-0.

C. Rigollier, O. Bauer, and L. Wald. On the clear sky model of the esra - european solar radiation atlas - with respect to the heliosat method. *Solar Energy*, 68(1):33 – 48, 2000. ISSN 0038-092X. doi: 10.1016/S0038-092X(99)00055-9.

S. Sayeef, T. Moore, S. Percy, D. Cornforth, J. Ward, and D. Rowe. Characterisation and integration of high penetration solar power in australia – a solar intermittency study. In *1st International Workshop on the Integration of Solar Power into Power Systems Aarhus, Denmark, 24 October 2011*, 2011.

J. Schmelter, M. Lange, and U. Focken. Weather class depending combinations of solar power forecasts – operational experiences. In *1st International Workshop on the Integration of Solar Power into Power Systems Aarhus, Denmark, 24 October 2011*, 2011.

G. Y. Yang, J. Østergaard, S. B. Kjær, A. Constantin, H. P. Ballegaard, R. D. Lazar, U. Borup, C. Stephansen, M. Mattesen, and J. B. Sørensen. Smart integration of photovoltaic power systems on the island of bornholm. In *1st International Workshop on the Integration of Solar Power into Power Systems Aarhus, Denmark, 24 October 2011*, 2011.

S. Younes, R. Claywell, and T. Muneer. Quality control of solar radiation data: Present status and proposed new approaches. *Energy*, 30(9):1533 – 1549, 2005. ISSN 0360-5442. doi: 10.1016/j.energy.2004.04.031. Measurement and Modelling of Solar Radiation and Daylight- Challenges for the 21st Century.

Y. Zong, D. Kullmann, A. Thavlov, O. Gehrke, and H. Bindner. Active load management in an intelligent building using model predictive control strategy. In *PowerTech, 2011 IEEE Trondheim*, pages 1 –6, june 2011. doi: 10.1109/PTC.2011.6019347.

K. Zweibel, J. Mason, and V. Fthenakis. A solar grand plan. *Scientific American*, 298(1):64–73, 2008.

J. Široký, F. Oldewurtel, J. Cigler, and S. Prívara. Experimental analysis of model predictive control for an energy efficient building heating system. *Applied Energy*, 88(9):3079 – 3087, 2011. ISSN 0306-2619. doi: 10.1016/j.apenergy.2011.03.009.

Paper A

A non-parametric method for correction of global radiation observations

Authors:
Peder Bacher[1], Henrik Madsen[1], Bengt Perers[2], and Henrik Aalborg Nielsen[3]

Submitted to:
Solar Energy (April 2012)

[1]DTU Informatics, Richard Pedersens Plads, Building 321, DK-2800 Lyngby, Denmark
[2]DTU Civil Engineering, Technical University of Denmark, DK-2800, Lyngby, Denmark
[3]ENFOR A/S, Lyngsø Allé 3, DK-2970 Hørsholm, Denmark (URL: www.enfor.eu)

Abstract

This paper presents a method for correction and alignment of global radiation observations based on information obtained from calculated global radiation, in the present study one-hour forecast of global radiation from a numerical weather prediction (NWP) model is used. Systematical errors detected in the observations are corrected. These are errors such as: tilt in the leveling of the sensor, shadowing from surrounding objects, clipping and saturation in the signal processing, and errors from dirt and wear. The method is based on a statistical non-parametric clear-sky model which is applied to both the observed and the calculated radiation in order to find systematic deviations between them. The method is applied to correct global radiation observations from a climate station located at a district heating plant in Denmark. The results are compared to observations recorded at the Danish Technical University. The method can be useful for optimized use of solar radiation observations for forecasting, monitoring, and modeling of energy production and load which are affected by solar radiation.

Nomenclature

G_t	Observed global radiation $[\mathrm{W/m^2}]$
G_t^{nwp}	Numerical weather predictions (NWPs) of global radiation $[\mathrm{W/m^2}]$
G_{cs}	Clear-sky global radiation $[\mathrm{W/m^2}]$
B_{cs}	Direct clear-sky global radiation $[\mathrm{W/m^2}]$
D_{cs}	Diffuse clear-sky global radiation $[\mathrm{W/m^2}]$
G	Global radiation $[\mathrm{W/m^2}]$
I_{ext}	Extraterrestrial radiation $[\mathrm{W/m^2}]$
G_t^{pr}	Projection of global radiation to the plane normal to the direct solar radiation $[\mathrm{W/m^2}]$
$\widehat{G}_t^{\mathrm{pr,cs}}$	Estimated clear-sky radiation on a plane normal to the direct solar radiation $[\mathrm{W/m^2}]$
$\widehat{G}_t^{\mathrm{cs}}$	Estimated clear-sky global radiation (modeled based on observations) $[\mathrm{W/m^2}]$
$\widehat{G}_t^{\mathrm{nwp,cs}}t$	Clear-sky global radiation for numerical weather predictions (NWPs) $[\mathrm{W/m^2}]$
$\widehat{G}_t^{\mathrm{co}}$	Corrected global radiation $[\mathrm{W/m^2}]$
$\theta_t^{\mathrm{zenith}}$	Solar zenith angle [rad]
$\tau_{\mathrm{a,B}}$	Transmittance function of the atmosphere for direct radiation under clear-sky conditions
τ_{c}	Transmittance function of clouds in the atmosphere
β_t	Parameter vector for the local quantile regression
$\rho_q(u)$	The quantile regression objective function
q	Sample quantile to be estimated in the local quantile regression
i	Counter of days [days]
j	Counter in samples
t	Time [hours]
t_{sp}	Sample period [hours]
h_{doy}	Bandwidth of kernel function in the *day of year* dimension [days]
h_{tod}	Bandwidth of kernel function in the *time of day* dimension [hours]

A.1 Introduction

The transition to a reliable and secure energy system based on weather dependent production technologies, especially wind and solar, will require new methods for automated handling of climate data recorded at, in most cases, unsupervised and uncalibrated stations. Reliable observations of solar radiation

are an important source of information for operation of the energy system, especially for the energy production and load which are dependent on the solar radiation, for example production from photovoltaics and solar collectors, and load from heating and cooling of buildings.

Observations of solar radiation are exposed to many sources of errors. Younes et al. (2005) list the most important types of errors and divide the errors into two major categories: equipment errors and operation related errors. The present solar radiation sensor technology makes it easy and cheap to install and connect sensors to the Internet, both for professional and amateur applications. Web sites already provide on-line data (DMI, 2012), which can become an important source of information for operation of energy systems. Such, mostly unsupervised and unvalidated installations, will be highly exposed to different error sources.

In the present study observations of global radiation from a station at a district heating plant in Sønderborg, Denmark, are used. Three types of errors are found in the observations: tilt in the leveling of the sensor, shadowing from surrounding objects, and clipping at a maximum level. A method is presented for correction of the observations on the basis of information extracted from global radiation calculated using a model based on physical principles. The method is based on a non-parametric statistical clear-sky model and requires no further information about the installation and sensor than the observed values and the location of the station. With the statistical clear-sky model the sensor output level under clear-sky conditions is modeled directly from the observations. This is compared to solar radiation calculated with a clear-sky model based on physical modeling of the optical effects through the atmosphere, such as the models described by Davies and McKay (1982), Bird (1984), Rigollier et al. (2000), Mueller et al. (2004), and Ineichen (2006). In the preset study forecasts from a numerical weather prediction (NWP) model is used. The result after correction of the observations is compared to high quality measurements recorded at the Danish Technical University.

Studies on quality control of measured solar radiation data can be found in the literature. The procedures are semi-automatic and are mostly based on comparison to physical models for detection of erroneous measurements (Geiger et al., 2002), (Younes et al., 2005), (Isaac and Moradi, 2009) and (Journée and Bertrand, 2011).

The paper is organized as follows: the data used in the study is presented in the next section. This is followed by a section in which the statistical clear-sky model is described and a section where the correction is presented. The paper ends with a discussion of the method and a conclusion.

Figure A.1: The weather station in Sønderborg, which is mounted on a pole on the roof of a single-storey district heating plant building (in the image it is on the left side of the building).

A.2 Data: Observations and numerical weather predictions of global radiation

The data used in this study consists of time series of global radiation observed at two weather stations: one located in Sønderborg (54.91°N and 9.80°E) and one located at DTU Byg in Lyngby (55.79°N and 12.52°E), both in Denmark. In addition NWPs of global radiation for the same locations are used. All values are hourly averages. All times are in UTC and the time points are set to the end of the hour.

A.2.1 Observations

The observations from Sønderborg are recorded with a weather station, which is located at a district heating plant. The weather station is mounted on a pole on a single-storey building as seen on the image in Figure A.1. No information about the type of the solar radiation sensor was available. The time series from Sønderborg is

$$\{G_t;\ t = 1, \ldots, N\} \tag{A.1}$$

where $N = 17520$ and G_t is the observed average global radiation between time t and $t - 1$. The upper plot in Figure A.2 shows the series which spans from

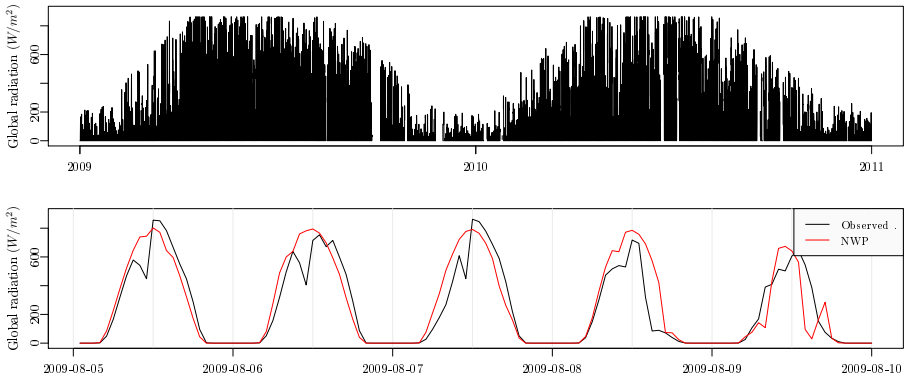

Figure A.2: The upper plot shows the time series of observed global radiation in Sønderborg. In the lower plot the observations and NWPs of global radiation in Sønderborg are shown for five days in August 2009.

2009-01-01 to 2011-01-01. From this plot it is readily seen that the observations are not without systematic errors, for example it can be seen that the values are clipped at a maximum level. This and other types of systematic errors are corrected for the Sønderborg observations using the method described in this paper.

The second series of observed global radiation is from a weather station at DTU Byg in Lyngby and is used as a reference to check the corrected data. The upper plot in Figure A.3 shows the series which spans from 2009-01-01 to 2010-01-01. It was measured with a Kipp & Zohnen CM10 pyranometer and the weather station was regularly supervised in the measuring period. The measurement error is in the range of maximum $\pm 3\%$ from the world standard and high class calibrated sensor inter-comparisons indicate an error within the range of $\pm 1\%$. The lower plot in Figure A.3 shows the observations together with the NWPs of global radiation (defined in the next section) for five days in August 2009. It is seen that the level of the observed global radiation is generally lower than the level of the NWPs, but that this there is no systematic difference between the deviation in the morning and in the afternoon. The lower level is most likely due to a bias in the NWPs. Since the accuracy of the DTU observations is high and no systematic errors, apart from the generally lower level, is seen, then it is found valid to assume that the DTU observations can used be as a reference to verify the NWPs and the results of the correction.

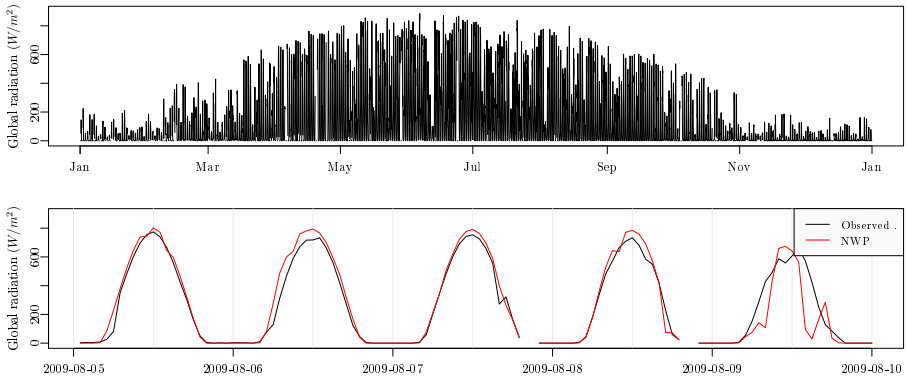

Figure A.3: The upper plot shows the time series of observed global radiation at DTU Byg covering the entire year 2009. In the lower plot the observations and NWPs of global radiation at DTU Byg are shown for five days in August 2009.

A.2.2 Numerical weather predictions

The numerical weather predictions (NWPs) used in the study are provided by the Danish Meteorological Institute (DMI). The NWP model used is DMI-HIRLAM-S05, which has a 5 kilometer grid and 40 vertical layers, see (DMI, 2011) and (Hansen Sass et al., 2002) for more details. The forecasts are updated four times per day and have a calculation delay of 4 hours (e.g. the forecast starting at 00:00 is available at 04:00). Two time series, consisting of the latest available forecast (lead times are 5 to 11 hours) of global radiation, are used: one for the location in Sønderborg and one for the location of DTU in Lyngby. The time series of NWPs for the Sønderborg location is used for the correction. It is denoted with

$$\{G_t^{\text{nwp}};\ t = 1, \ldots, N\} \tag{A.2}$$

The time series for DTU Byg in Lyngby is shown, together with the observations, in the lower plot of Figure A.3 for five days in August.

A.2.3 Systematic errors in Sønderborg observations

The lower plot in Figure A.2 shows the Sønderborg observations and the NWPs of global radiation for five days in August 2009. From the first day, which is a clear-sky day, at least two types of errors can be seen in the observations:

compared to the NWPs the observed level is too low in the morning and too high in the afternoon, which is most likely due to the sensor being tilted. It could also be due to a shift in time of the sensor, however it was thoroughly checked that the night hours, where the radiation was zero (or very close to zero), are with only a few exceptions the same hours for both the observed and the NWPs, indicating that they are well synchronized. The second type of error is seen just before noon, where the observations have a drop, which is repeated at the same *time of day* on following clear-sky day. The drop is caused by shading from the chimney, which is located close to the weather station, as seen on the image in Figure A.1.

The scatter plot in Figure A.4 shows the observed values versus the NWPs, together with two lines indicating the relation between the variables in the morning and in the afternoon. The lines are calculated using locally weighted least squares regression between the observations and the NWPs, using the function `loess()` in R (R Development Core Team, 2011) with a bandwidth: `span=0.9`. A similar plot for the DTU observations is found in Figure A.5. The following three distinct systematic errors can be seen from the scatter plot for the Sønderborg observations:

1. Firstly, the observations are clipped at a maximum level around 860 W/m^2.

2. Secondly, the level of the morning observations is generally lower than the level of the afternoon observations. This is confirmed by the fitted regression lines, which mostly have a difference of at least 50 to 75 W/m^2. This is clearly a larger difference than seen for the two fitted lines for the DTU observations in Figure A.5.

3. Finally, the morning values are significantly lower in the NWP range of 700 to 900 W/m^2. These values are the observations in the drop before noon, which, as described earlier, is caused by shadowing from the chimney right next to the weather station.

Considering the scatter plot for the DTU observations in Figure A.5 it is seen that these systematic errors are not found in the DTU observations. As noted before the level of the DTU observations is generally a bit lower than the level of NWPs, which is most likely due to a bias of the NWPs, since the accuracy of the DTU observations is verified to be in the range of $\pm 3\%$. For correction of the systematical errors, as the listed above, a statistical clear-sky model fitted to the observations can be used, as outlined in the following sections.

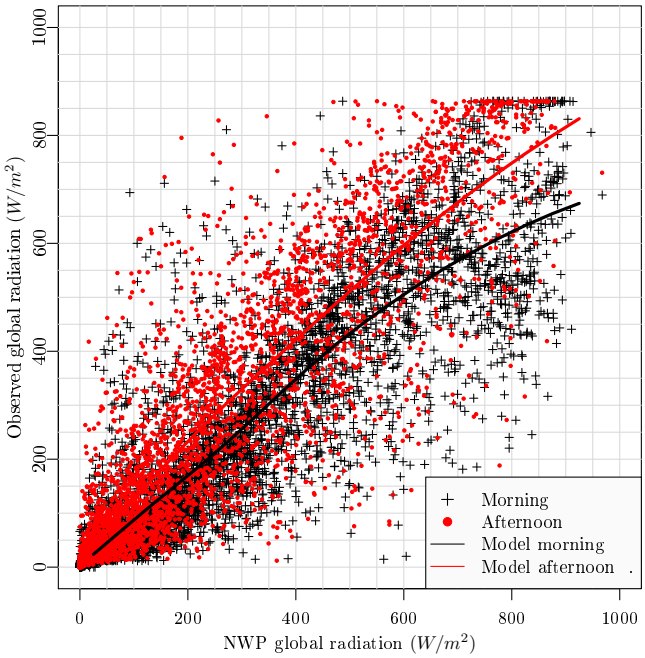

Figure A.4: The values of the Sønderborg observations versus the NWPs covering the entire year 2009. The morning values and the afternoon values are indicated by different symbols and colors. The two lines show a locally weighted least squares regression estimate of the relation between the variables in the morning and the afternoon.

A.3 Statistical clear-sky model

In this section it is described how the clear-sky global radiation is modeled using a statistical model. With the statistical clear-sky model the level under clear-sky conditions at time t is estimated for the particular series of observations. It is the output of the sensor under clear-sky conditions which is estimated. This implies that if an observation is affected by a systematical error, for example shadowing from an object in the surroundings, the estimated clear-sky output will be lowered. It is this feature which enables the model to be used for correction. The statistical clear-sky model is a non-parametric model based on local polynomial quantile regression (Koenker, 2005) similar to the clear-sky model presented in (Bacher et al., 2009).

Usually, clear-sky models are models with which the global radiation in clear

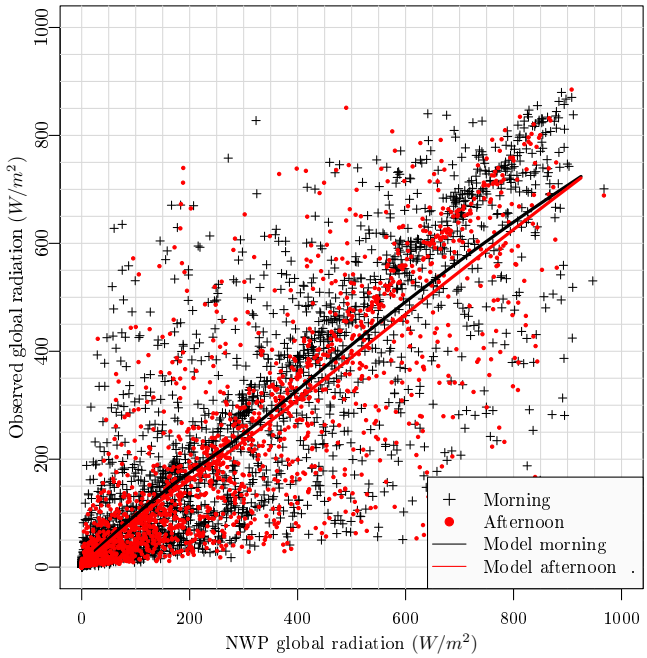

Figure A.5: The values of observed versus NWP global radiation at DTU Byg in Lyngby, Denmark. The morning values and the afternoon values are plotted with different symbols and colors. The two lines are indicating the relation between the variables: one for the morning and one for the afternoon.

(non-overcast) sky at any given time can be calculated based on physical modeling of the atmosphere. Usually the clear-sky global radiation G_{cs} is separated into a direct (or beam) B_{cs} and diffuse D_{cs} component

$$G_{\mathrm{cs}} = B_{\mathrm{cs}} + D_{\mathrm{cs}} \tag{A.3}$$

which are then modeled separately. The direct component by

$$B_{\mathrm{cs}} = I_{\mathrm{ext}} \cos(\theta_{\mathrm{zenith}})\, \tau_{\mathrm{a,B}} \tag{A.4}$$

where I_{ext} is the extraterrestrial radiation, θ_{zenith} is the solar zenith angle and $\tau_{\mathrm{a,B}}$ is a transmittance function of the atmosphere for direct radiation under clear-sky conditions, which for example can be modeled taking Rayleigh scattering, aerosol extinction, and ozone, water and uniformly mixed gas absorption into account Bird and Riordan (1984).

The diffuse component can be modeled by adding several contributions from

reflections and scattering through the atmosphere.

The global radiation (at the surface of the earth) can be modeled by

$$G = G_{\mathrm{cs}}\,\tau_{\mathrm{c}} \tag{A.5}$$

where τ_{c} is a transmittance function of clouds in the atmosphere, which can be modeled with "layer models" (Davies and McKay, 1982) where cloud layer transmittance and reflections are taken into account.

A clear-sky model, similar to the one proposed by Bacher et al. (2009) for observations of solar power, is here proposed for observations of global radiation. The proposed clear-sky model does not include any prior physical knowledge, it is based solely on the information obtained from the observations. It is denoted as a statistical clear-sky model, since it is based on a non-parametric statistical model of clear-sky radiation. Information embedded in the observations, which is particular for the sensor and its location, can be modeled with the statistical clear-sky model, for example shadowing and non-horizontal leveling of the sensor. This is a fundamental difference to the clear-sky models based on prior physical knowledge, which implies that the statistical clear-sky model can be used for different applications.

The statistical clear-sky model is based on time series of global radiation observations (or simulated values) and is defined by

$$G_t = \widehat{G}_t^{\mathrm{cs}}\,\tau_t \tag{A.6}$$

where the t is used to indicate that the variables the time series of actual observations, G_t is observed global radiation, $\widehat{G}_t^{\mathrm{cs}}$ is estimated clear-sky global radiation and τ_t is a factor, which is much to alike τ_{c}, but different due to the fact that it is estimated based on information from observations and not calculated based on prior physical knowledge. It is noted here that the clear-sky model could be defined for the direct component solely, which would be obvious since nearly all local systematic effects have a much higher impact on the direct component compared to the diffuse component. However, since the application of the clear-sky model in the present study is for observations of global radiation and since the systematic errors would propagate into both the direct and diffuse component calculated with a splitting scheme, such as suggested by Ruiz-Arias et al. (2010), the clear-sky model is applied to the global radiation directly.

Considering the observed global radiation as samples of a random variable with a probability distribution function, which is a function of the *day of year* x_t and the *time of day* y_t, the observed clear-sky global radiation can be estimated as a quantile

$$\widehat{G}_t^{\mathrm{cs}} = Q_q(x_t, y_t) \tag{A.7}$$

of this distribution function, where the quantile $q \in [0, \ldots, 1]$ must be close to one

$$q \lesssim 1 \tag{A.8}$$

Assuming that the quantile function is a smooth function it can be approximated with local quantile regression Koenker (2005). The result in the three-dimensional space formed by global radiation, *day of year* and *time of day*, can be seen as a surface which follows the observed global radiation under clear-sky conditions and is located "on top" of the point cloud of observed global radiation.

In order to decrease the gradient and curvature of the estimated clear-sky radiation surface a projection is carried out. The projection is from the horizontal plane to the plane which is normal to the direct solar radiation (i.e. the plane tracking the sun position)

$$G_t^{\text{pr}} = \frac{G_t}{\cos(\theta_t^{\text{zenith}})} \tag{A.9}$$

where θ_t^{zenith} is the average solar zenith angle in the sample period between $t-1$ and t. Values where $\cos(\theta_t^{\text{zenith}}) < 0.01$ are removed: this corresponds to sun elevation below 0.5°. The quantile close to one is then estimated for the projected values. A general form of the proposed statistical clear-sky model is formulated in A.7, which is based on a local quantile regression model with second order polynomials and a two-dimensional kernel in both the *day of year* and *time of day* dimensions.

For correction of hourly values a local quantile regression model based only on a one-dimensional kernel, where on the *day of year* dimension is used, was found most suitable. The reason for using only a one-dimensional kernel, and not including the *time of day* dimension in the local weighting, is that the model becomes too biased and the estimated clear-sky global radiation does not follow the drop before noon caused by shadowing (the systematic error described on page 50) very well. Hence only values lagged in steps of 24 hours from t are used as input, which is a similar approach as in classical decomposition of seasonal time series (Cleveland and Tiao, 1976). Furthermore, it is noted that this is equivalent to using a bandwidth in the *time of day* dimension below one hour (i.e. below the sample period) for the two-dimensional model presented in A.7, hence for time series with a shorter sample period a two-dimensional model should be considered. The applied local quantile regression model based on a third order polynomial is

$$\hat{\beta}_t = \underset{\beta \in \mathbb{R}^4}{\operatorname{argmin}} \sum_{i=-\infty}^{\infty} \rho_q\big(G_{t+24i}^{\text{tr}} - (\beta_{0,t} + \beta_{1,t} i + \beta_{2,t} i^2 + \beta_{3,t} i^3)\big) K(i) \tag{A.10}$$

where $\rho_q(u) = u\big(q - I(u < 0)\big)$ is the quantile regression objective function (see (Koenker, 2005) and (Koenker, 2011)), $q \in [0, \ldots, 1]$ is the sample quantile to be estimated, $i \in \mathbb{N}$ is a counter of days, and $K(i)$ is a kernel function. The estimated projected clear-sky radiation is then found as the local intercept

$$\widehat{G}_t^{\mathrm{pr,cs}} = \hat{\beta}_{0,t} \tag{A.11}$$

The weights are calculated with the Epanechnikov kernel function

$$K(i) = \begin{cases} \frac{3}{4}\left(1 - \left[\frac{|i|}{h_{\mathrm{doy}}}\right]^2\right) & \text{for } \frac{|i|}{h_{\mathrm{doy}}} \geq 1 \\ 0 & \text{for } \frac{|i|}{h_{\mathrm{doy}}} < 1 \end{cases} \tag{A.12}$$

where h_{doy} is the bandwidth.

The R package `quantreg` implementation of quantile regression was used for the estimation (Koenker, 2011). Finally, the estimated projected clear-sky radiation on the projected plane is projected back to the horizontal plane by

$$\widehat{G}_t^{\mathrm{cs}} = \widehat{G}_t^{\mathrm{pr,cs}} \cos(\theta_t^{\mathrm{zenith}}) \tag{A.13}$$

Finally, in order to take the clipping at a maximum level into account, the estimated clear-sky radiation is limited to the maximum value of the observations

$$\widehat{G}_t^{\mathrm{cs}} = \begin{cases} \widehat{G}_t^{\mathrm{cs}} & \text{for } \widehat{G}_t^{\mathrm{cs}} \leq G_t^{\max} \\ G_t^{\max} & \text{for } \widehat{G}_t^{\mathrm{cs}} > G_t^{\max} \end{cases} \tag{A.14}$$

where $G_t^{\max}$ is the maximum value of global radiation observations.

The selection of suitable values for the parameters (here the quantile and the kernel bandwidth) for the fitting of the local quantile regression model, would preferably be based on a measure of performance for estimation clear-sky global radiation. Then the parameters could be optimized in order to achieve the best performance. However thorough studies are required in order to define such a measure. Therefore the parameter values are selected based on visual inspection of the estimated clear-sky global radiation for days with only clear-sky. These days are chosen such that they are distributed evenly over the entire period. The selected values are

$$q = 0.97, \quad h_{\mathrm{doy}} = 125 \tag{A.15}$$

which gives the estimate of the clear-sky global radiation for the observations $\widehat{G}_t^{\mathrm{cs}}$ shown in Figure A.6 and for the NWPs $\widehat{G}_t^{\mathrm{nwp,cs}}$ shown in Figure A.7. Note, that the estimated surface for the observations is clipped at the maximum value of the observations, which gives the "flat" top. Furthermore, notice that the drop due to shadowing is clearly seen in the estimated clear-sky radiation for the observations.

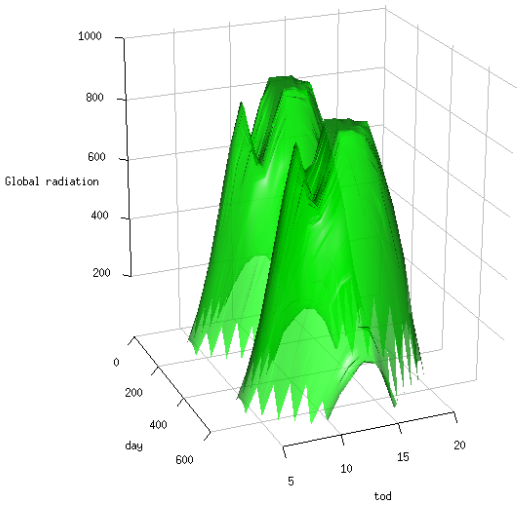

Figure A.6: The clear-sky global radiation estimated for the Sønderborg observations. Shown as a surface parametrized in the two dimensions: day (days since 2009-01-01) and tod (*time of day*).

A.4 Correction of observations

The correction of the observations is carried out by multiplying the observations with the ratio between the estimated clear-sky radiation for the NWPs and the observations

$$\widehat{G}_t^{\mathrm{co}} = \frac{\widehat{G}_t^{\mathrm{nwp,cs}}}{\widehat{G}_t^{\mathrm{cs}}} \, G_t \tag{A.16}$$

The level of the correction applied, i.e. $\widehat{G}_t^{\mathrm{nwp,cs}}/\widehat{G}_t^{\mathrm{cs}}$, is shown as function of days since 2009-01-01 and the *time of day* in Figure A.8. The systematical error caused by a tilt of the sensor, resulting in a too low level of the observations in the morning and too high level in the afternoon, can be directly seen in the correction, since in the morning the correction is generally above one and the afternoon level below one. Also apparent is the drop in the observed level due to shadowing objects, especially seen between 9 to 10 am.

The corrected observations are plotted versus the NWPs in Figure A.9, including the local least squares estimate of the relation in the morning and in the afternoon. This plot is similar to the plot in Figure A.4. By comparison of

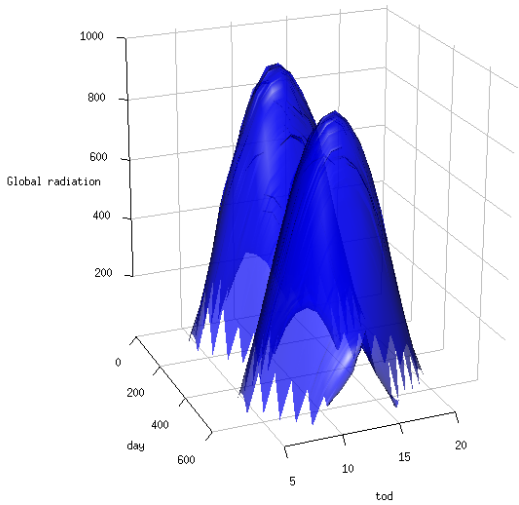

Figure A.7: The clear-sky global radiation estimated for the NWPs for Sønderborg. Shown as a surface parametrized in the two dimensions: day (days since 2009-01-01) and tod (*time of day*).

the two plots it is seen that the difference between the estimated relation in the morning and the estimated relation in the afternoon has been decreased significantly. A visual comparison to the similar plot of the high quality DTU observations in Figure A.5 verifies that the pattern of the scatter after the correction is much closer to the pattern found there. It can also be seen that the clipping at a maximum level has been corrected. Finally, it is found that the overall scattering has been reduced. This is confirmed by a comparison of the errors for an estimated relation similar to the ones in Figure A.4 and A.9, but using all data points (except nighttime values), i.e. no distinction between morning and afternoon. Note here that the this measure is only used to give a rough indication of the performance of the correction. The root mean square error (RMSE) and mean absolute error (MAE) before the correction are

$$\mathrm{RMSE}_{\mathrm{before}} = 114 \text{ W/m}^2, \quad \mathrm{MAE}_{\mathrm{before}} = 79 \text{ W/m}^2 \tag{A.17}$$

and after the correction

$$\mathrm{RMSE}_{\mathrm{after}} = 101 \text{ W/m}^2, \quad \mathrm{MAE}_{\mathrm{after}} = 67 \text{ W/m}^2 \tag{A.18}$$

Hence a notably reduction in RMSE and MAE is achieved by applying the correction.

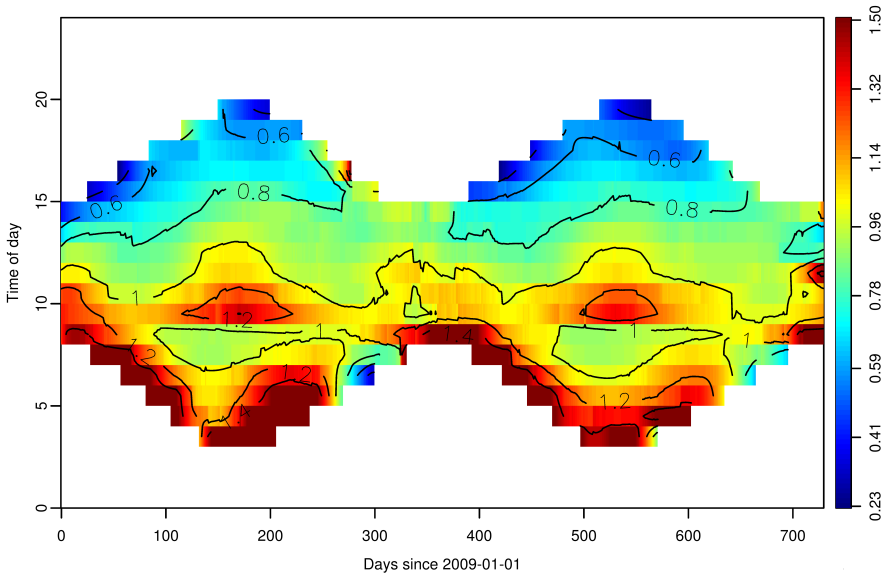

Figure A.8: The applied correction, which is the ratio between the estimated clear-sky radiation of the observations and the NWPs, as a function of days and *time of day*.

A.4.1 On-line operation

For on-line operation the model has to be applied causally, such that only past values can be used for the correction. A causal correction was calculated with slightly different parameter values for the clear-sky model, again selecting the parameters from visual inspection. The estimated quantile q was decreased and the kernel bandwidth h_{doy} increased slightly to

$$q = 0.95, \quad h_{\text{doy}} = 150 \tag{A.19}$$

Using a one-sided kernel will increase the bias of the estimates, which is also reflected by a slightly increased RMSE and MAE of the `loess` fit for the corrected observations to

$$\text{RMSE}_{\text{after}} = 103 \text{ W/m}^2, \quad \text{MAE}_{\text{after}} = 67 \text{ W/m}^2 \tag{A.20}$$

Considering the similar plots as presented for the causal correction showed only a small visual difference. Hence it is found that the method works well for on-line operation.

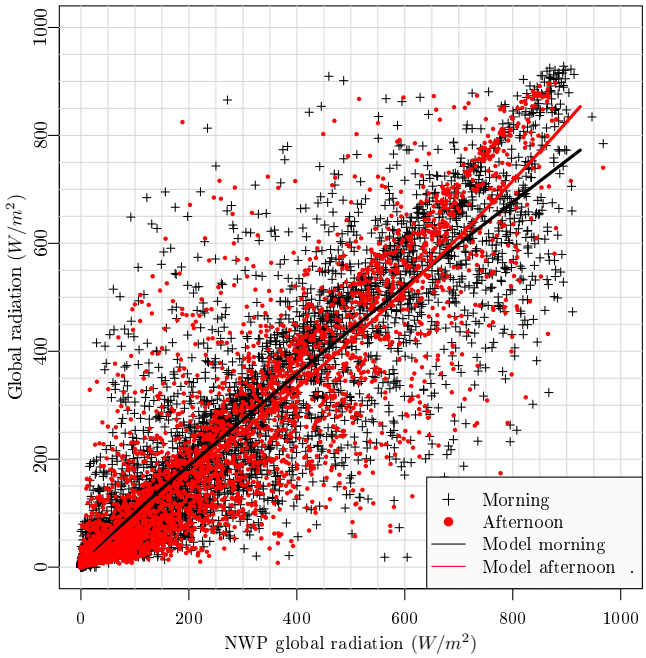

Figure A.9: The values of the corrected observations versus NWPs of global radiation. The morning values and the afternoon values are indicated by different symbols and colors. The two lines show a locally weighted least squares regression estimate of the relation between the variables in the morning and the afternoon.

A.5 Discussion

In this section the correction method and results are discussed together with considerations on how to improve the method.

Considering the fitting of the clear-sky model it is noted that the model which should be applied, is dependent on the time resolution of the data. For resolutions higher than hourly a two-dimensional kernel, which also includes the *time of day* dimension, should be used, as in (Bacher et al., 2009) where a similar clear-sky model was applied to fifteen minutes values. Regarding the parameters needed to be tuned in the clear-sky model - the quantile, kernel bandwidth, and order of the polynomial - some manual interaction is required. However the method could be based on a parameter optimization criteria, hence an objective measure to evaluate the performance of the correction, possibly based

on cross validation (Friedman et al., 2001), and applied automatically for the general case. Hence it can also be used for monitoring and data quality classification for sub-daily solar data. Clearly, an objective measure of performance of the correction is needed in order to further develop and improve the correction method.

Improvements of the method could be formed by combining it with a prior step in which a parametric model is fitted to correct for drift in time and tilt in the leveling of the sensor. Another possibility for improvement is to treat the direct and diffuse radiation separately, since most of the systematic errors, for example tilt and shadowing, will have a different impact on direct and diffuse radiation. This will require, if the direct and diffuse are not measured separately, a splitting into a diffuse and direct component, which could be carried out with a scheme such as suggested by Ruiz-Arias et al. (2010) and Duffie and Beckman (2006, p. 75-77). However applying such a scheme will cause the effect of the systematic errors to propagate into both the direct and the diffuse components. Another approach would be to enhance the correction method by using more than one quantile, in the presented approach only a single quantile close to one is used. Several quantiles can be estimated for both the observed and calculated radiation, which, together with an interpolation scheme, will form a more extensive correction. Clearly this also requires that the calculated global radiation, i.e. here the NWPs, describes the distribution well over the entire range of global radiation. Finally, it is mentioned that for on-line operation the method can be implemented computationally very efficient using time-adaptive quantile regression (Møller et al., 2008).

A.6 Conclusion

A correction method based on statistical non-parametric modeling techniques is presented and applied on hourly observations of global radiation. Several typical errors in the observations can be corrected with the method, including: tilt in the leveling of the sensor, shadowing from objects in the surroundings and clipping of the observations at a maximum level. The method works semi-automatically and no prior information about the sensor and its surroundings, besides the observations and location, is required. Furthermore only a few parameters needs to be tuned. Information embedded in NWPs of global radiation is used for the correction, but this could be replaced with any calculated clear-sky global radiation model. The method is well suited as part of monitoring and operation applications for which local solar radiation observations provide valuable information, e.g. for forecasting of climate dependent renewables such as solar thermal, PV and heating systems. Finally, it is briefly discussed how

the method can be improved or extended in several ways.

Acknowledgement

The observations of global radiation was very kindly provided by Sønderborg Fjernvarme and we also thank the Danish Meteorological Institute for making their numerical weather predictions available. Finally, acknowledgments are given to the The Danish Council for Strategic Research, which have provided the financial support for the project "Solar/electric heating systems in the future energy system" under which the work was carried out.

A.7 Two-dimensional local statistical clear-sky model

The proposed statistical clear-sky model in a general form is described in this section. It is based on a two-dimensional second-order polynomial local quantile regression model. In this form the local weighting is carried out with a two-dimensional multiplicative kernel function in the *day of year* and *time of day* dimensions.

The model

$$\hat{\beta}_t = \underset{\beta\in\mathbb{R}^5}{\operatorname{argmin}} \sum_{i=-\infty}^{\infty}\sum_{j=-\infty}^{\infty} \rho_q\big(G^{\mathrm{tr}}_{t+\frac{24}{t_{\mathrm{sp}}}i+j} - (\beta_{0,t} + \beta_{1,t}i + \beta_{2,t}i^2 + \beta_{3,t}j + \beta_{4,t}j^2)\big)K(i,j) \tag{A.21}$$

where t_{sp} is the sample period of the time series in hours, $\rho_q(u) = u\big(q - I(u<0)\big)$ is the quantile regression objective function (see (Koenker, 2005) and (Koenker, 2011)), $q \in [0,\ldots,1]$ is the sample quantile to be estimated, $i \in \mathbb{N}$ is a counter of days, $j \in \mathbb{N}$ is a counter in steps of the sample period, and $K(i,j)$ is a kernel function. The model could easily be reduced or expanded to polynomials of different orders. The estimated projected clear-sky radiation is then found as the local intercept

$$\widehat{G}^{\mathrm{pr,cs}}_t = \hat{\beta}_{0,t} \tag{A.22}$$

The weights are calculated with the Epanechnikov kernel function

$$K(i,j) = \begin{cases} \frac{9}{16}\left(1 - \left[\frac{|i|}{h_{\mathrm{doy}}}\right]^2\right)\left(1 - \left[\frac{|j|t_{\mathrm{sp}}}{h_{\mathrm{tod}}}\right]^2\right) & \text{for } \frac{|i|}{h_{\mathrm{doy}}} < 1 \wedge \frac{|j|}{h_{\mathrm{tod}}} < 1 \\ 0 & \text{for } \frac{|i|}{h_{\mathrm{doy}}} \geq 1 \vee \frac{|j|}{h_{\mathrm{tod}}} \geq 1 \end{cases} \tag{A.23}$$

where h_{doy} is the bandwidth in the *day of year* dimension (in days) and h_{tod} is the bandwidth in the *time of day* dimension (in hours).

References

P. Bacher, H. Madsen, and H. A. Nielsen. Online short-term solar power forecasting. *Solar Energy*, 83(10):1772–1783, 2009. ISSN 0038092x.

R. Bird and C. Riordan. Simple solar spectral model for direct and diffuse irradiance on horizontal and tilted planes at the earth's surface for cloudless atmospheres. Technical report, Solar Energy Research Inst., Golden, CO (USA), 1984.

R. E. Bird. A simple, solar spectral model for direct-normal and diffuse horizontal irradiance. *Solar Energy*, 32(4):461 – 471, 1984. ISSN 0038-092X. doi: 10.1016/0038-092X(84)90260-3. URL `http://www.sciencedirect.com/science/article/pii/0038092X84902603`.

W. Cleveland and G. Tiao. Decomposition of seasonal time series: A model for the census x-11 program. *Journal of the American statistical Association*, pages 581–587, 1976.

J. A. Davies and D. C. McKay. Estimating solar irradiance and components. *Solar Energy*, 29(1):55 – 64, 1982. ISSN 0038-092X. doi: 10.1016/0038-092X(82)90280-8. URL `http://www.sciencedirect.com/science/article/pii/0038092X82902808`.

DMI. Danish Meteorological Institute, DMI-HIRLAM-S05, 2011. URL `http://www.dmi.dk/eng/index/research_and_development/dmi-hirlam-2009.htm`.

DMI. Danish Meteorological Institute, Borgervejr. `www.borgervejr.dk`, Feb. 2012.

J. A. Duffie and W. A. Beckman. *Solar Engineering of Thermal Processes, 3rd Edition*. Wiley, 2006.

J. Friedman, T. Hastie, and R. Tibshirani. *The elements of statistical learning*, volume 1. Springer Series in Statistics, 2001.

M. Geiger, L. Diabaté, L. Ménard, and L. Wald. A web service for controlling the quality of measurements of global solar irradiation. *Solar Energy*, 73(6): 475 – 480, 2002. ISSN 0038-092X. doi: 10.1016/S0038-092X(02)00121-4.

B. Hansen Sass, N. Woetmann Nielsen, J. U. Jørgensen, B. Amstrup, M. Kmit, and K. S. Mogensen. *The operational DMI-HIRLAM system 2002-version*. DMI, 2002.

P. Ineichen. Comparison of eight clear sky broadband models against 16 independent data banks. *Solar Energy*, 80(4):468 – 478, 2006. ISSN 0038-092X. doi: 10.1016/j.solener.2005.04.018.

Isaac and Moradi. Quality control of global solar radiation using sunshine duration hours. *Energy*, 34(1):1 – 6, 2009. ISSN 0360-5442. doi: 10.1016/j.energy.2008.09.006.

M. Journée and C. Bertrand. Quality control of solar radiation data within the RMIB solar measurements network. *Solar Energy*, 85(1):72 – 86, 2011. ISSN 0038-092X. doi: 10.1016/j.solener.2010.10.021.

R. Koenker. *Quantile Regression*. Cambridge University Press, 2005.

R. Koenker. *quantreg: Quantile Regression*, 2011. URL `http://CRAN.R-project.org/package=quantreg`. R package version 4.76.

R. Mueller, K. Dagestad, P. Ineichen, M. Schroedter-Homscheidt, S. Cros, D. Dumortier, R. Kuhlemann, J. Olseth, G. Piernavieja, C. Reise, L. Wald, and D. Heinemann. Rethinking satellite-based solar irradiance modelling: The solis clear-sky module. *Remote Sensing of Environment*, 91(2):160 – 174, 2004. ISSN 0034-4257. doi: 10.1016/j.rse.2004.02.009.

J. K. Møller, H. A. Nielsen, and H. Madsen. Time-adaptive quantile regression. *Computational Statistics and Data Analysis*, 52(3):1292–1303, 2008. ISSN 01679473.

R Development Core Team. *R: A Language and Environment for Statistical Computing*. R Foundation for Statistical Computing, Vienna, Austria, 2011. URL `http://www.R-project.org/`. ISBN 3-900051-07-0.

C. Rigollier, O. Bauer, and L. Wald. On the clear sky model of the esra - european solar radiation atlas - with respect to the heliosat method. *Solar Energy*, 68(1):33 – 48, 2000. ISSN 0038-092X. doi: 10.1016/S0038-092X(99)00055-9.

J. Ruiz-Arias, H. Alsamamra, J. Tovar-Pescador, and D. Pozo-Vázquez. Proposal of a regressive model for the hourly diffuse solar radiation under all sky conditions. *Energy Conversion and Management*, 51(5):881–893, 2010. ISSN 01968904. doi: 10.1016/j.enconman.2009.11.024.

S. Younes, R. Claywell, and T. Muneer. Quality control of solar radiation data: Present status and proposed new approaches. *Energy*, 30(9):1533 – 1549, 2005. ISSN 0360-5442. doi: 10.1016/j.energy.2004.04.031. Measurement and Modelling of Solar Radiation and Daylight- Challenges for the 21st Century.

Paper B

Online Short-term Solar Power Forecasting

Authors:
Peder Bacher[1], Henrik Madsen[1], and Henrik Aalborg Nielsen[2]

Published in:
Solar Energy, 2009, 83(10), pp. 1772-1783.

[1]DTU Informatics, Richard Pedersens Plads, Building 321, DK-2800 Lyngby, Denmark
[2]ENFOR A/S, Lyngsø Allé 3, DK-2970 Hørsholm, Denmark (URL: www.enfor.eu)

Abstract

This paper describes a new approach to online forecasting of power production from PV systems. The method is suited to online forecasting in many applications and in this paper it is used to predict hourly values of solar power for horizons of up to 36 hours. The data used is fifteen-minute observations of solar power from 21 PV systems located on rooftops in a small village in Denmark. The suggested method is a two-stage method where first a statistical normalization of the solar power is obtained using a clear sky model. The clear sky model is found using statistical smoothing techniques. Then forecasts of the normalized solar power are calculated using adaptive linear time series models. Both autoregressive (AR) and AR with exogenous input (ARX) models are evaluated, where the latter takes numerical weather predictions (NWPs) as input. The results indicate that for forecasts up to two hours ahead the most important input is the available observations of solar power, while for longer horizons NWPs are the most important input. A root mean square error improvement of around 35 % is achieved by the ARX model compared to a proposed reference model.

B.1 Introduction

Efforts to increase the capacity of solar power production in Denmark are concentrating on installing grid connected PV systems on rooftops. The peak power of the installed PV systems is in the range of 1 to 4 kWp, which means that the larger systems will approximately cover the electricity consumption (except heating) of a typical family household in Denmark. The PV systems are connected to the main electricity grid and thus the output from other power production units has to be adjusted in order to balance the total power production. The cost of these adjustments increases as the horizon of the adjustments decreases and thus improved forecasting of solar power will result in an optimized total power production, and in future power production systems where energy storage is implemented, power forecasting is an important factor in optimizing utilization of storage facilities (Koeppel and Korpas, 2006).

The total electricity power production in Denmark is balanced by the energy market Nord Pool, where electricity power is traded on two markets: the main market Elspot and a regulation market Elbas. On Nord Pool the producers release their bids at 12:00 for production each hour the following day, thus the relevant solar power forecasts are updated before 12:00 and consist of hourly values at horizons of 12 to 36 hours. The models in this paper focus on such forecasts, but with the 1-to-11-hour horizons also included.

Interest in forecasting solar power has increased and several recent studies deal with the problem. Many of these consider forecasts of the global irradiance which is essentially the same problem as forecasting solar power. Two approaches are dominant:

- a two-stage approach in which the solar power (or global irradiance) is normalized with a clear sky model in order to form a more stationary time series and such that the classical linear time series methods for forecasting can be used.
- another approach in which neural networks (NNs) with different types of input are used to predict the solar power (or global irradiance) directly.

In a study Chowdhury and Rahman (1987) make sub-hourly forecasts by normalizing with a clear sky model. The solar power is divided into a clear sky component, which is modelled with a physical parametrization of the atmosphere, and a stochastic cloud cover component which is predicted using ARIMA models. Sfetsos and Coonick (2000) use NNs to make one-step predictions of hourly values of global irradiance and compare these with linear time series models that work by predicting clearness indexes. Heinemann et al. (2006) use satellite images for horizons below 6 hours, and in (Lorenz et al., 2007) numerical weather predictions (NWPs) for longer horizons, as input to NNs to predict global irradiance. This is transformed into solar power by a simulation model of the PV system. Hocaoglu et al. (2008) investigate feed-forward NNs for one-step predictions of hourly values of global irradiance and compare these with seasonal AR models applied on solar power directly. Cao and Lin (2008) use NNs combined with wavelets to predict next day hourly values of global irradiance. Different types of meteorological observations are used as input to the models; among others the daily mean global irradiance and daily mean cloud cover of the day to be forecasted.

This paper describes a new two-stage method where first the clear sky model approach is used to normalize the solar power and then adaptive linear time series models are applied for prediction. Such models are linear functions between values with a constant time difference, where the model coefficients are estimated by minimizing a weighted residual sum of squares. The coefficients are updated regularly, and newer values are weighted higher than old values, hence the models adapt over time to changing conditions.

Normalization of the solar power is obtained by using a clear sky model which gives an estimate of the solar power in clear (non-overcast) sky at any given point in time. The clear sky model is based on statistical smoothing techniques and quantile regression, and the observed solar power is the only input. The adaptive linear prediction is obtained using recursive least squares (RLS) with

forgetting. It is found that the adaptivity is necessary, since the characteristics of a PV-system are subject to changes due to snow cover, leaves on trees, dirt on the panel, etc., and this has to be taken into account by an online forecasting system.

The data used in the modelling is described in Section B.2. The clear sky model used for normalizing the solar power is defined in Section B.3 followed by Section B.4 where the adaptive time series models used for prediction are identified. In Section B.5 an approach to modelling of the uncertainty in the forecasts is outlined. The evaluation of the models and a discussion of the results are found in Section B.6 and finally the conclusions of the study are drawn in Section B.7.

Nomenclature

p	Solar power	W
p_{cs}	Clear sky solar power	W
τ	Normalized solar power	-
t	Time index	-
k	Forecast horizon index	-
i, j	Miscellaneous indexes	-
p_t	Observation of average solar power	W
$\hat{p}_{t+k\|t}$	k-step prediction of solar power	W
$\hat{p}_t^{\mathrm{cs}}$	Estimated clear sky solar power	W
$\hat{g}_{i,k}$	i'th update of NWP of global irradiance	W/m^2
$\hat{g}_{k,t}^{00}$	NWP of global irradiance updated at 00:00	W/m^2
$\hat{g}_{k,t}^{12}$	NWP of global irradiance updated at 12:00	W/m^2
$p_{k,t}^{00}$	Observation of solar power corresponding to $\hat{g}_{k,t}^{00}$	W
$p_{k,t}^{12}$	Observation of solar power corresponding to $\hat{g}_{k,t}^{12}$	W
τ_t	Normalized solar power	-
$\hat{\tau}_{t+k\|t}$	k-step prediction of normalized solar power	-
$\hat{\tau}_t^{\mathrm{nwp}}$	NWPs transformed into normalized solar power	-
x_t	Day of year	-
y_t	Time of day	-
e_{t+k}	k-step prediction error	-
q	Quantile level	-
h	Bandwidth of smoothing kernel	-
λ	Forgetting factor	-

B.2 Data

The data used in this study is observations of solar power from 21 PV systems located in a small village in Jutland, Denmark. The data covers the entire year 2006. Forecasts of global irradiance are provided by the Danish Meteorological Institute using the HIRLAM mesoscale NWP model.

The PV array in each the 21 PV systems is composed of "BP 595" PV modules and the inverters are of the type "BP GCI 1200". The installed peak power of

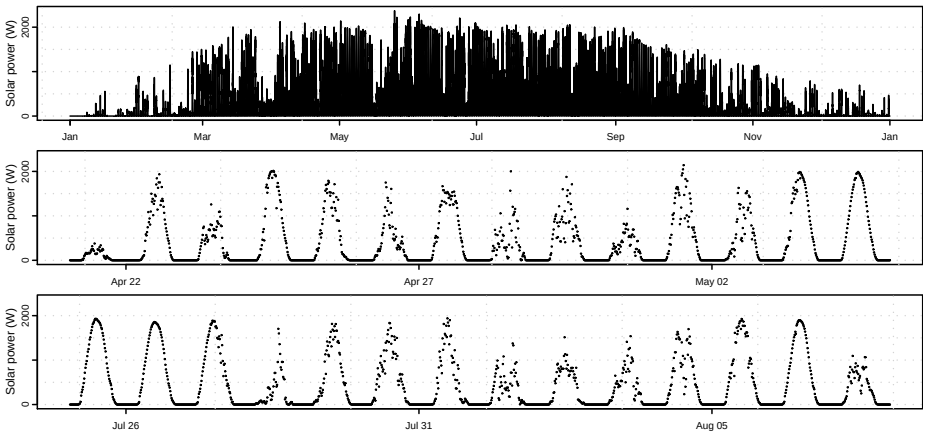

Figure B.1: The observations of average solar power used in the study. Upper plot: The solar power over the entire year 2006. Lower plots: The solar power in two selected periods.

the PV arrays is between 1020 Watt peak and 4080 Watt peak, and the average is 2769 Watt peak. Let $p_{i,t}$ denote the average value of solar power (W) over 15 minutes observed for the i'th PV system at time t. These observations are used to form the time series

$$\{p_t;\ t = 1, \ldots, N\} \tag{B.1}$$

where

$$p_t = \frac{1}{21} \sum_{i=1}^{21} p_{i,t}\ . \tag{B.2}$$

This time series is used throughout the modelling. The time series covers the period from 01 January 2006 to 31 December 2006. The observations are fifteen-minute values, ie. $N = 35040$. Plots of $\{p_t\}$ are shown in Figure B.1 for the entire period and for two shorter periods.

The NWPs of global irradiance are given in forecasts of average values for every third hour, and the forecasts are updated at 00:00 and 12:00 each day. The i'th update of the forecasts is the time series

$$\{\hat{g}_{i,k}, k = 1, \ldots, 12\} \tag{B.3}$$

which then covers the forecast horizons up to 36 hours ahead, and is given in $(\mathrm{W/m^2})$.

Time series are resampled to lower sample frequencies by mean values and when the resampled values are used this is noted in the text. In order to synchronize

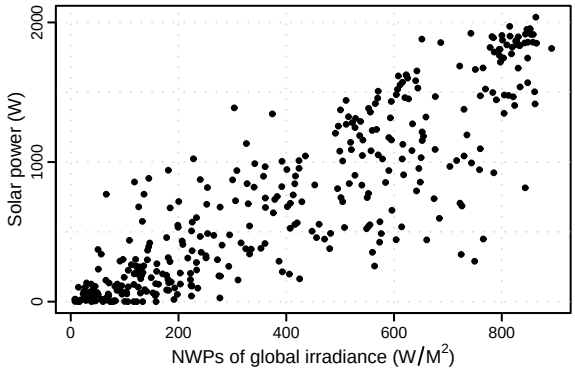

Figure B.2: All three hour interval values of solar power at time of day 10:30 versus the corresponding NWPs of global irradiance with 24 hour horizon. Hence the plot shows observations and predictions of values covering identical time intervals.

data with different sample frequencies, the time point for a given mean value is assigned to the middle of the period that it covers, e.g. the time point of an hourly value of solar power from 10:00 to 11:00 is assigned to 10:30.

As an example of the NWPs of global irradiance Figure B.2 shows values at time of day 10:30 of $\{p_t\}$ resampled to three hour interval values plotted versus the corresponding $\{\hat{g}_{i,k}\}$ values with a 24 hour horizon. Clearly the plot indicates a significant correlation. Hence it is seen that there is information in the NWPs, which can be utilized to forecast the solar power.

B.3 Clear sky model

A clear sky model is usually a model which estimates the global irradiance in clear (non-overcast) sky at any given time. Chowdhury and Rahman (1987) divide the global irradiance into a clear sky component and a cloud cover component by

$$G = G_{\text{cs}} \cdot \tau_c \tag{B.4}$$

where G is the global irradiance (W/m^2), and G_{cs} is the clear sky global irradiance (W/m^2). Finally τ_c is the transmissivity of the clouds which they model as a stochastic process using ARIMA models. The clear sky global irradiance is found by

$$G_{\text{cs}} = I_0 \cdot \tau_a \tag{B.5}$$

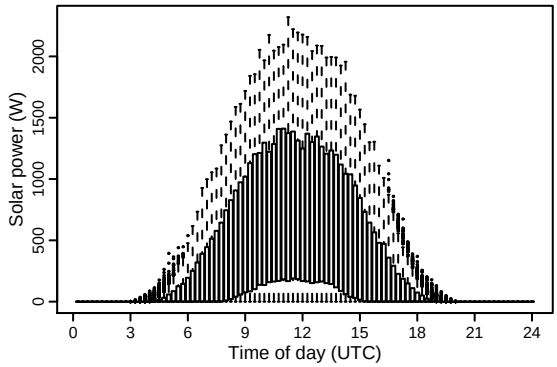

Figure B.3: Modified boxplots of the distribution of the solar power as a function of time of day. The boxplots are calculated with all the fifteen-minutes values of solar power, i.e. covering all of 2006. At each time of the day the box represents the center half of the distribution, from the first to the third quantile. The lower and upper limiting values of the distribution are marked with the ends of the vertical dotted lines, and dots beyond these indicate outliers.

where I_0 is the extraterrestrial irradiance (W/m^2). τ_a is the total sky transmissivity in clear sky which is modelled by atmospheric dependent parametrization.

In this study the same approach is used, but instead of applying the factor on global irradiance it is applied on solar power, i.e.

$$p = p_{\text{cs}} \cdot \tau \tag{B.6}$$

where p is the solar power (W) and p_{cs} is the clear sky solar power (W). The factors τ and τ_c are much alike, but since the clear sky model developed in the present study estimates p_{cs} by statistical smoothing techniques rather than using physics, the method is mainly viewed as a statistical normalization technique and τ is referred to as normalized solar power.

The motivation behind the proposed normalization of the solar power with a clear sky model is that the normalized solar power (the ratio of solar power to clear sky solar power) is more stationary than the solar power, so that classical time series models assuming stationarity (Madsen, 2007) can be used for predicting the normalized values. The non-stationarity is illustrated by Figure B.3 where modified boxplots indicate the distribution of solar power p_t as a function of time of day. Clearly a change in the distributions over the day is seen and this non-stationarity must be considered. Figure B.4 shows the same type of plot for the normalized solar power and it is seen that the distributions over the

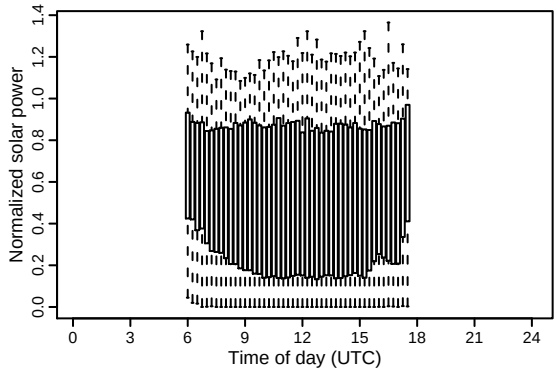

Figure B.4: Modified boxplots of the distribution of the normalized solar power as a function of time of day. The boxplots are calculated with all fifteen-minutes values available, i.e. covering all of 2006.

day are closer to being identical. Thus the effect of the changes over the day is much lower for the normalized solar power than for the solar power.

The clear sky model is defined as

$$p_{\text{cs}} = f_{\max}(x, y) \tag{B.7}$$

where p_{cs} is the clear sky solar power (W), x is the day of year and y is the time of day. The function $f_{\max}(\cdot, \cdot)$ is assumed to be a smooth function and thus $f_{\max}(\cdot, \cdot)$ can be estimated as a local maximum (Koenker, 2005). Figure B.5 shows the solar power plotted as a function of x and y, and the estimated clear sky solar power $\hat{f}_{\max}(\cdot, \cdot)$ is shown as a surface in Figure B.6. Due to outliers the weighted quantile regression method outlined in Section B.8 is used to find the local maximum. The $\hat{f}_{\max}(\cdot, \cdot)$ is then used to form the output of the clear sky model as the time series

$$\{\hat{p}_t^{\text{cs}}, t = 1, \ldots, N\}, \tag{B.8}$$

where $\hat{p}_t^{\text{cs}}$ is the estimated clear sky solar power (W) at time t, and $N = 35040$. The normalized solar power is now defined as

$$\tau_t = \frac{p_t}{\hat{p}_t^{\text{cs}}} \tag{B.9}$$

and this is used to form time series of normalized solar power

$$\{\tau_t, t = 1, \ldots, 35040\}. \tag{B.10}$$

For each (x_t, y_t) corresponding to the solar power observation p_t, weighted quantile regression estimates the q quantile by a Gaussian two dimensional smoothing kernel, defined in Section B.8. The smoothing kernel is used to form the

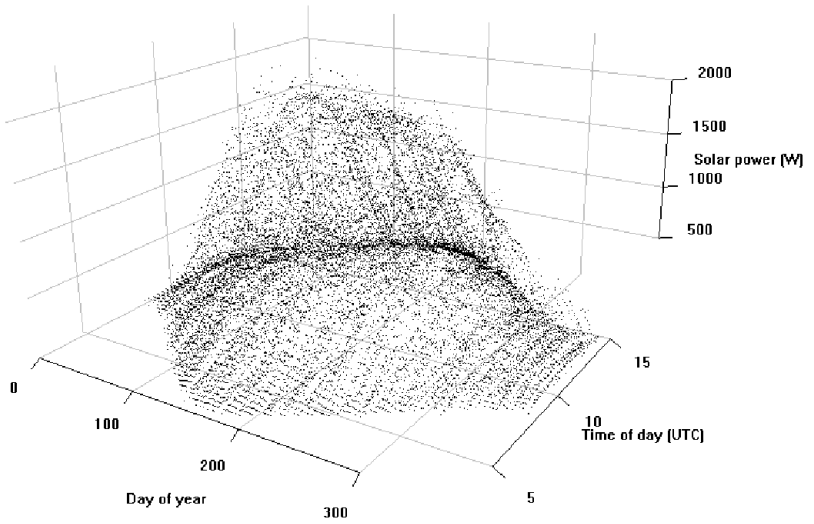

Figure B.5: The solar power as a function of the day of year, and the time of day. Note that only positive values of solar power are plotted.

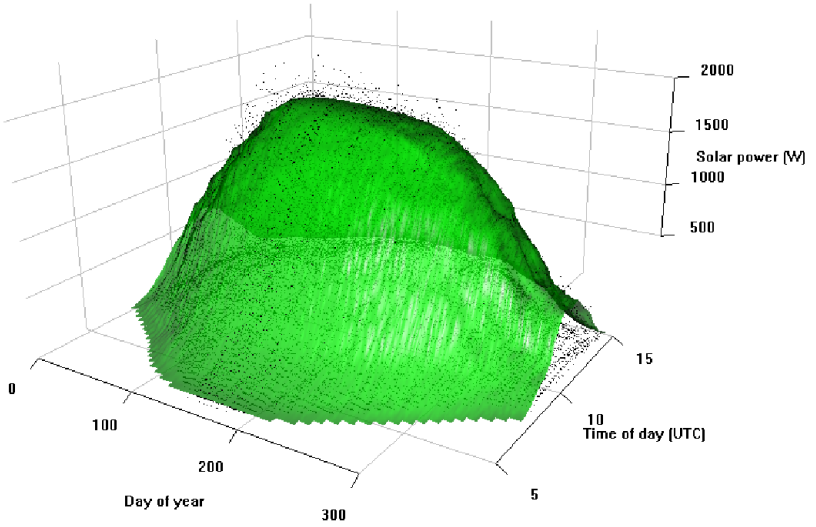

Figure B.6: The estimated clear sky solar power shown as a surface. The solar power is shown as points.

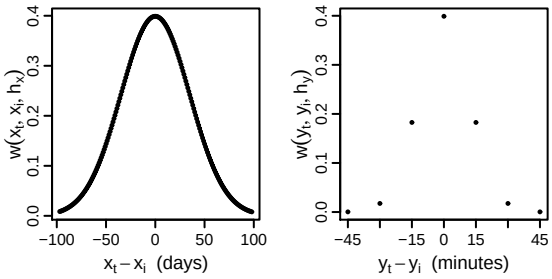

Figure B.7: The one dimensional smoothing kernels used. Left plot is the kernel in the day of year (x) dimension. Right plot is the kernel in the time of day (y) dimension. They are multiplied to form the applied two dimensional smoothing kernel.

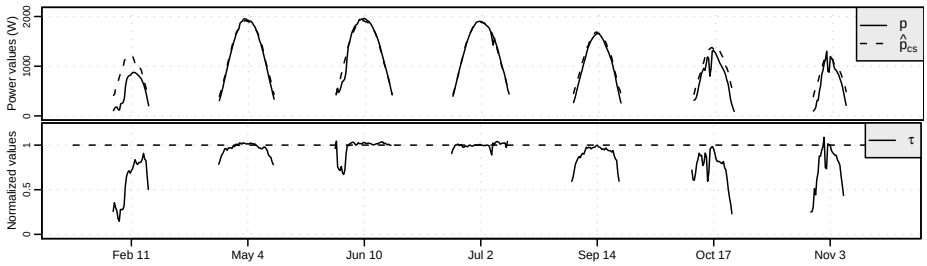

Figure B.8: The result of the normalization for selected clear sky days over the year. The time-axis ticks refer to midday points, i.e. at 12:00. The upper plot shows the solar power p and the estimated clear sky solar power $\hat{p}_{\mathrm{cs}}$. The lower plot shows the normalized solar power τ.

weights applied in the quantile regression. As seen in Figure B.7, which shows the smoothing kernel used, the weights in the day of year dimension $w(x_t, x_i, h_{\mathrm{x}})$, are decreasing as the absolute time differences are increasing. Similarly for the weights in the time of day dimension $w(y_t, y_i, h_{\mathrm{y}})$. The applied weights are finally found by multiplying the weigths from the two dimensions. The choice of the quantile level q to be estimated and the bandwidth in each dimension, h_{x} and h_{y}, is based on a visual inspection of the results. A level of $q = 0.85$ was used since this gives $\tau_t \approx 1$ for days with clear sky all day, as seen in Figure B.8. The plot for days with varying cloud cover in Figure B.9 show that estimates where $\tau_t > 1$ occur. These are ascribed to reflections from clouds and varying level of water vapour in the atmosphere. Future work should elaborate on the inclusion of such effects in the clear sky model.

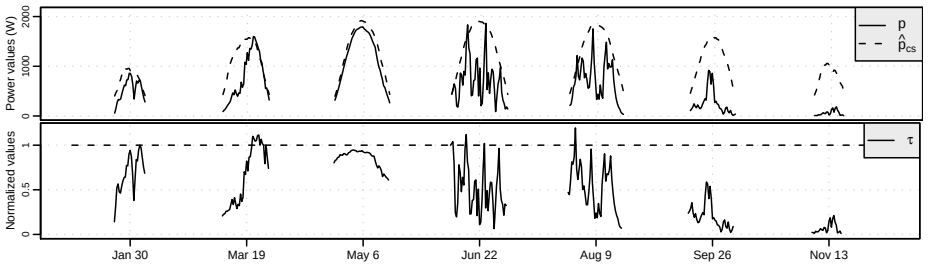

Figure B.9: The result of the normalization for days evenly distributed over the year. The time-axis ticks refer to midday points, i.e. at 12:00. The upper plot shows the solar power p and the estimated clear sky solar power $\hat{p}_{\text{cs}}$. The lower plot shows the normalized solar power τ.

For small $\hat{p}_t^{\text{cs}}$ values the error of τ_t is naturally increasing and at nighttime the error is infinite. Therefore all values of $\hat{p}_t^{\text{cs}}$ where

$$\frac{\hat{p}_t^{\text{cs}}}{\max(\{\hat{p}_t^{\text{cs}}\})} < 0.2 \tag{B.11}$$

are removed from $\{\tau_t\}$. The function $\max(\{\hat{p}_t^{\text{cs}}\})$ gives the maximum value in $\{\hat{p}_t^{\text{cs}}\}$.

The estimates of clear sky solar power are best in the summer period. The bad estimates in winter periods are caused by the sparse number of clear sky observations. It should also be possible to improve the normalization toward dusk and dawn, and thus lower the limit where values in $\{\hat{p}_{\text{cs}}\}$ are removed, either by refining the modelling method or by including more explanatory variables such as e.g. air mass.

Finally it is noted that the deterministic changes of solar power are really caused by the geometric relation between the earth and the sun, which can be represented in the current problem by the sun elevation as x and sun azimuth as y. The clear sky solar power was also modelled in the space spanned by these two variables, by applying the same statistical methods as for the space spanned by day of year and time of day. The result was not satisfactory, i.e. the estimated clear sky solar power was less accurate, probably because neighboring values in this space are not necessarily close in time and thus changes in the surroundings to the PV system blurred the estimates.

B.4 Prediction models

Adaptive linear time series models (Madsen, 2007) are applied to predict future values of the normalized solar power τ_t. The inputs are: lagged observations of τ_t and transformed NWPs $\hat{\tau}_t^{\text{nwp}}$. Three types of models are identified:

- a model which has only lagged observations of τ_t as input. This is an autoregressive (AR) model and it is referred to as the AR model.
- a model with only $\hat{\tau}_t^{\text{nwp}}$ as input. This is referred to as the LM_{nwp} model.
- a model with both types of input. This is an autoregressive with exogenous input (ARX) model and it is referred to as the ARX model.

The best model of each type is identified by using the autocorrelation function (ACF).

B.4.1 Transformation of NWPs into predictions of normalized solar power

In order to use the NWPs of global irradiation $\hat{g}_{i,k}$ as input to the prediction models, these are transformed into $\hat{\tau}_t^{\text{nwp}}$ which are meteorological based hourly predictions of τ_t. This is done by first transforming $\hat{g}_{i,k}$ into solar power predictions and then transforming these by the clear sky model. The time series $\{\hat{g}_{i,k}\}$, defined in (B.3), holds the i'th NWP forecast of three hour interval values, and was updated at

$$\text{time}_i = t_0 + (i-1) \cdot 12\text{h} \tag{B.12}$$

where t_0 = 2006-01-01 00:00. Thus the time series with sample period of one day

$$\{\hat{g}_{k,t}^{00},\ t = 1, \ldots, 364\} = \{\hat{g}_{i,k},\ i = 1, 3, \ldots, 727\}, \tag{B.13}$$

consist of all the NWPs updated at time of day 00:00 at horizon k, i.e. the superscript "00" forms part of the name of the variable. Similarly the time series

$$\{\hat{g}_{k,t}^{12},\ t = 1, \ldots, 364\} = \{\hat{g}_{i,k},\ i = 2, 4, \ldots, 728\}, \tag{B.14}$$

consist of all the NWPs updated at time of day 12:00. The corresponding time series of solar power covering the identical time intervals are respectively

$$\{p_{k,t}^{00},\ t = 1, \ldots, 364\} = \{p_t,\ t = k, (1 \cdot 8 + k), \ldots, (363 \cdot 8 + k)\} \tag{B.15}$$

and

$$\{p_{k,t}^{12},\ t = 1, \ldots, 364\} = \{p_t,\ t = k+4, (1 \cdot 8 + k + 4), \ldots, (363 \cdot 8 + k + 4)\}, \tag{B.16}$$

where $\{p_t\}$ has been resampled to three hour interval values. The NWPs are modelled into solar power predictions by the adaptive linear model

$$\hat{p}_{k,t}^{00} = \beta_t \ + \ \alpha_t \ \hat{g}_{k,t}^{00} \ + \ e_t \ , \tag{B.17}$$

note that the hat above the variable indicates that these values are predictions (estimates) of the solar power. A similar model is made for the NWP updates at time of day 12:00 giving $\hat{p}_{k,t}^{12}$. The interpretion of the coefficients β_t and α_t is not further elaborated here, but it is noted that they are time dependent in order to account for the effects of changing conditions over time, e.g. the changing geometric relation between the earth and the sun, dirt on the solar panel. This adaptivity is obtained by fitting the model with k-step recursive least squares (RLS) with forgetting, which is described in Section B.9. In order to use the RLS algorithm, $p_{k,t}^{00}$ has to be lagged depending on k. Each RLS estimation is optimized by choosing the value of the forgetting factor λ from $0.9, 0.905, \ldots, 1$ that minimizes the root mean square error (*RMSE*).

The last steps in the transformation of the NWPs is to normalize $\hat{p}_{k,t}^{00}$ and $\hat{p}_{k,t}^{12}$ with the clear sky model, and resample up to hourly values by linear interpolation. Finally the time series

$$\{\hat{\tau}_t^{\text{nwp}}, t = 1, \ldots, 8760\} \tag{B.18}$$

of the NWPs of global irradiance transformed into predictions of normalized solar power is formed, and this is used as input to the *ARX* prediction models as described in the following. More details can be found in (Bacher, 2008).

B.4.2 *AR* model identification

To investigate the time dependency in $\{\tau_t\}$, i.e. dependency between values with a constant time difference, the ACF is calculated and plotted in Figure B.10. Clearly an AR(1) component is indicated by the exponential decaying pattern of the first few lags and a seasonal diurnal AR component by the exponential decaying peaks at lag $= 24, 48, \ldots$. By considering only first-order terms this leads to the 1-step AR model

$$\tau_{t+1} = m + a_1 \tau_t + a_2 \tau_{t-23} + e_{t+1} \ . \tag{B.19}$$

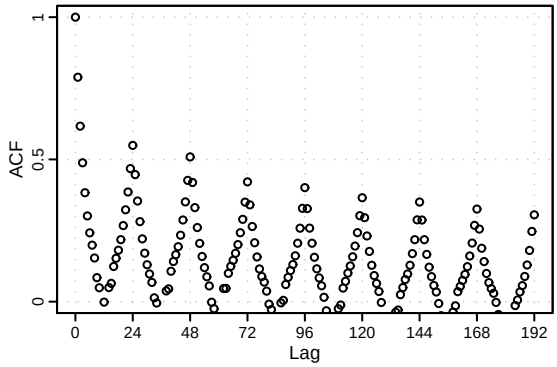

Figure B.10: ACF of the time series of normalized solar power $\{\tau_t\}$.

And a reasonable 2-step AR model is

$$\tau_{t+2} = m + a_1\tau_t + a_2\tau_{t-22} + e_{t+2} \ . \tag{B.20}$$

Note that here the 1-step lag cannot be used, since this is τ_{t+1} i.e. a future value, and thus the latest observed value τ_t is included instead. Formulated as a k-step AR model

$$\tau_{t+k} = m + a_1\tau_t + a_2\tau_{t-s(k)} + e_{t+k} \tag{B.21}$$

$$s(k) = 24 + k \bmod 24 \tag{B.22}$$

where the function $s(k)$ ensures that the latest observation of the diurnal component is included. This is needed, since for $k = 25$ the diurnal 24 hour AR component cannot be used and instead the 48 hour AR component is used. This model is referred to as the AR model.

Figure B.11 shows the ACF of $\{e_{t+k}\}$, which is the time series of the errors in the model for horizon k, for six selected horizons after fitting the AR model with RLS, which is described in Section B.9. The vertical black lines indicate which lags are included in the model. For $k = 1$ the correlation of the AR(1) component is removed very well and the diurnal AR component has also been decreased considerably. There is high correlation left at lag $= 24, 48, \ldots$. This can most likely be ascribed to systematic errors caused by non-stationarity effects left in $\{\tau_t\}$, and it indicates that the clear sky model normalization can be further optimized. For $k = 2$ and 3 the grayed points show the lags that cannot be included in the model and the high correlation of these lags indicate that information is not exploited. The AR model was extended with higher order AR and diurnal AR terms without any further improvement in performance, see (Bacher, 2008).

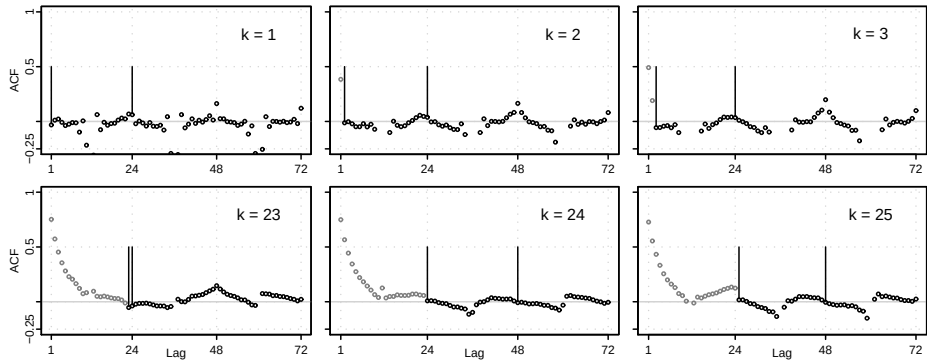

Figure B.11: ACF of the time series of errors $\{e_{t+k}\}$ for selected horizons k of the AR model. The vertical bars indicate the lags included in each of the models, and the grayed points show the lags which cannot be included in the model.

B.4.3 LM_{nwp} model identification

The model using only NWPs as input

$$\tau_{t+k} = m + b_1 \hat{\tau}^{\text{nwp}}_{t+k|t} + e_{t+k} \tag{B.23}$$

is referred to as LM_{nwp} . It is fitted using RLS and the ACF of $\{e_{t+k}\}$ is shown in Figure B.12 for two horizons. For $k = 1$ clearly correlation is left from an AR(1) component, but as seen for both horizons the actual NWP input removes diurnal correlation very well.

B.4.4 *ARX* model identification

The model using both lagged observations of τ_t and NWPs as input is an ARX model. The LM_{nwp} revealed an exponential decaying ACF for short horizons and thus an AR(1) term is clearly needed, whereas adding the diurnal AR component has only a small effect. The results show that in fact the diurnal AR component can be left out, but it is retained since this clarifies that no improvement is achieved by adding it, this is showed later. The model

$$\tau_{t+k} = m + a_1 \tau_t + a_2 \tau_{t-s(k)} + b_1 \hat{\tau}^{\text{nwp}}_{t+k|t} + e_{t+k}, \tag{B.24}$$

is referred to as the *ARX* model. The model is fitted using RLS and the ACF of $\{e_{t+k}\}$ is plotted in Figure B.13. It is seen that the AR(1) component removes

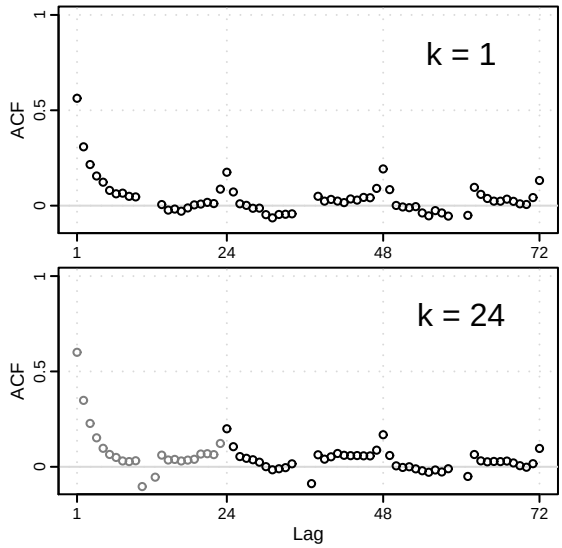

Figure B.12: ACF of the time series of errors $\{e_{t+k}\}$ at horizon $k = 1$ and $k = 24$ of the LM_{nwp} model. The grayed points show the lags which cannot be included in the model.

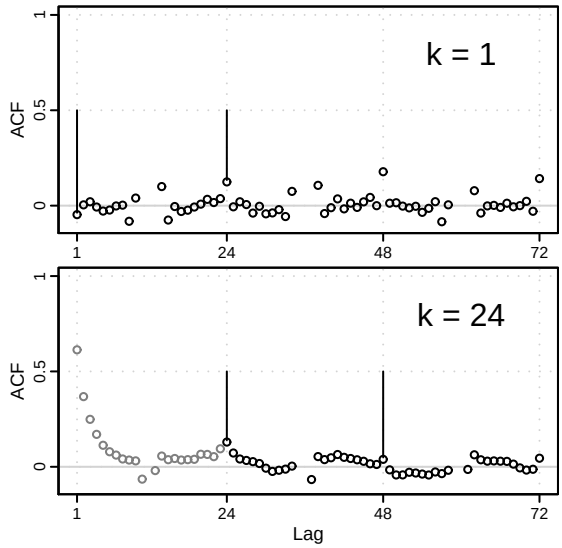

Figure B.13: ACF of the time series of errors $\{e_{t+k}\}$ at horizons $k = 1$ and $k = 24$ of the ARX model. The vertical bars indicate the lags included in each of the models, and the grayed points show the lags which cannot be included in the model.

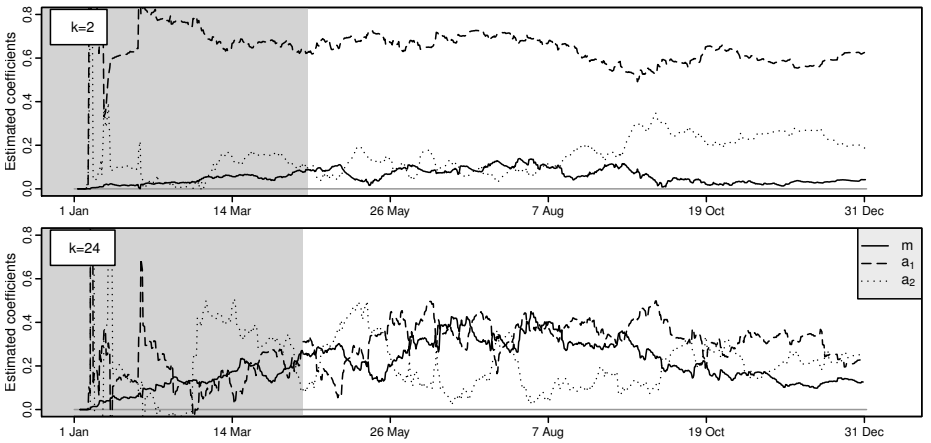

Figure B.14: The online estimates of the coefficients in the AR model as a function of time. Two selected horizons are shown. The grayed period in the beginning marks the burn-in period.

the correlation for the short horizons very well. The *ARX* was extended with higher order AR and diurnal AR terms without any further improvements in performance.

B.4.5 Adaptive coefficient estimates

The plots in Figure B.14 show the online coefficient estimates for the *AR* model, where a value of $\lambda = 0.995$ is used since this is the value that minimizes the $RMSE_k$ best for all horizons in the current setting. Clearly the values of the coefficient estimates change over time and this indicates that the adaptivity is needed to make an optimal model for online forecasting.

B.5 Uncertainty modelling

Extending the solar power forecasts, from predicting a single value (a point forecast) to predicting a distribution increases their usefulness. This can be achieved by modelling the uncertainties of the solar power forecasts and a simple approach is outlined here. The classical way of assuming normal distribution of the errors will in this case not be appropriate since the distribution of the errors has finite limits. Instead, quantile regression is used, inspired by Møller et al.

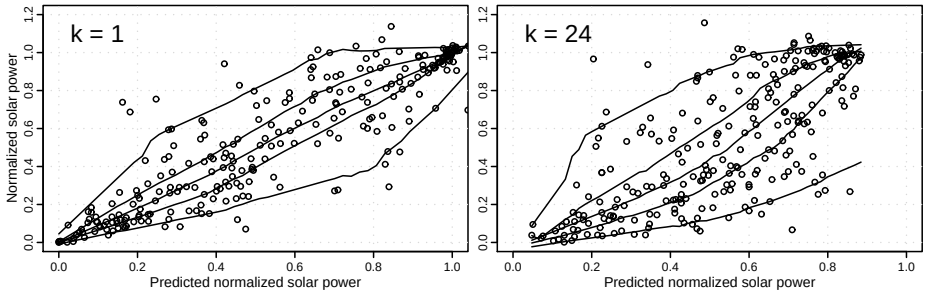

Figure B.15: Normalized solar power versus the predicted normalized solar power at horizons $k = 1$ and $k = 24$. The predictions are made with the ARX model. The lines are estimates of the $0.05, 0.25, 0.50, 0.75$ and 0.95 quantiles of $f_\tau(\hat{\tau})$.

(2008) where it is applied to wind power forecasts. Plots of $\{\tau_t\}$ versus $\{\hat{\tau}_t\}$ for a given horizon reveal that the uncertainties depend on the level of $\hat{\tau}$. Figure B.15 shows such plots for horizons $k = 1$ and $k = 24$. The lines in the plot are estimates of the $0.05, 0.25, 0.50, 0.75$ and 0.95 quantiles of the probability distribution function of τ as a function of $\hat{\tau}$. The weighted quantile regression with a one dimensional kernel smoother, described in Section B.8, is used.

Figure B.15 illustrates that the uncertainties are lower for $\hat{\tau}$ close to 0 and 1, than for the mid-range values around 0.5. Thus forecasts of values toward overcast or clear sky have less uncertainty than forecasts of a partly overcast sky, which agrees with results by Lorenz et al. (2007). Further work should extend the uncertainty model to include NWPs as input.

B.6 Evaluation

The methods used for evaluating the prediction models are inspired by Madsen et al. (2005) where a framework for evaluation of wind power forecasting is suggested. The RLS fitting of the prediction models does not use any degrees of freedom and the dataset is therefore not divided into a training set and a test set. It is, however, noted that the clear sky model and the optimization of λ does use the entire dataset, and thus the results can be a little optimistic. The values in the burn-in period are not used in calculating the error measures. In Figure B.14 the burn-in periods for the AR model are shown.

B.6.1 Error measures

The k-step prediction error is

$$e_{t+k} = p_{t+k} - \hat{p}_{t+k|t} \tag{B.25}$$

The Root Mean Square Error for the k'th horizon is

$$RMSE_k = \left(\frac{1}{N} \sum_{t=1}^{N} e_{t+k}^2 \right)^{\frac{1}{2}}. \tag{B.26}$$

The $RMSE_k$ is used as the main evaluation criterion (EC) for the performance of the models. The Normalized Root Mean Square Error is found by

$$NRMSE_k = \frac{RMSE_k}{p_{\text{norm}}} \tag{B.27}$$

where either

$$p_{\text{norm}} = \bar{p} = \frac{1}{N} \sum_{t=1}^{N} p_t. \tag{B.28}$$

or p_{norm} is the average peak power of the 21 PV systems.

The mean value of the $RMSE_k$ for a range of horizons

$$\overline{RMSE}_{k_\text{s},k_\text{e}} = \frac{1}{k_\text{e} - k_\text{s} + 1} \sum_{k=k_\text{s}}^{k_\text{e}} RMSE_k \tag{B.29}$$

is used as a summary error measure. When comparing the performance of two models the improvement

$$I_{\text{EC}} = 100 \cdot \frac{EC_{\text{ref}} - EC}{EC_{\text{ref}}} (\%) \tag{B.30}$$

is used, where EC is the considered evaluation criterion.

B.6.2 Reference model

To compare the performance of prediction models, and especially when making comparisons between different studies, a common reference model is essential. A reference model for solar power is here proposed as the best performing naive predictor for the given horizon. Three naive predictors of solar power are found to be relevant. Persistence

$$p_{t+k} = p_t + e_{t+k}, \tag{B.31}$$

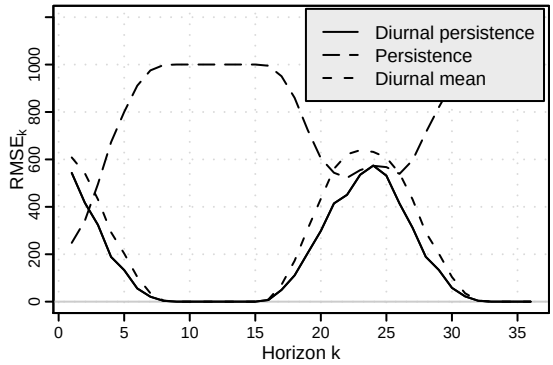

Figure B.16: $RMSE_k$ for the three naive predictors used in the Reference model.

diurnal persistence

$$p_{t+k} = p_{t-s(k)} + e_{t+k} \tag{B.32}$$

$$s(k) = f_{\text{spd}} + k \bmod f_{\text{spd}} \tag{B.33}$$

where $s(k)$ ensures that the latest diurnal observation is used and f_{spd} is the sample frequency in number of samples per day, and diurnal mean

$$p_{t+k} = \frac{1}{n}\sum_{i=1}^{n} p_{t-s(k,i)} \; + e_{t+k} \tag{B.34}$$

$$s(k,i) = i \cdot f_{\text{spd}} + k \bmod f_{\text{spd}} \tag{B.35}$$

which is the mean of solar power of the last n observations at the time of day of $t+k$. The value of n is chosen such that all past samples are included.

Figure B.16 shows the $RMSE_k$ for each of the three naive predictors. It is seen that for $k \leq 2$ the persistence predictor is the best while the best for $k > 2$ is the diurnal persistence predictor. This model is referred to as the *Reference* model.

B.6.3 Results

Examples of solar power forecasts made with the *ARX* model are shown in Figure B.17 for short horizons and in Figure B.18 for next day horizons. It is found that the forecasted solar power generally follows the main level of the solar power, but the fluctuations caused by sudden changes in cloud cover are not fully described by the model.

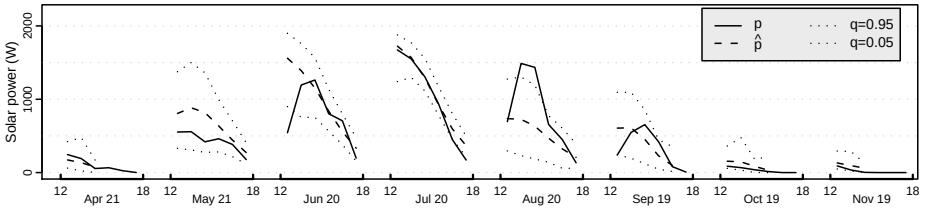

Figure B.17: Forecasts of solar power at short horizons $k = 1, \ldots, 6$ made with the ARX model.

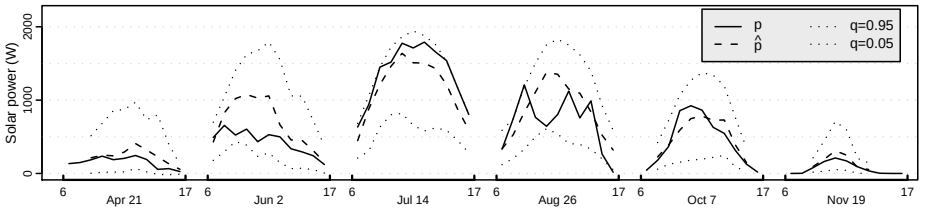

Figure B.18: Forecasts of solar power at next day horizons $k = 19, \ldots, 29$ made with the ARX model.

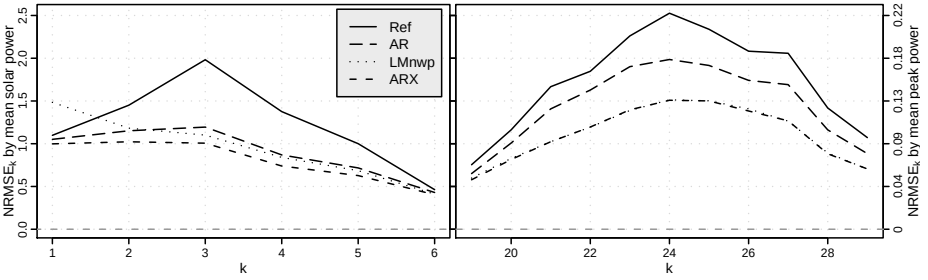

Figure B.19: The $NRMSE_k$ for each of the three models and the Reference model. The left plot show the short horizons and the right the next day horizons. The left scale show $RMSE_k$ normalized by the mean solar power $\bar{p} = 248$ W/h and the right scale show $RMSE_k$ normalized by 2769W, which is the mean peak power of the 21 PV systems.

Models	$I_{\overline{RMSE}_{1,6}}$	$I_{\overline{RMSE}_{19,29}}$
AR over *Reference*	27%	17%
LM_{nwp} over *Reference*	25%	36%
ARX over *Reference*	35%	36%
LM_{nwp} over AR	-2%	23%
ARX over AR	12%	23%
ARX over LM_{nwp}	13%	1%

Table B.1: Summary error measures of improvements compared to the *Reference* model for short horizons $k = 1, \ldots, 6$ and next day horizons $k = 19, \ldots, 29$.

The $NRMSE_k$ is plotted for each model in Figure B.19. Clearly the performance is increasing from the *Reference* model to the AR model and further to the ARX model. The differences from using either the solar power or the NWPs, or both, as input become apparent from these results.

At $k = 1$ the AR model that only uses solar power as input is better than the LM_{nwp} which only uses NWPs as input, but at $k = 2, \ldots, 6$ the LM_{nwp} is better, though only slightly. This indicates that for making forecasts of horizons shorter than 2 hours, solar power is the most important input, whereas for 2 to 6 hours horizons, forecasting systems using either solar power or NWPs can perform almost equally. The ARX model using both types of input does have an increased performance at all $k = 1, \ldots, 6$ and thus combining the two types of input is found to be the superior approach.

For $k = 19, \ldots, 29$, which are the next day horizons, very clearly the LM_{nwp} model and the ARX model perform better than the AR model. Since the LM_{nwp} model and the ARX model perform almost equally, it is seen that no improvement is achieved from adding the solar power as input, and thus using only the NWPs as input is found to be adequate for next day horizons.

A summary of the improvement in performance is calculated using (B.29) and (B.30). The improvements compared to the *Reference* model are calculated for the four models by $I_{\overline{RMSE}_{1,6}}$ for short horizons and $I_{\overline{RMSE}_{19,29}}$ for next day horizons. The results are shown in Table B.1. These results naturally show the same as stated above, though the difference at $k = 1$ from AR to LM_{nwp} cannot be seen. These results show that a RMSE improvement of around 35 % over the *Reference* model can be achieved by using the ARX model.

B.7 Conclusions

Inspired by previous studies, the present method for solar power forecasting has been developed from scratch. A new approach to clear sky modelling with statistical smoothing techniques has been proposed, and an adaptive prediction model based on RLS makes a solid framework allowing for further refinements and model extensions e.g. by including NWPs of temperature as input. The adaptivity of the method makes it suited to online forecasting and ensures comprehension of changing conditions of the PV system and its surroundings. Furthermore the RLS algorithm is not computer intensive, which makes updating of forecasts fast. The clear sky model used to normalize the solar power delivers a useful result, but can be improved, especially for the estimates toward dawn and dusk, by using polynomial-based kernel regression. A procedure based on quantile regression is suggested for calculating the varying intervals of the uncertainty of the solar power predictions and the results agree with other studies. The best performing prediction model is an ARX model where both solar power observations and NWPs are used as input. The results indicate that for horizons below 2 hours solar power is the most important input, but for next day horizons no considerable improvement is achieved from using available values of solar power, so it is adequate just to use NWPs as input. Thus, depending on the application of the forecasting system using only either of the inputs can be considered, and a lower limit of the latency, at which solar power observations are needed for the forecasting system, can be different. Finally it is noted that a comparison to other online solar power forecasting methods, e.g. (Lorenz et al., 2007) and (Hocaoglu et al., 2008), has not been carried out, but that such a study would be informative in order to describe strengths and accuracy of the different proposed methods.

B.8 Weighted quantile regression

The solar power time series $\{p_t, t = 1, \ldots, N\}$ is the realization of a stochastic process $\{P_t, t = 1, \ldots, N\}$. The estimated clear sky solar power at time t is $\hat{p}_t^{\text{cs}}$ and it is found as the q quantile of f_{P_t}, the probability distribution function of P_t. The problem is reduced to estimating $\hat{p}_t^{\text{cs}}$ as a local constant for each (x_t, y_t), where x is the day of year and y the time of day. This is done by weighted quantile regression in which the loss function is

$$\rho(q, \epsilon_i) = \begin{cases} q\epsilon_i & , \quad \epsilon_i \geq 0 \\ (1-q)\epsilon_i & , \quad \epsilon_i < 0 \end{cases} \tag{B.36}$$

where $\epsilon_i = p_i - \hat{p}_t^{\text{cs}}$. The fitting of $\hat{p}_t^{\text{cs}}$ is then done by

$$\hat{p}_t^{\text{cs}} = \arg\min_{\hat{p}_t^{\text{cs}}} \sum_{i=1}^{N} k(x_t, y_t, x_i, y_i) \cdot \rho(q, \epsilon_i). \tag{B.37}$$

where

$$k(x_t, y_t, x_i, y_i) = \frac{w(x_t, x_i, h_{\text{x}}) \cdot w(y_t, y_i, h_{\text{y}})}{\sum_{i=1}^{N} w(x_t, x_i, h_{\text{x}}) \cdot w(y_t, y_i, h_{\text{y}})} \tag{B.38}$$

is the two dimensional multiplicative kernel function which weights the observations locally to (x_t, y_t), (Hastie and Tibshirani, 1993). Details of the minimization are found in (Koenker, 2005). In each dimension a Gaussian kernel is used

$$w(x_t, x_i, h_x) = f_{\text{std}}\left(\frac{|x_t - x_i|}{h_x}\right) \tag{B.39}$$

where f_{std} is the standard normal probability density function. A similar kernel function is used in the y dimension, and the final two dimensional kernel is found by multiplying the two kernels as shown in (B.37).

B.9 Recursive least squares

Fitting of the prediction models is done using k-step recursive least squares (RLS) with forgetting, which is described in the following using the ARX model

$$\tau_{t+k} = m + a_1\tau_t + a_2\tau_{t-s(k)} + b_1\hat{\tau}_{t+k|t}^{\text{nwp}} + e_{t+k}, \tag{B.40}$$

as an example. The regressor at time t is

$$\mathbf{X}_t^T = (1,\ \tau_t,\ \tau_{t-s(k)},\ \hat{\tau}_{t+k|t}^{\text{nwp}}), \tag{B.41}$$

the parameter vector is

$$\theta^T = (m,\ a_1,\ a_2,\ b_1), \tag{B.42}$$

and the dependent variable

$$Y_t = \tau_t. \tag{B.43}$$

Hence the model can be written as

$$Y_t = \mathbf{X}_t^T\theta + e_t. \tag{B.44}$$

The estimates of the parameters at t are found such that

$$\hat{\theta}_t = \arg\min_{\theta} S_t(\theta), \tag{B.45}$$

where the loss function is

$$S_t(\theta) = \sum_{s=1}^{t} \lambda^{t-s}(Y_s - \mathbf{X}_s^T\theta)^2. \tag{B.46}$$

This provides weighted least squares with exponential forgetting. The solution at time t leads to

$$\hat{\theta}_t = \mathbf{R}_t^{-1}\mathbf{h}_t, \tag{B.47}$$

see (Madsen, 2007), where

$$\mathbf{R}_t = \textstyle\sum_{s=1}^{t} \lambda^{t-s}\mathbf{X}_s\mathbf{X}_s^T, \qquad \mathbf{h}_t = \textstyle\sum_{s=1}^{t} \lambda^{t-s}\mathbf{X}_s Y_s. \tag{B.48}$$

The k-step RLS-algorithm with exponential forgetting is then

$$\mathbf{R}_t = \lambda\mathbf{R}_{t-1} + \mathbf{X}_{t-k}\mathbf{X}_{t-k}^T \tag{B.49}$$

$$\hat{\theta}_t = \hat{\theta}_{t-1} + \mathbf{R}_t^{-1}\mathbf{X}_{t-k}(Y_t - \mathbf{X}_{t-k}^T\hat{\theta}_{t-1}) \tag{B.50}$$

and the k-step prediction at t is

$$\hat{Y}_{t+k} = \mathbf{X}_t^T\hat{\theta}_t. \tag{B.51}$$

References

P. Bacher. Short-term solar power forecasting. Master's thesis, Technical University of Denmark, 2008. IMM-M.Sc.-2008-13.

J. Cao and X. Lin. Study of hourly and daily solar irradiation forecast using diagonal recurrent wavelet neural networks. *Energy Conversion and Management*, 49(6):1396–1406, 2008. ISSN 01968904.

B. Chowdhury and S. Rahman. Forecasting sub-hourly solar irradiance for prediction of photovoltaic output. In *IEEE Photovoltaic Specialists Conference, 19th, New Orleans, LA, May 4-8, 1987, Proceedings (A88-34226 13-44). New York, Institute of Electrical and Electronics Engineers, Inc., 1987, p. 171-176.*, pages 171–176, 1987.

T. Hastie and R. Tibshirani. Varying-coefficient models. *Journal of the Royal Statistical Society. Series B (Methodological)*, 55(4):757–796, 1993. ISSN 00359246.

D. Heinemann, E. Lorenz, and M. Girodo. Forecasting of solar radiation. In E. Dunlop, L. Wald, and M. Suri, editors, *Solar Resource Management for Electricity Generation from Local Level to Global Scale*, pages 83–94, New York, 2006. Nova Science Publishers.

F. O. Hocaoglu, Ö. N. Gerek, and M. Kurban. Hourly solar radiation forecasting using optimal coefficient 2-d linear filters and feed-forward neural networks. *Solar Energy*, 82(8):714–726, 2008. ISSN 0038092x.

R. Koenker. *Quantile Regression*. Cambridge University Press, 2005.

G. Koeppel and M. Korpas. Using storage devices for compensating uncertainties caused by non-dispatchable generators. *2006 International Conference on Probabilistic Methods Applied to Power Systems*, pages 1–8, 2006.

E. Lorenz, D. Heinemann, H. Wickramarathne, H. Beyer, and S. Bofinger. Forecast of ensemble power production by grid-connected pv systems. In *Proc. 20th European PV Conference, September 3-7, 2007, Milano*, 2007.

H. Madsen. *Time Series Analysis*. Chapman & Hall, 2007.

H. Madsen, P. Pinson, G. Kariniotakis, H. A. Nielsen, and T. S. Nielsen. Standardizing the performance evaluation of shortterm wind power prediction models. *Wind Engineering*, 29(6):475, 2005. ISSN 0309524x.

J. K. Møller, H. A. Nielsen, and H. Madsen. Time-adaptive quantile regression. *Computational Statistics and Data Analysis*, 52(3):1292–1303, 2008. ISSN 01679473.

A. Sfetsos and A. Coonick. Univariate and multivariate forecasting of hourly solar radiation with artificial intelligence techniques. *Solar Energy*, 68(2): 169–178, 2000. ISSN 0038092x.

Paper C

Online Short-term Solar Power Forecasting

Authors:
Peder Bacher[1], Henrik Madsen[1], and Henrik Aalborg Nielsen[2]

In proceedings:
1st International Workshop on the Integration of Solar Power into Power Systems. Aarhus, 2011.

[1]DTU Informatics, Richard Pedersens Plads, Building 321, DK-2800 Lyngby, Denmark
[2]ENFOR A/S, Lyngsø Allé 3, DK-2970 Hørsholm, Denmark (URL: www.enfor.eu)

Abstract

This paper describes two methods for online forecasting of power production from PV systems. The methods are suited for online forecasting in many applications and in this paper they are used to predict hourly values of solar power for horizons up to 32 hours. The data used is hourly observations of solar power from a single PV system located on a rooftop in a small village in Denmark. One approach is a two-stage method in which a statistical normalization of the solar power is obtained using a clear sky model. The clear sky model is found using statistical smoothing techniques, which ensure that local phenomena are directly modelled from data, as opposed to applying a deterministically derived clear sky model. In the second stage forecasts of the normalized solar power are calculated using adaptive linear time series models. A second approach is to apply conditional parametric models with both autoregressive input and NWPs exogenous input. The results indicate that for forecasts up to two hours ahead the most important input is the available observations of solar power, while for longer horizons NWPs are the most important input. A root mean square error improvement over a persistence model around 40 % is achieved for 1 and 2 hour horizons and around 35 % for longer horizons.

C.1 Introduction

The increasing installed solar power capacity rises the challenges of grid integration. The need for efficient forecasting methods is evident and the research activities within the topic is increasing, see for example (Sfetsos and Coonick, 2000), (Hocaoglu et al., 2008), (Lorenz et al., 2009), and (Ji and Chee, 2011). In this paper methods for online forecasting are presented. The methods are suited for forecasting of solar power for different systems and here they are applied to forecast the power production of a single 4 kW-peak PV-system installed on a rooftop of a single family house. Due to the fluctuating nature of solar power such forecasts are essential for optimal grid integration and will be essential for solar power smart grid technology. The applications include energy trading for large solar power producers, and diurnal peak-shaving and cost optimization for smaller systems with storage capacity in battery packs (e.g. provided in an electrical car). Two approaches are considered. One is based on a two-stages approach: first the systematic dependency of the position of the sun relative to the PV panel are removed with a clear sky model, and secondly the resulting process is forecasted with time-adaptive linear time series methods. The clear sky model is calculated with non-linear statistical techniques, which will also model the local conditions, such as e.g. shadows from elements in the surrounding

environment and snow cover. In the second approach numerical weather predictions (NWPs) are used as input to conditional parametric non-linear models (Nielsen et al., 2002) to forecast the solar power. Finally, the two approaches are combined by normalizing the forecast with the clear sky model, and finally using this as input to the linear forecasting model, such that an ARX model is formed.

The paper is organized as follows. First the data and how it is preprocessed is described. The next section contains an outline of the clear sky model, followed by a section where all the forecasting models are described. Then an evaluation is given and the results are presented, followed by a discussion of the results and ideas for further work. Finally, the paper ends with a conclusion.

C.2 Data

The data used in this study consist of hourly mean values of solar power from a 4 kW-peak PV-system and NWPs of global irradiance. The NWPs are provided by the Danish Meteorological Institute using the HIRLAM mesoscale NWP model. The data covers the entire year 2006.

The time series of hourly observed solar power is

$$\{P_t;\ t = 1, \ldots, N\} \tag{C.1}$$

where $N = 8760$. The NWPs have a calculation time of 4 hours, which is taken into consideration, such that e.g. the forecast from 2009-01-01 00:00 are only available from 2009-01-01 04:00. The NWPs are provided in a time resolution of 3 hours. They are pre-processed into time series of hourly values, such that the most recent available forecast k hours ahead is selected each hour. The time series for a given k of the direct radiation is

$$\left\{G^{\text{nwp}}_{t+k|t};\ t = 1, \ldots, N\right\} \tag{C.2}$$

C.2.1 Pre-processing

The solar power data is plotted for each hour of the day in Figure C.1. The solar radiation is zero at night, hence the observed solar power is also zero. For the current data set only periods, for a given hour of the day longer than 40 days in which the solar power is different from zero, are included for evaluation of the model performance. This is illustrated in Figure C.1, where the non-included periods are grayed out.

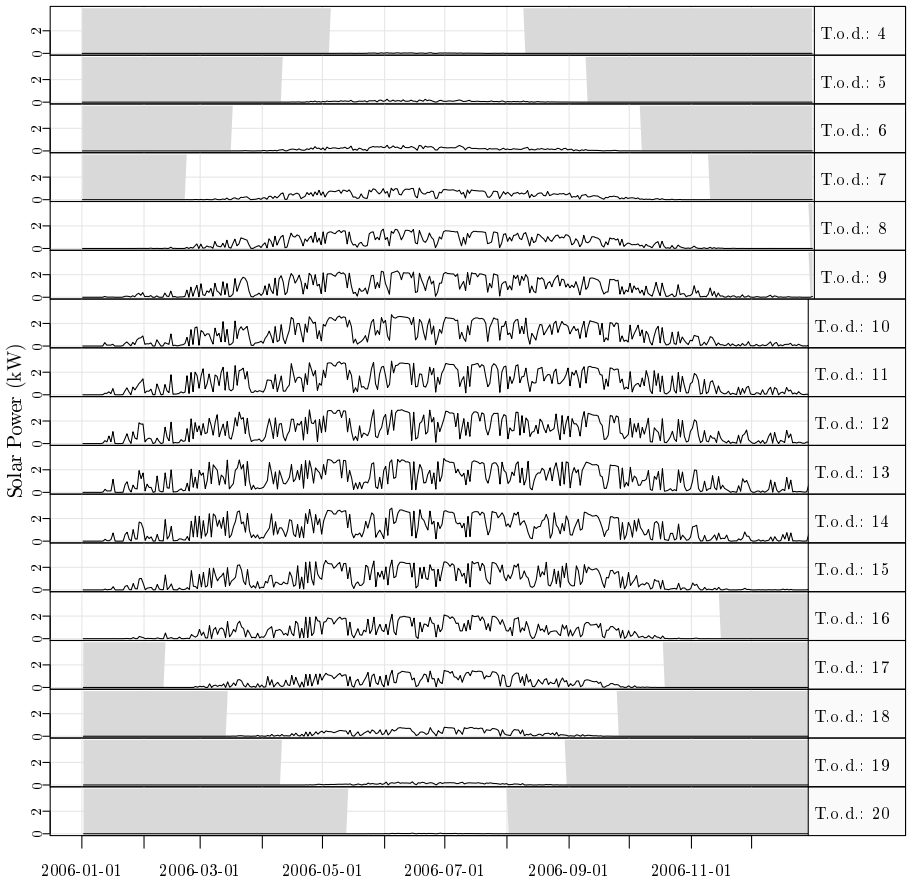

Figure C.1: The solar power data. The greyed area are not included in the evaluation of the model performance.

C.3 Clear sky model

Forecasting effectively using linear time series methods calls for stationarity of the underlying process Madsen (2007). The process that generates the solar power is not stationary, which is seen by plotting quantiles of the distribution of solar power conditioned on the time of day, see Figure C.2. Clearly the distribution of solar power is not independent of the time of day.

Most of this dependency can be removed by a normalization using a clear sky

model

$$\tau_t = \frac{P_t}{P_t^{\text{cs}}} \tag{C.3}$$

where P_t is the observed solar power, P_t^{cs} is the estimated clear sky solar power, and τ_t is the normalized solar power.

C.3.1 Statistically estimated clear sky solar power

The clear sky solar power is estimated using a statistical non-linear and adaptive model. Quantile regression Koenker (2005) locally weighted in the day of year and time of day dimension is applied. This is carried out fully causal, i.e. only past values are used. The clear sky model is

$$\hat{P}_t^{\text{cs}} = q_{0.99}(P_1, P_2, \ldots, P_t, h_{\text{y}}, h_{\text{tod}}) \tag{C.4}$$

where $q_{0.99}$ is the 99% quantile based on the solar power values up to time t. The bandwidths h_{day} and h_{tod}, are in the day of year and time of day dimension, respectively. The bandwidths control how "locally" the model is fitted, i.e. a lower bandwidth puts more emphasis on data which is close in the two dimensions. The local weighting function is an Epanechnikov kernel. The applied bandwidths are

$$h_{\text{day}} = 100 \text{ days}, \quad h_{\text{tod}} = 3 \text{ hours} \tag{C.5}$$

which were found by visual inspection of the fitted clear sky curve. Finally, it is noted that second-order polynomials were applied in the time of day dimension to include curvature into the model. The estimated clear sky solar power is shown in Figure C.3.

One advantage of the normalization is that it will automatically adapt to changes in the system, such as degraded performance or changes in the surroundings e.g. snow cover and shadowing effects. It can as well be used for monitoring of the solar system, since degraded performance from the same time of year will result in a lower clear sky solar power curve. Plots of the quantiles of the distribution of normalized solar power conditional on the time of day are shown in Figure C.2, from which it is seen that the normalized solar power process is considerably less dependent on the time of day and therefore a much more stationary process. It is noted that further work could include physical considerations into the clear sky model.

[t]

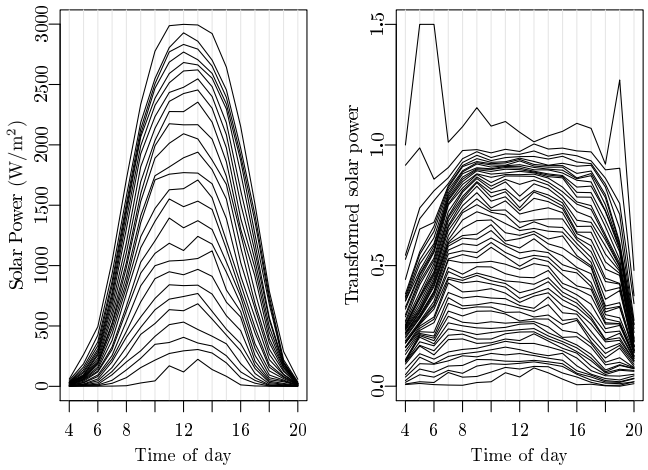

Figure C.2: The $0, 4\%, ..., 100\%$ quantiles of the distribution of the solar power and the normalized solar power conditioned on the time of day. Values above 1.5 has been clipped, which was the case for 6 values.

C.4 Forecasting models

In this section a description of the applied forecasting models is given. The models can be divided into models using linear time series models to forecast the normalized solar power: autoregressive (AR) and autoregressive with exogenous inputs (ARX) models - and models which forecast in a single stage: conditional parametric (CP) models. Each model is fitted separately for each horizon, such that the same model structure is used, but the parameters are estimated separately for each horizon.

C.4.1 Reference model

To compare the performance of prediction models, and especially when making comparisons between different studies, a common reference model is essential. The reference model for solar power used in this study is the best performing naive predictor for a given horizon. Two naive predictors of solar power are found to be relevant. Persistence

$$p_{t+k} = p_t + e_{t+k}, \tag{C.6}$$

and diurnal persistence

$$p_{t+k} = p_{t-s(k)} + e_{t+k} \tag{C.7}$$
$$s(k) = 24 + k \bmod 24 \tag{C.8}$$

where $s(k)$ ensures that the latest diurnal observation is used, i.e. the value which, depending on the horizon, is either 24 or 48 hours before the time point that is to be forecasted.

C.4.2 Autoregressive models

Autoregressive (AR) models are applied to forecast the normalized solar power. These models can include either the latest available observation or the latest available diurnal observation, or both, as input. The models are fitted with k-step recursive least squares with forgetting factor Bacher et al. (2009). The model formulated as a k-step AR model

$$\tau_{t+k} = m + a_1\tau_t + a_{24}\tau_{t-s(k)} + e_{t+k} \tag{C.9}$$
$$s(k) = 24 + k \bmod 24 \tag{C.10}$$

where the function $s(k)$ ensures that the latest observation of the diurnal component is included. The model without the diurnal component, denoted AR, performs best on short horizons

$$\tau_{t+k} = m + a_1\tau_t + e_{t+k} \tag{C.11}$$

and is included in the evaluation. The AR model with only the diurnal performs better on longer horizons, but is inferior to the models including the NWPs.

C.4.3 Conditional parametric models

Conditional parametric (CP) models where the coefficients are conditional on the time of day and time of year are applied with both past solar power observations and NWPs as inputs. The CP model with the latest solar power observation as input is

$$P_{t+k} = m + a\big(t_{\text{day}}, t_{\text{tod}}, P_t\big)P_t + e_{t+k} \tag{C.12}$$

where the coefficient function is a non-linear function of the solar power. It is denoted as CP_P. The CP model with NWPs of global radiation as input is

$$P_{t+k} = m + b\Big(t_{\text{day}}, t_{\text{tod}}, G^{\text{nwp}}_{t+k|t}\Big)G^{\text{nwp}}_{t+k|t} + e_{t+k} \tag{C.13}$$

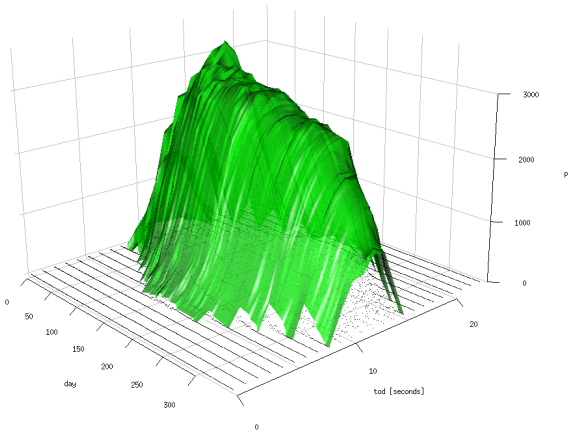

Figure C.3: The estimated clear sky solar power.

where $G^{\text{nwp}}_{t+k|t}$ is the k-hour ahead NWP of global radiation. This model is denoted CP_{NWP}. Finally, the model with both inputs

$$\begin{aligned} P_{t+k} =& m + a\big(t_{\text{day}}, t_{\text{tod}}, P_t\big)P_t \\ &+ b\Big(t_{\text{day}}, t_{\text{tod}}, G^{\text{nwp}}_{t+k|t}\Big)G^{\text{nwp}}_{t+k|t} + e_{t+k} \end{aligned} \tag{C.14}$$

is denoted $CP_{NWP,P}$.

In the following the coefficients dependency of the time of day for CP_{NWP} is elaborated on. It is noted that the bandwidths are optimized for each horizon. Plots of the fitted forecasting function $b\Big(t_{\text{day}}, t_{\text{tod}}, G^{\text{nwp}}_{t+k|t}\Big)$ for $k = 24$ hours are shown in Figure C.4. It is seen how the slope of the function is lower in the morning, than in the middle of the day. This is naturally caused by the higher angle of incidence in the morning, which cause less horizontal radiation to be absorbed due to reflection. Likewise for the afternoon. Finally, non-linearity in the fitted function is seen.

C.4.4 Autoregressive model with exogenous input

The AR model is be expanded to include the forecast of the CP models, thus combining information in past observed solar power and NWPs. The solar power

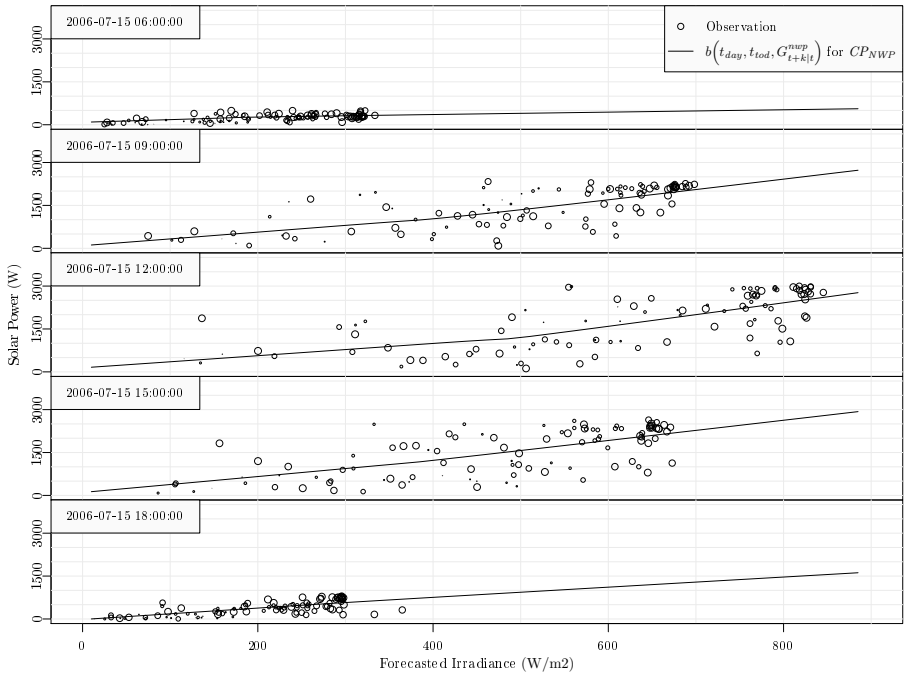

Figure C.4: Examples of the function fitted for $k = 24$ hours forecasting with the NWPs of global radiation at different times of the day on the 15'th of July 2010 with the CP_{NWP} model. For each observation the size of circle indicates the weighting of the observation in the CP models. Thus observations with a larger circle have more influence on the fitted function.

forecasts from the CP is normalized with the clear sky model by

$$\hat{\tau}^{\text{nwp}}_{t+k|t} = \frac{\hat{P}^{\text{nwp}}_{t+k|t}}{P^{\text{cs}}_{t-s(k)}} \tag{C.15}$$

$$s(k) = f_{\text{spd}} + k \bmod f_{\text{spd}} \tag{C.16}$$

where $f_{\text{spd}} = 24$ is the sample frequency in number of samples per day. The *ARX1* model is

$$\tau_{t+k} = m + a_1\tau_t + b_1\tau^{\text{nwp}}_{t+k|t} + e_{t+k} \tag{C.17}$$

C.5 Evaluation

The methods used for evaluating the prediction models are inspired by Madsen et al. (2005). The clear sky model, RLS, and CP fitting do not use any degrees of freedom and the data set is therefore not divided into a training set and a test set. It is only for the optimization of the kernel bandwidths and the forgetting factor that the entire data set is used. The period before 2006-03-01 is considered as a burn-in period and not used for calculating the error measures.

C.5.1 Error measures

The Root Mean Square Error for the k'th horizon is

$$RMSE_k = \left(\frac{1}{N} \sum_{t=1}^{N} e_{t+k}^2 \right)^{\frac{1}{2}} \tag{C.18}$$

where e_{t+k} is the k-hourly prediction error. The $RMSE_k$ is used as the main evaluation criterion (EC) for the performance of the models. The Normalized Root Mean Square Error is found by

$$NRMSE_k = \frac{RMSE_k}{p_{\max}} \tag{C.19}$$

where $p_{\max}$ is the maximum observed solar power output. The mean value of the $RMSE_k$ for a range of horizons

$$\overline{RMSE}_{k_{\text{start}},k_{\text{end}}} = \frac{1}{k_{\text{end}} - k_{\text{start}} + 1} \sum_{k=k_{\text{start}}}^{k_{\text{end}}} RMSE_k \tag{C.20}$$

is used as a summary error measure. When comparing the performance of two models the improvement

$$I_{\text{EC}} = 100 \cdot \frac{EC_{\text{ref}} - EC}{EC_{\text{ref}}} (\%) \tag{C.21}$$

is used, where EC is the considered evaluation criterion. When calculating the error measures it is important to consider how to handle missing values for the solar power forecasts. The problem is handled by replacing missing forecast values with forecast values from the reference model *Ref*.

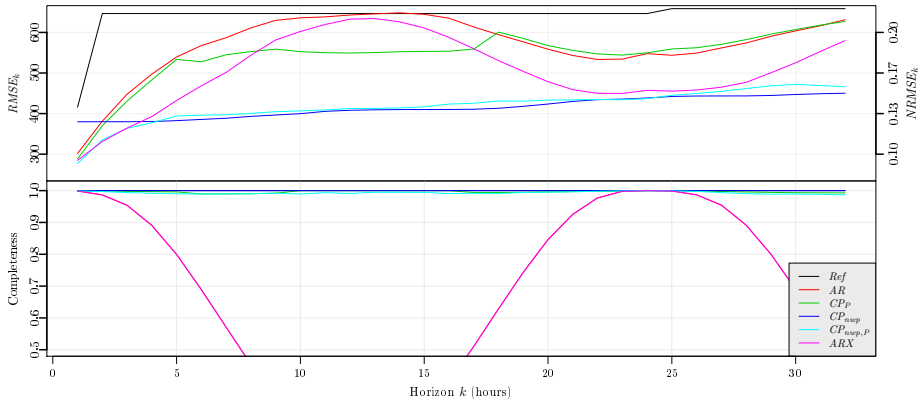

Figure C.5: The upper plot is $\boldsymbol{RMSE_k}$ for the forecasting models. On the right side the $\boldsymbol{NRMSE_k}$ is indicated. The lower plot is completeness $\boldsymbol{C_k}$.

C.5.2 Completeness

In order to evaluate a model for its performance regarding missing forecast values a measure is defined. It is denoted completeness. The completeness of a forecast for horizon k, is the ratio of the total sum of solar power and the summed solar power for time points where the forecasts are not missing

$$C_k = \frac{\sum_{t=1}^{N} P_t \; I\big(\hat{P}_{t|t-k}\big)}{\sum_{t=1}^{N} P_t} \tag{C.22}$$

where $I(\hat{P}_{t|t-k})$ is the indicator function which is 0 if $\hat{P}_{t|t-k}$ is missing, and 1 if not. Only the included values are used, i.e. not values during nighttime.

C.6 Results

In this section the results are presented and evaluated. The $\overline{RMSE}_{k_{\text{start}},k_{\text{end}}}$ improvements for relevant ranges of horizons are listed in Table C.1. For selected models the $RMSE_k$ is shown in the upper plot of Figure C.5 and the completeness in the lower.

Considering the improvements it is seen that most of the models perform very well on either the short horizons or the longer horizons. Starting with short horizons (1 to 2 hours) the four models using the latest observed solar power

have better performance than CP_{NWP}, which only uses the NWPs. Using the combination of observed solar power and NWPs improves the performance, except on longer horizons where using only NWPs are slightly better. Considering the performance of AR, CP_P, and ARX it is seen that the $RMSE_k$ increase really fast as the horizon increases and reach the reference model around a horizon of 10 hours. This is simply because the models are using night values (which are missing) to forecast day values. This is also seen in the completeness of the AR and ARX model.

C.7 Discussion and applications

This section contains a short discussion of the results and ideas for further work, and ends with an outline of applications.

Considering the improvement achieved over the reference model the forecasting models are found to perform very well. Clearly the quality of the NWPs of solar radiation is the most influential source of error, hence improved NWPs will improve the performance. Especially using NWPs of direct and diffuse radiation should be tried. Regarding further improvement of the forecasting models, it is suggested that the following should be considered:

- Application of regime models and hidden Markov models to handle different aspects of forecasting for e.g. low and high radiation values, and it might be useful to use different forecasting models for different types of cloud conditions. This is ideal to apply in the setting of the CP models.
- For the CP models using higher order polynomials in the day of year and time of day dimensions should improve the models. It was tried but didn't improve the performance, but as the NWPs are getting better this will most likely be important.

Table C.1: Improvements in percent for selected ranges of horizons.

Model	$I_{\overline{RMSE}_{1,2}}$	$I_{\overline{RMSE}_{3,17}}$	$I_{\overline{RMSE}_{18,32}}$
AR	34.3	7.4	12.6
CP_P	36.7	17	11.5
CP_{NWP}	25	38.4	33.1
$CP_{NWP,P}$	40.8	37.6	31.4
ARX	40.1	15.9	25

- A thorough evaluation of the forecast errors to find ideas for how the models can be improved.

The applications for solar power forecasting include the integration of PV systems into the electricity grid, especially for smart grids. The solar power forecasts can be used as input to model predictive control to optimize the operation of the PV system. This will enable diurnal peak-shaving and cost optimization for smaller systems with storage capacity in battery packs (e.g. provided in an electrical car). For large solar power producers forecasting is essential for optimized energy trading.

The method is furthermore well suited for monitoring the performance of PV systems. Measures of the performance can be derived from the CP models, with which systems can be compared on an absolute scale. Sudden high deviation from the CP forecasting model will allow for very fast detection of failures in the system. For an individual system the change in performance over time can also be assessed by monitoring the clear sky curve for unusual behavior, and compare the change from year to year.

C.8 Conclusion

Two approaches for solar power forecasting are presented and applied to forecast hourly values for horizons up to 32 hours. Both a method based on a two-stage approach, where first the solar power is normalized with a statistical clear-sky model, and a method in which the solar power is forecasted in a single step. The normalization with a clear sky model removes most of the non-stationarity caused by the changing position of the sun relative to the PV panel. This a pre-requisite for optimal application of linear time series models. Conditional parametric models are used to include NWPs of global radiation, and a one-stage approach, solely based on conditional parametric models, is presented. A root mean square improvement over a persistence reference model on short horizons (1 to 2 hours) is in average 40%, and in average 35% on the longer horizons. The method can furthermore be applied to monitor and check the performance of PV systems.

References

P. Bacher, H. Madsen, and H. A. Nielsen. Online short-term solar power forecasting. *Solar Energy*, 83(10):1772–1783, 2009. ISSN 0038092x.

F. O. Hocaoglu, Ö. N. Gerek, and M. Kurban. Hourly solar radiation forecasting using optimal coefficient 2-d linear filters and feed-forward neural networks. *Solar Energy*, 82(8):714–726, 2008. ISSN 0038092x.

W. Ji and K. C. Chee. Prediction of hourly solar radiation using a novel hybrid model of arma and tdnn. *Solar Energy*, 85(5):808–817, 2011. ISSN 0038092x. doi: 10.1016/j.solener.2011.01.013.

R. Koenker. *Quantile Regression*. Cambridge University Press, 2005.

E. Lorenz, J. Hurka, D. Heinemann, and H. Beyer. Irradiance forecasting for the power prediction of grid-connected photovoltaic systems. *IEEE Journal of Selected Topics in Applied Earth Observations and Remote Sensing*, 2(1): 2–10, 2009. ISSN 19391404, 21511535.

H. Madsen. *Time Series Analysis*. Chapman & Hall, 2007.

H. Madsen, P. Pinson, G. Kariniotakis, H. A. Nielsen, and T. S. Nielsen. Standardizing the performance evaluation of shortterm wind power prediction models. *Wind Engineering*, 29(6):475, 2005. ISSN 0309524x.

T. S. Nielsen, H. Madsen, and H. A. Nielsen. Prediction of wind power using time-varying coefficient-functions. *Proceedings of the 15th IFAC World Congress on Automatic Control*, 2002.

A. Sfetsos and A. Coonick. Univariate and multivariate forecasting of hourly solar radiation with artificial intelligence techniques. *Solar Energy*, 68(2): 169–178, 2000. ISSN 0038092x.

Paper D

Short-term solar collector power forecasting

Authors:
Peder Bacher[1], Henrik Madsen[1], and Bengt Perers[2]

In proceedings:
ISES Solar World Congress 2011.

[1]DTU Informatics, Richard Pedersens Plads, Building 321, DK-2800 Lyngby, Denmark
[2]DTU Civil Engineering, Brovej, Building 118, DK-2800 Lyngby, Denmark

Abstract

This paper describes a new approach to online forecasting of power output from solar thermal collectors. The method is suited for online forecasting in many applications and in this paper it is applied to predict hourly values of power from a standard single glazed large area flat plate collector. The method is applied for horizons of up to 42 hours.

Solar heating systems naturally come with a hot water tank, which can be utilized for energy storage also for other energy sources. Thereby such systems can become an important part of energy systems with a large share of uncontrollable energy sources, such as wind power. In such a scenario online forecasting is a vital tool for optimal control and utilization of solar heating systems.

The method is a two-step scheme, where first a non-linear model is applied to transform the solar power into a stationary process, which then is forecasted with robust time-adaptive linear models. The approach is similar to the one by Bacher et al. (2009), but contains additional effects due to differences between solar thermal collectors and photovoltaics. Numerical weather predictions provided by Danish Meteorological Institute are used as input. The applied models adapt over time enabling tracking of changes in the system and in the surrounding conditions, such as decreasing performance due to wear and dirt, and seasonal changes such as leaves on trees. This furthermore facilitates remote monitoring and check of the system.

D.1 Introduction

Forecasting of energy production is vital for optimization of energy systems which include wind and solar energy production. This paper describes an approach to online forecasting of power production from solar thermal collectors. In Denmark the level of wind power penetration already now gives periods with a surplus of energy and facilities to absorb this energy are needed. Solar heating systems with a hot water tank and auxiliary electrical heating can provide energy storage, which can facilitate absorption of wind energy and peak shaving, especially for levelling out diurnal energy consumption. The method is planned to be part of the control system for such heating systems (Perers et al., 2011). The study is carried out with climate data observed at a weather station at Danish Technical University. From this data, simulated hourly average values of solar thermal power is generated with a very detailed simulation model. Furthermore numerical weather predictions (NWPs) provided by Danish Meteorological In-

stitute data is used. The forecasting method is a two-step scheme, where first a statistical clear sky model is applied to transform the solar power into a more stationary process, which then is forecasted with robust time-adaptive linear models. The NWPs are used as input to conditional parametric time-adaptive models to forecast the solar power. These forecasts are then transformed with the clear sky model, such that they can be applied as inputs to the linear forecasting models. Finally, a combined model, which is the most optimal for all horizons, is formed.

The paper is organized as follows. First the data and how it is preprocessed is described in a section. The next section contains an outline of the clear sky model, and this is followed by a section where all the forecasting models are described. Then an evaluation is given and the results are presented, each in a section. The second last section contains a discussion of the results and ideas for further work, and finally, the paper ends with a conclusion.

Nomenclature

P_t	Hourly solar thermal power, $\left[\mathrm{W/m^2}\right]$.
P_t^{cs}	Estimated clear sky solar power, $\left[\mathrm{W/m^2}\right]$.
τ_t	Normalized solar power.
t	Time index, [h].
k	Forecast horizon index, [h].
t_{tod}	Time of day.
$F'(\tau\alpha)_{\mathrm{en}}$	Zero loss efficiency of collector for direct radiation at normal incidence
$K_{\tau\alpha\mathrm{b}}(\theta)$	Incidence angle modifier for direct radiation
$K_{\tau\alpha\mathrm{d}}$	Incidence angle modifier for diffuse radiation
$F'U_0$	Heat loss coefficient at $(T_{\mathrm{a}} - T_{\mathrm{f}}) = 0$, $\left[\mathrm{W/(m^2K)}\right]$.
$G_{t+k\|t}^{\mathrm{nwp}}$	NWP of global radiation, $\left[\mathrm{W/m^2}\right]$.
$G_{t+k\|t}^{\mathrm{b,nwp}}$	NWP of direct solar radiation, $\left[\mathrm{W/m^2}\right]$.
$G_{t+k\|t}^{\mathrm{d,nwp}}$	NWP of diffuse solar radiation, $\left[\mathrm{W/m^2}\right]$.
$T_{t+k\|t}^{\mathrm{a,nwp}}$	NWP of ambient temperature, [°C].
$\hat{P}_{t+k\|t}^{\mathrm{nwp}}$	k-hour prediction of solar power, $\left[\mathrm{W/m^2}\right]$.
$\hat{\tau}_{t+k\|t}$	k-hour prediction of normalized solar power.
e_{t+k}	k-step prediction error.

D.2 Data

The forecasting method is applied on simulated solar output power data for a flat plate collector carefully tested and modelled at DTU. A validated collector model and longterm climate data from the DTU Byg climate station was used to create realistic operating data for a solar collector during the year. The simulation model and weather data was introduced in TRNSYS 16 and the collector output power was calculated as hourly mean values. The simulation model is dynamic, such that dynamical effects - introduced when the collector starts and stops and during rapidly varying solar radiation conditions - are modelled.

In this study all time series are hourly average values and all units are implicitly per hour. Time points are set to the end of their respective sample period and all are in UTC. The units for radiation are $\frac{\mathrm{W}}{\mathrm{m}^2}$ and for temperatures °C.

D.2.1 Solar power

The simulated solar power time series is plotted for each hour of the day in Figure D.1. A few short periods are with missing values.

D.2.2 Numerical weather predictions

The numerical weather predictions (NWPs) used in the study are provided by Danish Meteorological Institute. The NWP model is DMI-HIRLAM-S05, which has a 5 kilometer grid and 40 vertical layers (DMI, 2011). NWPs are updated every 6'th hour and are up to a 48 hours horizon. They consist of hourly predictions of ambient temperature, and horizontal direct- and diffuse solar radiation. A couple of the considered forecasting models use the global radiation as input, which is simply the direct and the diffuse radiation summed. The scatter plots in Figure D.2 shows the solar power versus the NWPs for a 24 hour horizon. Clearly, the solar power is highly correlated with both the global and direct radiation, whereas the effect of diffuse and ambient temperature are not as apparent.

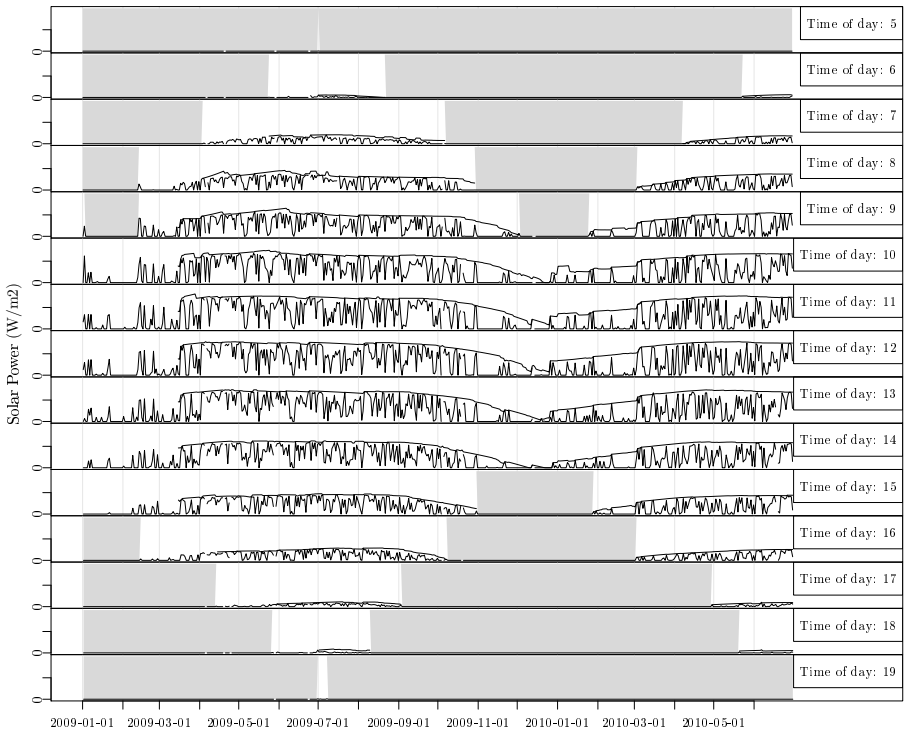

Figure D.1: The observed solar power for each hour of the day. The grayed area shows the periods not included in the modelling. The curve following the highest values of solar power is the estimated clear sky power, which is referred to in later parts of the paper.

D.2.3 Pre-processing

On most locations on earth the solar radiation is zero at night time, hence the observed solar power is also zero. For the current dataset only periods, for a given hour of the day longer than 40 days in which the solar power is different from zero, are included. This is illustrated in Figure D.1, where the non-included periods are grayed out. Furthermore a few short periods are missing from the observations. The time series of hourly observed solar power spanning the period from 2009-01-01 to 2010-07-01 is

$$\{P_t;\ t = 1, \ldots, N\} \tag{D.1}$$

where $N = 13104$. The NWPs have a calculation time of 4 hours, which is taken into consideration, such that e.g. the forecast from 2009-01-01 00:00 are only available from 2009-01-01 04:00. The NWPs are pre-processed into time series

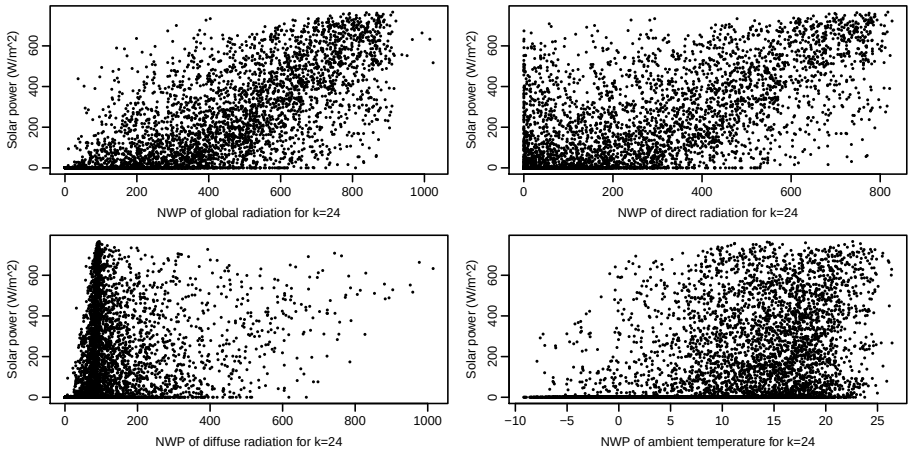

Figure D.2: The observed solar power versus the NWPs for $k = 24$, which are used as inputs to forecasting models.

of hourly values, such that the most recent available forecast k hours ahead is selected each hour. The time series are for a given k: the direct radiation

$$\left\{G^{\mathrm{b,nwp}}_{t+k|t};\ t = 1, \ldots, N\right\} \tag{D.2}$$

the diffuse radiation

$$\left\{G^{\mathrm{d,nwp}}_{t+k|t};\ t = 1, \ldots, N\right\} \tag{D.3}$$

and the ambient temperature

$$\left\{T^{\mathrm{a,nwp}}_{t+k|t};\ t = 1, \ldots, N\right\} \tag{D.4}$$

Due to the 6 hours interval the NWPs for horizons longer than 42 hours are not complete and therefore the solar power forecasting are only carried out up to 42 hours.

D.3 Clear sky model

For effective forecasting with classical linear time series methods stationarity of the process is required (Madsen, 2007). The process that generates the solar power is not stationary, which is seen by plotting quantiles of the distribution of solar power conditioned on the time of day. Such a plot is shown in Figure D.3.

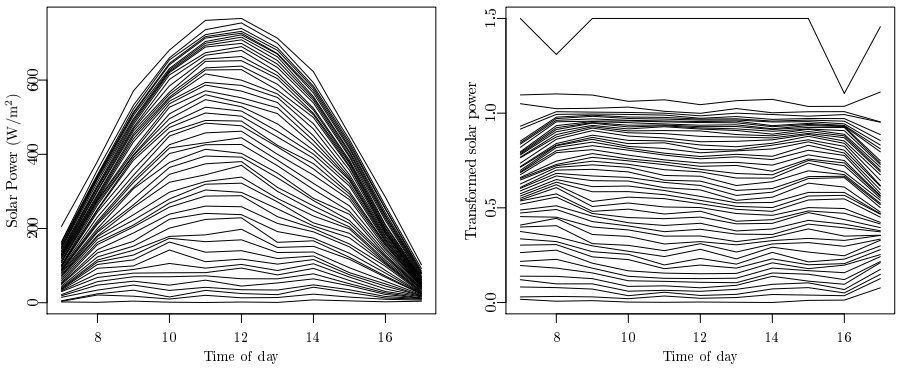

Figure D.3: The $0, 2\%, ..., 100\%$ quantiles of the distribution of the solar power and the transformed solar power conditioned on the time of day. Values above 1.5 has been clipped, which was the case for 17 values.

Clearly the distribution of solar power is not independent of the time of day. The dependency can be removed by a transformation with a clear sky model

$$\tau_t = \frac{P_t}{P_t^{\text{cs}}} \tag{D.5}$$

where P_t is the observed solar power, P_t^{cs} is the estimated clear sky solar power, and τ_t is the transformed solar power.

D.3.1 Statistically estimated clear sky solar power

The clear sky solar power is estimated with a statistical non-linear and adaptive model. Quantile regression locally weighted in the day of year and time of day dimension is applied. In the present study this is carried out fully causal. The clear sky model is

$$P_t^{\text{cs}} = q_{0.99}(P_1, P_2, \ldots, P_t, h_{\text{t}}, h_{\text{tod}}, h_{\text{y}}) \tag{D.6}$$

where $q_{0.99}$ is the 99% quantile of all the solar power values up to t. The bandwidths h_{t}, h_{tod}, and h_{y}, are in the time-, time of day-, and year-dimension, respectively. The bandwidths control how "locally" the model is fitted, i.e. a lower bandwidth puts more emphasis on data which is close in time. The local weighting function is an Epanechnikov kernel. The applied bandwidths are

$$h_t = 120 \text{ days}, \quad h_{\text{tod}} = 2 \text{ hours}, \quad h_{\text{y}} = 1.7 \text{ years} \tag{D.7}$$

which were found by visual inspection of the fitted clear sky curve. Finally, it is noted that second-order polynomials were applied in the time- and time of day-dimension to include curvature into the model. The estimate of the clear sky solar power is shown in Figure D.1. From the plot it is seen that it follows the highest values of solar power quite well. Clearly, the clear sky power is most easily carried out in the periods with a high level of solar power. One advantage of the transformation is that it will automatically adapt to changes in the system, such as degraded performance or changes in the surroundings e.g. snow cover and shadowing effects. It can as well be used for monitoring of the solar system, since degraded performance from the same time of year will result in a lower clear sky solar power curve. Quantile plots of the transformed solar power conditioned on the time of day are shown in Figure D.3, from which it is seen that the transformed solar power process is considerably less dependent of the time of day and therefore a much more stationary process. It is noted that further work could include physical considerations e.g. by using the air mass as an input.

D.4 Forecasting models

In this section a description of the applied forecasting models is given. The models can be divided into models without NWPs as input - autoregressive (AR) models - and models with NWPs as input: conditional parametric (CP) and autoregressive with exogenous inputs (ARX) models. Each model is fitted seperately for each horizon, such that the same model structure is used, but the parameters are estimated separately for each horizon. In the final model, a combination of models are used to achieve the most optimal performance for all horizon.

D.4.1 Reference model

To compare the performance of prediction models, and especially when making comparisons between different studies, a common reference model is essential. The reference model for solar power used in this study is the best performing naive predictor for a given horizon. Two naive predictors of solar power are found to be relevant. Persistence

$$p_{t+k} = p_t + e_{t+k}, \tag{D.8}$$

and diurnal persistence

$$p_{t+k} = p_{t-s(k)} + e_{t+k} \tag{D.9}$$
$$s(k) = f_{\text{spd}} + k \bmod f_{\text{spd}} \tag{D.10}$$

where $f_{\text{spd}} = 24$ is the sample frequency in number of samples per day and $s(k)$ ensures that the latest diurnal observation is used, i.e. the value which, depending on the horizon, is either 24 or 48 hours before the time point that is to be forecasted.

D.4.2 Autoregressive models

Autoregressive (AR) models are applied to forecast the transformed solar power. These models can include either the latest available observation or the latest available diurnal observation, or both, as input. The models are fitted with k-step recursive least squares with forgetting factor (Bacher et al., 2009). The model formulated as a k-step AR model

$$\tau_{t+k} = m + a_1\tau_t + a_{24}\tau_{t-s(k)} + e_{t+k} \tag{D.11}$$
$$s(k) = 24 + k \bmod 24 \tag{D.12}$$

where the function $s(k)$ ensures that the latest observation of the diurnal component is included. It was found that depending on the horizon better performance was achieved by only using one input. Thus for short horizons (1 and 2 hours) the model without the diurnal component

$$\tau_{t+k} = m + a_1\tau_t + e_{t+k} \tag{D.13}$$

was found to have the best performance, it is denoted *AR1*, and for longer horizons the model with only the diurnal component

$$\tau_{t+k} = m + a_{24}\tau_{t-s(k)} + e_{t+k} \tag{D.14}$$

was found to have the best performance, it is denoted *ARDiurnal*.

D.4.3 Conditional parametric models with NWPs as input

Models based on NWPs of solar radiation and ambient temperature are described in this section. It is known from physics (Perers, 1997) that the power

output of a solar collector can be described by

$$P = F'(\tau\alpha)_{\mathrm{en}} K_{\tau\alpha\mathrm{b}}(\theta) G_{\mathrm{b,col}} + F'(\tau\alpha)_{\mathrm{en}} K_{\tau\alpha\mathrm{d}} G_{\mathrm{d,col}} - F'U_0 \left(\frac{T_{\mathrm{o}} + T_{\mathrm{i}}}{2} - T_{\mathrm{a}} \right) \tag{D.15}$$

where the $G_{\mathrm{b,col}}$ and $G_{\mathrm{d,col}}$ are respectively direct and diffuse solar radiation normal to the collector plane. This is formed into a forecasting model based on NWPs by rewriting as follows. First, both the the angle of incidence modifier $K_{\tau\alpha\mathrm{b}}(\theta)$ and the transformation of solar radiation from horizontal to the collector plane are modelled by letting the coefficients - for the radiation effects - become a function of time t and time of day t_{tod}. Furthermore, assuming that the outlet temperature is a function of the solar radiation

$$T_{\mathrm{o}} = f_{\mathrm{b}}(G_{\mathrm{b,col}}) + f_{\mathrm{d}}(G_{\mathrm{d,col}}) \tag{D.16}$$

this give the total effect of direct radiation as a non-linear function

$$a(t, t_{\mathrm{tod}}, G_{\mathrm{b}}, G_{\mathrm{d}}) G_{\mathrm{b}} = F'(\tau\alpha)_{\mathrm{en}} K_{\tau\alpha\mathrm{b}}(\theta) G_{\mathrm{b,col}} - F'U_0 \frac{1}{2} f_{\mathrm{b}}(G_{\mathrm{b,col}}) \tag{D.17}$$

and for the diffuse radiation

$$b(t, t_{\mathrm{tod}}, G_{\mathrm{b}}, G_{\mathrm{d}}) G_{\mathrm{d}} = F'(\tau\alpha)_{\mathrm{en}} K_{\tau\alpha\mathrm{d}} G_{\mathrm{b,col}} - F'U_0 \frac{1}{2} f_{\mathrm{d}}(G_{\mathrm{d,col}}) \tag{D.18}$$

Finally, the effect of the ambient temperature is kept as

$$cT_{\mathrm{a}} = F'U_0 T_{\mathrm{a}} \tag{D.19}$$

and by assuming a constant inlet temperature this part becomes a constant effect

$$m = -F'U_0 \frac{T_{\mathrm{i}}}{2} \tag{D.20}$$

Thus the CP model structure used for forecasting is

$$P = m + a(t, t_{\mathrm{tod}}, G_{\mathrm{b}}, G_{\mathrm{d}}) G_{\mathrm{b}} + b(t, t_{\mathrm{tod}}, G_{\mathrm{b}}, G_{\mathrm{d}}) G_{\mathrm{d}} + cT_{\mathrm{a}} \tag{D.21}$$

Since the time-dependency and non-linearity are smooth functions in the parameters, it is modelled with conditional parametric (CP) models. The time varying effect is modelled by conditioning on t and t_{tod} - this is equivalent of a local constant effect - and the dependency of the radiation is modelled with 1-order local polynomials. A kernel method is applied, using a nearest neighbor approach to find the bandwidth of an Epanechnikov weighting function. From Equation (D.15) it is seen that the output can be negative if little radiation hits the collector and the ambient temperature is low. In this case the output is zero

since the system stops. This effect can be seen on the plot in Figure D.2. It is handled by the non-linearity of the models and by setting negative forecasts to zero.

The simplest considered conditional parametric model is

$$P_{t+k} = m + a\Big(t, t_{\text{tod}}, G^{\text{nwp}}_{t+k|t}\Big) G^{\text{nwp}}_{t+k|t} + e_{t+k} \tag{D.22}$$

where $G^{\text{nwp}}_{t+k|t}$ is the k-hour NWP of global radiation and denoted as *CP1* in the following. This second CP model has NWPs of direct and the diffuse radiation as inputs

$$\begin{aligned} P_{t+k} = m &+ a\Big(t, t_{\text{tod}}, G^{\text{b,nwp}}_{t+k|t}, G^{\text{d,nwp}}_{t+k|t}\Big) G^{\text{b,nwp}}_{t+k|t} \\ &+ b\Big(t, t_{\text{tod}}, G^{\text{b,nwp}}_{t+k|t}, G^{\text{d,nwp}}_{t+k|t}\Big) G^{\text{d,nwp}}_{t+k|t} + e_{t+k} \end{aligned} \tag{D.23}$$

where $G^{\text{b,nwp}}_{t+k|t}$ is the k-hour NWP of direct radiation and $G^{\text{d,nwp}}_{t+k|t}$ is the k-hour NWP of diffuse radiation, and denoted as *CP2*. Finally the model is expanded with NWPs of ambient temperature

$$\begin{aligned} P_{t+k} = m &+ a\Big(t, t_{\text{tod}}, G^{\text{b,nwp}}_{t+k|t}, G^{\text{d,nwp}}_{t+k|t}\Big) G^{\text{b,nwp}}_{t+k|t} \\ &+ b\Big(t, t_{\text{tod}}, G^{\text{b,nwp}}_{t+k|t}, G^{\text{d,nwp}}_{t+k|t}\Big) G^{\text{d,nwp}}_{t+k|t} + c\Big(t, t_{\text{tod}}\Big) T^{\text{a,nwp}}_{t+k|t} + e_{t+k} \end{aligned} \tag{D.24}$$

where $T^{\text{a,nwp}}_{t+k|t}$ is the k-hour NWPs of the ambient temperature and the model is denoted as *CP3*.

In the following the coefficients dependency of the time of day is elaborated on. Plots of the fitted forecasting function $a\Big(t, t_{\text{tod}}, G^{\text{b,nwp}}_{t+k|t}, G^{\text{d,nwp}}_{t+k|t}\Big)$ are shown in Figure D.4. It is seen how the slope of the function is lower in the morning, than in the middle of the day. This is naturally caused by the higher angle of incidence in the morning, which cause less horizontal radiation to be absorbed due to reflection. Likewise for the afternoon. Finally, non-linearity in the fit is seen, which is caused by the non-negativity of the solar power (mentioned above) and varying uncertainty of the NWPs.

D.4.4 Autoregressive model with exogenous input

The AR model is be expanded to include the forecast of the CP models, thus combining information in past observed solar power and NWPs. The solar power

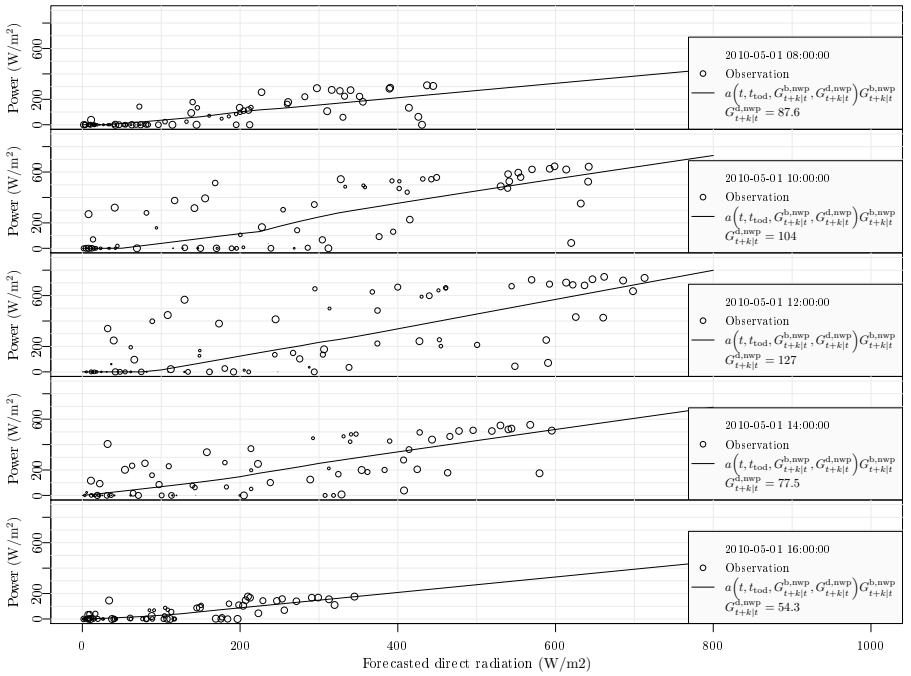

Figure D.4: Examples of the function fitted for forecasting of the effect of direct radiation at different times of the day the 1'th of May 2010 with the *CP2* model. For each observation the size of circle indicates the weighting of the observation in the CP models. Thus observations with a larger circle have more influence on the fitted function.

forecasts from the CP is transformed with the clear sky model by

$$\hat{\tau}^{\text{nwp}}_{t+k|t} = \frac{\hat{P}^{\text{nwp}}_{t+k|t}}{P^{\text{cs}}_{t-s(k)}} \tag{D.25}$$

$$s(k) = f_{\text{spd}} + k \bmod f_{\text{spd}} \tag{D.26}$$

where $f_{\text{spd}} = 24$ is the sample frequency in number of samples per day. This is applied as an input to the ARX model

$$\tau_{t+k} = m + a_1\tau_t + a_{24}\tau_{t-s(k)} + b_1\tau^{\text{nwp}}_{t+k|t} + e_{t+k} \tag{D.27}$$

Again, as for the AR models, different performance is found depending on the horizon. The *ARX1* model is best for short horizons

$$\tau_{t+k} = m + a_1\tau_t + b_1\tau^{\text{nwp}}_{t+k|t} + e_{t+k} \tag{D.28}$$

ARXDiurnal for horizons up to 24 hours

$$\tau_{t+k} = m + a_{24}\tau_{t-s(k)} + b_1\tau^{\text{nwp}}_{t+k|t} + e_{t+k} \tag{D.29}$$

and *ARX*

$$\tau_{t+k} = m + b_1\tau^{\text{nwp}}_{t+k|t} + e_{t+k} \tag{D.30}$$

for longer horizons.

D.4.5 Combined model

The final model is a combination of the previously described models. The model is denoted *ARXCombined*. First, missing values in forecasts from *ARX1* are replaced with forecast values from *ARXDiurnal*. These missing values are in the morning, since they were tried to be forecasted based on night values, which are zero. For horizons longer than 30 hours forecasts from *ARX* are used. Finally, any remaining missing values - which are only where the diurnal lag was not present for *ARXDiurnal* - are replaced with forecasted values from *CP2*.

D.5 Evaluation

The methods used for evaluating the prediction models are inspired by Madsen et al. (2005). They suggest a framework for evaluation of wind power forecasting. The clear sky model, RLS, and CP fitting do not use any degrees of freedom and the dataset is therefore not divided into a training set and a test set. It is only for the optimization of the kernel bandwidths and the forgetting factor that the entire dataset is used. The period before 2009-03-15 is considered as a burn-in period and are not used when calculating the error measures.

D.5.1 Error measures

The Root Mean Square Error for the k'th horizon is

$$RMSE_k = \left(\frac{1}{N}\sum_{t=1}^{N} e^2_{t+k}\right)^{\frac{1}{2}} \tag{D.31}$$

where e_{t+k} is k-hourly prediction error. The $RMSE_k$ is used as the main evaluation criterion (EC) for the performance of the models. The Normalized Root Mean Square Error is found by

$$NRMSE_k = \frac{RMSE_k}{p_{\max}} \tag{D.32}$$

where $p_{\max}$ is the maximum observed solar power output. The mean value of the $RMSE_k$ for a range of horizons

$$\overline{RMSE}_{k_{\text{start}},k_{\text{end}}} = \frac{1}{k_{\text{end}} - k_{\text{start}} + 1} \sum_{k=k_{\text{start}}}^{k_{\text{end}}} RMSE_k \tag{D.33}$$

is used as a summary error measure. When comparing the performance of two models the improvement

$$I_{\text{EC}} = 100 \cdot \frac{EC_{\text{ref}} - EC}{EC_{\text{ref}}}(\%) \tag{D.34}$$

is used, where EC is the considered evaluation criterion. When calculating the error measures it is important to consider how to handle missing values for the solar power forecasts. The problem is handled by replacing missing forecast values with forecast values from the reference model *Ref.*

D.5.2 Completeness

In order to evaluate a model for its performance regarding missing forecast values a measure is defined, it is denoted completeness. The completeness of a forecast for horizon k, is the ratio of the the summed solar power for time points where the forecasts are not missing to the total sum of solar power

$$C_k = \frac{\sum_{t=1}^{N} P_t \; I\big(\hat{P}_{t|t-k}\big)}{\sum_{t=1}^{N} P_t} \tag{D.35}$$

where $I(\hat{P}_{t|t-k})$ is the indicator function which is 0 if $\hat{P}_{t|t-k}$ is missing, and 1 if not. Only the included values are used, i.e. not night values.

D.6 Results

In this section the results are presented and evaluated. The $\overline{RMSE}_{k_{\text{start}},k_{\text{end}}}$ improvement for relevant ranges of horizons are listed in Table D.1. For selected models the $RMSE_k$ is shown in the upper plot of Figure D.5 and the completeness in the lower.

Considering the improvements it is seen that most of the models perform very well on either the short horizons or the longer horizons. Starting with short horizons (1 to 2 hours), the *AR1* and *ARX1* are clearly superior, which is due to their inclusion of the most present autoregressive lag. Their performance on longer horizons are not good. The reason for this is found by considering the plot of $RMSE_k$ and completeness. Here it is seen that the completeness of *AR1* and *ARX1* drops really quickly as the horizon increase, which cause the $RMSE_k$ to increase and reach the reference model at the 10 hours horizon. This is simply due to missing forecast values, since for e.g. the 10 to 14 hours horizons the models use night values (which are missing) to forecast day values with.

For horizons longer than three hours the best performance is seen for the models, that doesn't include the most present AR lag. The *ARDiurnal* is a clear improvement from the *AR1*, and the CP and ARX models - which include the NWPs - are superior for these horizons. An improved performance is found from *CP1* to *CP2* mainly for 3 to 24 hours horizons, whereas no clear increase in improvement is found from *CP2* to *CP3*. The CP models are slightly improved by using them as input to the ARX models, since autocorrelation of the errors are modelled.

Finally, the combined model *ARXCombined* utilizes the best parts of: *ARX1*, *ARX*, *ARXDiurnal*, and *CP2*. Especially the replacement of missing forecast values improves the performance for horizons up to 5 hours. The completeness of the combined model is as high as any of the others.

Table D.1: Improvements in percent for selected ranges of horizons.

Model	$I_{\overline{RMSE}_{1,2}}$	$I_{\overline{RMSE}_{3,24}}$	$I_{\overline{RMSE}_{25,42}}$	$I_{\overline{RMSE}_{1,42}}$
AR1	30.8	7.1	6.1	7.8
ARDiurnal	-10.7	15	18	15.1
CP1	13.5	30	30.6	29.5
CP2	16.2	31.4	30.9	30.5
CP3	15.5	31.6	30.8	30.5
ARX	17.1	32	31.3	31
ARX1	34.4	11.6	8.7	11.4
ARXDiurnal	17.8	32.4	30.5	30.9
ARXCombined	39.3	33.3	31.5	32.8

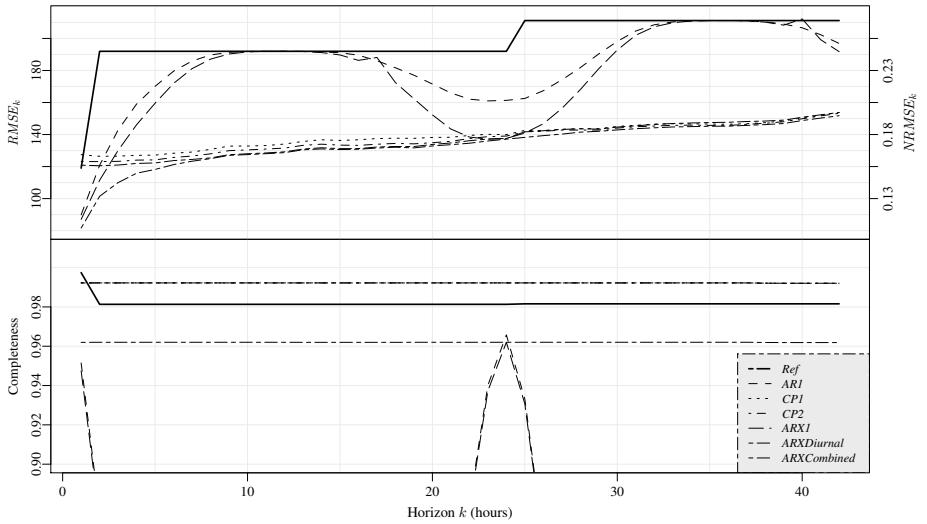

Figure D.5: The upper plot is $\boldsymbol{RMSE_k}$ for the forecasting models. On the right side the $\boldsymbol{NRMSE_k}$ is indicated. The lower plot is completeness $\boldsymbol{C_k}$.

D.7 Discussion and applications

This section contains a short discussion of the results and ideas for further work, and ends with an outline of applications.

Considering the improvement achieved over the reference model the forecasting method is found to perform very well. Clearly the quality of the NWPs of solar radiation is the most influential source of error, hence improved NWPs will improve the forecasting performance. Regarding improvement of the forecasting models, the following are considered:

- A thorough evaluation of the forecast errors to clarify how the models can be improved.
- Optimization of forgetting factor of the RLS has not been carried out, this will improve the performance of the AR and ARX models.
- Application of regime models to handle different aspects of forecasting for low and high radiation values.
- More optimal ways to combine the models. Utilizing a linear combination instead of the simple replacement currently carried out.

- It might be possible to improve performance by including a third-stage, where modelling of the errors are carried out.

The applications for this type of solar thermal power forecasting counts the integration of solar thermal energy systems with auxiliary electrical heating into smart grid systems (Perers et al., 2011). The solar power forecasts will be used for model predictive control to optimize the operation of the system. Other applications include optimal control of large solar heating plants.

The method is furthermore well suited for monitoring the performance of solar thermal systems. Measures of the performance can be derived from the CP models, with which systems can be compared on an absolute scale. Sudden high deviation from the CP forecasting model will allow for very fast detection of failures in the system. For an individual system the change in performance over time can also be assessed by monitoring the clear sky curve for unusual behavior, and compare the change from year to year.

D.8 Conclusion

A method for forecasting of solar thermal power output is presented. It is applied to forecast hourly values for horizons up to 42 hours. The method is based on conditional parametric models. Both models without and with NWPs of solar radiation and ambient temperature are considered. The NWPs are included by using a non-linear conditional parametric model, which are formed from prior physical knowledge. The forecast models which do not use NWPs achieve an improvement on short horizons (1 to 2 hours) in average 30% over a persistence reference model, and in average 15% on horizons up to 42 hours. Applying the NWPs an improvement around 39 % is achieved in average for short horizons and around 32% in average for longer horizons. The method can furthermore be applied to monitor and check the performance of solar thermal collectors.

References

P. Bacher, H. Madsen, and H. A. Nielsen. Online short-term solar power forecasting. *Solar Energy*, 83(10):1772–1783, 2009. ISSN 0038092x.

DMI. Danish Meteorological Institute, DMI-HIRLAM-S05, 2011. URL `http://www.dmi.dk/eng/index/research_and_development/dmi-hirlam-2009.htm`.

H. Madsen. *Time Series Analysis*. Chapman & Hall, 2007.

H. Madsen, P. Pinson, G. Kariniotakis, H. A. Nielsen, and T. S. Nielsen. Standardizing the performance evaluation of shortterm wind power prediction models. *Wind Engineering*, 29(6):475, 2005. ISSN 0309524x.

B. Perers. An improved dynamic solar collector test method for determination of non-linear optical and thermal characteristics with multiple regression. *Solar Energy*, 59(4-6):163–178, 1997. ISSN 0038092x.

B. Perers, S. Furbo, J. Fan, E. Andersen, and Z. Chen. Solar combisystems with forecast control to increase the solar fraction and lower the auxiliary energy cost. In *ISES Solar World Congress 2011 Proceedings*, page , 2011. ISBN 978-3-9814659-0-7. Presented at: ISES Solar World Congress, SWC ; 30 : Kassel, Germany, 2011.

Paper E

Models of the heat dynamics of solar collectors for performance testing

Authors:
Peder Bacher[1], Henrik Madsen[1], and Bengt Perers[2]

In proceedings:
ISES Solar World Congress 2011.

[1]DTU Informatics, Richard Pedersens Plads, Building 321, DK-2800 Lyngby, Denmark
[2]DTU Civil Engineering, Brovej, Building 118, DK-2800 Lyngby, Denmark

Abstract

The need for fast and accurate performance testing of solar collectors is increasing. This paper describes a new technique for performance testing which is based on non-linear continuous time models of the heat dynamics of the collector. It is shown that all important performance parameters can be accurately estimated with measurements from a single day. The estimated parameters are compared with results from standardized test methods (Fischer et al., 2004).

Modelling the dynamics of the collector is carried out using stochastic differential equations, which is a well proven efficient method to obtain accurate estimates of parameters in physical models. The applied method is described by Kristensen et al. (2004) and implemented in the software CTSM[1]. Examples of successful applications of the method includes modelling the of the heat dynamics of integrated photo-voltaic modules (Friling et al., 2009) and modelling of the heat dynamics of buildings (Madsen and Holst, 1995).

Measurements obtained at a test site in Denmark during the spring 2010 are used for the modelling. The tested collector is a single glazed large area flat plate collector with selective absorber and Teflon anti convection layer. The test rig is described in Fan et al. (2009).

The modelling technique provides uncertainty estimates such as confidence intervals for the parameters, and furthermore enables statistical validation of the results. Such tests can also facilitate procedures for selecting the best model to use, which is a very non-trivial task.

E.1 Introduction

This paper presents a new statistical approach for modelling the heat dynamics of a solar thermal collector. The applied modelling technique facilitates application of detailed models on data sampled with a relatively high sample rate. It is demonstrated that this allows for parameter estimation with high accuracy to be achieved with measurements from a single day. In the present study 2 seconds values averaged to 30 seconds values are used. Conventional non-dynamical models - by some called pseudo-dynamical models - of solar collectors cannot use such a high sample rate due to auto-correlation of the errors caused by non-modelled dynamical effects. The applied models are based on stochastic differential equations (SDEs), which gives the possibility to combine physical

[1] www2.imm.dtu.dk/~ctsm/

and data-driven statistical modelling. Such models are called grey-box models. A very strong feature of grey-box models is that they provide the possibility to estimate hidden state variables, i.e. variables in the model which are not measured. This allows using the same data for fitting models, with which the system is lumped differently, i.e. the physical model of the system can either be a single-state or a multi-state lumped model, which can be required for different types of collectors. Furthermore the modelling technique facilitates application of statistical tests to determine which model is most suitable for the given data. This is important for model identification and the approach is demonstrated in the paper. The modelling is carried out based on measurements from a period of 9 consecutive days in the beginning of May 2010. None of the days could have been used for stationary testing that is still the most common test method for solar collectors. Stationary testing requires perfect stable clear weather around noon. The measurements were performed on a single glazed large area flat plate collector with selective absorber and Teflon anti convection layer. The collector was not brand new, but has been in operation for 15 years, which affects the parameter values compared to todays products of the similar design. The results from the grey-box models are compared with results from the standardized EN 12975 Quasi Dynamic Test Method (CEN, European committee for standardization, 2006), which is based on multiple linear regression (MLR) modelling, to see if the estimation results matches current test standards. Finally, a thorough discussion and perspectives of the technique are given.

The paper is arranged as follows. The next section is a presentation of the theory of the applied grey-box models, with a simple example. This is followed by a section with a description of the MLR models used and thereafter a section with a description of all the considered grey-box models. Then the results are presented, and finally a discussion and perspective is given before the paper ends with a conclusion.

Nomenclature

The same notation as in Perers (1997) are used as widely as possible.

Collector model parameters:

$F'(\tau\alpha)_{\mathrm{en}}$	Zero loss efficiency for direct radiation at normal incidence
$K_{\tau\alpha\mathrm{b}}(\theta)$	Incidence angle modifier for direct radiation
$K_{\tau\alpha\mathrm{d}}$	Incidence angle modifier for diffuse radiation
$F'U_0$	Heat loss coefficient at $(T_{\mathrm{a}} - T_{\mathrm{f}}) = 0$, $\left[\mathrm{W/(m^2K)}\right]$.
$F'U_1$	Temperature dependence of the heat loss coefficient, $\left[\mathrm{W/(m^2K^2)}\right]$.
$F'U_{\mathrm{w}}$	Wind dependence of the heat loss coefficient, $\left[\mathrm{Ws/(m^3K)}\right]$.
$(mC)_{\mathrm{e}}$	Effective thermal capacitance including piping for the collector, $\left[\mathrm{J/(m^2K)}\right]$.
C_{f}	Fluid thermal capacitance, $\left[\mathrm{J/(m^2K)}\right]$.
C_{m}	Collector thermal capacitance, $\left[\mathrm{J/(m^2K)}\right]$.
U_{fa}	Heat transmission coefficient from fluid to ambient, $\left[\mathrm{J/(Km^2)}\right]$.
U_{fm}	heat transmission coefficient from fluid to module, $\left[\mathrm{J/(Km^2)}\right]$.
U_{ma}	heat transmission coefficient from module to ambient, $\left[\mathrm{J/(Km^2)}\right]$.
n_{c}	Number of compartments

Measured variables:

G_{d}	Diffuse radiation onto the collector plane, $\left[\mathrm{W/m^2}\right]$.
G_{b}	Direct radiation onto the collector plane, $\left[\mathrm{W/m^2}\right]$.
T_{a}	Ambient air temperature near the collector, [°C].
T_{o}	Outlet temperature of the collector, [°C].
T_{i}	Temperature of the inlet to the collector, [°C].
Q_{f}	Flow of the fluid per square meter of collector, $\left[\mathrm{l/(sm^2)}\right]$.
θ	incidence angle for the direct solar radiation onto the collector plane, [radians].
w	Wind speed, [m/s].

Derived variables etc.:

T_{f}	Average temperature of the collector fluid, [°C].
T_{m}	Average temperature of the collector, [°C].
q_{u}	Collector power output, $\left[\mathrm{W/m^2}\right]$.
c_{f}	Specific heat capacity of the fluid, [J/(lK)].

E.2 Grey-box models of a dynamic system

A grey-box model is established using a combination of prior physical knowledge and statistics, i.e. information embedded in data Kristensen et al. (2004). The prior physical knowledge is formulated by a set of non-linear stochastic differential equations (SDEs), also called a stochastic non-linear state-space model in continuous time. The equations describe a lumped model of the heat dynamics of the system.

The output of the solar collector is calculated by

$$q_{\mathrm{u}} = c_{\mathrm{f}} Q_{\mathrm{f}} (T_{\mathrm{o}} - T_{\mathrm{i}}) \tag{E.1}$$

where T_{o} is the outlet temperature and T_{i} is the inlet temperature of the fluid. The output q_{u} is power output per square meter of collector aperture area and Q_{f} is flow per the same area. From Perers (1997) it is known that the output of a standard flat plate collector in first order accuracy level can be described by the heat balance

$$\begin{aligned} c_{\mathrm{f}} Q_{\mathrm{f}} (T_{\mathrm{o}} - T_{\mathrm{i}}) = {} & F'(\tau\alpha)_{\mathrm{en}} K_{\tau\alpha\mathrm{b}}(\theta) G_{\mathrm{b}} + F'(\tau\alpha)_{\mathrm{en}} K_{\tau\alpha\mathrm{d}} G_{\mathrm{d}} \\ & - F' U_0 (T_{\mathrm{f}} - T_{\mathrm{a}}) - (mC)_{\mathrm{e}} \frac{dT_{\mathrm{f}}}{dt} \end{aligned} \tag{E.2}$$

For explanation of the symbols, see page 128. A linear temperature profile through the collector is applied by modelling the fluid temperature as a simple average

$$T_{\mathrm{f}} = \frac{T_{\mathrm{o}} + T_{\mathrm{i}}}{2} \tag{E.3}$$

The differential of the fluid temperature can then be written as

$$\frac{dT_{\mathrm{f}}}{dt} = \frac{1}{2}\frac{dT_{\mathrm{o}}}{dt} + \frac{1}{2}\frac{dT_{\mathrm{i}}}{dt} \tag{E.4}$$

which for a constant inlet temperature is

$$\frac{dT_{\mathrm{f}}}{dt} = \frac{1}{2}\frac{dT_{\mathrm{o}}}{dt} \tag{E.5}$$

This substitution, together with the addition of a noise term, is used to form the SDE

$$\begin{aligned} dT_{\mathrm{o}} = {} & \Big(F' U_0 (T_{\mathrm{a}} - T_{\mathrm{f}}) + c_{\mathrm{f}} Q_{\mathrm{f}} (T_{\mathrm{i}} - T_{\mathrm{o}}) \\ & + F'(\tau\alpha)_{\mathrm{en}} K_{\tau\alpha\mathrm{b}}(\theta) G_{\mathrm{b}} + F'(\tau\alpha)_{\mathrm{en}} K_{\tau\alpha\mathrm{d}} G_{\mathrm{d}} \Big) \frac{2}{(mC)_{\mathrm{e}}} dt + \sigma d\omega \end{aligned} \tag{E.6}$$

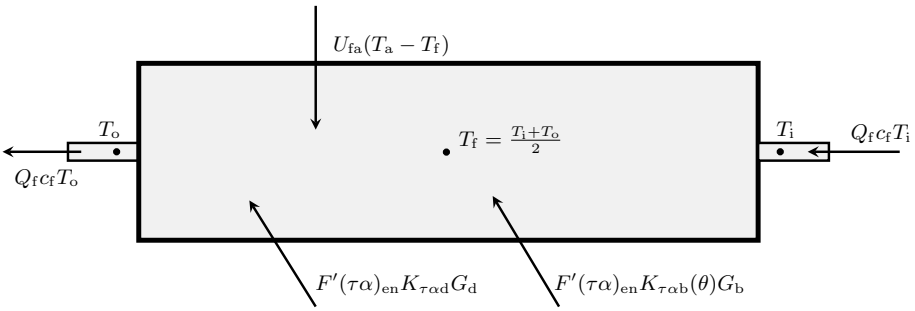

Figure E.1: Diagram of *ToComp1* illustrating all the energy flows included in the model.

which describes the heat dynamics for the collector in the simplest grey-box model considered in the paper. It is denoted as *ToComp1*. In grey-box terminology this is called the system equation of the state-space model. The noise term $\sigma d\omega$ is called the system noise and consist of increments of $\{\omega\}$, which is a standard Wiener process, and σ^2, which is the incremental variance of the Wiener process. In this model the collector is lumped into one single part and the state variable is the outlet temperature T_{o}. An illustration of the model is found in Figure E.1.

The physical model part is coupled with the data-driven model part with which the information embedded in observed data is used for parameter estimation. The data-driven part in the considered example is represented by the discrete time measurement equation

$$Y_k = T_{\mathrm{o}k} + e_k \tag{E.7}$$

where k is the point in time t_k of a measurement, Y_k is the measured outlet temperature, and e_k is the measurement error, which is assumed to be a Gaussian white noise process with variance σ^2. This assumption - plus the assumption that W is a Wiener process - enables evaluation and tests of the performance of the model, since such tests can show if the physical model is consistent with the observed heat dynamics of the collector.

E.2.1 Maximum likelihood estimation of parameters

Given a grey-box model, as described above, maximum likelihood estimates of the parameters can be obtained. Let the N observations be represented by

$$\mathcal{Y}_N = [Y_N, Y_{N-1}, \ldots, Y_1, Y_0] \tag{E.8}$$

then the likelihood function is the joint probability density

$$L(\theta; \mathcal{Y}_N) = \left(\prod_{k=1}^{N} p(Y_k | \mathcal{Y}_{k-1}, \theta) \right) p(Y_0 | \theta) \tag{E.9}$$

where $p(Y_k|\mathcal{Y}_{k-1}, \theta)$ is a conditional density denoting the probability of observing Y_k given the previous observations and the parameters θ, and where $p(Y_0|\theta)$ is a parameterization of the starting conditions Kristensen et al. (2004). The maximum likelihood estimates of the parameters are then found by

$$\hat{\theta} = \arg\max_{\theta} \left\{ L(\theta; \mathcal{Y}_N) \right\} \tag{E.10}$$

Due to the previously mentioned assumptions about the system and measurement noise, it follows that the conditional densities in Equation (E.10) can be well approximated by Gaussian densities. Hence an extended Kalman filter can be used to calculate the likelihood function, and an optimization algorithm can be applied to maximize it, thereby calculating the maximum likelihood estimates, see Kristensen et al. (2004) for a detailed discussion. This is implemented in the computer software CTSM, which has been used for carrying out the parameter estimation. See more about the methods and software at [2] and in Kristensen and Madsen (2003).

E.3 Experimental setup and data

The experiments are described by Fan et al. (2009) and were carried out in the spring of 2010. The measurements were obtained with a 2 seconds sample interval. For the present study models are identified for both 30 seconds and 10 minutes average values. The data resampled to 10 minute average values is plotted in Figure E.2. Only time points where the angle of incidence is lower than 84 degrees are used. For the parameter estimation it is important to acquire a period, for which the input signals are as uncorrelated as possible and cover the typical range of operation. Periods with full cloud cover are not feasible, since there is not enough variation in the direct radiation and in periods with no cloud cover the radiation and the module temperature is highly correlated. Hence days with varying cloud cover are most appropriate and these days are the most common in most locations where people traditionally live.

[2] `www.imm.dtu.dk/~ctsm`

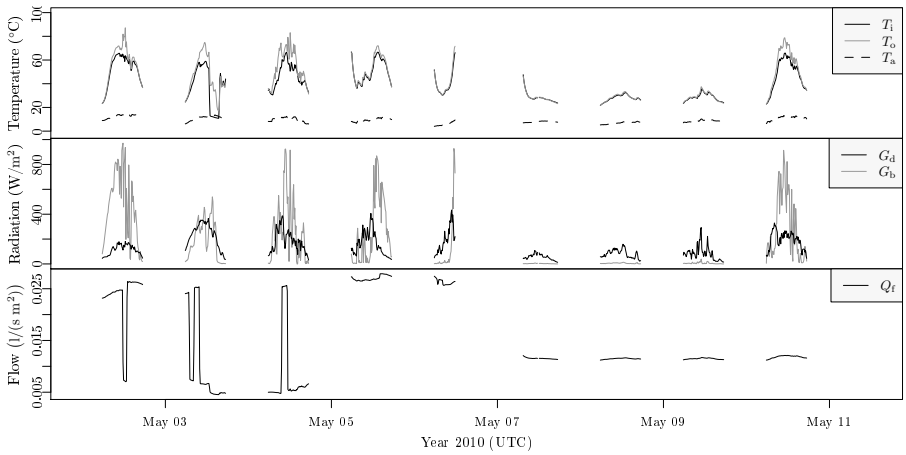

Figure E.2: The data as 10 minutes averaged values. The upper plot is the measured temperatures, the middle plot is the diffuse and direct (beam) radiation, and the lowest plot is the fluid flow.

E.4 Multiple linear regression models

The EN 12975 Quasi Dynamic Test Method (CEN, European committee for standardization, 2006) is applied to have a reference for the results from the new proposed method. The method is based on multiple linear regression (MLR) modelling, where down to 5 minutes average values are recommended. The data was resampled to 10 minutes averages, which for all 9 days gives 593 time points. MLR modelling with 5 minutes averages was tried and the results were only marginally different. The following model structure is applied

$$q_t^{\mathrm{u}} = F'(\tau\alpha)_{\mathrm{en}} K_{\tau\alpha\mathrm{b}}(\theta) G_t^{\mathrm{b}} + F'(\tau\alpha)_{\mathrm{en}} K_{\tau\alpha\mathrm{d}} G_t^{\mathrm{d}} + F'U_0 \Delta T_t + F'U_1 \Delta T_t^2 - F'U_{\mathrm{w}} \Delta T_t w_t - (mC)_{\mathrm{e}} \frac{dT_t^{\mathrm{f}}}{dt} + e_t \tag{E.11}$$

where $\Delta T_t = T_t^{\mathrm{a}} - T_t^{\mathrm{f}}$. Three models are fitted: *MLR1* without $F'U_1$ and $F'U_{\mathrm{w}}$, *MLR2* without $F'U_1$, and *MLR3* with all inputs.

E.5 Applied grey-box models

This section gives an overview of the applied grey-box models and the parts of the data on which the parameter estimation was carried out. First the single

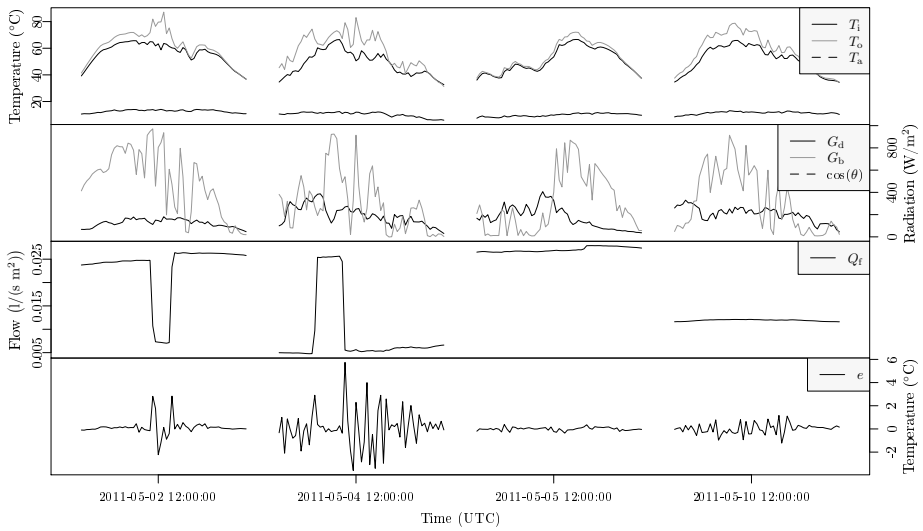

Figure E.3: The 10 minutes averaged values from days where the model *ToComp1* is fitted. The upper plot is of the inlet-, outlet-, and the ambient temperature. Below this is shown a plot of the direct- and diffuse solar radiation, followed by a plot of the fluid flow. The lowest plot is the residuals from the fit from each day, this is referred to in a later in the paper.

state grey-box model *ToComp1*, described in Section E.2 was fitted to 10 minutes average values on the days with varying cloud cover. This data is plotted in Figure E.3. The model was fitted to data from each day separately and finally to all the data from four days pooled together. In addition to the *ToComp1* model four other grey-box models have been fitted to the data from the 10'th of May resampled to 30 second average values. This gives $N = 1413$ data points, which are plotted in Figure E.4. The additional four models are expanded as more detailed versions of *ToComp1*. There are two ways to expand the model: either more inputs (explanatory variables) can be used, or - since the models are lumped models - a better representation can maybe be achieved by lumping the system into more parts (also called compartments, states, zones, or nodes). The latter approach is considered in the following. The first two expanded models are made more detailed by lumping the collector into more than one compartment in the flow direction of the collector fluid, such that the temperature of the collector is represented by two or more temperature state variables. This allows for a better representation of the temperature differences between the inlet - the cold side when solar radiation level is high - and the outlet of the collector. Furthermore this also gives a better description of the delay introduced since it takes time for the fluid to flow through the collector. For the current setup

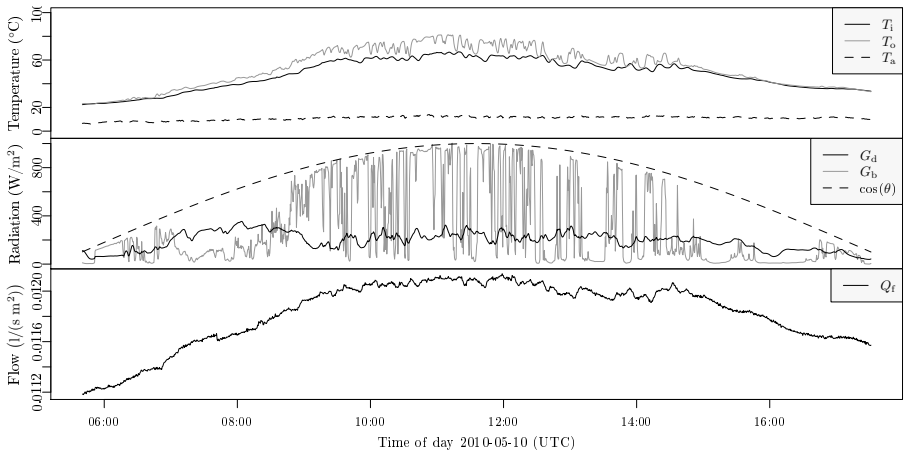

Figure E.4: The 30 seconds averaged data for which the modelling is applied. The upper plot is of the inlet-, outlet-, and the ambient temperature. Below this is a plot of the direct- and diffuse solar radiation, followed by the plot of the fluid flow.

and the flow of the 10'th of May, this is around 1 minute. These two models are denoted by *ToComp2* and *ToComp3*. The third expanded model is denoted by *ToTmComp1* and in this model the collector is lumped in two parts: one representing the fluid and one representing the solid part of the collector. This is a better description of the system, in which the solar radiation first heats up the collector which then heats up the fluid. Finally, the fourth expanded model *TmToComp2* is a combination of the two approaches, where the collector is first divided in two parts - one for the fluid and one for the collector - which then each are divided into two compartments in the flow direction of the fluid.

E.5.1 Models with multiple compartments in the flow direction

The *ToComp1* model can be expanded to a n_c compartment model with the system equations

$$\begin{aligned}
dT_{o1} &= \Big(F'U_0(T_a - T_{f1}) + n_c c_f Q_f(T_i - T_{o1}) + F'(\tau\alpha)_{en}K_{\tau\alpha b}(\theta)G_b \\
&\quad + F'(\tau\alpha)_{en}K_{\tau\alpha d}G_d\Big)\frac{2}{(mC)_e}dt + \sigma_1 d\omega_1 \\
dT_{o2} &= \Big(F'U_0(T_a - T_{f2}) + n_c c_f Q_f(T_{o1} - T_{o2}) + F'(\tau\alpha)_{en}K_{\tau\alpha b}(\theta)G_b \\
&\quad + F'(\tau\alpha)_{en}K_{\tau\alpha d}G_d\Big)\frac{2}{(mC)_e}dt + \sigma_2 d\omega_2 \\
&\vdots \\
dT_{on_c} &= \Big(F'U_0(T_a - T_{fn_c}) + n_c c_f Q_f(T_{o(n_c-1)} - T_{on_c}) + F'(\tau\alpha)_{en}K_{\tau\alpha b}(\theta)G_b \\
&\quad + F'(\tau\alpha)_{en}K_{\tau\alpha d}G_d\Big)\frac{2}{(mC)_e}dt + \sigma_{n_c} d\omega_{n_c}
\end{aligned} \tag{E.12}$$

where n_c is the number of compartments. The accompanying measurement equation is

$$Y_k = T_{on_c k} + e_k \tag{E.13}$$

Two models of this type are fitted to the data: *ToComp2* with two compartments, and *ToComp3* with three compartments. A diagram illustrating *ToComp2* is shown in Figure E.5

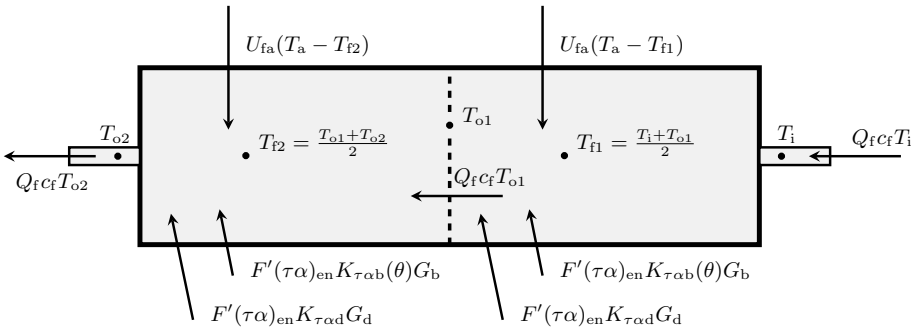

Figure E.5: The *ToComp2* model with two compartments in the flow direction of the fluid.

E.5.2 Models divided into a collector and a fluid part

The *TmToComp1* model illustrated in Figure E.6, where the panel is divided into two parts, has the system equation

$$\begin{aligned} dT_{\mathrm{m}} &= \Big(F'(\tau\alpha)_{\mathrm{en}}K_{\tau\alpha\mathrm{b}}(\theta)G_{\mathrm{b}} + F'(\tau\alpha)_{\mathrm{en}}K_{\tau\alpha\mathrm{d}}G_{\mathrm{d}} + U_{\mathrm{fm}}(T_{\mathrm{f}} - T_{\mathrm{m}}) \\ &\quad + U_{\mathrm{ma}}(T_{\mathrm{a}} - T_{\mathrm{m}})\Big)\frac{1}{(mC)_{\mathrm{e}}}dt + \sigma_m d\omega_m \\ dT_{\mathrm{o}} &= \Big(U_{\mathrm{fm}}(T_{\mathrm{m}} - T_{\mathrm{f}}) + c_{\mathrm{f}}Q_{\mathrm{f}}(T_{\mathrm{i}} - T_{\mathrm{o}})\Big)\frac{2}{(mC)_{\mathrm{e}}}dt + \sigma_o d\omega_o \end{aligned} \tag{E.14}$$

It is seen that the solar radiation enters the collector part, which then heats up the fluid by conduction. Of the considered models the most detailed model is *TmToComp2*, in which the collector is both divided into two parts and 2 compartments in the fluid flow direction for each part. The following system equations is formulated for a model with two parts having each n_{c} compartments

$$\begin{aligned} dT_{\mathrm{m1}} &= \Big(F'(\tau\alpha)_{\mathrm{en}}K_{\tau\alpha\mathrm{b}}(\theta)G_{\mathrm{b}} + F'(\tau\alpha)_{\mathrm{en}}K_{\tau\alpha\mathrm{d}}G_{\mathrm{d}} + U_{\mathrm{fm}}(T_{\mathrm{f1}} - T_{\mathrm{m1}}) \\ &\quad + U_{\mathrm{ma}}(T_{\mathrm{a}} - T_{\mathrm{m1}})\Big)\frac{1}{(mC)_{\mathrm{e}}}dt + \sigma_{\mathrm{m1}}d\omega_{\mathrm{m1}} \\ dT_{\mathrm{o1}} &= \Big(U_{\mathrm{fm}}(T_{\mathrm{m1}} - T_{\mathrm{f1}}) + n_{\mathrm{c}}c_{\mathrm{f}}Q_{\mathrm{f}}(T_{\mathrm{i}} - T_{\mathrm{o1}})\Big)\frac{2}{(mC)_{\mathrm{e}}}dt + \sigma_{\mathrm{o1}}d\omega_{\mathrm{o1}} \\ dT_{\mathrm{m2}} &= \Big(F'(\tau\alpha)_{\mathrm{en}}K_{\tau\alpha\mathrm{b}}(\theta)G_{\mathrm{b}} + F'(\tau\alpha)_{\mathrm{en}}K_{\tau\alpha\mathrm{d}}G_{\mathrm{d}} + U_{\mathrm{fm}}(T_{\mathrm{f2}} - T_{\mathrm{m2}}) \\ &\quad + U_{\mathrm{ma}}(T_{\mathrm{a}} - T_{\mathrm{m2}})\Big)\frac{1}{(mC)_{\mathrm{e}}}dt + \sigma_{\mathrm{m2}}d\omega_{\mathrm{m2}} \\ dT_{\mathrm{o2}} &= \Big(U_{\mathrm{fm}}(T_{\mathrm{m2}} - T_{\mathrm{f2}}) + n_{\mathrm{c}}c_{\mathrm{f}}Q_{\mathrm{f}}(T_{\mathrm{o1}} - T_{\mathrm{o2}})\Big)\frac{2}{(mC)_{\mathrm{e}}}dt + \sigma_{\mathrm{o2}}d\omega_{\mathrm{o2}} \\ &\vdots \\ dT_{\mathrm{mn_c}} &= \Big(F'(\tau\alpha)_{\mathrm{en}}K_{\tau\alpha\mathrm{b}}(\theta)G_{\mathrm{b}} + F'(\tau\alpha)_{\mathrm{en}}K_{\tau\alpha\mathrm{d}}G_{\mathrm{d}} + U_{\mathrm{fm}}(T_{\mathrm{fn_c}} - T_{\mathrm{mn_c}}) \\ &\quad + U_{\mathrm{ma}}(T_{\mathrm{a}} - T_{\mathrm{mn_c}})\Big)\frac{1}{(mC)_{\mathrm{e}}}dt + \sigma_{\mathrm{mn_c}}d\omega_{\mathrm{mn_c}} \\ dT_{\mathrm{on_c}} &= \Big(U_{\mathrm{fm}}(T_{\mathrm{mn_c}} - T_{\mathrm{fn_c}}) + n_{\mathrm{c}}c_{\mathrm{f}}Q_{\mathrm{f}}(T_{\mathrm{o1}} - T_{\mathrm{on_c}})\Big)\frac{2}{(mC)_{\mathrm{e}}}dt + \sigma_{\mathrm{on_c}}d\omega_{\mathrm{on_c}} \end{aligned} \tag{E.15}$$

i.e. the *TmToComp2* model has $n_{\mathrm{c}} = 2$.

E.6 Results

In this section the results of the parameter estimation with the described models are presented. Firstly, the results from the traditional MLR models fitted on the entire data set of 10 minutes values is presented, secondly from grey-box model *ToComp1* fitted on individual days of 10 minutes values, and finally all grey-box models fitted on 30 seconds values from the 10'th of May. The parameter estimates together with the their standard deviation are presented in tables, and time series of the residuals together with other relevant error measures are plotted. A short outline of the model identification carried out is also provided.

E.6.1 MLR models

The parameter estimates are listed in Table E.1. The estimates are clearly within the typical range for this type of collector, see Perers (1993) and Solar Keymark homepage (Solar Keymark, 2011). The collector under test has been in operation for 15 years, this affects the parameter values compared to todays products. The standard deviations show that the parameters are very accurately determined. The only non-significant term are $F'U_1$ in *MLR3*, which leads the conclusion that *MLR2* is the most appropriate model of the three. For evaluation of the model fit the measured collector output versus the predicted is plotted in Figure E.7. It is seen that the measured output is predicted very well, although it does seems like the variance increase slightly with the output. This is most likely due to the periods with low flow rate for some of the days. Furthermore the inlet temperature variation range is not fully as high as specified in the standard for the selected days.

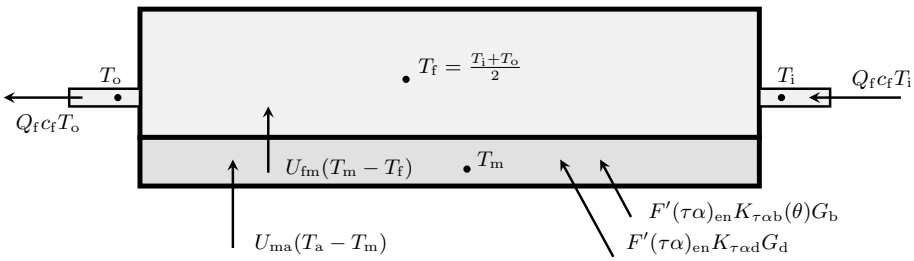

Figure E.6: Diagram illustrating the *TmToComp1* model. The collector is divided into a part representing the fluid and another part representing the collector.

Parameter	*MLR1*		*MLR2*		*MLR3*		Units
$F'(\tau\alpha)_{\mathrm{en}}$	0.737	(0.0031)	0.741	(0.0030)	0.746	(0.0043)	
b_0	0.166		0.172		0.175		
$K_{\tau\alpha\mathrm{d}}$	0.891		0.904		0.895		
$F'U_0$	2.18	(0.45)	2.13	(0.045)	2.02	(0.082)	$[\mathrm{W/(m^2K)}]$
$F'U_1$					0.0031*	(0.0020)	$[\mathrm{W/(m^2K)}]$
$F'U_{\mathrm{w}}$			0.192	(0.034)	0.179	(0.035)	$[\mathrm{W/(m^2K)}]$
$(mC)_{\mathrm{e}}$	4699	(130)	4751	(127)	4788	(129)	$[\mathrm{J/(m^2K)}]$

Table E.1: Parameter estimates with MLR models. The standard deviation of the estimate is in parenthesis to the right of the estimated value. Insignificant terms are marked with *.

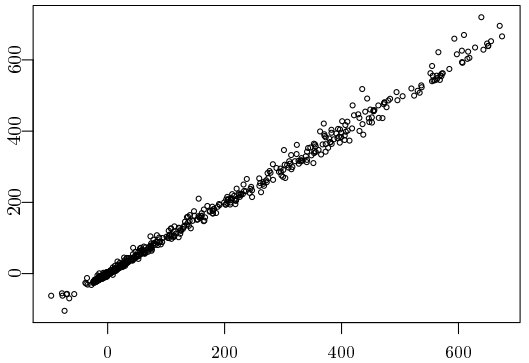

Figure E.7: Measured versus the predicted collector output from *MLR2*.

E.6.2 ToComp1 fitted to 10 minutes values

The single state grey-box model defined in Equation (E.6) is fitted to both 10 minutes values from four separate days and all four pooled together. The estimated parameter are listed in Table E.2. Clearly the parameter estimates matches the estimates from the MLR models quite well considering the standard deviations, especially the parameters $F'(\tau\alpha)_{\mathrm{en}}$ and $F'U_0$, which are the most important parameters for evaluation of the collector performance. A very apparent deviation of the results between the days is that the lowest uncertainty is found on the 5'th of May. This is not a surprise considering a plot of the residuals, which is shown in the lowest plot of Figure E.3. The level of the residuals from the fit to this day are smaller than for the other days, and this is apparently due to the level of the fluid flow, which is plotted above the residuals in the figure. The parameter estimates based on the four days pooled together seems like a compromise between the estimates from the single days.

	2011-05-02		2011-05-04		2011-05-05	
$F'(\tau\alpha)_{\mathrm{en}}$	0.755	(0.032)	0.785	(0.032)	0.746	(0.0086)
b_0	0.204	(0.039)	0.201	(0.046)	0.18	(0.017)
$K_{\tau\alpha\mathrm{d}}$	0.903	(0.42)	0.857	(0.11)	0.819	(0.027)
$F'U_0$	2.07	(1.1)	2.4	(0.35)	1.73	(0.13)
$(mC)_{\mathrm{e}}$	6050	(1060)	6200	(1130)	5040	(279)
	2011-05-10		Pooled			
$F'(\tau\alpha)_{\mathrm{en}}$	0.758	(0.014)	0.763	(0.011)		
b_0	0.182	(0.023)	0.195	(0.020)		
$K_{\tau\alpha\mathrm{d}}$	0.867	(0.049)	0.839	(0.034)		
$F'U_0$	2.16	(0.26)	2.05	(0.18)		
$(mC)_{\mathrm{e}}$	5020	(92)	5666	(638)		

Table E.2: Parameter estimates from *ToComp1* fitted to 10 minutes values from single days and all four days pooled. The standard deviation is given in parenthesis to the right of the estimate.

E.6.3 Grey-box models fitted to 30 seconds values

The five grey-box models described are fitted to the data from the 10'th of May resampled to 30 seconds averages. The parameter estimates are listed in Table E.3. First, it is noticed that the parameters of the three models prefixed with *To* are not representing the same physical entities as they do in the models prefixed with *ToTm*, since the collector is lumped differently in the models. The increase of the value of $F'(\tau\alpha)_{\mathrm{en}}$ from *To* to *ToTm* models is found to be consistent with the physical representation, since the reference temperature is closer to the absorber surface. This means that the estimated optical parameter for the *ToTm* models is rather $\tau\alpha$. The value F' is in the range of 0.95 for this collector design, which leads to an estimate of $F'(\tau\alpha)_{\mathrm{en}}$ to 0.752 for *ToTmComp2*.

Plots of the residual series from each model are shown in Figure E.8. Clearly the level of the residuals decrease from the upper to the lower plot and the highest errors occur when a cloud passes by and the level of direct solar radiation shifts rapidly. The decreased level of the variation of the residuals indicates that the more detailed models are better. To verify this, statistical likelihood-ratio tests is applied as described by Bacher and Madsen (2011). The log-likelihood of the fit for each model is listed in Table E.4, together with the number of parameters, and the p-value of tests for model expansion. The tests for expansion is a model versus the expanded model a single step to the right in the table, except for *nl2TmToComp1*, from which the expansion is from *nl2ToComp2*. The results of the tests are very clear, all expansions are significant. Hence it is concluded

Prm.	ToComp1		ToComp2		ToComp3	
$F'(\tau\alpha)_{\mathrm{en}}$	0.767	(0.0036)	0.751	(0.0027)	0.743	(0.0015)
b_0	0.172	(0.0063)	0.177	(0.0017)	0.18	(0.00044)
$K_{\tau\alpha\mathrm{d}}$	0.942	(0.015)	0.933	(0.0042)	0.931	(0.002)
U_{fa}	2.55	(0.076)	2.31	(0.049)	2.2	(0.023)
U_{fm}						
U_{ma}						
C_{f}	6960	(80)	8020	(17)	8580	(36)
C_{m}						
Prm.	TmToComp1		TmToComp2			
$F'(\tau\alpha)_{\mathrm{en}}$	0.816	(0.0025)	0.792	(0.00096)		
b_0	0.188	(0.0038)	0.189	(0.00067)		
$K_{\tau\alpha\mathrm{d}}$	0.929	(0.008)	0.927	(0.0021)		
U_{fa}						
U_{fm}	49.8	(2.5)	83.7	(0.83)		
U_{ma}	2.37	(0.042)	2.22	(0.016)		
C_{f}	3750	(114)	3390	(54)		
C_{m}	962	(64)	1690	(22)		

Table E.3: The parameter estimates from the grey-box models fitted to 30 seconds values from the 10'th of May. Note that the parameters represent different physical entities from the three first model (prefixed with *To*) to the last two models (prefixed with *TmTo*) and therefore cannot be directly compared. For each estimate the standard deviation is given in parenthesis to the right of the estimate.

that *nl2TmToComp2* is the most suitable model of these five models and that it might very well be, that the model could be further expanded. Finally, the auto-correlation function (ACF) and the cumulated periodogram (CP) Madsen (2007) of the residuals are shown in Figure E.9. The dashed blue lines indicate 95% confidence intervals for a white noise. According to theory, presented in Section E.2, then if the residual series are white noise this indicates that the grey-box model is consistent with the observed heat dynamics of the collector. From the ACF and CP it is seen that the residuals are close to having white noise properties. Interestingly it is seen that residuals from *ToComp1* are more white noise like than the residuals from *TmToComp1*. It is found that this is caused by a low signal to noise ratio in the residuals for *ToTmComp1*, i.e. the dominating errors are on a high frequency which have characteristics like white noise. As the detailed models includes the faster dynamics, the high frequency errors are decreased, and they do not "hide" the remaining signal components in the residuals. However for the most detailed model almost all the systematic variation in the data is described.

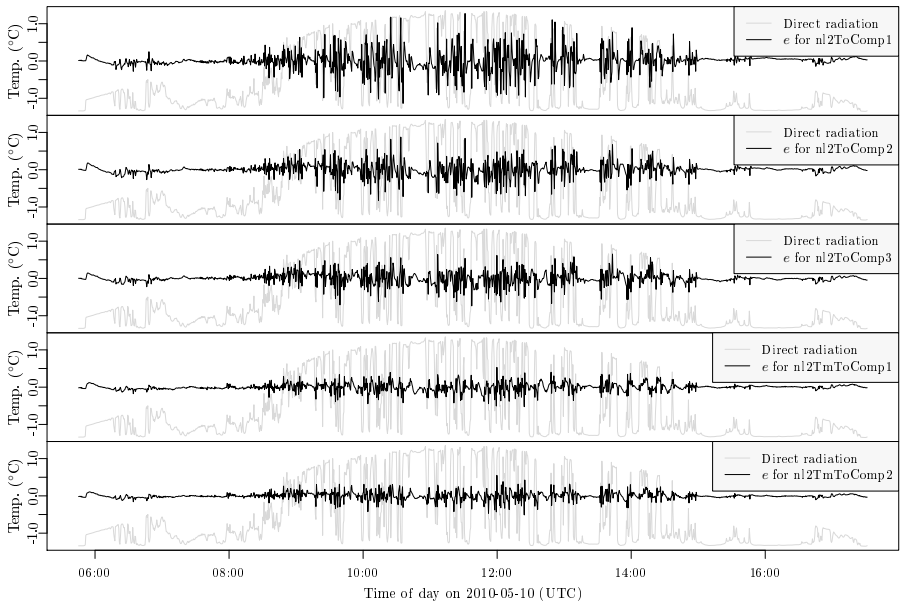

Figure E.8: The residual series from the grey-box models fitted to 30 seconds values from the 10'th of May. The greyed series are the direct solar radiation.

	nl2ToComp1	nl2ToComp2	nl2ToComp3
Log-likelihood	-35.51	454.8	661
Number of prm.	9	12	14
p-value		≈ 0	≈ 0
	nl2TmToComp1	nl2TmToComp2	
Log-likelihood	1185	1307	
Number of prm.	13	18	
p-value	≈ 0	≈ 0	

Table E.4: Log-likelihood, number of parameters, and p-value of likelihood-ratio tests for model expansion for each of the grey-box models.

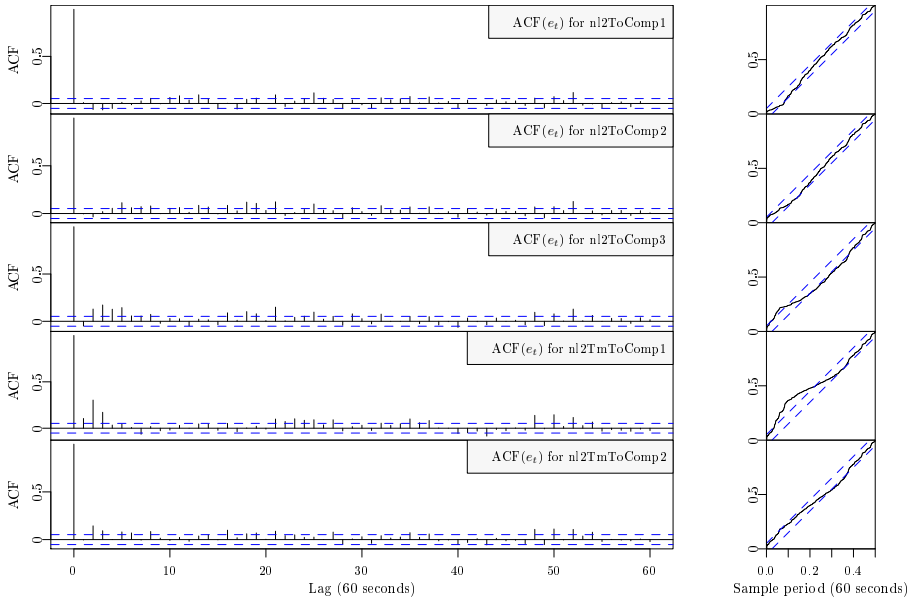

Figure E.9: Plots of the auto-correlation function (ACF) and the cumulated periodogram of the residuals from each of the grey-box models fitted on 30 seconds values.

E.7 Discussion and applications

In general the results from the MLR models and the grey-box are found to match well, but it is noted that the result the from grey-box model *ToComp1* fitted on separate days - which have different conditions, especially in the fluid flow level - gives some variation to the estimates. Therefore it is concluded that attention has to be put on the experimental design in order to ensure stable and accurate parameter estimation for collector testing with grey-box models. Regarding the more detailed grey-box models fitted to 30 seconds values, it is found that since the likelihood is not saturated, i.e. the likelihood-ratio tests are very significant, further expansion of the *TmToComp2* is still possible. From the plots of the residuals in Figure E.8, it is seen that the error level certainly is highest just after the direct radiation shifts its level very rapidly, and it is this effect that seems to be improved as the more detailed models are used. Hence the main improvement from the one-state model *ToComp1* to the multi-state models are in the description of the fast dynamics, which includes the delay caused by movement of the fluid through the collector, e.g. when the direct radiation shifts from a high to a low level, the fluid passing out of the collector are still hot for some time. This also indicates the importance of the experiment design, since for dynamic condition the frequency, with which the system is excited, affect which grey-box model is optimal. For example if the direct radiation varies with a lower frequency, a simpler model might be in favour over more complex models, whereas for variation with a higher frequency the inclusion of the fast dynamics are more important. Therefore if the main excitation of the system, i.e. the direct radiation, can be controlled, it will be possible to achieve fast and accurate parameter estimation. This could be carried out with a simple shadowing device, which should be controlled with PRBS signal to gain maximum information of the heat dynamics of the system (Madsen and Holst, 1995). Higher accuracy can also be achieved with more systematic variation of the inlet temperature, this also applies for the MLR modelling. The right experiment design will allow inclusion of night measurements - which will improve the separation of heat loss and radiation effects and thereby more accurate estimation - and furthermore allow for inclusion of more effects, such as wind and non-linear radiation effects between the collector and the surroundings. Finally, dividing the collector into more parts, e.g. one representing the fluid, one representing the metal, and one representing the surrounding collector body could be tried.

E.7.1 Applications

The most apparent application of grey-box modelling of the heat dynamics of solar collectors are for the development of fast and accurate performance testing,

especially for some types of collectors multi-state models are needed to obtain a required level of accuracy. Especially vacuum tube collectors of dewar type can have an extra time delay due to the high thermal resistance between the heat transfer fluid and absorber surface that is not fully taken up by the present collector model used for performance testing. The new approach described here, particularly with the *TmTo* models, has the potential to deal with this in an accurate way. Additional applications include optimization of operation with model predictive control, which the grey-box models are perfectly suited for. Especially larger solar thermal plants might be able to gain much in performance by applying grey-box modelling and model predictive control.

E.8 Conclusion

Successful modelling of a the heat dynamics of a solar collector with grey-box models has been carried out. The results have been compared to the EN-standard MLR modelling and they are in agreement. It is shown that high accuracy parameter estimates was obtained with measurements from a single day resampled to 30 seconds average values. This will enable lowering of testing time significantly compared to current test methods. Highly detailed models of the heat dynamics of the solar collector can be applied, which can be useful for many types of collectors. It is found that the conditions under which the experiment was carried out influence the parameter estimates. Therefore it is concluded that experiment design is the key to achievement of fast, reliable and high accuracy collector testing methods with grey-box models. Experiments with PRBS variation of direct radiation with shadowing device should be carried out to obtain higher accuracy and reproducibility of the results, and finally models with more explanatory variables, such as wind and long-wave radiation should be further elaborated.

References

P. Bacher and H. Madsen. Identifying suitable models for the heat dynamics of buildings. *Energy & Buildings*, 43(7):1511–1522, 2011. ISSN 03787788. doi: 10.1016/j.enbuild.2011.02.005.

CEN, European committee for standardization. En 12975-2:2006, thermal solar systems and components - collectors - part 2: Test methods, 2006.

J. Fan, Z. Chen, S. Furbo, B. Perers, and B. Karlsson. Efficiency and lifetime of

solar collectors for solar heating plants. Proceedings of the ISES Solar World Congress 2009: Renewable Energy Shaping Our Future, 2009.

S. Fischer, W. Heidemann, H. Müller-Steinhagen, B. Perers, P. Bergquist, and B. Hellström. Collector test method under quasi-dynamic conditions according to the european standard en 12975-2. *Solar Energy*, 76(1-3):117–123, 2004. ISSN 0038092x. doi: 10.1016/j.solener.2003.07.021.

N. Friling, M. J. Jiménez, H. Bloem, and H. Madsen. Modelling the heat dynamics of building integrated and ventilated photovoltaic modules. *Energy and Buildings*, 41(10):1051–1057, 2009. ISSN 03787788.

N. R. Kristensen and H. Madsen. Continuous time stochastic modelling, CTSM 2.3 - mathematics guide. Technical report, DTU, 2003.

N. R. Kristensen, H. Madsen, and S. B. Jørgensen. Parameter estimation in stochastic grey-box models. *Automatica*, 40(2):225 – 237, 2004. ISSN 0005-1098. doi: DOI:10.1016/j.automatica.2003.10.001.

H. Madsen. *Time Series Analysis*. Chapman & Hall, 2007.

H. Madsen and J. Holst. Estimation of continuous-time models for the heat dynamics of a building. *Energy and Buildings*, 22(1):67–79, 1995. ISSN 03787788.

B. Perers. Dynamic method for solar collector array testing and evaluation with standard database and simulation programs. *Solar Energy*, 50(6):517–526, 1993. ISSN 0038092x.

B. Perers. An improved dynamic solar collector test method for determination of non-linear optical and thermal characteristics with multiple regression. *Solar Energy*, 59(4-6):163–178, 1997. ISSN 0038092x.

Solar Keymark. Homepage and database (all tested collectors according to EN12975 in Europe), 2011. URL `http://solarkey.dk/solarkeymarkdata/qCollectorCertificates/ShowQCollectorCertificatesTable.aspx`.

Paper F

Short-term heat load forecasting for single family houses

Authors:
Peder Bacher[1], Henrik Madsen[1], Henrik Aalborg Nielsen[2], and Bengt Perers[3]

Submitted to:
Buildings and Energy (April 2012).

[1]DTU Informatics, Richard Pedersens Plads, Building 321, DK-2800 Lyngby, Denmark
[2]ENFOR A/S, Lyngsø Allé 3, DK-2970 Hørsholm, Denmark (URL: www.enfor.eu)
[3]DTU Civil Engineering, Brovej, Building 118, DK-2800 Lyngby, Denmark

Abstract

This paper present a method for forecasting the load for space heating in a single-family house. The forecasting model is built using data from sixteen houses in Sønderborg, Denmark, combined with local climate measurements and weather forecasts. Every hour the hourly heat load for each house the following two days is forecasted. The underlying basis of the method is physical knowledge of building heat dynamics, which, combined with statistical models, leads to a grey-box modelling approach. The forecast models are adaptive linear time-series models and the climate inputs used are: ambient temperature, global radiation, and wind speed. The adaptivity over time is achieved with a recursive least squares scheme, which is computationally very efficient. Also included is a diurnal curve for modelling patterns in the residents behavior, for example a nightly setback. The models are optimized to fit the individual characteristics for each house, such as the level of optimal adaptivity and the thermal dynamical response of the building, which are modelled with simple transfer functions. The identification of a model, which is suitable for application to all the houses, is carried out. The results show that the one-step (one hour) ahead errors are close to white noise and that practically all correlation to the climate variables are removed with the model. Furthermore the analysis of the results shows that the main sources to forecast errors are related to: unpredictable high frequency variations in the heat load signal (predominant only for some houses), shifts in resident behavior, and uncertainty of the weather forecasts for longer horizons, especially the solar radiation is a challenge.

F.1 Introduction

The transition to an energy system based on renewables requires methods for forecasting of energy load and production. In Denmark around 40% of the total energy consumption is related to buildings and around 29% of the energy for space heating is covered by individual oil or gas fired furnaces (Danish Commission on Climate Change Policy, 2010b), which is neither an economically feasible nor environmentally friendly technology. The Danish Commission on Climate Change Policy recommends replacement with alternative technologies, especially heat pumps, since this is one of the socio-economically cheapest initiatives in the transition to an energy system without fossil fuels in Denmark. Hence, new and alternative technologies for building space heating based on renewable energy production are of high interest, both for individual and district heating. Especially electrical heating systems since large amounts of wind power are available, which creates a need for flexible load in order to absorb the

volatile production. As the level of electrical load increase, even load-shifting in shorter periods of time for peak-shaving of the diurnal electrical consumption is a valuable service to the grid (Danish Commission on Climate Change Policy, 2010a). Flexible load can be achieved with thermal energy buffering, both in individual heating and district heating, where huge thermal storage capacity is available. Several studies are considering the possibilities for flexible heating, for example Pedersen et al. (2011) and Chen (2001) who presents methods for energy storage in the thermal mass of the building, and Reddy et al. (1991) and Henze et al. (2004) who consider load-shifting for cooling of buildings. The present paper presents a method for forecasting of the power load for space heating in a single-family house. The heat load forecasts can be used as input to model predictive control, which can be used for load-shifting, for example for operation under energy markets, where relocation of load to periods with cheap energy will be rewarded. The method can just as well be used for forecasting of cooling load and used for load-shifting with cool thermal storage. Perers et al. (2011) presents solar combisystems, which is a heating system based on a solar thermal collector and electrical heating, where a hot water tank is used for thermal energy storage. Forecasting of the heat load is vital for optimal and effective use of the thermal storage in such a system.

Forecasting of the load for space heating is carried out for sixteen houses in Sønderborg, Denmark. Every hour a new forecast is calculated of the hourly heat load up to 42 hours ahead. The houses are generally built in the sixties and seventies, with a floor plan in the range of 85 to 170 m^2, and constructed in bricks. Climate observations - which are measured at the local district heating plant within 10 kilometers from the houses - together with numerical weather predictions (NWPs) are used as input to the forecasting model. The NWPs are from the HIRLAM-S05 model and provided by the Danish Meteorological Institute. For each house only the total heat load, including both space heating and water heating, is available. The heat load signal is first separated into two signals: a signal for space heating and a signal for water heating. The space heating signal is then forecasted. The splitting allows for a clear view of the effects stemming from heat loss to the ambient and heat gains from solar radiation etc., since the noisy peaks from how water heating is filtered out. The indoor temperature is not available, which is accounted for in the models by including a diurnal curve to model nightly setback and behavioral patterns of the residents e.g. heat from electrical appliances used for cooking.

Very many approaches to load forecasting are found in the literature. A good overview of references are given by Mestekemper (2011), who built load forecasting models using dynamic factor models. Dotzauer (2002) use a model based on the ambient temperature and a weekly pattern for forecasting of the heat load in district heating, i.e. the total heat load for many houses. Zhou et al. (2008) use a grey-box model based on transfer functions for building thermal load predic-

tion and validates it on a 50 floors multi purpose building. The models applied in the present study are originally developed and used for forecasting of heat load in district heating, as described in (Nielsen et al., 2000) and (Nielsen and Madsen, 2006). The total heat load for many houses together have less high frequency variation, due to the averaging effects, compared to the heat load for a single house. Emphasis in the present study is put on the variability in heat load among the individual houses, for example some react more than others to solar radiation, and especially the diurnal pattern is very different among the studied houses.

The paper starts with a section in which the data and the NWPs are described. This is followed by a presentation of the modelling approach and the model identification, where a suitable forecasting model is found together with a dynamic model for the remaining noise. Finally the results are presented, and the method is discussed and concluded.

F.2 Data

The data used in the study consist of heat load measurements from sixteen houses in Sønderborg, Denmark, and local climate measurements and NWPs. All times are in UTC and the time stamp for average values are set to the end of the time interval.

F.2.1 Heat load measurements

The houses are typical Danish single family houses from the sixties and seventies. Only houses with radiator heating is considered. A single signal for each house is used, which consist of both the energy for space heating and hot water heating. The heat load measurements consist of 10 minutes average values. Time series plots over the entire period, spanning nearly two and a half years, for four of the houses are shown in Figure F.1. Also shown, with red lines, is the distribution over time, which are estimates of the $0\%, 2\%, \ldots, 98\%, 100\%$ quantiles. They are estimated using local quantile regression (Koenker, 2005), where the weighting is local in time. They clearly indicate that the distribution of the heat load is heavily skewed, for example only two percent of the values are between the two upper lines, which cover more than half of the range. The reason for this skewness is seen from Figure F.2, where 10 days of heat load for the same four houses is plotted. The heat load for water heating consist of high frequency spikes added to the more slowly varying space heating signal. The highest peaks

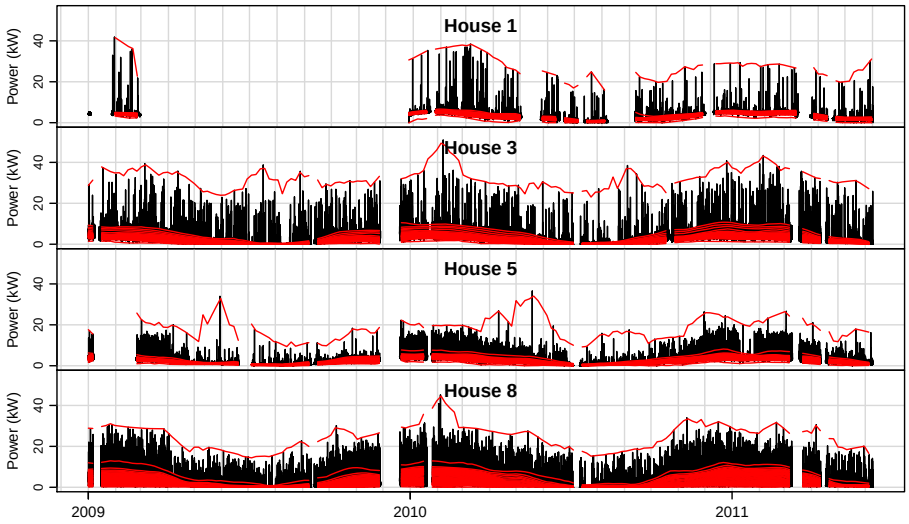

Figure F.1: The heat load for four selected houses over the entire period, which is nearly spanning two and a half years. The red lines are estimates of the $0\%, 2\%, \ldots, 98\%, 100\%$ quantiles, which indicate the distribution of the heat load at a given time.

are from showers and cause the high skewness. Since it is wanted to study the space heating part, then each signal is splitted into a space heating part and a water heating part - with the method described in (Saint-Aubain, 2011) used causally. On the figure the part of the signal identified as water heating is marked with red, note that it is added on top of the space heating signal in the plot. After the splitting the series are resampled into hourly average values. The hourly space heating for a single house is denoted by

$$\{Q_t;\ t = 1, \ldots, N\} \tag{F.1}$$

where $N = 21144$ and the unit is kW. Notice that no distinguishment in between the houses is used in the notation, but when the results are presented the house number, ranging from 1 to 16, is clearly stated.

F.2.2 Local climate observations

The local climate observations are from a weather station at the district heating plant in Sønderborg, which is less than 10 kilometers from the houses. The data

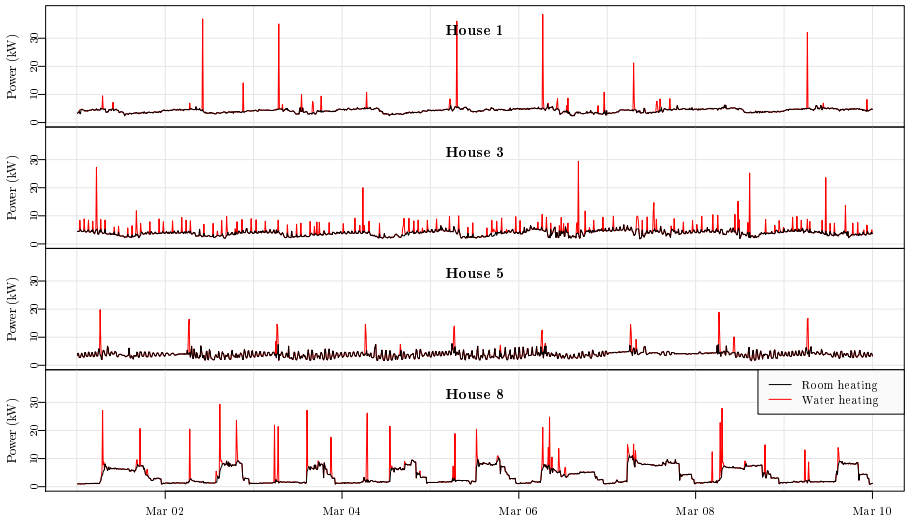

Figure F.2: Heat load for four selected houses for the first 10 days of March in 2010. The peaks marked with red are the parts which are identified as water heating and the black line is the space heating part. Note that the water heating is added on top the space heating signal.

is resampled to hourly average values and the following time series are used:

$$\begin{aligned} \text{Ambient temperature:} \quad & \left\{T_t^{\text{a,obs}}; t = 1, \ldots, N\right\} \\ \text{Global radiation:} \quad & \left\{G_t^{\text{obs}}; t = 1, \ldots, N\right\} \\ \text{Wind speed:} \quad & \left\{W_t^{\text{s,obs}}; t = 1, \ldots, N\right\} \end{aligned} \tag{F.2}$$

F.2.3 Numerical weather predictions

The numerical weather predictions (NWPs) used for the forecasting are provided by the Danish Meteorological Institute. The NWP model used is DMI-HIRLAM-S05, which has a 5 kilometer grid and 40 vertical layers (DMI, 2011). The NWPs consist of time series of hourly values for climate variables, which are updated four times per day and have a 4 hour calculation delay (e.g. the forecast starting at 00:00 is available at 04:00). Since a new two day heat load forecast is calculated every hour, then - in order to use the latest available information - every hour the latest available NWP value for the k'th horizon at

time t is picked as

$$\begin{aligned} \text{Ambient temperature (°C):} \quad & T^{\mathrm{a,nwp}}_{t+k|t} \\ \text{Global radiation (W/m}^2\text{):} \quad & G^{\mathrm{nwp}}_{t+k|t} \\ \text{Wind speed (m/s):} \quad & W^{\mathrm{s,nwp}}_{t+k|t} \\ \text{Wind direction (°azimuth):} \quad & W^{\mathrm{d,nwp}}_{t+k|t} \end{aligned} \tag{F.3}$$

F.2.4 Combining local observations with NWPs

To include the building heat dynamics in an efficient way, the inputs are low-pass filtered as explained in Section F.3.3. Hence, for the forecast calculated at time t, past values of the inputs are being used. In order to use the information embedded in the local measurements they are combined with the NWPs. The combining is carried out by forming the time series for each of the inputs at time t, for a specific horizon k, by

$$\begin{aligned} \left\{T^{\mathrm{a}}_{t+k|t}\right\} &= \left\{\ldots, T^{\mathrm{a,obs}}_{t-1}, T^{\mathrm{a,obs}}_{t}, T^{\mathrm{a,nwp}}_{t+1|t}, T^{\mathrm{a,nwp}}_{t+2|t}, \ldots, T^{\mathrm{a,nwp}}_{t+k|t}\right\} \\ \left\{G_{t+k|t}\right\} &= \left\{\ldots, G^{\mathrm{obs}}_{t-1}, G^{\mathrm{obs}}_{t}, G^{\mathrm{nwp}}_{t+1|t}, G^{\mathrm{nwp}}_{t+2|t}, \ldots, G^{\mathrm{nwp}}_{t+k|t}\right\} \\ \left\{W^{\mathrm{s}}_{t+k|t}\right\} &= \left\{\ldots, W^{\mathrm{s,obs}}_{t-1}, W^{\mathrm{s,obs}}_{t}, W^{\mathrm{s,nwp}}_{t+1|t}, W^{\mathrm{s,nwp}}_{t+2|t}, \ldots, W^{\mathrm{s,nwp}}_{t+k|t}\right\} \\ \left\{W^{\mathrm{d}}_{t+k|t}\right\} &= \left\{\ldots, W^{\mathrm{d,nwp}}_{t-1|t}, W^{\mathrm{d,nwp}}_{t|t}, W^{\mathrm{d,nwp}}_{t+1|t}, W^{\mathrm{d,nwp}}_{t+2|t}, \ldots, W^{\mathrm{d,nwp}}_{t+k|t}\right\} \end{aligned} \tag{F.4}$$

Notice that local observations are not available for the wind direction.

F.3 Models

As mentioned earlier the applied models are similar to the models used by Nielsen and Madsen (2006) for modelling of the total heat load for many houses. The models are based on prior physical knowledge of the heat dynamics of buildings, which in combination with statistical time series models, forms a grey-box modelling approach. This allows for inclusion of heat transfer effects related to the climate variables in a combination with time adaptivity for modelling of changing condition. Furthermore, in order to describe of patterns in resident behavior, a diurnal curve is included. The forecasting models are fitted, by optimizing the parameters to minimize the RMSE in an off-line setting. The fitting is carried out separately for each house and for each horizon k, which means that the same model formulation - i.e. same inputs and model structure - is used, but the parameter values for each house and horizon can be different.

F.3.1 Time adaptive models

The models are fitted with the k-step recursive least squares scheme described by Bacher et al. (2009). This means that the coefficients in the model can change over time and thereby adapt optimally to changing conditions. The coefficients are recursively updated, which means that only a few matrix operations are required to make a new forecast, hence the scheme is computationally very fast. It is a recursive implementation of a weighted least squares estimation, where the weights are exponentially decaying over time. A single parameter is required, the forgetting factor λ, which determines how fast input data is down-weighted. The weights are equal to

$$w(\Delta t) = \lambda^{\Delta t} \tag{F.5}$$

where Δt is the age of the data in hours. This means that for $\lambda = 0.98$ the weights are halved in 34 hours, for $\lambda = 0.995$ they are halved in 138 hours (~ 6 days), and for $\lambda = 0.999$ in 693 hours (~ 29 days).

F.3.2 Diurnal curve

A curve for describing systematic diurnal patterns in the heat load is included in the models, which for example can be caused by a nightly setback and free heat from electrical appliances. The curve is modelled as a harmonic function using a Fourier series

$$\mu(t_{\mathrm{tod}}, \alpha_{\mathrm{diu}}) = \sum_{i=1}^{n_{\mathrm{har}}} \alpha_{i,1}^{\mathrm{diu}} \sin\left(\frac{t_{\mathrm{tod}} i\pi}{12}\right) + \alpha_{i,2}^{\mathrm{diu}} \cos\left(\frac{t_{\mathrm{tod}} i\pi}{12}\right) \tag{F.6}$$

where t_{tod} is the time of day in hours at time t and n_{har} is the number of harmonics included in the Fourier series. For all the applied models a curve is fitted for working days and another curve for weekends.

F.3.3 Low-pass filtering for modelling of building dynamics

The heat dynamics of a building can be described by lumped parameter RC-models, see for example (Madsen and Holst, 1995), (Braun and Chaturvedi, 2002), and (Jiménez et al., 2008). As described by Nielsen and Madsen (2006) the response in the heat load to changes in the climate variables can be modelled with rational transfer functions, which is a description of the low-pass filtering

effect of the building with an RC-model. In the present models the simplest first order low-pass filter, with a stationary gain equal to one, is used. This is a model of the building heat dynamics formed by an RC-model with a single resistance and a single capacitor. As an example the transfer function from the ambient temperature to the heat load is

$$Q_t = H_{\mathrm{a}}(q) T_t^{\mathrm{a}} \tag{F.7}$$

where

$$H_{\mathrm{a}}(q) = \frac{1 - a_{T_{\mathrm{a}}}}{1 - a_{T_{\mathrm{a}}} q^{-1}} \tag{F.8}$$

and where q^{-1} is the backward shift operator ($q^{-1} x_t = x_{t-1}$) (see (Madsen, 2007)) and $a_{T_{\mathrm{a}}} \in [0, 1]$ is a parameter, which is equivalent to the time constant for the part of the building affected by changes in ambient temperature. A building with a high thermal mass and good insulation will have a relatively high $a_{T_{\mathrm{a}}}$, hence the filter parameter needs to be estimated for each building in order to describe the heat dynamics properly. First order low-pass filters are also applied for wind speed and global radiation, with the filter parameter is estimated for matching of the response of the building to each of the climate variable separately.

F.3.4 Parameter optimization

As described above several parameters needs to be optimized for each house and horizon. The optimization is carried out in an off-line setting by minimizing the root mean square error for each of the sixteen houses and for each horizon $k = 1, \ldots, 42$ separately. This does require some computational power, especially the low-pass filtering of the inputs. Therefore a simple bisectioning scheme is applied for the optimization, since this allows for performing a filtering of the inputs only once for parameter values in a given range. Then these series can be used for optimization for all the houses and horizons.

The following parameters are optimized

- The forgetting coefficient: λ
- The number of harmonics in the diurnal curve: n_{har}
- The coefficients for input low-pass filters: $a_{T_{\mathrm{a}}}, a_{\mathrm{G}}$, and $a_{\mathrm{W_s}}$

F.4 Model identification

Forecasting models, which include different types of heat transfer effects related to the climate variables, are applied to identify which of the inputs are important to include. Furthermore different ways for the inputs to enter the model are tried. See (Nielsen and Madsen, 2006) for a description of how a physical model can be rewritten into the identifiable models, which are used here. The model which include all energy contributions is

$$Q_{t+k} = \widehat{Q}_{t+k|t} + e_{t+k} \tag{F.9}$$

where

$$\widehat{Q}_{t+k|t} = Q_{\mathrm{a}} + Q_{\mathrm{g}} + Q_{\mathrm{w}} \tag{F.10}$$

where the Q_{name} variables on the right side of the equation represents the heat contributions from the considered heat transfers, which are described below.

F.4.1 First step in model selection

To select a suitable forecasting model a forward selection approach is used. In the first step the $model_{\mathrm{D}}$

$$\widehat{Q}_{t+k|t} = \alpha_{\mathrm{ia}} + \mu(t_{\mathrm{tod}}, \alpha_{\mathrm{diu}}) \tag{F.11}$$

which do not include the climate inputs, is fitted. In this model the heat load is simply modelled as a diurnal curve with an offset. Note that α_{ia} then represents a constant difference between the indoor and the ambient temperature and the diurnal part will try to capture diurnal patterns in both the indoor and ambient temperature. Due to the time adaptive scheme the model will be able to track the slow changes in the temperatures over the year. Finally note also that the coefficients could have been denoted with: a t to indicate that they are changing over time, a house number to indicate that they are fitted to each house, and a k to indicate that the model is fitted for each horizon separately, but this have been left out for better readability.

To find out if there is useful information available in the climate series as inputs to the model, the cross-correlation function (CCF), see (Box et al., 1976), between the one-step ahead ($k = 1$ hour) error for $model_{\mathrm{D}}$ and the available input series is calculated - which is prefered over the NWPs, as it is mainly the observations which are used for the one-step ahead forecast. Since it is too

cumbersome to analyze the error series for each house separately, the average error

$$\bar{e}_{t+k} = \frac{1}{n_{\text{houses}}} \sum_{i=1}^{n_{\text{houses}}} e_{t+k}^{\text{House } i} \tag{F.12}$$

where $n_{\text{houses}} = 16$ are the number of houses and $e_{t+k}^{\text{House } i}$ is the error series for House i, is used. In this way the CCF to the inputs is summarized for all the houses in a single plot. This will of course only show if an input is generally important to include and not the effects for each individual house. The effects related to each house - which are different - are considered in later parts of the paper.

The CCF between the average errors from $model_{\text{D}}$ to the inputs can be seen in Figure F.3a. Clearly very significant correlations between the error and both the ambient temperature and the global radiation, but apparently none to the wind speed, are found. It is decided to add the ambient temperature as input to the model, which leads to $model_{\text{A}}$

$$\widehat{Q}_{t+k|t} = Q_{\text{a}} \tag{F.13}$$

where

$$Q_{\text{a}} = \alpha_{\text{i}} + \mu(t_{\text{tod}}, \alpha_{\text{diu}}) + \alpha_{\text{a}} H_{\text{a}}(q) T^{\text{a}}_{t+k|t} \tag{F.14}$$

The $H_{\text{a}}(q)$ is the low-pass filter modelling the dynamics of the building envelope, i.e. the response of in heat load to changes in ambient temperature. Notice that the intercept α_{i} is representing a constant indoor temperature modified by the diurnal curve.

In order to find out if any gain in forecasting performance is achieved from $model_{\text{D}}$ to $model_{\text{A}}$ the root mean square error is used for evaluation as described in the following.

F.4.1.1 Root mean square error evaluation

To evaluate the models the root mean square error (RMSE) for the k'th horizon

$$\text{RMSE}_k = \left(\frac{1}{N} \sum_{t=1}^{N} e_{t+k}^2 \right)^{\frac{1}{2}} \tag{F.15}$$

is used together with the RMSE_k improvement

$$I_{\text{RMSE}} = 100 \cdot \frac{\text{RMSE}_{\text{ref}} - \text{RMSE}}{\text{RMSE}_{\text{ref}}} (\%) \tag{F.16}$$

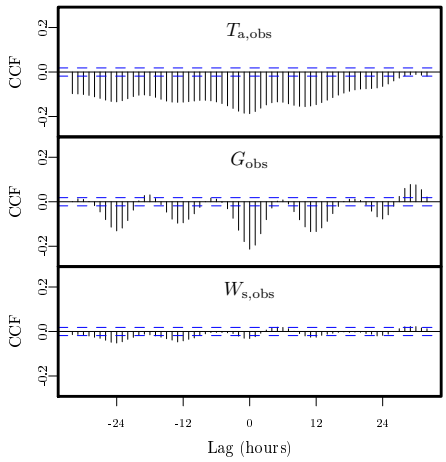

(a) Step one: CCF for $model_{D}$ errors to the inputs.

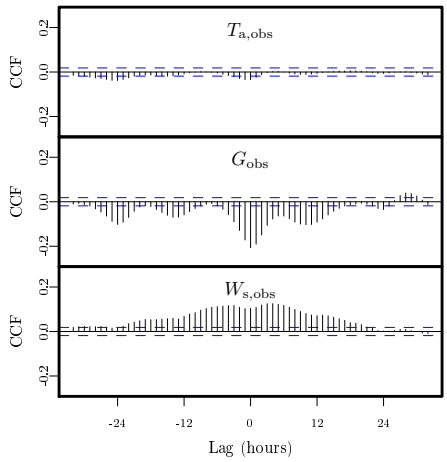

(b) Step two: CCF for $model_{A}$ errors to the inputs.

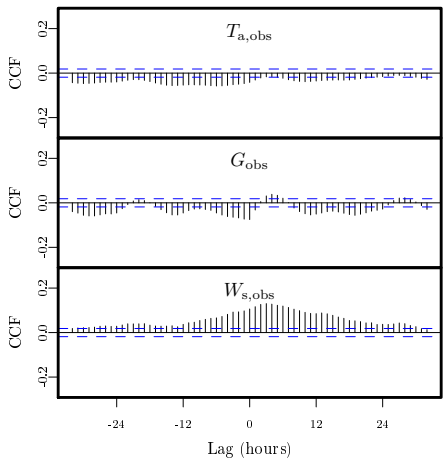

(c) Step three: CCF for $model_{A.G}$ errors to the inputs.

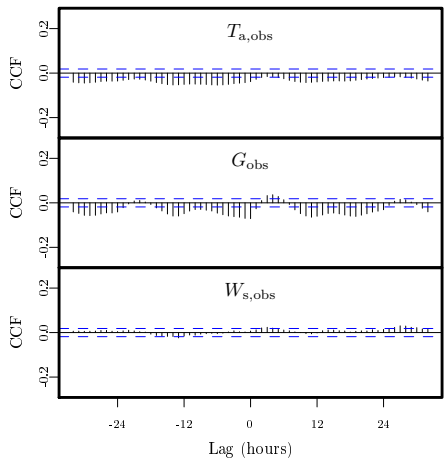

(d) Step four: CCF for $model_{A.G.W}$ errors to the inputs.

Figure F.3: The cross-correlation function (CCF) between the average error series for the one-step ahead forecast (horizon $k = 1$) and the local observations of the inputs, since the inputs for the one-step ahead forecasts are primarily formed by the observations. The plots are for the errors from the selected model in the four steps of model identification carried out.

over the currently selected model as reference. It is noted values not in the heating season - which starts the 15'th of September and ends 15'th of May in Denmark - and values before the 15'th of March 2009, which is used as a burn-in period, are excluded from the RMSE_k calculation. For evaluation of the inclusion of ambient temperature, the RMSE_k improvement for $model_{\text{A}}$ over $model_{\text{D}}$ is calculated. The average improvement for all horizons (from $k = 1$ to $k = 42$) for each house is plotted in Figure F.4a. A RMSE_k improvement for the each house in the range from 5 to 25 percent and around 14 percent in average is achieved. This is clearly a significant improvement, hence $model_{\text{A}}$ is preferred over $model_{\text{D}}$.

F.4.2 Second step in model selection

To explore the possibilities for further expansion of $model_{\text{A}}$ the CCFs from the average errors (defined in Equation (F.12)) to each of the climate series are calculated. They are plotted in Figure F.3b. The correlation to the ambient temperature is much lower than for $model_{\text{D}}$ and the correlation to the global radiation is more or less the same. The correlation to the wind speed has increased, most likely this correlation was "overshadowed" by the correlation to the ambient temperature for the $model_{\text{D}}$ errors. Notice that there is a significant correlation decaying over 12 to 24 hours to the lagged inputs, which indicates that dynamics should be included by low-pass filtering.

To find the most important extension of $model_{\text{A}}$ several extensions involving the global radiation or the wind speed are fitted (i.e. the RMSE_k is minimized by tuning the parameters listed in Section F.3.4 for each house).

The first considered expansion is $model_{\text{A.G}}$

$$\widehat{Q}_{t+k|t} = Q_{\text{a}} + \alpha_{\text{g}} H_{\text{g}}(q) G_{t+k|t} \tag{F.17}$$

where the heat gain from solar radiation is included by letting the global radiation enter through a low-pass filter, which models the dynamic response from the global radiation to the heat load of the building. The second expansion is $model_{\text{A.W}}$

$$\widehat{Q}_{t+k|t} = Q_{\text{a}} + \alpha_{\text{ws}} H_{\text{w}}(q) W^{\text{s}}_{t+k|t} \tag{F.18}$$

where the cooling of the building from wind is modelled by letting the wind speed enter through a low-pass filter. This is a model of wind cooling not depending on the ambient temperature, however - due to the time-adaptive modelling scheme - is does include the slow changes in temperature difference between indoor and

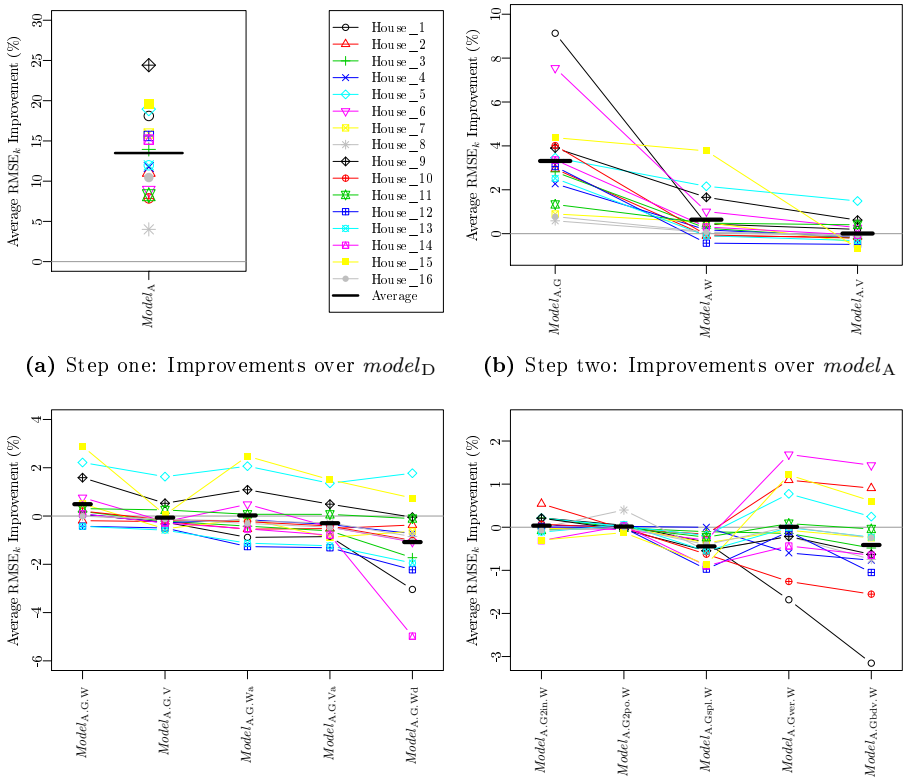

(a) Step one: Improvements over $model_{\mathrm{D}}$ **(b)** Step two: Improvements over $model_{\mathrm{A}}$

(c) Step three: Improvements over $model_{\mathrm{A.G}}$ **(d)** Step four: Improvements over $model_{\mathrm{A.G.W}}$

Figure F.4: Improvements over the previously selected model for the models in each step of the selection.

ambient temperature. The third expansion is $model_{\mathrm{A.V}}$

$$\widehat{Q}_{t+k|t} = Q_{\mathrm{a}} + \alpha_{\mathrm{vent}} W^{\mathrm{s}}_{t+k|t} \tag{F.19}$$

which include an effect of ventilation modelled by inputting the instant effect of wind speed to the heat load.

The RMSE_k improvements averaged over all horizons for each house for the considered expansions is plotted in Figure F.4b. It is seen that the performance increase is highest for all the houses for $model_{\mathrm{A.G}}$, hence this model is preferred and used for expansion in the following step. In the remaining of the paper the heat contribution from solar radiation is denoted by

$$Q_{\mathrm{g}} = \alpha_{\mathrm{g}} H_{\mathrm{g}}(q) G_{t+k|t} \tag{F.20}$$

F.4.3 Step three: Inclusion of wind speed in the model

In the third step of the model identification several ways of including the wind speed is considered. First the CCFs between the one-step ahead error, from the model selected in the previous step, $model_{\mathrm{A.G}}$ and the inputs, are studied to see if any useful information is remaining in the climate series.

First it is noted that the correlation to the global radiation has decreased compared to the CCF plot for $model_{\mathrm{A}}$, but that some is still left, indicating that the dynamic effects are not entirely described by the model. Secondly it is noted that there is a significant cross-correlation to the wind speed and therefore it is chosen to seek an expansion which include the wind speed. Five different ways of letting the wind speed enter the model are tried as described in the following.

The first expansion is formed by adding the wind speed through a low-pass filter for modelling of cooling of the building in $model_{\mathrm{A.G.W}}$

$$\widehat{Q}_{t+k|t} = Q_{\mathrm{a}} + Q_{\mathrm{g}} + \alpha_{\mathrm{ws}} H_{\mathrm{w}}(q) W^{\mathrm{s}}_{t+k|t} \tag{F.21}$$

and, for modelling ventilation, the instant effect of wind speed is added in $model_{\mathrm{A.G.V}}$

$$\widehat{Q}_{t+k|t} = Q_{\mathrm{a}} + Q_{\mathrm{g}} + \alpha_{\mathrm{ws}} W^{\mathrm{s}}_{t+k|t} \tag{F.22}$$

In the two models above the wind speed enter the model without the interaction with ambient temperature, which means that the temperature difference between the indoor and ambient temperature is modelled as constant and that

changes are only tracked with the adaptivity of the model. In the following two expansions the interaction is also included, with a filter in $model_{\text{A.G.Wa}}$

$$\widehat{Q}_{t+k|t} = Q_{\text{a}} + Q_{\text{g}} + \alpha_{\text{ws}} H_{\text{w}}(q) W^{\text{s}}_{t+k|t} + \alpha_{\text{wsa}} H_{\text{w}}(q) W^{\text{s}}_{t+k|t} T^{\text{a}}_{t+k|t} \tag{F.23}$$

and as an instant effect in $model_{\text{A.G.Va}}$

$$\widehat{Q}_{t+k|t} = Q_{\text{a}} + Q_{\text{g}} + \alpha_{\text{ws}} W^{\text{s}}_{t+k|t} + \alpha_{\text{wsa}} W^{\text{s}}_{t+k|t} T^{\text{a}}_{t+k|t} \tag{F.24}$$

Finally the wind speed input coefficient is conditioned on the wind direction in $model_{\text{A.G.Wd}}$

$$\widehat{Q}_{t+k|t} = Q_{\text{a}} + Q_{\text{g}} + \sum_{i=1}^{4} \alpha_{\text{i}} H_{\text{w}}(q) K(u) W^{\text{s}}_{t+k|t} T^{\text{a}}_{t+k|t} \tag{F.25}$$

where the kernel function

$$K(u) = (1 - |u|)\mathbf{1}_{\{|u| \leq 1\}} \tag{F.26}$$

with

$$u = \Big(\big(W^{\text{d,nwp}}_{t+k|t} + 45 + (i-1) \cdot 90 \big) \bmod 4 \Big) - 1 \tag{F.27}$$

makes four input series, which are linearly interpolated as a function of the wind direction. The center of the kernels is thus at the most prevailing wind directions in Denmark, especially southwest in the winter period (Cappelen and Jørgensen, 1999).

The plot in Figure F.4c shows the improvements over $model_{\text{A.G}}$ for the five models. The improvement is quite different for each house, for some it is negative, which is because the forecasting model becomes over-parametrized. It is also seen that the pattern of the improvement among the houses are quite similar for the five models, which indicates that for some houses the wind have a more prevalent effect than for others. Since $model_{\text{A.G.W}}$ generally have the most positive improvement and since it is the simplest extension, it is preferred over the others. In the remaining of the paper the model part describing the effect of wind is denoted with

$$Q_{\text{w}} = \alpha_{\text{ws}} H_{\text{w}}(q) W^{\text{s}}_{t+k|t} \tag{F.28}$$

F.4.4 Step four: Enhancement of the solar model part

In the final step the model part for solar radiation is enhanced in different ways, as described in the following. Studying the CCFs for $model_{\text{A.G.W}}$ in Figure F.3d

only very little correlation between the errors and the inputs are seen. There is a little left to the ambient temperature and solar radiation. From studying plots of the forecasts it is found that it could be possible to improve the model part, where the effect of solar radiation is included.

First an additional input for the solar gain is added the model, this is $model_{\text{A.G2in.W}}$

$$\widehat{Q}_{t+k|t} = Q_{\text{a}} + Q_{\text{g}} + \alpha_{\text{g2}} H_{\text{g2}}(q) G_{t+k|t} + Q_{\text{w}} \tag{F.29}$$

This will allow for an additional dynamic response of the building to solar radiation. Notice that an additional filter coefficient for the $H_{\text{g2}}(q)$ filter is fitted here.

Secondly the solar radiation part is enhanced by using a two-pole filter instead of the one-pole filter

$$\widehat{Q}_{t+k|t} = Q_{\text{a}} + \alpha_{\text{g}} H_{\text{2pol}}(q) G_{t+k|t} + Q_{\text{w}} \tag{F.30}$$

where

$$H_{\text{2pol}}(q) = \frac{1 - a_1 - a_2}{1 - a_1 q^{-1} - a_2 q^{-2}} \tag{F.31}$$

and

$$a_1 = a_{g_1} + a_{g_2} \quad \text{and} \quad a_2 = -a_{g_2} \tag{F.32}$$

The two filter coefficients thereby relate to different dynamics: a_{g_1} is related to the highest time constant (slow response) and a_{g_2} is related to the lowest time constant of the building (fast response).

In the third model the solar radiation is separated into three inputs: one for the morning, one for the noon, and one for the evening. This allows for the building to have different solar gains during the day. The $model_{\text{A.Gspl.W}}$ is

$$\begin{aligned} \widehat{Q}_{t+k|t} = Q_{\text{a}} &+ \alpha_{\text{g1}} H_{\text{g}}(q) G^{\text{morning}}_{t+k|t} + \alpha_{\text{g2}} H_{\text{g}}(q) G^{\text{noon}}_{t+k|t} \\ &+ \alpha_{\text{g3}} H_{\text{g}}(q) G^{\text{evening}}_{t+k|t} + Q_{\text{w}} \end{aligned} \tag{F.33}$$

The three inputs are

$$\begin{aligned} G^{\text{morning}}_{t+k|t} &= G_{t+k|t}\ \mathbf{1}_{\{t+k \in [t_{\text{rise}},\ t_{\text{rise}}+\Delta t]\}} \\ G^{\text{noon}}_{t+k|t} &= G_{t+k|t}\ \mathbf{1}_{\{t+k \in [t_{\text{rise}}+\Delta t,\ t_{\text{set}}-\Delta t]\}} \\ G^{\text{evening}}_{t+k|t} &= G_{t+k|t}\ \mathbf{1}_{\{t+k \in [t_{\text{set}}-\Delta t,\ t_{\text{set}}]\}} \end{aligned} \tag{F.34}$$

where $\mathbf{1}_{\{\}}$ is the indicator function, t_{rise} and t_{set} is the time of sunrise and sunset, respectively, and $\Delta t = (t_{\text{set}} - t_{\text{rise}})/3$ is a third of the day length.

Finally two more possible enhancement is applied by projecting the solar radiation onto a vertical surface tracking the solar azimuth angle. The projection to vertical is carried out by first splitting the global radiation into a direct and a diffuse component as in (Ruiz-Arias et al., 2010) and onto a vertical surface with the Hay and Davies model (Hay and Davies, 1980), see also (Reindl et al., 1990). The effect of the projections is mostly an increased level of solar radiation in the morning and in the evening (or afternoon), when the sun elevation is low. In $model_{\text{A.Gver.W}}$

$$\widehat{Q}_{t+k|t} = Q_{\text{a}} + \alpha_{\text{g}} H_{\text{g}}(q) G^{\text{ver,tr}}_{t+k|t} + Q_{\text{w}} \tag{F.35}$$

the total vertical radiation is inputted and in $model_{\text{A.Gbdv.W}}$

$$\widehat{Q}_{t+k|t} = Q_{\text{a}} + \alpha_{\text{g1}} H_{\text{g}}(q) G^{\text{beam,tr}}_{t+k|t} + \alpha_{\text{g2}} H_{\text{g}}(q) G^{\text{diffuse,tr}}_{t+k|t} + Q_{\text{w}} \tag{F.36}$$

the direct (or beam) and the diffuse component is inputted separately.

The models are fitted to each house and the improvements over $model_{\text{A.G.W}}$ are calculated and plotted in Figure F.4d. For $model_{\text{A.G2in.W}}$ and $model_{\text{A.G2po.W}}$ only a little difference in performance is seen, and for $model_{\text{A.Gspl.W}}$ the performance has decreased. These three models become over-parametrized, however it is noted that for short horizons the improvement for $model_{\text{A.Gin2.W}}$ is positive for all the houses. For the last two: $model_{\text{A.Gver.W}}$ and $model_{\text{A.Gbdv.W}}$, the change in performance depends on the house. One interesting pattern is that the houses with the highest change (both decreased and increased) are the houses which benefit most from addition of the solar radiation to the model, as seen in the plot in Figure F.4b. This indicates that increased performance can be gained with a model which modifies the solar gain over the day. Such a model should learn an optimal diurnal solar gain curve for each house. In general no significant overall increase in performance is found for any of the five models, hence the model selection is ended and the results in the remaining of the paper are from $model_{\text{A.G.W}}$, together with a model of the noise, which is described in the following section.

F.5 Noise model

Considering the auto-correlation for the one-step ahead error for the houses, shown in the upper plot of Figure F.5, it is found that a model is useful for describing dynamical information embedded in the errors. A simple auto-regressive (AR) model is fitted to the errors with the recursive least squares scheme (Bacher et al., 2009). The AR(1) model

$$e_{t+k} = a_{\text{e}} e_t + e^{\text{noise}}_{t+k} \tag{F.37}$$

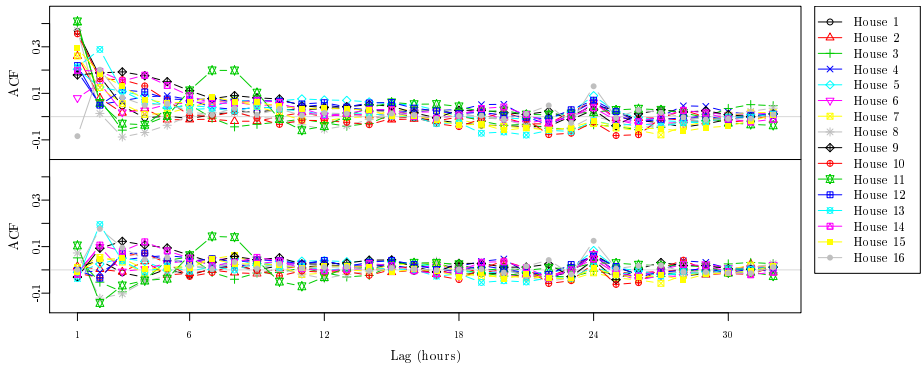

Figure F.5: The auto-correlation function (ACF) for each house. The upper plot is the ACF of the errors before the AR(1) noise model is applied and the lower plot shows the ACF of the errors after.

is fitted for the errors from the selected model $model_{\text{A.G.W}}$ for each horizon k. The ACF of the noise error e^{noise}_{t+k} can be seen in the lower plot of Figure F.5. Compared to the upper plot almost all of the auto-correlation is for lag 1 is removed. Clearly, some of the houses still have significant auto-correlation left and for the short horizons an error model, which include more lags could improve the performance. However it was tried to include one more lag (lag 2), but this did only improve the overall performance marginally, mainly because no performance improvement is achieved on longer horizons. The houses which have the highest ACF (in particular House 11 and 16) have some high frequency oscillations embedded in the heat load signal, as described in the following section where the results are discussed. The average RMSE_k improvement over all horizons is in the range of 0.35% to 6.7%, hence a quite significant improvement, especially for some of the houses. The RMSE_k improvement for the one-step ahead forecasts is in the range 1.3% to 19%, which clearly shows that the noise model is most important for short horizons.

F.6 Results

In this section the results from forecasting with the selected model are presented and discussed. First the parameters, which are fitted for each house, are reported and then the performance for individual houses is discussed.

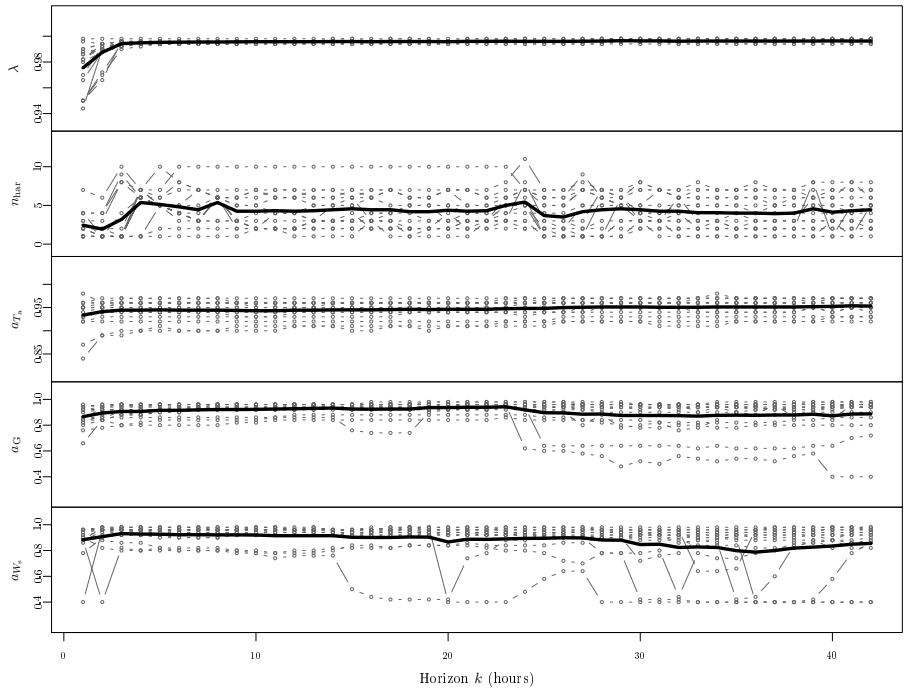

Figure F.6: Values of the parameters fitted for each house.

F.6.1 Model parameters

The parameters which are fitted for each house are listed in Section F.3.4. Since there is a value for each horizon for each house for each parameter, they are reported with the plots in Figure F.6. It is the general patterns which are discussed in the following. Starting with the upper most plot in the figure, which is of the forgetting coefficient λ in the recursive least squares scheme, it can be seen that it has a tendency to be lower for the first couple of horizons: for $k = 1$ the average over all the house is 0.9755, which means that the weighting of the input data is halved in only 28 hours. This fast forgetting is most likely optimal, because it is profitable for the forecasting model to be able to react fast to changes in to the system, e.g. residents increase the indoor temperature or open the windows, which can be tracked on short horizons. On longer horizons the forgetting is on a stable level: for $k = 5$ the average is 0.9953 increasing to 0.9963 for $k = 42$, which means that the weighting of the input data is halved in around 8 days.

The second plot from the top in Figure F.6 is of the optimized number of

House	1	2	3	4	5	6	7	8
a_{T_a}	0.96	0.91	0.91	0.96	0.94	0.96	0.95	0.96
τ_{T_a} (hours)	27	11	10	25	16	27	21	26
House	9	10	11	12	13	14	15	16
a_{T_a}	0.94	0.97	0.95	0.96	0.95	0.94	0.96	0.92
τ_{T_a} (hours)	17	32	18	24	19	15	25	13

Table F.1: Values of optimized low-pass filter coefficient for the response from ambient temperature to heat load and corresponding RC time constant τ_{T_a} in hours.

harmonics in the diurnal curve: a higher number means that it is profitable to include harmonics up to higher frequencies in the diurnal curve. Clearly, a huge variation among the houses is found, which is very reasonable, since the diurnal patterns are very different as shown later in the paper.

The middle plot of the figure is of the optimized coefficient for the low-pass filter transfer function from the ambient temperature to the heat load. Except for the two lowest lines the variation for each house as a function of the horizon k is actually quite little (in the range of ± 0.01), which leads to the conclusion that this does describe very well, how fast the response of heat load is to changes in ambient temperature for the house. In Table F.1 the average coefficient for each house is listed together with the equivalent RC time constants. The values are within a reasonable range compared to values found in other studies (Nielsen and Madsen, 2006), (Reddy et al., 1991).

The fitted values of low-pass filter coefficient for global radiation a_G and for wind speed a_{W_s} are shown in the lower two plots of Figure F.6. The values are all in the same range, generally between 0.8 and up to near 1, but with some lower values for a couple of the houses, which are houses where the solar radiation and wind speed are not very important inputs.

F.6.2 Forecasting performance

In this section the forecasting performance is presented and discussed, especially the differences in performance among the houses. For evaluation of the performance the normalized root mean square error for each horizon

$$\mathrm{NRMSE}_k = \frac{\mathrm{RMSE}_k}{\bar{Q}_t} \tag{F.38}$$

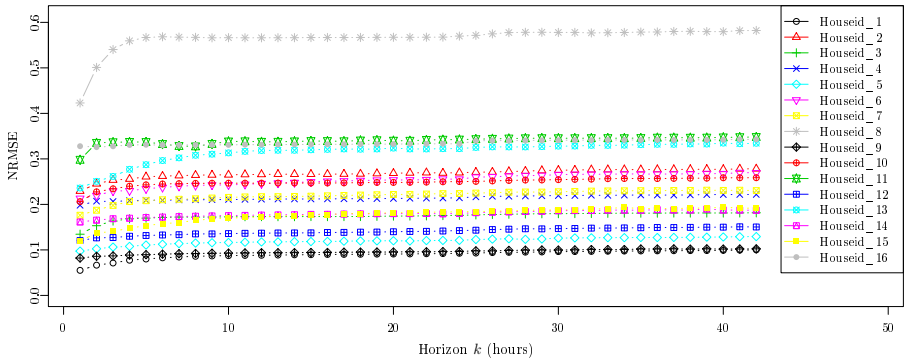

Figure F.7: The NRMSE_k as a function of the horizon k for $model_{\text{A.G.W}}$ for each house.

is used, where $\bar{Q}_t$ is the average heat load for the house, which is calculated with the same values as used for calculation of the RMSE_k (see the text below Equation (F.15)).

The plot in Figure F.7 shows the NRMSE_k as a function of the horizon k for each house using the selected $model_{\text{A.G.W}}$. Clearly the poorest forecasting performance is for House 8. The explanation is found by considering the plot for House 8 in Figure F.8, which shows the heat load together with the 1 hour and 24 hour forecasts. The main reason for the poor forecasts is a very irregular diurnal curve. A nightly setback makes a huge difference in heat load from day to night and furthermore the time of day, where the heat is turned high again, varies among the days and is probably controlled manually by the residents. This is opposed to the nightly setback for House 10, which have a much more regular pattern that can be much better forecasted.

Another source for high errors is seen in the plots for House 2 and 16, where noisy fluctuations occur on the higher frequencies in the signals. The smaller fluctuations are probably partly from water heating, which was not well separated from the space heating, but clearly higher peaks not related to water heating are seen. For House 11 a more steady, but still quite unpredictable, fluctuation is seen, which is likely to come from some oscillation in the thermostatic control of the heat system.

The heat load signals for House 1, 9, and 15 are much less volatile. These houses are also the ones with a lower NRMSE_k, as seen from the plot in Figure F.7. The most obvious thing to notice is the deviation between the 1 and the 24 hour forecasts. Starting with the drop on the 21'st of February, which is followed well by the 1 hour forecast, but not by the 24 hour forecast. This drop is clearly

caused by solar radiation. It is a clear-sky day as seen by the high level of observed global radiation (the second uppermost plot of Figure F.8), which is also predicted by the 24 hour NWP. However the drop is not followed by the 24 hour load forecast, since the previous day was also forecasted as a clear-sky day by the 24 hour NWP, but it was not a clear-sky day as seen by the low observed level. Hence there is a much higher uncertainty on the global radiation input to the 24 hour model compared to the 1 hour model, which use mostly observations as input, and therefore the global radiation is not given much weight in the 24 hour forecasting model. From the 1'st of March a sunny period begins and it can be seen how the 24 hour forecasts starts to track the mid-day drops in heat load, as more weight is put on the global radiation input due to the time adaptivity of the modelling scheme. Finally it is noted that the drop the 23'th of February and the peak the 27'th of February in the heat load for House 15 are not seen in the other heat loads. It is attributed to residents behavior, which cannot be forecasted - though it is tracked in the 1 hour forecast, but with a delay.

F.7 Discussion

For the data used in the study the indoor temperature was not available and it is therefore modelled as constant modified with a diurnal curve. If the indoor temperature is available it will allow for advancements of the method by including it as an input to the model. The estimation of a time constant for the building can be carried out with higher accuracy, which will allow the method to be used for smart grid applications, such as load-shifting by use of the building structure for thermal storage.

Regarding the model part in which the solar radiation is entering, further advancements could be tried. For example more information about the individual buildings such as the azumuth angle of the walls, would provide a more detailed projection of the radiation from horizontal to vertical surfaces. However it will be favorable for operation if no specific information about the buildings is needed. The possibilities are then to try non-linear functions, which could be applied with piecewise linear or regime switching functions depending on the level of solar radiation, or a non-parametric approach could also taken with an off-line method for learning how the building respond to solar radiation over the day. Finally it is found that performance can be increased by using different models depending on the horizon, especially it is more relevant to increase the model complexity for shorter horizons.

F.8 Conclusion

A method for forecasting the load for space heating in a single-family house is presented. It is formed by adaptive linear time-series modelling techniques, using local observations and weather forecasts as input. Based on measurements from sixteen houses a model, which is suitable for all the houses, is identified by using a forward selection approach. It is shown how the forecasting performance increases when the ambient temperature, global radiation, and wind speed are added as inputs to the model. For inclusion of the heat dynamics of the building into the model simple transfer functions are used. Several further advancements to the model are tried, but this makes the model over-parametrized and results in decreased performance. In a second step an auto-regressive model is applied for modelling of the remaining dynamic information in the error. After this it is shown that almost no auto-correlation is left in the errors and thereby that the heat load is modelled very well. The model parameters, which have been fitted individually for each house, are analyzed and it is found that they provide reliable information about the dynamic response of the building. The forecasting results are then analyzed thoroughly to give insight into the sources of error, for example unpredictable behavior of the residents and uncertainty in the inputs, especially from the solar radiation weather forecasts. Finally, a discussion is given with ideas for further advancements.

Acknowledgement

Acknowledgements are given to the The Danish Council for Strategic Research, which have provided the financial support for the project "Solar/electric heating systems in the future energy system" (2104-07-0021) under which the work was carried out. The heat load and climate data was very kindly provided by Sønderborg Fjernvarme and the Danish Meteorological Institute is thanked for making their numerical weather predictions available.

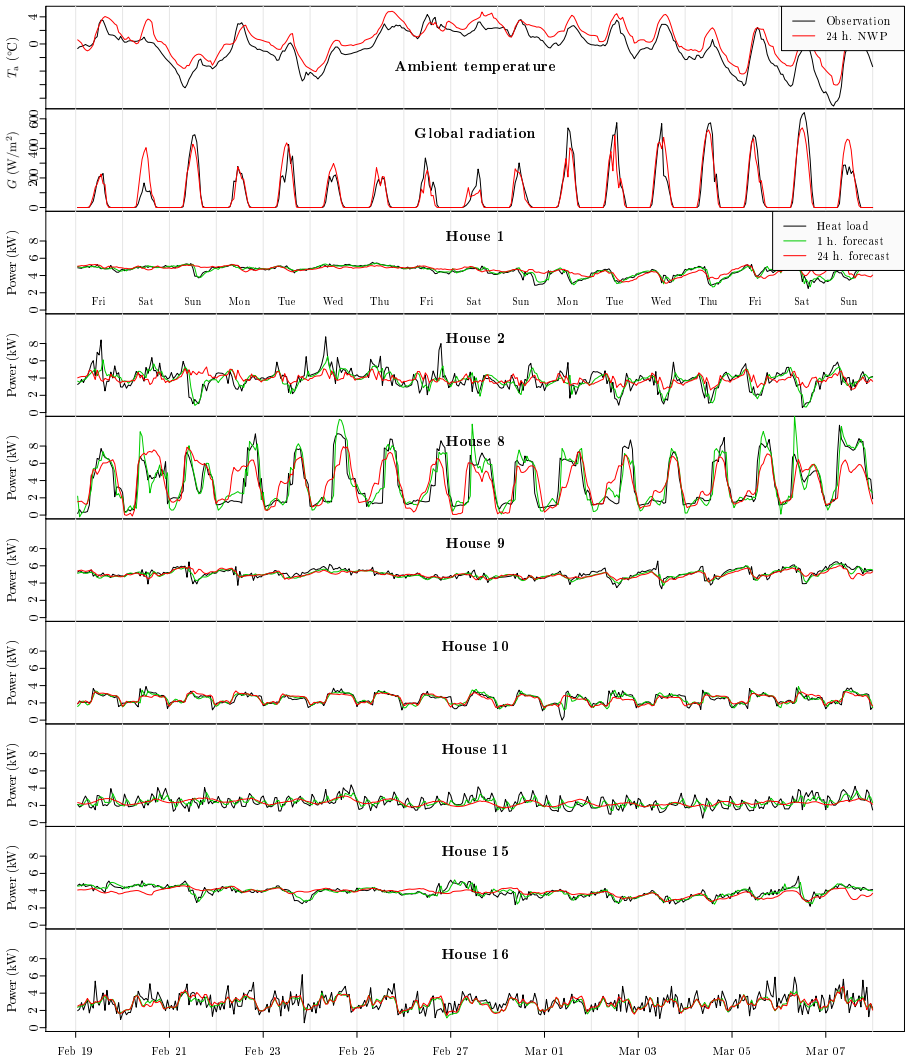

Figure F.8: Plots of inputs and forecasts for sixteen days starting at the 19'th February 2010. The upper two plots are observations and the 24 hour NWP forecasts of the two most significant inputs: the ambient temperature and the global radiation. The plots below are for eight the houses of: observed heat load, 1 hour forecasts, and 24 hour forecasts.

References

P. Bacher, H. Madsen, and H. A. Nielsen. Online short-term solar power forecasting. *Solar Energy*, 83(10):1772–1783, 2009. ISSN 0038092x.

G. Box, G. Jenkins, and G. Reinsel. *Time series analysis*. Holden-day San Francisco, 1976.

J. E. Braun and N. Chaturvedi. An inverse gray-box model for transient building load prediction. *HVAC&R Research*, 8(1):73–99, 2002. doi: 10.1080/10789669.2002.10391290.

J. Cappelen and B. Jørgensen. Observed wind speed and direction in denmark - with climatoligical standards normals, 1961-90. Technical report, Danish Meteorological Institute, 1999.

T. Chen. Real-time predictive supervisory operation of building thermal systems with thermal mass. *ENERGY AND BUILDINGS*, 33(2):141–150, JAN 2001. ISSN 0378-7788.

Danish Commission on Climate Change Policy. Green energy – the road to a danish energy system without fossil fuels, September 2010a.

Danish Commission on Climate Change Policy. Grøn energi - vejen mod et dansk energisystem uden fossile brændsler. Technical report, Danish Energy Agency, September 2010b. Dokumentationsdelen til Klimakommissionens samlede rapport.

DMI. Danish Meteorological Institute, DMI-HIRLAM-S05, 2011. URL `http://www.dmi.dk/eng/index/research_and_development/dmi-hirlam-2009.htm`.

E. Dotzauer. Simple model for prediction of loads in district-heating systems. *Applied Energy*, 73(3–4):277 – 284, 2002. ISSN 0306-2619. doi: 10.1016/S0306-2619(02)00078-8.

J. Hay and J. Davies. Calculation of the solar radiation incident on an inclined surface. In *Proc. 1st Canadian Solar Radiation Data Workshop*, volume 59, page , 1980.

G. P. Henze, C. Felsmann, and G. Knabe. Evaluation of optimal control for active and passive building thermal storage. *International Journal of Thermal Sciences*, 43(2):173 – 183, 2004. ISSN 1290-0729. doi: 10.1016/j.ijthermalsci.2003.06.001.

M. Jiménez, H. Madsen, and K. Andersen. Identification of the main thermal characteristics of building components using matlab. *Building and Environment*, 43(2):170–180, 2008. ISSN 03601323, 1873684x. doi: 10.1016/j.buildenv.2006.10.030.

R. Koenker. *Quantile Regression*. Cambridge University Press, 2005.

H. Madsen. *Time Series Analysis*. Chapman & Hall, 2007.

H. Madsen and J. Holst. Estimation of continuous-time models for the heat dynamics of a building. *Energy and Buildings*, 22(1):67–79, 1995. ISSN 03787788.

T. Mestekemper. *Energy demand forecasting and dynamic water temperature management*. PhD thesis, Bielefeld University, 2011.

H. Nielsen, H. Madsen, and D. E. F. P. og Fordeling af El og Varme. Predicting the heat consumption in district heating systems using meteorological forecasts. Technical report, DTU IMM, 2000.

H. A. Nielsen and H. Madsen. Modelling the heat consumption in district heating systems using a grey-box approach. *Energy & Buildings*, 38(1):63–71, 2006. ISSN 03787788. doi: 10.1016/j.enbuild.2005.05.002.

T. Pedersen, P. Andersen, K. Nielsen, H. Starmose, and P. Pedersen. Using heat pump energy storages in the power grid. In *Control Applications (CCA), 2011 IEEE International Conference on*, pages 1106 –1111, sept. 2011. doi: 10.1109/CCA.2011.6044504.

B. Perers, S. Furbo, J. Fan, E. Andersen, and Z. Chen. Solar combisystems with forecast control to increase the solar fraction and lower the auxiliary energy cost. In *ISES Solar World Congress 2011 Proceedings*, page , 2011. ISBN 978-3-9814659-0-7. Presented at: ISES Solar World Congress, SWC ; 30 : Kassel, Germany, 2011.

T. Reddy, L. Norford, and W. Kempton. Shaving residential air-conditioner electricity peaks by intelligent use of the building thermal mass. *Energy*, 16 (7):1001 – 1010, 1991. ISSN 0360-5442. doi: 10.1016/0360-5442(91)90060-Y.

D. Reindl, W. Beckman, and J. Duffie. Evaluation of hourly tilted surface radiation models. *Solar Energy*, 45(1):9 – 17, 1990. ISSN 0038-092X. doi: 10.1016/0038-092X(90)90061-G.

J. Ruiz-Arias, H. Alsamamra, J. Tovar-Pescador, and D. Pozo-Vázquez. Proposal of a regressive model for the hourly diffuse solar radiation under all sky conditions. *Energy Conversion and Management*, 51(5):881–893, 2010. ISSN 01968904. doi: 10.1016/j.enconman.2009.11.024.

P. d. Saint-Aubain. Adaptive load forecasting. Master's thesis, Technical University of Denmark, 2011.

Q. Zhou, S. Wang, X. Xu, and F. Xiao. A grey-box model of next-day building thermal load prediction for energy-efficient control. *International Journal of Energy Research*, 32(15):1418–1431, 2008. ISSN 1099-114X. doi: 10.1002/er.1458.

Paper G

Identifying suitable models for the heat dynamics of buildings

Authors:
Peder Bacher and Henrik Madsen

Published in:
Energy and Buildings, 2011, 43(7), pp. 1511-1522.

Revisions

Compared to the originally published paper the included paper has the following revisions:

- The estimates of the parameters related to the system and measurement noise have been included in Appendix G.9 together with a short discussion.

Abstract

The present paper suggests a procedure for identification of suitable models for the heat dynamics of a building. Such a procedure for model identification is essential for better usage of readings from smart meters, which is expected to be installed in almost all buildings in the coming years. The models can be used for different purposes, e.g. control of the indoor climate, forecasting of energy consumption, and for accurate description of energy performance of the building. Grey-box models based on prior physical knowledge and data-driven modelling are applied. This facilitates insight into otherwise hidden information about the physical properties of the building. A hierarchy of models of increasing complexity is formulated based on prior physical knowledge and a forward selection strategy is suggested enabling the modeller to iteratively select suitable models of increasing complexity. The performance of the models is compared using likelihood ratio tests, and they are validated using a combination of appropriate statistics and physical interpretation of the results. A case study is described in which a suitable model is sought after for a single storey 120 m^2 building. The result is a set of different models of increasing complexity, with which building characteristics, such as: thermal conductivity, heat capacity of different parts, and window area, are estimated.

G.1 Introduction

This paper describes a new method for obtaining detailed information about the heat dynamics of a building based frequent readings of the heat consumption, indoor temperature, ambient air temperature, and other climate variables. Such a method is considered to be of uttermost importance as a key procedure for better usage of readings from smart meters, which is expected to be installed in almost all buildings in the coming years. The method is based on a procedure for selecting a suitable model of the heat dynamics for a building. Rabl (1988) gives an overview of techniques for steady state and for dynamic analysis of energy use in a building, the latter implicate modelling of the heat dynamics of the building. Such dynamic models can be realized with a set of differential equations, as carried out by Sonderegger (1978) and Boyer et al. (1996). Parameter estimation in dynamical models is known as system identification and a survey of different approaches for buildings is found in Bloem (1994). The applied models in the present method are grey-box models, which consist of a set of continuous time stochastic differential equations coupled with a set of discrete time measurement equations. Grey-box modelling is well proven as a comprehensive and accurate method to model dynamical systems and thereby obtain knowledge of

the thermal properties of a building, see Madsen and Holst (1995), Andersen et al. (2000), and Jiménez et al. (2008). The problem of identifying a suitable model is both finding a model that is in agreement with the physical reality and finding a model, which has a complexity that is in agreement with the level of information embedded in data, which means that the model should neither be under-fitted nor over-fitted. The most suitable model is identified from a set of models of increasing complexity. A forward selection strategy is used, in which the modeller starts out with the simplest feasible model and iteratively selects models of increasing complexity. In each iteration the models are compared using likelihood-ratio tests and the models performances are evaluated. The selection procedure runs until no significant improvement of the model is found. See Pawitan (2001) and Madsen and Thyregod (2010) for an in-depth assessment of likelihood theory and model selection. The procedure is demonstrated by identifying a suitable model for a single storey 120 m^2 building. The building is part of the experimental distributed energy system, Syslab, at Risø DTU in Denmark. It is constructed of wood on the outside and plaster boards on the inside, with a layer of insulation wool in between. The data used spans 6 days and stems from a set of experiments for building energy performance, which was carried out in the winter period of 2009. It is thoroughly described in Bacher and Madsen (2010).

The remaining of the article is organized as follows. The applied grey-box modelling technique is described in Section G.2, and in Section G.3 the statistical test used for model selection is described. Then the suggested procedure for identifying a suitable model is outlined in Section G.4. The following section is devoted to a case-study, where the procedure is applied. It starts with a description of the building and the data, followed by an outline of the applied models and the selection, and ends with a discussion of the results. Finally a perspective of the applications are given in Section G.6 and the conclusions are drawn in Section G.7.

G.2 Grey-box models of a dynamic system

A grey-box model is established using a combination of prior physical knowledge and statistics, i.e. information embedded in data. The prior physical knowledge is formulated by a set of first-order stochastic differential equations, also called a stochastic linear state-space model in continuous time. The equations describe a lumped model of the heat dynamics of the building. It is emphasized that the physical interpretation of the parameters is dependent on how the building is divided into entities in the model.

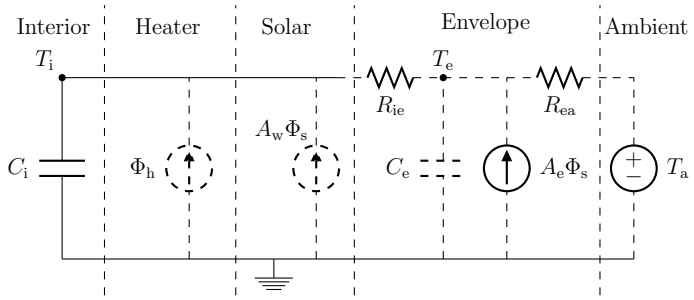

Figure G.1: RC-network of the model described by Equation (G.1) and (G.2). The model is divided into different parts indicating the corresponding part of the building.

An example of a feasible model is given here. It has two state variables, one describing the interior temperature T_i and one representing the temperature of the building envelope T_e. The first-order dynamics are represented by the stochastic differential equations

$$dT_\mathrm{i} = \frac{1}{R_\mathrm{ie}C_\mathrm{i}}(T_\mathrm{e} - T_\mathrm{i})dt + \frac{1}{C_\mathrm{i}}\Phi_\mathrm{h}dt + \frac{1}{C_\mathrm{i}}A_\mathrm{w}\Phi_\mathrm{s}dt + \sigma_\mathrm{i}d\omega_\mathrm{i} \tag{G.1}$$

$$dT_\mathrm{e} = \frac{1}{R_\mathrm{ie}C_\mathrm{e}}(T_\mathrm{i} - T_\mathrm{e})dt + \frac{1}{R_\mathrm{ea}C_\mathrm{e}}(T_\mathrm{a} - T_\mathrm{e})dt + \sigma_\mathrm{e}d\omega_\mathrm{e} \tag{G.2}$$

where t is the time, R_ie is the thermal resistance between the interior and the building envelope, R_ea is the thermal resistance between the building envelope and the ambient air, C_i is the heat capacity of the interior, C_e is the heat capacity of the building envelope, Φ_h is the energy flux from the heating system, A_w is the effective window area, Φ_s is the energy flux from solar radiation, T_a is the ambient air temperature, $\{\omega_{\mathrm{i},t}\}$ and $\{\omega_{\mathrm{e},t}\}$ are standard Wiener processes, and σ_i^2 and σ_e^2 are the incremental variances of the Wiener processes. The model can be represented with the RC-network depicted in Figure G.1, where the model is divided into different parts to show the corresponding parts of the building.

The physical model part is coupled with the data-driven model part with which the information embedded in observed data is used for parameter estimation. The data-driven part in the considered example is represented by the discrete time measurement equation

$$Y_k = T_{\mathrm{i}k} + e_k \tag{G.3}$$

where k is the point in time t_k of a measurement, Y_k is the measured interior temperature and e_k is the measurement error, which is assumed to be a Gaussian white noise process with variance σ^2. This assumption enables evaluation and tests of the performance of the model, since if it is met, this indicates that the physical model is consistent with the observed heat dynamics of the building.

G.2.1 Maximum likelihood estimation of parameters

Given a grey-box model, as described above, maximum likelihood estimates of the parameters can be obtained. Let the observations be represented by

$$\mathcal{Y}_N = [Y_N, Y_{N-1}, \ldots, Y_1, Y_0] \tag{G.4}$$

then the likelihood function is the joint probability density

$$L(\theta; \mathcal{Y}_N) = \left(\prod_{k=1}^{N} p(Y_k | \mathcal{Y}_{k-1}, \theta) \right) p(Y_0 | \theta) \tag{G.5}$$

where $p(Y_k|\mathcal{Y}_{k-1}, \theta)$ is a conditional density denoting the probability of observing Y_k given the previous observations and the parameters θ, and where $p(Y_0|\theta)$ is a parameterization of the starting conditions. The maximum likelihood estimates of the parameters are then found by

$$\hat{\theta} = \arg\max_{\theta} \left\{ L(\theta; \mathcal{Y}_N) \right\} \tag{G.6}$$

Due to the previously mentioned assumptions about the noise process and the fact that the model is linear, it follows that the conditional densities in Equation (G.6) are Gaussian densities. Since the conditional densities are Gaussian a Kalman filter can be used to calculate the likelihood function, and an optimization algorithm can be applied to maximize it, thereby calculating the maximum likelihood estimates, see Kristensen et al. (2004) for a detailed discussion. This is implemented in the computer software CTSM, which has been used for carrying out the parameter estimation, see more about the software at [1] and in Kristensen and Madsen (2003).

G.3 A statistical test for model selection

Statistical tests can be utilized in the search for the most suitable model. If a model is a sub-model of larger model, then a likelihood ratio test can determine if the larger model performs significantly better than the sub-model. Using a sequence of such tests a strategy for selection of the best model can be evolved.

G.3.1 Likelihood ratio tests

Let a model have parameters $\theta \in \Omega_0$ where $\Omega_0 \in \mathbb{R}^r$ is the parameter space and $r = \dim(\Omega_0)$ is the number of parameters in the model. Let a larger model have

[1] www.imm.dtu.dk/~ctsm

parameters $\theta \in \Omega$ where $\Omega \in \mathbb{R}^m$ and $\dim(\Omega) = m$, and assume that

$$\Omega_0 \subset \Omega \tag{G.7}$$

i.e. the first model is a sub-model of the second model and $r < m$.

The likelihood ratio test

$$\lambda(\mathcal{Y}_N) = \frac{\sup_{\theta \in \Omega_0} L(\theta; \mathcal{Y}_N)}{\sup_{\theta \in \Omega} L(\theta; \mathcal{Y}_N)} \tag{G.8}$$

where $\mathcal{Y}_N$ is the observed values, can then be used to test the hypothesis

$$H_0 : \theta \in \Omega_0 \quad \text{vs.} \quad H_\text{a} : \theta \in \Omega \setminus \Omega_0 \tag{G.9}$$

since under H_0 the test statistic $-2\log\big(\lambda(\mathcal{Y}_N)\big)$ converges to a χ^2 distributed random variable with $(m - r)$ degrees of freedom as the number of samples in $\mathcal{Y}_N$ goes to infinity. If H_0 is rejected then the likelihood of the larger model is significantly higher than the likelihood of the sub-model, and it is concluded that $\mathcal{Y}_N$ is more likely to be observed with the larger model. Hence the larger model is needed over the sub-model to describe the information embedded in data. For more details see Madsen and Thyregod (2010).

G.3.2 Forward selection

In a forward selection procedure the modeller starts with the smallest feasible model and then in each step extends the model with the part that gives the lowest p-value, i.e. the most significant improvement. The possible candidates for improvement that are selected in each iteration are the smallest possible extensions to the current model. The procedure stops when no extensions to the model yields a p-value below a pre-specified limit, usually set to 5%.

G.4 Model selection procedure

Different strategies for identifying a suitable model is proposed in the literature and finding an appropriate strategy depends on the specific modelling setup. An purely algorithmic and exhaustive selection procedure is seldomly feasible, hence iterative methods, in which the modeller is partly involved in the selection, are commonly applied. Here, a forward selection procedure is suggested for identification of a suitable model for the heat dynamics. It is based on likelihood ratio testing, which is described in Section G.3.1.

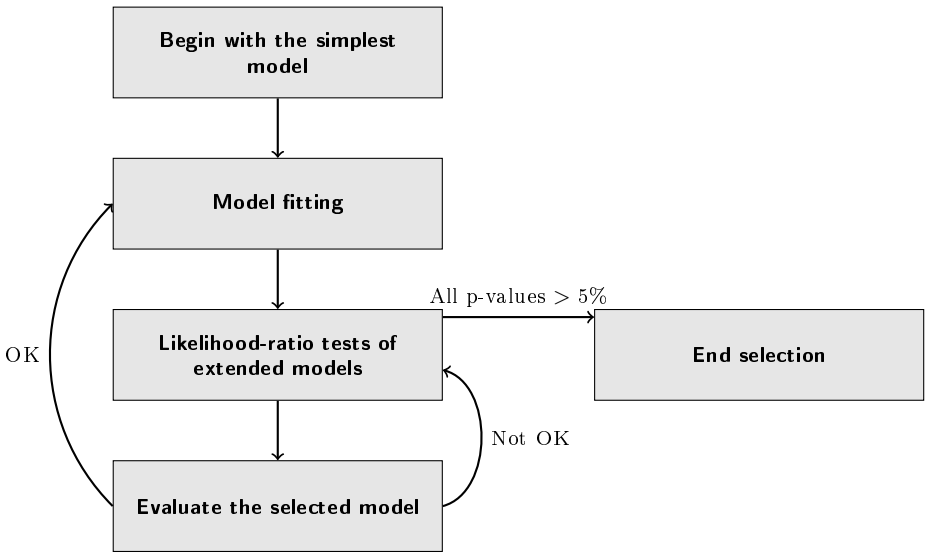

Figure G.2: Illustration of the model selection procedure

G.4.1 Model selection

The procedure starts by a formulation of the simplest feasible model having parameter space Ω_{m} and a full model with parameter space Ω_{full}, such that

$$\Omega_{\mathrm{m}} \subset \Omega_{\mathrm{full}}. \tag{G.10}$$

Within this range a set of models can be formed, in which a suitable model is to be identified. A suitable model is a sufficient model, which is the smallest model that describes all information embedded in the data (Madsen and Thyregod, 2010). The selection is initiated with the simplest model and then extensions of the model are iteratively added. The selection stops when all of the extensions to the selected model, gives a likelihood-ratio test p-value above the pre-specified limit. Hence the procedure will stop with a model from which no larger model can be found, with which it is significantly more likely to observe the data. As mentioned above a purely algorithmic procedure is not possible, hence the modeller must be involved to evaluate the models estimated in each iteration. The evaluation is carried out by analyzing the properties of residuals and parameter estimates, and if some of the properties are not in line with the assumptions and physical reality, then the modeller may have to influence the choice of model. The procedure is illustrated in Figure G.2 and the steps are

Model fitting The models which are extended from the current model are

fitted to the data by maximum likelihood estimation of the parameters.

Likelihood-ratio tests Calculate the likelihood-ratio test statistic for the current model versus each of the extended models. Stop if none of the tests have a p-value below 5% and use the current model as the final model, else then select the extended model which yield the lowest p-value.

Evaluate The modeller evaluates the selected extended model. If the result is satisfactory the model is kept and next iteration can be started; if not, the previous step should be repeated to select another extension.

If two extensions show an almost identical improvement, i.e. the p-values of the tests are nearly equal, the selection can be branched and extensions with different parts examined separately. The procedure will then end with several models, which cannot be tested directly against each other, and it is then up to the modeller to decide which should be preferred. This should be done by comparing the likelihoods, where if two models have almost equal likelihoods the smaller model should be preferred, and furthermore by an evaluation of the residuals and parameter estimates. It can also happen that several models have only marginal difference in performance and that each of them can be considered to be a sufficient model.

G.4.2 Model evaluation

In each step the selected model must be evaluated. This serves both to check if the model meet the assumptions and if it gives reasonable estimates from a physical point of view. Furthermore the evaluation can reveal model deficiencies from which it can be learned which parts of the model should be further elaborated. The evaluation should consist of the following:

- The assumption of white noise residuals should be inferred upon using the auto-correlation function (ACF) and the cumulated periodogram (CP), which can also reveal how well dynamics on different timescales are modelled.
- Plots of the inputs, outputs, and residuals. These plots can be used to understand which effects are not described properly by the model.
- Evaluation of the estimated physical parameters. Clearly the results should be consistent among different models, e.g. estimate of the thermal resistance of the building envelope should not change significantly among the models. Furthermore the modeller have to judge if the results are consistent with reality.

(a) (b)

Figure G.3: (a) the north facade and (b) is the south facade of the building.

G.5 Case study: model identification for a building

The method is demonstrated by applying it to identify a suitable model for a building. The building, named FlexHouse, is part of the experimental energy system Syslab, at Risø DTU in Denmark. It is well suited for such experiments since it has a controllable electrical heating system. Measurements consisting of five minute values over a period of six days are used, for further details see Bacher and Madsen (2010), in which a thorough description of the experiments and data is given. This section starts with a description of the building and measurement equipment, then the data is presented, followed by an outline of the considered models, and finally the model identification and evaluation is given.

G.5.1 Description of the building and measurement equipment

The outer walls of the building are constructed of wood on the outside and plaster boards on the inside, with a layer of insulation wool in between. An image of the north facade and an image of the south facade of the building can be seen in Figure G.3. The building rests on piles, leaving an air gab between the ground and the building. The roof is flat and covered with roofing felt. The dimensions of the floor plan is approximately 7.5 times 16 meters. In Figure G.4 the floor plan of the building is shown. A server system is installed in the building, which can control the electrical heaters located as indicated on the floor

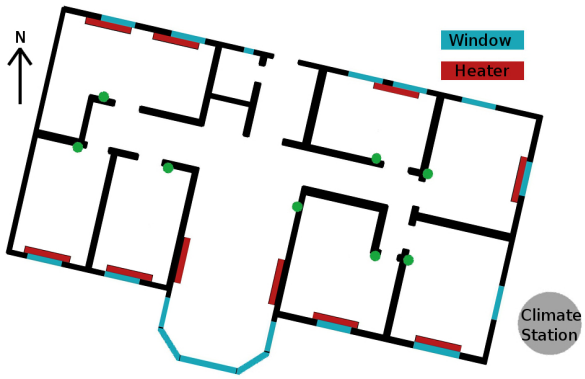

Figure G.4: The floor plan of the building.

plan. To measure the indoor temperature Hobo U12-012 Temp/RH/Light/Ext sensors mounted on a small piece of wood was hanged freely in the middle of each each room. A small climate station is located two meters east of the building, the position relative to the building is indicated in Figure G.4.

G.5.2 Data

The present study is based on data collected during a series of experiments carried out in February to April 2009. The following time series consisting of five minute average values are used:

y (°C) A single signal representing the indoor temperature. It is formed as the first principal component of the measurements of the indoor temperature from the Hobo sensors.

T_a (°C) Observed ambient air temperature at the climate station.

Φ_h (kW) Total heat input from the electrical heaters in the building.

Φ_s (kW/m^2) The global irradiance measured at the climate station.

Plots of the time series can be found in Figure G.5. The controlled heat input is a pseudo-random binary sequence (PRBS), which has white noise properties and no correlation with the other inputs. It is designed to excite the heat dynamics at several ranges of frequencies in which the time constants of the building is expected to be, such that the information embedded in data is optimized

for estimation of the heat dynamic properties of the building, see Madsen and Schultz (1993).

G.5.3 Applied models

The proposed procedure is such, that the modeller starts with the simplest model and iteratively selects more complex models. This implies fitting a set of models from the simplest model to the most feasible complex model, denoted the full model. In this section the set of applied models and the result of the iterative selection procedure is described. All the models are grey-box models, in which the physical part is stochastic linear state-space model (as presented in Section G.2) and where the dynamics of the states can be written

$$d\mathbf{T} = \mathbf{A}\mathbf{T}dt + \mathbf{B}\mathbf{U}dt + d\boldsymbol{\omega} \tag{G.11}$$

where $\mathbf{T}$ is the state vector and $\mathbf{U}$ is the input vector, and none of the state variables or input variables are in $\mathbf{A}$ or $\mathbf{B}$ which only consist of parameters. All the considered models have an input vector with three inputs

$$\mathbf{U} = [T_{\mathrm{a}}, \Phi_{\mathrm{s}}, \Phi_{\mathrm{h}}]^T \tag{G.12}$$

All the models are lumped, but with a different structure, which implies that a given parameter does not necessarily represent the same physical entity in each model. For example the parameter C_{i} is representing the heat capacity of the entire building in the simplest model, whereas this heat capacity is divided into five heat capacities in the full model, in which the parameter C_{i} represents the heat capacity of the indoor air. This is elaborated further in Section G.5.5.2, where the parameter estimates for the models are presented. Furthermore it should be kept in mind that these models are linear approximations to the real system.

In the following sections the full and the simplest model are described, since they represent the range of applied models. First the full model is outlined to give a complete overview of all the individual parts, which is included in the models. Then the simplest model is presented, since it is the first model applied in the selection procedure and furthermore it illustrates how the models are lumped. Each model is named from its state vector and where needed a few parameter names. See G.8 for a list of RC-networks corresponding to all applied models.

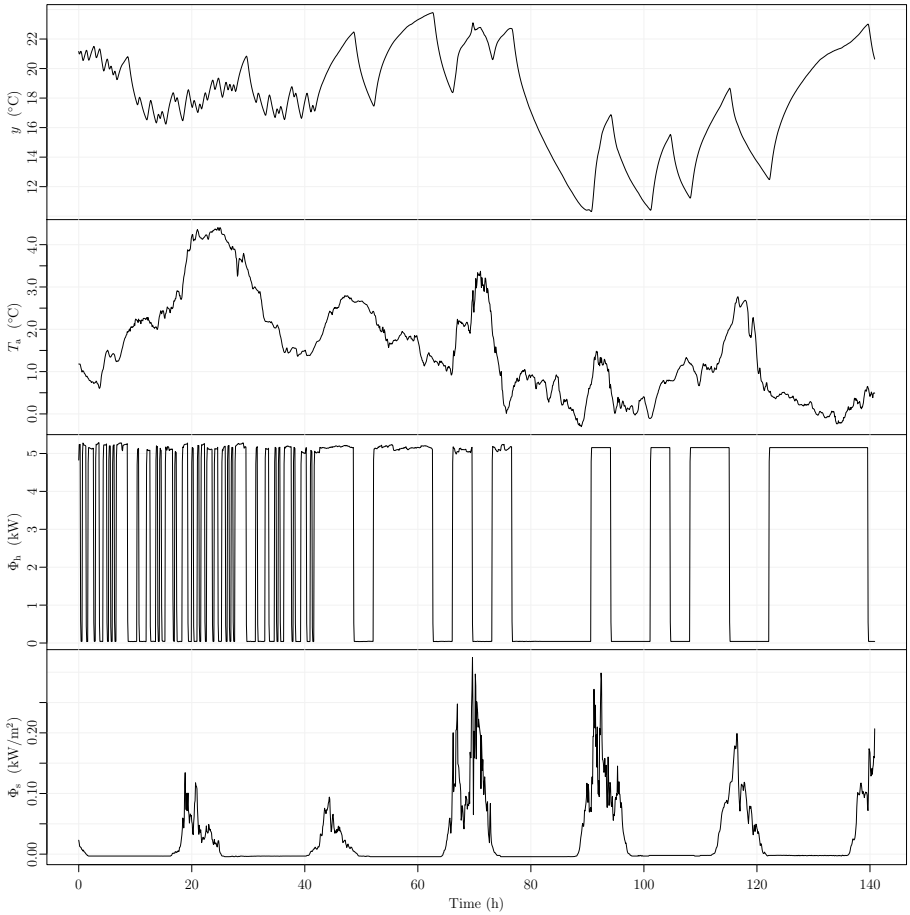

Figure G.5: The data set. From the top, the first plot shows the observed indoor temperature y, the second shows the ambient air temperature T_a, followed by a plot of the heat input Φ_h, and finally the lower plot shows the global irradiance Φ_s.

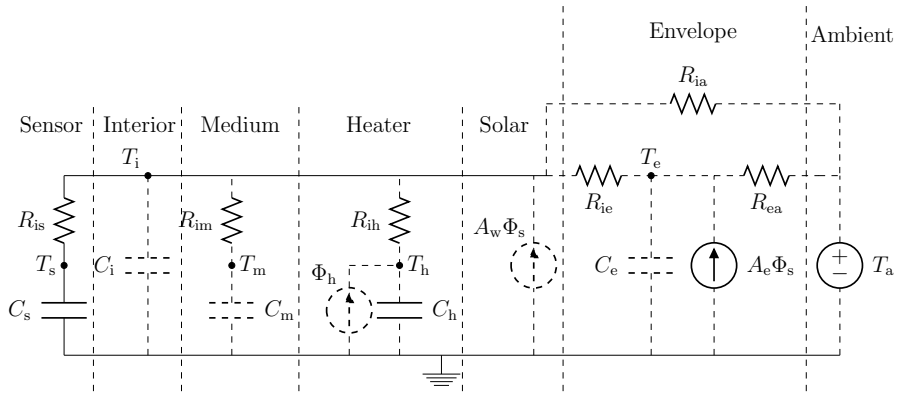

Figure G.6: The full model *TiTmTeThTsAeRia* with the individual model parts indicated. This model includes all parts which is included in any of the applied models.

G.5.3.1 The full model *TiTmTeThTsAeRia*

The RC-network of the full model, which is the most complex model applied, is illustrated in Figure G.6. This model includes all the individual parts of the building, which it is found feasible to include in linear models, with the current available data. The individual model parts are indicated on the figure. The model parts are:

Sensor The temperature sensors are modelled with a heat capacity and a thermal resistance to the interior.

Interior In the full model the interior is considered to be the indoor air (again remember that, since the models are lumped models, the building part represented by "Interior" is mostly different for each model) and it is modelled as a heat capacity connected to other parts by thermal resistances.

Medium A thermal medium inside the building is the interior walls and furniture, which is modelled with a heat capacity and a thermal resistance to the interior.

Heater The heaters are modelled by a heat capacity and a thermal resistance to the interior.

Solar The heat input from solar radiation is modelled by the global irradiance multiplied with the effective window area.

Envelope The building envelope is modelled with a heat capacity and thermal resistances to both the interior and the ambient. A thermal resistance directly coupled to the ambient is also included.

Ambient The ambient is represented by the observed ambient air temperature.

The full model includes five state variables, that each represents the temperature in a part of the building, and they are:

T_{s} The temperature of the sensor, which for the full model is used as the model output, i.e. Y_k in the measurement equation (Equation (G.19)).

T_{i} The temperature of the interior, i.e. the indoor air.

T_{m} The temperature of an interior thermal medium, i.e. interior walls and furniture.

T_{h} The temperature of the heaters.

T_{e} The temperature of the building envelope.

The parameters of the model represent different thermal properties of the building. This includes thermal resistances:

R_{is} between the interior and the sensor,

R_{im} between the interior and the interior thermal medium,

R_{ih} between the heaters and the interior,

R_{ia} between the interior and the ambient,

R_{ie} between from the interior and the building envelope,

R_{ea} between the building envelope and the ambient.

The heat capacities of different parts of the building are represented by:

C_{s} for the temperature sensor,

C_{i} for the interior,

C_{m} for the interior walls and furniture,

C_{h} for the electrical heaters,

C_e for the building envelope.

Finally two coefficients are included, each representing an estimate of an effective area in which the energy from solar radiation enters the building. They are:

A_w The effective window area of the building.

A_e The effective area in which the solar radiation enters the building envelope.

The set of stochastic differential equations describing the heat flows in the full model are

$$dT_s = \frac{1}{R_{is}C_s}(T_i - T_s)dt + \sigma_s d\omega_s \tag{G.13}$$

$$dT_i = \frac{1}{R_{is}C_i}(T_s - T_i)dt + \frac{1}{R_{im}C_i}(T_m - T_i)dt + \frac{1}{R_{ih}C_i}(T_h - T_i) \tag{G.14}$$

$$\frac{1}{R_{ie}C_i}(T_e - T_i)dt + \frac{1}{R_{ia}C_i}(T_a - T_i)dt + \frac{1}{C_i}A_w\Phi_s dt + \sigma_i d\omega_i \tag{G.15}$$

$$dT_m = \frac{1}{R_{im}C_m}(T_i - T_m)dt + \sigma_m d\omega_m \tag{G.16}$$

$$dT_h = \frac{1}{R_{ih}C_h}(T_i - T_h)dt + \frac{1}{C_h}\Phi_h dt + \sigma_h d\omega_h \tag{G.17}$$

$$dT_e = \frac{1}{R_{ie}C_e}(T_i - T_e)dt + \frac{1}{R_{ea}C_e}(T_a - T_e)dt + \frac{1}{C_e}A_e\Phi_s dt + \sigma_e d\omega_e \tag{G.18}$$

and the measurement equation is

$$Y_k = T_{s,k} + e_k \tag{G.19}$$

since the observed temperature is encumbered with some measurement error.

G.5.3.2 The simplest model *Ti*

The simplest model considered is illustrated by the RC-network in Figure G.7. The model has one state variable T_i and the following parameters:

R_{ia} The thermal resistance from the interior to the ambient.

C_i The heat capacity of the entire building, including the indoor air, interior walls, furniture etc., and the building envelope.

A_w is the effective window area of the building.

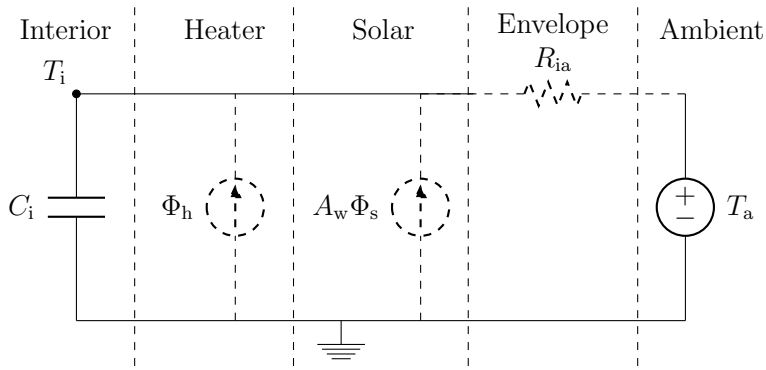

Figure G.7: RC-network of the model *Ti*, which is the simplest feasible model.

The stochastic differential equation describing the heat flow is

$$\frac{dT_\mathrm{i}}{dt} = \frac{1}{R_\mathrm{ia}C_\mathrm{i}}(T_\mathrm{a} - T_\mathrm{i}) + \frac{1}{C_\mathrm{i}}A_\mathrm{w}\Phi_\mathrm{s} + \frac{1}{C_\mathrm{i}}\Phi_\mathrm{h} + \sigma_\mathrm{i}\frac{d\omega_\mathrm{i}}{dt} \tag{G.20}$$

and the measurement equation is

$$Y_k = T_{\mathrm{i},k} + e_k \tag{G.21}$$

Note the differences in representation of the building parts between the simplest and full model, e.g. R_ia represent the thermal resistance of the building envelope in the simplest model, whereas this is represented by a coupling of $R_\mathrm{ia}, R_\mathrm{ie}$, and R_ea in the full model.

G.5.4 Model identification

The identification procedure is applied to find a sufficient model in the set of models ranging from *Ti* to *TiTmTeThTsAeRia*. The log-likelihood of each model, which is fitted, is listed in Table G.1 ordered by the iterations of the model selection. The procedure begins with the simplest model. Then in the first iteration four extended models are fitted and *TiTh* is selected since it has the highest log-likelihood, hence the lowest p-value of the likelihood-ratio tests (the four models have the same number of parameters). The selection procedure is carried out until no significant extension can be found, which occurs in iteration number five. During each iteration the current selected model is evaluated, see Section G.5.5. It is found that the models selected in each iteration are all satisfying the evaluation with respect to improvement of the results etc. In Table G.2 the result of likelihood-ratio tests for model expansion in each iteration is

Iteration	Models			
Start	*Ti*			
$l(\theta; \mathcal{Y}_N)$	2482.6			
m	6			
1	*TiTe*	*TiTm*	*TiTs*	*TiTh*
	3628.0	3639.4	3884.4	3911.1
	10	10	10	10
2	*TiThTs*	*TiTmTh*	*TiTeTh*	
	4017.0	5513.1	5517.1	
	14	14	14	
3	*TiTeThRia*	*TiTeThAe*	*TiTmTeTh*	*TiTeThTs*
	5517.3	5520.5	5534.5	5612.4
	15	15	18	18
4	*TiTeThTsRia*	*TiTmTeThTs*	*TiTeThTsAe*	
	5612.5	5612.9	5614.6	
	19	22	19	
5	*TiTmTeThTsAe*	*TiTeThTsAeRia*		
	5614.6	5614.7		
	23	20		

Table G.1: Log-likelihood $l(\theta; \mathcal{Y}_N)$ for the fitted models ordered by iterations of the model selection procedure and in each row by log-likelihood. In each iteration the extended model with highest log-likelihood is selected, which is the rightmost models in the table. The number of estimated parameters for each model is indicated by m.

listed. Clearly, the expansions carried out in the first three iterations indicate very significant improvements of the model. In iteration four, the improvement is still below 5%, whereas no significant improvement is found in iteration five. The procedure thus ends with *TiTeThTsAe* as a sufficient model, which is illustrated by the RC-network in Figure G.8.

G.5.5 Model evaluation

In the following the selected models are evaluated as outlined in Section G.4.2.

Iteration	Sub-model	Model	$m-r$	$-2log(\lambda(y))$	p-value
1	Ti	$TiTh$	4	2857	$< 10^{-16}$
2	$TiTh$	$TiTeTh$	4	3212	$< 10^{-16}$
3	$TiTeTh$	$TiTeThTs$	4	190.5	$< 10^{-16}$
4	$TiTeThTs$	$TiTeThTsAe$	1	4.5	0.035
5	$TiTeThTsAe$	$TiTeThTsAeRia$	1	0.12	0.73

Table G.2: Tests carried out in the model selection procedure.

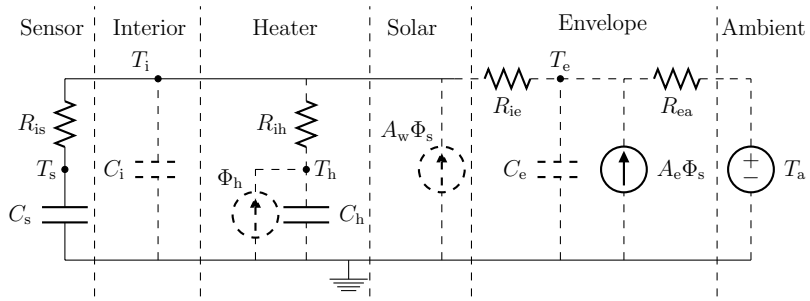

Figure G.8: The final selected model $TiTeThTsAe$ with the individual model parts indicated.

G.5.5.1 Residuals

Plots of output, inputs, and residuals for each model can be seen in Figure G.9. For each model the auto-correlation function (ACF) of the residuals is plotted in Figure G.10 and the cumulated periodogram (CP) in Figure G.11. It is seen directly from the plot of the residuals from the simplest model Ti, that they do not have white noise properties and that they are not independent of the inputs. The ACF of the residuals also clearly show a high lag dependency, and the CP reveals that the model is not detailed enough to describe the dynamics. Examining the plot of the residuals for the model selected in the first iteration, $TiTh$, it is seen that the level of the residuals is reduced compared to the residuals for Ti. The ACF and CP indicate that the assumption of white noise residuals is not fulfilled. From the plot of the residuals for the model selected in the second iteration, $TiTeTh$, it is seen that the level of the residuals is reduced dramatically, but that some dependency of the inputs is still seen, mostly from the solar irradiance. The ACF reveals that the characteristics of the residuals are much closer to white noise, which is also seen from the CP, indicating that the model now describes the heat dynamics of the building quite well. The plot of the residuals, ACF, and CP for the model selected in the third iteration

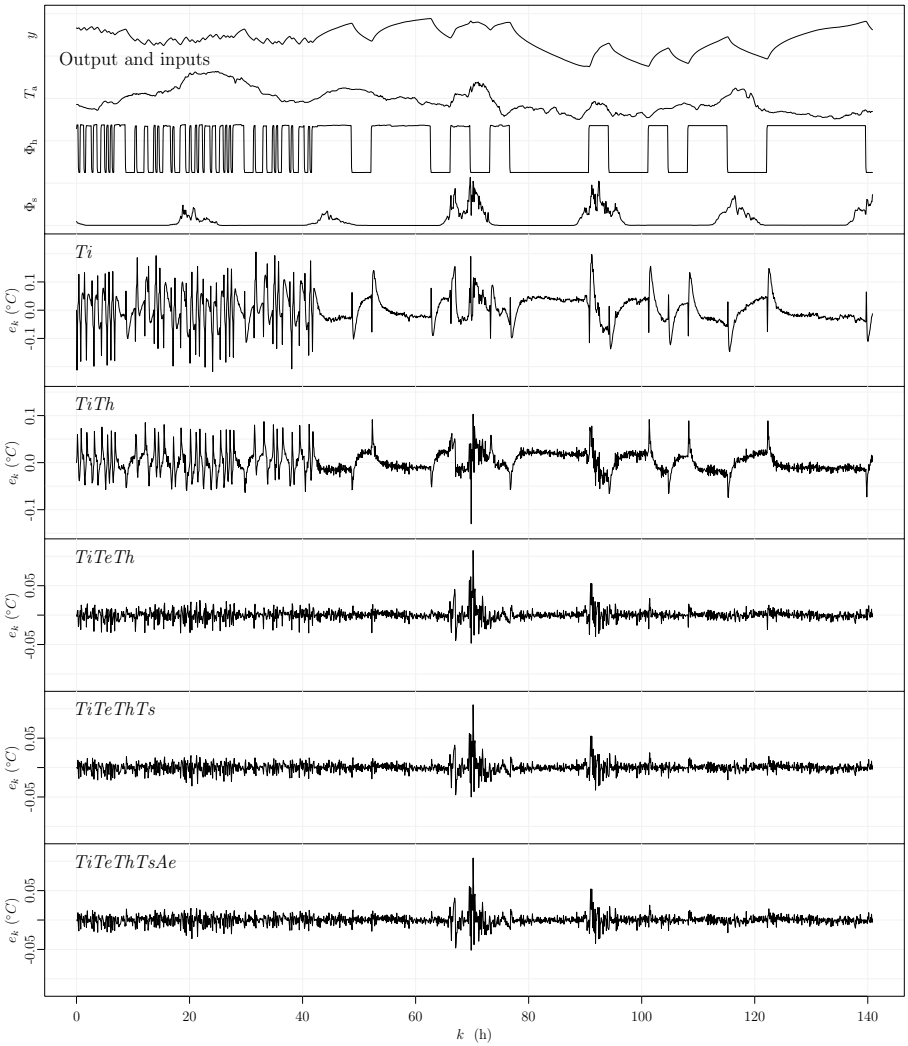

Figure G.9: The upper plot is of the output and inputs, and the following plots are of the residuals for each of the selected models. On each plot of the residuals the model name is indicated.

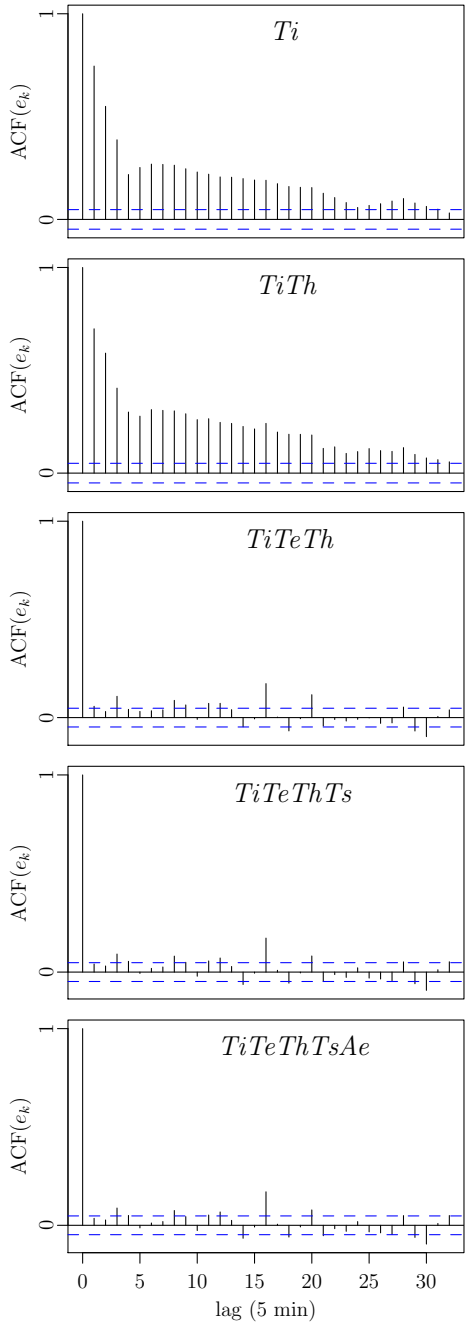

Figure G.10: The auto-correlation function of the residuals for each of the selected models.

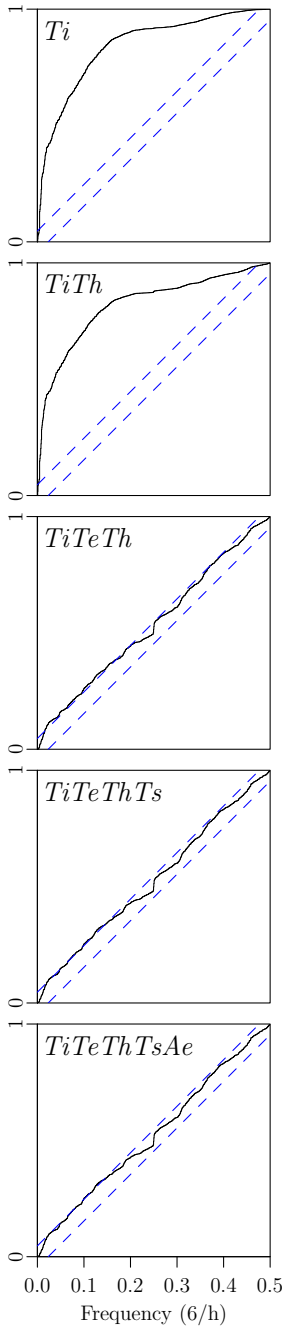

Figure G.11: The cumulated periodogram of the residuals for each of the selected models.

TiTeThTs, reveals only slight improvements compared to the previous model. Finally the plots for the final selected model *TiTeThTsAe*, show that almost no differences can be observed from the previous model. The highest level of error can be observed where the solar irradiance is high, hence it is found that further improvement of the model should be focused on the part in which the solar radiation enters the building, or alternatively in letting the incremental variance of the Wiener process depend on the solar radiation.

G.5.5.2 Parameter estimates

The parameter estimates of the selected models are evaluated in the following. The estimates are presented in Table G.3 together with the time constants calculated for each of the selected models. The total heat capacity and thermal resistance of the building envelope estimated by the selected models are presented in Table G.4. As found by evaluating the residuals, see previous section, the models *Ti* and *TiTh* do not describe the dynamics of the system very well, which implies that the estimates of the heat capacities are not reliable. Esti-

Model	*Ti*	*TiTh*	*TiTeTh*	*TiTeThTs*	*TiTeThTsWithAe*
C_{i}	2.07	1.36	1.07	0.143	0.0928
C_{e}	-	-	2.92	3.24	3.32
C_{h}	-	0.309	0.00139	0.321	0.889
C_{s}	-	-	-	0.619	0.0549
R_{ia}	5.29	5.31	-	-	-
R_{ie}	-	-	0.863	0.909	0.897
R_{ea}	-	-	4.54	4.47	4.38
R_{ih}	-	0.639	93.4	0.383	0.146
R_{is}	-	-	-	0.115	1.89
A_{w}	7.89	6.22	5.64	6.03	5.75
A_{e}	-	-	-	-	3.87
τ_1	10.9	0.16	0.129	0.0102	0.0102
τ_2	-	8.9	0.668	0.105	0.105
τ_3	-	-	18.4	0.786	0.788
τ_4	-	-	-	19.6	19.3

Table G.3: The estimated parameters. The heat capacities, C_{x}, are in [kWh/°C]. The thermal resistances, R_{xx}, are in [°C/kW]. The areas, A_{x}, are in $[\mathrm{m}^2]$. The time constants, τ_x, are in hours. Note that the physical interpretation for many of the parameters is different for each model.

Model	*Ti*	*TiTh*	*TiTeTh*	*TiTeThTs*	*TiTeThTsAe*
C_{total}	2.07	1.67	3.99	4.32	4.36
R_{envelope}	5.29	5.31	5.40	5.38	5.28
α_{UA}	1.55	1.55	1.52	1.53	1.55

Table G.4: The total heat capacity [kWh/°C] and thermal resistance [°C/kW] of the building envelope estimated by the selected models. The UA-values α_{UA} are in $\left[\text{W}/(^\circ\text{Cm}^2)\right]$.

mates of the heat capacities found by the tree larger models are more credible, especially it is seen that the time constants are almost equal, indicating that the models comprise the same dynamics. The exact physical interpretation of the smaller heat capacities $C_{\text{i}}, C_{\text{h}}$, and C_{s} cannot be given, but it is noted that their sum, for each of the three larger models, is quite close ranging from 1.03 to 1.08 [kWh/°C].

The estimated total thermal resistance of the building envelope and thereby the UA-values is quite similar for all models, as seen in Table G.4.

G.6 Applications

Identification of a suitable model of the heat dynamics of a building based on frequent readings of heat consumption, indoor temperature, ambient air temperature, and climate variables, will be very useful for different purposes. Important fields of application are:

Accurate description of energy performance of the building An energy signature of buildings can provide important information for energy- and cost effective improvements of the building. The most effective actions to be taken for an individual building can be identified. Furthermore the heat consumption due to physical effects, such as a poor isolated building envelope, can be separated from behavioral effects, e.g. a high indoor temperature.

Forecasting of energy consumption for heating Forecasting of energy consumption for heating can be used for integration of large amounts of renewable energy, such as wind- and solar energy. Implementation of electrical heating with hot water tanks for heat storage in individual houses can be profitable in the near future. Knowledge of the heat dynamics of buildings is essential to forecasting and control of such systems.

Indoor climate control Control of the indoor temperature, ventilation etc. to provide a good indoor climate conditions can be carried out with methods which include models of the heat dynamics. The models can also be extended to include the effect of wind and thereby provide information of the air tightness of buildings.

G.7 Conclusion

A procedure for identification of the most suitable models for the heat dynamics of a building has been described and applied on the basis of data from an experiment carried out in February 2009. The procedure is based on likelihood-ratio testing combined with a forward selection strategy. The proposed models are grey-box models, where a combination of prior physical knowledge and data-driven modelling is utilized. The data used for the modelling consist of: climate data measured at the location, measurements of the indoor temperature, and a PRBS controlled heat input.

The results of the identification procedure are evaluated and discussed, both in a statistical and physical context. The evaluation reveal that the selected model meet the assumptions of white noise residuals, hence it can be applied to give reliable estimates consistent with reality and the results are statistically validated. Furthermore model deficiencies are pointed out, from which further advancement of the model should be pursued. For the considered building this is primarily on the model part where the solar radiation input enters the building.

It has been shown that the method is able to provide rather detailed knowledge of the heat dynamics of the building. This includes for instance the thermal resistance of the envelope and thereby the UA-value, parameters describing the capabilities for storing heat, and the time constants of the building.

G.8 RC-networks of applied models

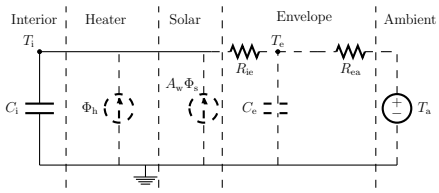

(a) RC-network network of *TiTe*.

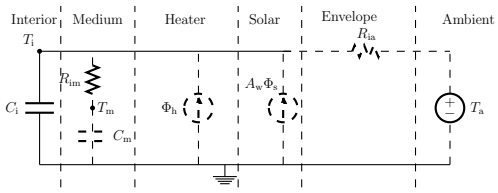

(b) RC-network network of *TiTm*.

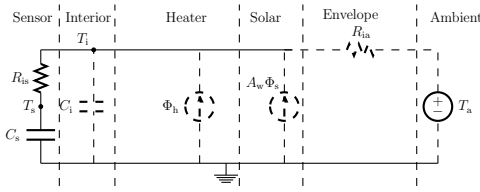

(c) RC-network network of *TiTs*.

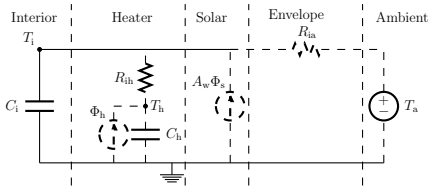

(d) RC-network network of *TiTh*.

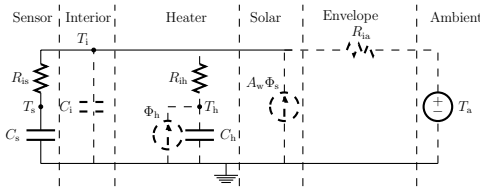

(e) RC-network network of *TiThTs*.

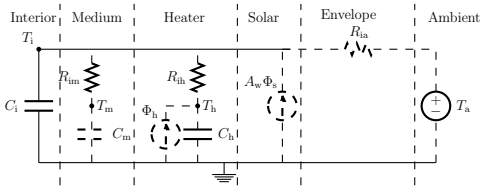

(a) RC-network network of $TiTmTh$.

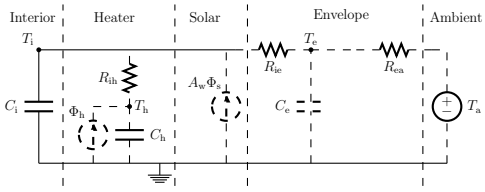

(b) RC-network network of $TiTeTh$.

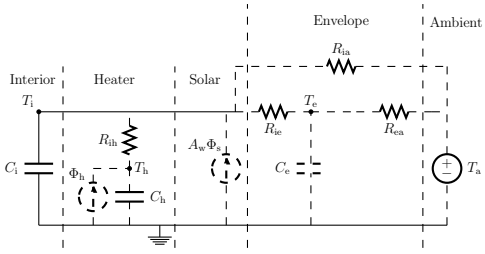

(c) RC-network network of $TiTeThRia$.

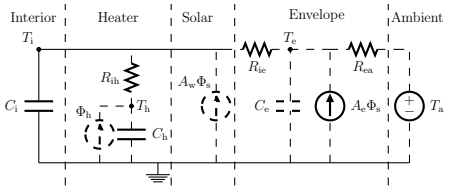

(d) RC-network network of $TiTeThAe$.

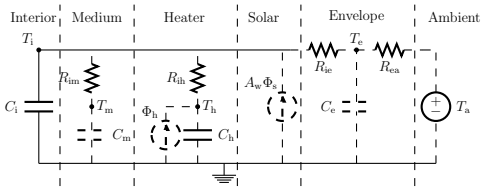

(e) RC-network network of $TiTmTeTh$.

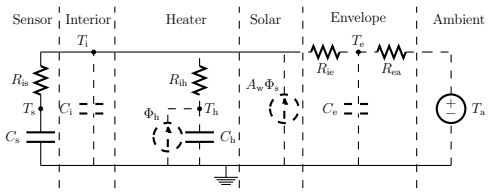

(a) RC-network network of *TiTeThTs*.

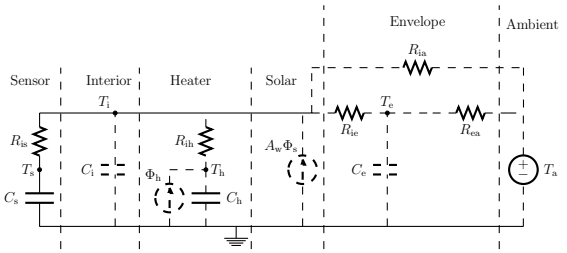

(b) RC-network network of *TiTeThTsRia*.

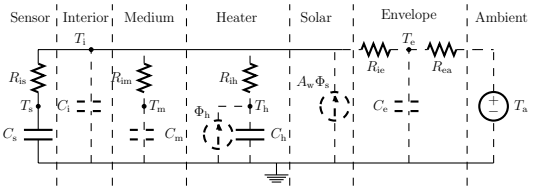

(c) RC-network network of *TiTmTeThTs*.

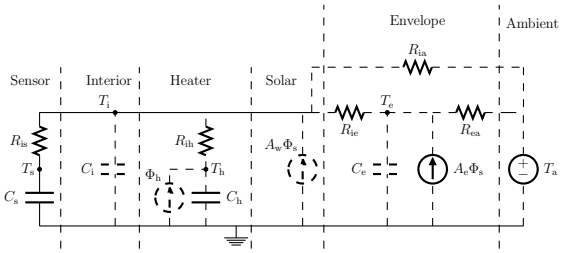

(d) RC-network network of *TiTeThTsAeRia*.

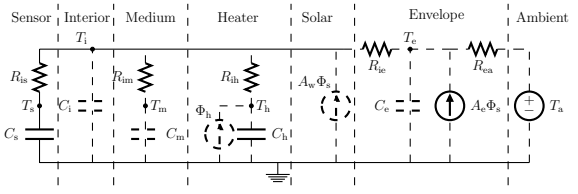

(e) RC-network network of *TiTmTeThTsAe*.

G.9 Estimates of system and observation noise parameters

The estimates of the scaling of the increments in the Wiener process in the system equations together with the standard deviation of the observation noise are listed in Table G.5. Considering the level of the estimated system noise for *Ti* and *TiTh* compared to the level of the estimated system noise for each of the three larger models, it should intuitively be higher, since *Ti* is a submodel of the larger models. However, since the residuals for *Ti* and *TiTe* are not white noise, then the system noise is almost surely not a Wiener process. Hence the definition of the parameters are not valid and a direct comparison not possible. For the three larger models *TiTeTh*, *TiTeThTs*, and *TiTeThTsWithAe* the estimated level of system noise is high compared to the level of measurement noise. This indicates that not all information is described by the model, hence that a more complicated and possibly non-linear model could be identified as more suitable than *TiTeThTsWithAe*.

Model	*Ti*	*TiTh*	*TiTeTh*	*TiTeThTs*	*TiTeThTsWithAe*
σ_{i}	0.19	$4.9 \cdot 10^{-6}$	0.017	0.13	0.18
σ_{e}			0.27	0.28	0.28
σ_{h}		1.4	$4.0 \cdot 10^{-5}$	$7.2 \cdot 10^{-5}$	$2.7 \cdot 10^{-5}$
σ_{s}				$3.8 \cdot 10^{-13}$	$2.0 \cdot 10^{-12}$
σ	$1.7 \cdot 10^{-11}$	$1.7 \cdot 10^{-11}$	$2.4 \cdot 10^{-6}$	$1.1 \cdot 10^{-6}$	$1.4 \cdot 10^{-6}$

Table G.5: The estimated values of system noise and measurement noise related parameters. The unit of the system noise parameters $\sigma_{\mathrm{i}}, \sigma_{\mathrm{e}}, \sigma_{\mathrm{h}}, \sigma_{\mathrm{s}}$ is $^{\circ}\mathrm{C}/\sqrt{\mathrm{h}}$ and the unit of the measurement noise σ is $^{\circ}\mathrm{C}$.

References

K. K. Andersen, H. Madsen, and L. H. Hansen. Modelling the heat dynamics of a building using stochastic differential equations. *Energy and Buildings*, 31 (1):13–24, 2000. ISSN 03787788.

P. Bacher and H. Madsen. Experiments and data for building energy performance analysis : Financed by the danish electricity saving trust. Technical report, DTU Informatics, Building 321, Kgs. Lyngby, 2010.

J. J. Bloem, editor. *System Identification Applied to Building Performance Data.* CEC-EUR 15885 EN, 1994.

H. Boyer, J. Chabriat, B. GrondinPerez, C. Tourrand, and J. Brau. Thermal building simulation and computer generation of nodal models. *BUILDING AND ENVIRONMENT*, 31(3):207–214, MAY 1996. ISSN 0360-1323.

M. Jiménez, H. Madsen, J. Bloem, and B. Dammann. Estimation of non-linear continuous time models for the heat exchange dynamics of building integrated photovoltaic modules. *Energy & Buildings*, 40(2):157–167, 2008. ISSN 03787788.

N. R. Kristensen and H. Madsen. Continuous time stochastic modelling, CTSM 2.3 - mathematics guide. Technical report, DTU, 2003.

N. R. Kristensen, H. Madsen, and S. B. Jørgensen. Parameter estimation in stochastic grey-box models. *Automatica*, 40(2):225 – 237, 2004. ISSN 0005-1098. doi: DOI:10.1016/j.automatica.2003.10.001.

H. Madsen and J. Holst. Estimation of continuous-time models for the heat dynamics of a building. *Energy and Buildings*, 22(1):67–79, 1995. ISSN 03787788.

H. Madsen and J. Schultz. Short time determination of the heat dynamics of buildings. Technical report, DTU, 1993.

H. Madsen and P. Thyregod. *Introduction to General and Generalized Linear Models.* CRC Press, 2010.

Y. Pawitan. *In All Likelihood: Statistical Modelling and Inference Using Likelihood.* Oxford University Press, 2001.

A. Rabl. Parameter-estimation in buildings - methods for dynamic analysis of measured energy use. *Journal of Solar Energy Engineering-transactions of the Asme*, 110(1):52–66, 1988. ISSN 0199-6231.

R. C. Sonderegger. *Dynamic models of house heating based on equivalent thermal parameters.* PhD thesis, Princeton Univ., NJ., 1978.

Peder Bacher, Henrik Madsen, Bengt Perers, Models of the heat dynamics of solar collectors for performance testing, ISES Solar World Congress 2011 Proceedings

MODELS OF THE HEAT DYNAMICS OF SOLAR COLLECTORS FOR PERFORMANCE TESTING

Peder Bacher[1], **Henrik Madsen**[1] **and Bengt Perers**[2]

[1]DTU Informatics, Richard Pedersens Plads, Building 321, DK-2800 Lyngby, Denmark
[2]DTU Civil Engineering, Brovej, Building 118, DK-2800 Lyngby, Denmark

Abstract

The need for fast and accurate performance testing of solar collectors is increasing. This paper describes a new technique for performance testing which is based on non-linear continuous time models of the heat dynamics of the collector. It is shown that all important performance parameters can be accurately estimated with measurements from a single day. The estimated parameters are compared with results from standardized test methods (Fischer et al., 2004).

Modelling the dynamics of the collector is carried out using stochastic differential equations, which is a well proven efficient method to obtain accurate estimates of parameters in physical models. The applied method is described by Kristensen et al. (2004) and implemented in the software CTSM[1]. Examples of successful applications of the method includes modelling the of the heat dynamics of integrated photo-voltaic modules (Friling et al., 2009) and modelling of the heat dynamics of buildings (Madsen and Holst, 1995).

Measurements obtained at a test site in Denmark during the spring 2010 are used for the modelling. The tested collector is a single glazed large area flat plate collector with selective absorber and Teflon anti convection layer. The test rig is described in Fan et al. (2009).

The modelling technique provides uncertainty estimates such as confidence intervals for the parameters, and furthermore enables statistical validation of the results. Such tests can also facilitate procedures for selecting the best model to use, which is a very non-trivial task.

1 Introduction

This paper presents a new statistical approach for modelling the heat dynamics of a solar thermal collector. The applied modelling technique facilitates application of detailed models on data sampled with a relatively high sample rate. It is demonstrated that this allows for parameter estimation with high accuracy to be achieved with measurements from a single day. In the present study 2 seconds values averaged to 30 seconds values are used. Conventional non-dynamical models - by some called pseudo-dynamical models - of solar collectors cannot use such a high sample rate due to auto-correlation of the errors caused by non-modelled dynamical effects. The applied models are based on stochastic differential equations (SDEs), which gives the possibility to combine physical and data-driven statistical modelling. Such models are called grey-box models. A very strong feature of grey-box models is that they provide the possibility to estimate hidden state variables, i.e. variables in the model which are not measured. This allows using the same data for fitting models, with which the system is lumped differently, i.e. the physical model of the system can either be a single-state or a multi-state lumped model, which can be required for different types of collectors. Furthermore the modelling technique facilitates application of statistical tests to determine which model is most suitable for the given data. This is important for model identification and the approach is demonstrated in the paper. The modelling is carried out based on measurements from a period of 9 consecutive days in the beginning of May 2010. None of the days could have been used for stationary testing that is still the most common test method for solar collectors. Stationary testing requires perfect stable clear weather around noon. The measurements were performed on a single glazed large area flat plate collector with selective absorber and Teflon anti convection layer. The collector was not brand new, but has been in operation for 15 years, which affects the parameter values compared to todays products of the similar design. The results from the grey-box models are compared with results from the standardized EN 12975 Quasi Dynamic Test Method (CEN, European committee for standardization, 2006), which is based on multiple linear regression (MLR) modelling, to see if the estimation results matches current test standards. Finally, a thorough discussion and perspectives of the technique are given.

The paper is arranged as follows. The next section is a presentation of the theory of the applied grey-box models, with a simple example. This is followed by a section with a description of the MLR models used and thereafter a section with a description of all the considered grey-box models. Then the results are presented, and finally a discussion and perspective is given before the paper ends with a conclusion.

[1]www2.imm.dtu.dk/~ctsm/

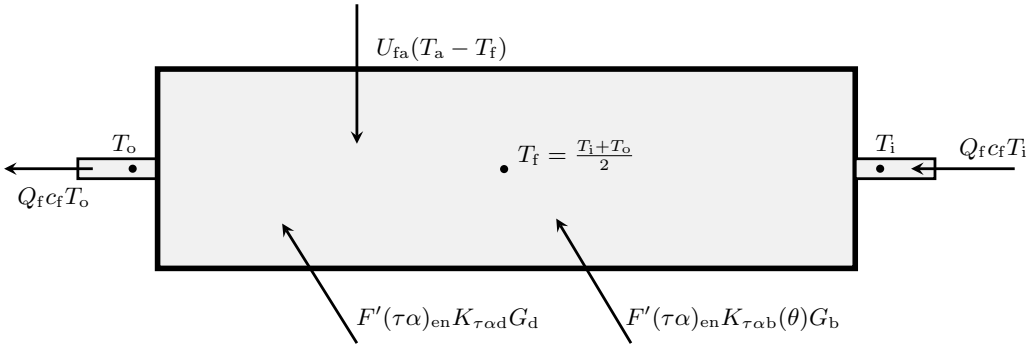

Figure 1: Diagram of *ToComp1* illustrating all the energy flows included in the model.

2 Grey-box models of a dynamic system

A grey-box model is established using a combination of prior physical knowledge and statistics, i.e. information embedded in data Kristensen et al. (2004). The prior physical knowledge is formulated by a set of non-linear stochastic differential equations (SDEs), also called a stochastic non-linear state-space model in continuous time. The equations describe a lumped model of the heat dynamics of the system.
The output of the solar collector is calculated by

$$q_{\mathrm{u}} = c_{\mathrm{f}}Q_{\mathrm{f}}(T_{\mathrm{o}} - T_{\mathrm{i}}) \tag{1}$$

where T_{o} is the outlet temperature and T_{i} is the inlet temperature. The output q_{u} is power output per square meter of collector aperture area and Q_{f} is flow per the same area. From Perers (1997) it is known that the output of a standard flat plate collector in first order accuracy level can be described by the heat balance

$$c_{\mathrm{f}}Q_{\mathrm{f}}(T_{\mathrm{o}} - T_{\mathrm{i}}) = F'(\tau\alpha)_{\mathrm{en}}K_{\tau\alpha\mathrm{b}}(\theta)G_{\mathrm{b}} + F'(\tau\alpha)_{\mathrm{en}}K_{\tau\alpha\mathrm{d}}G_{\mathrm{d}} - F'U_0(T_{\mathrm{f}} - T_{\mathrm{a}}) - (mC)_{\mathrm{e}}\frac{dT_{\mathrm{f}}}{dt} \tag{2}$$

For explanation of the symbols, see page 11. A linear temperature profile through the collector is applied by modelling the fluid temperature as a simple average

$$T_{\mathrm{f}} = \frac{T_{\mathrm{o}} + T_{\mathrm{i}}}{2} \tag{3}$$

The differential of the fluid temperature can then be written as

$$\frac{dT_{\mathrm{f}}}{dt} = \frac{1}{2}\frac{dT_{\mathrm{o}}}{dt} + \frac{1}{2}\frac{dT_{\mathrm{i}}}{dt} \tag{4}$$

which for a constant inlet temperature is

$$\frac{dT_{\mathrm{f}}}{dt} = \frac{1}{2}\frac{dT_{\mathrm{o}}}{dt} \tag{5}$$

This substitution, together with the addition of a noise term, is used to form the SDE

$$dT_{\mathrm{o}} = \Big(F'U_0(T_{\mathrm{a}} - T_{\mathrm{f}})dt + c_{\mathrm{f}}Q_{\mathrm{f}}(T_{\mathrm{i}} - T_{\mathrm{o}})dt + F'(\tau\alpha)_{\mathrm{en}}K_{\tau\alpha\mathrm{b}}(\theta)G_{\mathrm{b}}dt + F'(\tau\alpha)_{\mathrm{en}}K_{\tau\alpha\mathrm{d}}G_{\mathrm{d}}dt\Big)\frac{2}{(mC)_{\mathrm{e}}} + \sigma d\omega \tag{6}$$

which describes the heat dynamics for the collector in the simplest grey-box model considered in the paper. It is denoted as *ToComp1*. In grey-box terminology this is called the system equation of the state-space model. The noise term $\sigma d\omega$ is called the system noise and consist of increments of $\{\omega\}$, which is a standard Wiener process, and σ^2, which is the incremental variance of the Wiener process. In this model the collector is lumped into one single part and the state variable is the outlet temperature T_{o}. An illustration of the model is found in Figure 1.

The physical model part is coupled with the data-driven model part with which the information embedded in observed data is used for parameter estimation. The data-driven part in the considered example is represented by the discrete time measurement equation

$$Y_k = T_{ok} + e_k \tag{7}$$

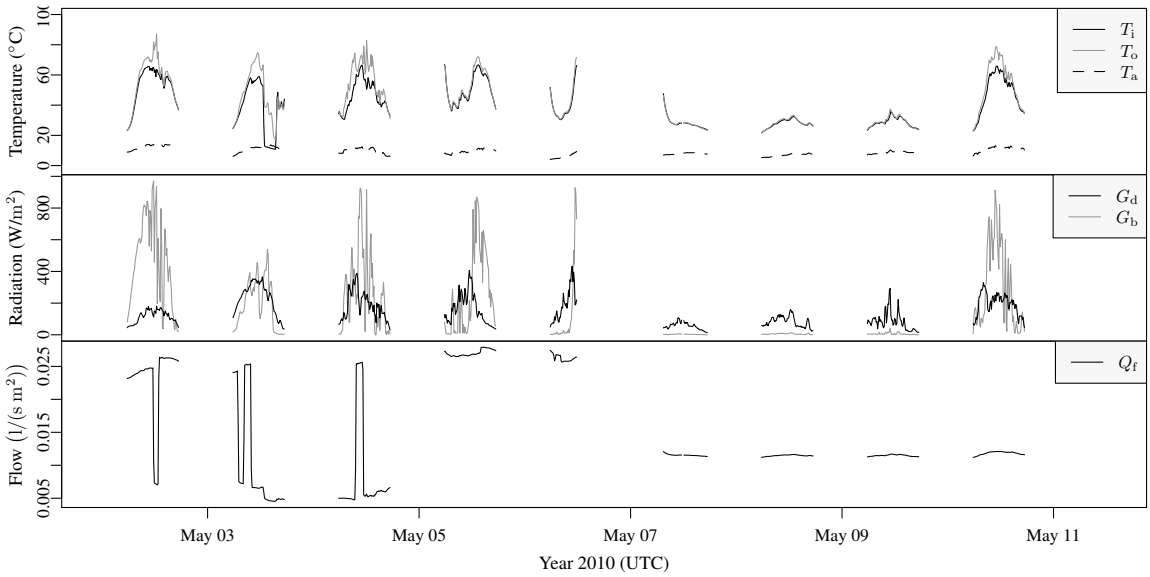

Figure 2: The data as 10 minutes averaged values. The upper plot is the measured temperatures, the middle plot is the diffuse and direct (beam) radiation, and the lowest plot is the fluid flow.

where k is the point in time t_k of a measurement, Y_k is the measured outlet temperature, and e_k is the measurement error, which is assumed to be a Gaussian white noise process with variance σ^2. This assumption - plus the assumption that W is a Wiener process - enables evaluation and tests of the performance of the model, since such tests can show if the physical model is consistent with the observed heat dynamics of the collector.

2.1 Maximum likelihood estimation of parameters

Given a grey-box model, as described above, maximum likelihood estimates of the parameters can be obtained. Let the N observations be represented by

$$\mathcal{Y}_N = [Y_N, Y_{N-1}, \ldots, Y_1, Y_0] \tag{8}$$

then the likelihood function is the joint probability density

$$L(\theta; \mathcal{Y}_N) = \left(\prod_{k=1}^{N} p(Y_k | \mathcal{Y}_{k-1}, \theta) \right) p(Y_0 | \theta) \tag{9}$$

where $p(Y_k|\mathcal{Y}_{k-1}, \theta)$ is a conditional density denoting the probability of observing Y_k given the previous observations and the parameters θ, and where $p(Y_0|\theta)$ is a parameterization of the starting conditions Kristensen et al. (2004). The maximum likelihood estimates of the parameters are then found by

$$\hat{\theta} = \arg\max_{\theta} \left\{ L(\theta; \mathcal{Y}_N) \right\} \tag{10}$$

Due to the previously mentioned assumptions about the system and measurement noise, it follows that the conditional densities in Equation (10) can be well approximated by Gaussian densities. Hence an extended Kalman filter can be used to calculate the likelihood function, and an optimization algorithm can be applied to maximize it, thereby calculating the maximum likelihood estimates, see Kristensen et al. (2004) for a detailed discussion. This is implemented in the computer software CTSM, which has been used for carrying out the parameter estimation. See more about the methods and software at [2] and in Kristensen and Madsen (2003).

3 Experimental setup and data

The experiments are described by Fan et al. (2009) and were carried out in the spring of 2010. The measurements were obtained with a 2 seconds sample interval. For the present study models are identified for both 30

[2] `www.imm.dtu.dk/~ctsm`

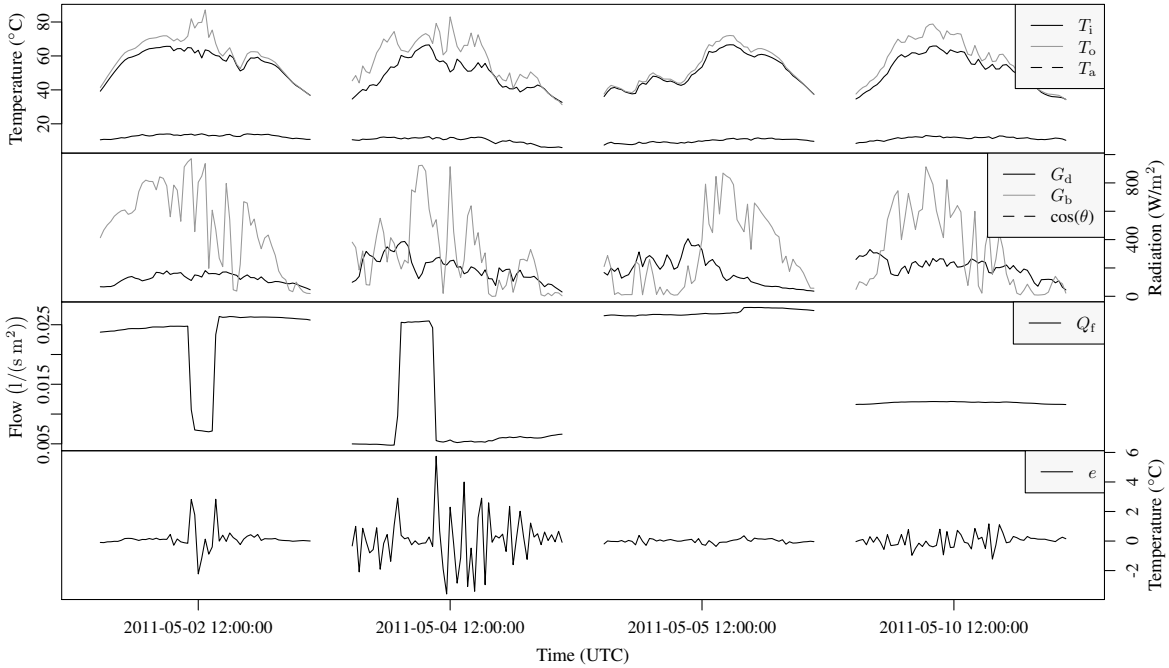

Figure 3: The 10 minutes averaged values from days where the model *ToComp1* is fitted. The upper plot is of the inlet-, outlet-, and the ambient temperature. Below this is shown a plot of the direct- and diffuse solar radiation, followed by a plot of the fluid flow. The lowest plot is the residuals from the fit from each day, this is referred to in a later in the paper.

seconds and 10 minutes average values. The data resampled to 10 minute average values is plotted in Figure 2. Only time points where the angle of incidence is lower than 84 degrees are used. For the parameter estimation it is important to acquire a period, for which the input signals are as uncorrelated as possible and cover the typical range of operation. Periods with full cloud cover are not feasible, since there is not enough variation in the direct radiation and in periods with no cloud cover the radiation and the module temperature is highly correlated. Hence days with varying cloud cover are most appropriate and these days are the most common in most locations where people traditionally live.

4 Multiple linear regression models

The EN 12975 Quasi Dynamic Test Method (CEN, European committee for standardization, 2006) is applied to have a reference for the results from the new proposed method. The method is based on multiple linear regression (MLR) modelling, where down to 5 minutes average values are recommended. The data was re-sampled to 10 minutes averages, which for all 9 days gives 593 time points. MLR modelling with 5 minutes averages was tried and the results were only marginally different. The following model structure is applied

$$q_t^{\mathrm{u}} = F'(\tau\alpha)_{\mathrm{en}} K_{\tau\alpha\mathrm{b}}(\theta) G_t^{\mathrm{b}} + F'(\tau\alpha)_{\mathrm{en}} K_{\tau\alpha\mathrm{d}} G_t^{\mathrm{d}} + F'U_0 \Delta T_t + F'U_1 \Delta T_t^2 - F'U_{\mathrm{w}} \Delta T_t w_t - (mC)_{\mathrm{e}} \frac{dT_t^{\mathrm{f}}}{dt} + e_t \tag{11}$$

where $\Delta T_t = T_t^{\mathrm{a}} - T_t^{\mathrm{f}}$. Three models are fitted: *MLR1* without $F'U_1$ and $F'U_{\mathrm{w}}$, *MLR2* without $F'U_1$, and *MLR3* with all inputs.

5 Applied grey-box models

This section gives an overview of the applied grey-box models and the parts of the data on which the parameter estimation was carried out. First the single state grey-box model *ToComp1*, described in Section 2 was fitted to 10 minutes average values on the days with varying cloud cover. This data is plotted in Figure 3. The model was fitted to each day separately and finally to all four days pooled together. In addition to the *ToComp1* model four other grey-box models have been fitted to the data from the 10'th of May resampled to 30 second average values. This gives $N = 1413$ data points, which are plotted in Figure 4. The additional four models are expanded as more detailed versions of *ToComp1*. There are two ways to expand the model: either more inputs

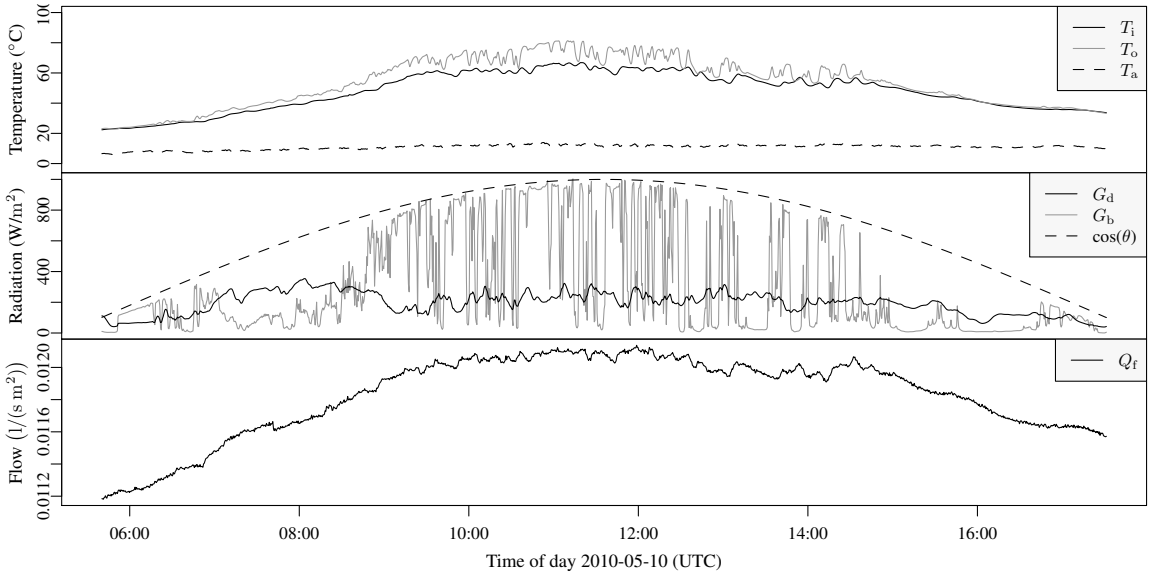

Figure 4: The 30 seconds averaged data for which the modelling is applied. The upper plot is of the inlet-, outlet-, and the ambient temperature. Below this is a plot of the direct- and diffuse solar radiation, followed by the plot of the fluid flow.

(explanatory variables) can be used, or - since the models are lumped models - a better representation can maybe be achieved by lumping the system into more parts (also called compartments, states, zones, or nodes). The latter approach is considered in the following. The first two expanded models are made more detailed by lumping the collector into more than one compartment in the flow direction of the collector fluid, such that the temperature of the collector is represented by two or more temperature state variables. This allows for a better representation of the temperature differences between the inlet - the cold side when solar radiation level is high - and the outlet of the collector. Furthermore this also gives a better description of the delay introduced since it takes time for the fluid to flow through the collector. For the current setup and the flow of the 10'th of May, this is around 1 minute. These two models are denoted by *ToComp2* and *ToComp3*. The third expanded model is denoted by *ToTmComp1* and in this model the collector is lumped in two parts: one representing the fluid and one representing the solid part of the collector. This is a better description of the system, in which the solar radiation first heats up the collector which then heats up the fluid. Finally, the fourth expanded model *TmToComp2* is a combination of the two approaches, where the collector is first divided in two parts - one for the fluid and one for the collector - which then each are divided into two compartments in the flow direction of the fluid.

5.1 Models with multiple compartments in the flow direction

The *ToComp1* model can be expanded to a n_c compartment model with the system equations

$$\begin{aligned}
dT_{\mathrm{o}1} &= \Big(F'U_0(T_\mathrm{a}-T_{\mathrm{f}1})+n_\mathrm{c}c_\mathrm{f}Q_\mathrm{f}(T_\mathrm{i}-T_{\mathrm{o}1})+F'(\tau\alpha)_\mathrm{en}K_{\tau\alpha\mathrm{b}}(\theta)G_\mathrm{b}+F'(\tau\alpha)_\mathrm{en}K_{\tau\alpha\mathrm{d}}G_\mathrm{d}\Big)\frac{2}{(mC)_\mathrm{e}}dt+\sigma_1 d\omega_1 \\
dT_{\mathrm{o}2} &= \Big(F'U_0(T_\mathrm{a}-T_{\mathrm{f}2})+n_\mathrm{c}c_\mathrm{f}Q_\mathrm{f}(T_{\mathrm{o}1}-T_{\mathrm{o}2})+F'(\tau\alpha)_\mathrm{en}K_{\tau\alpha\mathrm{b}}(\theta)G_\mathrm{b}+F'(\tau\alpha)_\mathrm{en}K_{\tau\alpha\mathrm{d}}G_\mathrm{d}\Big)\frac{2}{(mC)_\mathrm{e}}dt+\sigma_2 d\omega_2 \\
&\vdots \\
dT_{on_\mathrm{c}} &= \Big(F'U_0(T_\mathrm{a}-T_{\mathrm{f}n_\mathrm{c}})+n_\mathrm{c}c_\mathrm{f}Q_\mathrm{f}(T_{\mathrm{o}(n_\mathrm{c}-1)}-T_{on_\mathrm{c}})+F'(\tau\alpha)_\mathrm{en}K_{\tau\alpha\mathrm{b}}(\theta)G_\mathrm{b}+F'(\tau\alpha)_\mathrm{en}K_{\tau\alpha\mathrm{d}}G_\mathrm{d}\Big)\frac{2}{(mC)_\mathrm{e}}dt+\sigma_2 d\omega_2
\end{aligned} \tag{12}$$

where n_c is the number of compartments. The accompanying measurement equation is

$$Y_k = T_{on_\mathrm{c}k}+e_k \tag{13}$$

Two models of this type are fitted to the data: *ToComp2* with two compartments, and *ToComp3* with three compartments. A diagram illustrating *ToComp2* is shown in Figure 5

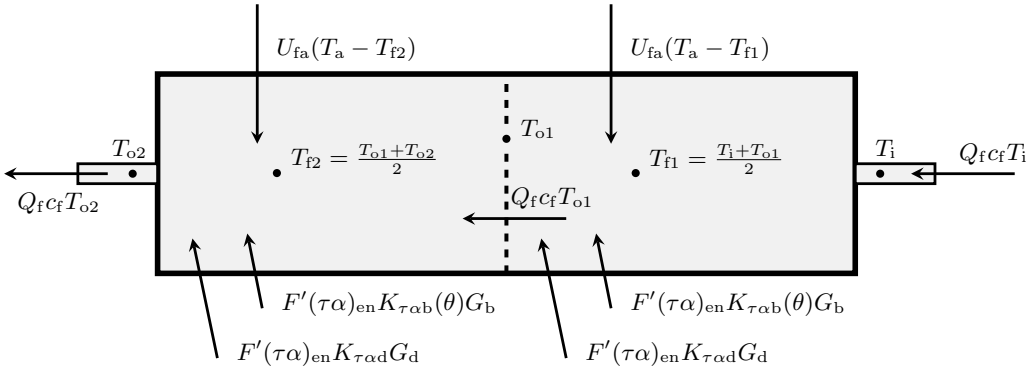

Figure 5: The *ToComp2* model with two compartments in the flow direction of the fluid.

5.2 Models divided into a collector and a fluid part

The *TmToComp1* model illustrated in Figure 6, where the panel is divided into two parts, has the system equation

$$dT_{\mathrm{m}} = \Big(F'(\tau\alpha)_{\mathrm{en}}K_{\tau\alpha\mathrm{b}}(\theta)G_{\mathrm{b}} + F'(\tau\alpha)_{\mathrm{en}}K_{\tau\alpha\mathrm{d}}G_{\mathrm{d}} + U_{\mathrm{fm}}(T_{\mathrm{f}} - T_{\mathrm{m}}) + U_{\mathrm{ma}}(T_{\mathrm{a}} - T_{\mathrm{m}})\Big)\frac{1}{(mC)_{\mathrm{e}}}dt + \sigma_m d\omega_m \tag{14}$$

$$dT_{\mathrm{o}} = \Big(U_{\mathrm{fm}}(T_{\mathrm{m}} - T_{\mathrm{f}}) + c_{\mathrm{f}}Q_{\mathrm{f}}(T_{\mathrm{i}} - T_{\mathrm{o}})\Big)\frac{2}{(mC)_{\mathrm{e}}}dt + \sigma_o d\omega_o$$

It is seen that the solar radiation enters the collector part, which then heats up the fluid by conduction. Of the considered models the most detailed model is *TmToComp2*, in which the collector is both divided into two parts and 2 compartments in the fluid flow direction for each part. The following system equations is formulated for a model with two parts having each n_{c} compartments

$$\begin{aligned}
dT_{\mathrm{m1}} &= \Big(F'(\tau\alpha)_{\mathrm{en}}K_{\tau\alpha\mathrm{b}}(\theta)G_{\mathrm{b}} + F'(\tau\alpha)_{\mathrm{en}}K_{\tau\alpha\mathrm{d}}G_{\mathrm{d}} + U_{\mathrm{fm}}(T_{\mathrm{f1}} - T_{\mathrm{m1}}) + U_{\mathrm{ma}}(T_{\mathrm{a}} - T_{\mathrm{m1}})\Big)\frac{1}{(mC)_{\mathrm{e}}}dt + \sigma_{\mathrm{m1}}d\omega_{\mathrm{m1}} \\
dT_{\mathrm{o1}} &= \Big(U_{\mathrm{fm}}(T_{\mathrm{m1}} - T_{\mathrm{f1}}) + n_{\mathrm{c}}c_{\mathrm{f}}Q_{\mathrm{f}}(T_{\mathrm{i}} - T_{\mathrm{o1}})\Big)\frac{2}{(mC)_{\mathrm{e}}}dt + \sigma_{\mathrm{o1}}d\omega_{\mathrm{o1}} \\
dT_{\mathrm{m2}} &= \Big(F'(\tau\alpha)_{\mathrm{en}}K_{\tau\alpha\mathrm{b}}(\theta)G_{\mathrm{b}} + F'(\tau\alpha)_{\mathrm{en}}K_{\tau\alpha\mathrm{d}}G_{\mathrm{d}} + U_{\mathrm{fm}}(T_{\mathrm{f2}} - T_{\mathrm{m2}}) + U_{\mathrm{ma}}(T_{\mathrm{a}} - T_{\mathrm{m2}})\Big)\frac{1}{(mC)_{\mathrm{e}}}dt + \sigma_{\mathrm{m2}}d\omega_{\mathrm{m2}} \\
dT_{\mathrm{o2}} &= \Big(U_{\mathrm{fm}}(T_{\mathrm{m2}} - T_{\mathrm{f2}}) + n_{\mathrm{c}}c_{\mathrm{f}}Q_{\mathrm{f}}(T_{\mathrm{o1}} - T_{\mathrm{o2}})\Big)\frac{2}{(mC)_{\mathrm{e}}}dt + \sigma_{\mathrm{o2}}d\omega_{\mathrm{o2}} \\
&\vdots \\
dT_{\mathrm{m}n_{\mathrm{c}}} &= \Big(F'(\tau\alpha)_{\mathrm{en}}K_{\tau\alpha\mathrm{b}}(\theta)G_{\mathrm{b}} + F'(\tau\alpha)_{\mathrm{en}}K_{\tau\alpha\mathrm{d}}G_{\mathrm{d}} + U_{\mathrm{fm}}(T_{\mathrm{f}n_{\mathrm{c}}} - T_{\mathrm{m}n_{\mathrm{c}}}) + U_{\mathrm{ma}}(T_{\mathrm{a}} - T_{\mathrm{m}n_{\mathrm{c}}})\Big)\frac{1}{(mC)_{\mathrm{e}}}dt + \sigma_{\mathrm{m}n_{\mathrm{c}}}d\omega_{\mathrm{m}n_{\mathrm{c}}} \\
dT_{\mathrm{o}n_{\mathrm{c}}} &= \Big(U_{\mathrm{fm}}(T_{\mathrm{m}n_{\mathrm{c}}} - T_{\mathrm{f}n_{\mathrm{c}}}) + n_{\mathrm{c}}c_{\mathrm{f}}Q_{\mathrm{f}}(T_{\mathrm{o1}} - T_{\mathrm{o}n_{\mathrm{c}}})\Big)\frac{2}{(mC)_{\mathrm{e}}}dt + \sigma_{\mathrm{o}n_{\mathrm{c}}}d\omega_{\mathrm{o}n_{\mathrm{c}}}
\end{aligned}$$

i.e. the *TmToComp2* model has $n_{\mathrm{c}} = 2$.

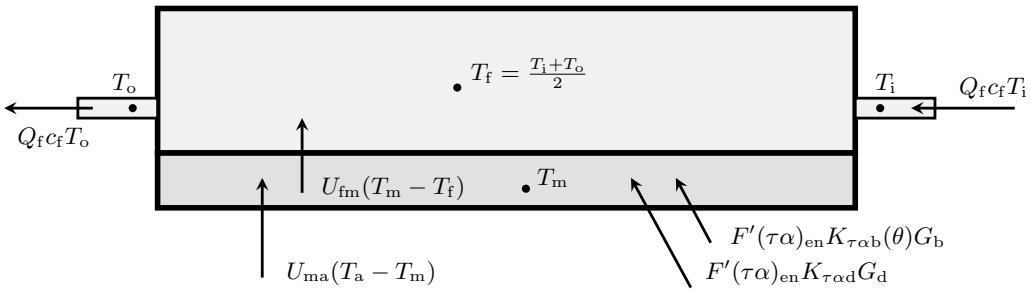

Figure 6: Diagram illustrating the *TmToComp1* model. The collector is divided into a part representing the fluid and another part representing the collector.

Table 1: Parameter estimates with MLR models. The standard deviation of the estimate is in parenthesis to the right of the estimated value. Insignificant terms are marked with *.

Parameter	*MLR1*		*MLR2*		*MLR3*		Units
$F'(\tau\alpha)_{\mathrm{en}}$	0.737	(0.0031)	0.741	(0.0030)	0.746	(0.0043)	
b_0	0.166		0.172		0.175		
$K_{\tau\alpha\mathrm{d}}$	0.891		0.904		0.895		
$F'U_0$	2.18	(0.45)	2.13	(0.045)	2.02	(0.082)	$[\mathrm{W/(m^2K)}]$
$F'U_1$					0.0031*	(0.0020)	$[\mathrm{W/(m^2K)}]$
$F'U_{\mathrm{w}}$			0.192	(0.034)	0.179	(0.035)	$[\mathrm{W/(m^2K)}]$
$(mC)_{\mathrm{e}}$	4699	(130)	4751	(127)	4788	(129)	$[\mathrm{J/(m^2K)}]$

6 Results

In this section the results of the parameter estimation with the described models are presented. Firstly, the results from the traditional MLR models fitted on the entire data set of 10 minutes values is presented, secondly from grey-box model *ToComp1* fitted on individual days of 10 minutes values, and finally all grey-box models fitted on 30 seconds values from the 10'th of May. The parameter estimates together with the their standard deviation are presented in tables, and time series of the residuals together with other relevant error measures are plotted. A short outline of the model identification carried out is also provided.

6.1 MLR models

The parameter estimates are listed in Table 1. The estimates are clearly within the typical range for this type of collector, see Perers (1993) and Solar Keymark homepage (Solar Keymark, 2011). The collector under test has been in operation for 15 years, this affects the parameter values compared to todays products. The standard deviations show that the parameters are very accurately determined. The only non-significant term are $F'U_1$ in *MLR3*, which leads the conclusion that *MLR2* is the most appropriate model of the three. For evaluation of the model fit the measured collector output versus the predicted is plotted in Figure 7. It is seen that the measured output is predicted very well, although it does seems like the variance increase slightly with the output. This is most likely due to the periods with low flow rate for some of the days. Furthermore the inlet temperature variation range is not fully as high as specified in the standard for the selected days.

6.2 ToComp1 fitted to 10 minutes values

The single state grey-box model defined in Equation (6) is fitted to both 10 minutes values from four separate days and all four pooled together. The estimated parameter are listed in Table 2. Clearly the parameter estimates matches the estimates from the MLR models quite well considering the standard deviations, especially the parameters $F'(\tau\alpha)_{\mathrm{en}}$ and $F'U_0$, which are the most important parameters for evaluation of the collector performance. A very apparent deviation of the results between the days is that the lowest uncertainty is found on the 5'th of May. This is not a surprise considering a plot of the residuals, which is shown in the lowest plot

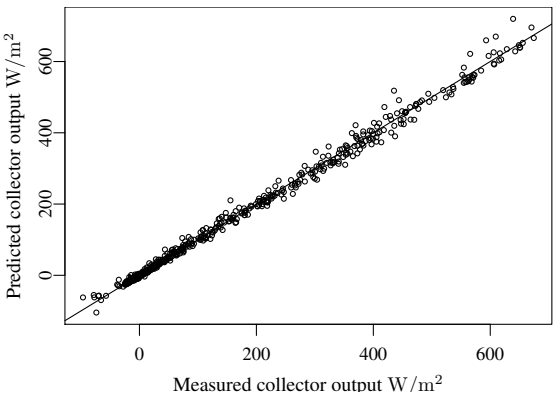

Figure 7: Measured versus the predicted collector output from *MLR2*.

Table 2: Parameter estimates from *ToComp1* fitted to 10 minutes values from single days and all four days pooled. The standard deviation is given in parenthesis to the right of the estimate.

	2011-05-02		2011-05-04		2011-05-05		2011-05-10		Pooled	
$F'(\tau\alpha)_{\mathrm{en}}$	0.755	(0.032)	0.785	(0.032)	0.746	(0.0086)	0.758	(0.014)	0.763	(0.011)
b_0	0.204	(0.039)	0.201	(0.046)	0.18	(0.017)	0.182	(0.023)	0.195	(0.020)
$K_{\tau\alpha\mathrm{d}}$	0.903	(0.42)	0.857	(0.11)	0.819	(0.027)	0.867	(0.049)	0.839	(0.034)
$F'U_0$	2.07	(1.1)	2.4	(0.35)	1.73	(0.13)	2.16	(0.26)	2.05	(0.18)
$(mC)_{\mathrm{e}}$	6050	(1060)	6200	(1130)	5040	(279)	5020	(92)	5666	(638)

Table 3: The parameter estimates from the grey-box models fitted to 30 seconds values from the 10'th of May. Note that the parameters represent different physical entities from the three first model (prefixed with *To*) to the last two models (prefixed with *TmTo*) and therefore cannot be directly compared. For each estimate the standard deviation is given in parenthesis to the right of the estimate.

	ToComp1		ToComp2		ToComp3		TmToComp1		TmToComp2	
$F'(\tau\alpha)_{\mathrm{en}}$	0.767	(0.0036)	0.751	(0.0027)	0.743	(0.0015)	0.816	(0.0025)	0.792	(0.00096)
b_0	0.172	(0.0063)	0.177	(0.0017)	0.18	(0.00044)	0.188	(0.0038)	0.189	(0.00067)
$K_{\tau\alpha\mathrm{d}}$	0.942	(0.015)	0.933	(0.0042)	0.931	(0.002)	0.929	(0.008)	0.927	(0.0021)
U_{fa}	2.55	(0.076)	2.31	(0.049)	2.2	(0.023)				
U_{fm}							49.8	(2.5)	83.7	(0.83)
U_{ma}							2.37	(0.042)	2.22	(0.016)
C_{f}	6960	(80)	8020	(17)	8580	(36)	3750	(114)	3390	(54)
C_{m}							962	(64)	1690	(22)

of Figure 3. The level of the residuals from the fit to this day are smaller than for the other days, and this is apparently due to the level of the fluid flow, which is plotted above the residuals in the figure. The parameter estimates based on the four days pooled together seems like a compromise between the estimates from the single days.

6.3 Grey-box models fitted to 30 seconds values

The five grey-box models described are fitted to the data from the 10'th of May resampled to 30 seconds averages. The parameter estimates are listed in Table 3. First, it is noticed that the parameters of the three models prefixed with *To* are not representing the same physical entities as they do in the models prefixed with *ToTm*, since the collector is lumped differently in the models. The increase of the value of $F'(\tau\alpha)_{\mathrm{en}}$ from *To* to *ToTm* models is found to be consistent with the physical representation, since the reference temperature is closer to the absorber surface. This means that the estimated optical parameter for the *ToTm* models is rather $\tau\alpha$. The value F' is in the range of 0.95 for this collector design, which leads to an estimate of $F'(\tau\alpha)_{\mathrm{en}}$ to 0.752 for *ToTmComp2*.

Plots of the residual series from each model are shown in Figure 8. Clearly the level of the residuals decrease from the upper to the lower plot and the highest errors occur when a cloud passes by and the level of direct solar radiation shifts rapidly. The decreased level of the variation of the residuals indicates that the more detailed models are better. To verify this, statistical likelihood-ratio tests is applied as described by Bacher and Madsen (2011). The log-likelihood of the fit for each model is listed in Table 4, together with the number of parameters, and the p-value of tests for model expansion. The tests for expansion is a model versus the expanded model a single step to the right in the table, except for *nl2TmToComp1*, from which the expansion is from *nl2ToComp2*. The results of the tests are very clear, all expansions are significant. Hence it is concluded that *nl2TmToComp2* is the most suitable model of these five models and that it might very well be, that the model could be further expanded. Finally, the auto-correlation function (ACF) and the cumulated periodogram (CP) Madsen (2007) of the residuals are shown in Figure 9. The dashed blue lines indicate 95% confidence intervals for a white noise. According to theory, presented in Section 2, then if the residual series are white noise this indicates that the grey-box model is consistent with the observed heat dynamics of the collector. From the ACF and CP it is seen that the residuals are close to having white noise properties. Interestingly it is seen that residuals from *ToComp1* are more white noise like than the residuals from *TmToComp1*. It is found that this is caused by a low signal to noise ratio in the residuals for *ToTmComp1*, i.e. the dominating errors are on a high frequency which have characteristics like white noise. As the detailed models includes the faster

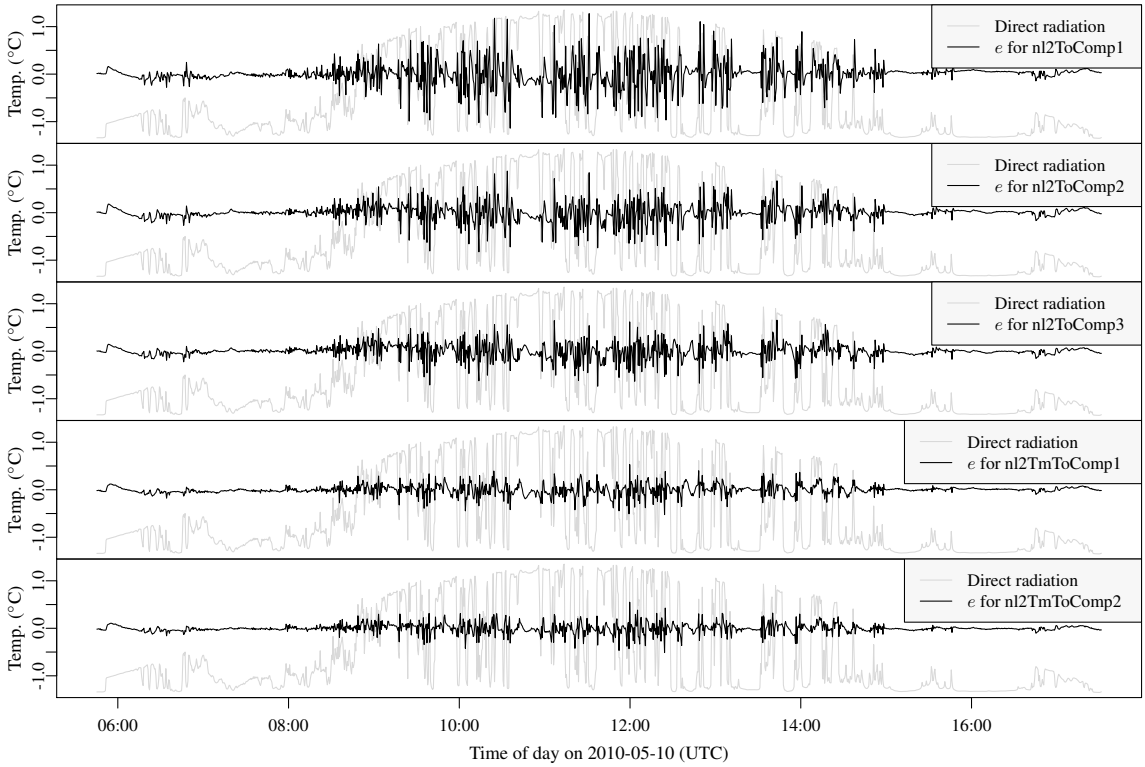

Figure 8: The residual series from the grey-box models fitted to 30 seconds values from the 10'th of May. The greyed series are the direct solar radiation.

dynamics, the high frequency errors are decreased, and they do not "hide" the remaining signal components in the residuals. However for the most detailed model almost all the systematic variation in the data is described.

7 Discussion and applications

In general the results from the MLR models and the grey-box are found to match well, but it is noted that the result the from grey-box model *ToComp1* fitted on separate days - which have different conditions, especially in the fluid flow level - gives some variation to the estimates. Therefore it is concluded that attention has to be put on the experimental design in order to ensure stable and accurate parameter estimation for collector testing with grey-box models. Regarding the more detailed grey-box models fitted to 30 seconds values, it is found that since the likelihood is not saturated, i.e. the likelihood-ratio tests are very significant, further expansion of the *TmToComp2* is still possible. From the plots of the residuals in Figure 8, it is seen that the error level certainly is highest just after the direct radiation shifts its level very rapidly, and it is this effect that seems to be improved as the more detailed models are used. Hence the main improvement from the one-state model *ToComp1* to the multi-state models are in the description of the fast dynamics, which includes the delay caused by movement of the fluid through the collector, e.g. when the direct radiation shifts from a high to a low level, the fluid passing out of the collector are still hot for some time. This also indicates the importance of the experiment design, since for dynamic condition the frequency, with which the system is excited, affect which grey-box model is optimal. For example if the direct radiation varies with a lower frequency, a simpler model might be in favour over more complex models, whereas for variation with a higher frequency the inclusion of the fast dynamics

Table 4: Log-likelihood, number of parameters, and p-value of likelihood-ratio tests for model expansion for each of the grey-box models.

	nl2ToComp1	nl2ToComp2	nl2ToComp3	nl2TmToComp1	nl2TmToComp2
Log-likelihood	-35.51	454.8	661	1185	1307
Number of prm.	9	12	14	13	18
p-value		≈ 0	≈ 0	≈ 0	≈ 0

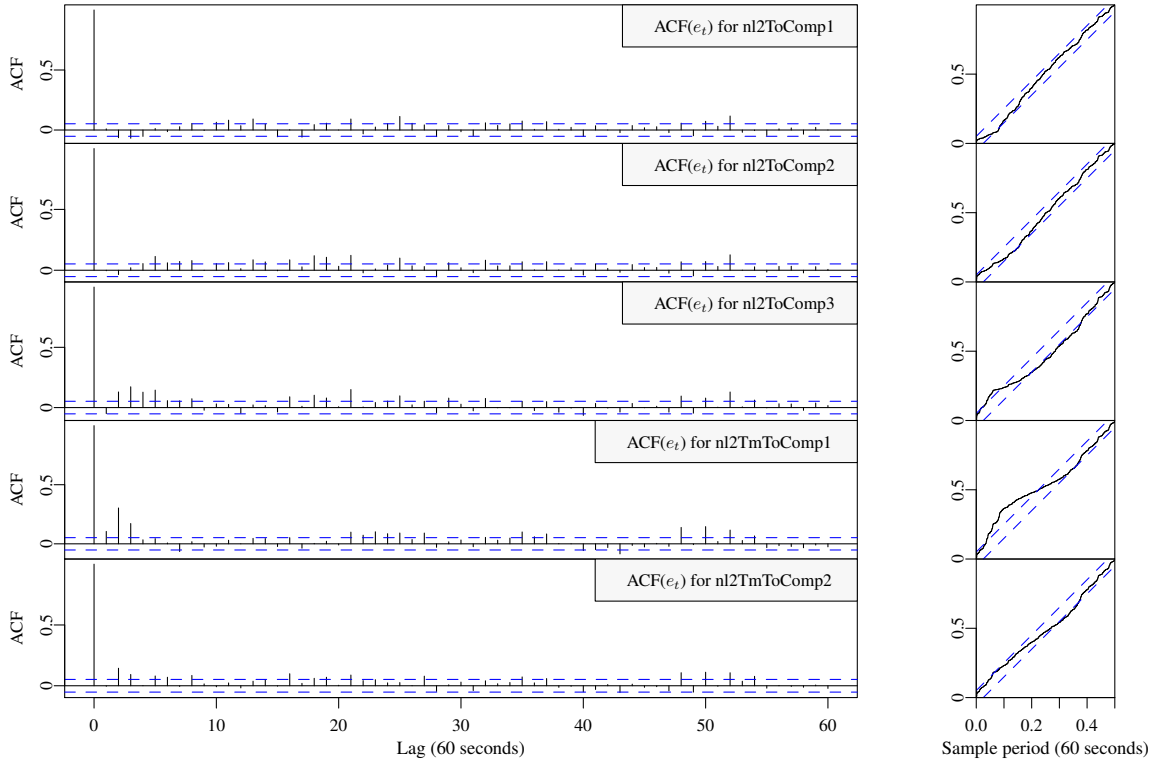

Figure 9: Plots of the auto-correlation function (ACF) and the cumulated periodogram of the residuals from each of the grey-box models fitted on 30 seconds values.

are more important. Therefore if the main excitation of the system, i.e. the direct radiation, can be controlled, it will be possible to achieve fast and accurate parameter estimation. This could be carried out with a simple shadowing device, which should be controlled with PRBS signal to gain maximum information of the heat dynamics of the system (Madsen and Holst, 1995). Higher accuracy can also be achieved with more systematic variation of the inlet temperature, this also applies for the MLR modelling. The right experiment design will allow inclusion of night measurements - which will improve the separation of heat loss and radiation effects and thereby more accurate estimation - and furthermore allow for inclusion of more effects, such as wind and non-linear radiation effects between the collector and the surroundings. Finally, dividing the collector into more parts, e.g. one representing the fluid, one representing the metal, and one representing the surrounding collector body could be tried.

7.1 Applications

The most apparent application of grey-box modelling of the heat dynamics of solar collectors are for the development of fast and accurate performance testing, especially for some types of collectors multi-state models are needed to obtain a required level of accuracy. Especially vacuum tube collectors of dewar type can have an extra time delay due to the high thermal resistance between the heat transfer fluid and absorber surface that is not fully taken up by the present collector model used for performance testing. The new approach described here, particularly with the *TmTo* models, has the potential to deal with this in an accurate way. Additional applications include optimization of operation with model predictive control, which the grey-box models are perfectly suited for. Especially larger solar thermal plants might be able to gain much in performance by applying grey-box modelling and model predictive control.

8 Conclusion

Successful modelling of a the heat dynamics of a solar collector with grey-box models has been carried out. The results have been compared to the EN-standard MLR modelling and they are in agreement. It is shown that high accuracy parameter estimates was obtained with measurements from a single day resampled to 30 seconds average values. This will enable lowering of testing time significantly compared to current test methods.

Highly detailed models of the heat dynamics of the solar collector can be applied, which can be useful for many types of collectors. It is found that the conditions under which the experiment was carried out influence the parameter estimates. Therefore it is concluded that experiment design is the key to achievement of fast, reliable and high accuracy collector testing methods with grey-box models. Experiments with PRBS variation of direct radiation with shadowing device should be carried out to obtain higher accuracy and reproducibility of the results, and finally models with more explanatory variables, such as wind and long-wave radiation should be further elaborated.

Nomenclature

The same notation as in Perers (1997) are used as widely as possible.

Collector model parameters:

$F'(\tau\alpha)_{\mathrm{en}}$	Zero loss efficiency for direct radiation at normal incidence
$K_{\tau\alpha\mathrm{b}}(\theta)$	Incidence angle modifier for direct radiation
$K_{\tau\alpha\mathrm{d}}$	Incidence angle modifier for diffuse radiation
$F'U_0$	Heat loss coefficient at $(T_{\mathrm{a}} - T_{\mathrm{f}}) = 0$, $\left[\mathrm{W}/(\mathrm{m}^2\mathrm{K})\right]$.
$F'U_1$	Temperature dependence of the heat loss coefficient, $\left[\mathrm{W}/(\mathrm{m}^2\mathrm{K}^2)\right]$.
$F'U_{\mathrm{w}}$	Wind dependence of the heat loss coefficient, $\left[\mathrm{Ws}/(\mathrm{m}^3\mathrm{K})\right]$.
$(mC)_{\mathrm{e}}$	Effective thermal capacitance including piping for the collector, $\left[\mathrm{J}/(\mathrm{m}^2\mathrm{K})\right]$.
C_{f}	Fluid thermal capacitance, $\left[\mathrm{J}/(\mathrm{m}^2\mathrm{K})\right]$.
C_{m}	Collector thermal capacitance, $\left[\mathrm{J}/(\mathrm{m}^2\mathrm{K})\right]$.
U_{fa}	Heat transmission coefficient from fluid to ambient, $\left[\mathrm{J}/(\mathrm{Km}^2)\right]$.
U_{fm}	heat transmission coefficient from fluid to module, $\left[\mathrm{J}/(\mathrm{Km}^2)\right]$.
U_{ma}	heat transmission coefficient from module to ambient, $\left[\mathrm{J}/(\mathrm{Km}^2)\right]$.
n_{c}	Number of compartments

Measured variables:

G_{d}	Diffuse radiation onto the collector plane, $\left[\mathrm{W}/\mathrm{m}^2\right]$.
G_{b}	Direct radiation onto the collector plane, $\left[\mathrm{W}/\mathrm{m}^2\right]$.
T_{a}	Ambient air temperature near the collector, $[^\circ\mathrm{C}]$.
T_{o}	Outlet temperature of the collector, $[^\circ\mathrm{C}]$.
T_{i}	Temperature of the inlet to the collector, $[^\circ\mathrm{C}]$.
Q_{f}	Flow of the fluid per square meter of collector, $\left[\mathrm{l}/(\mathrm{sm}^2)\right]$.
θ	incidence angle for the direct solar radiation onto the collector plane, $[\mathrm{radians}]$.
w	Wind speed, $[\mathrm{m}/\mathrm{s}]$.

Derived variables etc.:

T_{f}	Average temperature of the collector fluid, $[^\circ\mathrm{C}]$.
T_{m}	Average temperature of the collector, $[^\circ\mathrm{C}]$.
q_{u}	Collector power output, $\left[\mathrm{W}/\mathrm{m}^2\right]$.
c_{f}	Specific heat capacity of the fluid, $[\mathrm{J}/(\mathrm{lK})]$.

References

P. Bacher and H. Madsen. Identifying suitable models for the heat dynamics of buildings. *Energy & Buildings*, 43(7): 1511–1522, 2011. ISSN 03787788. doi: 10.1016/j.enbuild.2011.02.005.

CEN, European committee for standardization. En 12975-2:2006, thermal solar systems and components - collectors - part 2: Test methods, 2006.

J. Fan, Z. Chen, S. Furbo, B. Perers, and B. Karlsson. Efficiency and lifetime of solar collectors for solar heating plants. Proceedings of the ISES Solar World Congress 2009: Renewable Energy Shaping Our Future, 2009.

S. Fischer, W. Heidemann, H. Müller-Steinhagen, B. Perers, P. Bergquist, and B. Hellström. Collector test method under quasi-dynamic conditions according to the european standard en 12975-2. *Solar Energy*, 76(1-3):117–123, 2004. ISSN 0038092x. doi: 10.1016/j.solener.2003.07.021.

N. Friling, M. J. Jiménez, H. Bloem, and H. Madsen. Modelling the heat dynamics of building integrated and ventilated photovoltaic modules. *Energy and Buildings*, 41(10):1051–1057, 2009. ISSN 03787788.

N. R. Kristensen and H. Madsen. Continuous time stochastic modelling, CTSM 2.3 - mathematics guide. Technical report, DTU, 2003.

N. R. Kristensen, H. Madsen, and S. B. Jørgensen. Parameter estimation in stochastic grey-box models. *Automatica*, 40 (2):225 – 237, 2004. ISSN 0005-1098. doi: DOI:10.1016/j.automatica.2003.10.001.

H. Madsen. *Time Series Analysis*. Chapman & Hall, 2007.

H. Madsen and J. Holst. Estimation of continuous-time models for the heat dynamics of a building. *Energy and Buildings*, 22(1):67–79, 1995. ISSN 03787788.

B. Perers. Dynamic method for solar collector array testing and evaluation with standard database and simulation programs. *Solar Energy*, 50(6):517–526, 1993. ISSN 0038092x.

B. Perers. An improved dynamic solar collector test method for determination of non-linear optical and thermal characteristics with multiple regression. *Solar Energy*, 59(4-6):163–178, 1997. ISSN 0038092x.

Solar Keymark. Homepage and database (all tested collectors according to EN12975 in Europe), 2011. URL `http://solarkey.dk/solarkeymarkdata/qCollectorCertificates/ShowQCollectorCertificatesTable.aspx`.

Peder Bacher, Henrik Madsen, Henrik Aalborg Nielsen, Online Short-term Solar Power Forecasting, 1st International Workshop on the Integration of Solar power into Power Systems Proceedings, Århus, Denmark, 2011

Online Short-term Solar Power Forecasting

Peder Bacher, Henrik Madsen, Henrik Aalborg Nielsen

***Abstract*—This paper describes two methods for online forecasting of power production from PV systems. The methods are suited for online forecasting in many applications and in this paper they are used to predict hourly values of solar power for horizons up to 32 hours. The data used is hourly observations of solar power from a single PV system located on a rooftop in a small village in Denmark. One approach is a two-stage method in which a statistical normalization of the solar power is obtained using a clear sky model. The clear sky model is found using statistical smoothing techniques, which ensure that local phenomena are directly modelled from data, as opposed to applying a deterministically derived clear sky model. In the second stage forecasts of the normalized solar power are calculated using adaptive linear time series models. A second approach is to apply conditional parametric models with both autoregressive input and NWPs exogenous input. The results indicate that for forecasts up to two hours ahead the most important input is the available observations of solar power, while for longer horizons NWPs are the most important input. A root mean square error improvement over a persistence model around 40 % is achieved for 1 and 2 hour horizons and around 35 % for longer horizons.**

***Index Terms*—Solar power, prediction, forecasting, time series, photovoltaic, numerical weather predictions, clear sky model**

I. Introduction

The increasing installed solar power capacity rises the challenges of grid integration. The need for efficient forecasting methods is evident and the research activities within the topic is increasing, see for example [1], [2], [3], and [4]. In this paper methods for online forecasting are presented. The methods are suited for forecasting of solar power for different systems and here they are applied to forecast the power production of a single 4 kW-peak PV-system installed on a rooftop of a single family house. Due to the fluctuating nature of solar power such forecasts are essential for optimal grid integration and will be essential for solar power smart grid technology. The applications include energy trading for large solar power producers, and diurnal peak-shaving and cost optimization for smaller systems with storage capacity in battery packs (e.g. provided in an electrical car). Two approaches are considered. One is based on a two-stages approach: first the systematic dependency of the position of the sun relative to the PV panel are removed with a clear sky model, and secondly the resulting process is forecasted with time-adaptive linear time series methods. The clear sky model is calculated with non-linear statistical techniques, which will also model the local conditions, such as e.g. shadows from elements in the surrounding environment and snow cover. In the second approach numerical weather predictions (NWPs) are used as input to conditional parametric non-linear models [5] to forecast the solar power. Finally, the two approaches are combined by normalizing the forecast with the clear sky model, and finally using this as input to the linear forecasting model, such that an ARX model is formed.

The paper is organized as follows. First the data and how it is preprocessed is described. The next section contains an outline of the clear sky model, followed by a section where all the forecasting models are described. Then an evaluation is given and the results are presented, followed by a discussion of the results and ideas for further work. Finally, the paper ends with a conclusion.

P. Bacher and H. Madsen are with the Department of Informatics, Technical University of Denmark, DK-2800 Lyngby, Denmark (e-mail: pb@imm.dtu.dk) H.A. Nielsen is with ENFOR A/S, Lyngsø Alle 3, DK-2970 Hørsholm, Denmark (URL: www.enfor.eu)

II. Data

The data used in this study consist of hourly mean values of solar power from a 4 kW-peak PV-system and NWPs of global irradiance. The NWPs are provided by the Danish Meteorological Institute using the HIRLAM mesoscale NWP model. The data covers the entire year 2006.

The time series of hourly observed solar power is

$$\{P_t;\ t = 1, \ldots, N\} \tag{1}$$

where $N = 8760$. The NWPs have a calculation time of 4 hours, which is taken into consideration, such that e.g. the forecast from 2009-01-01 00:00 are only available from 2009-01-01 04:00. The NWPs are provided in a time resolution of 3 hours. They are pre-processed into time series of hourly values, such that the most recent available forecast k hours ahead is selected each hour. The time series for a given k of the direct radiation is

$$\left\{G^{\mathrm{nwp}}_{t+k|t};\ t = 1, \ldots, N\right\} \tag{2}$$

A. Pre-processing

The solar power data is plotted for each hour of the day in Figure 1. The solar radiation is zero at night, hence the observed solar power is also zero. For the current data set only periods, for a given hour of the day longer than 40 days in which the solar power is different from zero, are included for evaluation of the model performance. This is illustrated in Figure 1, where the non-included periods are grayed out.

III. Clear sky model

Forecasting effectively using linear time series methods calls for stationarity of the underlying process [6]. The process that generates the solar power is not stationary, which is seen by plotting quantiles of the distribution of solar power conditioned on the time of day, see Figure 2. Clearly the distribution of solar power is not independent of the time of day.

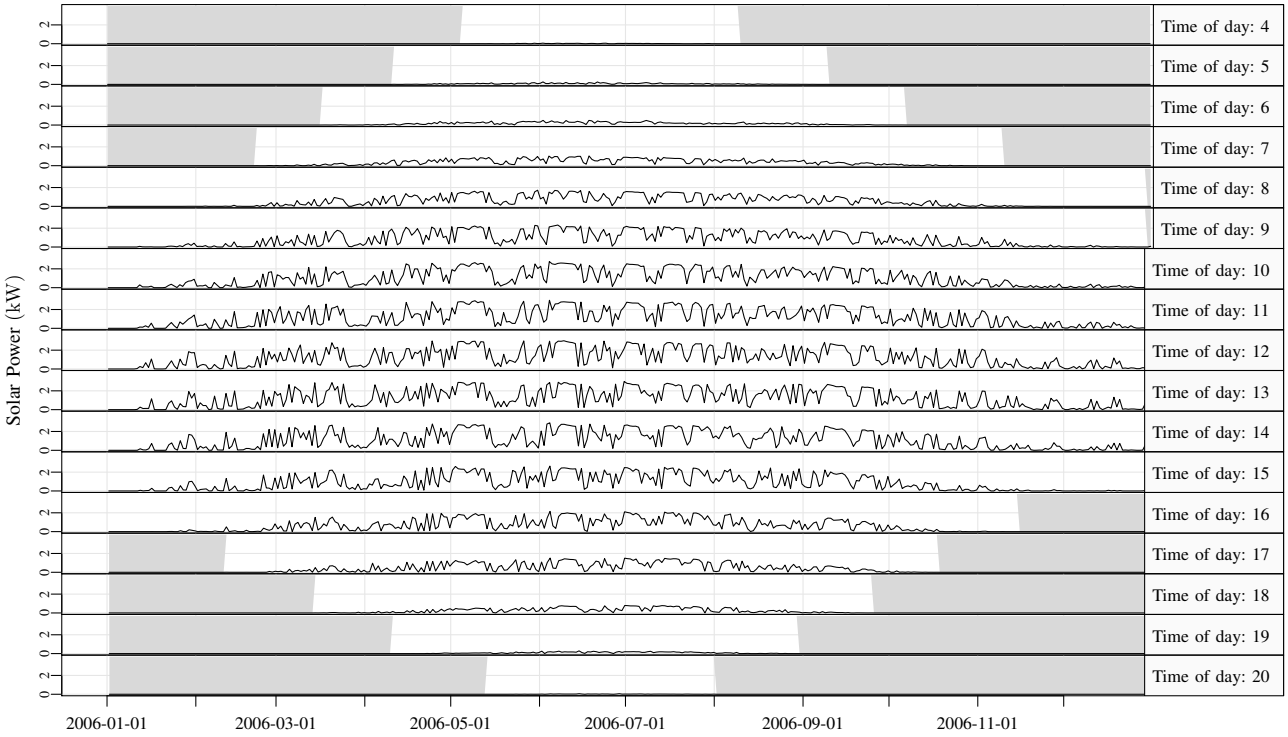

Fig. 1. The solar power data. The greyed area are not included in the evaluation of the model performance.

Most of this dependency can be removed by a normalization using a clear sky model

$$\tau_t = \frac{P_t}{P_t^{\text{cs}}} \tag{3}$$

where P_t is the observed solar power, P_t^{cs} is the estimated clear sky solar power, and τ_t is the normalized solar power.

A. Statistically estimated clear sky solar power

The clear sky solar power is estimated using a statistical non-linear and adaptive model. Quantile regression [7] locally weighted in the day of year and time of day dimension is applied. This is carried out fully causal, i.e. only past values are used. The clear sky model is

$$\hat{P}_t^{\text{cs}} = q_{0.99}(P_1, P_2, \ldots, P_t, h_{\text{y}}, h_{\text{tod}}) \tag{4}$$

where $q_{0.99}$ is the 99% quantile based on the solar power values up to time t. The bandwidths h_{day} and h_{tod}, are in the day of year and time of day dimension, respectively. The bandwidths control how "locally" the model is fitted, i.e. a lower bandwidth puts more emphasis on data which is close in the two dimensions. The local weighting function is an Epanechnikov kernel. The applied bandwidths are

$$h_{\text{day}} = 100 \text{ days}, \quad h_{\text{tod}} = 3 \text{ hours} \tag{5}$$

which were found by visual inspection of the fitted clear sky curve. Finally, it is noted that second-order polynomials were applied in the time of day dimension to include curvature into the model. The estimated clear sky solar power is shown in Figure 3.

One advantage of the normalization is that it will automatically adapt to changes in the system, such as degraded performance or changes in the surroundings e.g. snow cover and shadowing effects. It can as well be used for monitoring of the solar system, since degraded performance from the same time of year will result in a lower clear sky solar power curve. Plots of the quantiles of the distribution of normalized solar power conditional on the time of day are shown in Figure 2, from which it is seen that the normalized solar power process is considerably less dependent on the time of day and therefore a much more stationary process. It is noted that further work could include physical considerations into the clear sky model.

[t]

IV. Forecasting models

In this section a description of the applied forecasting models is given. The models can be divided into models using linear time series models to forecast the normalized solar power: autoregressive (AR) and autoregressive with exogenous inputs (ARX) models - and models which forecast in a single stage: conditional parametric (CP) models. Each model is fitted separately for each horizon, such that the same model structure is used, but the parameters are estimated separately for each horizon.

A. Reference model

To compare the performance of prediction models, and especially when making comparisons between different studies, a common reference model is essential. The reference model for solar power used in this study is the best performing naive

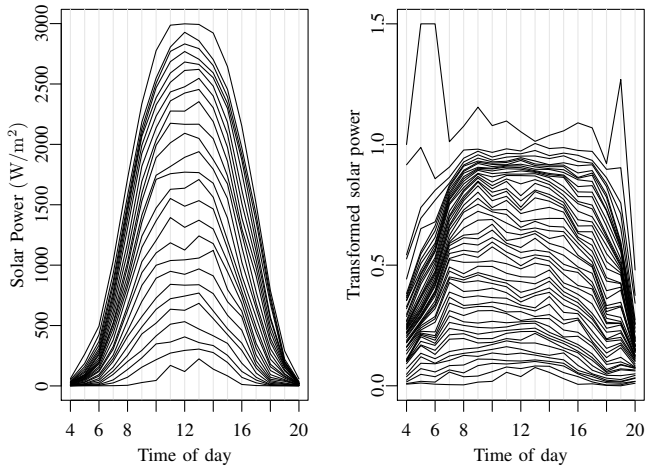

Fig. 2. The $0, 4\%, ..., 100\%$ quantiles of the distribution of the solar power and the normalized solar power conditioned on the time of day. Values above 1.5 has been clipped, which was the case for 6 values.

predictor for a given horizon. Two naive predictors of solar power are found to be relevant. Persistence

$$p_{t+k} = p_t + e_{t+k}, \tag{6}$$

and diurnal persistence

$$p_{t+k} = p_{t-s(k)} + e_{t+k} \tag{7}$$
$$s(k) = 24 + k \bmod 24 \tag{8}$$

where $s(k)$ ensures that the latest diurnal observation is used, i.e. the value which, depending on the horizon, is either 24 or 48 hours before the time point that is to be forecasted.

B. Autoregressive models

Autoregressive (AR) models are applied to forecast the normalized solar power. These models can include either the latest available observation or the latest available diurnal observation, or both, as input. The models are fitted with k-step recursive least squares with forgetting factor [8]. The model formulated as a k-step AR model

$$\tau_{t+k} = m + a_1\tau_t + a_{24}\tau_{t-s(k)} + e_{t+k} \tag{9}$$
$$s(k) = 24 + k \bmod 24 \tag{10}$$

where the function $s(k)$ ensures that the latest observation of the diurnal component is included. The model without the diurnal component, denoted AR, performs best on short horizons

$$\tau_{t+k} = m + a_1\tau_t + e_{t+k} \tag{11}$$

and is included in the evaluation. The AR model with only the diurnal performs better on longer horizons, but is inferior to the models including the NWPs.

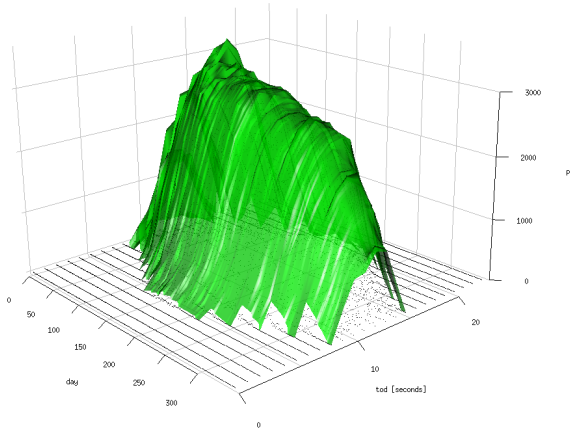

Fig. 3. The estimated clear sky solar power.

C. Conditional parametric models

Conditional parametric (CP) models where the coefficients are conditional on the time of day and time of year are applied with both past solar power observations and NWPs as inputs. The CP model with the latest solar power observation as input is

$$P_{t+k} = m + a\big(t_{\text{day}}, t_{\text{tod}}, P_t\big)P_t + e_{t+k} \tag{12}$$

where the coefficient function is a non-linear function of the solar power. It is denoted as CP_P. The CP model with NWPs of global radiation as input is

$$P_{t+k} = m + b\Big(t_{\text{day}}, t_{\text{tod}}, G^{\text{nwp}}_{t+k|t}\Big)G^{\text{nwp}}_{t+k|t} + e_{t+k} \tag{13}$$

where $G^{\text{nwp}}_{t+k|t}$ is the k-hour ahead NWP of global radiation. This model is denoted CP_{NWP}. Finally, the model with both inputs

$$P_{t+k} = m + a\big(t_{\text{day}}, t_{\text{tod}}, P_t\big)P_t \tag{14}$$
$$+ b\Big(t_{\text{day}}, t_{\text{tod}}, G^{\text{nwp}}_{t+k|t}\Big)G^{\text{nwp}}_{t+k|t} + e_{t+k} \tag{15}$$

is denoted $CP_{NWP,P}$.

In the following the coefficients dependency of the time of day for CP_{NWP} is elaborated on. It is noted that the bandwidths are optimized for each horizon. Plots of the fitted forecasting function $b\Big(t_{\text{day}}, t_{\text{tod}}, G^{\text{nwp}}_{t+k|t}\Big)$ for $k = 24$ hours are shown in Figure 4. It is seen how the slope of the function is lower in the morning, than in the middle of the day. This is naturally caused by the higher angle of incidence in the morning, which cause less horizontal radiation to be absorbed due to reflection. Likewise for the afternoon. Finally, non-linearity in the fitted function is seen.

D. Autoregressive model with exogenous input

The AR model is be expanded to include the forecast of the CP models, thus combining information in past observed solar power and NWPs. The solar power forecasts from the

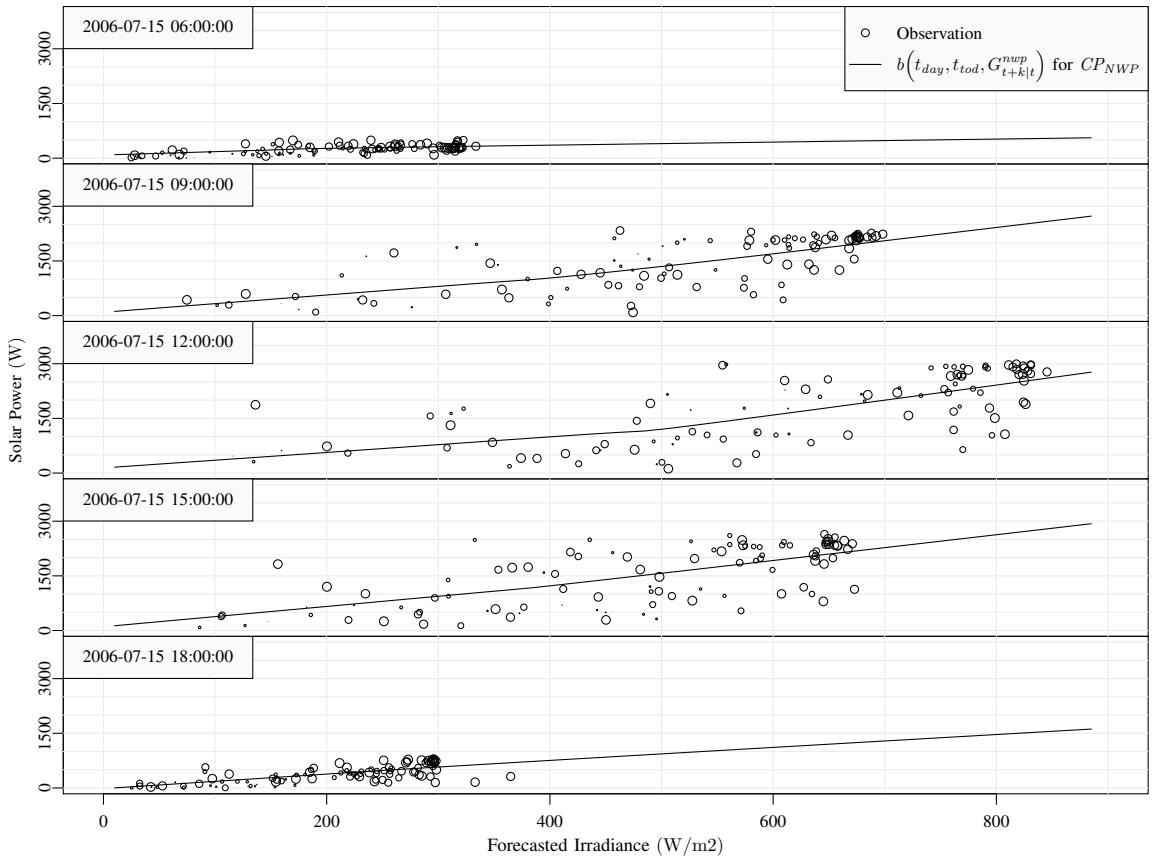

Fig. 4. Examples of the function fitted for $k = 24$ hours forecasting with the NWPs of global radiation at different times of the day on the 15'th of July 2010 with the CP_{NWP} model. For each observation the size of circle indicates the weighting of the observation in the CP models. Thus observations with a larger circle have more influence on the fitted function.

CP is normalized with the clear sky model by

$$\hat{\tau}^{\mathrm{nwp}}_{t+k|t} = \frac{\hat{P}^{\mathrm{nwp}}_{t+k|t}}{P^{\mathrm{cs}}_{t-s(k)}} \tag{16}$$

$$s(k) = f_{\mathrm{spd}} + k \bmod f_{\mathrm{spd}} \tag{17}$$

where $f_{\mathrm{spd}} = 24$ is the sample frequency in number of samples per day. The *ARX1* model is

$$\tau_{t+k} = m + a_1\tau_t + b_1\tau^{\mathrm{nwp}}_{t+k|t} + e_{t+k} \tag{18}$$

V. Evaluation

The methods used for evaluating the prediction models are inspired by [9]. The clear sky model, RLS, and CP fitting do not use any degrees of freedom and the data set is therefore not divided into a training set and a test set. It is only for the optimization of the kernel bandwidths and the forgetting factor that the entire data set is used. The period before 2006-03-01 is considered as a burn-in period and not used for calculating the error measures.

A. Error measures

The Root Mean Square Error for the k'th horizon is

$$RMSE_k = \left(\frac{1}{N}\sum_{t=1}^{N} e^2_{t+k}\right)^{\frac{1}{2}} \tag{19}$$

where e_{t+k} is the k-hourly prediction error. The $RMSE_k$ is used as the main evaluation criterion (EC) for the performance of the models. The Normalized Root Mean Square Error is found by

$$NRMSE_k = \frac{RMSE_k}{p_{\max}} \tag{20}$$

where $p_{\max}$ is the maximum observed solar power output. The mean value of the $RMSE_k$ for a range of horizons

$$\overline{RMSE}_{k_{\mathrm{start}},k_{\mathrm{end}}} = \frac{1}{k_{\mathrm{end}} - k_{\mathrm{start}} + 1}\sum_{k=k_{\mathrm{start}}}^{k_{\mathrm{end}}} RMSE_k \tag{21}$$

is used as a summary error measure. When comparing the performance of two models the improvement

$$I_{\mathrm{EC}} = 100 \cdot \frac{EC_{\mathrm{ref}} - EC}{EC_{\mathrm{ref}}}(\%) \tag{22}$$

is used, where EC is the considered evaluation criterion. When calculating the error measures it is important to consider how to handle missing values for the solar power forecasts. The problem is handled by replacing missing forecast values with forecast values from the reference model *Ref*.

B. Completeness

In order to evaluate a model for its performance regarding missing forecast values a measure is defined. It is denoted

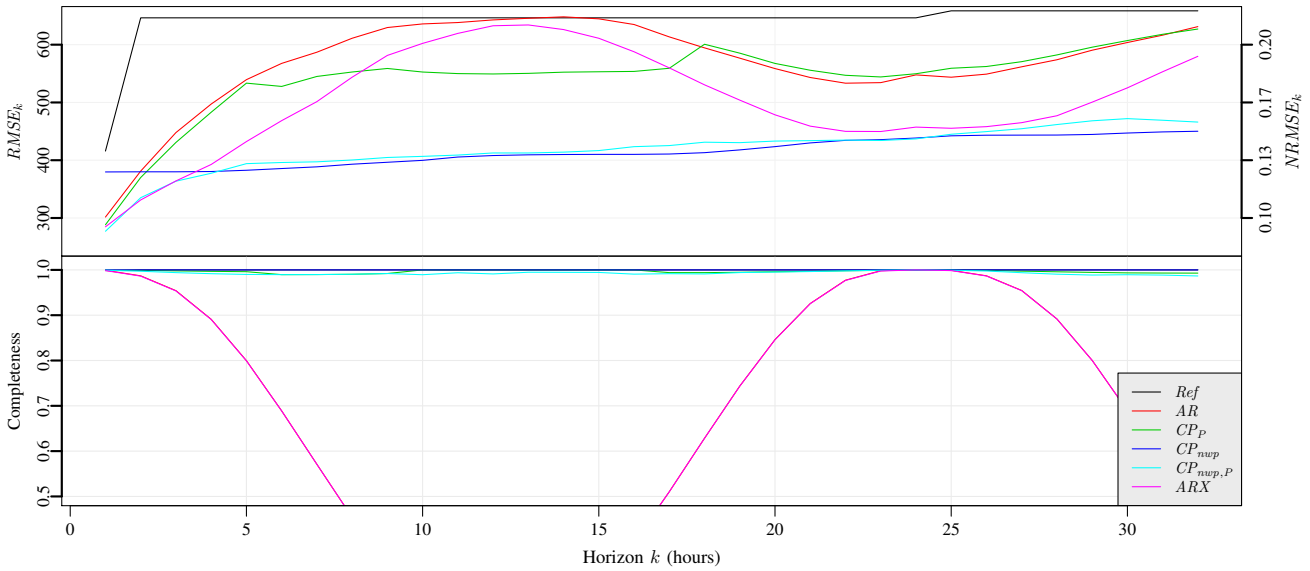

Fig. 5. The upper plot is $\boldsymbol{RMSE_k}$ for the forecasting models. On the right side the $\boldsymbol{NRMSE_k}$ is indicated. The lower plot is completeness $\boldsymbol{C_k}$.

completeness. The completeness of a forecast for horizon k, is the ratio of the total sum of solar power and the summed solar power for time points where the forecasts are not missing

$$C_k = \frac{\sum_{t=1}^{N} P_t \; I\big(\hat{P}_{t|t-k}\big)}{\sum_{t=1}^{N} P_t} \tag{23}$$

where $I()$ is the indicator function which is 0 if $\hat{P}_{t|t-k}$ is missing, and 1 if not. Only the included values are used, i.e. not values during nighttime.

VI. Results

In this section the results are presented and evaluated. The $\overline{RMSE}_{k_{\text{start}},k_{\text{end}}}$ improvements for relevant ranges of horizons are listed in Table I. For selected models the $RMSE_k$ is shown in the upper plot of Figure 5 and the completeness in the lower.

Considering the improvements it is seen that most of the models perform very well on either the short horizons or the longer horizons. Starting with short horizons (1 to 2 hours) the four models using the latest observed solar power have better performance than CP_{NWP}, which only uses the NWPs. Using the combination of observed solar power and NWPs improves the performance, except on longer horizons where using only NWPs are slightly better. Considering the performance of AR, CP_P, and ARX it is seen that the $RMSE_k$ increase really fast as the horizon increases and reach the reference model around a horizon of 10 hours. This is simply because the models are using night values (which are missing) to forecast day values. This is also seen in the completeness of the AR and ARX model.

TABLE I
Improvements in percent for selected ranges of horizons.

Model	$I_{\overline{RMSE}_{1,2}}$	$I_{\overline{RMSE}_{3,17}}$	$I_{\overline{RMSE}_{18,32}}$
AR	34.3	7.4	12.6
CP_P	36.7	17	11.5
CP_{NWP}	25	38.4	33.1
$CP_{NWP,P}$	40.8	37.6	31.4
ARX	40.1	15.9	25

VII. Discussion and applications

This section contains a short discussion of the results and ideas for further work, and ends with an outline of applications.

Considering the improvement achieved over the reference model the forecasting models are found to perform very well. Clearly the quality of the NWPs of solar radiation is the most influential source of error, hence improved NWPs will improve the performance. Especially using NWPs of direct and diffuse radiation should be tried. Regarding further improvement of the forecasting models, it is suggested that the following should be considered:

- Application of regime models and hidden Markov models to handle different aspects of forecasting for e.g. low and high radiation values, and it might be useful to use different forecasting models for different types of cloud conditions. This is ideal to apply in the setting of the CP models.
- For the CP models using higher order polynomials in the day of year and time of day dimensions should improve the models. It was tried but didn't improve the performance, but as the NWPs are getting better this will most likely be important.
- A thorough evaluation of the forecast errors to find ideas for how the models can be improved.

The applications for solar power forecasting include the integration of PV systems into the electricity grid, especially for smart grids. The solar power forecasts can be used as input to model predictive control to optimize the operation

of the PV system. This will enable diurnal peak-shaving and cost optimization for smaller systems with storage capacity in battery packs (e.g. provided in an electrical car). For large solar power producers forecasting is essential for optimized energy trading.

The method is furthermore well suited for monitoring the performance of PV systems. Measures of the performance can be derived from the CP models, with which systems can be compared on an absolute scale. Sudden high deviation from the CP forecasting model will allow for very fast detection of failures in the system. For an individual system the change in performance over time can also be assessed by monitoring the clear sky curve for unusual behavior, and compare the change from year to year.

VIII. Conclusion

Two approaches for solar power forecasting are presented and applied to forecast hourly values for horizons up to 32 hours. Both a method based on a two-stage approach, where first the solar power is normalized with a statistical clear-sky model, and a method in which the solar power is forecasted in a single step. The normalization with a clear sky model removes most of the non-stationarity caused by the changing position of the sun relative to the PV panel. This a pre-requisite for optimal application of linear time series models. Conditional parametric models are used to include NWPs of global radiation, and a one-stage approach, solely based on conditional parametric models, is presented. A root mean square improvement over a persistence reference model on short horizons (1 to 2 hours) is in average 40%, and in average 35% on the longer horizons. The method can furthermore be applied to monitor and check the performance of PV systems.

References

[1] A. Sfetsos and A. Coonick, "Univariate and multivariate forecasting of hourly solar radiation with artificial intelligence techniques," *Solar Energy*, vol. 68, no. 2, pp. 169–178, 2000.

[2] F. O. Hocaoglu, Ö. N. Gerek, and M. Kurban, "Hourly solar radiation forecasting using optimal coefficient 2-d linear filters and feed-forward neural networks," *Solar Energy*, vol. 82, no. 8, pp. 714–726, 2008.

[3] E. Lorenz, J. Hurka, D. Heinemann, and H. Beyer, "Irradiance forecasting for the power prediction of grid-connected photovoltaic systems," *IEEE Journal of Selected Topics in Applied Earth Observations and Remote Sensing*, vol. 2, no. 1, pp. 2–10, 2009.

[4] W. Ji and K. C. Chee, "Prediction of hourly solar radiation using a novel hybrid model of arma and tdnn," *Solar Energy*, vol. 85, no. 5, pp. 808–817, 2011.

[5] T. S. Nielsen, H. Madsen, and H. A. Nielsen, "Prediction of wind power using time-varying coefficient-functions," *Proceedings of the 15th IFAC World Congress on Automatic Control*, 2002.

[6] H. Madsen, *Time Series Analysis*. Chapman & Hall, 2007.

[7] R. Koenker, *Quantile Regression*. Cambridge University Press, 2005.

[8] P. Bacher, H. Madsen, and H. A. Nielsen, "Online short-term solar power forecasting," *Solar Energy*, vol. 83, no. 10, pp. 1772–1783, 2009.

[9] H. Madsen, P. Pinson, G. Kariniotakis, H. A. Nielsen, and T. S. Nielsen, "Standardizing the performance evaluation of shortterm wind power prediction models," *Wind Engineering*, vol. 29, no. 6, p. 475, 2005.

Peder Bacher, Henrik Madsen, Henrik Aalborg Nielsen, Online Short-term Solar Power Forecasting, Solar Energy 83, p. 1772-1783, 2009

Available online at www.sciencedirect.com
ScienceDirect
Solar Energy 83 (2009) 1772–1783
SOLAR ENERGY
www.elsevier.com/locate/solener

Online short-term solar power forecasting

Peder Bacher [a,*], Henrik Madsen [a], Henrik Aalborg Nielsen [b]

[a] *Informatics and Mathematical Modelling, Richard Pedersens Plads, Technical University of Denmark, Building 321, DK-2800 Lyngby, Denmark*
[b] *ENFOR A/S, Lyngsø Allé 3, DK-2970 Hørsholm, Denmark*

Received 2 September 2008; received in revised form 16 March 2009; accepted 22 May 2009
Available online 22 July 2009

Communicated by: Associate Editor Frank Vignola

Abstract

This paper describes a new approach to online forecasting of power production from PV systems. The method is suited to online forecasting in many applications and in this paper it is used to predict hourly values of solar power for horizons of up to 36 h. The data used is 15-min observations of solar power from 21 PV systems located on rooftops in a small village in Denmark. The suggested method is a two-stage method where first a statistical normalization of the solar power is obtained using a clear sky model. The clear sky model is found using statistical smoothing techniques. Then forecasts of the normalized solar power are calculated using adaptive linear time series models. Both autoregressive (AR) and AR with exogenous input (ARX) models are evaluated, where the latter takes numerical weather predictions (NWPs) as input. The results indicate that for forecasts up to 2 h ahead the most important input is the available observations of solar power, while for longer horizons NWPs are the most important input. A root mean square error improvement of around 35% is achieved by the *ARX* model compared to a proposed reference model.

Keywords: Solar power; Prediction; Forecasting; Time series; Photovoltaic; Numerical weather predictions; Clear sky model; Quantile regression; Recursive least squares

1. Introduction

Efforts to increase the capacity of solar power production in Denmark are concentrating on installing grid connected PV systems on rooftops. The peak power of the installed PV systems is in the range of 1- to 4-kWp, which means that the larger systems will approximately cover the electricity consumption (except heating) of a typical family household in Denmark. The PV systems are connected to the main electricity grid and thus the output from other power production units has to be adjusted in order to balance the total power production. The cost of these adjustments increases as the horizon of the adjustments decreases and thus improved forecasting of solar power will result in an optimized total power production, and in future power production systems where energy storage is implemented, power forecasting is an important factor in optimizing utilization of storage facilities (Koeppel and Korpas, 2006).

The total electricity power production in Denmark is balanced by the energy market Nord Pool, where electricity power is traded on two markets: the main market Elspot and a regulation market Elbas. On Nord Pool the producers release their bids at 12:00 for production each hour the following day, thus the relevant solar power forecasts are updated before 12:00 and consist of hourly values at horizons of 12- to 36-h. The models in this paper focus on such forecasts, but with the 1- to 11-h horizons also included.

Interest in forecasting solar power has increased and several recent studies deal with the problem. Many of these consider forecasts of the global irradiance which is

* Corresponding author. Tel.: +45 60774725.
E-mail address: pb@imm.dtu.dk (P. Bacher).
URLs: http://www.imm.dtu.dk/~hm (H. Madsen), http://www.enfor.eu (H.A. Nielsen).

0038-092X/$ - see front matter © 2009 Elsevier Ltd. All rights reserved.
doi:10.1016/j.solener.2009.05.016

Nomenclature

p	solar power (W)
p_{cs}	clear sky solar power (W)
τ	normalized solar power (–)
t	time index (–)
k	forecast horizon index (–)
i, j	miscellaneous indexes (–)
p_t	observation of average solar power (W)
$\hat{p}_{t+k\|t}$	k-step prediction of solar power (W)
$\hat{p}_t^{cs}$	estimated clear sky solar power (W)
$\hat{g}_{i,k}$	ith update of NWP of global irradiance (W/m^2)
$\hat{g}_{k,t}^{00}$	NWP of global irradiance updated at 00:00 (W/m^2)
$\hat{g}_{k,t}^{12}$	NWP of global irradiance updated at 12:00 (W/m^2)
$p_{k,t}^{00}$	observation of solar power corresponding to $\hat{g}_{k,t}^{00}$ (W)
$p_{k,t}^{12}$	observation of solar power corresponding to $\hat{g}_{k,t}^{12}$ (W)
τ_t	normalized solar power (–)
$\hat{\tau}_{t+k\|t}$	k-step prediction of normalized solar power (–)
$\hat{\tau}_t^{nwp}$	NWPs transformed into normalized solar power (–)
x_t	day of year (–)
y_t	time of day (–)
e_{t+k}	k-step prediction error (–)
q	quantile level (–)
h	bandwidth of smoothing kernel (–)
λ	forgetting factor (–)

essentially the same problem as forecasting solar power. Two approaches are dominant:

- A two-stage approach in which the solar power (or global irradiance) is normalized with a clear sky model in order to form a more stationary time series and such that the classical linear time series methods for forecasting can be used.
- Another approach in which neural networks (NNs) with different types of input are used to predict the solar power (or global irradiance) directly.

In a study, Chowdhury and Rahman (1987) make subhourly forecasts by normalizing with a clear sky model. The solar power is divided into a clear sky component, which is modelled with a physical parametrization of the atmosphere, and a stochastic cloud cover component which is predicted using ARIMA models. Sfetsos and Coonick (2000) use NNs to make one-step predictions of hourly values of global irradiance and compare these with linear time series models that work by predicting clearness indexes. Heinemann et al. (2006) use satellite images for horizons below 6 h, and in (Lorenz et al., 2007) numerical weather predictions (NWPs) for longer horizons, as input to NNs to predict global irradiance. This is transformed into solar power by a simulation model of the PV system. Hocaoglu et al. (2008) investigate feed-forward NNs for one-step predictions of hourly values of global irradiance and compare these with seasonal AR models applied on solar power directly. Cao and Lin (2008) use NNs combined with wavelets to predict next day hourly values of global irradiance. Different types of meteorological observations are used as input to the models; among others the daily mean global irradiance and daily mean cloud cover of the day to be forecasted.

This paper describes a new two-stage method where first the clear sky model approach is used to normalize the solar power and then adaptive linear time series models are applied for prediction. Such models are linear functions between values with a constant time difference, where the model coefficients are estimated by minimizing a weighted residual sum of squares. The coefficients are updated regularly, and newer values are weighted higher than old values, hence the models adapt over time to changing conditions.

Normalization of the solar power is obtained by using a clear sky model which gives an estimate of the solar power in clear (non-overcast) sky at any given point in time. The clear sky model is based on statistical smoothing techniques and quantile regression, and the observed solar power is the only input. The adaptive linear prediction is obtained using recursive least squares (RLS) with forgetting. It is found that the adaptivity is necessary, since the characteristics of a PV system are subject to changes due to snow cover, leaves on trees, dirt on the panel, etc., and this has to be taken into account by an online forecasting system.

The data used in the modelling is described in Section 2. The clear sky model used for normalizing the solar power is defined in Section 3 followed by Section 4 where the adaptive time series models used for prediction are identified. In Section 5 an approach to modelling of the uncertainty in the forecasts is outlined. The evaluation of the models and a discussion of the results are found in Section 6 and finally the conclusions of the study are drawn in Section 7.

2. Data

The data used in this study is observations of solar power from 21 PV systems located in a small village in Jutland, Denmark. The data covers the entire year 2006. Forecasts of global irradiance are provided by the Danish

Meteorological Institute using the HIRLAM mesoscale NWP model.

The PV array in each the 21 PV systems is composed of "BP 595" PV modules and the inverters are of the type "BP GCI 1200". The installed peak power of the PV arrays is between 1020 W peak and 4080 W peak, and the average is 2769 W peak. Let $p_{i,t}$ denote the average value of solar power (W) over 15 min observed for the ith PV system at time t. These observations are used to form the time series

$$\{p_t;\ \ t = 1, \ldots, N\}, \tag{1}$$

where

$$p_t = \frac{1}{21}\sum_{i=1}^{21} p_{i,t}. \tag{2}$$

This time series is used throughout the modelling. The time series covers the period from 01 January 2006 to 31 December 2006. The observations are 15-min values, i.e. $N = 35040$. Plots of $\{p_t\}$ are shown in Fig. 1 for the entire period and for two shorter periods.

The NWPs of global irradiance are given in forecasts of average values for every third hour, and the forecasts are updated at 00:00 and 12:00 each day. The ith update of the forecasts is the time series

$$\{\hat{g}_{i,k},\ \ k = 1, \ldots, 12\}, \tag{3}$$

which then covers the forecast horizons up to 36 h ahead, and is given in W/m^2.

Time series are resampled to lower sample frequencies by mean values and when the resampled values are used this is noted in the text. In order to synchronize data with different sample frequencies, the time point for a given mean value is assigned to the middle of the period that it covers, e.g. the time point of an hourly value of solar power from 10:00 to 11:00 is assigned to 10:30.

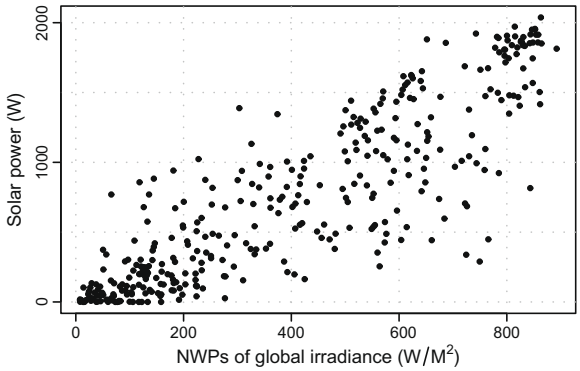

Fig. 2. All 3-h interval values of solar power at time of day 10:30 versus the corresponding NWPs of global irradiance with 24-h horizon. Hence the plot shows observations and predictions of values covering identical time intervals.

As an example of the NWPs of global irradiance Fig. 2 shows values at time of day 10:30 of $\{p_t\}$ resampled to 3-h interval values plotted versus the corresponding $\{\hat{g}_{i,k}\}$ values with a 24-h horizon. Clearly the plot indicates a significant correlation. Hence it is seen that there is information in the NWPs, which can be utilized to forecast the solar power.

3. Clear sky model

A clear sky model is usually a model which estimates the global irradiance in clear (non-overcast) sky at any given time. Chowdhury and Rahman (1987) divide the global irradiance into a clear sky component and a cloud cover component by

$$G = G_{\mathrm{cs}} \cdot \tau_c, \tag{4}$$

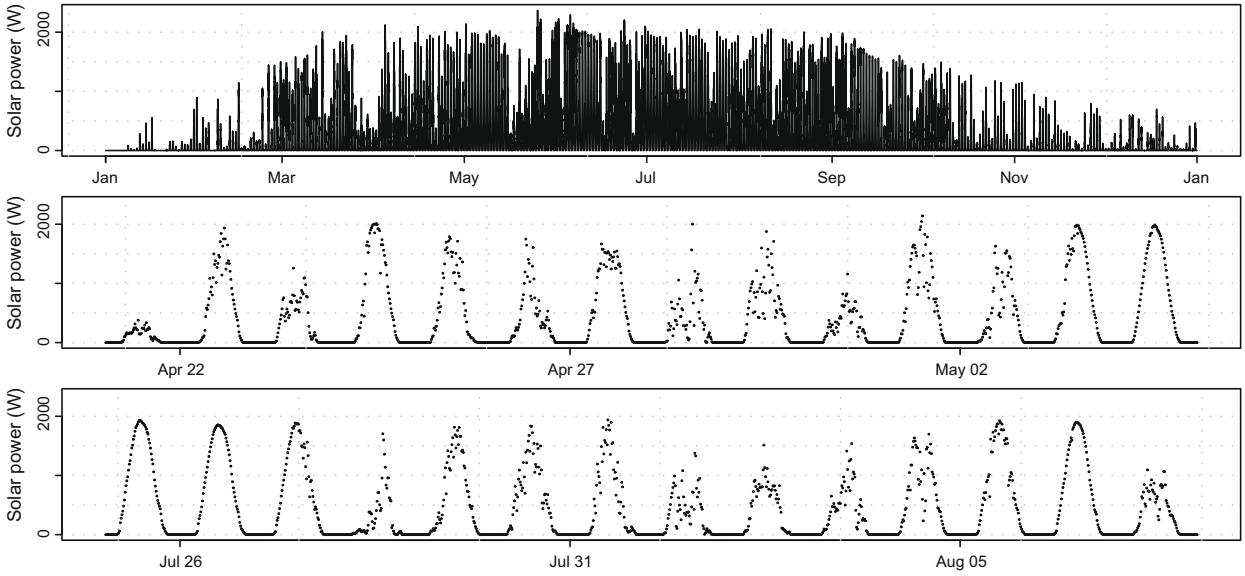

Fig. 1. The observations of average solar power used in the study. Top: The solar power over the entire year 2006. Bottom: The solar power in two selected periods.

where G is the global irradiance (W/m^2), and G_{cs} is the clear sky global irradiance (W/m^2). Finally, τ_c is the transmissivity of the clouds which they model as a stochastic process using ARIMA models. The clear sky global irradiance is found by

$$G_{cs} = I_0 \cdot \tau_a, \tag{5}$$

where I_0 is the extraterrestrial irradiance (W/m^2). τ_a is the total sky transmissivity in clear sky which is modelled by atmospheric dependent parametrization.

In this study the same approach is used, but instead of applying the factor on global irradiance it is applied on solar power, i.e.

$$p = p_{cs} \cdot \tau, \tag{6}$$

where p is the solar power (W) and p_{cs} is the clear sky solar power (W). The factors τ and τ_c are much alike, but since the clear sky model developed in the present study estimates p_{cs} by statistical smoothing techniques rather than using physics, the method is mainly viewed as a statistical normalization technique and τ is referred to as normalized solar power.

The motivation behind the proposed normalization of the solar power with a clear sky model is that the normalized solar power (the ratio of solar power to clear sky solar power) is more stationary than the solar power, so that classical time series models assuming stationarity (Madsen, 2007) can be used for predicting the normalized values. The non-stationarity is illustrated in Fig. 3 where modified boxplots indicate the distribution of solar power p_t as a function of time of day. Clearly a change in the distributions over the day is seen and this non-stationarity must be considered. Fig. 4 shows the same type of plot for the normalized solar power and it is seen that the distributions over the day are closer to being identical. Thus the effect of the changes over the day is much lower for the normalized solar power than for the solar power.

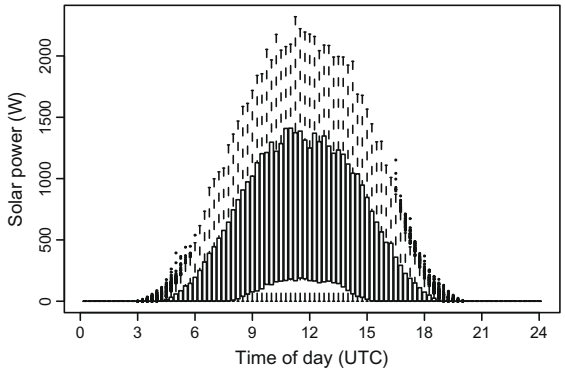

Fig. 3. Modified boxplots of the distribution of the solar power as a function of time of day. The boxplots are calculated with all the 15-min values of solar power, i.e. covering all of 2006. At each time of the day the box represents the center half of the distribution, from the first to the third quantile. The lower and upper limiting values of the distribution are marked with the ends of the vertical dotted lines, and dots beyond these indicate outliers.

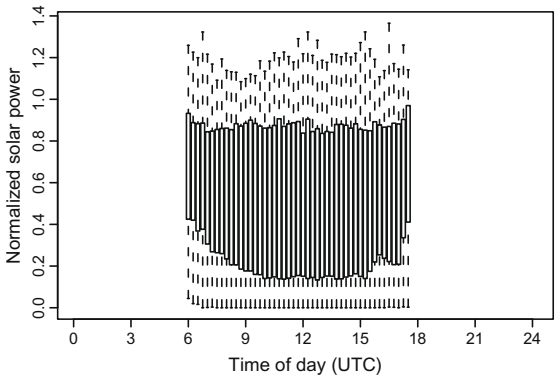

Fig. 4. Modified boxplots of the distribution of the normalized solar power as a function of time of day. The boxplots are calculated with all 15-min values available, i.e. covering all of 2006.

The clear sky model is defined as

$$p_{cs} = f_{max}(x, y), \tag{7}$$

where p_{cs} is the clear sky solar power (W), x is the day of year and y is the time of day. The function $f_{max}(\cdot,\cdot)$ is assumed to be a smooth function and thus $f_{max}(\cdot,\cdot)$ can be estimated as a local maximum (Koenker, 2005). Fig. 5 shows the solar power plotted as a function of x and y, and the estimated clear sky solar power $\hat{f}_{max}(\cdot,\cdot)$ is shown as a surface in Fig. 6. Due to outliers the weighted quantile regression method outlined in Appendix A is used to find the local maximum. The $\hat{f}_{max}(\cdot,\cdot)$ is then used to form the output of the clear sky model as the time series

$$\{\hat{p}_t^{cs},\ \ t = 1, \ldots, N\}, \tag{8}$$

where $\hat{p}_t^{cs}$ is the estimated clear sky solar power (W) at time t, and $N = 35040$. The normalized solar power is now defined as

$$\tau_t = \frac{p_t}{\hat{p}_t^{cs}}, \tag{9}$$

and this is used to form time series of normalized solar power

$$\{\tau_t,\ \ t = 1, \ldots, 35040\}. \tag{10}$$

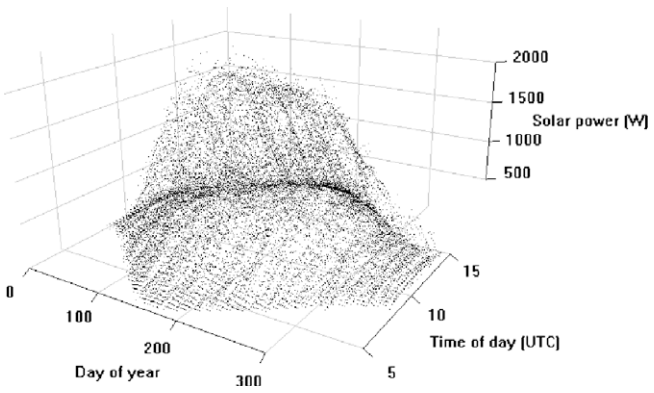

Fig. 5. The solar power as a function of the day of year, and the time of day. Note that only positive values of solar power are plotted.

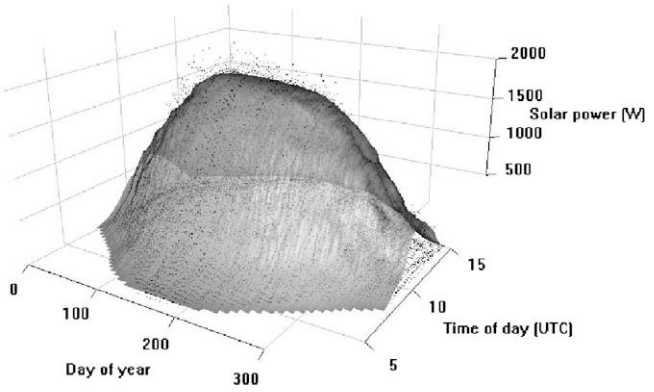

Fig. 6. The estimated clear sky solar power shown as a surface. The solar power is shown as points.

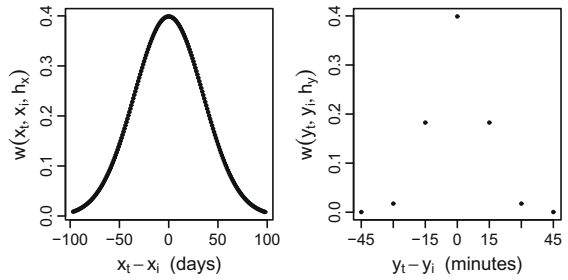

Fig. 7. The one-dimensional smoothing kernels used. Left plot is the kernel in the day of year (x) dimension. Right plot is the kernel in the time of day (y) dimension. They are multiplied to form the applied two dimensional smoothing kernel.

For each (x_t, y_t) corresponding to the solar power observation p_t, weighted quantile regression estimates the q quantile by a Gaussian two-dimensional smoothing kernel, defined in Appendix A. The smoothing kernel is used to form the weights applied in the quantile regression. As seen in Fig. 7, which shows the smoothing kernel used, the weights in the day of year dimension $w(x_t, x_i, h_x)$, are decreasing as the absolute time differences are increasing. Similarly for the weights in the time of day dimension $w(y_t, y_i, h_y)$. The applied weights are finally found by multiplying the weights from the two dimensions. The choice of the quantile level q to be estimated and the bandwidth in each dimension, h_x and h_y, is based on a visual inspection of the results. A level of $q = 0.85$ was used since this gives $\tau_t \approx 1$ for days with clear sky all day, as seen in Fig. 8. The plot for days with varying cloud cover in Fig. 9 shows that estimates where $\tau_t > 1$ occur. These are ascribed to reflections from clouds and varying level of water vapour in the atmosphere. Future work should elaborate on the inclusion of such effects in the clear sky model.

For small $\hat{p}_t^{cs}$ values the error of τ_t is naturally increasing and at nighttime the error is infinite. Therefore all values of $\hat{p}_t^{cs}$ where

$$\frac{\hat{p}_t^{cs}}{\max\left(\{\hat{p}^{cs}t\}\right)} < 0.2, \tag{11}$$

are removed from $\{\tau_t\}$. The function $\max\left(\{\hat{p}_t^{cs}\}\right)$ gives the maximum value in $\{\hat{p}_t^{cs}\}$.

The estimates of clear sky solar power are best in the summer period. The bad estimates in winter periods are caused by the sparse number of clear sky observations. It should also be possible to improve the normalization toward dusk and dawn, and thus lower the limit where values in $\{\hat{p}_{cs}\}$ are removed, either by refining the modelling method or by including more explanatory variables such as e.g. air mass.

Finally, it is noted that the deterministic changes of solar power are really caused by the geometric relation between the earth and the sun, which can be represented in the current problem by the sun elevation as x and sun azimuth as y. The clear sky solar power was also modelled in the space spanned by these two variables, by applying the same statistical methods as for the space spanned by day of year and time of day. The result was not satisfactory, i.e. the estimated clear sky solar power was less accurate, probably because neighboring values in this space are not necessarily close in time and thus changes in the surroundings to the PV system blurred the estimates.

4. Prediction models

Adaptive linear time series models (Madsen, 2007) are applied to predict future values of the normalized solar power τ_t. The inputs are: lagged observations of τ_t and transformed NWPs $\hat{\tau}_t^{nwp}$. Three types of models are identified:

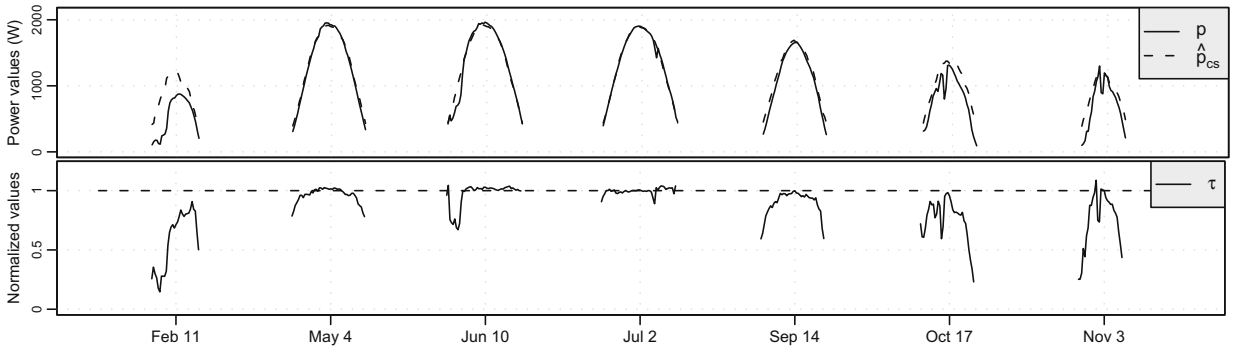

Fig. 8. The result of the normalization for selected clear sky days over the year. The time-axis ticks refer to midday points, i.e. at 12:00. The upper plot shows the solar power p and the estimated clear sky solar power $\hat{p}_{cs}$. The lower plot shows the normalized solar power τ.

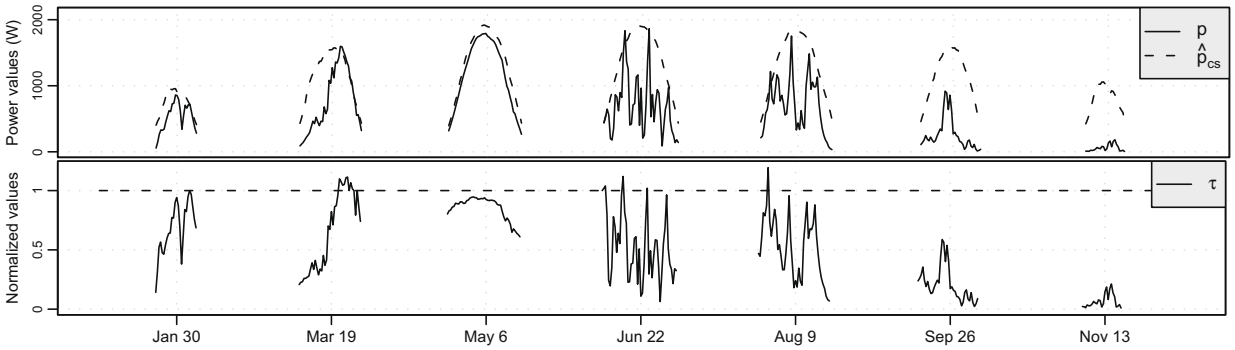

Fig. 9. The result of the normalization for days evenly distributed over the year. The time-axis ticks refer to midday points, i.e. at 12:00. The upper plot shows the solar power p and the estimated clear sky solar power $\hat{p}_{cs}$. The lower plot shows the normalized solar power τ.

- A model which has only lagged observations of τ_t as input. This is an autoregressive (AR) model and it is referred to as the *AR* model.
- A model with only $\hat{\tau}_t^{nwp}$ as input. This is referred to as the LM_{nwp} model.
- A model with both types of input. This is an autoregressive with exogenous input (ARX) model and it is referred to as the *ARX* model.

The best model of each type is identified by using the autocorrelation function (ACF).

4.1. Transformation of NWPs into predictions of normalized solar power

In order to use the NWPs of global irradiation $\hat{g}_{i,k}$ as input to the prediction models, these are transformed into $\hat{\tau}_t^{nwp}$ which are meteorological based hourly predictions of τ_t. This is done by first transforming $\hat{g}_{i,k}$ into solar power predictions and then transforming these by the clear sky model. The time series $\{\hat{g}_{i,k}\}$, defined in (3), holds the ith NWP forecast of 3-h interval values, and was updated at

$$\text{time}_i = t_0 + (i-1)\cdot 12\text{h}, \tag{12}$$

where $t_0 =$ 2006-01-0 100:00. Thus the time series with sample period of one day

$$\left\{\hat{g}_{k,t}^{00},\ \ t=1,\ldots,364\right\} = \{\hat{g}_{i,k},\ \ i=1,3,\ldots,727\}, \tag{13}$$

consist of all the NWPs updated at time of day 00:00 at horizon k, i.e. the superscript "00" forms part of the name of the variable. Similarly the time series

$$\left\{\hat{g}_{k,t}^{12},\ \ t=1,\ldots,364\right\} = \{\hat{g}_{i,k},\ \ i=2,4,\ldots,728\}, \tag{14}$$

consist of all the NWPs updated at time of day 12:00. The corresponding time series of solar power covering the identical time intervals are, respectively

$$\{p_{k,t}^{00},\ \ t=1,\ldots,364\} = \{p_t, t=k,(1\cdot 8+k),\ldots,(363\cdot 8+k)\} \tag{15}$$

and

$$\left\{p_{k,t}^{12},\ \ t=1,\ldots,364\right\} = \{p_t, t=k+4,(1\cdot 8+k+4),\ldots,(363\cdot 8+k+4)\}, \tag{16}$$

where $\{p_t\}$ has been resampled to 3-h interval values. The NWPs are modelled into solar power predictions by the adaptive linear model

$$\hat{p}_{k,t}^{00} = \beta_t + \alpha_t \hat{g}_{k,t}^{00} + e_t. \tag{17}$$

Note that the hat above the variable indicates that these values are predictions (estimates) of the solar power. A similar model is made for the NWP updates at time of day 12:00 giving $\hat{p}_{k,t}^{12}$. The interpretion of the coefficients β_t and α_t is not further elaborated here, but it is noted that they are time dependent in order to account for the effects of changing conditions over time, e.g. the changing geometric relation between the earth and the sun, dirt on the solar panel. This adaptivity is obtained by fitting the model with k-step recursive least squares (RLS) with forgetting, which is described in Appendix B. In order to use the RLS algorithm, $p_{k,t}^{00}$ has to be lagged depending on k. Each RLS estimation is optimized by choosing the value of the forgetting factor λ from 0.9,0.905,...,1 that minimizes the root mean square error (*RMSE*).

The last steps in the transformation of the NWPs is to normalize $\hat{p}_{k,t}^{00}$ and $\hat{p}_{k,t}^{12}$ with the clear sky model, and resample up to hourly values by linear interpolation. Finally, the time series

$$\left\{\hat{\tau}_t^{nwp},\ \ t=1,\ldots,8760\right\} \tag{18}$$

of the NWPs of global irradiance transformed into predictions of normalized solar power is formed, and this is used as input to the *ARX* prediction models as described in the following. More details can be found in Bacher (2008).

4.2. AR model identification

To investigate the time dependency in $\{\tau_t\}$, i.e. dependency between values with a constant time difference, the ACF is calculated and plotted in Fig. 10. Clearly an AR(1) component is indicated by the exponential decaying

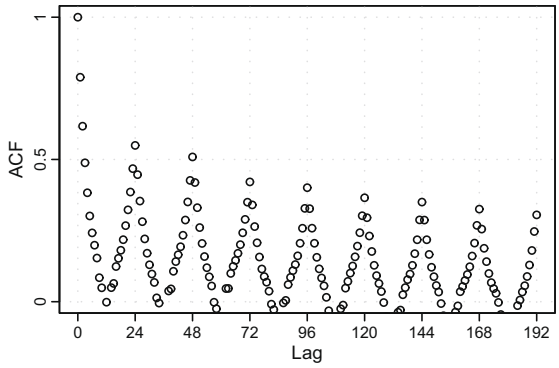

Fig. 10. ACF of the time series of normalized solar power $\{\tau_t\}$.

pattern of the first few lags and a seasonal diurnal AR component by the exponential decaying peaks at lag = 24,48,.... By considering only first-order terms this leads to the 1-step AR model

$$\tau_{t+1} = m + a_1\tau_t + a_2\tau_{t-23} + e_{t+1}. \tag{19}$$

And a reasonable 2-step AR model is

$$\tau_{t+2} = m + a_1\tau_t + a_2\tau_{t-22} + e_{t+2}. \tag{20}$$

Note that here the 1-step lag cannot be used, since this is τ_{t+1}, i.e. a future value, and thus the latest observed value is included instead. Formulated as a k-step AR model

$$\tau_{t+k} = m + a_1\tau_t + a_2\tau_{t-s(k)} + e_{t+k}, \tag{21}$$

$$s(k) = 24 + k \bmod 24, \tag{22}$$

where the function $s(k)$ ensures that the latest observation of the diurnal component is included. This is needed, since for $k = 25$ the diurnal 24-h AR component cannot be used and instead the 48-h AR component is used. This model is referred to as the AR model.

Fig. 11 shows the ACF of $\{e_{t+k}\}$, which is the time series of the errors in the model for horizon k, for six selected horizons after fitting the AR model with RLS, which is described in Appendix B. The vertical black lines indicate which lags are included in the model. For $k = 1$ the correlation of the AR(1) component is removed very well and the diurnal AR component has also been decreased considerably. There is high correlation left at lag = 24,48,.... This can most likely be ascribed to systematic errors caused by non-stationarity effects left in $\{\tau_t\}$, and it indicates that the clear sky model normalization can be further optimized. For $k = 2$ and 3 the grayed points show the lags that cannot be included in the model and the high correlation of these lags indicate that information is not exploited. The AR model was extended with higher order AR and diurnal AR terms without any further improvement in performance, see Bacher (2008).

4.3. LM_{nwp} model identification

The model using only NWPs as input

$$\tau_{t+k} = m + b_1\hat{\tau}^{\text{nwp}}_{t+k|t} + e_{t+k} \tag{23}$$

is referred to as LM_{nwp}. It is fitted using RLS and the ACF of $\{e_{t+k}\}$ is shown in Fig. 12 for two horizons. For $k = 1$ clearly correlation is left from an AR(1) component, but as seen for both horizons the actual NWP input removes diurnal correlation very well.

4.4. ARX model identification

The model using both lagged observations of τ_t and NWPs as input is an ARX model. The LM_{nwp} revealed an exponential decaying ACF for short horizons and thus an AR(1) term is clearly needed, whereas adding the diurnal AR component has only a small effect. The results show that in fact the diurnal AR component can be left out, but

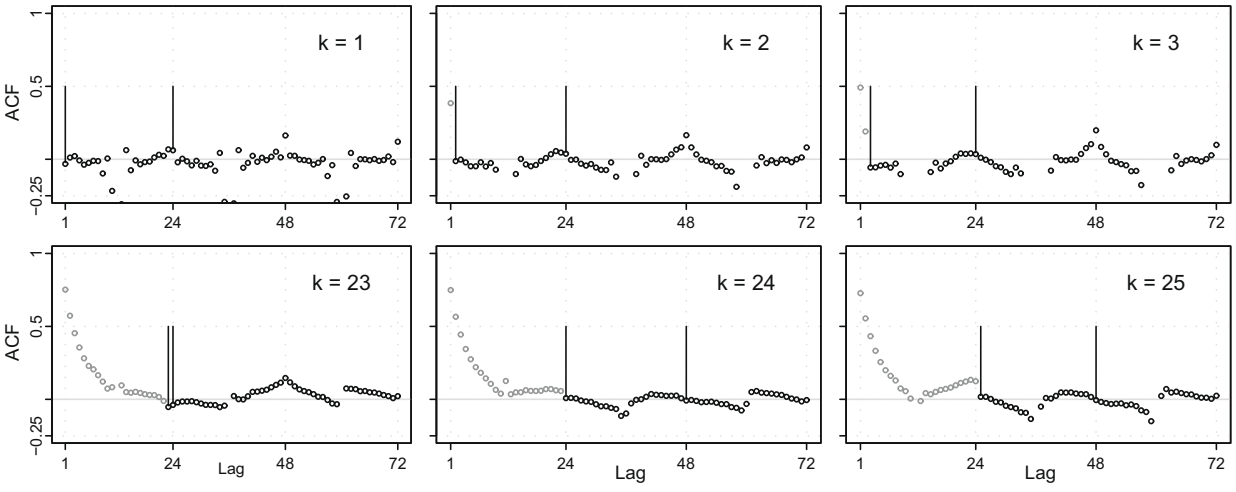

Fig. 11. ACF of the time series of errors $\{e_{t+k}\}$ for selected horizons k of the AR model. The vertical bars indicate the lags included in each of the models, and the grayed points show the lags which cannot be included in the model.

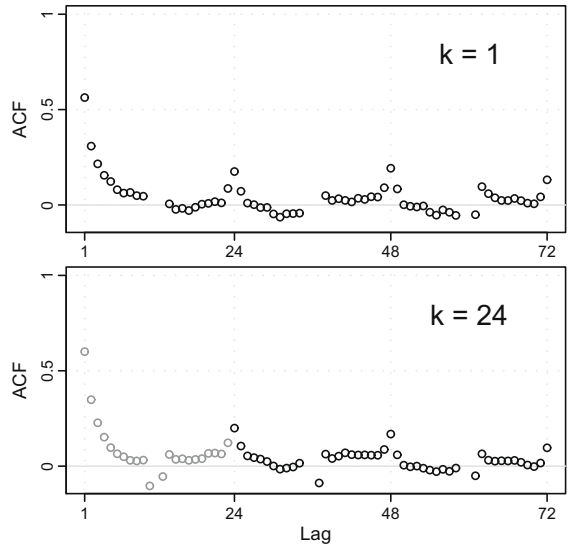

Fig. 12. ACF of the time series of errors $\{e_{t+k}\}$ at horizon $k = 1$ and $k = 24$ of the LM_{nwp} model. The grayed points show the lags which cannot be included in the model.

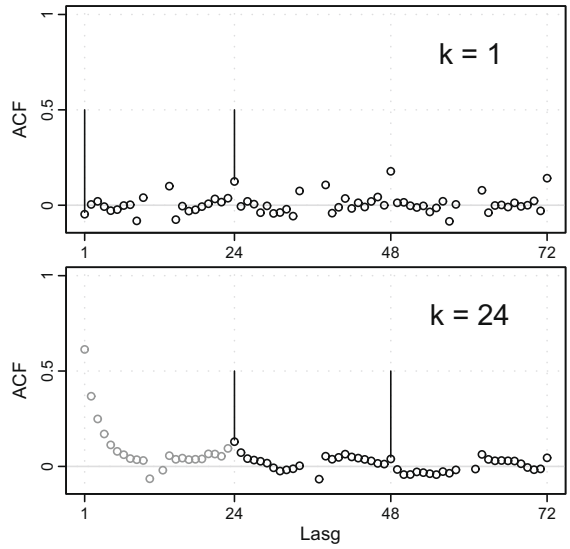

Fig. 13. ACF of the time series of errors $\{e_{t+k}\}$ at horizons $k = 1$ and $k = 24$ of the ARX model. The vertical bars indicate the lags included in each of the models, and the grayed points show the lags which cannot be included in the model.

it is retained since this clarifies that no improvement is achieved by adding it, this is showed later. The model

$$\tau_{t+k} = m + a_1\tau_t + a_2\tau_{t-s(k)} + b_1\hat{\tau}^{\text{nwp}}_{t+k|t} + e_{t+k} \tag{24}$$

is referred to as the ARX model. The model is fitted using RLS and the ACF of $\{e_{t+k}\}$ is plotted in Fig. 13. It is seen that the AR(1) component removes the correlation for the short horizons very well. The ARX was extended with higher order AR and diurnal AR terms without any further improvements in performance.

4.5. Adaptive coefficient estimates

The plots in Fig. 14 show the online coefficient estimates for the AR model, where a value of $\lambda = 0.995$ is used since this is the value that minimizes the $RMSE_k$ best for all horizons in the current setting. Clearly the values of the coefficient estimates change over time and this indicates that the adaptivity is needed to make an optimal model for online forecasting.

5. Uncertainty modelling

Extending the solar power forecasts, from predicting a single value (a point forecast) to predicting a distribution increases their usefulness. This can be achieved by modelling the uncertainties of the solar power forecasts and a simple approach is outlined here. The classical way of assuming normal distribution of the errors will in this case not be appropriate since the distribution of the errors has finite limits. Instead, quantile regression is used, inspired by Møller et al. (2008) where it is applied to wind power forecasts. Plots of $\{\tau_t\}$ versus $\{\hat{\tau}_t\}$ for a given horizon reveal that the uncertainties depend on the level of $\hat{\tau}$. Fig. 15 shows such plots for horizons $k = 1$ and $k = 24$. The lines in the plot are estimates of the 0.05, 0.25, 0.50, 0.75 and 0.95 quantiles of the probability distribution function of τ as a function of $\hat{\tau}$. The weighted quantile regression with a one-dimensional kernel smoother, described in Appendix A, is used.

Fig. 15 illustrates that the uncertainties are lower for $\hat{\tau}$ close to 0 and 1, than for the mid-range values around 0.5. Thus forecasts of values toward overcast or clear sky have less uncertainty than forecasts of a partlyovercast sky, which agrees with results by Lorenz et al. (2007). Further work should extend the uncertainty model to include NWPs as input.

6. Evaluation

The methods used for evaluating the prediction models are inspired by Madsen et al. (2005) where a framework for evaluation of wind power forecasting is suggested. The RLS fitting of the prediction models does not use any degrees of freedom and the dataset is therefore not divided into a training set and a test set. It is, however, noted that the clear sky model and the optimization of λ does use the entire dataset, and thus the results can be a little optimistic. The values in the burn-in period are not used in calculating the error measures. In Fig. 14 the burn-in periods for the AR model are shown.

6.1. Error measures

The k-step prediction error is

$$e_{t+k} = p_{t+k} - \hat{p}_{t+k|t}. \tag{25}$$

The root mean square error ($RMSE$) for the kth horizon is

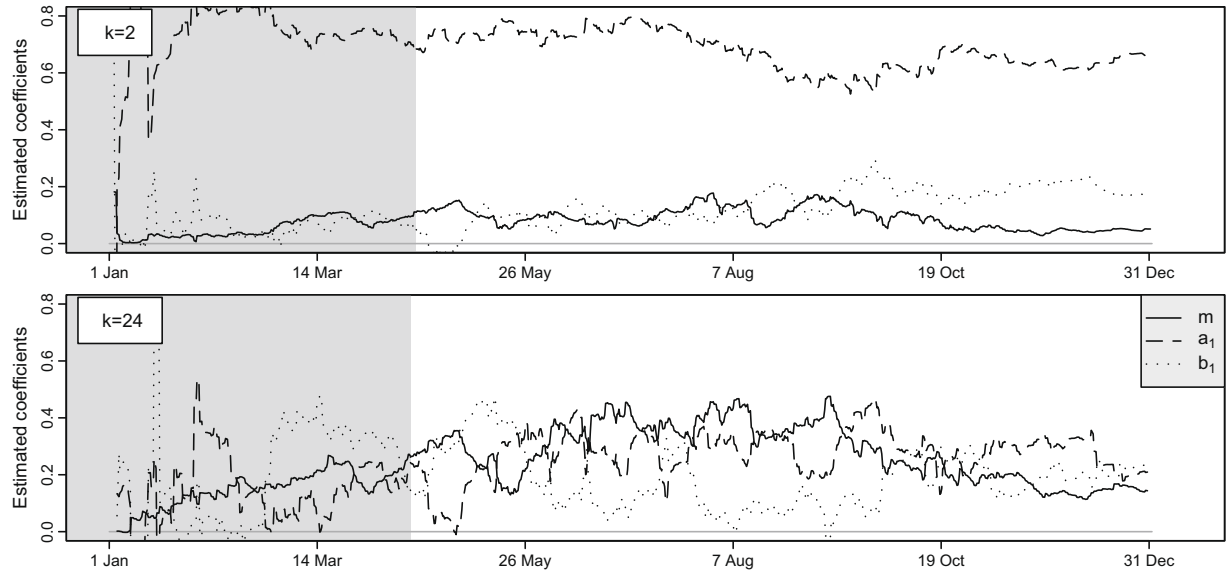

Fig. 14. The online estimates of the coefficients in the *AR* model as a function of time. Two selected horizons are shown. The grayed period in the beginning marks the burn-in period.

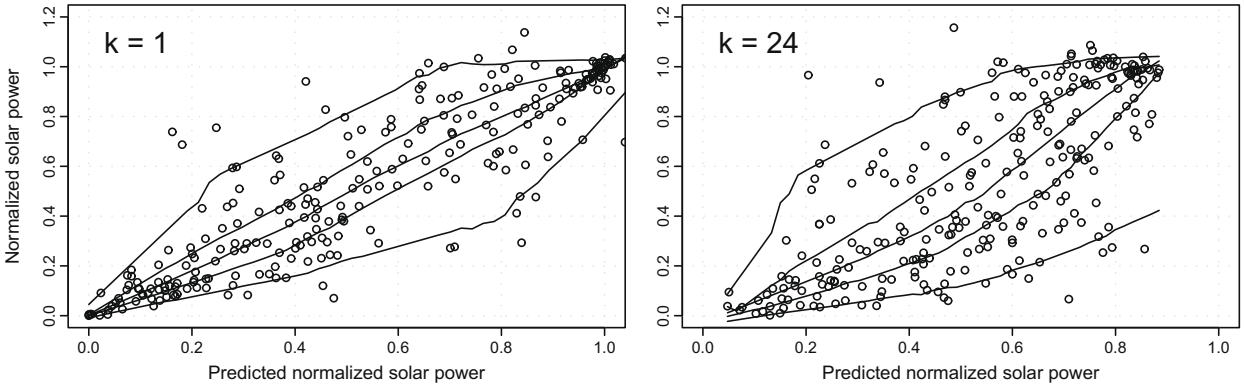

Fig. 15. Normalized solar power versus the predicted normalized solar power at horizons $k = 1$ and $k = 24$. The predictions are made with the *ARX* model. The lines are estimates of the 0.05, 0.25, 0.50, 0.75 and 0.95 quantiles of $f_\tau(\hat{\tau})$.

$$RMSE_k = \left(\frac{1}{N} \sum_{t=1}^{N} e_{t+k}^2 \right)^{\frac{1}{2}}. \tag{26}$$

The $RMSE_k$ is used as the main evaluation criterion (EC) for the performance of the models. The normalized root mean square error (NRMSE) is found by

$$NRMSE_k = \frac{RMSE_k}{p_{\text{norm}}}, \tag{27}$$

where either

$$p_{\text{norm}} = \bar{p} = \frac{1}{N} \sum_{t=1}^{N} p_t, \tag{28}$$

or p_{norm} is the average peak power of the 21 PV systems.

The mean value of the $RMSE_k$ for a range of horizons

$$\overline{RMSE}_{k_s,k_e} = \frac{1}{k_e - k_s + 1} \sum_{k=k_s}^{k_e} RMSE_k \tag{29}$$

is used as a summary error measure. When comparing the performance of two models the improvement

$$I_{\text{EC}} = 100 \cdot \frac{EC_{\text{ref}} - EC}{EC_{\text{ref}}} (\%) \tag{30}$$

is used, where EC is the considered evaluation criterion.

6.2. Reference model

To compare the performance of prediction models, and especially when making comparisons between different studies, a common reference model is essential. A reference model for solar power is here proposed as the best perform-

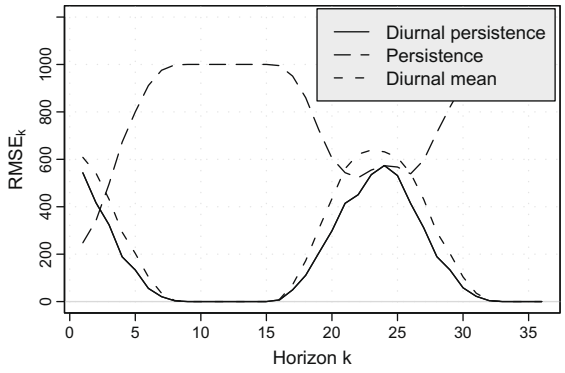

Fig. 16. $RMSE_k$ for the three naive predictors used in the *Reference* model.

ing naive predictor for the given horizon. Three naive predictors of solar power are found to be relevant. Persistence

$$p_{t+k} = p_t + e_{t+k}, \tag{31}$$

diurnal persistence

$$p_{t+k} = p_{t-s(k)} + e_{t+k}, \tag{32}$$

$$s(k) = f_{\text{spd}} + k \bmod f_{\text{spd}}, \tag{33}$$

where $s(k)$ ensures that the latest diurnal observation is used and f_{spd} is the sample frequency in number of samples per day, and diurnal mean

$$p_{t+k} = \frac{1}{n}\sum_{i=1}^{n} p_{t-s(k,i)} + e_{t+k} \tag{34}$$

$$s(k,i) = i \cdot f_{\text{spd}} + k \bmod f_{\text{spd}}, \tag{35}$$

which is the mean of solar power of the last n observations at the time of day of p_{t+k}. The value of n is chosen such that all past samples are included.

Fig. 16 shows the $RMSE_k$ for each of the three naive predictors. It is seen that for $k \leqslant 2$ the persistence predictor is the best while the best for $k > 2$ is the diurnal persistence predictor. This model is referred to as the *Reference* model.

6.3. Results

Examples of solar power forecasts made with the *ARX* model are shown in Fig. 17 for short horizons and in Fig. 18 for next day horizons. It is found that the forecasted solar power generally follows the main level of the solar power, but the fluctuations caused by sudden changes in cloud cover are not fully described by the model.

The $NRMSE_k$ is plotted for each model in Fig. 19. Clearly the performance is increasing from the *Reference* model to the *AR* model and further to the *ARX* model. The differences from using either the solar power or the NWPs, or both, as input become apparent from these results.

At $k = 1$ the *AR* model that only uses solar power as input is better than the LM_{nwp} which only uses NWPs as input, but at $k = 2,\ldots,6$ the LM_{nwp} is better, though only slightly. This indicates that for making forecasts of horizons shorter than 2 h, solar power is the most important input, whereas for 2- to 6-h horizons, forecasting systems using either solar power or NWPs can perform almost equally. The *ARX* model using both types of input does have an increased performance at all $k = 1,\ldots,6$ and thus

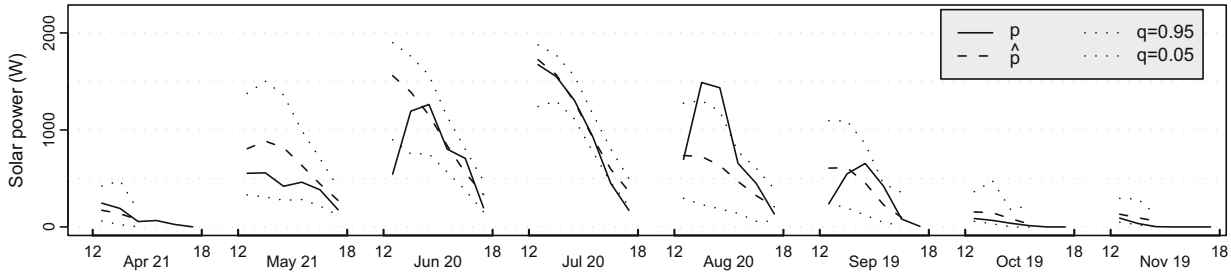

Fig. 17. Forecasts of solar power at short horizons $k = 1,\ldots,6$ made with the *ARX* model.

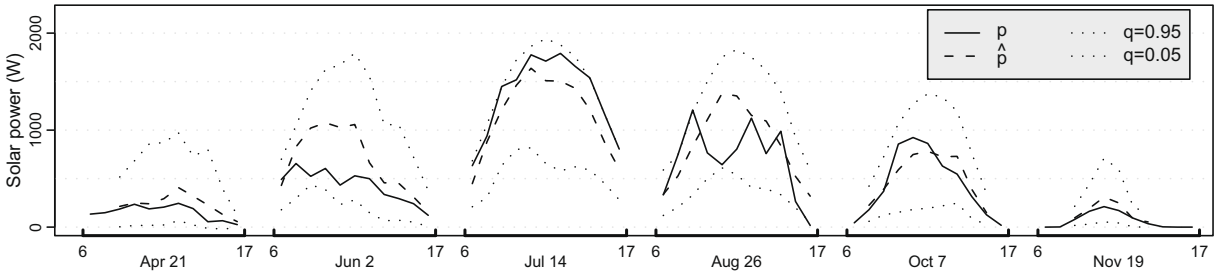

Fig. 18. Forecasts of solar power at next day horizons $k = 19,\ldots,29$ made with the *ARX* model.

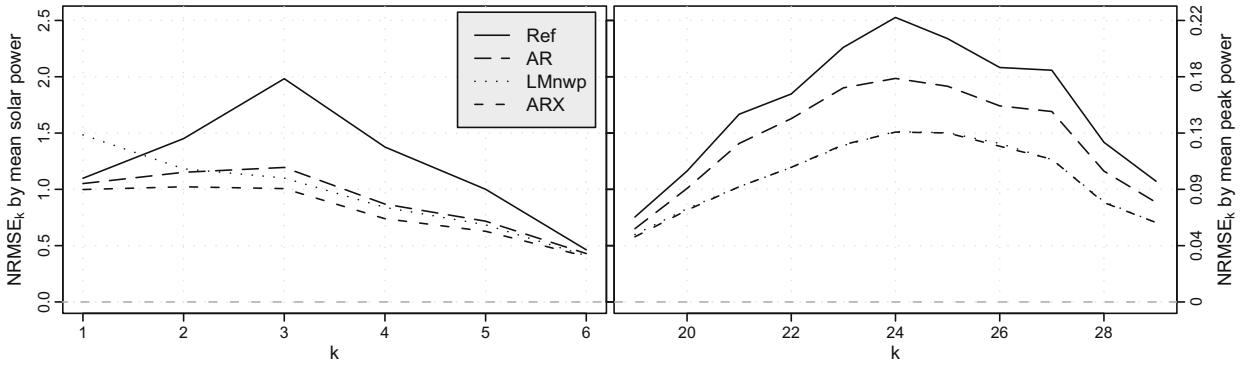

Fig. 19. The $NRMSE_k$ for each of the three models and the *Reference* model. The left plot show the short horizons and the right the next day horizons. The left scale show $RMSE_k$ normalized by $\bar{p} = 248$ W/h and the right scale show $RMSE_k$ normalized by 2769 W which is the mean peak power of the 21 PV systems.

Table 1
Summary error measures of improvements compared to the *Reference* model for short horizons $k = 1,\ldots,6$ and next day horizons $k = 19,\ldots,29$.

Models	$I_{\overline{RMSE}_{1,6}}$ (%)	$I_{\overline{RMSE}_{19,29}}$ (%)
AR over *Reference*	27	17
LM_{nwp} over *Reference*	25	36
ARX over *Reference*	35	36
LM_{nwp} over *AR*	−2	23
ARX over *AR*	12	23
ARX over LM_{nwp}	13	1

combining the two types of input is found to be the superior approach.

For $k = 19,\ldots,29$, which are the next day horizons, very clearly the LM_{nwp} model and the *ARX* model perform better than the *AR* model. Since the LM_{nwp} model and the *ARX* model perform almost equally, it is seen that no improvement is achieved from adding the solar power as input, and thus using only the NWPs as input is found to be adequate for next day horizons.

A summary of the improvement in performance is calculated using (29) and (30). The improvements compared to the *Reference* model are calculated for the four models by $I_{\overline{RMSE}_{1,6}}$ for short horizons and $I_{\overline{RMSE}_{19,29}}$ for next day horizons. The results are shown in Table 1. These results naturally show the same as stated above, though the difference at $k = 1$ from *AR* to LM_{nwp} cannot be seen. These results show that a RMSE improvement of around 35% over the *Reference* model can be achieved by using the *ARX* model.

7. Conclusions

Inspired by previous studies, the present method for solar power forecasting has been developed from scratch. A new approach to clear sky modelling with statistical smoothing techniques has been proposed, and an adaptive prediction model based on RLS makes a solid framework allowing for further refinements and model extensions, e.g. by including NWPs of temperature as input. The adaptivity of the method makes it suited to online forecasting and ensures comprehension of changing conditions of the PV system and its surroundings. Furthermore, the RLS algorithm is not computer intensive, which makes updating of forecasts fast. The clear sky model used to normalize the solar power delivers a useful result, but can be improved, especially for the estimates toward dawn and dusk, by using polynomial-based kernel regression. A procedure based on quantile regression is suggested for calculating the varying intervals of the uncertainty of the solar power predictions and the results agree with other studies. The best performing prediction model is an *ARX* model where both solar power observations and NWPs are used as input. The results indicate that for horizons below 2-h solar power is the most important input, but for next day horizons no considerable improvement is achieved from using available values of solar power, so it is adequate just to use NWPs as input. Thus, depending on the application of the forecasting system using only either of the inputs can be considered, and a lower limit of the latency, at which solar power observations are needed for the forecasting system, can be different. Finally, it is noted that a comparison to other online solar power forecasting methods, e.g. Lorenz et al. (2007) and Hocaoglu et al. (2008), has not been carried out, but that such a study would be informative in order to describe strengths and accuracy of the different proposed methods.

Appendix A. Weighted quantile regression

The solar power time series $\{p_t,\ t = 1,\ldots,N\}$ is the realization of a stochastic process $\{P_t,\ t = 1,\ldots,N\}$. The estimated clear sky solar power at time t is $\hat{p}_t^{\text{cs}}$ and it is found as the q quantile of f_{P_t}, the probability distribution function of P_t. The problem is reduced to estimating $\hat{p}_t^{\text{cs}}$ as a local constant for each (x_t, y_t), where x is the day of year and y the time of day. This is done by weighted quantile regression in which the loss function is

$$\rho(q,\epsilon_i) = \begin{cases} q\epsilon_i, & \epsilon_i \geqslant 0, \\ (1-q)\epsilon_i, & \epsilon_i < 0, \end{cases} \tag{36}$$

where $\epsilon_i = p_i - \hat{p}_t^{cs}$. The fitting of $\hat{p}_t^{cs}$ is then done by

$$\hat{p}_t^{cs} = \arg\min_{\hat{p}_t^{cs}} \sum_{i=1}^{N} k(x_t, y_t, x_i, y_i) \cdot \rho(q, \epsilon_i), \tag{37}$$

where

$$k(x_t, y_t, x_i, y_i) = \frac{w(x_t, x_i, h_x) \cdot w(y_t, y_i, h_y)}{\sum_{i=1}^{N} w(x_t, x_i, h_x) \cdot w(y_t, y_i, h_y)} \tag{38}$$

is the two-dimensional multiplicative kernel function which weights the observations locally to (x_t, y_t) (Hastie and Tibshirani, 1993). Details of the minimization are found in Koenker (2005). In each dimension a Gaussian kernel is used

$$w(x_t, x_i, h_x) = f_{\text{std}}\left(\frac{|x_t - x_i|}{h_x}\right), \tag{39}$$

where f_{std} is the standard normal probability density function. A similar kernel function is used in the y dimension, and the final two-dimensional kernel is found by multiplying the two kernels as shown in (37).

Appendix B. Recursive least squares

Fitting of the prediction models is done using k-step recursive least squares (RLS) with forgetting, which is described in the following using the ARX model

$$\tau_{t+k} = m + a_1\tau_t + a_2\tau_{t-s(k)} + b_1\hat{\tau}_{t+k|t}^{\text{nwp}} + e_{t+k}, \tag{40}$$

as an example. The regressor at time t is

$$\mathbf{X}_t^T = \left(1, \tau_t, \tau_{t-s(k)}, \hat{\tau}_{t+k|t}^{\text{nwp}}\right). \tag{41}$$

The parameter vector is

$$\theta^T = (m, a_1, a_2, b_1), \tag{42}$$

and the dependent variable

$$Y_t = \tau_t. \tag{43}$$

Hence the model can be written as

$$Y_t = \mathbf{X}_t^T\theta + e_t. \tag{44}$$

The estimates of the parameters at t are found such that

$$\hat{\theta}_t = \arg\min_{\theta} S_t(\theta), \tag{45}$$

where the loss function is

$$S_t(\theta) = \sum_{s=1}^{t} \lambda^{t-s}\left(Y_s - \mathbf{X}_s^T\theta\right)^2. \tag{46}$$

This provides weighted least squares with exponential forgetting. The solution at time t leads to

$$\hat{\theta}_t = \mathbf{R}_t^{-1}\mathbf{h}_t, \tag{47}$$

see Madsen (2007), where

$$\mathbf{R}_t = \sum_{s=1}^{t} \lambda^{t-s}\mathbf{X}_s\mathbf{X}_s^T, \quad \mathbf{h}_t = \sum_{s=1}^{t} \lambda^{t-s}\mathbf{X}_s Y_s. \tag{48}$$

The k-step RLS-algorithm with exponential forgetting is then

$$\mathbf{R}_t = \lambda\mathbf{R}_{t-1} + \mathbf{X}_{t-k}\mathbf{X}_{t-k}^T, \tag{49}$$

$$\hat{\theta}_t = \hat{\theta}_{t-1} + \mathbf{R}_t^{-1}\mathbf{X}_{t-k}\left(Y_t - \mathbf{X}_{t-k}^T\hat{\theta}_{t-1}\right), \tag{50}$$

and the k-step prediction at t is

$$\widehat{Y}_{t+k} = \mathbf{X}_t^T\hat{\theta}_t. \tag{51}$$

References

Bacher, P., 2008. Short-term solar power forecasting. Master's Thesis, Technical University of Denmark, IMM-M.Sc.-2008-13.

Cao, J., Lin, X., 2008. Study of hourly and daily solar irradiation forecast using diagonal recurrent wavelet neural networks. Energy Conversion and Management 49 (6), 1396–1406.

Chowdhury, B., Rahman, S., 1987. Forecasting sub-hourly solar irradiance for prediction of photovoltaic output. In: IEEE Photovoltaic Specialists Conference, 19th, New Orleans, LA, May 4–8, 1987, Proceedings (A88-34226 13-44). New York, Institute of Electrical and Electronics Engineers, Inc., 1987, pp. 171–176.

Hastie, T., Tibshirani, R., 1993. Varying-coefficient models. Journal of the Royal Statistical Society Series B (Methodological) 55 (4), 757–796.

Heinemann, D., Lorenz, E., Girodo, M., 2006. Forecasting of solar radiation. In: Dunlop, E., Wald, L., Suri, M. (Eds.), Solar Resource Management for Electricity Generation from Local Level to Global Scale. Nova Science Publishers, New York, pp. 83–94.

Hocaoglu, F.O., Gerek, O.N., Kurban, M., 2008. Hourly solar radiation forecasting using optimal coefficient 2-D linear filters and feed-forward neural networks. Solar Energy 82 (8), 714–726.

Koenker, R., 2005. Quantile Regression. Cambridge University Press, Cambridge.

Koeppel, G., Korpas, M., 2006. Using storage devices for compensating uncertainties caused by non-dispatchable generators. 2006 International Conference on Probabilistic Methods Applied to Power Systems, pp. 1–8.

Lorenz, E., Heinemann, D., Wickramarathne, H., Beyer, H., Bofinger, S., 2007. Forecast of ensemble power production by grid-connected PV systems. In: Proceedings of the 20th European PV Conference, Milano, September 3–7, 2007.

Madsen, H., 2007. Time Series Analysis. Chapman & Hall, London.

Madsen, H., Pinson, P., Kariniotakis, G., Nielsen, H.A., Nielsen, T.S., 2005. Standardizing the performance evaluation of shortterm wind power prediction models. Wind Engineering 29 (6), 475.

Møller, J.J.K., Nielsen, H.A., Madsen, H., 2008. Time-adaptive quantile regression. Computational Statistics and Data Analysis 52 (3), 1292–1303.

Sfetsos, A., Coonick, A., 2000. Univariate and multivariate forecasting of hourly solar radiation with artificial intelligence techniques. Solar Energy 68 (2), 169–178.

Peder Bacher, Bengt Perers, Opensource software for MLR-modelling of solar collectors, ISES Solar World Congress 2011 Proceedings

OPENSOURCE SOFTWARE FOR MLR-MODELLING OF SOLAR COLLECTORS

Peder Bacher
DTU Informatics, Richard Pedersens Plads, Building 321, DK-2800 Lyngby, Denmark
Bengt Perers
DTU Civil Engineering, Brovej, Building 118, DK-2800 Lyngby

Abstract

A first research version is now in operation of a software package for multiple linear regression (MLR) modeling and analysis of solar collectors according to ideas originating all the way from Walletun et. al. (1986), Perers, (1987 and 1993). The tool has been implemented in the free and open source program R http://www.r-project.org/. Applications of the software package includes: visual validation, resampling and conversion of data, collector performance testing analysis according to the European Standard EN 12975 (Fischer et al., 2004), statistical validation of results, and the determination of collector incidence angle modifiers without the need of a mathematical function (Perers, 1997). The paper gives a demonstration with examples of the applications, based on measurements obtained at a test site at DTU in Denmark (Fan et al., 2009). The tested collector is a single glazed large area flat plate collector with selective absorber and teflon anti convection layer.

The package is intended to enable fast and reliable validation of data, and provide a united implementation for MLR testing of solar collectors. This will furthermore make it simple to replicate the calculations by a third party in order to validate the results. Finally more advanced methods can be implemented and easily shared as extensions to the package, for example methods for statistical estimation of the incidence angle modifier with non-linear functions for collectors with more complicated optics.

The overall advantage of this kind of tool and analysis is that it is almost the inverse of simulation. Therefore the model and parameters will be very well validated for application in later use for system simulation, even if the test is no real system test. Also for annual collector performance calculations with a new Excel tool connected to EN 12975 (Kovacs, 2011) this built in validation gives an extra quality assurance.

Introduction

A large database is created during a normal solar collector test according to the EN12975 (2006) standard. To have a fast check and efficient evaluation of the data there is a need for a software that can run through the data quickly. Some of the steps are check and selection of OK data points, scaling of units and conversion of raw data to an appropriate MLR input form and finally statistically estimated collector parameters can be reported. When applying stationary testing (SS) a larger amount of data, has to be collected compared to a quasi dynamic test (QDT). But the number of data points finally used in the analysis to get the collector parameters is much larger in the QDT method. Therefore a fast and efficient evaluation tool is very desirable.

For the QDT method several parameter identification methods can be used. One of them is Multiple Linear Regression (MLR). In opposition to what you normally think, due to the word Linear, the collector model can still be highly nonlinear in the terms, when using MLR. Also stepwise identification using so called "dummy variables" can be applied to identify a parameter in different ranges of the database in the same run. This is for example very useful for collectors with an incidence angle behavior that can't be described with a simple mathematical function. A big advantage of the MLR method proposed in the QDT method is also that a time sequence of data without gaps is not needed. Therefore the deselection of data points due intermittent problems with for example the test rig, test object or sensors is no problem.

In Sweden an Excel tool has been developed at SP www.sp.se for the analysis of QDT test results. This is used for all kinds of collectors. When the database becomes large, and when highly asymmetric collectors are investigated, Excel has limitations in capacity and the first steps have been taken to develop an alternative tool using the open source statistical and graphical software "R" http://www.r-project.org/

Some of the ideas implemented here come from the period when the first steps towards the MLR/QDT method was taken and access to the Minitab statistical software was available. This work was done in connection to the IEA SH&C Task III cooperation for collector and system testing. Walletun et. al. (1986), Perers, (1987 and 1993).

The overall advantage of this kind of tool and analysis is that it is almost the opposite of simulation so the model and parameters will be very well validated for application in later use for system simulation even if

the test is no real system test. Also for standardized annual collector performance calculations with a newly developed Excel tool for EN 12975 Perers et. al. (2011) this built in validation in the QDT method and this tool gives an extra quality assurance.

The test design is also very important and should be a systematic emulator of all normal operating states for the collector in a real system, plus some extra extreme states of high and low operating temperature to separate the model parameters from each other.

This principle can be further improved in the EN12975 QDT method. The QDT method was very much restricted in the standard writing to also give stationary test (SS) data points in the same test period. Therefore a perfect constant inlet temperature was specified during all test days. In this respect the SS method is far from an all day model plus parameter validation, even if the model plus parameters are very well defined for clear sky conditions within a certain diffuse fraction range, that is the requirement during testing. The built in error due to varying diffuse fraction during an SS test, is quantified and a correction method is proposed in Kovacs et. al. (2011)

The proposed evaluation tool can be extended to also select and evaluate stationary collector test data if the test sequence is run according to the SS method. MLR is already applied to determine the stationary collector parameters and efficiency curve in an SS test, but in a limited form for only tree parameters.

1. Description of the main parts of the tool

The tool can be divided in a number of important steps from reading of raw data until final results.

1) Raw test data reading into the software
2) Input of collector parameters as Aperture area, Tilt and Orientation. Latitude and Longitude of the test site.
3) Organisation of the data in a standardized format including units for further analysis
4) Check of data and removing obviously wrong data points like negative solar radiaton, temperatures or other variables out of range. (This can be caused by power failures or repair of sensors or wires for example). Plots of raw data can be a very efficient check too to see strange or wrong values.
5) Creation of the collector model terms in a standardized way like the term (Tm-Ta) or $(Tm-Ta)^2$ or the dTf/Dt capacitance term. Note that the collector model terms are set up in ***output power*** form and not *efficiency* form so that the parameters set derived in the analysis will minimize the error in collector output power and not the error in efficiency like in the SS method.
6) Re-sampling from the time step in raw data like 30 sec averages or 2 sec instantaneous values to a time step suitable for the model analysis, normally 5-10 min averages, presently when using just a one node capacitance correction term.
7) Check of the cross correlation of the input series in the collector model to see that the requirement for independency is fulfilled and that the input variables like inlet temperature and incidence angles are varied enough during the test to achieve reliable parameter values. This is an often forgotten requirement not only for an MLR analysis. It is not possible to identify accurate and reliable parameters if for example the inlet temperature variations has been too limited like in most cases in system operation of a collector.
8) Selection of data according to specific rules in the standard or research requirements. It can be positive collector output, incidence angles smaller than 85 deg or solar radiation greater than 50W/m2 for example.
9) Run the MLR routine. Check if the parameter values and statistical results are reasonable. For example the t-ratio should be greater than 2 to keep a parameter and term in the collector equation.
10) Plot of the statistical results and model output power versus measured output. Check for outliers that can indicate wrong data in some way. For example visitors shading the collector sample for some minutes unintentionally or a bird sitting on a solar sensor for some time. A lose wire or connector can also give intermittent measurement errors. There are many more examples in real testing life that has to be removed from data before accurate results can be achieved. In this step the R tool is very efficient in plotting the data and finding the strange points. Also the allowance in the MLR procedure to have data gaps when data has to be removed is very useful.

2. Some examples of results from the MLR/QDT- R tool

Below are some diagrams showing results of an analysis of measurements on a large area flat plate collector at DTU, (Fan et. al. 2009). The test was done according to the SS method, but as different operating temperatures were present within the test period also the QDT and MLR method could be used to analyse data. In this case as it was a research test also data points during the night could be used to check the future

possibilities to shorten the testing time, by varying the inlet temperature during night and estimate the heat loss parameters more accurately and faster.

Figure 1-3 gives all day and also night results showing that the analysis method gives a very good model fit to real measurements of collector output. Also some large fluctuations in inlet temperature and flow are shown to be handled well as rapid fluctuations in solar radiation.

Figure 4 gives an example of the option in the tool to determine the incidence angle modifier with statistical estimation of non-linear functions without the need of a simple mathematical function (black and red points). Also the separation of morning and afternoon values are shown to give an impression of the reproducibility that the method can give. As a comparison the standard b0 equation is shown for the same data set. It is interesting to note the cut off before 90 degrees that is caused by shading of the absorber from the frame of the collector. This detailed evaluation of the measurements, require a test rig and sensors in very good shape. Small errors will otherwise show up here like a test rig not oriented due south for example or bad adjustment or mounting of a shading ring or misalignment of solar sensors. Also other measurement problems or errors will show up and this is also one advantage with this tool that the quality of the test rig can be improved step by step based on this kind of results.

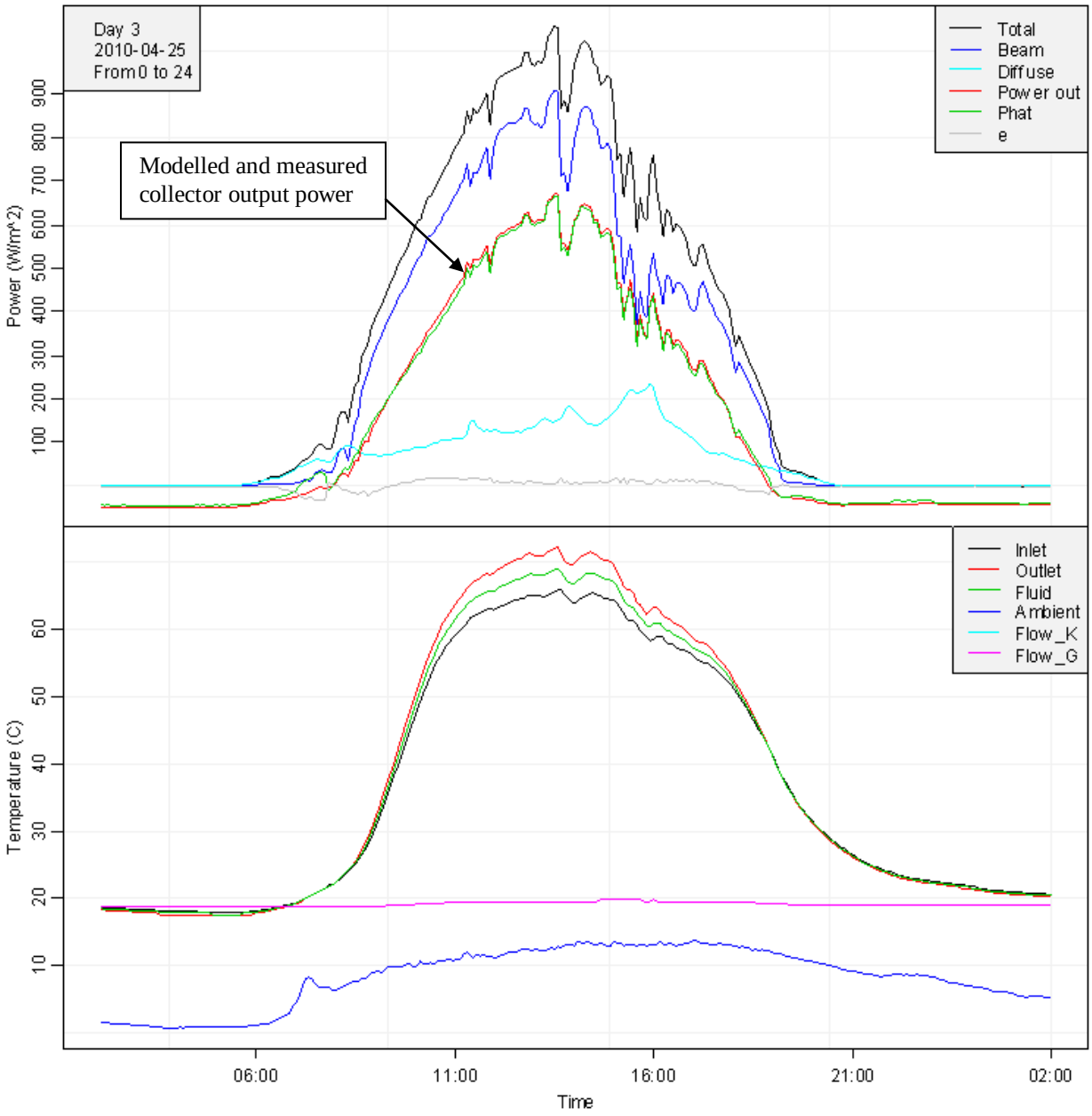

Fig. 1: All day measurements and validation of the method and model plus parameters. The red curve in the upper diagram is measured collector output and the green curve is the model output with the identified parameters for the whole test period

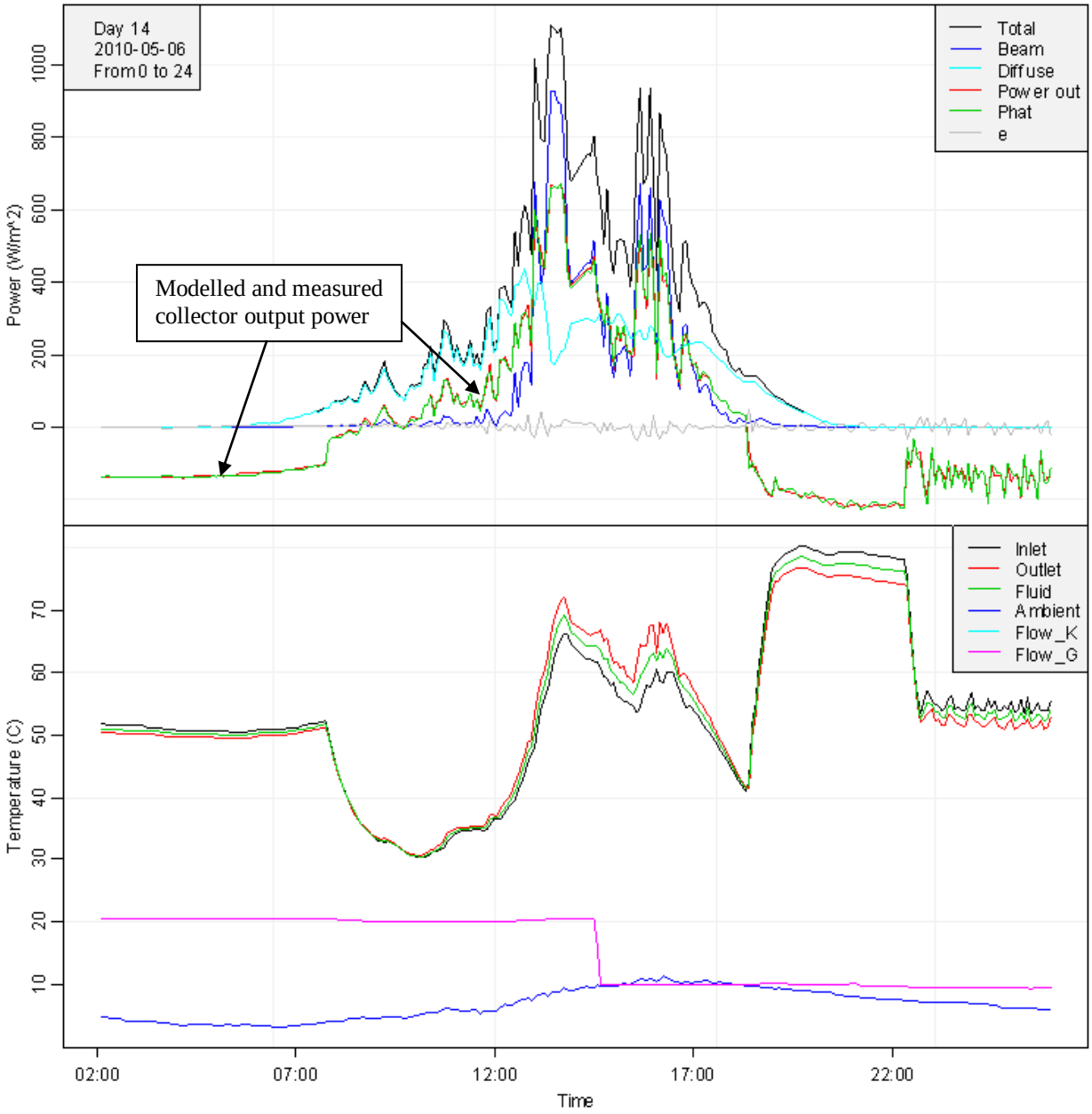

Fig. 2: All day measurements and validation of the method and model plus parameters. The red curve in the upper diagram is measured collector output and the green curve is the model output with the identified parameters for the whole test period

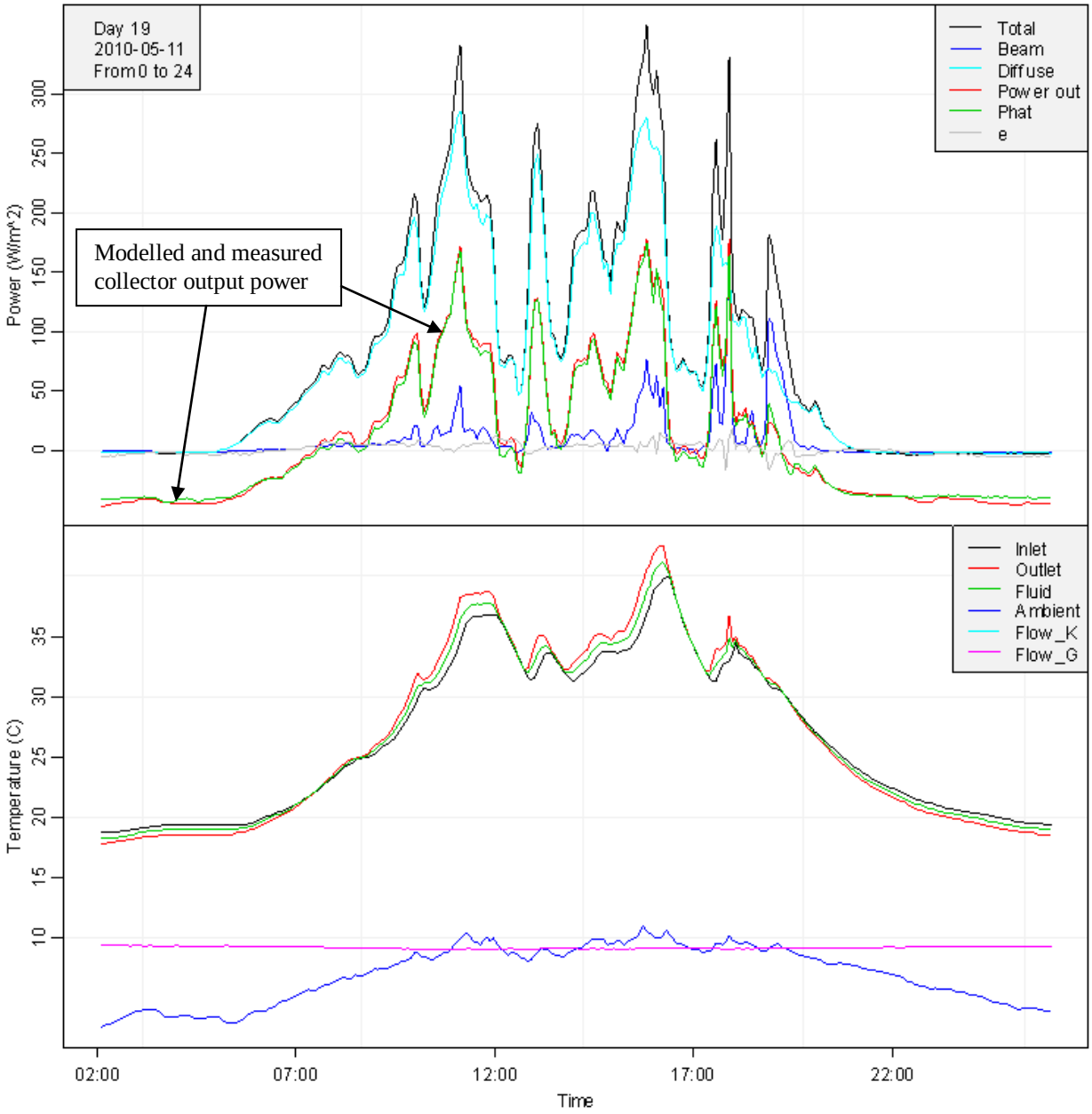

Fig. 3: All day measurements and validation of the method and model plus parameters. The red curve in the upper diagram is measured collector output and the green curve is the model output with the identified parameters for the whole test period

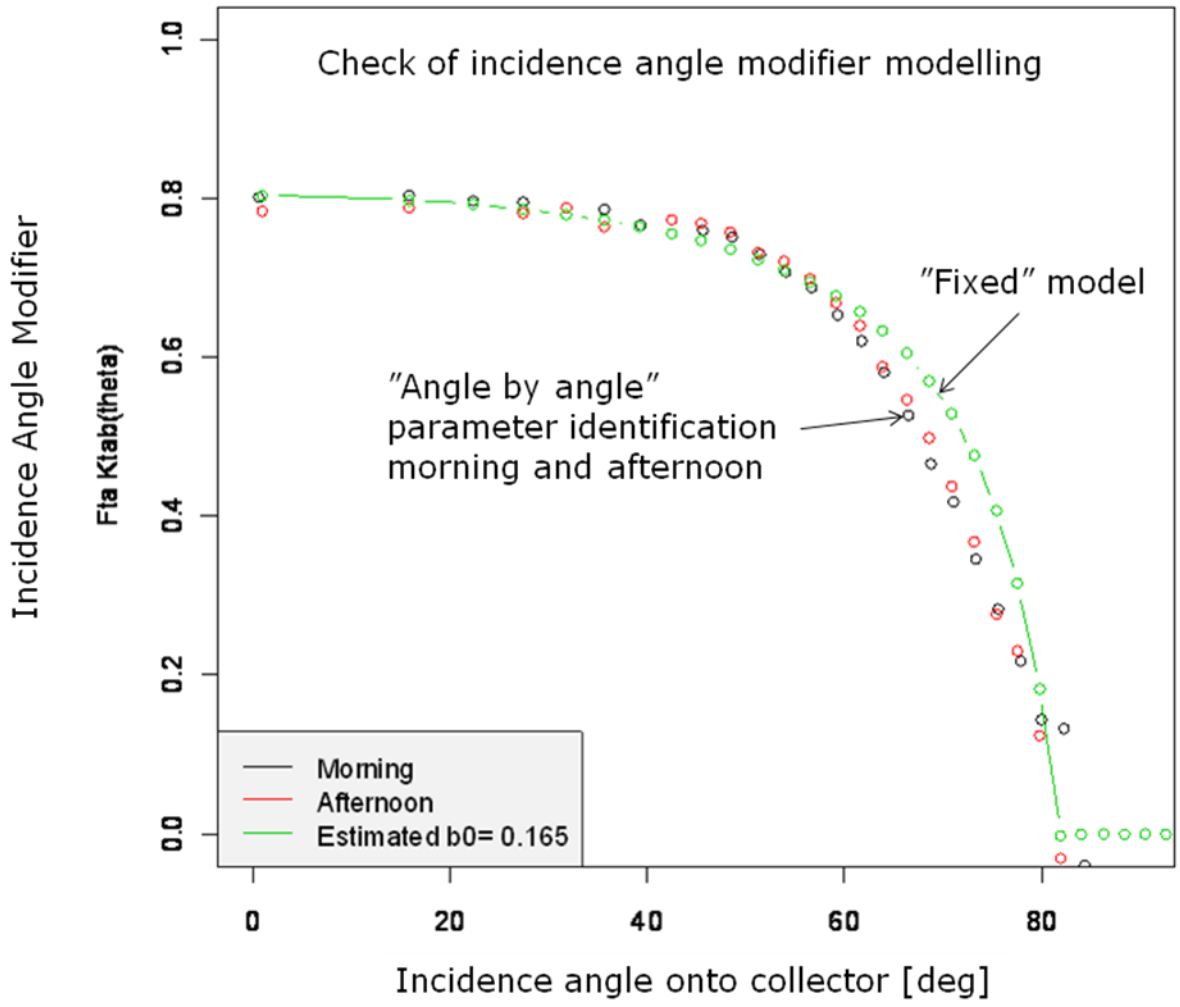

Figure 4. Example of the option to determine the Incidence angle modifier with statistical estimation of non-linear functions without the need of a simple mathematical function (black and red points). Also the separation of morning and afternoon values are shown to give an impression of the reproducibility that the method can give. As a comparison the standard b0 equation is shown.

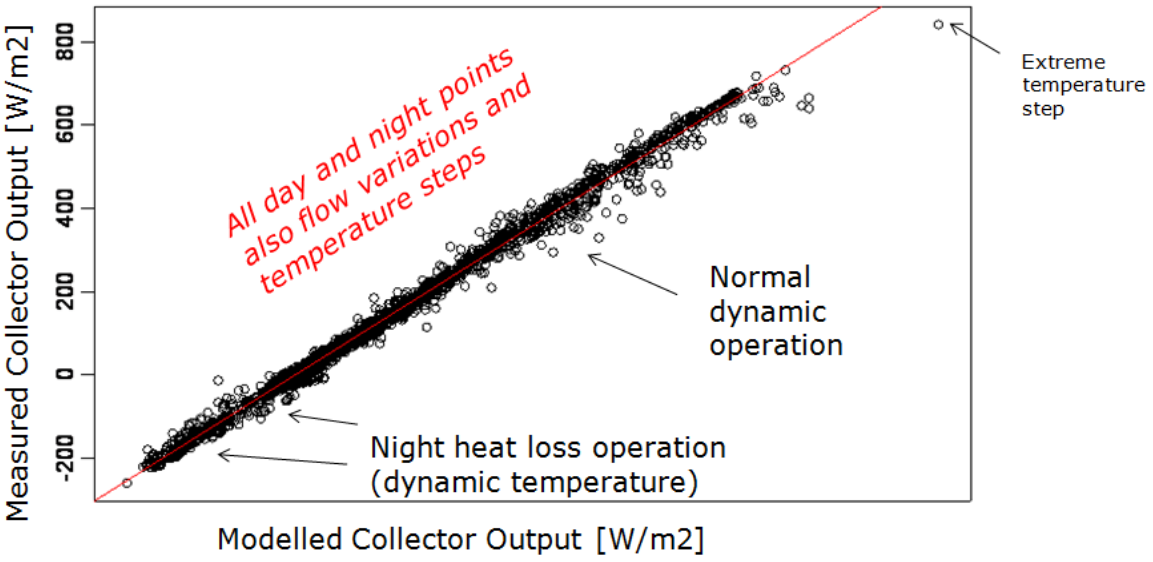

Fig. 5: Model versus measurements including also night heat loss measurements. (Points with negative collector output).

3. Discussion and Conclusions

A first version of a tool has been developed and tested, for all day test data evaluation according to the QDT option in the EN 12975 standard .

The tool contains all steps from import of data to display of final parameters with statistical information.

In the tool the built in model plus parameter validation in the EN12975 QDT method can be applied and displayed. This helps a lot to assure reliable results and especially to find intermittent errors in the test rig, collector samples (like condensation or micro fluid leaks), measurement equipment problems or even unusual occasions like visitors or birds shading the test instruments or collector.

The tool is prepared to deselect obviously wrong data from the analysis and use the advantage with the QDT and MLR method to allow data gaps if needed.

The development has been done with no dedicated project for the work. Therefore further improvements and refinements, as more user friendliness, are possible if a project could be created for this. Also the addition of the EN12975 stationary test SS evaluation could be an option.

References

Fan, J., Chen, Z., Furbo, S., Perers, B., B., K., 2009. Efficiency and lifetime of solar collectors for solar heating plants.

CEN, European committee for standardization. (2006) *"EN 12975-2:2006, Thermal solar systems and components - Collectors - Part 2: Test methods"*

Fischer, S., Heidemann, W., Müller-Steinhagen, H., Perers, B., Bergquist, P., Hellstr□om, B., 2004. Collector test method under quasi-dynamic conditions according to the European standard en 12975-2. Solar Energy 76 (1-3), 117{123.

P. Kovacs, B. Perers, U. Pettersson, (2011). Improving the compatibility of collector parameters between Steady state and Quasi dynamic testing for new collector designs. ISES Kassel (this conference)

Perers, B., Kovacs, P., Olsson, M., Persson M., Pettersson, U. (2011). A new tool for standardized collector performance calculations. ISES Solar World Congress, Kassel 2011.

Perers, B., 1993. Dynamic method for solar collector array testing and evaluation with standard database and simulation programs. Solar Energy 50 (6), 517{526.

Perers, B., 1997. An improved dynamic solar collector test method for determination of non-linear optical and thermal characteristics with multiple regression. Solar Energy 59 (4-6), 163{178.

Walletun, H. Eriksson, Leif. Perers, B. Zinko, H. (1986) Vindens inflytande på oglasade solfångare respektive solfångare med konvektionshinder. Studsvik Technical Note ED-86/15.

Perers, B. (1987). Performance testing of Unglased Collectors. Wind and Longwave Radiation Influence IEA Task III. Studsvik 1987.

Peder Bacher, Henrik Madsen, Henrik Aalborg Nielsen, Bengt Perers, Short-term heat load forecasting for single family houses, submitted to Buildings and Energy, 2012

Short-term heat load forecasting for single family houses

Peder Bacher, Henrik Madsen

DTU Compute, Technical University of Denmark, DK-2800 Lyngby, Denmark

Henrik Aalborg Nielsen

ENFOR A/S, DK-2970 Hørsholm, Denmark

Bengt Perers

DTU Civil Engineering, Technical University of Denmark, DK-2800, Lyngby, Denmark

Abstract

This paper presents a method for forecasting the load for space heating in a single-family house. The forecasting model is built using data from sixteen houses located in Sønderborg, Denmark, combined with local climate measurements and weather forecasts. Every hour the hourly heat load for each house the following two days is forecasted. The forecast models are adaptive linear time-series models and the climate inputs used are: ambient temperature, global radiation and wind speed. A computationally efficient recursive least squares scheme is used. The models are optimized to fit the individual characteristics for each house, such as the level of adaptivity and the thermal dynamical response of the building, which is modeled with simple transfer functions. Identification of a model, which is suitable for all the houses, is carried out. The results show that the one-step ahead errors are close to white noise and that practically all correlation to the climate variables are removed. Furthermore, the results show that the forecasting errors mainly are related to: unpredictable high frequency variations in the heat load signal (predominant only for some houses), shifts in resident behavior patterns and uncertainty of the weather forecasts for longer horizons, especially for solar radiation.

Keywords: Heat load, single-family house, building heat dynamics, forecasting, numerical weather predictions, thermal, cooling

1. Introduction

The transition to an energy system based on renewables requires methods for forecasting of power load and generation. In Denmark around 40% of the total energy consumption is related to buildings and around 29% of the energy used for space heating is covered by individual oil or gas fired furnaces [1], which is neither economically feasible nor environmentally friendly technologies. The Danish Commission on Climate Change Policy recommends replacement with alternative technologies, especially with electric heat pumps since this is one of the socio-economically cheapest

Email address: pbac@dtu.dk (Peder Bacher)
URL: www.imm.dtu.dk/∼hm (Henrik Madsen), www.enfor.eu (Henrik Aalborg Nielsen)

alternatives in the transition to an energy system without fossil fuels in Denmark. Hence, new and alternative technologies for building space heating based on renewable energy production are of high interest, both for individual and district heating. Especially electrical heating systems since large amounts of wind power are available, which creates a need for flexible load in order to absorb the increasingly volatile production. As the level of electrical load increase, load-shifting in shorter periods of time for peak-shaving of the diurnal electrical consumption is a valuable service to the grid [2]. Flexible load can be achieved with thermal energy buffering, both in individual heating and district heating, where huge thermal storage capacity is available. Several studies consider the possibilities for flexible heating, for example [3] and [4] who present methods for energy storage in the thermal mass of buildings, and [5] and [6] who consider load-shifting for cooling of buildings. The present paper presents a method for forecasting of the power load for space heating in a single-family house, referred to as the space heat load or simply heat load. The heat load forecasts can be used as input to model predictive control, which can be used for optimized load-shifting, for example for operation under energy markets where relocation of load to periods with cheap energy is rewarded. The method can just as well be used for forecasting of cooling load and used for load-shifting with cool thermal storage. [7] presents solar a combisystem, which is a heating system based on a solar thermal collector and electrical heating, where a hot water tank is used for thermal energy storage. Forecasting of the heat load is vital for optimal and effective use of the thermal storage in such a system.

Forecasting of the heat load is carried out for sixteen houses located in Sønderborg, Denmark. Every hour a new forecast is calculated of the hourly heat load up to 42 hours ahead. The houses are generally built in the sixties and seventies, with a floor plan in the range of 85 to 170 m^2 and constructed in bricks. Climate observations - which are measured at the local district heating plant within 10 kilometers from the houses - together with numerical weather predictions (NWPs) are used as input to the forecasting model. The NWPs are from the HIRLAM-S05 [15] model and provided by the Danish Meteorological Institute. For each house only the total heat load, including both space heating and hot water heating in a single signal, is available. The total heat load signal is separated into two signals: one for space heating and one for hot water heating, and then the space heating is forecasted. The splitting allows for a clear view of the effects stemming from heat loss to the ambient and heat gains from solar radiation etc., since the noisy peaks from hot water heating are filtered out. The indoor temperature is not available, but this is accounted for in the models by including a diurnal curve to model nightly setback and behavioral patterns of the residents e.g. heat from electrical appliances used for cooking.

Many approaches to load forecasting are found in the literature. A good overview of references are given by [8], who also built load forecasting models using dynamic factor models. [9] use a model based on the ambient temperature and a weekly pattern for forecasting of the heat load in district heating, i.e. the total heat load for many houses. [10] use a grey-box model based on transfer functions for building thermal load prediction and validates it on a 50 floors multi-purpose building. The models applied in the present study are originally developed and used for forecasting of heat load in district heating, as described in [11] and [12]. The heat load summed for many houses have less high frequency variation, due to the averaging effects, compared to the heat load for a single house. Emphasis in the present study is put on the variability in heat load among the individual houses, for example some react more than others to solar radiation and especially the diurnal pattern is very different among the studied houses.

The paper starts with a section in which the data and the NWPs are described. This is

followed by a presentation of the modeling approach and the model identification, where a suitable forecasting model is found together with a dynamic model for the remaining noise. Finally, the results are presented, and the method is discussed and concluded.

2. Data

The data used in the study consists of measurements from sixteen houses located in Sønderborg, Denmark, local climate measurements and NWPs. All times are in UTC and the time stamp for average values are set to the end of the time interval.

2.1. Heat load measurements

The houses are typical Danish single family houses from the sixties and seventies. Only houses with radiator heating are considered. A single signal for each house is used. It consists of the total energy for both space heating and hot water heating. The measurements consist of 10 minutes average values. Time series plots of the entire period, spanning nearly two and a half years, for four of the houses are shown in Figure 1. Also shown, with red lines, is the distribution over time as smoothing estimates of the $0\%, 2\%, \ldots, 98\%, 100\%$ quantiles. They are estimated using local quantile regression [13], where the weighting is local in time. They clearly show that the distribution of the measurements is heavily skewed, as only two percent of the values are between the two upper lines, which cover more than half of the range. The reason for this skewness is seen from Figure 2, where the measurements from a period of 10 days for the same four houses are plotted. The hot water heat load consists of high frequency spikes added to the more slowly varying space heat load. The highest peaks are from showers and cause the high skewness. Since it is wanted to study the space heating part, then each signal is separated into a space heating part and a hot water heating part - with the method described in [14] applied causally. On the figure the part of the signal identified as hot water heat load is marked with red, note that it is added on top of the space heat load in the plot. After the splitting the series are re-sampled into hourly average values. The hourly space heating for a single house is denoted by

$$\{Q_t;\ t = 1, \ldots, N\} \tag{1}$$

where $N = 21144$ and the unit is kW. Notice that no distinction in between the houses is used in the notation, but when the results are presented the house number, ranging from 1 to 16, is clearly stated.

2.2. Local climate observations

The local climate observations are from a weather station at the district heating plant in Sønderborg, which is less than 10 kilometers from the houses. The observations are re-sampled to hourly average values and the following time series are used:

$$\begin{aligned} \text{Ambient temperature:} &\quad \left\{T_t^{\mathrm{a,obs}};\ t = 1, \ldots, N\right\} \\ \text{Global radiation:} &\quad \left\{G_t^{\mathrm{obs}};\ t = 1, \ldots, N\right\} \\ \text{Wind speed:} &\quad \left\{W_t^{\mathrm{s,obs}};\ t = 1, \ldots, N\right\} \end{aligned} \tag{2}$$

2.3. Numerical weather predictions

The numerical weather predictions (NWPs) used for the forecasting are provided by the Danish Meteorological Institute. The NWP model used is DMI-HIRLAM-S05, which has a 5 kilometer grid and 40 vertical layers [15]. The NWPs consist of time series of hourly values for climate variables, which are updated four times per day and have a 4 hour calculation delay (e.g. the forecast starting at 00:00 is available at 04:00). Since a new two-day heat load forecast is calculated every hour, then - in order to use the latest available information - every hour the latest available NWP value for the k'th horizon at time t is picked as

$$\begin{aligned} \text{Ambient temperature (°C):} \quad & T^{\mathrm{a,nwp}}_{t+k|t} \\ \text{Global radiation (W/m}^2\text{):} \quad & G^{\mathrm{nwp}}_{t+k|t} \\ \text{Wind speed (m/s):} \quad & W^{\mathrm{s,nwp}}_{t+k|t} \\ \text{Wind direction (°azimuth):} \quad & W^{\mathrm{d,nwp}}_{t+k|t} \end{aligned} \tag{3}$$

2.4. Combining local observations with NWPs

To include the building heat dynamics in an efficient way, the inputs are low-pass filtered as explained in Section 3.3. Hence, for the forecast calculated at time t, past values of the inputs are being used. In order to use the information embedded in the local measurements they are combined with the NWPs. The combining is carried out by forming the time series for each of the inputs at time t, for a specific horizon k, by

$$\begin{aligned} \left\{T^{\mathrm{a}}_{t+k|t}\right\} &= \left\{\ldots, T^{\mathrm{a,obs}}_{t-1}, T^{\mathrm{a,obs}}_{t}, T^{\mathrm{a,nwp}}_{t+1|t}, T^{\mathrm{a,nwp}}_{t+2|t}, \ldots, T^{\mathrm{a,nwp}}_{t+k|t}\right\} \\ \left\{G_{t+k|t}\right\} &= \left\{\ldots, G^{\mathrm{obs}}_{t-1}, G^{\mathrm{obs}}_{t}, G^{\mathrm{nwp}}_{t+1|t}, G^{\mathrm{nwp}}_{t+2|t}, \ldots, G^{\mathrm{nwp}}_{t+k|t}\right\} \\ \left\{W^{\mathrm{s}}_{t+k|t}\right\} &= \left\{\ldots, W^{\mathrm{s,obs}}_{t-1}, W^{\mathrm{s,obs}}_{t}, W^{\mathrm{s,nwp}}_{t+1|t}, W^{\mathrm{s,nwp}}_{t+2|t}, \ldots, W^{\mathrm{s,nwp}}_{t+k|t}\right\} \\ \left\{W^{\mathrm{d}}_{t+k|t}\right\} &= \left\{\ldots, W^{\mathrm{d,nwp}}_{t-1|t}, W^{\mathrm{d,nwp}}_{t|t}, W^{\mathrm{d,nwp}}_{t+1|t}, W^{\mathrm{d,nwp}}_{t+2|t}, \ldots, W^{\mathrm{d,nwp}}_{t+k|t}\right\} \end{aligned} \tag{4}$$

Notice that local observations are not available for the wind direction and that the most recent NWP is used for past values instead.

3. Models

As mentioned earlier the applied models are similar to the models used in [12] for forecasting of the summed total heat load for many houses. The models are based on prior physical knowledge of the heat dynamics of buildings, which in combination with statistical time series models, forms a grey-box modeling approach. This allows for inclusion of heat transfer effects related to the climate variables in combination with a time adaptive estimation scheme applied to meet changing condition. Furthermore, in order to describe of patterns in resident behavior, a diurnal curve is included. The forecasting models are fitted, by optimizing the parameters to minimize the root mean square error (RMSE) in an off-line setting. The fitting is carried out separately for each house and for each horizon k, which means that the same model formulation - i.e. same inputs and model structure - is used, only the parameter values for each house and horizon can vary.

3.1. Time adaptive models

The models are fitted with the k-step recursive least squares scheme described in [16]. This means that the coefficients in the model can change over time and adapt optimally, in a least squares sense, to changing conditions. The coefficients are recursively updated, which means that only a few matrix operations are required to compute an updated forecast, hence the scheme is computationally very fast. It is a recursive implementation of a weighted least squares estimation, where the weights are exponentially decaying over time. A single parameter is required, the forgetting factor λ, which determines how fast input data is down-weighted. The weights are equal to

$$w(\Delta t) = \lambda^{\Delta t} \tag{5}$$

where Δt is the age of the data in hours. This implies that for $\lambda = 0.98$ the weights are halved in 34 hours, for $\lambda = 0.995$ they are halved in 138 hours ($\sim$ 6 days) and for $\lambda = 0.999$ in 693 hours ($\sim$ 29 days).

3.2. Diurnal curve

A diurnal curve is included in the models for describing systematic diurnal patterns in the heat load, which for example can be caused by a nightly setback and free heat from electrical appliances. The curve is modeled as a harmonic function using a Fourier series

$$\mu(t_{\text{tod}}, n_{\text{har}}, \alpha_{\text{diu}}) = \sum_{i=1}^{n_{\text{har}}} \alpha_{i,1}^{\text{diu}} \sin\left(\frac{t_{\text{tod}} i\pi}{12}\right) + \alpha_{i,2}^{\text{diu}} \cos\left(\frac{t_{\text{tod}} i\pi}{12}\right) \tag{6}$$

where t_{tod} is the time of day in hours at time t, n_{har} is the number of harmonics included in the Fourier series and α_{diu} is a vector consisting of the coefficients for the included harmonics. For all the applied models a curve is fitted for working days and another curve for weekends.

3.3. Low-pass filtering for modeling of building heat dynamics

The heat dynamics of a building can be described by lumped parameter RC-models, see for example [17], [18] and [19]. As described by [12] the response in the heat load to changes in the climate variables can be modeled with a rational transfer function, which is a description with an RC-model of the low-pass filtering effect through the building. In the applied models the simplest first order low-pass filter, with a stationary gain equal to one, is used. This is a model of the building heat dynamics formed by an RC-model with a single resistance and a single capacitor. As an example the transfer function from the ambient temperature to the heat load is

$$Q_t = \alpha_{\text{a}} H_{\text{a}}(q) T_t^{\text{a}} \tag{7}$$

where

$$H_{\text{a}}(q) = \frac{1 - a_{T_{\text{a}}}}{1 - a_{T_{\text{a}}} q^{-1}} \tag{8}$$

and where q^{-1} is the backward shift operator ($q^{-1} x_t = x_{t-1}$) (see [20]), α_{a} is the stationary gain from the ambient temperature to heat load and $a_{T_{\text{a}}} \in [0, 1]$ is a parameter, which is corresponding to the time constant for the part of the building affected by changes in ambient temperature. A building with a high thermal mass and good insulation will have a relatively high $a_{T_{\text{a}}}$, hence the filter parameter needs to be tuned for each building in order to describe the heat dynamics properly. First order low-pass filters are also applied for wind speed and global radiation, with the filter parameter tuned to match the response of the building to each effect separately.

3.4. Parameter optimization

As described above several parameters need to be optimized for each house and horizon. The optimization is carried out in an off-line setting by minimizing the RMSE for each of the sixteen houses and for each horizon $k = 1, \ldots, 42$ separately. This does require some computational power, for example for the low-pass filtering of the inputs. Therefore a simple bisectioning scheme is applied for the optimization, since this allows for performing a filtering of the inputs only once for parameter values in a given range. Then these series can be used for optimization for all the houses and horizons. The properties of the optimization is not studied in detail in this work, however some remarks regarding an operational implementation are given in the discussion in Section 7.

The following parameters are optimized:

- The forgetting factor: λ,
- The number of harmonics in the diurnal curve: n_{har},
- The coefficients for input low-pass filters: $a_{T_{\text{a}}}, a_{\text{G}}$ and $a_{\text{W}_{\text{s}}}$.

4. Model identification

Forecasting models, which include different types of heat transfer effects related to the climate variables, are applied in order to identify which of the inputs are important to include. Furthermore, models in which the inputs enters differently are tried. See [12] for a description of how a physical model can be rewritten into the identifiable models, which are applied here. The model which include all energy contributions is

$$Q_{t+k} = \widehat{Q}_{t+k|t} + e_{t+k} \tag{9}$$

where

$$\widehat{Q}_{t+k|t} = Q_{\text{a}} + Q_{\text{g}} + Q_{\text{w}} \tag{10}$$

where the Q_{name} variables on the right side of the equation represent the heat contributions from the considered heat transfers as described in the following.

4.1. First step in model selection

To select a suitable forecasting model a forward selection approach is used. In the first step the $model_{\text{D}}$

$$\widehat{Q}_{t+k|t} = \alpha_{\text{ia}} + \mu(t_{\text{tod}}, n_{\text{har}}, \alpha_{\text{diu}}) \tag{11}$$

which do not include any climate inputs, is fitted. In this model the heat load is simply modeled as a diurnal curve with an offset. Note that the offset α_{ia} then represents a difference, which is constant over 24 hours, between the indoor and the ambient temperature, and that the diurnal curve will then capture diurnal patterns in both the indoor and ambient temperature in this model. Due to the time adaptive scheme this model will be able to track the slow changes in temperatures over the year. Finally, note also that the coefficients could have been denoted with a t to indicate that they are changing over time, a house number to indicate that they are fitted to each house,

and a k to indicate that the model is fitted for each horizon separately, however these have been left out for better readability.

To find out if useful information can be gained from applying climate series as inputs to the model, the cross-correlation function (CCF), see [21], between the one-step ahead ($k = 1$ hour) prediction residuals for $model_{\mathrm{D}}$ and the available input series is calculated. Since there is a series of residuals for each house the average over all houses

$$\bar{e}_{t+k} = \sum_{i=1}^{n_{\mathrm{houses}}} e_{t+k}^{\mathrm{House}\, i} \tag{12}$$

where $n_{\mathrm{houses}} = 16$ are the number of houses and $e_{t+k}^{\mathrm{House}\, i}$ is the residual series for House i, is used. In this way the CCF to each of the inputs can be summarized for all the houses in a single plot. This will of course only show if an input is generally important to include and not the effects for each individual house. The effects related to each house - which are different - are considered in later parts of the paper.

The CCF between the average residuals from $model_{\mathrm{D}}$ to the inputs can be seen in Figure 3a. Clearly, very significant correlations between the residuals and both the ambient temperature, and the global radiation, but apparently none to the wind speed, are found. It is decided to add the ambient temperature as input to the model, which leads to $model_{\mathrm{A}}$

$$\widehat{Q}_{t+k|t} = Q_{\mathrm{a}} \tag{13}$$

where

$$Q_{\mathrm{a}} = \alpha_{\mathrm{ia}} + \mu(t_{\mathrm{tod}}, n_{\mathrm{har}}, \alpha_{\mathrm{diu}}) + \alpha_{\mathrm{a}} H_{\mathrm{a}}(q) T_{t+k|t}^{\mathrm{a}} \tag{14}$$

The $H_{\mathrm{a}}(q)$ is the low-pass filter describing the heat dynamics of the building envelope, i.e. the response of in heat load to changes in ambient temperature. Notice that the intercept α_{ia} is representing a 24 hour constant indoor temperature modified by the diurnal curve.

In order to find out if any gain in forecasting performance is achieved from $model_{\mathrm{D}}$ to $model_{\mathrm{A}}$ the RMSE is used for evaluation as described in the following.

4.1.1. Root mean square error evaluation

To evaluate the models the root mean square error (RMSE) for the k'th horizon

$$\mathrm{RMSE}_k = \left(\frac{1}{N} \sum_{t=1}^{N} e_{t+k}^2 \right)^{\frac{1}{2}} \tag{15}$$

is used together with the RMSE_k improvement

$$I_{\mathrm{RMSE}} = 100 \cdot \frac{\mathrm{RMSE}_{\mathrm{ref}} - \mathrm{RMSE}}{\mathrm{RMSE}_{\mathrm{ref}}} (\%) \tag{16}$$

over the currently selected model as reference. It is noted values not in the heating season - which starts the 15'th of September and ends 15'th of May in Denmark - and values before the 15'th of March 2009, which is used as a burn-in period, are excluded from the RMSE_k calculation. For evaluation of the inclusion of ambient temperature, the RMSE_k improvement for $model_{\mathrm{A}}$ over $model_{\mathrm{D}}$ is calculated. The average improvement for all horizons (from $k = 1$ to $k = 42$) for each house is plotted in Figure 4a. A RMSE_k improvement for the each house in the range from 5 to 25 percent and around 14 percent in average is achieved. This is clearly a significant improvement, hence $model_{\mathrm{A}}$ is preferred over $model_{\mathrm{D}}$.

4.2. Second step in model selection

To explore the possibilities for further expansion of $model_{\mathrm{A}}$ the CCF from the average residuals (defined in Equation (12)) to each of the climate series is calculated and plotted in Figure 3b. The correlation to the ambient temperature is much lower than for $model_{\mathrm{D}}$ and the correlation to the global radiation is more or less the same. The correlation to the wind speed has increased, most likely this correlation was "covered" by the correlation to the ambient temperature for $model_{\mathrm{D}}$ residuals. Notice, that there is a significant correlation decaying over 12 to 24 hours to the lagged inputs indicating that dynamics should be included by low-pass filtering.

To find the most important extension of $model_{\mathrm{A}}$ several extensions involving the global radiation or the wind speed are fitted (i.e. the RMSE_k is minimized by tuning the parameters listed in Section 3.4 for each house).

The first considered expansion is $model_{\mathrm{A.G}}$

$$\widehat{Q}_{t+k|t} = Q_{\mathrm{a}} + \alpha_{\mathrm{g}} H_{\mathrm{g}}(q) G_{t+k|t} \tag{17}$$

where the heat gain from solar radiation is included by letting the global radiation enter through a low-pass filter, which describes the dynamic response from the global radiation to the heat load. The second expansion is $model_{\mathrm{A.W}}$

$$\widehat{Q}_{t+k|t} = Q_{\mathrm{a}} + \alpha_{\mathrm{ws}} H_{\mathrm{w}}(q) W^{\mathrm{s}}_{t+k|t} \tag{18}$$

where the cooling of the building from wind is described by letting the wind speed enter through a low-pass filter. This is a model of wind cooling not depending on the ambient temperature, however - due to the time-adaptive modeling scheme - is does include the slow changes in temperature difference between indoor and ambient temperature. The third expansion is $model_{\mathrm{A.V}}$

$$\widehat{Q}_{t+k|t} = Q_{\mathrm{a}} + \alpha_{\mathrm{vent}} W^{\mathrm{s}}_{t+k|t} \tag{19}$$

which includes the effect of ventilation by inputting the instant effect of wind speed to the heat load.

The RMSE_k improvements averaged over all horizons for each house for the considered expansions are plotted in Figure 4b. It is seen that the increase in performance is highest for all the houses using $model_{\mathrm{A.G}}$, hence this model is preferred and used for expansion in the following step. In the remaining of the paper the heat contribution from solar radiation is denoted by

$$Q_{\mathrm{g}} = \alpha_{\mathrm{g}} H_{\mathrm{g}}(q) G_{t+k|t} \tag{20}$$

4.3. Step three: Inclusion of wind speed in the model

In the third step of the model identification several ways of including the wind speed is considered. First the CCF between the one-step ahead residuals, from the model selected in the previous step, $model_{\mathrm{A.G}}$ and the inputs, are studied to see if any useful information is remaining in the climate series.

Firstly, it is noted that the correlation to the global radiation has decreased compared to the CCF plot for $model_{\mathrm{A}}$, but that some is still left, indicating that the dynamic effects are not entirely described by the model. Secondly, it is noted that there is a significant cross-correlation to the wind speed and therefore an expansion which includes the wind speed is sought. Five different ways of letting the wind speed enter the model are tried as described in the following.

The first expansion is formed by adding the wind speed through a low-pass filter for modeling of cooling of the building in $model_{\text{A.G.W}}$

$$\widehat{Q}_{t+k|t} = Q_{\text{a}} + Q_{\text{g}} + \alpha_{\text{ws}} H_{\text{w}}(q) W^{\text{s}}_{t+k|t} \tag{21}$$

and, for modeling ventilation, the instant effect of wind speed is added in $model_{\text{A.G.V}}$

$$\widehat{Q}_{t+k|t} = Q_{\text{a}} + Q_{\text{g}} + \alpha_{\text{ws}} W^{\text{s}}_{t+k|t} \tag{22}$$

In the two models above the wind speed enter the model without the interaction with ambient temperature, which means that the temperature difference between the indoor and ambient temperature is modeled as constant and that changes are only tracked due to the adaptivity of the model. In the following two expansions the interaction is also included, with a filter in $model_{\text{A.G.Wa}}$

$$\widehat{Q}_{t+k|t} = Q_{\text{a}} + Q_{\text{g}} + \alpha_{\text{ws}} H_{\text{w}}(q) W^{\text{s}}_{t+k|t} + \alpha_{\text{wsa}} H_{\text{w}}(q) W^{\text{s}}_{t+k|t} T^{\text{a}}_{t+k|t} \tag{23}$$

and as an instant effect in $model_{\text{A.G.Va}}$

$$\widehat{Q}_{t+k|t} = Q_{\text{a}} + Q_{\text{g}} + \alpha_{\text{ws}} W^{\text{s}}_{t+k|t} + \alpha_{\text{wsa}} W^{\text{s}}_{t+k|t} T^{\text{a}}_{t+k|t} \tag{24}$$

Finally, the wind speed input coefficient is conditioned on the wind direction in $model_{\text{A.G.Wd}}$

$$\widehat{Q}_{t+k|t} = Q_{\text{a}} + Q_{\text{g}} + \sum_{i=1}^{4} \alpha_{\text{i}} H_{\text{w}}(q) K(u) W^{\text{s}}_{t+k|t} T^{\text{a}}_{t+k|t} \tag{25}$$

where the kernel function

$$K(u) = (1 - |u|)\mathbf{1}_{\{|u| \leq 1\}} \tag{26}$$

with

$$u = \left(\left(W^{\text{d,nwp}}_{t+k|t} + 45 + (i-1) \cdot 90 \right) \bmod 4 \right) - 1 \tag{27}$$

is used to create four input series, which are linearly interpolated as a function of the wind direction. The center of the kernels is thus at the most prevailing wind directions in Denmark, especially southwest in the winter period [22].

The plot in Figure 4c shows the improvements over $model_{\text{A.G}}$ for the five models. The improvement is quite different for each house, for some it is negative, which is because the forecasting model becomes over-parameterized. It is also seen that the pattern of the improvement among the houses are quite similar for the five models, indicating that for some houses the wind have a more prevalent effect than for others. Since $model_{\text{A.G.W}}$ generally have the most positive improvement and since it is the simplest extension, it is preferred over the others. In the remaining of the paper the model part describing the effect of wind is denoted with

$$Q_{\text{w}} = \alpha_{\text{ws}} H_{\text{w}}(q) W^{\text{s}}_{t+k|t} \tag{28}$$

4.4. Step four: Enhancement of the solar model part

In the final step the model part for solar radiation is enhanced in different ways, as described in the following. Studying the CCFs for $model_{\text{A.G.W}}$ in Figure 3d it is seen that the correlation between the residuals and the inputs has been decreased compared to the CCFs for the smaller models, however there is some left to the ambient temperature and solar radiation. From studying plots of the forecasts it is found that it might be possible to improve the model part in which the effect of solar radiation is included.

Firstly, an additional input for the solar gain is added and $model_{\text{A.G2in.W}}$

$$\widehat{Q}_{t+k|t} = Q_{\text{a}} + Q_{\text{g}} + \alpha_{\text{g2}} H_{\text{g2}}(q) G_{t+k|t} + Q_{\text{w}} \tag{29}$$

is formed. This allows for an additional dynamic response of the building to solar radiation. Notice that an additional filter coefficient for the $H_{\text{g2}}(q)$ filter is fitted.

Secondly, the solar radiation part is enhanced by using a two-pole filter instead of a one-pole filter

$$\widehat{Q}_{t+k|t} = Q_{\text{a}} + \alpha_{\text{g}} H_{\text{2pol}}(q) G_{t+k|t} + Q_{\text{w}} \tag{30}$$

where

$$H_{\text{2pol}}(q) = \frac{1 - a_1 - a_2}{1 - a_1 q^{-1} - a_2 q^{-2}} \tag{31}$$

and

$$a_1 = a_{g_1} + a_{g_2} \quad \text{and} \quad a_2 = -a_{g_2} \tag{32}$$

The two filter coefficients thereby relate to different dynamics: a_{g_1} is related to the highest time constant and a_{g_2} is related to a faster time constant of the building.

In the third extension the solar radiation is separated into three inputs: one for the morning, one for the noon and one for the evening. This allows for the building to have different solar gains during the day. The $model_{\text{A.Gspl.W}}$ is

$$\begin{aligned} \widehat{Q}_{t+k|t} = Q_{\text{a}} &+ \alpha_{\text{g1}} H_{\text{g}}(q) G^{\text{morning}}_{t+k|t} + \alpha_{\text{g2}} H_{\text{g}}(q) G^{\text{noon}}_{t+k|t} \\ &+ \alpha_{\text{g3}} H_{\text{g}}(q) G^{\text{evening}}_{t+k|t} + Q_{\text{w}} \end{aligned} \tag{33}$$

The three inputs are

$$\begin{aligned} G^{\text{morning}}_{t+k|t} &= G_{t+k|t}\ \mathbf{1}_{\{t+k \in [t_{\text{rise}},\ t_{\text{rise}}+\Delta t]\}} \\ G^{\text{noon}}_{t+k|t} &= G_{t+k|t}\ \mathbf{1}_{\{t+k \in [t_{\text{rise}}+\Delta t,\ t_{\text{set}}-\Delta t]\}} \\ G^{\text{evening}}_{t+k|t} &= G_{t+k|t}\ \mathbf{1}_{\{t+k \in [t_{\text{set}}-\Delta t,\ t_{\text{set}}]\}} \end{aligned} \tag{34}$$

where $\mathbf{1}_{\{\cdot\}}$ is the indicator function, t_{rise} and t_{set} is the time of sunrise and sunset, respectively and $\Delta t = (t_{\text{set}} - t_{\text{rise}})/3$ is a third of the day length.

Finally, two enhancement are formed by projecting the solar radiation onto a vertical surface tracking the solar azimuth angle. The projection to vertical is carried out by first splitting the global radiation into a direct and a diffuse component as in [23] and onto a vertical surface with

the Hay and Davies model [24], see also [25]. The effect of the projections is first of all an increase in the level of solar radiation when the sun elevation is low, i.e. in the morning and in the evening (or afternoon). In $model_{\text{A.Gver.W}}$

$$\widehat{Q}_{t+k|t} = Q_{\text{a}} + \alpha_{\text{g}} H_{\text{g}}(q) G^{\text{ver,tr}}_{t+k|t} + Q_{\text{w}} \tag{35}$$

the total vertical radiation is inputted and in $model_{\text{A.Gbdv.W}}$

$$\widehat{Q}_{t+k|t} = Q_{\text{a}} + \alpha_{\text{g1}} H_{\text{g}}(q) G^{\text{beam,tr}}_{t+k|t} + \alpha_{\text{g2}} H_{\text{g}}(q) G^{\text{diffuse,tr}}_{t+k|t} + Q_{\text{w}} \tag{36}$$

the direct (or beam) and the diffuse component is inputted separately.

The models are fitted to each house and the RMSE improvements over $model_{\text{A.G.W}}$ are calculated and plotted in Figure 4d. For $model_{\text{A.G2in.W}}$ and $model_{\text{A.G2po.W}}$ only a little difference in performance is seen, and for $model_{\text{A.Gspl.W}}$ the performance has decreased. These three models become over-parameterized, however it is noted that for short horizons the improvement for $model_{\text{A.Gin2.W}}$ is positive for all the houses. For the last two models: $model_{\text{A.Gver.W}}$ and $model_{\text{A.Gbdv.W}}$, the change in performance depends on the house. One interesting pattern is that the houses with the highest change (both decreased and increased) are the houses, which benefited most from addition of the solar radiation in the step second step of the model selection, as seen in the plot in Figure 4b. This indicates that increased performance can be obtained by modifying the solar gain over the day by learning an optimal diurnal solar gain curve for each house, however this is beyond the scope of the present study. In general no significant overall increase in performance is found for any of the five suggested enhancements, hence the model selection is ended. The presented results in the remaining of the paper are from $model_{\text{A.G.W}}$, together with a model of the noise, which is described in the following section.

5. Noise model

Considering the auto-correlation function (ACF) for the one-step prediction residuals for the houses, shown in the upper plot of Figure 5, it is found that a model is useful for describing dynamical information embedded in the residuals. A simple auto-regressive (AR) model is fitted to the residuals with the recursive least squares scheme [16]. The AR(1) model

$$e_{t+k} = a_{\text{e}} e_t + e^{\text{noise}}_{t+k} \tag{37}$$

is fitted for the residuals from the selected model $model_{\text{A.G.W}}$ for each horizon k. The ACF of the noise residuals e^{noise}_{t+k} can be seen in the lower plot of Figure 5. Compared to the upper plot the auto-correlation for lag 1 is significantly lower indicating that the noise model improves performance. Clearly, some of the houses still have significant auto-correlation left and for the short horizons a noise model, which include more lags would improve performance further. However it was tried to include one more lag (lag 2), but this did only improve the overall performance marginally, mainly because no performance improvement is achieved on longer horizons. The houses which have the highest ACF (in particular House 11 and 16) have some high frequency oscillations embedded in the heat load signal, as described in the following section where the results are discussed. The average RMSE_k improvement over all horizons is in the range of 0.35% to 6.7%, hence a quite significant improvement, especially for some of the houses. The RMSE_k improvement for the one-step ahead forecasts is in the range 1.3% to 19%, which clearly shows that the noise model is most important for short horizons.

6. Results

In this section the results from forecasting with the selected model are presented and discussed. First the parameters, which are fitted for each house, are reported and then the performance for individual houses is discussed.

6.1. Model parameters

The parameters, which are fitted for each house, are listed in Section 3.4. Since there is a value for each horizon for each house and for each parameter, they are reported with the plots in Figure 6. The general patterns are discussed in the following. Starting with the upper most plot in the figure, which is of the forgetting factor λ in the recursive least squares scheme, it can be seen that it has a tendency to be lower for the first couple of horizons: for $k = 1$ the average over all the house is 0.9755, which implies that the weighting of the input data is halved in only 28 hours. This quick forgetting is most likely optimal, because it is profitable for the forecasting model to be able to react fast to changes in the system, e.g. residents increase the indoor temperature or open the windows, which can be tracked on short horizons. On longer horizons the forgetting is on a stable level: for $k = 5$ the average is 0.9953 increasing to 0.9963 for $k = 42$, which implies that the weighting of the input data is halved in around 8 days.

The second plot from the top in Figure 6 is of the optimized number of harmonics in the diurnal curve: a higher number means that it is profitable to include higher frequencies in the curve. Clearly, a huge variation among the houses is found, which is very reasonable, since the diurnal patterns are very different, this is shown below.

The middle plot of the figure is of the optimized coefficient for the low-pass filter transfer function from the ambient temperature to the heat load. Except for the two lower lines the variation for each house as a function of the horizon k is quite small (in the range of ± 0.01), which leads to the conclusion that the applied low-pass filtering describes the response of heat load to changes in ambient temperature for each house appropriately. In Table 1 the average coefficient for each house is listed together with the equivalent RC time constants. The values are within a reasonable range compared to values found in other studies [12], [5]. The fitted values of low-pass filter coefficient for global radiation a_{G} and for wind speed $a_{W_{\mathrm{s}}}$ are shown in the lower two plots of Figure 6. The values are all in the same range, generally between 0.8 and up to near 1, but with some lower values for a couple of the houses, which are houses where the solar radiation and wind speed are not very important inputs.

6.2. Forecasting performance

In this section the forecasting performance is analyzed and discussed, especially the differences in performance among the houses. For evaluation of the performance the normalized root mean square error for each horizon

$$\mathrm{NRMSE}_k = \frac{\mathrm{RMSE}_k}{\bar{Q}_t} \tag{38}$$

is used, where $\bar{Q}_t$ is the average heat load for the house, which is calculated with the same values as used for calculation of the RMSE_k (see the text below Equation (15)).

The plot in Figure 7 shows the NRMSE_k as a function of the horizon k for each house using the selected $model_{\mathrm{A.G.W}}$ and the noise model. Clearly, the poorest forecasting performance is for House 8. The explanation is found by considering the plot for House 8 in Figure 8, which shows the

heat load together with the 1 hour and 24 hour forecasts. The main reason for the poor forecasts is a very irregular diurnal curve. A nightly setback results in a high difference between day and night and the time of day at which the heat is switched to a high level again is not following a regular pattern. It is probably controlled manually by the residents. This is opposed to the nightly setback for House 10, which have a much more regular pattern which can be much better forecasted.

Another source for high errors is seen in the plots for House 2 and 16, where noisy fluctuations occur on the higher frequencies in the signals. The smaller fluctuations are probably partly from hot water heating, which was not well separated from the space heating, but clearly higher peaks which are not related to hot water heating are seen. For House 11 a more steady, but still quite unpredictable, pattern is seen, which is likely to come from some oscillation in the thermostatic control of the heat system.

The heat load signals for House 1, 9 and 15 are much less volatile. These houses are also the ones with a lower NRMSE_k, as seen from the plot in Figure 7. The most obvious point to notice is the deviation between the 1 and the 24 hour forecasts. Starting with the drop on the 21'st of February, which is followed well by the 1 hour forecast, but not by the 24 hour forecast. This drop is clearly caused by solar radiation. It is a clear-sky day, as seen by the high level of observed global radiation (the second uppermost plot of Figure 8), which is also predicted well by the 24 hour NWP. However the drop is not followed by the 24 hour load forecast, since the previous day was also forecasted as a clear-sky day by the 24 hour NWP, but it was not a clear-sky day as seen by the low observed level. Hence, there is a much higher uncertainty on the global radiation input to the 24 hour forecast model compared to the 1 hour forecast, which use mostly observations as input, and therefore the global radiation input is not given much weight in the 24 hour forecasting model. From the 1'st of March a sunny period begins and it can be seen how the 24 hour forecasts starts to track the mid-day drops in heat load, as more weight is put on the global radiation input due to the time adaptivity of the modeling scheme. Finally, it is noted that the drop the 23'th of February and the peak the 27'th of February in the heat load for House 15 are not seen in the other heat loads. It is attributed to residents behavior, which cannot be predicted. However, it is tracked with a delay in the 1 hour forecast.

7. Discussion

The presented heat load forecasts can be used to form the input for optimization of the heat supply to buildings in smart grid applications. Such optimization can be based on model predictive control. It is especially useful for optimization of heating systems with a thermal storage medium, for example a hot water tank. For the data used in the study the indoor temperature was not available and it is therefore modeled as constant offset modified by a diurnal curve. If the indoor temperature is available it will allow for advancements of the method by including it as an input to the model. Thereby the estimation of a time constant for the building can be carried out with higher accuracy, which will allow the method to be used for optimization, where the thermal mass of the building is used for thermal storage. It is also noted that the type of linear time-adaptive models applied for the forecasting furthermore can be used for characterization and monitoring of the thermal performance of buildings [26]. Especially, the inclusion of user behavior is an important issue and should be further elaborated in studies focusing on such applications.

The forecasting method is found feasible to implement operationally and can be automatized to a high degree. Certainly, flawed data can cause problems, however schemes for identifying issues which needs manual handling can be implemented. Alarms could for example be triggered by

unusual changes in coefficient estimates or unusually highly auto-correlated residuals. It is noted that the current implementation in R [1] is not compiled code and can be further optimized. However, a test shows that around 1000 forecast updates (including the recursive parameter estimation) of the 42 hours forecasts using the selected $model_{\text{A.G.W}}$ can be calculated in approximately 10 seconds on a 2.4 GHz single CPU computer. This is due to the computationally light recursive least squares scheme. If an update is needed every hour the time in-between updating can be used for data handling and off-line parameter optimization of the parameters listed in Section 3.4. The off-line optimization can be implemented with a recursive scheme and do not require updating very often, perhaps once a week. Based on this very coarse assessment it is found that operational implementation for a very large number of houses can be carried out with feasible amounts of computational power.

Regarding the model part in which the solar radiation is entering, is should be possible to achieve improvements in forecasting performance. For example more information about the individual buildings, such as the azimuth angle of the walls, would provide the possibility for projection of the radiation from horizontal to the vertical wall surfaces. However, it will be favorable for operation if no specific information about the buildings is needed. The non-linear functions, which could be applied with piecewise linear or regime switching functions depending on the level of solar radiation, or a non-parametric approach, could also taken with an off-line method for learning how the building respond to solar radiation over the day. Furthermore, it might be that performance can be increased by using different models depending on the horizon, especially it is more relevant to increase the model complexity for shorter horizons.

Finally, further work could be focused on modeling the uncertainties of the heat load forecasts. As found in the analysis of the results the two most important effects related to the uncertainties seems to be user behavior and solar radiation. Modeling the uncertainties is no trivial task since the uncertainties of the inputs propagates through the model and the relations change over time. One approach would be to characterize the uncertainties of the forecasted inputs and use this to build a model of the heat load forecast uncertainties. For example the uncertainties related to the user behavior will most likely have diurnal and regime shifting patterns which could be modeled with hidden Markov models.

8. Conclusion

A method for forecasting the load for space heating in a single-family house is presented. It is formed by adaptive linear time-series modeling techniques, using local observations and weather forecasts as input. Based on measurements from sixteen houses, a model, which is suitable for all the houses, is identified by using a forward selection approach. It is shown how the forecasting performance increases when the ambient temperature, global radiation and wind speed are added as inputs to the model. For inclusion of the heat dynamics of the building in the model a simple low-pass filter transfer function is used. In the last step of the model selection several enhancements of the model are tested, resulting in over-parameterization and decreased forecasting performance. In a second stage a noise model formed by an auto-regressive model is applied for modeling of the remaining dynamic information in the residuals. After applying the noise model, it is shown that almost no auto-correlation remains. The model parameters, which have been fitted individually for

[1] `www.r-project.org`

each house, are analyzed and it is found that they provide reliable information about the dynamic response of the buildings. The forecasting results are then analyzed thoroughly to give insight into the error sources, for example unpredictable behavior of the residents and uncertainty in the inputs, especially from the solar radiation weather forecasts. Finally, a discussion is given with ideas for applications and further advancements of the method.

Acknowledgement

Acknowledgements are given to the The Danish Council for Strategic Research, which have provided the financial support for the project "Solar/electric heating systems in the future energy system" (2104-07-0021) under which the work was carried out. The heat load and climate data was very kindly provided by Sønderborg Fjernvarme and the Danish Meteorological Institute is thanked for making their numerical weather predictions available.

References

[1] Danish Commission on Climate Change Policy, Grøn energi - vejen mod et dansk energisystem uden fossile brændsler, Tech. rep., Danish Energy Agency, dokumentationsdelen til Klimakommissionens samlede rapport (September 2010).

[2] Danish Commission on Climate Change Policy, Green energy – the road to a danish energy system without fossil fuels (September 2010).

[3] T. Pedersen, P. Andersen, K. Nielsen, H. Starmose, P. Pedersen, Using heat pump energy storages in the power grid, in: Control Applications (CCA), 2011 IEEE International Conference on, 2011, pp. 1106 –1111. doi:10.1109/CCA.2011.6044504.

[4] T. Chen, Real-time predictive supervisory operation of building thermal systems with thermal mass, ENERGY AND BUILDINGS 33 (2) (2001) 141–150.

[5] T. Reddy, L. Norford, W. Kempton, Shaving residential air-conditioner electricity peaks by intelligent use of the building thermal mass, Energy 16 (7) (1991) 1001 – 1010. doi:10.1016/0360-5442(91)90060-Y.

[6] G. P. Henze, C. Felsmann, G. Knabe, Evaluation of optimal control for active and passive building thermal storage, International Journal of Thermal Sciences 43 (2) (2004) 173 – 183. doi:10.1016/j.ijthermalsci.2003.06.001.

[7] B. Perers, S. Furbo, J. Fan, E. Andersen, Z. Chen, Solar combisystems with forecast control to increase the solar fraction and lower the auxiliary energy cost, in: ISES Solar World Congress 2011 Proceedings, 2011, p. , presented at: ISES Solar World Congress, SWC ; 30 : Kassel, Germany, 2011.

[8] T. Mestekemper, Energy demand forecasting and dynamic water temperature management, Ph.D. thesis, Bielefeld University (2011).

[9] E. Dotzauer, Simple model for prediction of loads in district-heating systems, Applied Energy 73 (3–4) (2002) 277 – 284. doi:10.1016/S0306-2619(02)00078-8.

[10] Q. Zhou, S. Wang, X. Xu, F. Xiao, A grey-box model of next-day building thermal load prediction for energy-efficient control, International Journal of Energy Research 32 (15) (2008) 1418–1431. doi:10.1002/er.1458.

[11] H. Nielsen, H. Madsen, D. E. F. P. og Fordeling af El og Varme, Predicting the heat consumption in district heating systems using meteorological forecasts, Tech. rep., DTU IMM (2000).

[12] H. A. Nielsen, H. Madsen, Modelling the heat consumption in district heating systems using a grey-box approach, Energy & Buildings 38 (1) (2006) 63–71. doi:10.1016/j.enbuild.2005.05.002.

[13] R. Koenker, Quantile Regression, Cambridge University Press, 2005.

[14] P. d. Saint-Aubain, Adaptive load forecasting, Master's thesis, Technical University of Denmark (2011).

[15] D. M. I. DMI, DMI-HIRLAM-S05 (2011).
URL http://www.dmi.dk/eng/index/research_and_development/dmi-hirlam-2009.htm

[16] P. Bacher, H. Madsen, H. A. Nielsen, Online short-term solar power forecasting, Solar Energy 83 (10) (2009) 1772–1783.

[17] H. Madsen, J. Holst, Estimation of continuous-time models for the heat dynamics of a building, Energy and Buildings 22 (1) (1995) 67–79.

[18] J. E. Braun, N. Chaturvedi, An inverse gray-box model for transient building load prediction, HVAC&R Research 8 (1) (2002) 73–99. arXiv:http://www.tandfonline.com/doi/pdf/10.1080/10789669.2002.10391290, doi:10.1080/10789669.2002.10391290.
[19] M. Jiménez, H. Madsen, K. Andersen, Identification of the main thermal characteristics of building components using matlab, Building and Environment 43 (2) (2008) 170–180. doi:10.1016/j.buildenv.2006.10.030.
[20] H. Madsen, Time Series Analysis, Chapman & Hall, 2007.
[21] G. Box, G. Jenkins, G. Reinsel, Time series analysis, Holden-day San Francisco, 1976.
[22] J. Cappelen, B. Jørgensen, Observed wind speed and direction in denmark - with climatoligical standards normals, 1961-90, Tech. rep., Danish Meteorological Institute (1999).
[23] J. Ruiz-Arias, H. Alsamamra, J. Tovar-Pescador, D. Pozo-Vázquez, Proposal of a regressive model for the hourly diffuse solar radiation under all sky conditions, Energy Conversion and Management 51 (5) (2010) 881–893. doi:10.1016/j.enconman.2009.11.024.
[24] J. Hay, J. Davies, Calculation of the solar radiation incident on an inclined surface, in: Proc. 1st Canadian Solar Radiation Data Workshop, Vol. 59, 1980, p. .
[25] D. Reindl, W. Beckman, J. Duffie, Evaluation of hourly tilted surface radiation models, Solar Energy 45 (1) (1990) 9 – 17. doi:10.1016/0038-092X(90)90061-G.
[26] H. A. Nielsen, Estimation of UA-values for single-family houses, Tech. rep., ENFOR (2008).

House	1	2	3	4	5	6	7	8
a_{T_a}	0.96	0.91	0.91	0.96	0.94	0.96	0.95	0.96
τ_{T_a} (hours)	27	11	10	25	16	27	21	26
House	9	10	11	12	13	14	15	16
a_{T_a}	0.94	0.97	0.95	0.96	0.95	0.94	0.96	0.92
τ_{T_a} (hours)	17	32	18	24	19	15	25	13

Table 1: Values of optimized low-pass filter coefficient for the response from ambient temperature to heat load and corresponding RC time constant τ_{T_a} in hours.

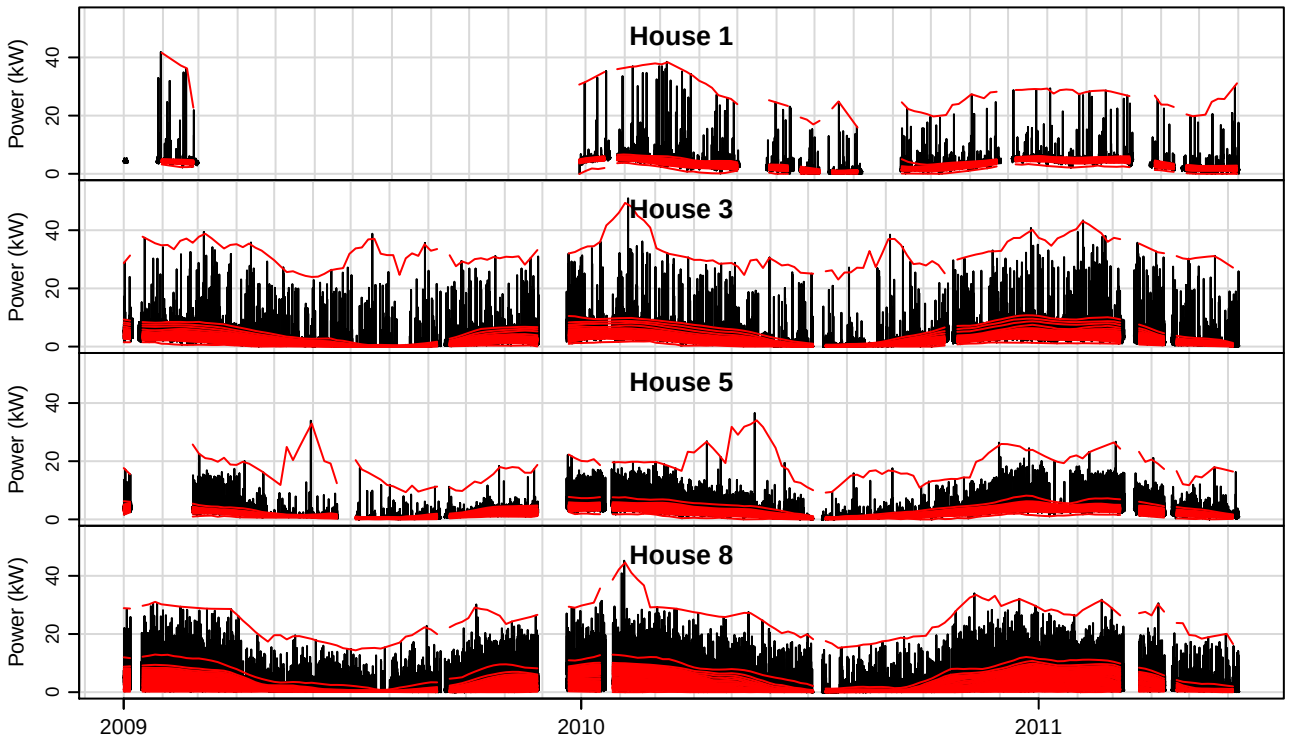

Figure 1: The heat load for four selected houses over the entire period, which is nearly spanning two and a half years. The red lines are estimates of the $0\%, 2\%, \ldots, 98\%, 100\%$ quantiles, which indicate the distribution of the heat load at a given time.

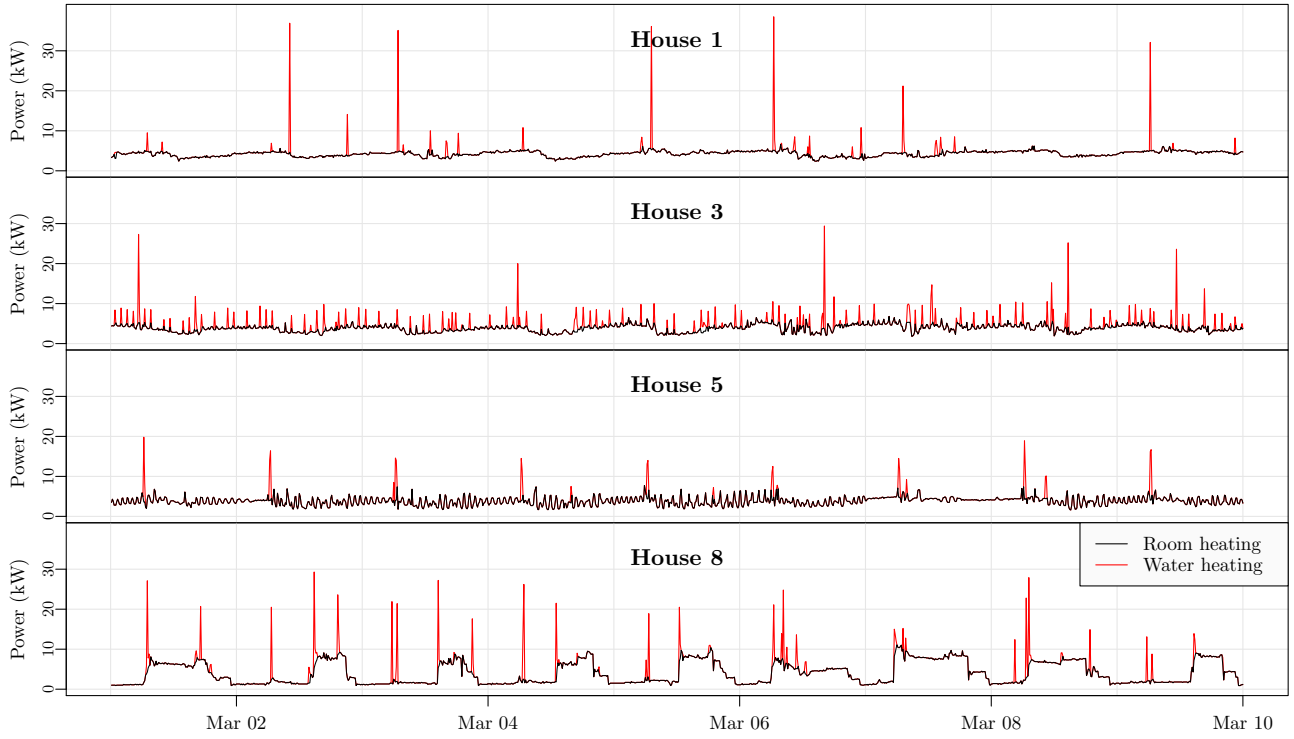

Figure 2: Heat load for four selected houses for the first 10 days of March in 2010. The peaks marked with red are the parts which are identified as hot water heating and the black line is the space heating part. Note that the hot water heating is added on top the space heating signal.

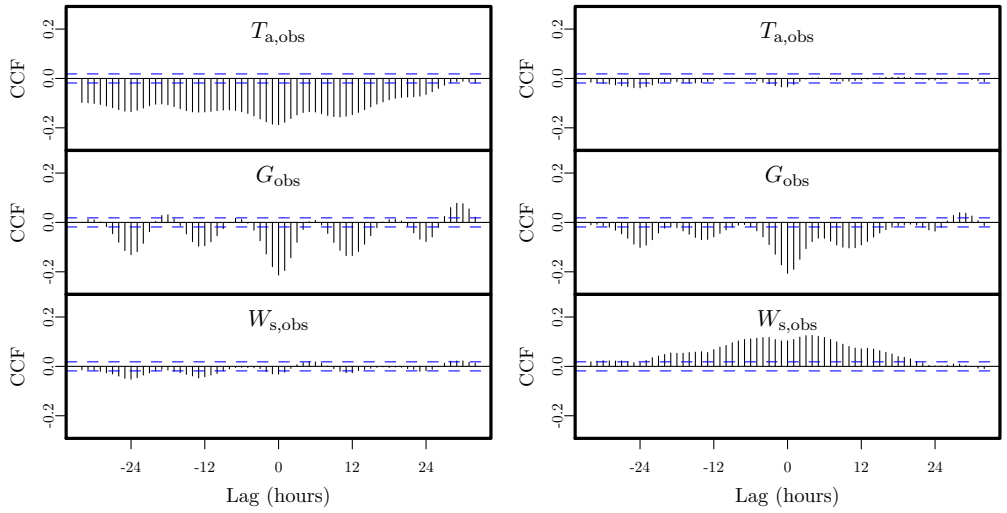

(a) Step one: CCF for $model_{\text{D}}$ errors to the inputs

(b) Step two: CCF for $model_{\text{A}}$ errors to the inputs.

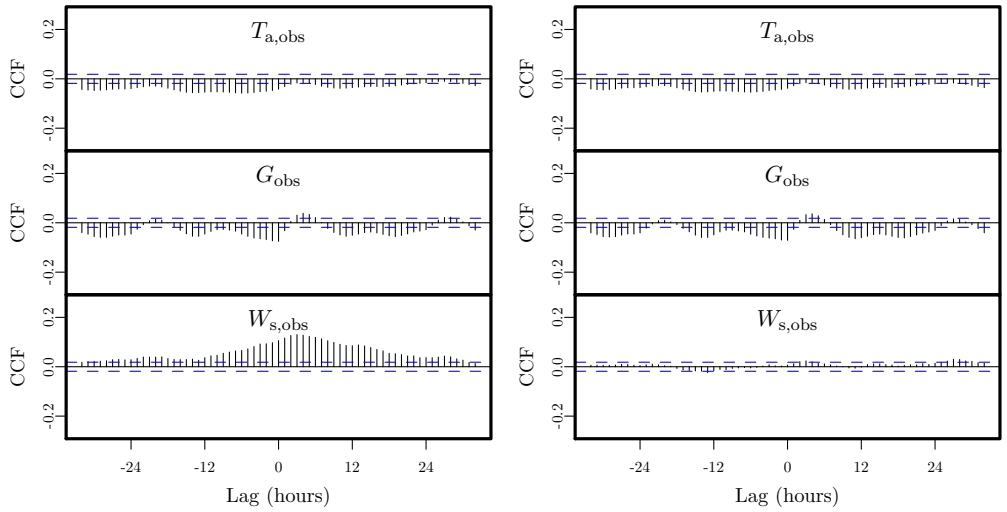

(c) Step three: CCF for $model_{\text{A.G}}$ errors to the inputs.

(d) Step four: CCF for $model_{\text{A.G.W}}$ errors to the inputs.

Figure 3: The cross-correlation function (CCF) between the average error series for the one-step ahead forecast (horizon $k = 1$) and the local observations of the inputs, since the inputs for the one-step ahead forecasts are primarily formed by the observations. The plots are for the errors from the selected model in the four steps of model identification carried out.

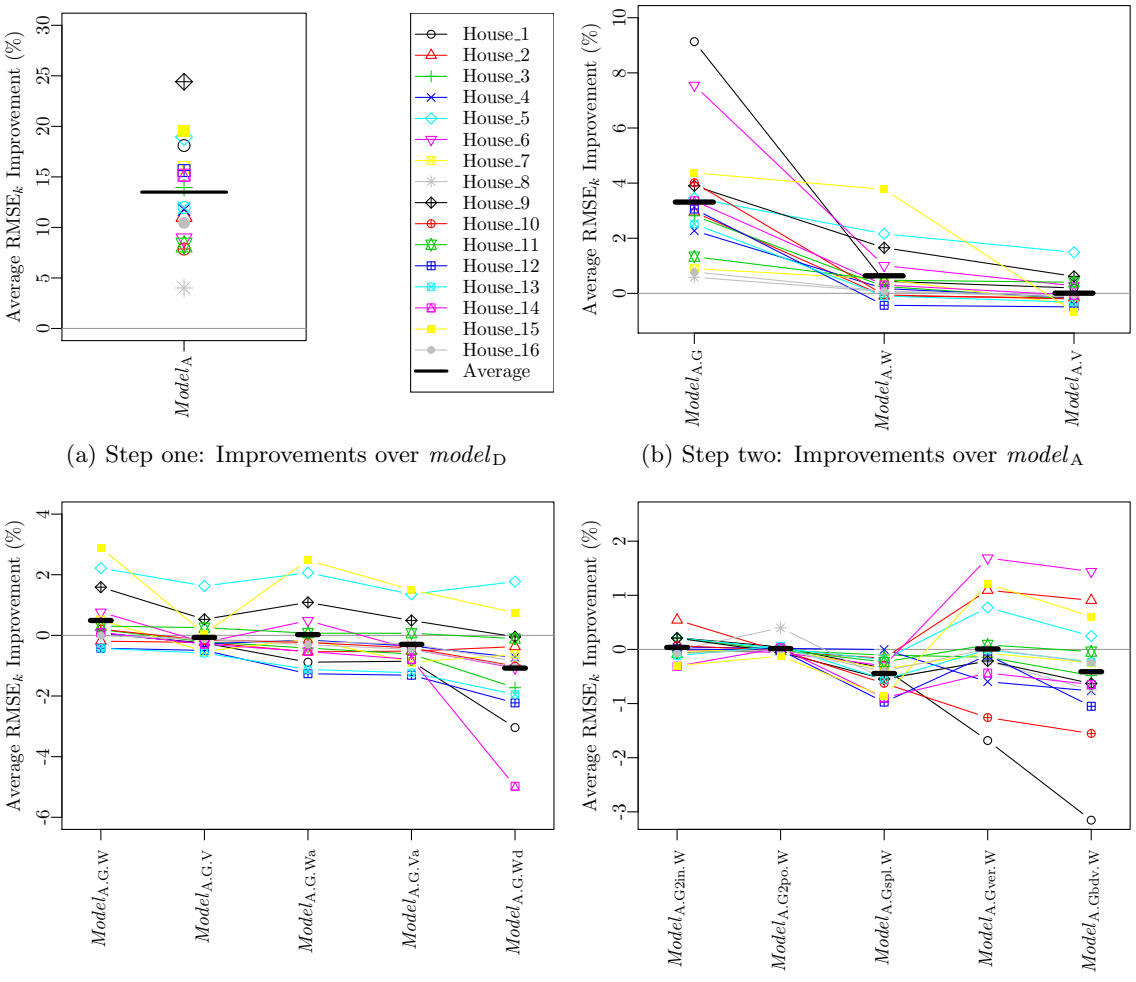

(a) Step one: Improvements over $model_{\mathrm{D}}$

(b) Step two: Improvements over $model_{\mathrm{A}}$

(c) Step three: Improvements over $model_{\mathrm{A.G}}$

(d) Step four: Improvements over $model_{\mathrm{A.G.W}}$

Figure 4: Improvements over the previously selected model for the models in each step of the selection.

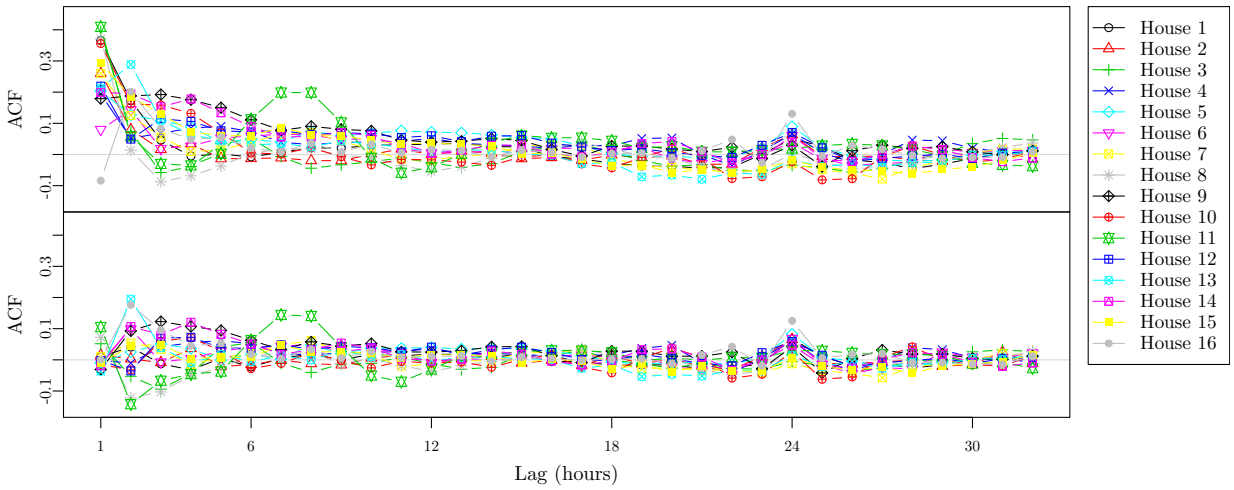

Figure 5: The auto-correlation function (ACF) for each house. The upper plot is the ACF of the errors before the AR(1) noise model is applied and the lower plot shows the ACF of the errors after.

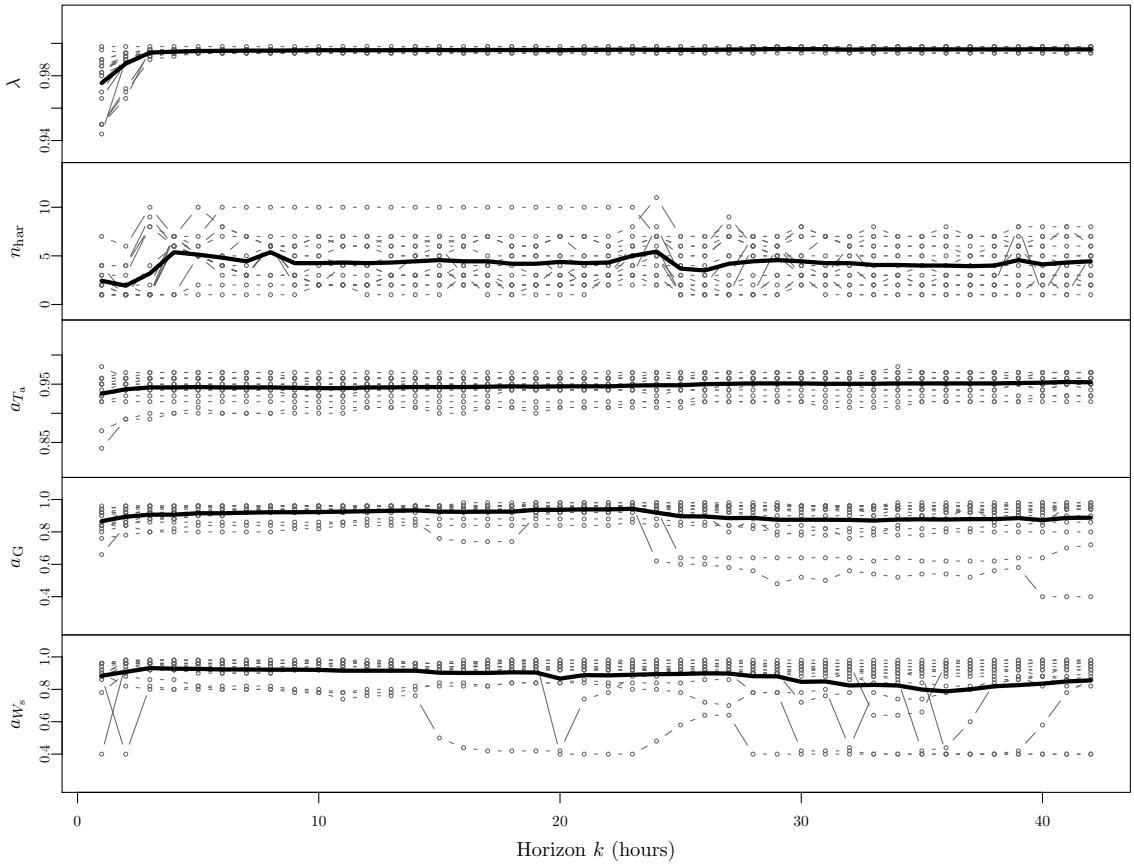

Figure 6: Values of the parameters fitted for each house.

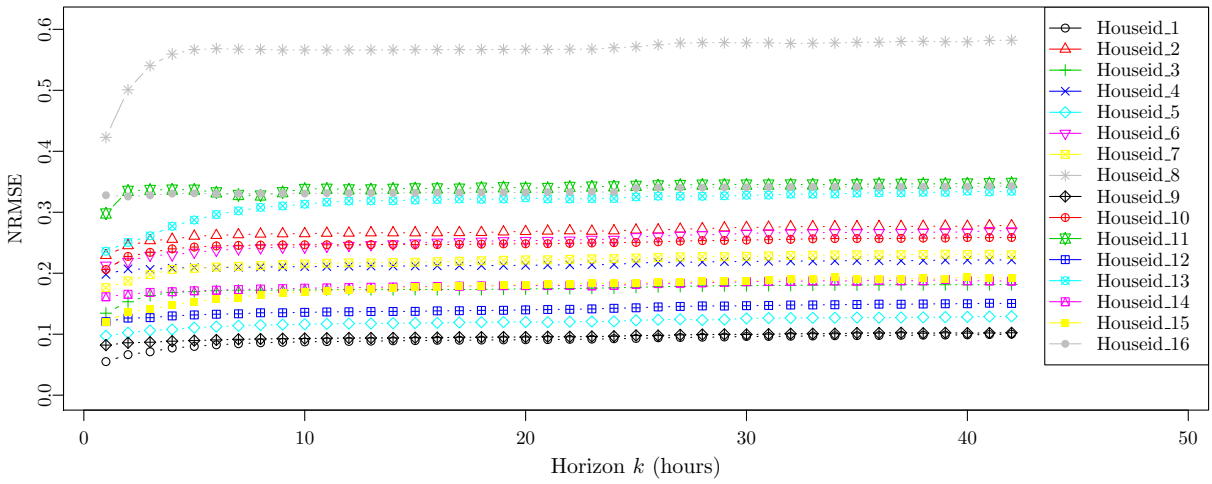

Figure 7: The NRMSE_k as a function of the horizon k for $model_{\text{A.G.W}}$ for each house.

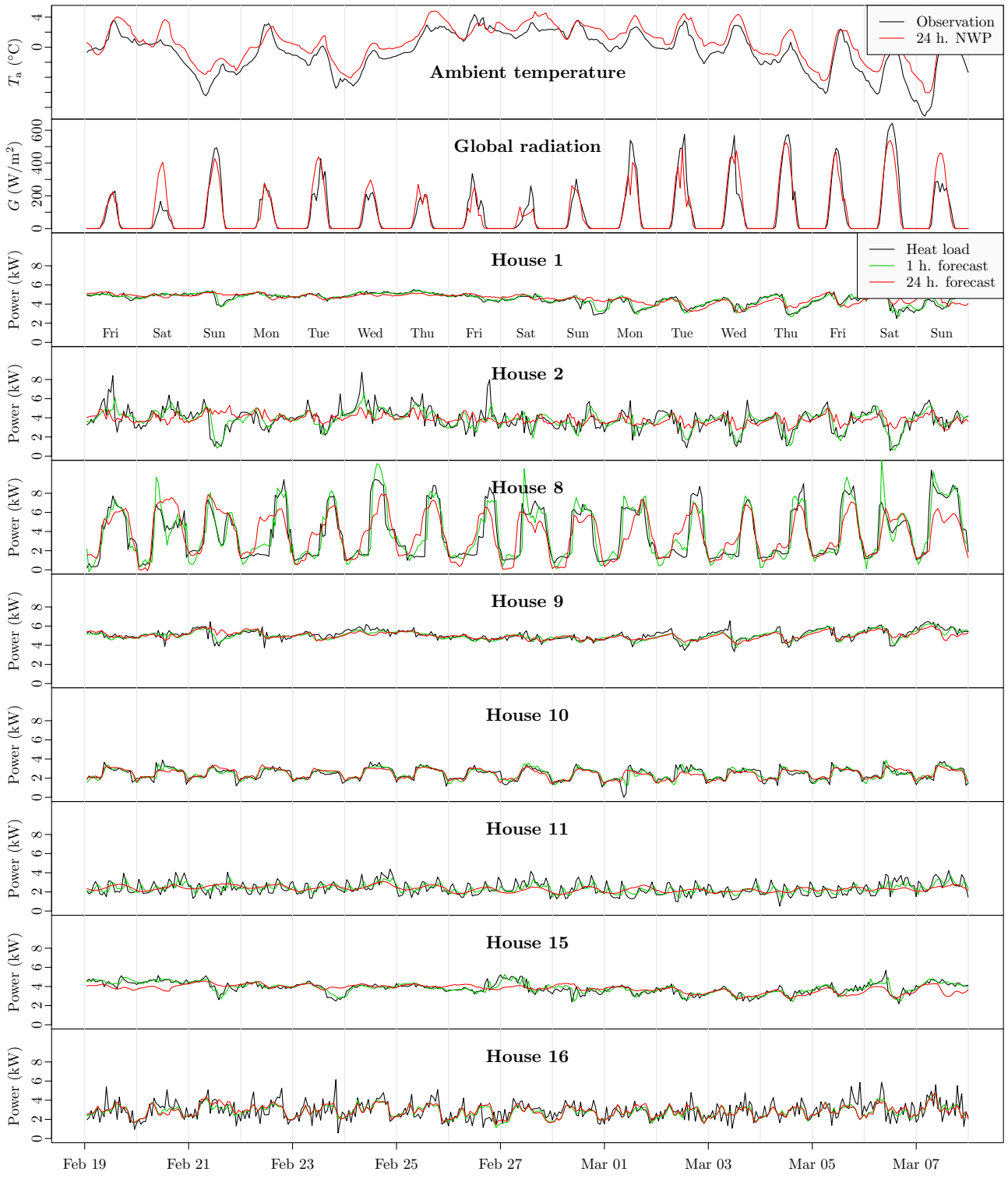

Figure 8: Plots of inputs and forecasts for sixteen days starting at the 19'th February 2010. The upper two plots are observations and the 24 hour NWP forecasts of the two most significant inputs: the ambient temperature and the global radiation. The plots below are for eight the houses of: observed heat load, 1 hour forecasts, and 24 hour forecasts.

Peder Bacher, Henrik Madsen, Bengt Perers, Short-term solar collector power forecasting, ISES Solar World Congress 2011 Proceedings

SHORT-TERM SOLAR COLLECTOR POWER FORECASTING

Peder Bacher[1], Henrik Madsen[1] and Bengt Perers[2]

[1]DTU Informatics, Richard Pedersens Plads, Building 321, DK-2800 Lyngby, Denmark
[2]DTU Civil Engineering, Brovej, Building 118, DK-2800 Lyngby, Denmark

Abstract

This paper describes a new approach to online forecasting of power output from solar thermal collectors. The method is suited for online forecasting in many applications and in this paper it is applied to predict hourly values of power from a standard single glazed large area flat plate collector. The method is applied for horizons of up to 42 hours.

Solar heating systems naturally come with a hot water tank, which can be utilized for energy storage also for other energy sources. Thereby such systems can become an important part of energy systems with a large share of uncontrollable energy sources, such as wind power. In such a scenario online forecasting is a vital tool for optimal control and utilization of solar heating systems.

The method is a two-step scheme, where first a non-linear model is applied to transform the solar power into a stationary process, which then is forecasted with robust time-adaptive linear models. The approach is similar to the one by Bacher et al. (2009), but contains additional effects due to differences between solar thermal collectors and photovoltaics. Numerical weather predictions provided by Danish Meteorological Institute are used as input. The applied models adapt over time enabling tracking of changes in the system and in the surrounding conditions, such as decreasing performance due to wear and dirt, and seasonal changes such as leaves on trees. This furthermore facilitates remote monitoring and check of the system.

1 Introduction

Forecasting of energy production is vital for optimization of energy systems which include wind and solar energy production. This paper describes an approach to online forecasting of power production from solar thermal collectors. In Denmark the level of wind power penetration already now gives periods with a surplus of energy and facilities to absorb this energy are needed. Solar heating systems with a hot water tank and auxiliary electrical heating can provide energy storage, which can facilitate absorption of wind energy and peak shaving, especially for levelling out diurnal energy consumption. The method is planned to be part of the control system for such heating systems (Perers et al., 2011). The study is carried out with climate data observed at a weather station at Danish Technical University. From this data, simulated hourly average values of solar thermal power is generated with a very detailed simulation model. Furthermore numerical weather predictions (NWPs) provided by Danish Meteorological Institute data is used. The forecasting method is a two-step scheme, where first a statistical clear sky model is applied to transform the solar power into a more stationary process, which then is forecasted with robust time-adaptive linear models. The NWPs are used as input to conditional parametric time-adaptive models to forecast the solar power. These forecasts are then transformed with the clear sky model, such that they can be applied as inputs to the linear forecasting models. Finally, a combined model, which is the most optimal for all horizons, is formed.

The paper is organized as follows. First the data and how it is preprocessed is described in a section. The next section contains an outline of the clear sky model, and this is followed by a section where all the forecasting models are described. Then an evaluation is given and the results are presented, each in a section. The second last section contains a discussion of the results and ideas for further work, and finally, the paper ends with a conclusion.

2 Data

The forecasting method is applied on simulated solar output power data for a flat plate collector carefully tested and modelled at DTU. A validated collector model and longterm climate data from the DTU Byg climate station was used to create realistic operating data for a solar collector during the year. The simulation model and weather data was introduced in TRNSYS 16 and the collector output power was calculated as hourly mean values. The simulation model is dynamic, such that dynamical effects - introduced when the collector starts and stops and during rapidly varying solar radiation conditions - are modelled.

In this study all time series are hourly average values and all units are implicitly per hour. Time points are set to the end of their respective sample period and all are in UTC. The units for radiation are $\frac{\mathrm{W}}{\mathrm{m}^2}$ and for temperatures $^\circ$C.

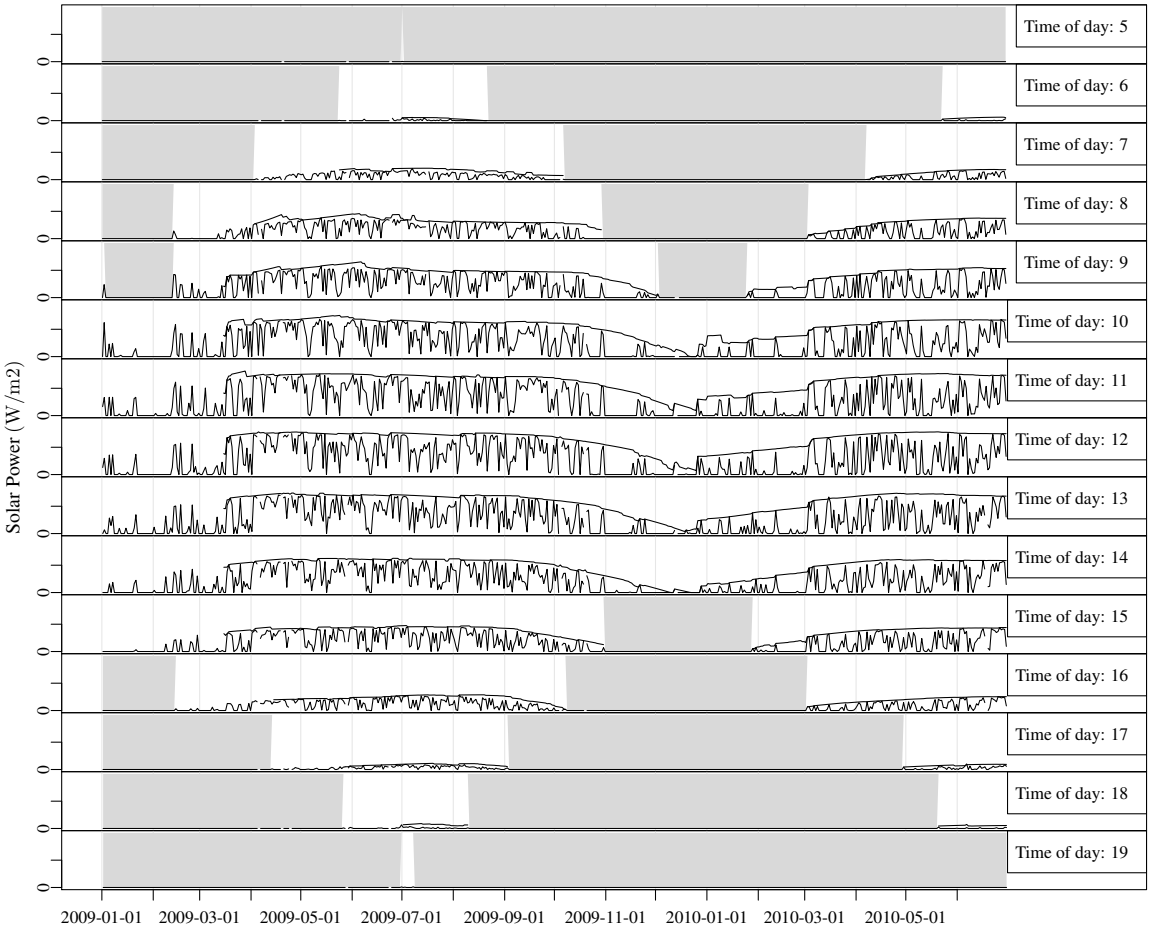

Figure 1: The observed solar power for each hour of the day. The grayed area shows the periods not included in the modelling. The curve following the highest values of solar power is the estimated clear sky power, which is referred to in later parts of the paper.

2.1 Solar power

The simulated solar power time series is plotted for each hour of the day in Figure 1. A few short periods are with missing values.

2.2 Numerical weather predictions

The numerical weather predictions (NWPs) used in the study are provided by Danish Meteorological Institute. The NWP model is DMI-HIRLAM-S05, which has a 5 kilometer grid and 40 vertical layers (Danish Meteorological Institute, 2011). NWPs are updated every 6'th hour and are up to a 48 hours horizon. They consist of hourly predictions of ambient temperature, and horizontal direct- and diffuse solar radiation. A couple of the considered forecasting models use the global radiation as input, which is simply the direct and the diffuse radiation summed. The scatter plots in Figure 2 shows the solar power versus the NWPs for a 24 hour horizon. Clearly, the solar power is highly correlated with both the global and direct radiation, whereas the effect of diffuse and ambient temperature are not as apparent.

2.3 Pre-processing

On most locations on earth the solar radiation is zero at night time, hence the observed solar power is also zero. For the current dataset only periods, for a given hour of the day longer than 40 days in which the solar power is different from zero, are included. This is illustrated in Figure 1, where the non-included periods are grayed out. Furthermore a few short periods are missing from the observations. The time series of hourly observed

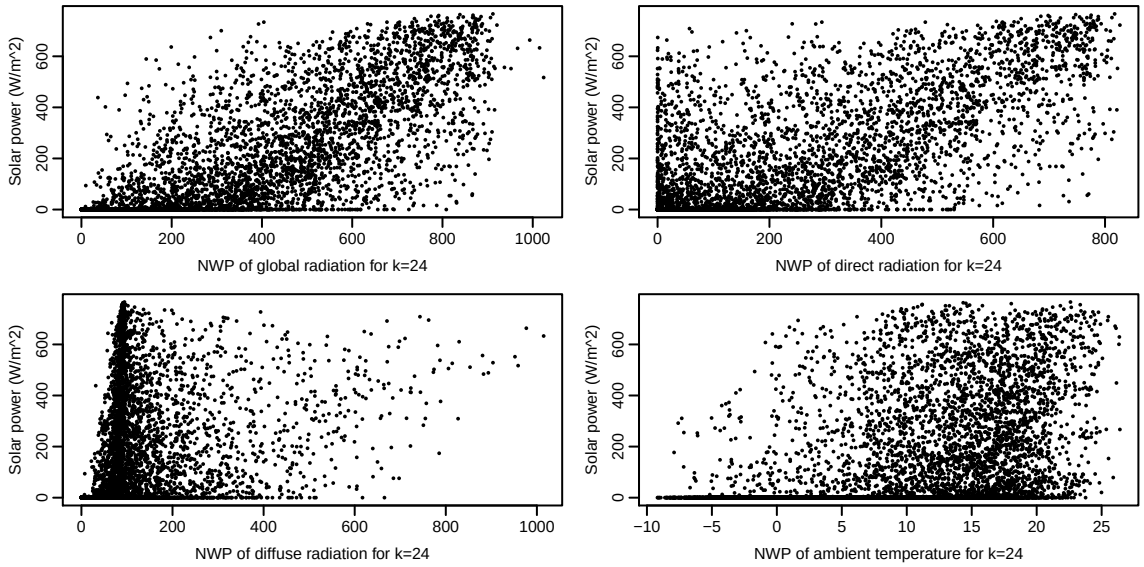

Figure 2: The observed solar power versus the NWPs for $k = 24$, which are used as inputs to forecasting models.

solar power spanning the period from 2009-01-01 to 2010-07-01 is

$$\{P_t;\ t = 1, \ldots, N\} \tag{1}$$

where $N = 13104$. The NWPs have a calculation time of 4 hours, which is taken into consideration, such that e.g. the forecast from 2009-01-01 00:00 are only available from 2009-01-01 04:00. The NWPs are pre-processed into time series of hourly values, such that the most recent available forecast k hours ahead is selected each hour. The time series are for a given k: the direct radiation

$$\left\{G^{\mathrm{b,nwp}}_{t+k|t};\ t = 1, \ldots, N\right\} \tag{2}$$

the diffuse radiation

$$\left\{G^{\mathrm{d,nwp}}_{t+k|t};\ t = 1, \ldots, N\right\} \tag{3}$$

and the ambient temperature

$$\left\{T^{\mathrm{a,nwp}}_{t+k|t};\ t = 1, \ldots, N\right\} \tag{4}$$

Due to the 6 hours interval the NWPs for horizons longer than 42 hours are not complete and therefore the solar power forecasting are only carried out up to 42 hours.

3 Clear sky model

For effective forecasting with classical linear time series methods stationarity of the process is required (Madsen, 2007). The process that generates the solar power is not stationary, which is seen by plotting quantiles of the distribution of solar power conditioned on the time of day. Such a plot is shown in Figure 3. Clearly the distribution of solar power is not independent of the time of day. The dependency can be removed by a transformation with a clear sky model

$$\tau_t = \frac{P_t}{P^{\mathrm{cs}}_t} \tag{5}$$

where P_t is the observed solar power, P^{cs}_t is the estimated clear sky solar power, and τ_t is the transformed solar power.

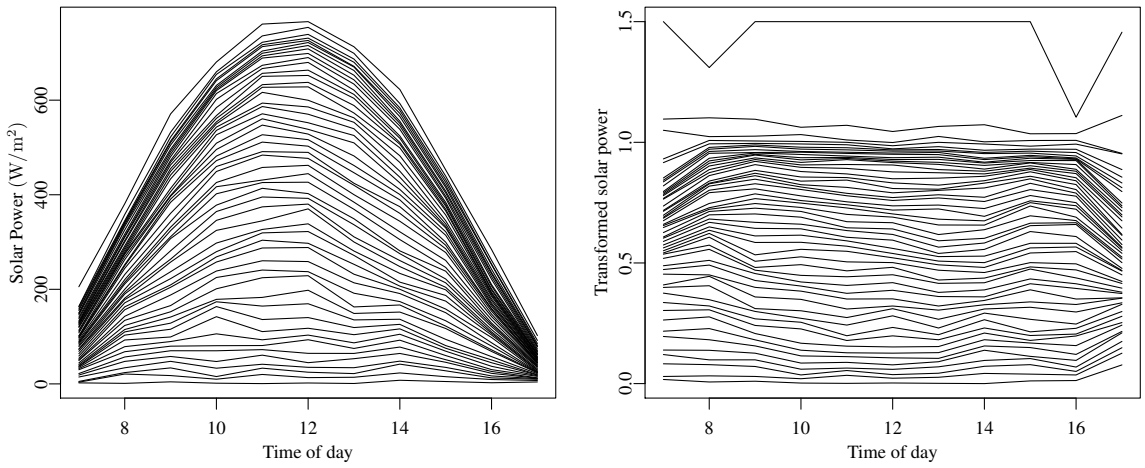

Figure 3: The $0, 2\%, ..., 100\%$ quantiles of the distribution of the solar power and the transformed solar power conditioned on the time of day. Values above 1.5 has been clipped, which was the case for 17 values.

3.1 Statistically estimated clear sky solar power

The clear sky solar power is estimated with a statistical non-linear and adaptive model. Quantile regression locally weighted in the day of year and time of day dimension is applied. In the present study this is carried out fully causal. The clear sky model is

$$P_t^{\mathrm{cs}} = q_{0.99}(P_1, P_2, \ldots, P_t, h_{\mathrm{t}}, h_{\mathrm{tod}}, h_{\mathrm{y}}) \tag{6}$$

where $q_{0.99}$ is the 99% quantile of all the solar power values up to t. The bandwidths h_{t}, h_{tod}, and h_{y}, are in the time-, time of day-, and year-dimension, respectively. The bandwidths control how "locally" the model is fitted, i.e. a lower bandwidth puts more emphasis on data which is close in time. The local weighting function is an Epanechnikov kernel. The applied bandwidths are

$$h_t = 120 \text{ days}, \quad h_{\mathrm{tod}} = 2 \text{ hours}, \quad h_{\mathrm{y}} = 1.7 \text{ years} \tag{7}$$

which were found by visual inspection of the fitted clear sky curve. Finally, it is noted that second-order polynomials were applied in the time- and time of day-dimension to include curvature into the model. The estimate of the clear sky solar power is shown in Figure 1. From the plot it is seen that it follows the highest values of solar power quite well. Clearly, the clear sky power is most easily carried out in the periods with a high level of solar power. One advantage of the transformation is that it will automatically adapt to changes in the system, such as degraded performance or changes in the surroundings e.g. snow cover and shadowing effects. It can as well be used for monitoring of the solar system, since degraded performance from the same time of year will result in a lower clear sky solar power curve. Quantile plots of the transformed solar power conditioned on the time of day are shown in Figure 3, from which it is seen that the transformed solar power process is considerably less depend end of the time of day and therefore a much more stationary process. It is noted that further work could include physical considerations e.g. by using the air mass as an input.

4 Forecasting models

In this section a description of the applied forecasting models is given. The models can be divided into models without NWPs as input - autoregressive (AR) models - and models with NWPs as input: conditional parametric (CP) and autoregressive with exogenous inputs (ARX) models. Each model is fitted seperately for each horizon, such that the same model structure is used, but the parameters are estimated separately for each horizon. In the final model, a combination of models are used to achieve the most optimal performance for all horizon.

4.1 Reference model

To compare the performance of prediction models, and especially when making comparisons between different studies, a common reference model is essential. The reference model for solar power used in this study is the

best performing naive predictor for a given horizon. Two naive predictors of solar power are found to be relevant. Persistence

$$p_{t+k} = p_t + e_{t+k}, \tag{8}$$

and diurnal persistence

$$p_{t+k} = p_{t-s(k)} + e_{t+k} \tag{9}$$
$$s(k) = f_{\mathrm{spd}} + k \bmod f_{\mathrm{spd}} \tag{10}$$

where $f_{\mathrm{spd}} = 24$ is the sample frequency in number of samples per day and $s(k)$ ensures that the latest diurnal observation is used, i.e. the value which, depending on the horizon, is either 24 or 48 hours before the time point that is to be forecasted.

4.2 Autoregressive models

Autoregressive (AR) models are applied to forecast the transformed solar power. These models can include either the latest available observation or the latest available diurnal observation, or both, as input. The models are fitted with k-step recursive least squares with forgetting factor (Bacher et al., 2009). The model formulated as a k-step AR model

$$\tau_{t+k} = m + a_1\tau_t + a_{24}\tau_{t-s(k)} + e_{t+k} \tag{11}$$
$$s(k) = 24 + k \bmod 24 \tag{12}$$

where the function $s(k)$ ensures that the latest observation of the diurnal component is included. It was found that depending on the horizon better performance was achieved by only using one input. Thus for short horizons (1 and 2 hours) the model without the diurnal component

$$\tau_{t+k} = m + a_1\tau_t + e_{t+k} \tag{13}$$

was found to have the best performance, it is denoted *AR1*, and for longer horizons the model with only the diurnal component

$$\tau_{t+k} = m + a_{24}\tau_{t-s(k)} + e_{t+k} \tag{14}$$

was found to have the best performance, it is denoted *ARDiurnal*.

4.3 Conditional parametric models with NWPs as input

Models based on NWPs of solar radiation and ambient temperature are described in this section. It is known from physics (Perers, 1997) that the power output of a solar collector can be described by

$$P = F'(\tau\alpha)_{\mathrm{en}}K_{\tau\alpha\mathrm{b}}(\theta)G_{\mathrm{b,col}} + F'(\tau\alpha)_{\mathrm{en}}K_{\tau\alpha\mathrm{d}}G_{\mathrm{d,col}} - F'U_0\left(\frac{T_{\mathrm{o}} + T_{\mathrm{i}}}{2} - T_{\mathrm{a}}\right) \tag{15}$$

where the $G_{\mathrm{b,col}}$ and $G_{\mathrm{d,col}}$ are respectively direct and diffuse solar radiation normal to the collector plane. This is formed into a forecasting model based on NWPs by rewriting as follows. First, both the the angle of incidence modifier $K_{\tau\alpha\mathrm{b}}(\theta)$ and the transformation of solar radiation from horizontal to the collector plane are modelled by letting the coefficients - for the radiation effects - become a function of time t and time of day t_{tod}. Furthermore, assuming that the outlet temperature is a function of the solar radiation

$$T_{\mathrm{o}} = f_{\mathrm{b}}(G_{\mathrm{b,col}}) + f_{\mathrm{d}}(G_{\mathrm{d,col}}) \tag{16}$$

this give the total effect of direct radiation as a non-linear function

$$a(t, t_{\mathrm{tod}}, G_{\mathrm{b}}, G_{\mathrm{d}})G_{\mathrm{b}} = F'(\tau\alpha)_{\mathrm{en}}K_{\tau\alpha\mathrm{b}}(\theta)G_{\mathrm{b,col}} + F'U_0\frac{1}{2}f_{\mathrm{b}}(G_{\mathrm{b,col}}) \tag{17}$$

and for the diffuse radiation

$$b(t, t_{\mathrm{tod}}, G_{\mathrm{b}}, G_{\mathrm{d}})G_{\mathrm{d}} = F'(\tau\alpha)_{\mathrm{en}}K_{\tau\alpha\mathrm{d}}G_{\mathrm{b,col}} + F'U_0\frac{1}{2}f_{\mathrm{d}}(G_{\mathrm{d,col}}) \tag{18}$$

Finally, the effect of the ambient temperature is kept as

$$cT_{\mathrm{a}} = F'U_0T_{\mathrm{a}} \tag{19}$$

and by assuming a constant inlet temperature this part becomes a constant effect

$$m = F'U_0\frac{T_{\mathrm{i}}}{2} \tag{20}$$

Thus the CP model structure used for forecasting is

$$P = m + a(t, t_{\mathrm{tod}}, G_{\mathrm{b}}, G_{\mathrm{d}})G_{\mathrm{b}} + b(t, t_{\mathrm{tod}}, G_{\mathrm{b}}, G_{\mathrm{d}})G_{\mathrm{d}} + cT_{\mathrm{a}} \tag{21}$$

Since the time-dependency and non-linearity are smooth functions in the parameters, it is modelled with conditional parametric (CP) models. The time varying effect is modelled by conditioning on t and t_{tod} - this is equivalent of a local constant effect - and the dependency of the radiation is modelled with 1-order local polynomials. A kernel method is applied, using a nearest neighbor approach to find the bandwidth of an Epanechnikov weighting function. From Equation (15) it is seen that the output can be negative if little radiation hits the collector and the ambient temperature is low. In this case the output is zero since the system stops. This effect can be seen on the plot in Figure 2. It is handled by the non-linearity of the models and by setting negative forecasts to zero.

The simplest considered conditional parametric model is

$$P_{t+k} = m + a\Big(t, t_{\mathrm{tod}}, G^{\mathrm{nwp}}_{t+k|t}\Big)G^{\mathrm{nwp}}_{t+k|t} + e_{t+k} \tag{22}$$

where $G^{\mathrm{nwp}}_{t+k|t}$ is the k-hour NWP of global radiation and denoted as *CP1* in the following. This second CP model has NWPs of direct and the diffuse radiation as inputs

$$P_{t+k} = m + a\Big(t, t_{\mathrm{tod}}, G^{\mathrm{b,nwp}}_{t+k|t}, G^{\mathrm{d,nwp}}_{t+k|t}\Big)G^{\mathrm{b,nwp}}_{t+k|t} + b\Big(t, t_{\mathrm{tod}}, G^{\mathrm{b,nwp}}_{t+k|t}, G^{\mathrm{d,nwp}}_{t+k|t}\Big)G^{\mathrm{d,nwp}}_{t+k|t} + e_{t+k} \tag{23}$$

where $G^{\mathrm{b,nwp}}_{t+k|t}$ is the k-hour NWP of direct radiation and $G^{\mathrm{d,nwp}}_{t+k|t}$ is the k-hour NWP of diffuse radiation, and denoted as *CP2*. Finally the model is expanded with NWPs of ambient temperature

$$P_{t+k} = m + a\Big(t, t_{\mathrm{tod}}, G^{\mathrm{b,nwp}}_{t+k|t}, G^{\mathrm{d,nwp}}_{t+k|t}\Big)G^{\mathrm{b,nwp}}_{t+k|t} + b\Big(t, t_{\mathrm{tod}}, G^{\mathrm{b,nwp}}_{t+k|t}, G^{\mathrm{d,nwp}}_{t+k|t}\Big)G^{\mathrm{d,nwp}}_{t+k|t} \tag{24}$$

$$+ c\Big(t, t_{\mathrm{tod}}\Big)T^{\mathrm{a,nwp}}_{t+k|t} + e_{t+k} \tag{25}$$

where $T^{\mathrm{a,nwp}}_{t+k|t}$ is the k-hour NWPs of the ambient temperature and the model is denoted as *CP3*.

In the following the coefficients dependency of the time of day is elaborated on. Plots of the fitted forecasting function $a\Big(t, t_{\mathrm{tod}}, G^{\mathrm{b,nwp}}_{t+k|t}, G^{\mathrm{d,nwp}}_{t+k|t}\Big)$ are shown in Figure 4. It is seen how the slope of the function is lower in the morning, than in the middle of the day. This is naturally caused by the higher angle of incidence in the morning, which cause less horizontal radiation to be absorbed due to reflection. Likewise for the afternoon. Finally, non-linearity in the fit is seen, which is caused by the non-negativity of the solar power (mentioned above) and varying uncertainty of the NWPs.

4.4 Autoregressive model with exogenous input

The AR model is be expanded to include the forecast of the CP models, thus combining information in past observed solar power and NWPs. The solar power forecasts from the CP is transformed with the clear sky model by

$$\hat{\tau}^{\mathrm{nwp}}_{t+k|t} = \frac{\hat{P}^{\mathrm{nwp}}_{t+k|t}}{P^{\mathrm{cs}}_{t-s(k)}} \tag{26}$$

$$s(k) = f_{\mathrm{spd}} + k \bmod f_{\mathrm{spd}} \tag{27}$$

where $f_{\mathrm{spd}} = 24$ is the sample frequency in number of samples per day. This is applied as an input to the ARX model

$$\tau_{t+k} = m + a_1\tau_t + a_{24}\tau_{t-s(k)} + b_1\tau^{\mathrm{nwp}}_{t+k|t} + e_{t+k} \tag{28}$$

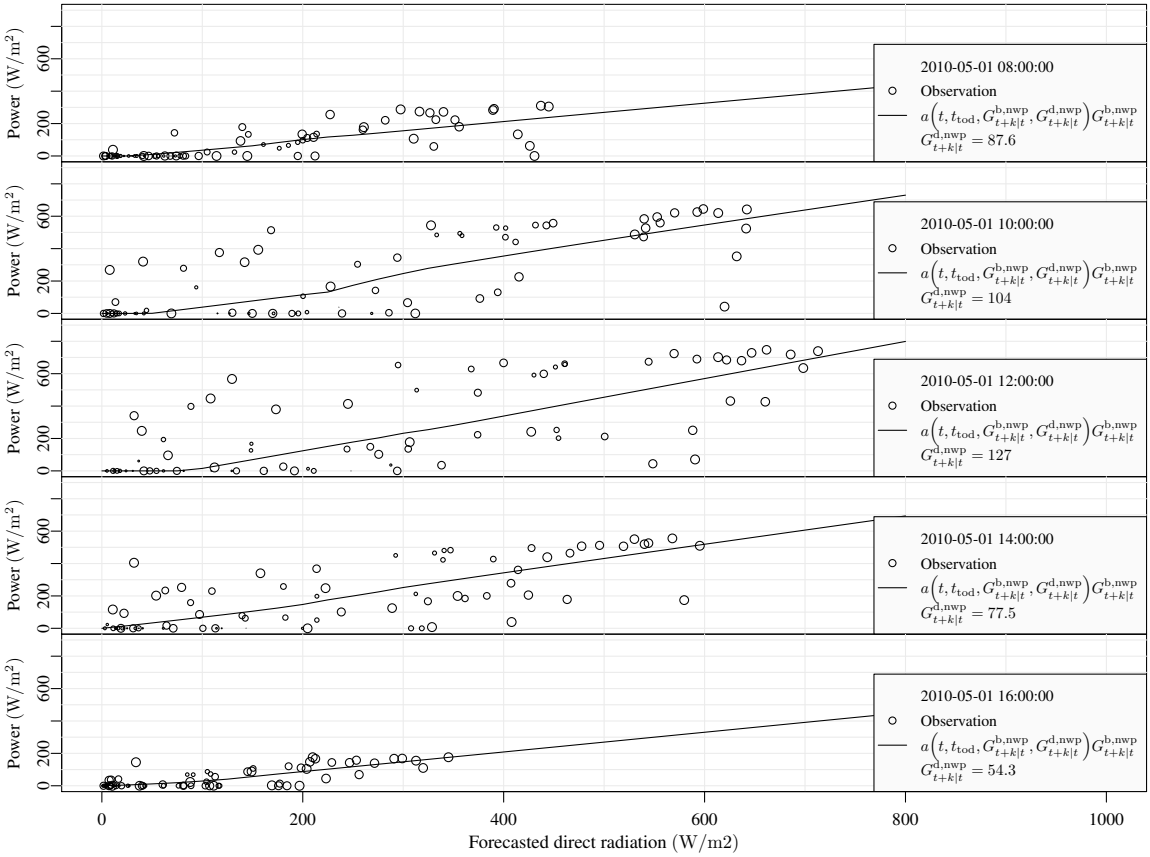

Figure 4: Examples of the function fitted for forecasting of the effect of direct radiation at different times of the day the 1'th of May 2010 with the *CP2* model. For each observation the size of circle indicates the weighting of the observation in the CP models. Thus observations with a larger circle have more influence on the fitted function.

Again, as for the AR models, different performance is found depending on the horizon. The *ARX1* model is best for short horizons

$$\tau_{t+k} = m + a_1\tau_t + b_1\tau^{\text{nwp}}_{t+k|t} + e_{t+k} \tag{29}$$

ARXDiurnal for horizons up to 24 hours

$$\tau_{t+k} = m + a_{24}\tau_{t-s(k)} + b_1\tau^{\text{nwp}}_{t+k|t} + e_{t+k} \tag{30}$$

and *ARX*

$$\tau_{t+k} = m + b_1\tau^{\text{nwp}}_{t+k|t} + e_{t+k} \tag{31}$$

for longer horizons.

4.5 Combined model

The final model is a combination of the previously described models. The model is denoted *ARXCombined*. First, missing values in forecasts from *ARX1* are replaced with forecast values from *ARXDiurnal*. These missing values are in the morning, since they were tried to be forecasted based on night values, which are zero. For horizons longer than 30 hours forecasts from *ARX* are used. Finally, any remaining missing values - which are only where the diurnal lag was not present for *ARXDiurnal* - are replaced with forecasted values from *CP2*.

5 Evaluation

The methods used for evaluating the prediction models are inspired by Madsen et al. (2005). They suggest a framework for evaluation of wind power forecasting. The clear sky model, RLS, and CP fitting do not use

any degrees of freedom and the dataset is therefore not divided into a training set and a test set. It is only for the optimization of the kernel bandwidths and the forgetting factor that the entire dataset is used. The period before 2009-03-15 is considered as a burn-in period and are not used when calculating the error measures.

5.1 Error measures

The Root Mean Square Error for the k'th horizon is

$$RMSE_k = \left(\frac{1}{N} \sum_{t=1}^{N} e_{t+k}^2 \right)^{\frac{1}{2}} \tag{32}$$

where e_{t+k} is k-hourly prediction error. The $RMSE_k$ is used as the main evaluation criterion (EC) for the performance of the models. The Normalized Root Mean Square Error is found by

$$NRMSE_k = \frac{RMSE_k}{p_{\max}} \tag{33}$$

where $p_{\max}$ is the maximum observed solar power output. The mean value of the $RMSE_k$ for a range of horizons

$$\overline{RMSE}_{k_{\text{start}},k_{\text{end}}} = \frac{1}{k_{\text{end}} - k_{\text{start}} + 1} \sum_{k=k_{\text{start}}}^{k_{\text{end}}} RMSE_k \tag{34}$$

is used as a summary error measure. When comparing the performance of two models the improvement

$$I_{\text{EC}} = 100 \cdot \frac{EC_{\text{ref}} - EC}{EC_{\text{ref}} =} (\%) \tag{35}$$

is used, where EC is the considered evaluation criterion. When calculating the error measures it is important to consider how to handle missing values for the solar power forecasts. The problem is handled by replacing missing forecast values with forecast values from the reference model *Ref*.

5.2 Completeness

In order to evaluate a model for its performance regarding missing forecast values a measure is defined, it is denoted completeness. The completeness of a forecast for horizon k, is the ratio of the total sum of solar power and the summed solar power for time points where the forecasts are not missing

$$C_k = \frac{\sum_{t=1}^{N} P_t \, I\big(\hat{P}_{t|t-k}\big)}{\sum_{t=1}^{N} P_t} \tag{36}$$

where $I()$ is the indicator function which is 0 if $\hat{P}_{t|t-k}$ is missing, and 1 if not. Only the included values are used, i.e. not night values.

6 Results

In this section the results are presented and evaluated. The $\overline{RMSE}_{k_{\text{start}},k_{\text{end}}}$ improvement for relevant ranges of horizons are listed in Table 1. For selected models the $RMSE_k$ is shown in the upper plot of Figure 5 and the completeness in the lower.

Considering the improvements it is seen that most of the models perform very well on either the short horizons or the longer horizons. Starting with short horizons (1 to 2 hours), the *AR1* and *ARX1* are clearly superior, which is due to their inclusion of the most present autoregressive lag. Their performance on longer horizons are not good. The reason for this is found by considering the plot of $RMSE_k$ and completeness. Here it is seen that the completeness of *AR1* and *ARX1* drops really quickly as the horizon increase, which cause the $RMSE_k$ to increase and reach the reference model at the 10 hours horizon. This is simply due to missing forecast values, since for e.g. the 10 to 14 hours horizons the models use night values (which are missing) to forecast day values with.

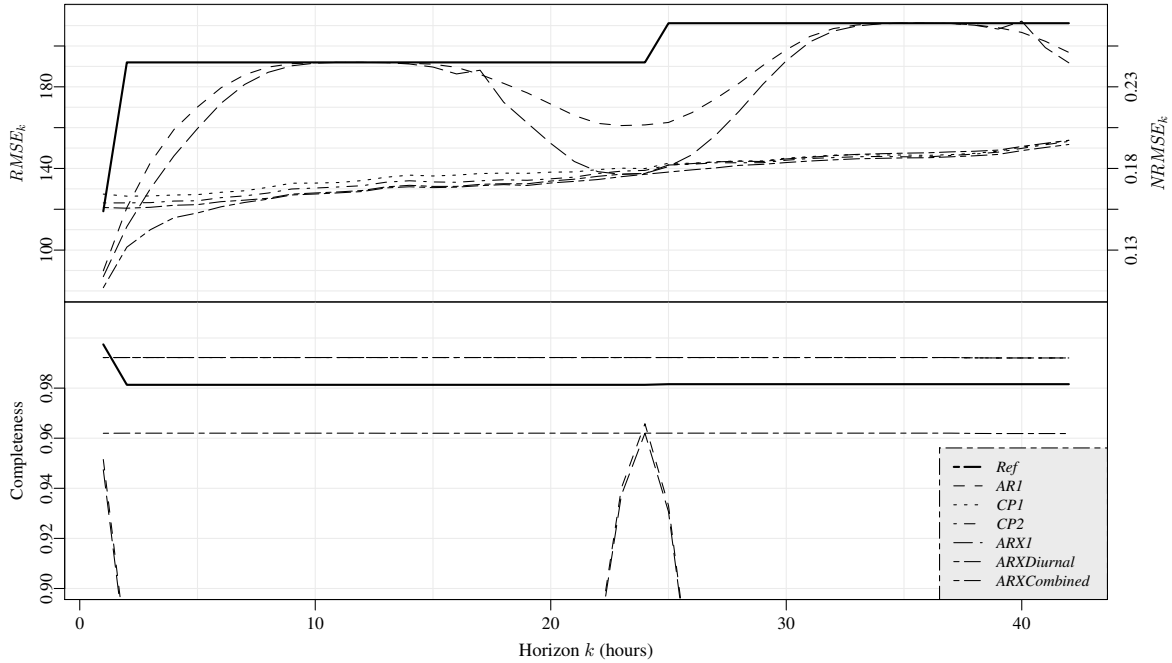

Figure 5: The upper plot is $RMSE_k$ for the forecasting models. On the right side the $NRMSE_k$ is indicated. The lower plot is completeness C_k.

For horizons longer than three hours the best performance is seen for the models, that doesn't include the most present AR lag. The *ARDiurnal* is a clear improvement from the *AR1*, and the CP and ARX models - which include the NWPs - are superior for these horizons. An improved performance is found from *CP1* to *CP2* mainly for 3 to 24 hours horizons, whereas no clear increase in improvement is found from *CP2* to *CP3*. The CP models are slightly improved by using them as input to the ARX models, since autocorrelation of the errors are modelled.

Finally, the combined model *ARXCombined* utilizes the best parts of: *ARX1*, *ARX*, *ARXDiurnal*, and *CP2*. Especially the replacement of missing forecast values improves the performance for horizons up to 5 hours. The completeness of the combined model is as high as any of the others.

7 Discussion and applications

This section contains a short discussion of the results and ideas for further work, and ends with an outline of applications.

Considering the improvement achieved over the reference model the forecasting method is found to perform very well. Clearly the quality of the NWPs of solar radiation is the most influential source of error, hence improved NWPs will improve the forecasting performance. Regarding improvement of the forecasting models, the following are considered:

Table 1: Improvements in percent for selected ranges of horizons.

Model	$I_{\overline{RMSE}_{1,2}}$	$I_{\overline{RMSE}_{3,24}}$	$I_{\overline{RMSE}_{25,42}}$	$I_{\overline{RMSE}_{1,42}}$
AR1	30.8	7.1	6.1	7.8
ARDiurnal	-10.7	15	18	15.1
CP1	13.5	30	30.6	29.5
CP2	16.2	31.4	30.9	30.5
CP3	15.5	31.6	30.8	30.5
ARX	17.1	32	31.3	31
ARX1	34.4	11.6	8.7	11.4
ARXDiurnal	17.8	32.4	30.5	30.9
ARXCombined	39.3	33.3	31.5	32.8

- A thorough evaluation of the forecast errors to clarify how the models can be improved.
- Optimization of forgetting factor of the RLS has not been carried out, this will improve the performance of the AR and ARX models.
- Application of regime models to handle different aspects of forecasting for low and high radiation values.
- More optimal ways to combine the models. Utilizing a linear combination instead of the simple replacement currently carried out.
- It might be possible improve performance by including a third-stage, where modelling of the errors are carried out.

The applications for this type of solar thermal power forecasting counts the integration of solar thermal energy systems with auxiliary electrical heating into smart grid systems (Perers et al., 2011). The solar power forecasts will be used for model predictive control to optimize the operation of the system. Other applications include optimal control of large solar heating plants.

The method is furthermore well suited for monitoring the performance of solar thermal systems. Measures of the performance can be derived from the CP models, with which systems can be compared on an absolute scale. Sudden high deviation from the CP forecasting model will allow for very fast detection of failures in the system. For an individual system the change in performance over time can also be assessed by monitoring the clear sky curve for unusual behavior, and compare the change from year to year.

8 Conclusion

A method for forecasting of solar thermal power output is presented. It is applied to forecast hourly values for horizons up to 42 hours. The method is based on a two-stage approach, where first the solar power is normalized with a statistical clear-sky model, and secondly forecasted with time-adaptive linear time series models. Both models without and with NWPs of solar radiation and ambient temperature are considered. The NWPs are included by using non-linear conditional parametric models, which are formed from prior physical knowledge. The forecast models which do not use NWPs achieve an improvement on short horizons (1 to 2 hours) in average 30% over a persistence reference model, and in average 15% on horizons up to 42 hours. Applying the NWPs an improvement around 39 % is achieved in average for short horizons and around 32% in average for longer horizons. The method can furthermore be applied to monitor and check the performance of solar thermal collectors.

Nomenclature

P_t	Hourly solar thermal power, $\left[\mathrm{W/m^2}\right]$.
P_t^{cs}	Estimated clear sky solar power, $\left[\mathrm{W/m^2}\right]$.
τ_t	Normalized solar power.
t	Time index, [h].
k	Forecast horizon index, [h].
t_{tod}	Time of day.
$F'(\tau\alpha)_{\mathrm{en}}$	Zero loss efficiency of collector for direct radiation at normal incidence
$K_{\tau\alpha\mathrm{b}}(\theta)$	Incidence angle modifier for direct radiation
$K_{\tau\alpha\mathrm{d}}$	Incidence angle modifier for diffuse radiation
$F'U_0$	Heat loss coefficient at $(T_{\mathrm{a}} - T_{\mathrm{f}}) = 0$, $\left[\mathrm{W/(m^2K)}\right]$.
$G^{\mathrm{nwp}}_{t+k\|t}$	NWP of global radiation, $\left[\mathrm{W/m^2}\right]$.
$G^{\mathrm{b,nwp}}_{t+k\|t}$	NWP of direct solar radiation, $\left[\mathrm{W/m^2}\right]$.
$G^{\mathrm{d,nwp}}_{t+k\|t}$	NWP of diffuse solar radiation, $\left[\mathrm{W/m^2}\right]$.
$T^{\mathrm{a,nwp}}_{t+k\|t}$	NWP of ambient temperature, $[^{\circ}\mathrm{C}]$.
$\hat{P}^{\mathrm{nwp}}_{t+k\|t}$	k-hour prediction of solar power, $\left[\mathrm{W/m^2}\right]$.
$\hat{\tau}_{t+k\|t}$	k-hour prediction of normalized solar power.
e_{t+k}	k-step prediction error.

References

P. Bacher, H. Madsen, and H. A. Nielsen. Online short-term solar power forecasting. *Solar Energy*, 83(10):1772–1783, 2009. ISSN 0038092x.

Danish Meteorological Institute. DMI-HIRLAM-S05, 2011. URL `http://www.dmi.dk/eng/index/research_and_development/dmi-hirlam-2009.htm`.

H. Madsen. *Time Series Analysis*. Chapman & Hall, 2007.

H. Madsen, P. Pinson, G. Kariniotakis, H. A. Nielsen, and T. S. Nielsen. Standardizing the performance evaluation of shortterm wind power prediction models. *Wind Engineering*, 29(6):475, 2005. ISSN 0309524x.

B. Perers. An improved dynamic solar collector test method for determination of non-linear optical and thermal characteristics with multiple regression. *Solar Energy*, 59(4-6):163–178, 1997. ISSN 0038092x.

B. Perers, S. Furbo, J. Fan, E. Andersen, and Z. Chen. Solar combisystems with forecast control to increase the solar fraction and lower the auxiliary energy cost. In *ISES Solar World Congress Proceedings*, 2011.

Kristian Pagh Nielsen, Verification of cloud physical properties, DMI, Poster from

Verification of cloud physical properties

Kristian Pagh Nielsen

Danish Meteorological Institute, Ministry of Climate and Energy, Copenhagen, Denmark

Abstract

For the first time, field verification of NWP cloud physical properties against measurements from the MSG satellite are presented. In classical observations clouds are described in terms of 1/8 fractions of cloud cover. The cloud fraction, however, is only one of the factors that determine the reflectance and transmittance of a cloud field. The other factors are the inherent cloud physical properties. These are particularly important with respect to shortwave radiative transfer. Therefore, satellite measurements of cloud physical properties, much improves the capability of cloud verification. With these measurements, processes such as aerosol indirect effects can also be assessed in detail. Results will be presented and discussed.

Introduction

- Clouds are affected by virtually all processes in the atmosphere;
- Cloud prediction is essential for prediction of radiative forcing and precipitation;
- New satellite data give 3D-information on clouds.

Theory

The equation of radiative transfer:

$$\mu\frac{dI_\lambda(\tau,\mu,\phi)}{d\tau} = I_\lambda(\tau,\mu,\phi) - (1-a)B_\lambda(T;\tau) - \frac{a}{4\pi}\int_{4\pi} d\omega' p(\tau,\mu',\phi')I_\lambda(\tau,\mu,\phi) - S^*_\lambda(\tau,\mu,\phi) \quad (1)$$

Inherent optical properties (IOPs):

- τ: Optical depth [-], the integrated extinction;
- a: Single scattering albedo = 1 - emittance [-];
- p: Phase function [-], in practice a function only of the asymmetry factor g (Henyey & Greenstein 1941);
- Lower boundary albedo / BRDF [-].
- "Cloud albedo" is not an inherent optical property!

The good news is that the cloud IOPs can be adequately derived from only two physical quatities

- Cloud liquid water path (CLWP) [kg/m^2];
- Effective cloud drop radius (r_e) [μm].

In the visible spectral range the following inherent optical properties can be derived from Mie-Debye theory.

$$\tau_{vis} = \frac{3CLWP}{2r_e\rho_l}, \quad a_{vis} = 1, \quad g_{vis} = 0.85 \quad (2)$$

$$r_e \equiv \int_0^\infty drn(r)r^3 / \int_0^\infty drn(r)r^2 \quad (3)$$

Satellite data

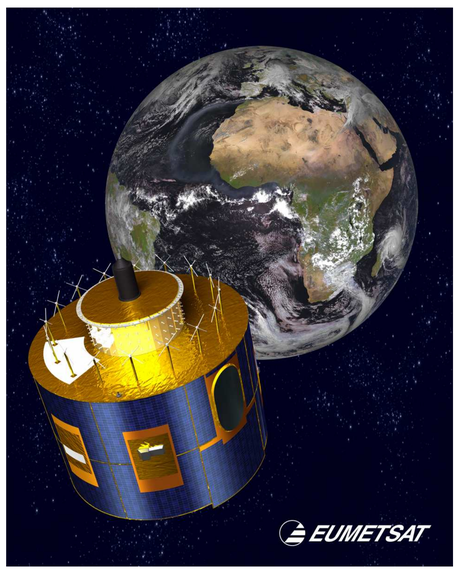

Figure 1: Meteosat Second Generation satellite.

- MSG Cloud mask;
- MSG Cloud physical products (CPP);
- CloudSat.

Results

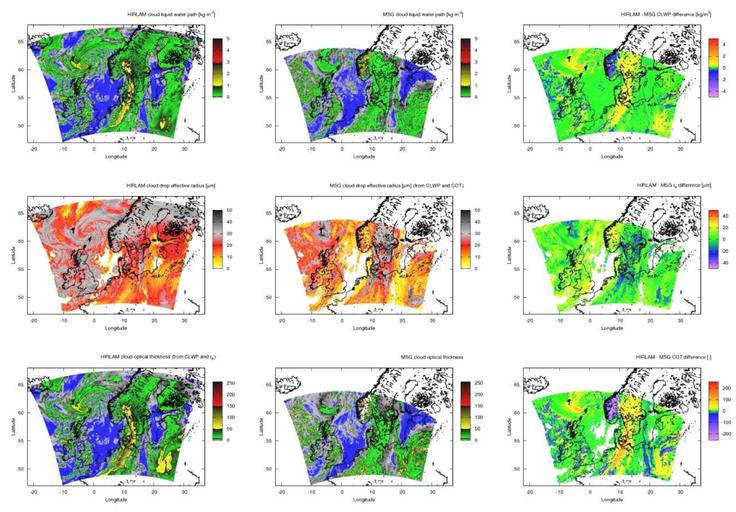

Figure 2: Comparision of DMI-HIRLAM forecast (2009-03-08 00:00 +12h) and MSG CPP data.

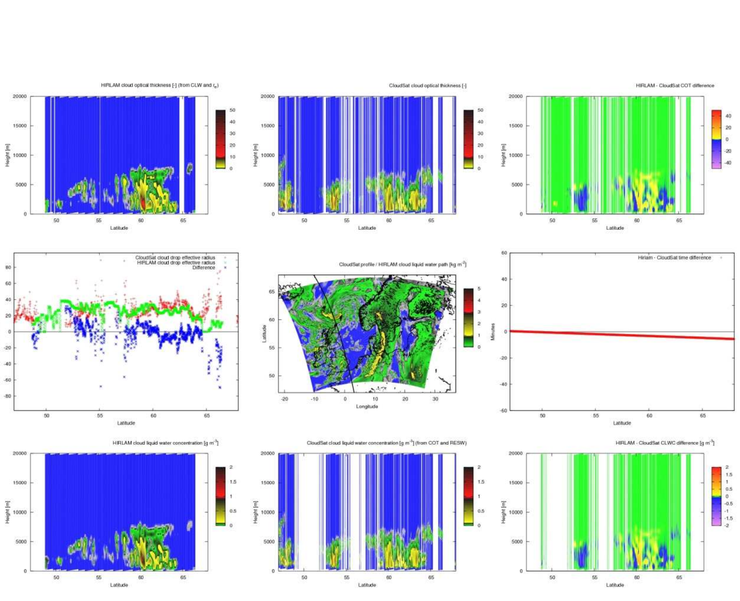

Figure 3: Comparision of DMI-HIRLAM forecast (2009-03-08 00:00 +13h) and Cloudsat CPP data.

Discussion and conclusion

- New satellite products with CPPs are very valuable in NWP verification;
- Continous variables - can be quantified;
- Possible MSG CPP issues:
  - Snow cover in northern Scandinavia - albedo bias.
  - Low sensitivity to high optical thickness ($\tau > 50$).
- Vertical variations of r_e not (yet) available;

Acknowledgements

Rainer Hollman, DWD;

Claus Petersen, Henrik Feddersen, Bjarne Stig Andersen, Mats Dahlblom, Anna Fitch, Xiaohua Yang, Bent Hansen Sass, K. Rune Larsen, Kai Sattler, DMI.

CloudSat Data Processing Center, CIRA;

Rob Roebeling, KNMI;

Kristian Pagh Nielsen, Verification of HIRLAM cloud forecasts with MSG cloud physical products, DMI, 2009

Verification of HIRLAM cloud forecasts with MSG cloud physical products

Kristian P. Nielsen, Danish Meteorological Institute

July 2, 2009

1 Introduction

For the first time, field verification of Cloud Physical Properties (CPP) forecast with Numerical Weather Prediction (NWP) models against measurements from the Meteosat Second Generation (MSG) satellite are presented. In classical observations, clouds are described in terms of 1/8 fractions of cloud cover. The cloud fraction, however, is only one of the factors that determine the reflectance and transmittance of a cloud field. The other factors are the inherent cloud physical properties. In the infrared spectral region, the temperature of the cloud also affects the radiative properties of clouds.

Clouds are affected by virtually all processes in the atmosphere, and they themselves strongly affect radiative forcing and precipitation. Thus, they are both one of the most difficult and important of the meteorological variables to simulate.

Today cloud verification is done by verifying the fractional cloud cover. Such verification does not account for one of the key cloud physical properties: The cloud optical thickness. This property is very important for the transmittance of short wave radiation. If only the cloud cover is considered, a very thick cloud layer is seen as no different from a very thin cloud layer, provided that they both cover 8/8 fractions of a given area. Clearly, this is not satisfactory.

Another problem with verification against cloud cover is that satellite data, *e.g.* the MSG cloud mask product is often given as either

- cloud free,
- partly cloudy, or
- cloudy.

Such data cannot be verified quantifically.

Satellite measurements of CPP, much improves the capability of cloud verification. Recently, algorithms for deriving CPP from MSG data have been made (Roebeling, Feijt & Stammes 2006). The CloudSat satellite data provide detailed tomographies of the clouds in its path (Stephens $et\ al.$ 2008). With these measurements CPP, and thereby processes such as aerosol indirect effects and stratocumulus clouds in the boundary layer can be assessed in detail. Results will be presented and discussed.

2 Theory

The equation of radiative transfer for a given wavelength (λ), direction (μ, ϕ) and optical depth (τ) is given by (Lommel 1889, Chandrasekhar 1960, Thomas & Stamnes 2002)

$$\mu \frac{dI_\lambda(\tau,\mu,\phi)}{d\tau} = I_\lambda(\tau,\mu,\phi) - (1-a(\tau))B_\lambda(T;\tau) - \frac{a(\tau)}{4\pi}\int_{4\pi} d\omega' p(\tau) I_\lambda(\tau,\mu',\phi') - S^*_\lambda(\tau,\mu,\phi) \quad [\frac{\text{W}}{\text{m}^2 \text{ nm sr}}]. \tag{1}$$

Here I_λ is the spectral radiance, $\mu \equiv \cos\theta$ is the cosine of the zenith angle, ϕ is the azimuth angle, a is the single scattering albedo, B_λ is the Planck function, T is the temperature, $d\omega'$ is the differential solid angle for the multiple scattering integral, and S^*_λ is the source function of direct sunlight scattered into the direction (μ, ϕ).

If the *inherent optical properties* (IOPs) are known for the column of interest, including the optical properties of the surface, Eq. (1) can be solved to a high degree of accuracy as shown by Hestenes *et al.* (2007).

The inherent optical properties (IOPs) are

- τ: Optical depth [-], the integrated extinction;
- $a(\tau)$: Single scattering albedo = 1 - emittance [-];
- $p(\tau)$: Phase function [-], for most practical purposes a function of the asymmetry factor only $g(\tau)$ (Henyey & Greenstein 1940).

The surface IOPs in NWP models are generally represented by their *flux albedo* and all surfaces are assumed to be Lambertian (Thomas & Stamnes 2002).

In recent literature the term “cloud albedo” is often used, in particular in relation to aerosol indirect effects (Seinfeld & Pandis 1997). This is a somewhat misleading term since “cloud albedo" or rather *cloud reflectance* is not an inherent optical property, *e.g.* it is important to remember that the same cloud may have a very different reflectance/albedo depending the optical properties of the surface below it; if the cloud is moved from being over the northern Atlantic Ocean to being over the Greenland ice sheet, its reflectance will increase significantly. Sagan & Pollack (1967) stated that:

> “The reflection spectra obtained from dispersed media - both clouds and powders - depend on the monochromatic single-scattering albedo, the single-scattering phase function, the particle-size distribution, the total optical depth, and the albedo of the underlying surface."

Later, it has been shown that it is not necessary to know the complete particle size distribution of clouds. In fact, the cloud IOPs can be adequately derived from only two physical quantities (Hu & Stamnes 1993)

- Cloud liquid water path (CLWP) [kg/m^2];
- Equivalent cloud drop radius (r_e) [μm],

where r_e is defined as the ratio between the third and second moments of the cloud drop size distribution (Hansen & Travis 1974)

$$r_e \equiv \int_0^\infty drn(r)r^3 / \int_0^\infty drn(r)r^2. \tag{2}$$

In the visible spectral range the following inherent optical properties of clouds can be derived from Mie-Debye theory (*e.g.* Ricchiazzi *et al.* 1998)

$$\tau_{vis} = \frac{3CLWP}{2r_e\rho_l}, \quad a_{vis} = 1, \quad g_{vis} = 0.85. \tag{3}$$

In the infrared spectral range the dependencies are more complicated, but parameterizations based on only $CLWP$ and r_e still yield very accurate results (Hu & Stamnes 1993).

These two cloud physical properties are derived in the MSG CPP product (Nakajima & King 1990, Roebeling *et al.* 2006). From the polar orbiting CloudSat satellite the optical thickness (τ_{vis}) of each vertical bin of approximately 240 meters thickness is given as output (Stephens $et\ \ al.$ 2008).

In HIRLAM $CLWP$ and r_e are derived as described by Wyser *et al.* (1999).

3 Results

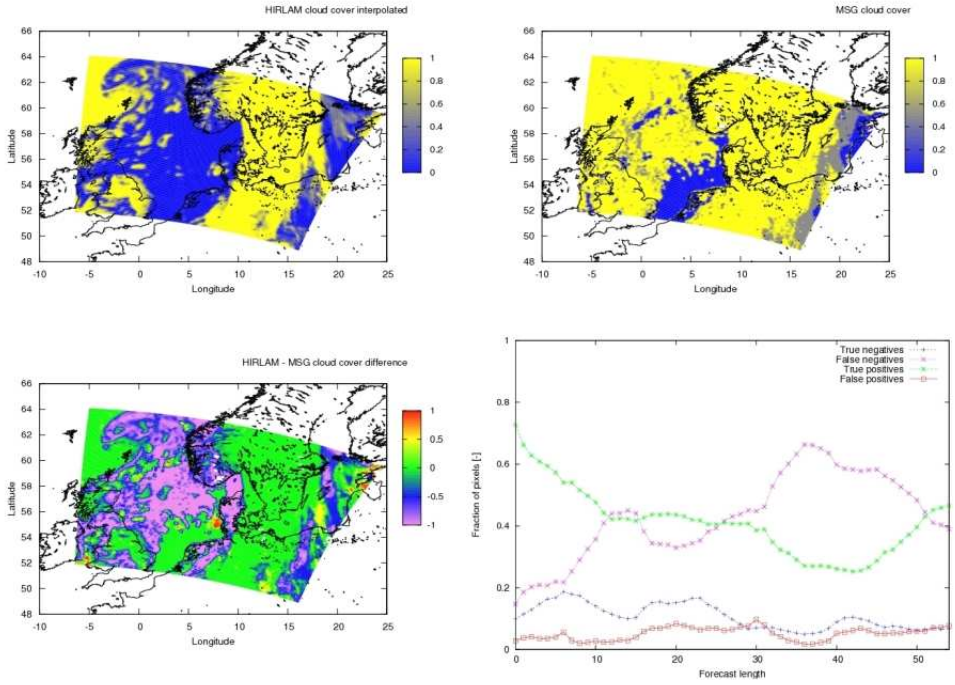

Figure 1: Comparision of DMI-HIRLAM cloud cover and the MSG cloudmask. **Upper left:** *The DMI-HIRLAM cloud cover forecast (2009-03-08 0 UTC +13h).* **Upper right:** *The MSG cloudmask, partially clouded pixels are given a value of 0.5.* **Lower left:** *The difference between the model and satellite data. Negative biases are blueish to purple, while positive biases are yellowish to red.* **Lower right:** *Discrete statistics for all forecast hours run at 2009-03-08 0 UTC. MSG pixels classified as partly cloudy are excluded from this statistics.*

In Fig. 1 an attempt of making quantitative statistics of the HIRLAM cloud cover fraction and the MSG cloud mask product is shown in the lower right panel. This should be taken with a large grain of salt for the reasons mentioned in the introduction section.

From the panels in Fig. 1 a large area with negative bias in the cloud cover over the North Sea is clearly seen. Negative bias in cloud cover over the North Sea is not unusual for the DMI-HIRLAM S model.

In Fig. 2 the CPP comparison for the same forecast as shown in Fig. 1 is shown. The large bias area seen in cloud cover over the North Sea is here seen not to correspond to a large bias in CLWP and τ_{VIS}. In Fig. 2 the most prominent bias is the positive bias and CLWP and τ_{VIS} seen in the frontal area that stretches from Oslo over Denmark to northern Germany. The same area can in Fig. 1 be seen as correctly forecast 8/8 fractions of cloud cover! A similar bias is seen for the smaller front strecthing between the Faroe islands and the Shetland islands.

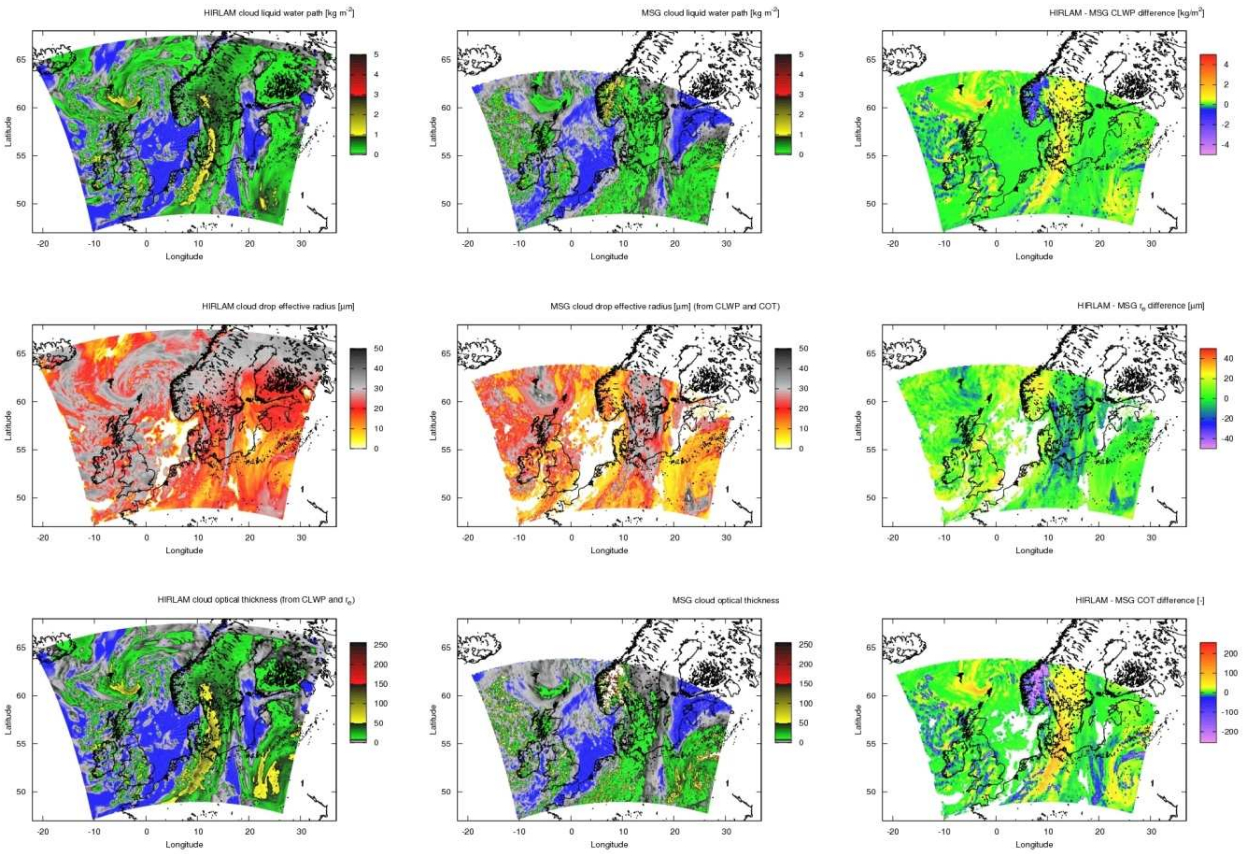

Figure 2: Comparision of DMI HIRLAM and MSG CPP data. **Left column:** *The DMI-HIRLAM CPP forecast for 2009-03-08 0 UTC +13h.* **Centre column:** *The MSG CPP values at 2009-03-08 13 UTC.* **Right column:** *The difference between the DMI-HIRLAM and the MSG CPP.* **Upper row:** *Cloud Liquid Water Path (CLWP) [kg/m^2].* **Centre row:** *Cloud drop equivalent radius, r_e [μm].* **Lower row:** *Cloud optical thickness, τ_{VIS} [-].*

Another prominent bias that can be seen in Fig. 2 is over southern Norway. Here a strong negative bias in CLWP ($\approx$ 3 kg/m^2) and a positive bias in r_e ($\approx$ 20 μm) is found. This from Eq. (3) leads to a negative bias in τ_{VIS} of more than 200.

In Fig. 3 a comparison of the DMI HIRLAM CPP data with the CloudSat CPP data along the CloudSat track across the DMI HIRLAM S area at 13h UTC on the 8th of March 2009 is shown. At this time CloudSat passed over the small frontal structure between the Shetland islands and the Faroe islands. In the frames showing the biases of $\tau_{VIS}/\Delta z$ and cloud liquid water concentration the “double penalty" of verification of high resolution data sets is clearly visible, with negative (bluish) biases scattered among positive (yellowish) biases. For the particular small frontal structure at 60°N, there is, however, a dominating positive bias. In the core of the structure DMI HIRLAM has a cloud liquid water concentration of more than 1 g/m^3, whereas the

CloudSat data show no more than 0.5 g/m^3. This corresponds to the positive bias seen in the CLWP at the same position in Fig. 2.

A negative bias in $\tau_{VIS}/\Delta z$ is seen at 54°N, *i.e.* over the East of England. In the central frame it can be seen that there are clouds over the East of England in the DMI-HIRLAM forecast, but these are laterally displaced eastwards of the CloudSat track.

The differences between cloud drop equivalent radius, r_e, simulated with DMI-HIRLAM and that from the CloudSat product are small along the track of the satellite. This is shown in the centre left frame of Fig. 3.

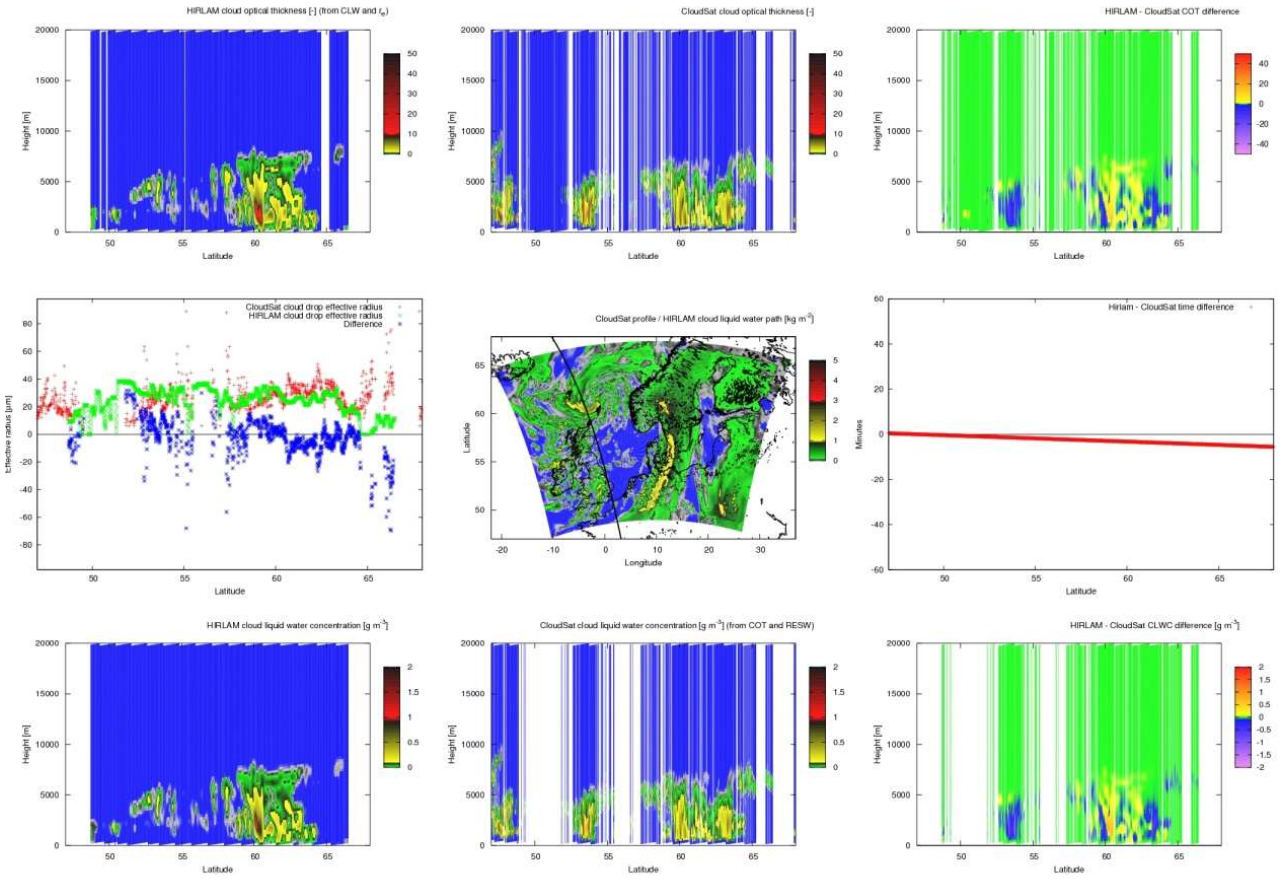

Figure 3: Comparision of the DMI HIRLAM forecast at 2009-03-08 0 UTC +13h and CPP data from the CloudSat satellite at approximately 2009-03-08 13 UTC. **Centre frame:** *The track of the CloudSat satellite across the DMI-HIRLAM S area plotted over the CLWP frame from Fig. 2.* **Centre right frame:** *The time difference in minutes between the forecast and the CloudSat overpass as a function of latitude. 0 minutes marks the forecast time.* **Centre left frame:** *The weigted vertical averages of r_e for DMI-HIRLAM (green points), CloudSat (red points) and the difference between them (blue points) along the CloudSat track as a function of latitude.* **Upper row** *Cloud optical thicknesses per vertical bins, $\Delta z = 240m$, for DMI HIRLAM (left), CloudSat (centre) and the difference between them (right), as a function of latitude and height from 0 - 20000 m.a.s.l.* **Lower row** *Cloud liquid water concentration [g/m^3] for DMI HIRLAM (left), CloudSat (centre) and the difference between them (right) in the same coordinates as the upper row figures.*

4 Discussion

By comparing Figs. 1 and 2 the advantages of using CPP for cloud verification, rather than using the fractional cloud cover only, should be clear: Clouds have a very large range of thicknesses, where an 8/8 fractional cover can represent both a very thin stratocumulus cloud layer or a 10 km thick frontal cloud system. The transmittance of radiation through these two cloud types will be very different. By using new CPP satellite products this shortcoming of fractional cloud cover can be overcome.

In Fig. 2 an area of negative bias is seen over southern Norway. On the 8^{th} of March 2009 the highlands in this part of Norway were covered by snow. The high albedo of a snow covered ground increases the reflectance strongly in the MSG spectral bands used in the MSG CPP algorithm. Therefore, it is likely that the bias is induced by either erroneous assumptions about the surface albedo, or, the heightened uncertainty of CPP retrieval over snow covered areas as described by King *et al.* (2006).

The frontal zones in Fig. 2 have a significant positive bias in CLWP and thereby τ_{VIS}. This could be due to the increasing uncertainty in retrieving the optical thickness of clouds with $\tau_{VIS} > 50$, as discussed by Deneke and Roebeling (2007). The same authors have, however, shown that the CPP retrieval algorithm performs very well, by validating it against surface solar irradiance measurements in the Nertherlands (Deneke, Feijt & Roebeling 2008). Therefore, it is not unlikely that the positive bias of DMI-HIRLAM CLWP is real. Further tests should be performed to certify this.

The CloudSat measurements (Fig. 3) provide cross sections of cloud features. These are extremely valuable for case studies. Their limitation is in the element of luck required that CloudSat has an overpass of the feature of interest at the correct time. Also, as with all tomographies, they give the best information when they are perpendicular to the feature of interest. This, of course, cannot be assured for a CloudSat overpass.

5 Conclusion

New satellite products with cloud physical properties (CPP) have been tested for verification of a NWP model for the first time, and shown to give very relevant information. In particular, many advantages of using CPP for cloud verification over using only fractional cloud cover for cloud verification, have been shown.

This new method of NWP verification is likely to provide information that will help improve parameterizations for cloud microphysics, precipitation and convection.

6 Acknowledgements

Rainer Hollman from Deutsche Wetter Dienst made the MSG CPP data available. The CloudSat Data Processing Center at CIRA provided the CloudSat CPP data.

K. Rune Larsen from DMI set up the ftp-transfer of data to DMI.

Help from colleagues at DMI: Claus Petersen, Henrik Feddersen, Bjarne Stig Andersen, Mats Dahlblom, Anna Fitch, Xiaohua Yang, Bent Hansen Sass and Kai Sattler is also appreciated.

References

Chandrasekhar, S. (1960), *Radiative Transfer*, Dover, New York.

Deneke, H. M., Feijt, A. J. & Roebeling, R. A. (2008), 'Estimating surface solar irradiance from meteosat seviri-derived cloud properties', *Rem. Sens. Environ.* **112**, 3131–3141.

Hansen, J. E. & Travis, L. D. (1974), 'Light scattering in planetary atmospheres', *Space Sci. Rev.* **16**, 527–610.

Henyey, L. G. & Greenstein, J. L. (1940), 'Diffuse radiation in the galaxy', *Ann. Astrophys.* **3**, 117–137.

Hestenes, K., Nielsen, K. P., Zhao, L., Stamnes, J. J. & Stamnes, K. (2007), 'Monte Carlo and discrete-ordinate simulations of spectral radiances in a coupled air-tissue system', *Appl. Opt.* **46**(12), 2333–2350.

Hu, Y. & Stamnes, K. (1993), 'An accurate parameterization of the radiative properties of water clouds suitable for use in climate models', *J. Climate* **6**, 728–742.

King, M. D., Platnick, D. S., Hubanks, P. A., Arnold, G. T., Moody, E. G., Wind, G. & Wind, B. (2006), 'Collection 005 change summary for the MODIS cloud optical property (06_OD) algorithm'.

Lommel, E. (1889), 'Die Photometrie der diffusen Zurückwerfung', *Ann. Phys. U. Chem.* **36**, 473–502.

Nakajima, T. & King, M. D. (1990), 'Determination of the optical thickness and effective particle radius of clouds from reflected solar radiation measurements. part I: Theory', *J. Atmos. Sci.* **47**(15), 1878–1893.

Ricchiazzi, P., Yang, S., Gautier, C. & Sowle, D. (1998), 'SBDART: A research and teaching software tool for plane-parallel radiative transfer in the Earth's atmosphere', *Bull. Amer. Meteor. Soc.* **79**(10), 2101–2114.

Roebeling, R. A., Feijt, A. J. & Stammes, P. (2006), 'Cloud property retrievals for climate monitoring: Implications of differences between Spinning Enhanced Visible and InfraRed Imager (SEVIRI) on METEOSAT-8 and Advanced Very High Resolution Radiometer (AVHRR) on NOAA-17', *J. Geophys. Res.* **111**, D20210.

Sagan, C. & Pollack, J. B. (1967), 'Anisotropic noncoservative scattering and the clouds of Venus', *J. Geophys. Res.* **72**(2), 469–477.

Seinfeld, J. H. & Pandis, S. N. (1997), *Atmospheric Chemistry and Physics: From Air Pollution to Climate Change*, Wiley-Interscience, Hoboken, NJ.

Stephens, G. $et\ al.$ (2008), 'CloudSat mission: Performance and early science after the first year of operation', *J. Geophys. Res.* **113**, D00A18.

Thomas, G. E. & Stamnes, K. (2002), *Radiative Transfer in the Atmosphere and Ocean*, Cambridge University Press, New York.

Wyser, K., Rontu, L. & Savijärvi, H. (1999), 'Introducing the effective radius into a fast radiation scheme of a mesoscale model', *Contr. Atmos. Phys.* **72**(3), 205–218.

Kristian Pagh Nielsen, Bent Hansen sass, Computationally efficient tilted independent column calculations of surface radiation, HIRLAM Newsletter no. 58, September 2011.

Computationally efficient tilted independent column calculations of surface radiation

Kristian P. Nielsen and Bent H. Sass

November 18, 2011

1 Introduction

As numerical weather prediction (NWP) models move to ever higher resolution, it is clear that ever larger errors will occur by using the current 1-dimensional radiation schemes, which keep all radiation calculations within independent vertical columns (Sass 2010). Full 3-dimensional radative calculations are, however, not feasible within the foreseeable future for the computation times required by NWP models. Hence smarter solutions are needed.

Várnai & Davies (1999) suggested that the errors in vertical independent column approximation (ICA) could be alleviated by performing the shortwave radiation calculations in columns tilted toward the Sun. This tilted independent column approximation (TICA) has been found to be a very good approximation for the direct solar radiation at the surface when compared to the results from a cloud-resolving model with full 3-dimensional radation calculations (Wapler 2007; Wapler & Mayer 2008). Wapler (2007) further found that the development of simulated convective clouds were significantly affected by correctly representing the cloud shadows, and, that convective clouds have shorter lifetimes when the TICA is not applied.

The effect of the TICA on super-cell thunderstorms has been studied by Markowski & Harrington (2005) and Frame & Markowski (2010). Oberthaler & Markowski (2010) studied the effect of the TICA on squall lines. They found that correctly representing the cloud shadows affects both the propagation and the structure of the squall lines.

As discussed by Sass (2010) the ICA also causes errors in the calculation of longwave radiation. Here, we will, however, focus only on the issues of shortwave radiation. We have simulated the month of August 2010 with both the DMI-HIRLAM S05 model and a version of this in which the TICA is applied for the calculation of the surface shortwave radiation (DMI-HIRLAM S05 TICA). August 2010 was chosen since several strong precipitation events occured in Denmark.

2 Theory

In order to apply the TICA in the calculation of the shortwave surface calculation, it is necessary to transform all the arrays that are important for this calculation from vertical arrays to arrays tilted toward the Sun. These arrays are: Cloud cover, cloud water, cloud ice, specific humidity and temperature.

(1) and (2) show the equations for the transformed array indices x_{tilt} and y_{tilt} of the tilted arrays as a function of the regular array indices x, y and z.

$$x_{tilt}(x,y,z) = \frac{Z(x,y,z)\tan(\theta_0(x,y))}{\lambda(x,y,z)}\sin(\phi_0(x,y) - \rho_{grid}(x,y)) \tag{1}$$

$$y_{tilt}(x,y,z) = \frac{Z(x,y,z)\tan(\theta_0(x,y))}{\phi(x,y,z)}\cos(\phi_0(x,y) - \rho_{grid}(x,y)) \quad (2)$$

$$\rho_{grid}(x,y) = -\tan^{-1}\left(\frac{\phi(x+1,y)-\phi(x-1,y)}{\cos(\phi(x,y))(\lambda(x+1,y)-\lambda(x-1,y))}\right) \quad (3)$$

ρ_{grid} is the local rotation between the modeling grid and the geographical grid, Z is the geopotential height, θ_0 is the solar zenith angle, ϕ_0 is the solar azimuth angle, ϕ is the latitude and λ is the longitude.

3 Practical issues with parallel computing

The array transformation obviously is limited by the edges of the model domain, at which it is necessary to use the standard vertical array indices. The errors caused by this are of course acceptable, as long as the domain edges are sufficiently far away from the area of interest of the limited area model. When the model physics is parallelized into several sub-domains, however, these errors deteriorate the forecast. An example of this is shown in Figure 1. In sub-domains with clouds at their egdes discontinuities in the surface shortwave radiation are seen.

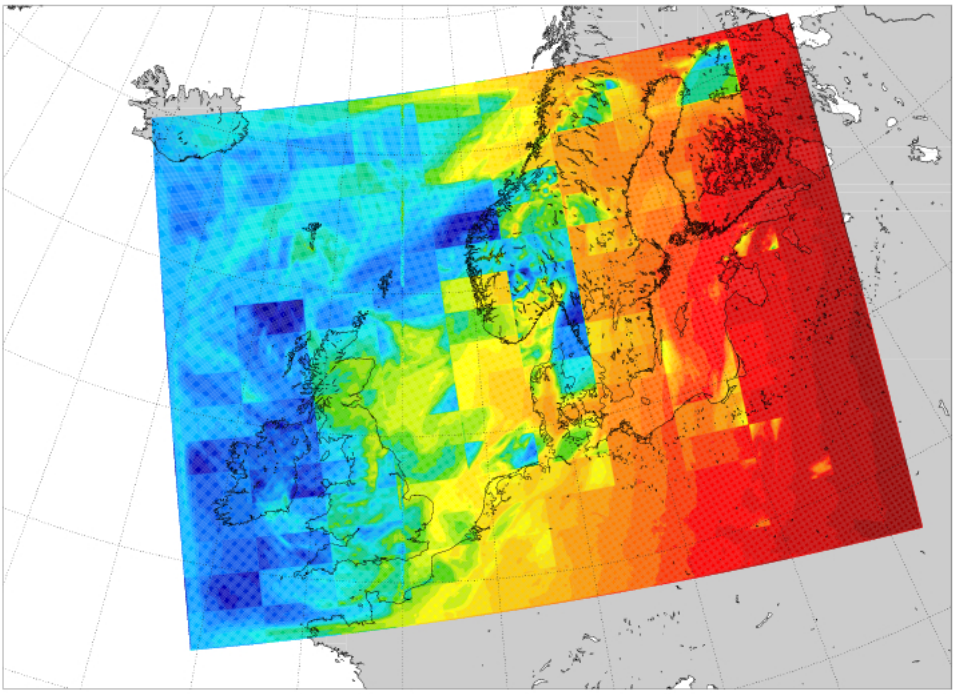

Figure 1: The first parallel processing simulation made with DMI-HIRLAM S05 with tilted arrays. The figure shows surface shortwave radiation in a 2-hour forecast started on 2010-08-01 at 6 UTC.

On the other hand, if the TICA calculations are not parallelized, the computation time increases by several hundred percent.

To solve this problem the halo zone points in the semi-Lagrangian advection scheme were utilized. Thus, the tilted arrays were calculated for sub-domains extended with the semi-Lagrangian halo zones. In

DMI-HIRLAM S05 the halo zones are 8 grid points wide corresponding to more than 40 km. In the simulations from August 2010 this was adequate for removing the effects shown in Figure 1. With the utilization of the halo zones in DMI-HIRLAM S05 TICA this is only 9% slower than DMI-HIRLAM S05.

4 Results and discussion

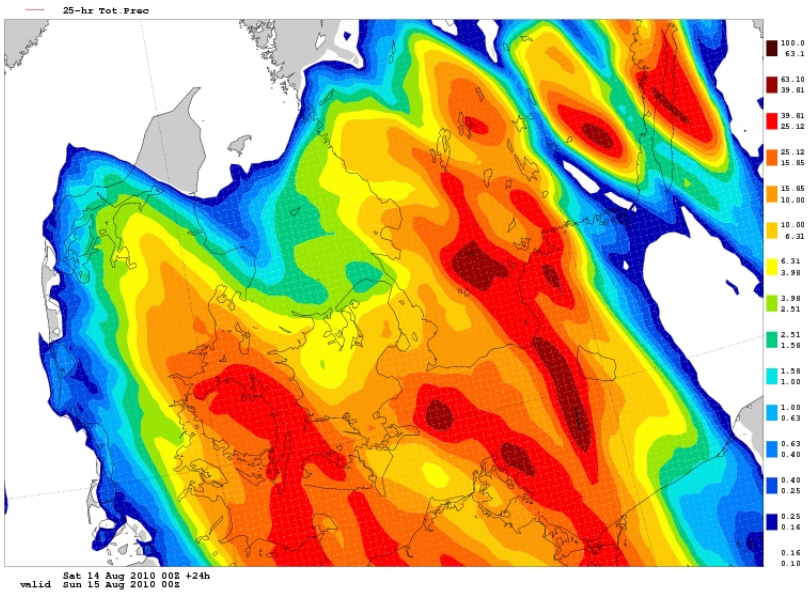

Figure 2: 24 hour accumulated precipitation over Denmark simulated with DMI-HIRLAM S05. The run was started 2010-08-14 at 0 UTC.

In the general verification statistics virtually no differences are seen between the DMI-HIRLAM S05 and the DMI-HIRLAM S05 TICA runs (results not shown here). For the convective events during August 2010, however, significant differences are seen in the precipitation patterns. In Figure 2 and Figure 3 an example of this is shown. Both figures show 24-forecasts of accumulated precipitation on the 14^{th} of August 2010. The difference in accumulated precipitation between the models is shown in Figure 4. Here it can be seen that the difference is up to 33 mm in North-East Zeeland.

Obviously, much cannot be concluded from a few convective cases during a single month. Further studies are needed before it may be concluded whether the TICA is needed in a 0.05° resolution model, or whether it may be sufficient with the regular ICA.

We plan to include the TICA model as a member in the DMI operational ensemble runs, in order to test this further.

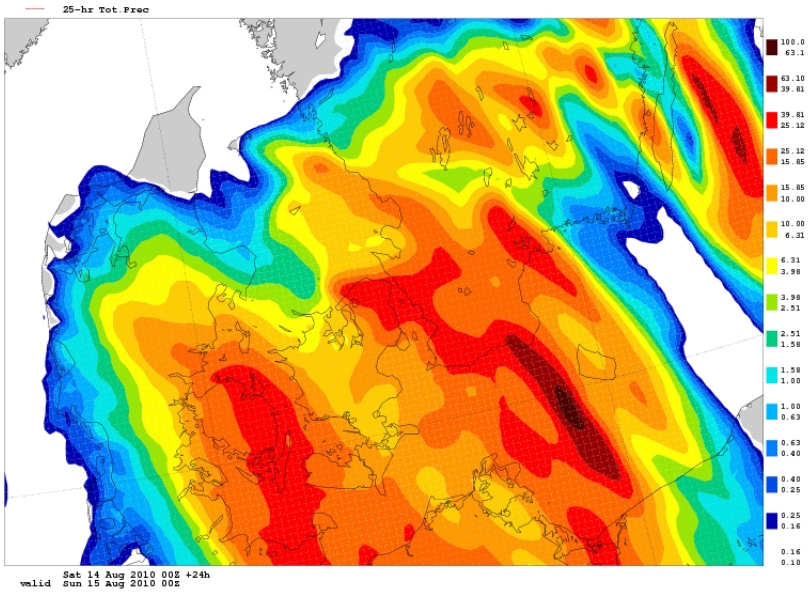

Figure 3: 24 hour accumulated precipitation over Denmark simulated with DMI-HIRLAM S05 TICA. The run was started 2010-08-14 at 0 UTC.

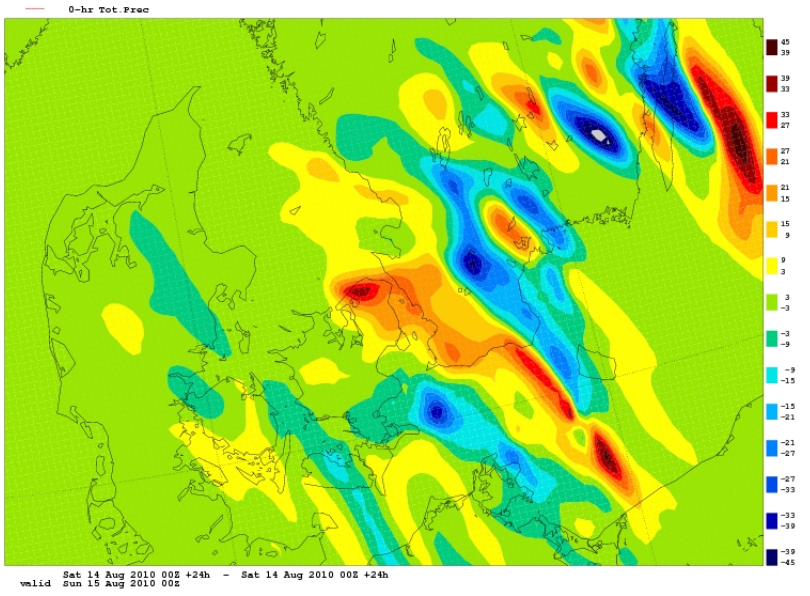

Figure 4: Difference in 24 hour accumulated precipitation over Denmark between the DMI-HIRLAM S05 TICA and the DMI-HIRLAM S05 run. Both runs were started 2010-08-14 at 0 UTC.

5 Concluding remarks

- We have deviced a method for implementing tilted array modeling, which is only 9 % slower than a regular NWP run;

- Tilted array modeling has virtually no effect on the general verification statisics of DMI-HIRLAM S05;
- Tilted array modeling significantly affects the strength and distribution of convective precipitation of DMI-HIRLAM S05;
- Further experiments are needed before anything conclusive can be stated in this matter.

6 Acknowledgements

Helpful suggestions from Ulrik S. Korsholm, DMI, Brian Sørensen, DMI and Copenhagen University, and Xiaohua Yang, DMI, are appreciated.

References

Frame, J., and P. M. Markowski, Numerical Simulations of Radiative Cooling beneath the Anvils of Supercell Thunderstorms, Monthly Weather Rev., 138, 3024–3047, 2010.

Markowski, P. M., and J. Y. Harrington, A Simulation of a Supercell Thunderstorm with Emulated Radiative Cooling beneath the Anvil, J. Atmos. Sci., 62, 2607–2617, 2005.

Oberthaler, A. J., and P. M. Markowski, Simulated squall lines with and without cloud shading effects, *in* 25th Conference on Severe Local Storms, American Meteorological Society, 2010.

Sass, B. H., Cloud/Radiation parameterization issues in high resolution NWP, HIRLAM Newsletter, 55 (B), 23–27, 2010.

Várnai, T., and R. Davies, Effects of Cloud Heteorgeneities on Shortwave Radiation: Comparison of Cloud-Top Variability and Internal Heterogeneity, J. Atmos. Sci., 56, 4206–4224, 1999.

Wapler, K., PhD-thesis: Der Einfluss des dreidimensionalen Strahlungstranportes auf Wolkenbildung und -entwicklung, der Ludwig-Maximilians-Universität, München, Germany, 2007.

Wapler, K., and B. Mayer, A Fast Three-Dimensional Approximation for the Calculation of Surface Irradiance in Large-Eddy Simulation Models, J. Appl. Meteorol. Climatol., 47, 3061–3071, 2008.

Kristian Pagh Nielsen, Testing cloud parametrizations in NWP models against satellite data, HIRLAM Newsletter no. 58, September 2011

Testing cloud parametrizations in NWP models against satellite data

Kristian P. Nielsen

November 18, 2011

1 Introduction

The classical meteorological description of clouds includes descriptive terms such as:

- Cloud cover in octas;
- Low, medium, and high clouds;
- Cloud types.

None of these terms give quantitative information about essential cloud parameters such as the shortwave transmittance, reflectance and absorptance, or the longwave transmittance, reflectance and emittance. Nevertheless, many numerical meteorologists still verify only the cloud cover from their models. Also, many operational meteorologist still use model output of 'high', 'medium' and 'low' clouds rather than utilizing the multilayer cloud output that is available from the models. Often only clouds shaded white as a function of the total cloud cover is presented to the public.

The physical description of clouds gives additional information to the classical description of clouds. Clouds physical properties are given either as 2-dimensional or 3-dimensional arrays. 2-dimensional properties include quantities such as:

- Integrated cloud water path [kg m^{-2}];
- Vertically averaged effective cloud particle size, r_e, [μm];
- Cloud top temperature [K];
- Cloud bottom temperature [K],

of which the former two are essential for the shortwave forcing of the clouds, and the latter two are also important for the longwave forcing of the clouds.

3-dimensional cloud physical properties include quantities such as:

- Cloud water concentration [g m^{-3}];
- Ice phase fraction [-];
- Effective cloud particle size, $r_{e,wat}$/$r_{e,ice}$, [μm];
- Detailed size distribution of cloud particles;

- Detailed shape distribution of cloud particles.

In numerical weather prediction models today, it is standard to include the concentration of cloud liquid water concentration and the cloud ice concentration as global variables. The effective cloud particle size (Hansen & Travis 1974) is, however, only included as a local variable in the radiation schemes of the models (e.g. Wyser *et al.* (1999); Sun & Rikus (1999); Sun (2001)). The shape distribution is important for cloud ice particles, whereas all cloud liquid drops may well be assumed to be spherical. The detailed size distribution of cloud particles has been show to be of little significance for shortwave radiation (Hu & Stamnes 1993). This is due to the fact that the cloud particles are much larger than the wavelength of shortwave radiation. In the longwave spectral region, however, this is not the case, as shown by Mitchell *et al.* (2002; 2010).

As discussed by Nielsen (2010) the inherent optical properties of clouds may be derived, when the physical properties of the clouds are known, *i.e.* the visible optical thickness of a cloud, τ_{vis}, is

$$\tau_{vis} = \frac{3CWP}{2r_e\rho_l}, \tag{1}$$

where CWP is the integrated cloud water path, r_e is the vertically averaged effective cloud partical size, and ρ_l is the density of water. From the inherent optical properties the cloud transmittance, reflectance and absorptance may then be calculated. Even when only the cloud water path and the vertically averaged effective cloud particle size are available, *i.e.* the 2-dimensional physical properties, these are sufficient to give good estimates of the cloud shortwave transmittance, as shown be Deneke *et al.* (2008).

In situ observations of clouds, *e.g.* from aircrafts, provide the most reliable measurements of 3-dimensional cloud microphysical properties (Baker & Lawson 2006; Lawson *et al.* 2006), however, such measurements are for practical reasons very limited in time and space. With recent advances in remote sensing and the launch of the A-Train satellites many more measurements of cloud physical properties have become available (Stephens *et al.* 2002; Stephens *et al.* 2008). In particular, the CloudSat satellite data provide detailed tomographies of the clouds in its path.

Here cloud physical property data will be presented from the European Satellite Application Facility on Climate Monitoring (CM SAF) Cloud Physical Product (CPP) (Roebeling *et al.* 2006) and the CloudSat Radar and Visible Optical Depth (RVOD) product (Wood 2008).

2 Results and discussion

2.1 Testing 2-D cloud physical properties

Figure 1 illustrates the degree of variability in the visible cloud optical thickess in the CM SAF CPP data. In large areas the clouds are optically thin with optical thicknesses between 1 and 10 (grey colors). In other areas local clouds with optical thicknesses over 50 (yellow colors) and 150 are seen (red colors). Such locally optically very thick clouds correspond to convective clouds.

The effect of the variability in cloud optical thickness on the integrated shortwave radiation, *i.e.* the global radiation, is illustrated in Figure 2. Where the measured global radiation is more than 700 W/m^2 at noon on cloud free days, it is less then 100 W/m^2 at noon on other days. This implies a local shortwave radiative forcing of more than 600 W/m^2 on days with optically very thick clouds. Clearly, this shows the importance of getting the cloud optical thickness right in meteorological and climate forecasting.

An example of comparing cloud water path from the HARMONIE Denmark model with cloud water path from CM SAF CPP data is shown in Figure 3. Both have a line of convective clouds going from the North Sea

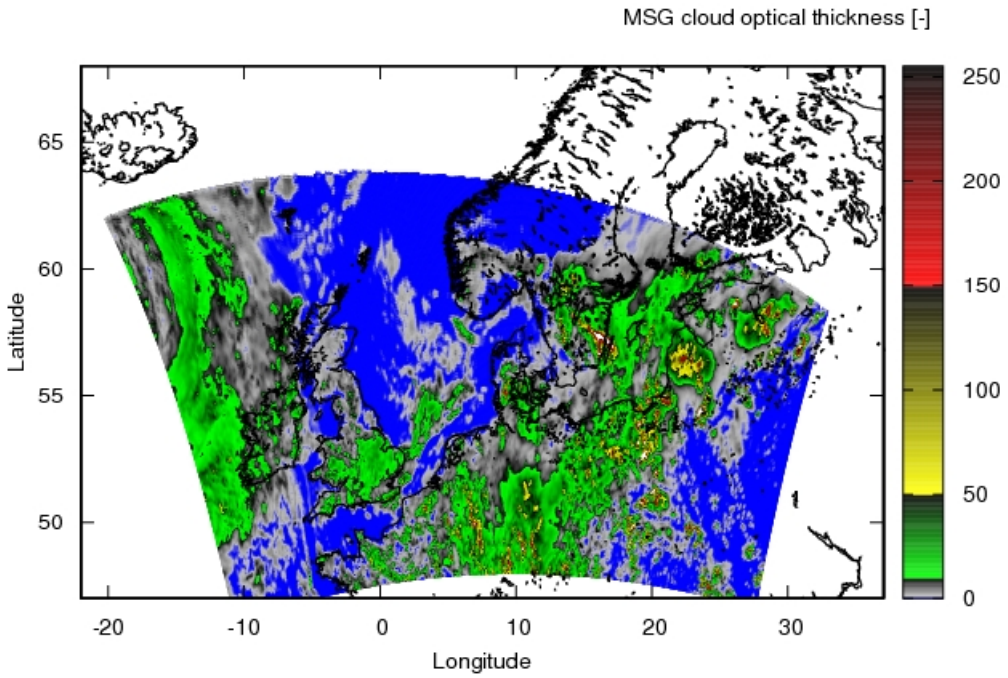

Figure 1: The visible cloud optical thicknesses (τ_{vis}) over NW-Europe on the 23rd of July 2010 at 15:00. The data is from the CM SAF CPP data. The blue color shows cloud free areas, the grey colors $\tau > 1$, the green colors $\tau > 10$, the yellow colors $\tau > 50$, and the red colors $\tau > 150$.

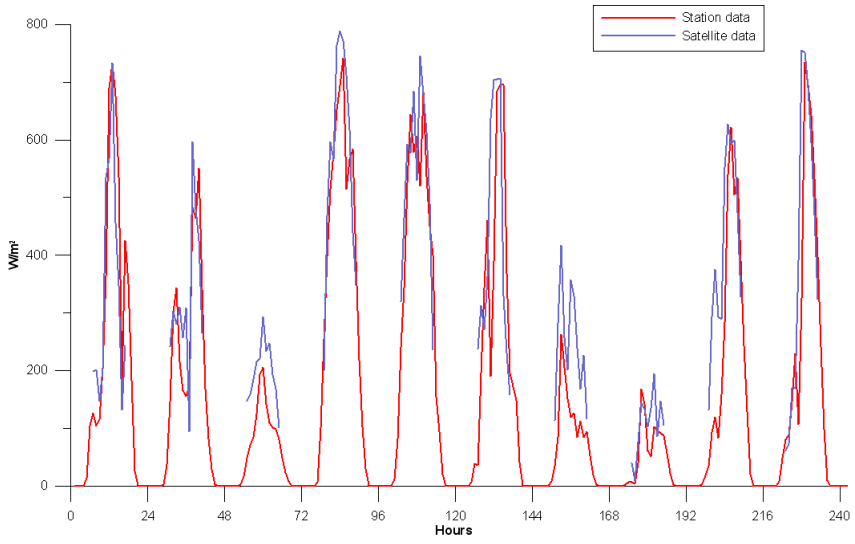

Figure 2: Measured and simulated global radiation at a station in Denmark during a 10 day period in August 2010.

across Southern Jutland to Northern Germany as a distinguishing feature. In the CM SAF CPP data this is,

however a 100 km further north than in the model data. Also, the CM SAF convective clouds contain more water (> 3 kg/m^2) than the modelled convective clouds (1-2 kg/m^2).

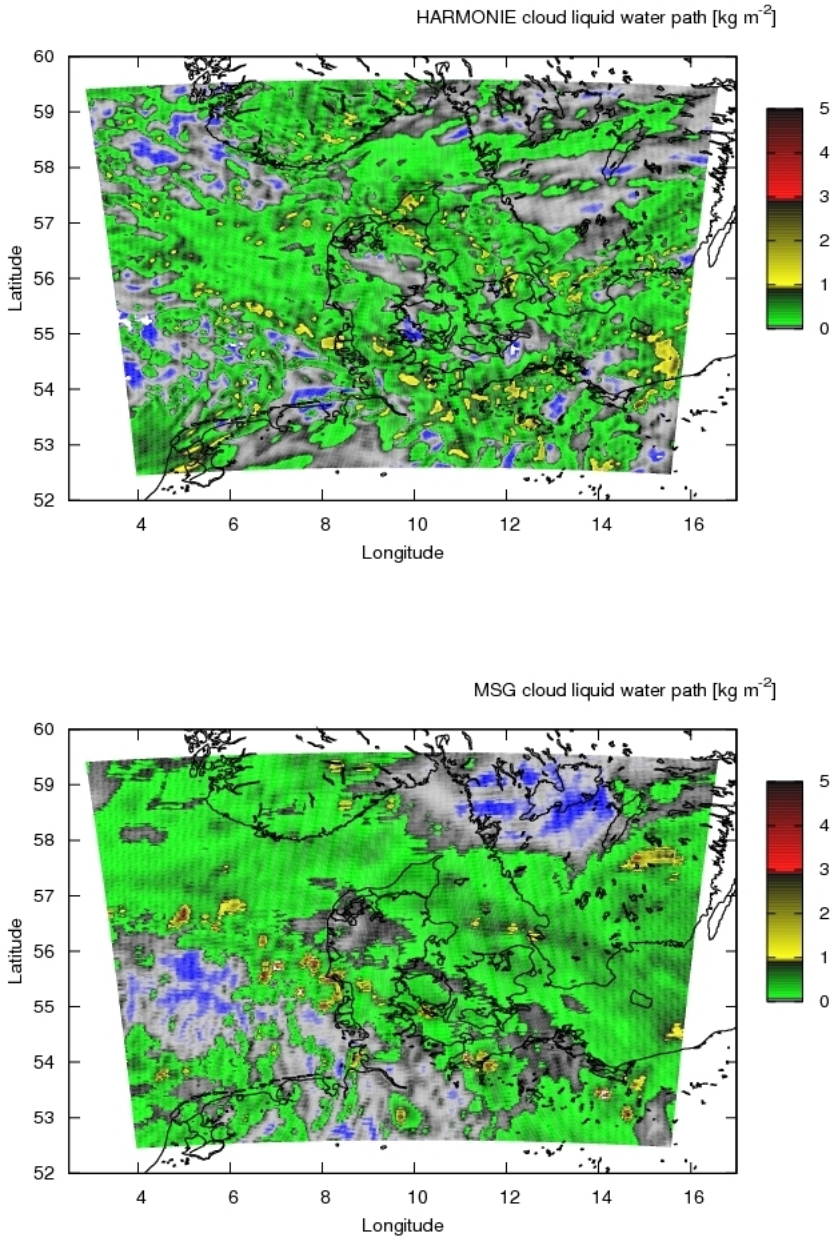

Figure 3: Comparison of modelled cloud water path from Harmonie 33h Denmark and cloud water path from CM SAF CPP. The data is from 2009-09-03 at 11 UTC, and the forecast was started at 0 UTC.

2.2 Testing 3-D cloud physical properties

In HIRLAM the cloud ice effective size is calculated as a third degree polynomial as a function of temperature (Ou & Liou 1995; Wyser *et al.* 1999):

$$r_{e,ice,Ou\&Liou} = 163.15 + 6.21T_C + 0.0985T_C^2 + 0.0006T_C^3, \quad T_C = T - 273.15 \tag{2}$$

The same expression is also an option in HARMONIE.

The CloudSat RVOD product contains both cloud liquid water effective sizes and cloud ice effective size. The latter can be compared to the the parameterization in Equation 2. Such a comparison is shown in Figures 4 and 5.

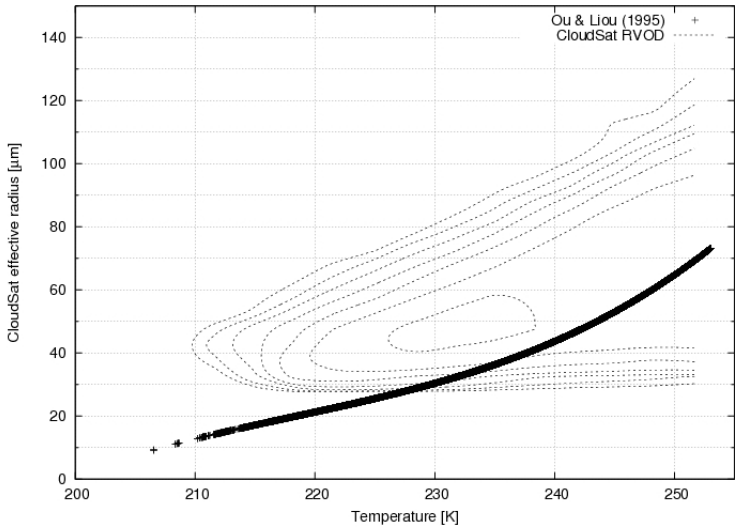

Figure 4: Comparison of 199371 measurements from the CloudsSat RVOD product of $r_{e,ice}$ as a function of the temperature and the equivalent values found with the parameterization of Ou & Liou (1995). The isolines in the plot show the density of the data with the density doubling for each isoline.

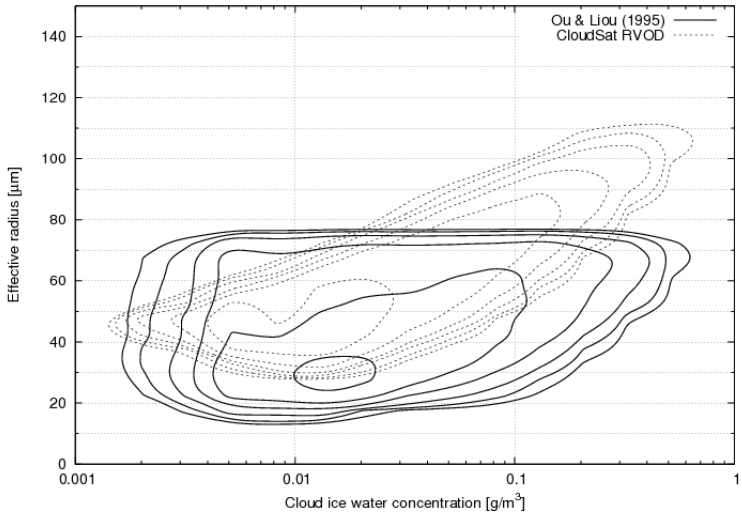

Figure 5: Comparison of 199371 measurements from the CloudsSat RVOD product of $r_{e,ice}$ as a function of the ice water concentration and the equivalent values found with the parameterization of Ou & Liou (1995). The isolines in the plot show the density of the data with the density doubling for each isoline.

(van Zadelhoff *et al*. 2004) showed that radar retrievals of $r_{e,ice}$ become biased if the lower limit of radar reflectivity is too high; unbiased retrievals can be made if the radar can detect signals that are -40 dBZ and stronger. Since the CloudSat radar can only detect signals stronger than -30 dBZ (L'Ecuyer *et al.* 2008). CloudSat estimates of $r_{e,ice}$ have a positive bias for ice clouds with very low ice water contration, *e.g.* high cirrus clouds. This has also been pointed out by (Protat *et al.* 2010), who found that the CloudSat $r_{e,ice}$-bias was 8-12 μm when compared to ground-based radar-lidar retrievals of ice clouds. Thus, the data shown in Figures 4 and 5 may be biased with the CloudSat data being approx. 10 μm too large, and we should be careful with drawing too strong conclusions from these data. Nevertheless - bias or no bias - it is clear that the Ou & Liou (1995) parametrization that is only a function of temperature does not adequately account for the variability of $r_{e,ice}$ as a function of the cloud ice water concentration that is seen in the CloudSat data. Thus, a parametrization that treats $r_{e,ice}$ as a function of both temperature and cloud ice water concentration, such a that of Sun & Rikus (1999) and Sun (2001), is likely to be a better choise than that of Ou & Liou. Here it should be noticed that this is possible to chose in HARMONIE by setting the switch NRADIP to 3.

3 Concluding remarks

- Accurate cloud physical properties in models are essential for prediciting cloud radiative forcing.
- MSG 2D cloud physical properties are useful for verifying NWP models.
- CloudSat 3D cloud physical properties are useful for verifying microphysical parametrizations.

4 Acknowledgements

The CloudSat Data Processing Center is acknowledged for access to the CloudSat RVOD data. Rainer Hollman at the DWD and CM SAF is acknowledged for sending the Cloud Physical Property data. K. Rune Larsen and Kai Sattler at DMI are acknowledged for help the processing of the CM SAF CPP data. Michael Scharling at DMI is acknowledged for the data and the figure of global radation measurements.

References

Baker, B. A., and R. P. Lawson (2006), In situ observations of the microphysical properties of wave, cirrus, and anvil clouds. Part I: Wave clouds, J. Atmos. Sci., 63, 3160–3185, 2006.

Deneke, H. M., A. J. Feijt, and R. A. Roebeling, Estimating surface solar irradiance from meteosat seviri-derived cloud properties, Rem. Sens. Environ., 112, 3131–3141, 2008.

Hansen, J. E., and L. D. Travis, Light scattering in planetary atmospheres, Space Sci. Rev., 16, 527–610, 1974.

Hu, Y., and K. Stamnes, An accurate parameterization of the radiative properties of water clouds suitable for use in climate models, J. Climate, 6, 728–742, 1993.

Lawson, R. P., B. A. Baker, B. Pilson, and Q. Mo, In situ observations of the microphysical properties of wave, cirrus, and anvil clouds. Part I: Cirrus clouds, J. Atmos. Sci., 63, 3186–3203, 2006.

L'Ecuyer, T. S., N. B. Wood, T. Haladay, G. L. Stephens, and P. W. S. Jr., Impact of clouds on atmospheric heating based on the r04 cloudsat fluxes and heating rates data set, J. Geophys. Res., 113, D00A15, 2008.

Mitchell, D. L. (2002), Effective diameter in radiation transfer: General definition, applications, and limitations, J. Atmos. Sci., 59, 2330–2346, 2002.

Mitchell, D. L., R. P. Lawson, and B. Baker, Understanding effective diameter and its application to terrestrial radiation in ice clouds, Atmos. Chem. Phys. Discuss., 10, 29,405–29,447, 2010.

Nielsen, K. P., Verification of hirlam cloud forecasts with msg cloud physical products, HIRLAM Newsletter, 58 (B), 11–17, 2010.

Ou, S., and K.-N. Liou, Ice microphysics and climatic temperature feedback, Atmos. Res., 35, 127–138, 1995.

Protat, A., J. Delanoë, E. J. O'Connor, and T. S. L'Ecuyer, The evaluation of CloudSat and CALIPSO ice microphysical products using ground-based cloud radar and lidar observations, J. Atmos. Oceanic. Tech., 27, 793–810, 2010.

Roebeling, R. A., A. J. Feijt, and P. Stammes, Cloud property retrievals for climate monitoring: Implications of differences between Spinning Enhanced Visible and InfraRed Imager (SEVIRI) on METEOSAT-8 and Advanced Very High Resolution Radiometer (AVHRR) on NOAA-17, J. Geophys. Res., 111, D20, 210, 2006.

Stephens, G. L., et al., The cloudSat mission and the A-train, Bull. Am. Meteorol. Soc., 83, 1771–1790, 2002.

Stephens, G. L., et al., CloudSat mission: Performance and early science after the first year of operation, J. Geophys. Res., 113, D00A18, 2008.

Sun, Z., Reply to comments by Greg M. McFarquhar on 'Parametrization of effective sizes of cirrus-cloud particles and its verification against observations', Q. J. R. Meteorol. Soc., 127, 267–271, 2001.

Sun, Z., and L. Rikus, Parametrization of effective sizes of cirrus-cloud particles and its verification against observations, Q. J. R. Meteorol. Soc., 125, 3037–3055, 1999.

van Zadelhoff, G.-J., D. P. Donovan, H. K. Baltink, and R. Boers, Comparing ice cloud microphysical properties using CloudNET and atmospheric radiation measurement program data, J. Geophys. Res., 109, D24,214, 2004.

Wood, N., Level 2B Radar-Visible Optical Depth Cloud Water Content (2B-CWC-RVOD) process description document, Tech. rep., NASA Earth System Science Pathfinder, 2008.

Wyser, K., L. Rontu, and H. Savijärvi, Introducing the effective radius into a fast radiation scheme of a mesoscale model, Contr. Atmos. Phys., 72 (3), 205–218, 1999.

Sisse Camilla Lundholm, Verification of global radiation forecasts from the ensemble prediction system at DMI, Ph.D. Thesis, 2013

Verification of Global Radiation Forecasts from the Ensemble Prediction System at DMI

Sisse Camilla Lundholm

Centre for Meteorological Modelling
The Danish Meteorological Institute
DMI

The PhD School of Science
Faculty of Science
University of Copenhagen

Denmark

February 18, 2013

To Kasper Vibild

Preface

This thesis was prepared at the Danish Meteorological Institute as part of acquiring a Ph.D. degree in science.

The Ph.D. project is part of the project "Solar/Electric heating systems in the future energy system" guided by the Technical University of Denmark and funded by The Danish Council for Strategic Research.

The thesis consists of two parts separated in time by a year of leave of absence.

København, February 2013

Sisse Camilla Lundholm

Supervisors: Aksel Walløe Hansen and Kristian Pagh Nielsen

Cover image from:
`http://en.cyberdodo.com/files/cyberdodo-and-solar-power/`

Acknowledgements

I would like to thank associate professor Simon Furbo at the Technical University of Denmark and head of the project "Solar/electric heating systems in the future energy system", of which my PhD project is a part, and I would also like to thank "The Danish Council for Strategic Research" under the "Danish Agency for Science Technology and Innovation" for funding the project. I would like to thank all partners within the project especially the Department of Civil Engineering and Informatics at The Technical University in Denmark, Innogie Aps, ENFOR A/S, and COWI A/S for their dedication at our follow-up meetings. I thank DMI for help and support during my work.

I am thankful for being given the opportunity to work on this highly prospective subject.

Abstract

To comply with an increasing demand for sustainable energy sources, a solar heating unit is being developed at the Technical University of Denmark. To make optimal use — environmentally and economically —, this heating unit is equipped with an intelligent control system using forecasts of the heat consumption of the house and the amount of available solar energy. In order to make the most of this solar heating unit, accurate forecasts of the available solar radiation are esstential. However, because of its sensitivity to local meteorological conditions, the solar radiation received at the surface of the Earth can be highly fluctuating and challenging to forecast accurately.

To comply with the accuracy requirements to forecasts of both global, direct, and diffuse radiation, the uncertainty of these forecasts is of interest. Forecast uncertainties can become accessible by running an ensemble of forecasts, and to this end, these three meteorological quantities have since August 2011 been output parameters from the high-resolution ensemble prediction system at the Danish Meteorological Institue.

The appropriateness of complementing forecast values with uncertainty estimates derived from the ensemble forecasts has been assessed by investigating the degree to which the ensemble members and the truth — here materialised by the verifying observation — are statistically indistinguishable. A degree of under-dispersion of the ensemble members is evident concerning global radiation, and the ensemble forecasts will therefore tend to express too little uncertainty in the forecast values. Under-dispersiveness is a well-known problem in ensemble prediction. Uncertainties on obsrvations may cause some of the under-dispersiveness of the ensemble forecasts of global radiation.

Referat (danish)

For at imødekomme en stigende efterspørgsel efter vedvarende energikilder er en særlig solvarmeenhed — udstyret med et intelligent styresystem — under udvikling på Danmarks Tekniske Universitet.

For at få optimalt udnytte af solvarmeenheden — klimamæssigt og økonomisk — anvender det intelligente styresystem prognoser af varmeforbruget i huset og af den solenergi, der er til rådighed. Præcise prognoser af solstrålingen er afgørende for bedst mulig brug af varmeenheden, men på grund af solstrålingens sensitivitet over for lokale meteorologisk forhold kan den være stærkt varierende og vanskelig at forudsige præcist.

I forbindelse med udviklingen af solvarmeenheden er det Danmarks Meteorologiske Instituts (DMI's) — og dermed mit Ph.d.-projekts — rolle at levere præcise prognoser af solstrålingen. En evaluering af prognoser af globalstrålingen og den direkte og den diffuse stråling har afsløret problemer i strålingsskemaet i DMI's HIRLAM modeller, og strålingsskemaet er efterfølgende blevet revideret.

En måde at efterkomme kravene til præcision af prognoser af globalstrålingen, den direkte og den diffuse strålingen, er ved at beskæftige sig med usikkerhederne for prognoserne. Disse usikkerheder kan blive tilgængelige ved at kører et ensemble af simultane prognoser. DMI's ensemble-prognose-system baseret på en højopløsningsmodel beregnet til at opfange lokale detaljer i vejret har siden august 2011 leveret prognoser af globalstrålingen, den direkte og den diffuse stråling.

Egnetheden af de estimater — udledt af ensemblemedlemmerne — af prognoseusikkerhederne er blevet vurderet ud fra en undersøgelse af i hvor høj grad ensemblemedlemmerne og den sande værdi — her observationen — er statistisk uafhængige. Spredningen blandt ensemblemedlemmerne er fundet for lille til at indeholde observationerne med en forventet andel, og ensembleprognoserne vil derfor være tilbøjelige til at give en for beskeden usikkerhed på de forudsagte værdier. For lille spredning blandt ensemlemedlemmerne er et velkendt problem i ensemble-prognose-systemer. En del af den begrænsede ensemblespredning kan muligvis skyldes usikkerheder på observationerne.

Hvad angår RMSE, skill score og diskrimination præsterer ensemble-

midlet bedre ens kontrolprognosen, og det kan være en ide at supplere værdien af en operationel prognose af globalstrålingen, men måske også relevant for andre meteorologiske parametre, med værdien af ensemble-midlet.

Contents

1 Introduction

Under the direction of the Department of Civil Engineering at the Technical University of Denmark, a project with the purpose of elucidating how to best design an individual heating unit based on solar energy was initiated in 2008. This solar heating unit is a so-called smart solar heating unit in the sense that it adjust its heated water volume according to forecasts of the heat consumption of the household and of the available solar energy.

The solar radiation available at the ground (and at the solar collectors) is highly variable due to the dependence on meteorological conditions (Lorenz et al., 2011), and in order to make optimal use — environmentally and economically — of this smart solar heating unit, accurate predictions of the available solar energy are essential. Within this project, the task of the Danish Meteorological Institute (DMI) — and thus my Ph.D. work — is to deliver accurate forecasts of the solar radiation reaching the surface of the Earth.

It is, however, highly challenging to forecast solar radiation at the surface of the Earth accurately even though the position of the Sun in the sky can be determined accurately from astronomical formulas and the transfer of solar radiation through an absorbing and scattering medium like the atmosphere is well established (Paltridge and Platt, 1976; Thomas and Stamnes, 1999). On the way through the atmosphere, the solar radiation interacts with atmospheric constituents such as molecules, ozone, water vapour, aerosols, and cloud particles (water droplets and/or ice particles) (Paltridge and Platt, 1976; Savijärvi, 1990; Stephens, 1984; Wyser et al., 1999), which all attenuate the solar radiation by absorption or scattering. The distribution of cloud particles and aerosols can be difficult to forecast to a high degree of accuracy, and especially cloud particles may reflect a large fraction of the incoming solar radiation (Juan and Da-Ren, 2012; Kasten and Czeplak, 1980).

Different approaches have been used to predict the solar surface radiation depending on the time scale of the forecast. Hammer et al. (1999) used cloud motion vectors derived from consecutive satellite pictures to make very short-range (30 minutes to 2 hours) forecasts of solar radiation reaching the surface. At forecast ranges beyond about 6 hours, numerical weather prediction (NWP) models have been found superior to other alternatives (Perez

et al., 2011). Apparently, the full coherent system of equations describing the evolution of the atmosphere is needed for these longer forecast ranges.

1.1 Ensemble Prediction

An inherent instability of an atmospheric state to small-scale perturbations (Lorenz, 1963) imposes a challenge to NWP forecasting of any meteorological parameter. This atmospheric instability — caused by non-linearity of the atmosphere — introduces a high degree of sensitivity to the initial conditions of an NWP forecast. The observations of the atmosphere, on which the initial conditions of an NWP forecast is based, are typically neither sufficiently exact nor sufficiently dense to consider the initial conditions as known with certainty (Epstein, 1969). Due to the imperfections in the observations, a multitude of nearly identical initial states will all be consistent with the observations, and each of these initial states may in time evolve into considerably different atmospheric states (Epstein, 1969; Lorenz, 1982). Because of the non-linearity of the atmosphere, the fate of NWP forecasting is that small errors in determining the initial state of the atmosphere, may with time lead to a forecasts that diverges from the true evolution of the atmosphere. Epstein (1969) concluded that the atmosphere could not be completely described with a single forecast run due to this uncertainty in the initial state, and in the following decades, the idea of running a collection, or an ensemble, of forecasts initiated from slightly perturbed states emerged (see e.g. Molteni et al. (1996); Toth and Kalnay (1993); Tracton and Kalnay (1993)).

Since the 1990s, ensemble prediction forecasts have become increasingly important as a mean of addressing forecast uncertainty, and ensemble predictions are made at most of the major operational weather prediction centres worldwide including the National Centers for Environmental Prediction (NCEP), the European Centre for Medium-Range Weather Forecasts (ECMWF), the United Kingdom Met Office and Meteo-France. Until recently, the main focus has been on global medium range (typically 10 days) forecasts, but with increased computer resources it has become relevant to pay attention to high resolution ensemble forecasts for a limited area (referred to as LAM models) (Bowler et al., 2008; Díaz et al., 2012; Feddersen, 2009). These model systems have the potential of addressing the uncertainty in both high impact weather and more detailed features of cloud fields and radiation up to about two days ahead (Díaz et al., 2012).

To access the uncertainty of solar radiation forecasts, DMI's high-resolution, limited area (LAM) ensemble prediction system (DMI-EPS) has since August 2011 made forecasts of the incoming solar radiation. DMI-EPS is aimed at capturing small-scale weather features of which a solar heating unit can be expected to be sensitive. Making forecasts of the future and providing

these with estimates of the uncertainty associated with them is fundamental in ensemble forecasting and is in line with the on-going transition within the field of meteorology from point prediction toward distributional prediction (Gneiting et al., 2008).

1.2 Organisation of the Thesis

In addressing the performance of forecasts of solar radiation, this thesis consists of two parts separated in time:

1. A part that describes the identification of shortcomings in the radiation scheme of DMI's NWP models that followed from evaluating model calculations of solar radiation against observations (a work performed during 2009). A short description of the subsequent revision of the radiation scheme finishes this part.

2. A part that describes a detailed verification of ensemble forecasts of solar radiation with the aim of investigating the prospects of complementing the forecasts with uncertainty estimates as derived from ensemble forecasts from DMI-EPS (a work performed during 2011–2012).

The organization of my thesis is as follows:

Chapter 2 describes the smart solar heating unit being the foundation of this work, and the role of the involved partners in developing this solar heating unit.

Chapter 3 defines global, direct, and diffuse radiation and describes the parametrisations of these quantities in the radiation scheme of DMI's NWP models.

Chapter 4 gives a general description of observations and model calculations of global radiation.

Chapter 5 describes the identification of problems of the radiation scheme of DMI's NWP models and the subsequent revision of the scheme.

Chapter 6 describes the configuration of DMI's ensemble prediction system, DMI-EPS.

Chapter 7 describes aspects of forecasts quality used to evaluate the ensemble forecasts.

Chapter 8 verifies by different means the forecasts of global radiation from DMI's ensemble prediction system.

Chapter 9 contains an assessment of the potential of DMI's ensemble forecasts of solar radiation and of the possibility of using the distribution of the ensemble members as estimates of the forecast uncertainties.

Chapter 10 concludes this work and provides some outlooks.

Most data analysis and plotting have been performed with the aid of the language for statistical computing R Development Core Team (2011) and associated packages to R: NCAR - Research Application Program (2010) and Weigel (2010).

2 Prelude: The Smart Solar Heating Unit

The project on developing a smart solar heating unit using forecasts of the heat consumption and the available solar energy is a collaboration between a number of partners. Beside the Department of Civil Engineering at the Technical University of Denmark (DTU) and DMI, other contributors include DTU Informatics (DTU), COWI A/S (*Consultancy Within Engineering, Environmental Science and Economics*), ENFOR A/S (*Forecasting and Optimization for the Energy Sector*), Ohmatex Aps, Ajva Aps, and Innogie Aps (Perers et al., 2009). In this brief description of the project and this smart solar heating unit, the role of the different partners will be outlined.

A solar heating unit illustrated in figure 2.1 includes a solar thermal collector plate and a water tank, where heat can be stored. If the solar energy cannot cover the full heat demand, which in the Danish climate probably will be the case on most days, an electricity based auxiliary energy source, such as an electric heating element or a heat pump, should provide the heat deficiency.

In Denmark, it is expected that an increasing part of the energy consumption in the future will be covered by wind farms (Perers et al., 2009). From the newly negotiated energy agreement (`http://www.kemin.dk/en-US/Climate_energy_and_building_policy_Denmark/energy_agreements/Sider/Forside.aspx`), it is evident that by 2020, just below 50 % of the Danish electricity consumption should be covered by wind energy. This will give an increased number of windy periods with a surplus of electricity and hence low electricity prices. These variable electricity prices, which contains a daily variation, are not yet of benefit to the customer. With the introduction in large scale of wind energy into the Danish electricity grid, fluctuating electricity prices at the customer level are expected to be a reality (Perers et al., 2009). The solar heating unit developed at DTU is optimized to make use of this occasional excess electricity produced in windy periods either through an electric heating element or via a heat pump. The smart solar heating unit can, if used in large numbers, facilitate the introduction of wind energy into the Danish energy system (Perers et al., 2009). In the future electricity

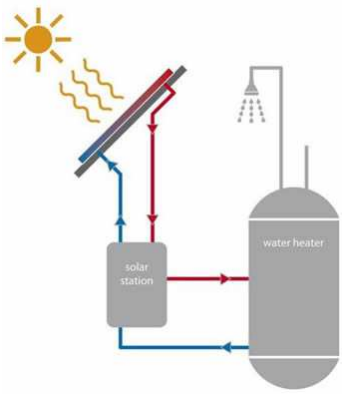

FIGURE 2.1: Illustration of the principle in a solar heating unit; cold water from the bottom of the tank gets heated by the solar collectors and re-enters in the top of the tank, which acts as a storage of energy. The hot water is used for domestic use and space heating (from the two top outlets). Typically, solar thermal collectors make use of solar radiation with wavelengths within the interval $300-4000\,nm$ (Badescu, 2008, Chap. 1), which is referred to as shortwave radiation. Note that here, no auxiliary heating of the water is shown.
The figure is from `http://www.terms-cz.com/en/thermal-collectors.php`.

grid, the customer will, equipped with a smart solar heating unit, be able to benefit from periods of low electricity prices.

In a traditional solar heating tank seen in figure 2.2(a)(left), a fixed volume in the top of the water tank is kept at a certain temperature either by solar energy or by the auxiliary heating. If the solar energy suffices, it also heats the remaining volume of the water. In the smart solar heating unit developed at DTU illustrated in figure 2.2(a)(right), the water is heated from above and has a flexible volume determined by the actual heat demand. This configuration lowers the heat loss of the tank and hence increases the thermal performance of the water tank compared to ordinary solar heating tanks (Furbo and Andersen, 2009). To lower the heat loss further, a strong thermal stratification within the tank is desirable. At the Department of Civil Engineering at DTU, simulations of solar heating units to identify the best design of the water tank, the optimal area of the solar collector, and the financial reduction for the costumer by introducing variable electricity prices have been performed and are described in Perers et al. (2009, 2010). At time of writing, a solar collector area of 9 m^2 and a water tank of 750 l produced by Ajva Aps (as the one seen in figure 2.2(b)) are chosen for the smart solar heating unit. Tests of stratification inlet pipes within the solar water tank resulted in fabric pipes from Ohmatex Aps, which are able to support a thermal stratification. To find the most favorable solution of the

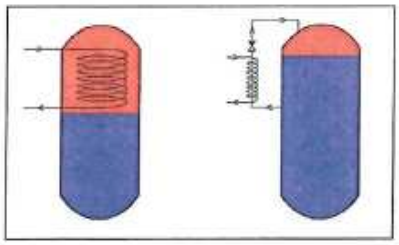

(a) Illustration of solar water tanks

(b) Picture of the solar water tank

FIGURE 2.2: To the left in figure (a), a standard, marketed solar hot water tank with a fixed volume of hot water is illustrated; to the right in figure (a), an advanced solar water tank with a flexible hot water volume heated from above and adjusted to the actual heat demand of the house is illustrated. In figure 2.2(b), a picture of a solar water tank is seen. Figure 2.2(a) is from Furbo and Andersen (2009) and figure 2.2(b) is from (Perers et al., 2011).

auxiliary heating concerning the degree of thermal stratification within the tank and thereby the heat balance of the tank and price of purchase and endurance, three different auxiliary systems are being tested at the test site at the Department of Civil Engineering at DTU.

At COWI A/S, a socio-economic analysis evaluating the advantages to society in terms of cost-savings and reductions in CO_2 emissions of implementing in large scale the smart solar heating unit into the Danish energy system has been performed for different types of houses with respect to the heat demand and for both types of auxiliary heating (electric heating element and heat pump). Without considering expenses to the solar heating unit, a unit using a heat pump as the auxiliary heating performs better with respect to reductions in socio-economic costs and to reductions in CO_2 emissions. The smart solar heating unit has the potential of being an appealing alternative to oil burners and natural gas boilers both from an environmental and an economical point of view (Perers et al., 2009).

Adjusting the hot water volume in the tank to always cover the heat demand requires knowledge of the future heat consumption. In co-cooperation, DTU Informatics and ENFOR A/S have developed a model described in Bacher (2012) to forecast the demand for space heating in a single-family house. The forecast model is based on observations of the space heat consumption in 16 single-family houses in Sønderborg in Denmark, knowledge of the heat dynamics of buildings, and weather forecasts of the ambient, i.e. outdoor, temperature (a low ambient temperature typically increases the heat demand), the global radiation (solar radiation entering through the

windows typically lowers the heat demand), and the wind speed (high wind speeds typically increase the ventilation of the house and thereby increase the heat demand).

If the solar energy available cannot cover the full heat demand of the house, the auxiliary heating will be activated by an advanced control system within the smart solar heating unit. To increase the fraction of solar energy usage in this smart solar heating unit and thereby reduce the use of the electricity based auxiliary heating, the advanced control system should activate the auxiliary heating only when solar energy is insufficient in covering the expected heat consumption and, if possible, only when electricity prices are favorable e.g. in windy periods or at night (Perers et al., 2009). For optimal use environmentally and economically of the smart solar heating unit, the advanced control system needs forecasts of the expected heat production in the solar collectors and forecasts of the electricity prices. Based on weather forecasts of the ambient temperature and of the direct and diffuse components of the solar radiation (described in chapter 3) provided by DMI, DTU Informatics and ENFOR A/S have provided an approach described in Bacher et al. (2011) to obtain forecasts of the heat production in the solar thermal collectors. The solar thermal collectors are sensitive to the characteristics of the solar radiation, that is, the amount and incidence angle of the direct radiation and the amount of diffuse radiation received at the collectors (illustrated in figure 3.1). Using variable electricity prices in an advanced control system, might imply considerable savings at the customer level. Perers et al. (2009) estimate annual reductions in the costs of the auxiliary heating of 300 € at Nord Pool Spot[1] prices. Nord Pool Spot is the Nordic electricity stock exchange, which sell electricity at prices that vary with fluctuating availability. Each day at 13:00 (local time), hourly electricity prices for the next 35 hours are determined.

From measured water temperatures within the tank, forecasts of the future heat demand of the house, forecasts of the disposable solar heat, and future electricity prices, the advanced control system developed by Innogie Aps should decide the optimal solution environmentally and economically of the water volume to heat, by which energy supply, and when. Central to the smart solar heating unit is the delivery of accurate forecasts of the solar radiation provided by DMI. These accurate predictions is the basis of my thesis.

[1] `http://www.nordpoolspot.com`

3 Global Radiation

As solar shortwave[1] radiation traverses the atmosphere of the Earth, interactions between the solar beam and the atmospheric constituents attenuates the solar radiation by either absorption or scattering of the radiation. Radiation that has been subjected to absorption is typically "lost" with respect to the amount of solar radiation penetrating the atmosphere. Radiation that has been scattered one or several times is referred to as diffuse. The remaining unabsorbed and unscattered radiation is called the direct radiation. The total downward solar radiation from the celestial sphere impinging upon a horizontal surface is called the global radiation.

The contributions to the diffuse radiation may vary with the position in the sky (Paltridge and Platt, 1976, Chap. 6), but is approximately isotropic (Paltridge and Platt, 1976, Chap. 6). The direct radiation varies likewise with the position in the sky, but its direction in definite and given by the zenith angle.

For a solar thermal collector, the direction of the direct beam relative to the normal of the solar collector plate is decisive for the amount of energy received at the solar collector. This is not the case for the diffuse radiation, which is approximately isotropic and therefore not sensitive to the slope of the solar collector. This is illustrated in figure 3.1. This difference in sensitivity to the slope of the solar collector between the direct and the diffuse radiation makes a distinction between them necessary.

In NWP models, detailed angular integrations of all the contributions to the diffuse radiation are not feasible. Typically in NWP models, and also the case for DMI's HIRLAM models, the contributions to the diffuse radiation is limited to either upward or downward diffuse radiation.

3.1 Definitions

By use of Paltridge and Platt (1976, TABLE 3), the following components of solar radiation (or solar irradiance) in $\frac{W}{m^2}$ to be used throughout the thesis are defined below.

[1] Radiation with wavelengths less than about 5 μm (Paltridge and Platt, 1976, TABLE 2.3), which constitutes most of the radiation from the Sun.

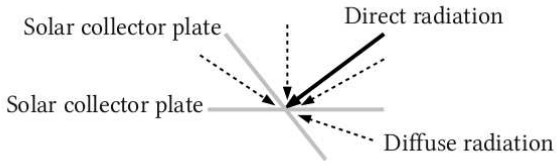

FIGURE 3.1: Illustration of the sensitivity of the direct radiation received at the solar collector to the slope of the collector relative to the direct radiation beam and the insensitivity of the diffuse radiation received at the solar collector to the slope of the collector; the two solar collectors receive (more or less) the same amount of diffuse radiation, but not the same amount of direct radiation.

- Direct normal solar radiation, F_{direct}:
  - solar radiation (or irradiance) that has not been subjected to scattering and is incident upon a surface perpendicular to the direction of the beam.
- Direct horizontal radiation, $F^{\downarrow}_{direct}$:
  - direct normal solar radiation incident on a horizontal surface, that is, $F^{\downarrow}_{direct} = F_{direct} \cdot \cos\theta$, when the angle of the direct solar beam and the normal to the surface is θ (see e.g. figure 3.2).
- Diffuse horizontal solar radiation, $F^{\downarrow}_{diffuse}$:
  - downward solar radiation (or irradiance) incident on a horizontal surface from a solid angle of 2 π (the sky) with the exception of the solid angle subtended by the Sun's disc.
- Global radiation, $F^{\downarrow}$
  - downward solar radiation (or irradiance) incident on a horizontal surface from a solid angle of 2 π (the sky). It is the sum of the direct horizontal, $F^{\downarrow}_{direct}$, and the diffuse horizontal radiation, $F^{\downarrow}_{diffuse}$.

Throughout this thesis, the direct horizontal radiation, $F^{\downarrow}_{direct}$ will be referred to as "direct radiation" and the diffuse horizontal radiation, $F^{\downarrow}_{diffuse}$, will be referred to as "diffuse radiation".

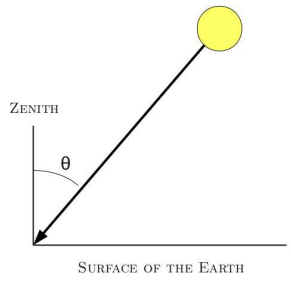

Figure 3.2: Definition of solar zenith angle θ as the angle between a solar beam of radiation impinging upon a horizontal surface and the normal to the surface

3.2 Shortwave Radiation in DMI's HIRLAM models

The attenuation of solar radiation in an absorbing and scattering medium — like the atmosphere — is described by a complex equation, "the transfer equation", involving detailed wavelength and angular integrations of the radiation (Thomas and Stamnes, 1999). To obtain the computational speed required in NWP forecasting, some sort of approximation to the this highly detailed transfer equation is often needed — the degree of which depends on the problem at hand. The transfer of radiation within the atmosphere is in DMI's operational NWP model calculated with a very fast radiation scheme (Savijärvi, 1990; Wyser et al., 1999), wherein the interaction between the solar shortwave radiation and the atmosphere is highly parametrised, and the diffuse radiation is treated as going either up or down. The radiation scheme is documented in Sass et al. (1994).

Since the distance between the Earth and the Sun has an annual change, so does the solar radiation at the Earth's distance from the Sun. This solar radiation is parametrised in terms of the running day from January 1, d, as

$$\begin{aligned} S =& S_0 \cdot (1 + 0.034221 \cdot \cos(\tfrac{2\pi \cdot d}{365}) + 0.00128 \cdot \sin(\tfrac{2\pi \cdot d}{365}) \\ &+ 0.00719 \cdot \cos(2\tfrac{2\pi \cdot d}{365})) \end{aligned} \tag{3.1}$$

(Paltridge and Platt, 1976; Savijärvi, 1990). S is the extraterrestrial radiation normal to the solar beam (Badescu, 2008). The annual change in the Earth-Sun distance and thereby in S is about ± 3.3 % (Paltridge and Platt, 1976, Chap. 3), which amounts to about $\pm 45 \frac{W}{m^2}$. The quantity S_0 is referred to as the "solar constant" and is the total solar radiation (that is, integrated over all wavelengths) at the mean distance of the Earth from

the Sun[2] (Thomas and Stamnes, 1999, Chap. 9). It is, in fact, not a constant and a more appropriate term is "total solar irradiance" (Thomas and Stamnes, 1999). In the radiation scheme of DMI's HIRLAM models, this total solar irradiance, S_0, is equal to 1365 $\frac{W}{m^2}$.

At a given solar zenith angle θ (defined in figure 3.2), the total downward solar radiation, that is, the global radiation (see e.g. chapter 3), received at the top of the atmosphere (toa), $\mathrm{F}^{\downarrow}(\mathrm{toa})$, before any attenuation by absorption or scattering of radiation, is

$$\mathrm{F}^{\downarrow}(\mathrm{toa}) = S \cdot \cos\theta \tag{3.2}$$

by the cosine law. Before atmospheric absorption and scattering, this radiation is all direct and coming from the direction of the Sun. The zenith angle θ (or cosine of the zenith angle) on a given location is parametrised in terms of the latitude, Φ, the solar declination, δ[3], and the local hour angle, $\mathcal{T}$ (described in Paltridge and Platt (1976, Chap. 3)), as

$$\cos(\theta) = \sin(\delta)\sin(\Phi) + \cos(\delta)\cos(\Phi)\cos(\mathcal{T}) \tag{3.3}$$

(Paltridge and Platt, 1976; Savijärvi, 1990). The solar declination, δ, is parametrised in terms of the running day from January 1, d, as

$$\begin{aligned}\delta =& 0.006918 - 0.399912 \cdot \cos(\tfrac{2\pi\cdot d}{365}) + 0.070257 \cdot \sin(\tfrac{2\pi\cdot d}{365}) - 0.006758 \cdot \cos(2\tfrac{2\pi\cdot d}{365}) \\ &+ 0.000907 \cdot \sin(2\tfrac{2\pi d}{365}) - 0.002697 \cdot \cos(3\tfrac{2\pi\cdot d}{365}) + 0.001480 \cdot \sin(3\tfrac{2\pi\cdot d}{365})\end{aligned} \tag{3.4}$$

(Paltridge and Platt, 1976, Chap. 3).

In a clear atmosphere, the diffuse radiation at the surface is found from the empirical formula

$$\mathrm{F}^{\downarrow}_{\mathrm{diffuse}} = 100 \cdot (1 - \exp(-2.865 \cdot \mathrm{h})),$$

where h is the solar elevation, which is $90° - \theta$. This equation an environmental adjustment of an equation in Paltridge and Platt (1976, Chap. 6). The direct radiation at the surface, $\mathrm{F}^{\downarrow}_{\mathrm{direct}}$, is the difference between the global radiation, $\mathrm{F}^{\downarrow}(\mathrm{surface})$, and the diffuse radiation, $\mathrm{F}^{\downarrow}_{\mathrm{diffuse}}(\mathrm{surface})$ at the surface.

[2]The mean distance of the Earth from the Sun is one astronomical unit, which is $1.5 \cdot 10^{11}$ m (Wallace and Hobbs, 2006).

[3]The solar declination is the angle between the plane spanned by the Earth and the Sun and the celestial equator, which is a projection of the terrestrial equator onto a celestial sphere surrounding the Earth. It varies between $+23.5°$ (on June 22) and $-23.5°$ (on December 22) (Paltridge and Platt, 1976, Chap. 3).

Cloud-free atmosphere In a cloud-free atmosphere, the total downward solar radiation received at the ground, $F^{\downarrow}(\text{surface})$, is obtained by reducing the radiation impinging upon the top of the atmosphere, $F^{\downarrow}(\text{toa}) = S \cdot \cos\theta$ according to equation (3.2), by atmospheric absorption (mainly by ozone, water vapour, and absorbing aerosols) and scattering (mainly by atmospheric molecules and scattering aerosols) parametrised as

$$\begin{aligned} F^{\downarrow}(\text{surface}) = \quad & F^{\downarrow}(\text{toa})\big(1 && \text{“top of atmosphere” radiation} \\ & -0.24(\cos\theta)^{-0.5} && \text{absorption by ozone} \\ & -aa \cdot 0.11\big(\tfrac{u}{\cos\theta}\big)^{0.25} && \text{absorption by water vapour and } CO_2 \\ & -as \cdot \tfrac{0.28}{1+6.42\cdot\cos\theta} && \text{atmospheric scatter} \\ & +as \cdot 0.07\alpha && \text{back-scattered reflected beam} \\ & \big) \end{aligned} \tag{3.5}$$

(Savijärvi, 1990). The parametrisation in equation (3.5) takes the following absorption and scattering into account: i) absorption by ozone of ultraviolet and visible solar radiation, the degree of which is determined by the solar zenith angle (and thereby by the path through the atmosphere) as $0.024 \cdot (\cos\theta)^{-0.5}$, ii) absorption of solar radiation by water vapour, CO_2, and O_2, which depends on the (scaled) water vapour amount u and the solar zenith angle, θ as $0.11 \cdot (\frac{u}{\cos\theta})^{0.25}$, iii) atmospheric scatter (in a cloud-free atmosphere this is scatter by atmospheric molecules — also referred to as Rayleigh scatter), which depends on the solar zenith angle as $\frac{0.28}{1+6.43\cdot\cos\theta}$, and iv) downward scatter of the reflected radiation given by $0.07 \cdot \alpha$, when the surface albedo is α. Reflection at the surface gives an upward radiation determined by the incident beam and the surface albedo, $F^{\downarrow}(\text{toa}) \cdot \alpha$. Atmospheric scatter will re-direct a small portion ($F^{\downarrow}(\text{toa}) \cdot \alpha \cdot 0.07$) of the reflected radiation back toward the surface.

Scattering and absorption by aerosols is included by enhancing the water vapour absorption by multiplying with aa, and the atmospheric scattering by multiplying the atmospheric scatter with as. In DMI's operational HIRLAM model, aa and as are equal to 1.2 and 1.25, respectively, thereby increasing the absorption by 20 % and the scattering by 25 %. These values are found by fitting model calculations to observations and should be applicable to North European conditions (Savijärvi, 1990).

Cloudy atmosphere The radiative properties of clouds depend strongly on the size of the cloud particles (Wyser et al., 1999). Compared to large cloud droplets, smaller cloud droplets increase the scatter and reflectivity of the cloud, so that more solar radiation is reflected back to space and less reaches the surface (Wyser et al., 1999). Transmission of radiation through a cloud is parametrised in terms of the vertically integrated cloud condensate (the total amount of water droplets and ice particles (in $\frac{g}{m^2}$)) within the

column of the model containing clouds, the cosine of the zenith angle, $\cos\theta$, and the effective radius, r_e, of the cloud particles. For radiation purposes, the effective radius is an appropriate measure of the average particle size in a distribution of spherical droplets in a water cloud (Wyser et al., 1999).

In calculating the effective radius, r_e, for a cloud, a distinction between cloud droplets and ice particles is made. At a given vertical level, only one effective radius is computed, which should then be representative of all cloud layers above the level in which r_e is calculated. To obtain this, the effective radius is found as a weighted average, where the weights consist of the amount of cloud condensate at the level under consideration normalised by the total amount of cloud condensate from the top of the atmosphere to that level. The full parametrisation of shortwave radiation through clouds can be found in Wyser et al. (1999).

4 Data

4.1 Observations

24 of DMI's pyranometers, situated on different locations in Denmark, measuring global radiation, form the observational basis for the evaluation and verification of global radiation forecasts treated in this work. Location and number of the pyranometers can be seen in figure 4.1. Data from the pyranometers are reported as an average of measurements during the preceding hour.

In the process of verifying model calculations of global radiation against observations, the first step has been to investigate the quality of the observations. For correct measurement of global radiation it is important that the pyranometer is in level (and not tilted toward or away from the Sun) and that the glass dome protecting the pyranometer is clear, see figure 4.2. To ensure the above, the pyranometers are inspected 2-12 times a year (Nordstrøm, 2005). There is in addition a continuous control of data from the pyranometers so that any evidently erroneous values are detected (John Cappelen, personal communication). This gives reasonable expectations to the measurements of DMI's pyranometers, which are of the type Star-pyranometer made in Austria by P. H. Schenk. They are sensitive to radiation with wavelengths in the interval 0.3-3 μm (Nielsen, 2005). After two years of running operationally (which was the case in 2005), the uncertainty on hourly values was reported to be ± 8.4 % at a confidence interval of 95 % (Nordstrøm et al., 2005). This value was found from propagation of uncertainty (Nordstrøm et al., 2005; Taylor, 1997) and a reported stability of 1 % per year of an operational pyranometer (Nielsen, 2005). Here, the uncertainty on the observations is estimated to be 10 %.

4.2 Matching Observations with Model Calculations

Forecasts from NWP models are typically calculated on a horizontal grid. The observations available to evaluate and verify the forecasts are located at points that are (most likely) not coincident with the forecast grid, and

FIGURE 4.1: Location and number of 24 of DMI's pyranometers

FIGURE 4.2: A pyranometer of the type Star pyranometer by Phillip Schenk

in such a case, it is necessary to select a method to match the observations to the forecast grid (Jolliffe and Stephenson, 2012, section 6.2). Two such methods exist: upscaling and downscaling. In upscaling, the observation is compared with the forecast value at the closest grid point thereby preserving the forecasted value and in downscaling, forecast values are calculated often by an interpolation method at the observation point. The result of matching forecast grid points with observation points depends on the method (upscaling or downscaling) being used (Jolliffe and Stephenson, 2012, Chap. 6). Likewise, the choice of downscaling (interpolation method) applied might influence the result of evaluation.

4.3 Model calculations

DMI is a member of the international program HIRLAM (High Resolution Limited Area Model), the aim of which it is to develop, maintain, and improve NWP models for operational use by the participating institutions (information on the HIRLAM corporation can be found at `http://www.hirlam.org`). A HIRLAM model is a high-resolution limited area (that is, covering a small domain) NWP model. At DMI, the HIRLAM models exist in a number of versions differing in horizontal and vertical resolution as well as in geographical coverage.

In 2009, the operational HIRLAM model, S03 (with a horizontal resolution of 0.03°), was nested into the lower resolution HIRLAM model, T15 (with a horizontal resolution of 0.15°), which again was nested into the global low-resolution model, IFS, at ECMWF (European Centre for Medium-Range Weather Forecasts). In 2011, the resolution of IFS was comparable with the HIRLAM model T15, and the S05 model (with a horizontal resolution of 0.05°) used in DMI-EPS is now directly nested into the global

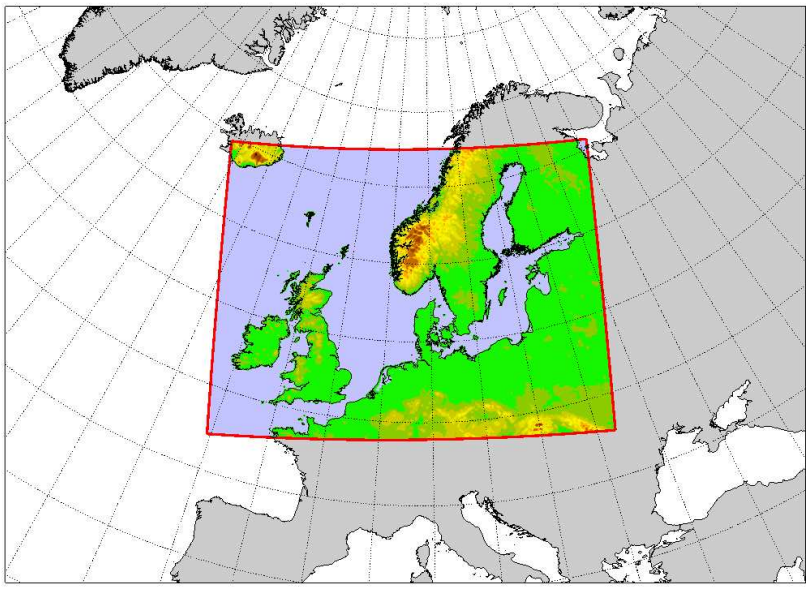

FIGURE 4.3: Model domain of HIRLAM model versions S03 and S05

IFS model. At time of verification, the global IFS model had a horizontal resolution of 0.15°and 91 vertical layers, while the S03 and the S05 models had 40 vertical layers. For model S03, S05, and T15, a new forecast was initiated at 00, 06, 12, 18 UTC. See table 4.1 for details on model setup and figure 4.3 for the model domain of S03 and S05, which are (almost) identical.

In DMI's HIRLAM models, calculations of the accumulated global, direct, and diffuse radiation are provided every hour. In taking differences of the accumulated radiation, values accumulated within the preceding hour are obtained.

4.4 Multidimensional Data

As often in meteorology, a data set contains some kind of multidimensionality — either by forecasts of several weather components at the same location or by the same weather component simultaneously forecasted at different locations, or a combination of this (Jolliffe and Stephenson, 2012). To match the global radiation measurements at the 24 pyranometers seen in figure 4.1, the data set — for either single or ensemble forecasts — consists of forecasts simultaneously predicted at 24 points, and this introduces multidimensionality into the data set.

Model name	**S05**	**S03**	**T15**
Number of vertical layers	40	40	40
Horizontal resolution	$0.05°(\approx 5\ km)$	$0.03°(\approx 3\ km)$	$0.15°(\approx 16\ km)$
Time step	150 s	150 s	400 s
Forecast length	54 hours	54 hours	60 hours
Number of forecasts per day	4	4	4
Global model	IFS	IFS	IFS

TABLE 4.1: Model setup at time of verification

5 Performance of Global Radiation Forecasts

The delivery of accurate forecasts of global, direct, and diffuse radiation to the solar heating unit developed at the Technical University of Denmark initiated an evaluation of the solar radiation forecasts from DMI's HIRLAM models. This evaluation had not previously been performed at DMI and was expected to unveil problems and successes in the model calculations. The performance of global radiation forecasts was evaluated against observations at the 24 DMI pyranometers.

5.1 Data

5.1.1 Observations

The period of verification was April 1 to June 1 2009. Inspection of the observations of this period revealed some obviously incorrect values: i) night values of a few $\frac{W}{m^2}$ over long periods of time and ii) individual values that are unrealistically high and which for some reason slipped through the data control. To compensate for these errors in the observations, night values of global radiation of a few $\frac{W}{m^2}$ have been set equal to zero and unrealistically high values of global radiation have been marked as invalid.

5.1.2 Model Calculations of Global Radiation

To investigate global radiation forecasts from the — at time of verification — operational HIRLAM model S03, a time series matching the observations have been constructed from a 24 hour long forecast for each 00 UTC forecast within the time period April 1 to June 1. Matching forecasts with observations, the method of upscaling (see e.g. section 4.2) has been applied.

It is highly challenging in model calculations to capture small scale clouds. Since they give rise to locally different atmospheric conditions and hence global radiation, some discrepancies between observations and model calculations are expected. To confine these discrepancies, a distinction between clear days and non-clear days is made. April 2009 was in Denmark

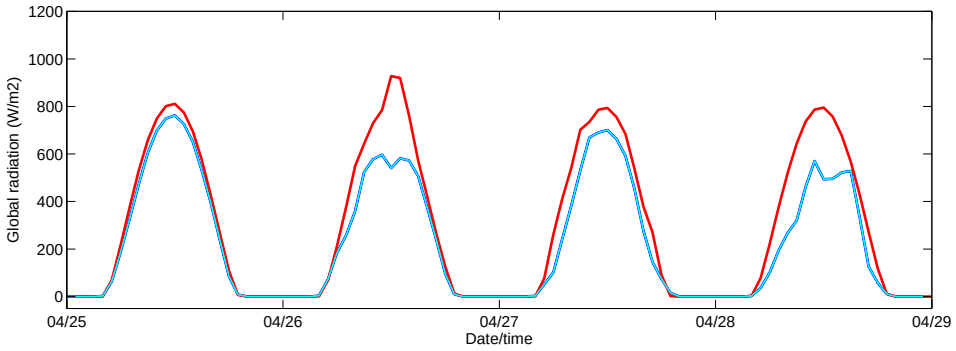

FIGURE 5.1: Global radiation at the verifying location 6188 (Sjælsmark); *blue*: observations; *cyan*: uncertainty on observations (±10.0 %); *red*: model calculations

characterized by sunny weather and is therefore considered appropriate for collecting a statistical sample of clear days[1].

5.2 Comparison of Model Calculations with Observations

Figure 5.1 shows the measured and calculated global radiation at the verifying location 6188 (Sjælsmark in Zealand) (see e.g. figure 4.1) on four days in April. April 25 was a clear day and exhibits the characteristics — a smooth curve peaking at noon — typical of clear days. In general, on clear days, and also valid for April 25, model calculations fit the observations within the uncertainties.

As expected, on cloudy days, the fit between model calculations and observations is reduced. This is illustrated in figure 5.2 for some days in May. The model tends to overestimate the global radiation compared to the observations, which might be related to HIRLAM's tendency to underestimate the cloud cover (Bent Hansen Sass, personal communication). On May 23 and 24, the shape of the curve representing model calculations (red) resembles the curve of the observations (blue), but the timing is a couple of hours off.

On April 26 in figure 5.1, the forecasted global radiation at noon exceeds the "noon-radiation" on clear days. This is the case for several verifying locations, but here only shown for station 6188. These values are unrealistically high and do not agree with observations, which show a depression in the

[1] A "clear day" is here loosely defined as a prevailing clear day, since actually only few days during sunny April 2009 were completely cloud-free in the whole country from sunrise to sunset.

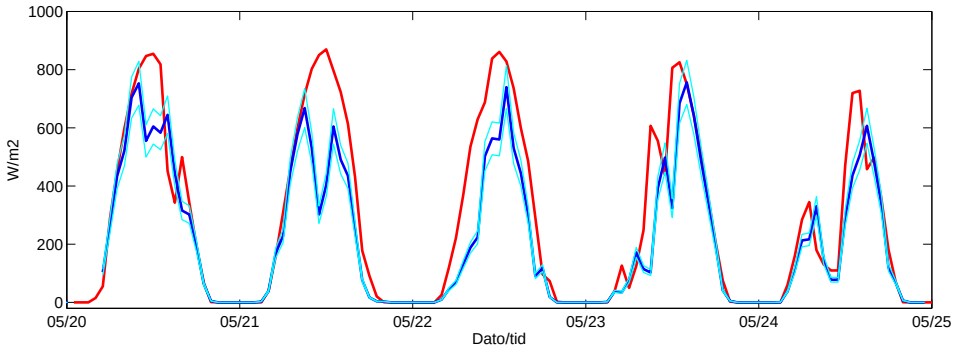

FIGURE 5.2: Global radiation at the verifying location 6188 (Sjælsmark); *blue*: observations; *cyan*: uncertainty on observations (±10.0 %); *red*: model calculations

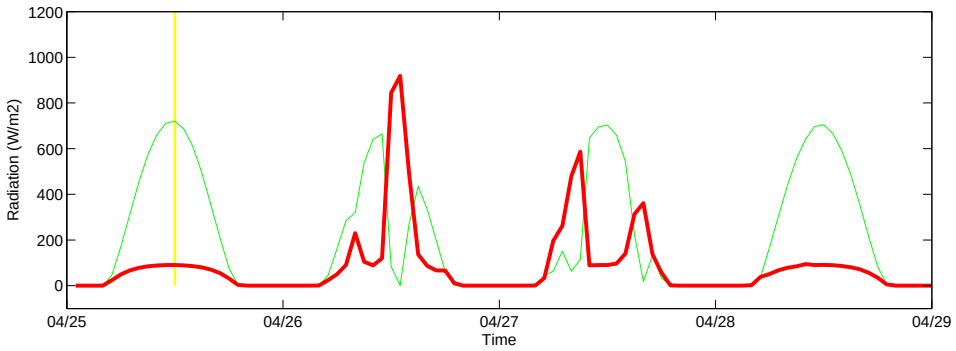

FIGURE 5.3: Calculations from DMI's operational model of diffuse (*thick red*) and direct (*thin green*) radiation at the verifying location station 6188 (Sjælsmark); Yellow, vertical bars mark clear days.

global radiation in the late morning in consistency with satellite pictures[2], which show a cloud cover over northern Zealand around that time.

5.3 Comparing Model Calculations with DTU Observations

Decomposing the global radiation into its direct and diffuse parts and analyzing them separately is expected to give a deeper understanding of shortcomings of the radiation scheme, some of which are displayed on April 26 in figure 5.3. According to figure 5.4, the peak in the calculated global

[2] www.sat.dundee.ac.uk

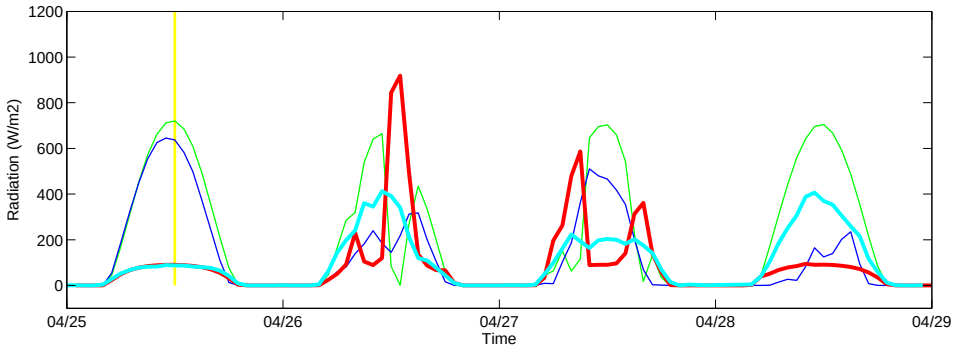

FIGURE 5.4: Calculations from DMI's operational model of diffuse (*thick red*) and direct (*thin green*) radiation at the grid point nearest to DTU and DTU measurements of diffuse (*thick cyan*) and direct (*thin blue*) radiation; Yellow, vertical bars mark clear days.

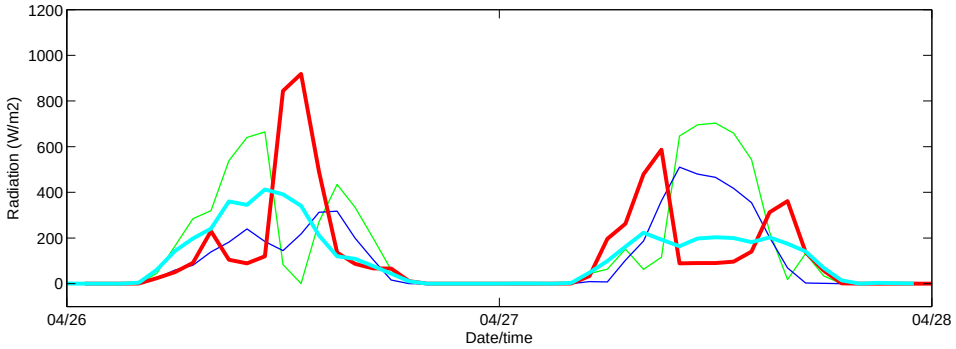

FIGURE 5.5: Zoom in of figure (5.4)

radiation at noon on April 26 consists of only diffuse radiation (the direct radiation is zero).

At DTU, global, direct and diffuse radiation are measured at the weather station at the Department of Civil Engineering at DTU. They have most kindly placed their radiation data from 1 April to 1 May 2009 at disposal for a comparison with DMI's diffuse and direct radiation computations.

In figure 5.4 and 5.5, this peak in global radiation on April 26 with zero direct radiation doesn't agree with DTU observations, which do show a depression around noon in the direct radiation (in accordance with satellite pictures), but which have a value of about 150 $\frac{W}{m^2}$.

Running test cases showed that the radiation scheme of HIRLAM gives 100 % diffuse radiation in case of a complete cloud cover — regardless of the optical thickness of the cloud.

Disagreements between observations and model calculations is also seen

on April 27 in figure 5.4 and 5.5. However, on April 27 the model is to some extent able to capture the shape oF the observations for both direct and diffuse radiation, although the model in general overestimates both quantities compared to the observed DTU values.

Another point to be made from figure 5.4 is that on certain days (e. g. on April 28), the model calculations result in a diffuse radiation typical of a clear day, while DTU observations show elevated diffuse radiation, characteristic of a day with some cloud cover. Satellite pictures[3] confirm the presence of clouds over Denmark for most of that day. The "clear day" seen in the model calculations might be related to HIRLAM's tendency to underestimate the cloud extent and hence overestimate the global radiation reaching the ground (Bent Hansen Sass, personal communication).

5.4 A Revision of the Radiation Scheme in DMI's HIRLAM models

In general, two problems of the radiation scheme have been encountered from this evaluation of global radiation forecasts: i) events of high values of global radiation consisting of only diffuse radiation, which do not agree with observations and ii) events of "clear days" in terms of radiation pattern that disagree with observations.

Since the commence of this evaluation, test cases with a revised radiation scheme by Bent Hansen Sass and Kristian Pagh Nielsen have been performed to deal with i) above. Before the implementation of the changes to the shortwave parametrisations, they made all radiation entering (and leaving) a cloud layer diffuse, and in case of a complete cloud cover, all radiation became diffuse. The revision has enabled a correction of a few errors within the radiation scheme — which should rectify the cases of very high values of global radiation — and has led to a change in the shortwave parametrisations to allow a transmission of direct radiation through a cloud layer depending on the integrated amount of cloud condensate, W, within the cloud, the effective radius, r_e, of the cloud particles, and the solar zenith angle, θ.

The major change in the shortwave parametrisations is to assume an exponential attenuation of the direct radiation traversing a cloud of optical thickness[4] $\tau_{\lambda,z}$[5] as

$$\mathrm{F}_{\mathrm{direct}}(\mathrm{surface}) = \mathrm{F}_{\mathrm{direct}}(\mathrm{at\ cloud\ top}) \cdot \exp(-\tfrac{\tau_{\lambda,z}}{\cos\theta})$$

[3] www.sat.dundee.ac.uk

[4] The optical thickness is a measure of the number and strength of optically active particles — that either absorb or scatter radiation — along the radiation beam (Thomas and Stamnes, 1999, Chap. 2).

[5] The relationship between an optical path, τ_λ, related to the direction of the solar beam, and an optical thickness, $\tau_{\lambda,z}$, related to the vertical axis of a typical NWP model, is given by $\tau_\lambda = \frac{\tau_{\lambda,z}}{\cos\theta}$.

(confer Beer's Law on exponential attenuation of a monochromatic beam of radiation entering an absorbing and/or scattering medium (Paltridge and Platt, 1976; Thomas and Stamnes, 1999) — described in appendix A). The optical thickness, $\tau_{\lambda,z}$, of a cloud can in the visible part of the solar spectrum be approximated by $\tau_{\lambda,z} \approx \frac{3W}{2 \cdot r_e}$ (Stephens, 1984), which gives

$$\mathrm{F}_{\mathrm{direct}}(\mathrm{surface}) = \mathrm{F}_{\mathrm{direct}}(\text{at cloud top}) \cdot \exp(-\tfrac{3W}{2 \cdot r_e \cdot \cos\theta}). \qquad (5.1)$$

Multiplying $\mathrm{F}_{\mathrm{direct}}(\mathrm{surface})$ with $\cos\theta$ gives $\mathrm{F}^{\downarrow}_{\mathrm{direct}}(\mathrm{surface})$.

A combination of a large value of integrated cloud condensate, W, and a small effective radius, r_e, (i.e. a large water content spread over many small cloud droplets) effectively impedes the direct radiation passing through the cloud layer. The cloud is said to be optically thick. The opposite — a small value of W and a large effective radius, r_e, (i.e. a small water content spread over a few large cloud droplets) — allows, to a large extent, transfer of direct radiation through the cloud. By comparison, the cloud is in this case optically thin. This is in accordance with results obtained by Wyser et al. (1999, Figure 2) showing the influence of the integrated cloud condensate, W, and the effective radius, r_e, on the transmission of global radiation through a water cloud.

This new parametrization (equation (5.1)) ensures that optically thin clouds can transfer direct radiation to the ground — also in case of a complete cloud cover. This is illustrated in figure 5.6, where the direct (horizontal) radiation — normalised by the value for zero cloud condensate — received at the surface, $\mathrm{F}^{\downarrow}_{\mathrm{direct}}(\mathrm{surface})$, is plotted against W in a case of a 100 % cloud cover. A value of integrated cloud condensate, W, below about 50 $\frac{g}{m^2}$ allows direct radiation at the ground. With the old radiation scheme, this was not possible, since radiation leaving a cloud was considered as diffuse and in case of a complete cloud cover, all radiation became diffuse.

A highly detailed radiative transfer model, the DISORT model (described in Stamnes et al. (1988)), has been run by Kristian Pagh Nielsen and is included in figure 5.6 for a comparison with the revised radiation scheme of DMI's HIRLAM model. The resemblance between the two is highly satisfying and indicates of a considerable improvement and success of the HIRLAM shortwave parametrisations of direct radiation. Note that the direct radiation from the old radiation scheme would be zero for any value of W in case of a complete cloud cover. This revised radiation scheme is now implemented in DMI's HIRLAM models.

A justification for implementing a simple exponential attenuation of the polychromatic (here, visible) direct radiation (as Beer's law describes for monochromatic radiation entering an absorbing and/or scattering medium — described in appendix A) can be found from the following considerations. When direct radiation enters a cloud, cloud droplets and ice particles attenuate the incident radiation primarily by scatter (Stephens, 1984). In

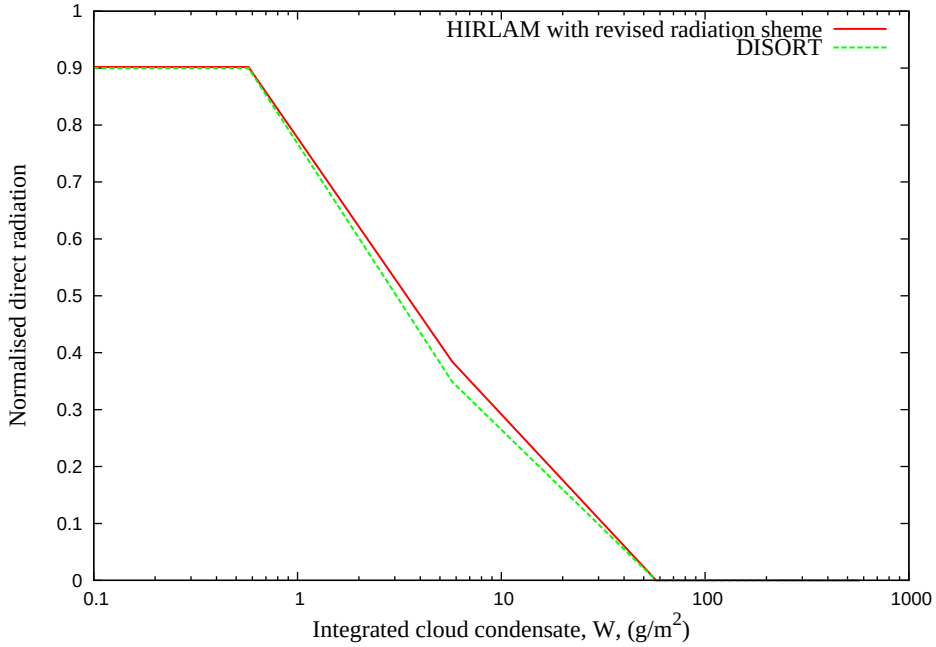

FIGURE 5.6: Normalised direct radiation as a function of the integrated amount of cloud condensate, W, within a 100 % cloud cover from 500 to 1000 m above the surface. The zenith angle is 30°and the surface albedo 0.35. The red full line shows results of the revised radiation scheme and the green dashed line the results of the DISORT model — a highly detailed radiation model in which the number of wavelengths and solid angles in which to discretise equation (A.6)can be chosen.

the visible part of the spectrum, this scatter is to a first approximation independent of wavelength. This condition that all visible wavelengths are scattered equally makes (most) clouds appear white. The transmission of direct radiation through a cloud can (at least in the visible part of the solar spectrum) be considered independent of wavelength, and this makes the application of a simple exponential attenuation of the direct radiation incident at the top of the cloud possible.

The remedy of point ii) above is an improvement in the prediction of clouds — their location, their horizontal and vertical extent, and their exact timing. All this may highly affect the global radiation received at a pyranometer or a solar collectors. The exact location of a cloud, its extent and exact timing might be some of the most difficult parameters to forecast in NWP modelling. Clouds may even appear on such a small scale, that they cannot (yet) be resolved in present NWP models despite their increasing resolution.

6 DMI's Ensemble Prediction System

An NWP forecast is in general subject to forecast uncertainties (or forecast errors) occurring from a combination of i) uncertainties in determining the initial state of the atmosphere arising from inaccuracy and incompleteness in the observations of the atmosphere (Epstein, 1969), and ii) uncertainties arising from deficiencies in the NWP model formulation (Leith, 1974). The information contained in a deterministic forecast is therefore best appreciated if complemented with estimates of these uncertainties in the forecast value.

Deficiencies in NWP models relate both to the errors introduced by the difference in resolution between a numerical model and the real atmosphere — illustrated in figure 6.1 — and to physical processes in the atmosphere appearing on such small scales, that they cannot be resolved by the NWP model (Wilks, 2006, Chap. 6). These physical processes must be parametrized in terms of variables that can be resolved by the model, and since these small-scale processes are often not fully determined by the resolved variable, all parametrisations might introduce uncertainties in the NWP formulation (Wilks, 2006, Chap. 6).

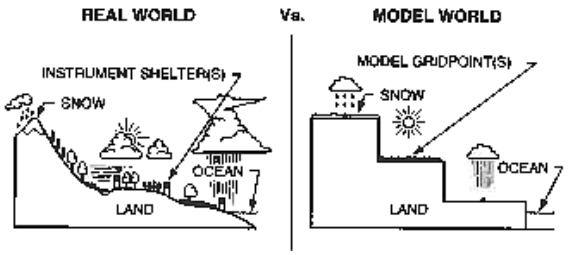

FIGURE 6.1: Illustration of the difference between a real world and the world as represented by an NWP model. From Wilks (2006, FIGURE 6.19)

6.1 Ensemble Prediction

Forecast uncertainties arising from model deficiencies are addressed in developing NWP models and ensemble prediction has (until recently) mainly focused on forecast uncertainties related to uncertainties in determining the initial state in an NWP model.

Because of the uncertainty in determining the initial state of the atmosphere, a multitude of states will all be consistent with the observations. In the high-dimensional phase space of a typical NWP model — in which an estimated state of the atmosphere is a point and its time evolution is along a trajectory in the phase space to another point — this multitude of states can be associated with a probability distribution function (PDF) characterizing the probability of each of these initial atmospheric states. At any time (initial or future), a PDF can be ascribed to the multitude of possible atmospheric states — a multitude in which the true atmospheric state is one. From the initial time to a given forecast time, the initial PDF transforms into a forecast PDF quantifying the uncertainty in the forecast.

A feasible way of addressing forecast uncertainty is by running an ensemble of forecasts initiated from slightly perturbed conditions. At the initial time, the PDF is assumed to be represented by a finite sample of all possible initial states (Molteni et al., 1996). Each of the ensemble members is then integrated forward in time by an NWP model, and at any forecast time, the properties of the PDF are assumed to be described by the ensemble members (Molteni et al., 1996).

Figure 6.2 attempts to illustrate the evolution of both the PDF of a two-dimensional phase space and the ensemble members representing the PDF. At "T = 0", the cyan cross represents the atmospheric state from which a traditional forecast would be initiated. This point in phase space represents only one in a number of atmospheric states all consistent with the uncertainty in the initial state. The PDF of these states is represented by the small ellipse (Wilks, 2006, Chap. 6). A time integration moves the three initial states through phase space along trajectories, which in this case diverge. From "T = 0" to "T = 24", the PDF expands implying less agreement between the three ensemble members on the atmospheric state at "T = 24". The shape, or spread, of the PDF is related to the uncertainty in the forecast. A small ensemble spread would generally imply little uncertainty in the forecast value and thereby a high confidence in it. Conversely, a large ensemble spread would imply large uncertainty and low confidence in the forecast value. In the high-dimensional phase space of a typical NWP model, some directions are associated with states that with time diverge and to sample the forecast PDF appropriately, a degree of dispersion of the ensemble members is necessary (Wilks, 2006, Chap. 7). In figure 6.2, if at "T = 0" the top black cross and the blue cross were sampled as an ensemble, their dispersion at "T = 24" would be too small to represent

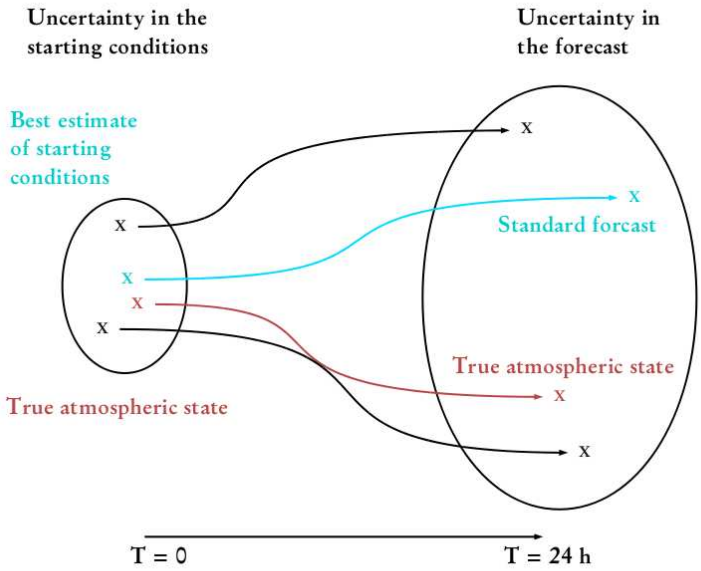

FIGURE 6.2: A simple illustration of the time evolution in a two-dimensional phase space (from 0 to 24 hours) of the true state of the atmosphere (red), and an ensemble prediction system consisting of three members: the standard forecast initiated from the "best estimate" of the initial conditions (T = 0) and two forecasts started from atmospheric states consistent with the uncertainty in the initial state (black). The ovals indicate the PDF and from left to right, its time evolution is illustrated.

The figure is inspired by a figure in: `http://www.metoffice/gov.uk/research/areas/data-assimilation-and-ensembles/ensembles/ensemble-forecasting/explanation`

the forecast uncertainty and to capture the true state of the atmosphere.

Generating ensemble members that at all time (initial and future) describe the features of the PDF, that is, behave as a random sample of the PDF, is the ideal goal in ensemble prediction (Gneiting et al., 2008; Tracton and Kalnay, 1993). If 1) the applied NWP model is accurate and 2) if the ensemble members a the initial time is a random sample of the PDF of the analysis[1] (Gombos and Hansen, 2007), that is, if the ensemble represents the uncertainty in the analysis (Toth and Kalnay, 1993), the ensemble members will approximate the PDF (Molteni et al., 1996; Wilks, 2006) and be able to capture its features. Requirement 2 above ensures that at the initial time, the ensemble members approximates the initial PDF, while requirement 1 ensures that after integrating these ensemble members forward in time, they will approximate the PDF at the forecast time. If the above two requirements are fulfilled, the true state of the atmosphere will behave as one more member of the ensemble, that is, the true state of the atmosphere will be statistically indistinguishable from the ensemble members (Wilks, 2006, Chap. 7). This condition, that the true atmospheric state behaves statistically like any of the ensemble members, is called consistency of the ensemble (Wilks, 2006, Chap. 7). A degree of ensemble dispersion is a prerequisite of ensemble consistency (Wilks, 2006, Chap. 7).

With no a priori information on the uncertainties in the initial state, generating ensemble members that reflect this uncertainty is challenging.

6.1.1 Initial Condition Perturbations

A number of methods differing in complexity of generating the initial ensemble members exist, but they all submit to the following form illustrated for ensemble member $\mathbf{y}_j$

$$\mathbf{y}_j(t=0) \equiv \mathbf{y}_0(t=0) + \delta\mathbf{y}_j(t=0), \tag{6.1}$$

(Buizza et al., 1999), where $\mathbf{y}_0$ is the unperturbed control forecast and $\delta\mathbf{y}_j(t=0)$ is the initial condition (IC) perturbation of the control forecast $\mathbf{y}_0$. The control forecast at time $t=0$, $\mathbf{y}_0(t=0)$, is the most recent analysis. A challenging in ensemble prediction is to generate ensemble pertubations that reflect the uncertainty in the analysis.

A model integration of equations of the type

$$\frac{\partial \mathbf{y}_j}{\partial t} = \mathbf{A}(\mathbf{y}_j, t) + \mathbf{P}(\mathbf{y}_j, t), \tag{6.2}$$

where $\mathbf{A}$ and $\mathbf{P}$ are the dynamic (non-parametrised) and physical (parametrised) processes, respectively, of the ensemble member $\mathbf{y}_j$ from the initial time and

[1] The analysis is the estimated state of the atmosphere that serves as the initial conditions of an NWP forecast.

to a time t gives

$$\mathbf{y}_j(t) = \int_{t=0}^{t} [\mathbf{A}(\mathbf{y}_j, t) + \mathbf{P}(\mathbf{y}_j, t)]dt.$$

Here, $\frac{\partial \mathbf{y}_j}{\partial t}$ in equation (6.2) could be the time derivative of either the velocity components as governed by the equation of motion (or momentum) originating from Newton's second law, of the temperature governed by the thermodynamic energy equation, or the density governed by the continuity equation. Combined, these three governing equations are often referred to as the primitive equations. "**A**" represents the causes of a change as described by the primitive equations and "**P**" represents additional forces from atmospherical processes that are less well described in a typical NWP model. These could be heating by solar radiation, changes of both heat and velocity components due to convection, and changes in velocity components due to turbulence and surface friction.

6.1.2 Model Perturbations

Until recently, the main focus in developing ensemble prediction systems (EPSs) has been on medium-range forecasts (Molteni et al., 1996; Tracton and Kalnay, 1993) that typically cannot resolve local features of the weather. Increased computer resources has created an interest in addressing forecast uncertainties in the local weather by developing short-range, high resolution, limited-area EPSs. These are now evolving rapidly in many centres (Bowler et al., 2008). The use of short-range, high-resolution EPSs has necessitated an additional simulation of deficiencies in the NWP model formulations (Bowler et al., 2008; Buizza et al., 1999). This concerns requirement 1 above. Generating an EPS that takes into account both the uncertainty in the analysis and the imperfections of the NWP model poses an additional challenge to ensemble prediction. Within the last decade, there has been enhanced focus on the effect of model deficiencies on forecast uncertainty, and on how to use ensemble prediction to address these model imperfections. Dealing with model errors in EPS is, however, thought to be an even greater challenge than simulating initial condition perturbations (Bowler et al., 2008).

One approach to simulate forecast uncertainty associated with model deficiencies is to include, besides the initial condition perturbations, multiple NWP models, which could, for example, consists of two or more competing model schemes describing some physical parametrisations (Bowler et al., 2008; Buizza et al., 1999; Feddersen, 2009; Wilks, 2006). Another approach to simulate this uncertainty is to introduce random perturbations to these physical parametrisations (Bowler et al., 2008; Feddersen, 2009; Wilks, 2006). These can be obtained by perturbing the total tendency $\frac{\partial \mathbf{y}_j}{\partial t}$

in equation (6.2) of each ensemble member $\mathbf{y}_j$ in the following way

$$\frac{\partial \mathbf{y}_j}{\partial t} = \mathbf{A}(\mathbf{y}_j, t) + \mathbf{P}(\mathbf{y}_j, t) + r_j(\lambda, \phi, z, t) \cdot \mathbf{P}(\mathbf{y}_j, t). \tag{6.3}$$

The term $r_j(\lambda, \phi, z, t)$ is a stochastic perturbation coefficient with λ and ϕ as horizontal coordinates and z as the vertical coordinate. To limit its growth, the time evolution in the perturbation coefficient $r_j(\lambda, \phi, z, t)$ is generated by an auto-regression model[2] as

$$r_j(\lambda, \phi, z, t + T) = a \cdot r_j(\lambda, \phi, z, t) + s_j, \tag{6.4}$$

where a is a coefficient and s_j is a uniformly distributed random number.

A time integration then gives for ensemble member $\mathbf{y}_j$

$$\mathbf{y}_j(t) = \int_{t=0}^{t} [\mathbf{A}(\mathbf{y}_j, t) + \mathbf{P}(\mathbf{y}_j, t) + r_j(\lambda, \phi, z, t) \cdot \mathbf{P}(\mathbf{y}_j, t)]dt \tag{6.5}$$

starting, (with $t = 0$), from the perturbed initial condition of equation (6.1).

6.2 Construction of DMI-EPS

At DMI, a short-range, high resolution ensemble prediction system (DMI-EPS) has during 2009 been developed and verified for the prognostic parameters temperature, wind speed, and precipitation (Feddersen, 2009).

6.2.1 Initial Condition Perturbations

Because of the limited forecast period of short-range, high-resolution ensemble forecasts, and more complex methods in which the model perturbations are developed in the early part of a forecast (as the singular-vector approach used at ECMWF (Molteni et al., 1996)) may not be suitable and other means of producing the ensemble perturbations must be applied (Bowler et al., 2008). In DMI-EPS, a scaled lagged average forecasting (SLAF) method (described in Ebisuzaki and Kalnay (1992)), to generate the initial perturbations, is used. In the SLAF method, the difference between a very-short-range forecast predicting the present analysis and this analysis (here denoted the forecast error) is used as perturbations ($\delta\mathbf{y}_j(t = 0)$) of the control analysis ($\mathbf{y}_0(t = 0)$) in equation (6.1) to estimate the uncertainty in the analysis. The perturbations have the following form

$$\delta\mathbf{y}_j(t = 0) = \pm\alpha_n(\mathbf{y}_{0_n}(n) - \mathbf{y}_0(t = 0)) \tag{6.6}$$

[2]An auto-regression model is, loosely speaking, a model to predict an outcome of a system at a time $T + t$ from the outcome of the system at a previous time t.

where $\mathbf{y}_{0_n}(n)$ is an n hour old and unperturbed (control) forecast propagated n hours forward in time to predict the present analysis[3]. Equation (6.1) can together with equation (6.6) be translated to

$$\text{initial condition} = \text{analysis} \pm \alpha_n \left(\text{forecast}_{\text{n hour old}}(n) - \text{analysis}\right) \tag{6.7}$$

(Feddersen, 2009).

An old forecast generally has larger forecast errors — it has become less skillful compared to a young forecast. Not to let these larger forecast errors influence the estimates of the uncertainty in the analysis, a scaling factor α is introduced to control the magnitude of the forecast error, so that larger forecast errors of older forecasts are damped more than smaller forecast errors of younger forecasts (Feddersen, 2009; Toth and Kalnay, 1993). Presently, a 6 hour old and a 12 hour old forecast generate through equation equation (6.7) four perturbed initial conditions in addition to the unperturbed control forecast, which have the form

$$\begin{aligned}
\text{IC}_0 &= \text{analysis} \\
\text{IC}_{6^+} &= \text{analysis} + \alpha_6 \cdot \left(\text{forecast}_{6 \text{ hour old}}(6) - \text{analysis}\right) \\
\text{IC}_{6^-} &= \text{analysis} - \alpha_6 \cdot \left(\text{forecast}_{6 \text{ hour old}}(6) - \text{analysis}\right) \\
\text{IC}_{12^+} &= \text{analysis} + \alpha_{12} \cdot \left(\text{forecast}_{12 \text{ hour old}}(6) - \text{analysis}\right) \\
\text{IC}_{12^-} &= \text{analysis} - \alpha_{12} \cdot \left(\text{forecast}_{12 \text{ hour old}}(12) - \text{analysis}\right).
\end{aligned} \tag{6.8}$$

The scaling factors were at time of verification

$$\alpha_6 = 0.80 \quad \text{and} \quad \alpha_{12} = 0.56$$

(Feddersen, 2009).

6.2.2 Model perturbations

In DMI-EPS, the perturbation coefficient, $r_j(\lambda, \phi, z, t)$, in equation (6.4) is allowed to vary horizontally, but not vertically, so $r_j(\lambda, \phi, z, t) = r_j(\lambda, \phi, t)$. To limit calculations, each horizontal domain D has its own perturbation coefficient, r_j, and random number, s_j, (associated with the ensemble member $\mathbf{y}_j$) – denoted by $\langle ... \rangle_D$ in equation (6.9), and T is the time interval between the updates of r_j. This gives the perturbation coefficient

$$r_j(\lambda, \phi, t + T) = a \langle r_j(\lambda, \phi, t) \rangle_D + \langle s_j \rangle_D. \tag{6.9}$$

Values presently employed in DMI-EPS can be found in table 6.1. In order to prevent the perturbation coefficients from escalating in the course of a forecast, r_j is limited to the interval {-0.5, 0.5} as indicated in table 6.1.

[3]Here n, which denotes a previous forecast that predicts the present analysis, is separated from t, which denotes a time integration from the present analysis and into the future, i.e. a forecast.

Parameter	Value
T	45 min
D	53 x 53 grid points
s_j	$\in$ {-0.15, 0.15}
a	0.9
r_j	$\in$ {-0.5, 0.5}

TABLE 6.1: Values used to construct the perturbation coefficients (Feddersen, 2009)

	STRACO		KF/RK		STRACO
	no stoc. phy.	stoc. physics	no stoc. phy.	stoc. physics	stoc. phy. + pert. rough
IC1 = IC_0	1	6	11	16	21
IC2 = IC_{6+}	2	7	12	17	22
IC3 = IC_{6-}	3	8	13	18	23
IC4 = IC_{12+}	4	9	14	19	24
IC5 = IC_{12-}	5	10	15	20	25
group	I	II	III	IV	V

TABLE 6.2: Configuration of the 25 ensemble members in DMI-EPS; IC: initial conditions; use and no use of stochastic physics ("stoc. phys." and "no stoc. phy.") and application of a perturbed roughness length ("pert. rough"); the computation of the initial conditions can be seen in equation (6.8).

In DMI-EPS, the total tendencies $\frac{\partial \mathbf{y}_j}{\partial t}$ in equation (6.3) of the four three-dimensional model variables of temperature, wind speed, humidity and cloud water are randomly perturbed according to equation (6.3) and (6.9).

To simulate model deficiencies, each of the five initial conditions emerging from the application of equation (6.6) and shown in equation (6.8) is combined with two different cloud schemes — the STRACO cloud scheme (documented in Sass (2002)) and the Kain-Fritsch/Rasch-Kristjánsson (KF/RK) cloud scheme (documented in Kain (2004); Rasch and Kristjánsson (1998)) — yielding a total of 10 ensemble members. Model deficiencies are further simulated by subjecting each ensemble member to stochastic perturbations, which increases the number of ensemble members to 20. According to Feddersen (2009), five ensemble members (members 21 to 25) have been dedicated to studying the impact of perturbing the roughness lengths for urban areas in addition to the application of stochastic physics. At the start of a forecast, a roughness length in meters in the interval {0.05, 1.1} is chosen at random for each of the ensemble members 21 to 25. The roughness length for the other 20 ensemble members (1 to 20) is equal to 1. An overview of the configuration of all 25 ensemble members can be seen in table 6.2.

7 A Framework for Forecast Verification

The purpose of forecast verification is to assess the quality of forecasts. Forecast quality describes the association between the forecasts and the corresponding observations for a number of forecast-observation pairs (Wilks, 2006). Forecast quality can be assessed in a number of ways each describing a different aspect of the quality of forecasts. Different approaches of assessing these aspects exist involving both measures and graphical displays.

Approaches of assessing forecast quality have been applied to both individual ensemble members of DMI-EPS as well as their derivatives as the ensemble mean and the ensemble median.

Aspects of forecast quality are described in section 7.1. In section 7.2, a description of some methods to address quality of ensemble forecasts is given.

7.1 Aspects of Forecast Quality

7.1.1 Traditional Measures of Forecast Quality

The more traditional measures of forecast quality applicable to continuous forecasts of a scalar variable (Wilks, 2006, Chap. 7) includes forecast bias, forecast accuracy, and forecast skill.

Bias

Forecast bias describes any systematic deviation between a forecast y and a matching observation x and is often measured by the mean error (ME), which is given by

$$\mathrm{ME} = \frac{1}{N}\sum_{i=1}^{N}(y_i - x_i). \tag{7.1}$$

In the forecast example illustrated in table 7.1, the forecasts display no bias since the difference between the mean of the observations and the mean of the forecasts is zero.

Accuracy

Forecast accuracy is often measured by the mean squared error (MSE) or its related root mean squared error (RMSE), which are defined as

$$\begin{aligned} \text{MSE} &= \frac{1}{N}\sum_{i=1}^{N}(y_i - x_i)^2 \\ \text{RMSE} &= \sqrt{\text{MSE}} \end{aligned} \tag{7.2}$$

respectively. Both ME, MSE, and RMSE will be equal to or above zero. They are all negatively oriented, so that small values are preferred to large values, and for perfect forecasts MSE, and RMSE, are all equal to zero. In the forecast example in table 7.1, the forecasts are not completely accurate, since neither MSE (nor RMSE) is zero. In taking the square in the MSE, and hence in the RMSE, large deviations between forecasts and observations will be highly penalised.

Skill

Forecast skill is often measured by a forecast skill score, SS, which is a relative accuracy measure, that is, the accuracy of a set of forecasts relative to a set of unskillful reference forecasts (Jolliffe and Stephenson, 2012; Wilks, 2006). For a given set of forecast-observation pairs, the skill score for a measure of accuracy, A, (which could be MSE or RMSE) with respect to the accuracy measure for a set of unskillful reference forecasts, A_{ref}, is

$$\text{SS} = \frac{\text{A} - \text{A}_{ref}}{\text{A}_{perf} - \text{A}_{ref}} \cdot 100\ \%, \tag{7.3}$$

where A_{perf} is the value of the accuracy measure that would be obtained for a set of perfect forecasts (Wilks, 2006, Chap. 7). The unskillful reference forecasts might be climatology or persistence (Wilks, 2006, Chap. 7). Skill scores, as defined here, can be interpreted as a percentage improvement over the unskillful reference forecasts.

In this work, a skill score based on MSE is generated. According to equation (7.3), the skill score can be written as

$$\text{SS} = \frac{\text{MSE} - \text{MSE}_{ref}}{\text{MSE}_{perf} - \text{MSE}_{ref}} \cdot 100\ \% = \left(1 - \frac{\text{MSE}}{\text{MSE}_{ref}}\right) \cdot 100\ \%. \tag{7.4}$$

The last equation follows from MSE being zero for perfect forecasts, that is $\text{MSE}_{perf} = 0$. If the MSE for the forecasts being evaluated equals the MSE for perfect forecasts, that is, $\text{MSE} = \text{MSE}_{perf}$, the skill score attains its maximum value of 100 %. If the forecast MSE equals the MSE for the unskillful reference forecasts, that is, $\text{MSE} = \text{MSE}_{ref}$, SS = 0 %, implying

Forecast	Observation
2.0	1.0
2.0	3.0
2.0	0.0
2.0	4.0

TABLE 7.1: A simple example illustrating forecasts with corresponding observations; the values could be *mm* of rain.

that the forecasts contain no improvement compared to the unskillful reference forecasts (Wilks, 2006, Chap. 7). If the forecasts being evaluated are inferior to the unskillful reference forecasts, the skill score becomes negative, so SS < 0 % (Wilks, 2006, Chap. 7).

7.1.2 General approach to Forecast Verification

The framework of verification introduced by Murphy and Winkler (1987), offers a general approach to forecast verification with access to other aspects of forecast quality than those described above. This approach of verification is based on the joint distribution of forecasts and observations. Denoting observations by x — and a specific value by X — and forecasts by y — and a specific value by Y, $p(x, y)$ denotes the joint distribution of all relevant values of X and Y. This joint distribution $p(x, y)$ contains information about the forecasts, the observations, and the relationships between the forecasts and the observations (Murphy et al., 1989). For a given data set, the joint distribution $p(x, y)$ is represented by a distribution of the relative occurrences (or relative frequencies) of the simultaneous events of forecasting a specific value Y, while observing a specific value X for all relevant combinations of X and Y.

Any joint distribution can be factored into a conditional and a marginal distribution in two ways (Murphy and Winkler, 1987; Wilks, 2006). The information contained in the joint distribution, $p(y, x)$ becomes more accessible, when it is factored in either of these ways (Murphy and Winkler, 1987; Murphy et al., 1989; Wilks, 2006).

One factorization is the *calibration-refinement* factorization, which has the form

$$p(x, y) = p(x|y) \cdot p(y) \tag{7.5}$$

(Murphy et al., 1989; Wilks, 2006). This factorization of $p(x, y)$ involves the conditional distribution $p(x|y)$, which is the distribution of the observations given a forecast value y, and the marginal distribution of the forecasts $p(y)$. The other factorization is called the *likelihood-base rate* factorization and has the form

$$p(x, y) = p(y|x) \cdot p(x) \tag{7.6}$$

(Murphy et al., 1989; Wilks, 2006). It involves the conditional distribution $p(y|x)$ of the forecasts given an observed value x and the marginal distribution of the observations $p(x)$.

Reliability

Forecast reliability (or forecast calibration) is related to the conditional distribution of the observations associated with a specific forecast value, Y, $p(x|y = Y)$ in equation (7.5) (Murphy, 1993).

Forecasts possess good reliability by a high degree of similarity between the mean of the observations associated with a specific forecast Y, $E(x|y = Y)$, and that forecast value Y (Murphy et al., 1989). According to Murphy (1993), evaluation of reliability can assess a question like this: "Does the mean observed temperature on those occasions on which the predicted temperature is 10°C correspond to that value?". If

$$E(x|y = Y) = Y \quad \text{for all} \quad Y, \tag{7.7}$$

where $E(x|y = Y)$ is the expected (or mean) value of the observations given a specific forecast value Y, the forecasts are said to be completely reliable (or perfectly calibrated) (Murphy and Winkler, 1987; Murphy et al., 1989). In table 7.1, the forecasts are completely reliable, since the mean of the observations on those occasions on which the predicted amount of rain is 0.2 equals 0.2.

In forecasting, two types of bias might be present: i) unconditional (or systematic or overall) bias and ii) conditional bias, that is, a forecast bias that depends on (or is conditional on) the forecast value. A presence of either of these biases imply a lack of reliability of the forecasts, which can be appreciated from the following considerations by use of the reliability criterion in equation (7.7). In a case of 10 forecasts, $Y_1, \ldots, Y_{10}$, if

$$\begin{aligned} E(x|y = Y) \quad &> \quad Y \text{ for } Y_1, Y_2, Y_3, Y_4, \text{ and } Y_5 \\ &\text{and} \\ E(x|y = Y) \quad &< \quad Y \text{ for } Y_6, Y_7, Y_8, Y_9, \text{ and } Y_{10} \end{aligned} \tag{7.8}$$

the forecasts values $Y_1, \ldots, Y_{10}$ are said to be conditionally biased (Murphy et al., 1989) and are not completely reliable according to equation (7.7). If

$$E(x|y = Y) > Y \text{ for } Y_1, \ldots, Y_8, \tag{7.9}$$

the forecasts $Y_1, \ldots, Y_8$ suffer from an unconditional (or a systematic or an overall) bias and the forecasts, $Y_1, \ldots, Y_{10}$, are not completely reliable — again with reference to equation 7.7. That is, either unconditional biases or conditional biases lead to forecasts that are not completely reliable.

Forecast	Observation	$p(y\|x = X)$
2.0	1.0	$p(y = 2.0\|x = 1.0) = 0.25$
2.0	3.0	$p(y = 2.0\|x = 3.0) = 0.25$
2.0	0.0	$p(y = 2.0\|x = 0.0) = 0.25$
2.0	4.0	$p(y = 2.0\|x = 4.0) = 0.25$

TABLE 7.2: A simple example illustrating completely reliable forecasts with no discriminative power and no sharpness; the values could be mm of rain.

Sharpness

Forecast sharpness, or refinement, is an attribute of the forecasts and is a characteristic of the marginal distribution of the forecast values $p(y)$ in equation (7.5) (Wilks, 2006, Chap 7). The distribution of forecasts indicates how often different forecast values are issued. A forecasting system that produces the same forecast on each forecast occasion is not sharp (Murphy et al., 1989). In table 7.2, the forecasts completely lack sharpness since only one value, the average of the observations, is forecast at all forecast occasions. Within the field of meteorology, sharp forecasts can easily be produced. The challenge is to ensure that these forecast values correspond to the subsequent observed values (Wilks, 2006, Chap. 7). Except for very simple forecasts as shown in table 7.1, that contain no variation and completely lack sharpness, evaluation of sharpness is usually applied to probability forecasts of a dichotomous (or binary) event and complete sharpness might be difficult to define for forecasts of continuous observations (Murphy et al., 1989). However, for perfectly accurate and reliable forecasts the distribution of forecast values, $p(y)$, should be identical to the distribution of the observed values, $p(x)$ (Murphy, 1993; Murphy et al., 1989).

Discrimination

Forecast discrimination measures the ability of the forecasts to discriminate between observations that differ (Murphy, 1993; Weigel and Manson, 2011) regardless of the actual forecast value. Discrimination is a fundamental quality attribute since it indicates the usefulness of a set of forecasts after being appropriately post-processed (Murphy, 1993; Weigel and Manson, 2011). Different measures of discrimination exists. Perfectly reliable forecasts are effectively useless if they lacks discriminative power (Weigel and Manson, 2011), which is illustrated by the simple example in table 7.2, which is an extension of table 7.1. The forecasts are completely reliable since $E(x|y = 2.0) = 2.0$ for all values of Y (in this case, there is just one value), but completely lack discriminative power, since the forecasts cannot discriminate between different observations and cases of rain and no rain.

Observation	18℃ [2]	Forecast	16℃ [2]	t = 1
Observation	23℃ [1]	Forecast	24℃ [1]	t = 2

TABLE 7.3: A comparison of two forecast-observations pairs; in square brackets, the corresponding rank of the observation and of the forecast is seen.

Within the framework of Murphy and Winkler (1987) discrimination is a characteristic of the conditional distribution of the forecasts for a specific value of the observations X, that is, $p(y|x = X)$. In table 7.2, the value of $p(y|x = X)$ is the same (0.25) for all four values of X. That is, a forecast value of 2.0 mm is with equal probability followed by an observation of either 1.0 mm, 3.0 mm, 0.0m, or 4.0 mm. When $p(y|x = X)$ is the same for all values of X, the forecasts are not able to discriminate between the different observations (Murphy et al., 1989). To clarify, an example of forecasts that are perfectly discriminatory, but not completely reliable is given in appdendix B. The forecast value is actually never observed. The forecasts would probably not be considered very informative despite their complete reliability, since they are all equal to the mean of the observations, and contain no variation. In real life, deductions about forecasts from only four forecast-observation pairs is, of course, questionable.

Another measure of discrimination is the generalised discrimination score proposed by Manson and Weigel (2009) with application to binary, categorical, and continuous observations and based on the joint distribution $p(x, y)$. In constructing the generalised discrimination score, D, all possible sets of two forecast-observation pairs are constructed from the verification data. For each of these sets, the question is asked whether the forecasts can be used to successfully distinguish (or rank) the observations (Weigel and Manson, 2011). In table 7.3, two forecast-observations pairs are compared, and the forecasts are able to correctly discriminate (or rank) the corresponding observations while in table 7.4, this is not the case. The proportion of times when two forecasts can be used to correctly rank the corresponding observations yields the generalised discrimination score, D, given by

$$D = \frac{1}{2}(\tau + 1), \tag{7.10}$$

(Weigel and Manson, 2011), where τ is Kendall's rank correlation coefficient (Bhattacharyya and Johnson, 1977, Chap. 15), which measures the degree of association between two variables. Since discrimination is not concerned with the forecasts taken at face value, a rank correlation coefficient will suffice in defining the generalised discrimination score.

By its definition, the generalised discrimination score, D, indicates how often the forecasts correctly discriminate the observations (Weigel and Manson, 2011). If the forecasts do not contain any useful information, the proba-

Observation	18℃ [1]	Forecast	16℃ [2]	t = 1
Observation	14℃ [2]	Forecast	17℃ [1]	t = 3

TABLE 7.4: A comparison of two forecast-observations pairs; in square brackets, the corresponding rank of observations and forecasts is seen.

	Continuous case		*Binary case*	
Day	Observations	Forecasts	Observations	Forecasts
t = July 10 14.00 UTC	22℃	23℃	1	1
t = July 11 14.00 UTC	23℃	21℃	1	1

TABLE 7.5: An example of forecasts and corresponding observations for continuous and binary observations

bility that the forecasts correctly discriminate two observations is equivalent to random guessing (which would be equal to 50 %) and one would obtain $D = 0.5$ (in this case there is no association between forecasts and observations, and so $\tau = 0$). The more successfully the forecasts are able to discriminate the observations, the closer the score is to 1, since a strong association (or correlation) between forecasts and observations will give τ close to 1. Forecasts that consistently rank the observations in the wrong way, will give $D = 0$ (in this case, a strong negative association between forecasts and observations will yield $\tau = -1$).

When the number of distinct observations increases — as from binary to categorical and to continuous observations, the discriminative power usually decreases (Weigel and Manson, 2011). This can be explained by the additional precision that is required to discriminate between continuous observations compared to binary observations (Weigel and Manson, 2011), which may be defined as observations being above or below some threshold. In the continuous case, the forecasts will have to successfully discriminate between values that might differ by only small amounts (Weigel and Manson, 2011). As an example, table 7.5 should illustrate the difference in precision required for continuous observations compared to binary observations. The table shows (fictitious) national average of maximum temperatures and corresponding observed events for two days in July. In creating the binary events, temperatures above the assumed average for July is 15℃ make an event (1) and temperatures below 15℃ no event (0). In the continuous case, the forecasts will have to correctly discriminate and therefore correctly forecast, which of the two days is the warmest. In the binary case, the forecasts will (only) have to discern between days when the national average temperature is above or below 15℃, which would (probably) be easier to forecast correctly.

7.2 Quality of Ensemble Forecasts

Methods to assess quality of ensemble forecasts exist. Multidimensional ensemble forecasts of continuous observations can be difficult to verify in a comprehensive manner (Jolliffe and Stephenson, 2012, Chap. 1). In this work, reliability and discrimination have been applied to ensemble forecasts of continuous observations.

7.2.1 Consistency

If the ensemble members can be considered as random samples of the PDF both at the initial time and at any later forecast time, the true state of the atmosphere will behave like one more member of the ensemble and the true atmospheric state will be statistically indistinguishable from the ensemble members (Gombos and Hansen, 2007; Wilks, 2006, Chap. 7). This condition is called consistency of the ensemble (Wilks, 2006, Chap. 7).

A common approach to assess the degree of consistency of ensemble forecasts, that is, to assess whether the ensemble members and the truth (materialised by the verifying observation) are statistically indistinguishable is by the shape of a scalar rank histogram (also known as a verification rank histogram or a Talagrand histogram) (Gombos and Hansen, 2007; Wilks, 2006). From consistent ensemble forecasts, questions like: "What is the probability that the daily accumulated global radiation tomorrow exceeds a given threshold?", or a more distributional question like: "Within what interval of global radiation values does 90 % of the forecasts lie in 12 hours?" can be answered. These questions, that is, the forecasts, will be reliable. The derivation of reliable probability forecasts is central to ensemble forecasting (Hamil and Colucci, 1997), and evaluation of ensemble consistency has over the years received special attention (see e.g. Gneiting et al. (2008); Hamill (2001); Jolliffe and Stephenson (2012); Wilks (2006)).

In the literature, consistency and reliability are used interchangeably to describe the statistical indistinguishability of the true state of the atmosphere and the ensemble members. Here, consistency describes this condition, while reliability characterises the reliability of the probability forecasts derived from the ensemble.

In constructing the scalar rank histogram, consider N ensemble forecasts, each of which consists of M ensemble members, and N corresponding observations (Jolliffe and Stephenson, 2012, Chap. 8). Now, for each of these N ensemble forecasts with corresponding observation, the value of the observation is ranked according to the values of the ensemble members. If the observation is smaller than all M ensemble members, then its rank is 1, and if the observation is larger than all ensemble members, then its rank is $M+1$ (Jolliffe and Stephenson, 2012, Chap. 8). If the M ensemble members and the verifying observation belong to the same distribution (the PDF),

that is, if ensemble members and the verifying observation are statistically indistinguishable, the rank of the observation within the $M+1$ values would be equally likely to take on any of the rank values $1, 2, \ldots, M+1$ (Jolliffe and Stephenson, 2012; Wilks, 2006). Determining the rank of the observation with respect to the ensemble members for N observations and N ensemble forecasts (of each M forecasts) gives when displayed in a histogram the rank histogram. If the ensemble forecasts are consistent, the ensemble members and the observations are statistically indistinguishable (Wilks, 2006, Chap. 7), and the histogram of the N observation ranks will be uniform with an expected number of $\frac{N}{M+1}$ counts per rank value apart from deviations due to sampling variability (Jolliffe and Stephenson, 2012; Wilks, 2006).

A uniform scalar rank histogram implies that the ensemble forecast and the verifying observation are random samples from the PDF — i.e. they are statistically indistinguishable. However, sampling the ensemble members from a distribution different from the PDF, can under special circumstances result in a uniform rank histogram (Hamill, 2001) and the interpretation of rank histograms should be treated carefully. Flatness of rank histograms is a necessary, but not sufficient criterion for ensemble consistency (Feddersen, 2009; Jolliffe and Stephenson, 2012; Wilks, 2006).

Deviations from uniformity of the rank histogram can be used to diagnose deficiencies of the ensemble consistency (Hamill, 2001; Jolliffe and Stephenson, 2012; Wilks, 2006). Bias in the ensemble (or systematic (or overall) deviations between the ensemble members and the observation) will result in a sloped rank histogram, since too, often the observation will be on one side of the ensemble, that is, either too often smaller than or too often larger than the ensemble forecasts, and this will too often occupy the smallest or the largest rank values (Hamill, 2001; Wilks, 2006) — see figure 7.1, where the ensemble forecasts have a tendency to over-forecast leaving the observations too often at one of the smallest rank values. An under-dispersive ensemble, will result in a U-shaped rank histogram, since too often the ensemble is not able to capture the observation, which will too often be either smaller than or larger than the ensemble forecasts (Hamill, 2001; Wilks, 2006) as may be caused by the presence of a conditional forecast bias among the ensemble members. This under-dispersion will overpopulate both the smallest and the largest rank values resulting in a rank histogram with a U-shaped appearance.

7.2.2 Multidimensional Consistency

The scalar rank histogram is in essence a verification tool to assess the consistency of ensemble forecasts of a scalar variable.

For the data set treated here, a multidimensionality is introduced by the 24 simultaneous forecasts corresponding to the 24 locations of the verifying observations (see e.g. section 4.3). To access the consistency of en-

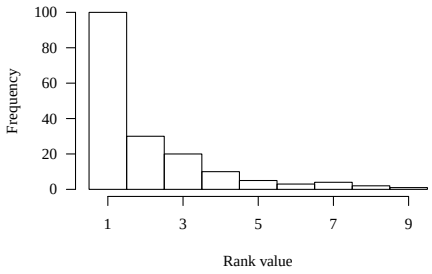

FIGURE 7.1: Illustration of a rank histogram when the 8 ensemble members have been sampled from a distribution, which is biased compared to the PDF. Here, the ensemble has a tendency to over-forecast, which leaves the observation too often as one of the smallest rank values.

semble forecasts of multidimensional data, a number of methods have been proposed. Two such methods are the multivariate rank (MVR) histogram (Gneiting et al., 2008; Jolliffe and Stephenson, 2012) and the minimum spanning tree (MST) histogram (Gneiting et al., 2008; Jolliffe and Stephenson, 2012) described below.

Multivariate Rank Histogram

The multivariate rank (MVR) histogram is a generalisation of the scalar rank histogram and assess — like their scalar counterpart — how the observations rank with respect to the individual ensemble members. Being a generalisation of the scalar rank histogram, the shape of the MVR histogram can be interpreted in the same way as the shape of the scalar rank histogram. In constructing MVR histograms, the challenge is to find a definition of how to rank multidimensional vectors (Jolliffe and Stephenson, 2012). Below, a procedure of determining the rank of a K-dimensional observation with respect to the M K-dimensional ensemble forecasts, is suggested (Gneiting et al., 2008; Jolliffe and Stephenson, 2012). In the K-dimensional space spanned by the $K = 24$ verifying locations simultaneously predicted, the K-dimensional vector, $x_{i,1} \ldots, x_{i,k} \ldots, x_{i,K}$, is denoted by $\mathcal{X}_i$ (with $i = 1, \ldots, N$) and the ensemble forecast $\mathcal{Y}_{i,j}$ denote the K-dimensional vector, $y_{i,j,1}, \ldots, y_{i,j,k}, \ldots, y_{i,j,K}$ is denoted by $\mathcal{Y}_{i,j}$ (with $i = 1, \ldots, N$). Table 7.6 attempts to illustrate how this work. Here, with $K = 4$ and $M = 3$, the K-dimensional observation vector, $\mathcal{X}_i$ would be equal to $(25, 23, 22, 24)$, and the K-dimensional vector for ensemble member 1, $\mathcal{Y}_{i,1}$, would be $(28, 27, 25, 25)$, and for ensemble member 2, $\mathcal{Y}_{i,2}$, the K-dimensional vector would be $(25, 22, 20, 25)$, and for ensemble member 3, $\mathcal{Y}_{i,3}$,

At time point i: forecast date **2011-08-06**, initial time **00**, and lead time **6 h**

Station	Member 1	Member 2	Member 3	Observation
6019	28	25	24	25
6031	27	22	23	23
6041	25	20	21	22
6049	25	25	24	25
	$\mathcal{V}_1$	$\mathcal{V}_2$	$\mathcal{V}_3$	$\mathcal{V}_0$

TABLE 7.6: Illustration of the K-dimensional vectors for an ensemble of three members at a given time point i corresponding to a certain forecast date, say 20110806, and a certain initial time, say 00, and a certain lead time, say 6 hours, which corresponds to the time 6 August 2011 06 UTC.

the K-dimensional vector would be $(24, 23, 21, 24)$ for the given combination of forecast date, initial time, and forecast length, i.

The procedure is then as follows (Jolliffe and Stephenson, 2012, Chap. 8):

1. Define $\mathcal{V}_0 = \mathcal{X}_i$ and $\mathcal{V}_j = \mathcal{Y}_{i,j}$ with $j \in 1, \ldots, M$. Now, $\mathcal{V}_{0,k}$ denotes the kth dimension of the observations and $\mathcal{V}_{j,k}$ the kth dimension of the jth ensemble member.

2. Then, determine the "pre-rank", ρ_j, of each vector $\mathcal{V}_j$ with $j \in 0, 1, \ldots, M$ by

$$\rho_j = 1 + \sum_{\substack{l=0 \\ l \neq j}}^{M} q_{j,l} \text{ with } q_{j,l} = \begin{cases} 1 & \text{if } \mathcal{V}_{j,k} \geq \mathcal{V}_{l,k} \text{ for all } k \in 1, \ldots, K \\ 0 & \text{otherwise} \end{cases} \tag{7.11}$$

   that is, if the K-dimensional ensemble vector $\mathcal{V}_j$ is larger than the K-dimensional ensemble vector $\mathcal{V}_l$ for all K-dimensions (in table 7.6 $K = 4$), the pre-rank, ρ_j, of ensemble member "j" is increased by 1. In the example illustrated in table 7.6, the pre-rank of ensemble member 1 is 4, since $\mathcal{V}_1$ is clearly larger than any of the other vectors, the pre-rank of the observations is 3, while the pre-ranks for ensemble member 2 and 3 are both 1.

3. Finally, the multivariate rank r is determined. If the pre-rank of the observation, ρ_0, is not tied, then r is given by ρ_0. If there are ties, these are solved at random. In the example in table 7.6, the pre-rank of the observations is in this case not tied, so $r = 3$.

Repeating these steps for N forecast-observation pairs and displaying the N multivariate ranks of the observations, r, in a histogram, yields the MVR histogram.

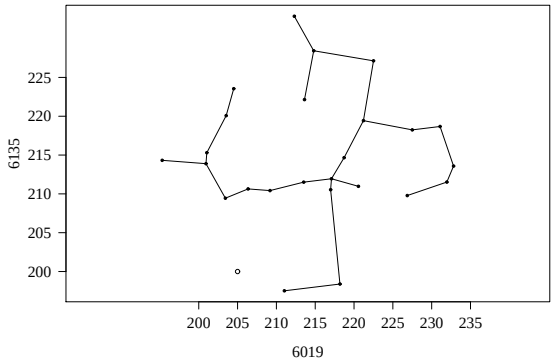

FIGURE 7.2: Illustration of a spanning tree of a data set with $K = 2$ dimensions (verifying location (number of pyranometers) 6019 and 6031) and 25 ensemble members (small, full circle); the open circle represents an observation.

Minimum Spanning Tree Histogram

Another method to evaluate the reliability of multidimensional ensemble forecasts is the minimum spanning tree (MST) histogram (Gneiting et al., 2008; Jolliffe and Stephenson, 2012). It is likewise applicable if a number of locations are simultaneously predicted by ensemble of forecasts.

When plotting a K-dimensional ensemble forecast in a diagram, a spanning tree can be constructed by connecting all K forecast points with line segments without generating any closed loops (Jolliffe and Stephenson, 2012, Chap. 8). There are several ways of generating a spanning tree (of connecting the points in figure 7.2 without any closed loops), but the one that gives the smallest sum, when adding the length of all the line segments, defines the minimum spanning tree (MST). This is best illustrated when the dimension of the data is 2 as in figure 7.2. Here, $K = 2$, and $M = 25$.

For a consistent EPS, the ensemble members should be statistically indistinguishable from the verifying observation, which according to Jolliffe and Stephenson (2012, Chap. 8) implies that the K dimensional distance of the observation from any of the ensemble members, should on average be similar to the average mutual distance of the ensemble members from each other. This relation is tested by the MST histogram. The statistical indistinguishability implies that the MST lengths should — on average — not be significantly affected if a random ensemble member is replaced by the verifying observation (Jolliffe and Stephenson, 2012). In figure 7.2, the distance of the observation from any of the ensemble members seems, on average, to exceed the average mutual distance of the ensemble members.

The procedure for generating MST is according to Jolliffe and Stephenson (2012, Chap. 8): the total length, l_0, of this minimum spanning tree spanned by the $M = 25$ ensemble members in the $K = 24$-dimensional space, is generated. Now, replacing the jth ensemble member by the verifying observation gives another total MST length, l_j. For consistent ensemble forecasts, l_0 should not be systematically larger or smaller than any $l_j \in \{l_1, \ldots, l_M\}$, that is, replacing any one of the ensemble members by the verifying observation should not affect the associated total MST length. Ranking l_0 within the set of MST lengths $\{l_0, l_1, \ldots, l_M\}$, it should be equally likely for the rank of l_0, which is denoted by r, to take on any of the values $\{1, \ldots, M + 1\}$. Whether this is the case can be assessed by determining r for all forecast-observation pairs and then displaying the values obtained in a histogram — the MST-histogram. If the forecasts are reliable, the MST histogram should be uniform (Jolliffe and Stephenson, 2012, Chap. 8).

MST histograms can generally not be considered as a multidimensional generalization of rank histograms, as is the case of the multivariable rank histogram, and they need to be interpreted differently (Jolliffe and Stephenson, 2012). Under-dispersive ensemble forecasts, which are often associated with U-shaped rank histograms, often yield negatively sloped MST histograms (Jolliffe and Stephenson, 2012).

7.2.3 Discrimination

Discrimination of ensemble forecast has often been accessed probabilistically, that is, after the ensemble has been transformed into probability forecasts (Weigel and Manson, 2011). A generalised discrimination score, D, applicable to ensemble forecasts of continuous observations has been proposed by Weigel and Manson (2011) as an expansion of the generalised discrimination score proposed by Manson and Weigel (2009) and described in section 7.1.2.

The construction of a generalised discrimination score, D, applicable to ensemble forecasts of a continuous observation, requires a definition of how to discriminate, or rank, two ensemble forecasts. For single deterministic forecasts, it is trivial to decide which one of two forecasts is larger and should (if the forecasts possess discriminative power) be associated with the larger one of the two corresponding observations (see e.g. table 7.3 and 7.4). This decision is less obvious for ensemble forecasts. Weigel and Manson (2011) consider 3 hypothetical 5-member ensemble forecasts of temperature (°C) with $\mathbf{y}_1 = (22, 23, 26, 27, 32)$, $\mathbf{y}_2 = (28, 31, 33, 24, 36)$, and $\mathbf{y}_3 = (24, 25, 26, 27, 28)$ (from Weigel and Manson (2011)). Most people would intuitive label $\mathbf{y}_2$ larger than both $\mathbf{y}_1$ and $\mathbf{y}_3$. The situation is less obvious when comparing $\mathbf{y}_1$ and $\mathbf{y}_3$. A method of ranking ensemble forecasts proposed by Weigel and Manson (2011) is described in appendix C, and makes the generalised discrimination score applicable to ensemble forecasts.

7.2.4 Summary of Aspects of Forecast Quality

In table 7.7, a summary of the aspects of forecasts quality described in this chapter can be found. A possibility of the quality aspect to handle multidimensional forecasts is indicated in the fourth and the fifth column for single forecast and ensemble forecasts, respectively.

Aspect	Measure	Definition	Multidimensionality	
			single forecasts	ensemble forecasts
Bias	ME	Describes the difference between mean forecast and mean observation	yes*	
Accuracy	MSE, RMSE	Describes the average correspondence between individual pairs of forecasts and observations	yes*	
Skill	SS	Describes the accuracy of forecasts relative to the accuracy of unskillful reference forecasts	yes*	
Reliability**		Describes the correspondence between the mean observation associated with a particular forecast and that forecast	no	yes
Discrimination	D	Describes the ability of the forecasts to discriminate between different observations	no	no
Sharpness		Describes the variability of the forecasts	yes*	

TABLE 7.7: Aspects of forecast quality with short definitions from Murphy (1993); the aspect of forecast quality is shown in column one, a typical measure of this quality aspect is shown in column two, a short definition of the aspect is given in column three, and in the fourth and fifth column, the application of the forecast aspect to multidimensional data sets is indicated for single forecasts in column four (single forecasts) and to ensemble forecasts in column five (ensemble forecasts). Here, an asterisk (*) indicates that the forecast aspect can handle multidimensional data, but only implicitly, that is, in the way the given measure or aspect of forecast quality is defined here. This is the case for the ME, MSE, and RMSE. A double asterisk (**) indicates that concerning ensemble forecasts, consistency (rather than reliability) of the ensemble, from which reliable probability forecasts can be derived (Wilks, 2006, Chap. 7), is evaluated.

8 Verification of Global Radiation from DMI-EPS

To comply with accuracy requirements to solar radiation forecasts arisen from the development of a smart solar heating unit, DMI-EPS has since August 2011 made hourly calculations of global, direct and diffuse radiation. With the aim of assessing the possibility of complementing forecasts of global radiation with uncertainty estimates as derived from ensemble forecasts of DMI-EPS, this chapter is devoted to verifying these ensemble forecasts.

8.1 The Data

The period of verfication is from August 5 2011 to November 14 2011, which amounts to 102 days and the ensemble forecasts are verified against global radiation measurements at the 24 DMI pyranometers.

8.1.1 Ensemble Calculations of Global Radiation

The data set consists of 100 days of forecasts (from August 5 2011 to November 12 2011) with 4 forecasts per day each consisting of 54 hourly values. This gives $N = 21600$ forecast occasions with corresponding observations within the period of verification from August 5 to November 14 2011. In verifying the S05 ensemble forecasts of global radiation against DMI's 24 observation stations, the forecasts have been downscaled by bilinear interpolation (see e.g. section 4.3) to the locations of the 24 verifying observations (that is, the 24 pyranometers shown in figure 4.1), which gives a data set of 24 simultaneous ensemble forecasts. The number of ensemble forecasts, M, is 25 (see e.g. table 6.2).

In generating ASCII files from the GRIB format of the DMI-EPS calculations, discontinuities in the data series have been introduced due to occasional storage problems. For all included time points, action has been taken to ensure that data for all 25 ensemble members exist, which makes $N = 19002$.

8.1.2 The Observations

Inspection of the observations covering the period of verification have revealed a few obviously incorrect values: i) night values of a few $\frac{\mathrm{W}}{\mathrm{m}^2}$ over long periods of time and ii) individual values that are unrealistically high, and which for some reason slipped through the data control — described in section 4.1. To compensate for the type i) errors, night values above zero have simply been set equal to zero and concerning errors of type ii), the "top of the atmosphere radiation" global radiation, $\mathrm{F}^{\downarrow}(\mathrm{toa})$, has been used to evaluate the ground measurements, and all values above $\mathrm{F}^{\downarrow}(\mathrm{toa})$ have been marked as invalid.

8.1.3 The Clearness Index

Global radiation reaching the surface of the Earth consists of a part governed by astronomical parameters giving rise to diurnal and seasonal variations and another part governed by short-term weather parameters such as frequency and height of clouds and their optical properties, atmospheric aerosols, atmospheric water vapour, and ground albedo (Badescu, 2008). The global radiation reaching the ground can be considered as a sum of two components — a deterministic (or astronomical) component and a stochastic (or meteorological) component. This meteorological or stochastic component can be isolated by introducing the clearness index defined by

$$\mathrm{K}_c = \frac{\mathrm{F}^{\downarrow}(\mathrm{surface})}{\mathrm{F}^{\downarrow}(\mathrm{toa})}, \tag{8.1}$$

where $\mathrm{F}^{\downarrow}(\mathrm{toa})$ is the extraterrestrial horizontal solar radiation (see e.g. equation (3.2)). $\mathrm{F}^{\downarrow}(\mathrm{surface})$ is the global radiation received at the surface of the Earth (Badescu, 2008). The clearness index K_c then accounts for all meteorological influences on the global radiation (Badescu, 2008) and has been calcualted in addition to the global radiation.

With this definition of the clearness index, it cannot be defined at night times, when $\mathrm{F}^{\downarrow}(\mathrm{toa})$ is zero. To eliminate any possible problems with model calculations for very high zenith angles (or for very low solar elevations), these invalid night values are expanded to zenith angles greater than 88°.

To avoid having night values — when the global radiation is zero for both observations and model calculations (i.e. a trivial forecast difference of zero) — influence the verification of global radiation from DMI-EPS, the undefined night values of the clearness index have been used to determine undefined night values of the global radiation, and, except if otherwise stated, these undefined night values are excluded from the verification.

In validating global radiation calculations from DMI-EPS, the clearness index data have been applied, when the elimination of the astronomical signal in the data was important.

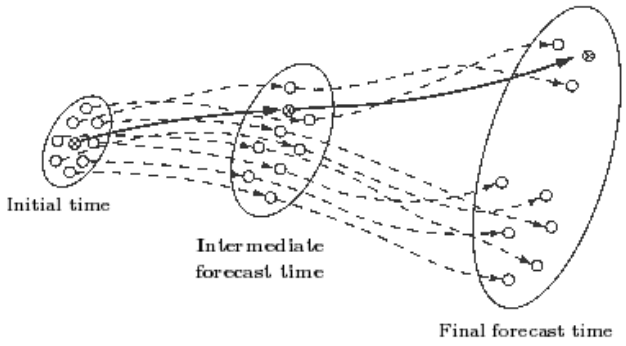

FIGURE 8.1: Illustration of the time evolution in a two-dimensional phase space. The full line illustrates the trajectory of the forecast initiated with the best estimate of the initial conditions. Dashed lines illustrates ensemble trajectories. From Wilks (2006, FIGURE 6.24)

8.2 Assessing the Performance of the Ensemble Mean

By averaging the ensemble members, some of the errors present in the individual forecasts should cancel, and the ensemble mean should, in general, provide an improved forecast compared to a traditional forecast (Toth and Kalnay, 1993; Wilks, 2006). Hence, the performance of the ensemble mean has been investigated.

In phase space, the ensemble mean will be the center of the distribution of all the ensemble members — at least until at clustering of the ensemble members appear (Wilks, 2006, Chap. 6), which is the case at the final forecast time in figure 8.1. In case of clustering, the ensemble mean will in phase space not be near any of the ensemble members (Wilks, 2006, Chap. 6), that is, the atmospheric state represented by the ensemble mean might be far from any predicted states. Being a more robust measure of centre, the ensemble median might in case of clustering do better compared to the ensemble mean. Depending on the distribution of the ensemble forecasts, the ensemble median is therefore speculated to be able to surpass the ensemble mean. Hence, both are calculated and together with the control forecast subjected to verification methods with the aim of investigating and comparing the performance of the three forecasts. Of course, the ensemble mean is *not* a real forecast, but a quantity derived from the ensemble. When sorting the 25 ensemble members, the ensemble median will be equal to the 13th member with 12 members above and 12 members below. In investigating the three forecasts, both the more traditional measures of forecast performance such as ME, RMSE, and skill score as well as aspects of forecast performance

such as sharpness, reliability, and discrimination are addressed.

8.2.1 Sharpness

Recall from section 7.1.2 that for continuous observations, complete sharpness of the forecasts is difficult to define, but that for completely accurate and reliable forecasts, the distribution of the forecasts $p(y)$ should be identical to the distribution of the observations $p(x)$ (Murphy et al., 1989).

In figure 8.2, the relative frequency distribution of the observations, $p(x)$ is seen in (a), and the relative frequency distribution, $p(y)$, of the control forecast is seen in (b), the ensemble mean in (c), and the ensemble median in (d). Here, the clearness index has been used to emphasize features in the distributions by a change of both the distribution and the scale of data. Although not identical, the distributions of clearness indices, bear an overall resemblance. However, the distribution of the ensemble mean, the control forecast, and the ensemble median are all characterized by a higher degree of symmetry as opposed to the corresponding distribution of the observations. High values of clearness index (greater than ≈0.8) found in the observations, are not seen in either of the three forecasts: the control forecast, the ensemble mean, and the ensemble median — best illustrated in the boxplot in figure 8.3. A more uniform distribution is exhibited by the ensemble mean and to some degree also by the ensemble median compared to the other two distributions. Smoothing by taking means and medians (not so pronounced for the ensemble median) seems to reduce the variability found in the observations and better captured by the control forecast. All three forecasts seem relatively broad and covers most values of the observations, but not values above ≈ 0.8. The distributions of the control forecast resembles the distribution of the observations more compared to the other two distributions, and therefore seems more sharp than both the ensemble mean and the ensemble median.

8.2.2 Bias, MSE, RMSE, and Skill Score

The more common measures of forecast quality as ME, MSE, and RMSE, are defined as

$$\mathrm{ME} = \frac{1}{\mathfrak{n}} \sum_{\substack{n=1 \\ \mathfrak{n} \in \mathcal{N}}}^{\mathfrak{n}} (y_n - x_n) \tag{8.2}$$

$$\mathrm{MSE} = \frac{1}{\mathfrak{n}} \sum_{\substack{n=1 \\ \mathfrak{n} \in \mathcal{N}}}^{\mathfrak{n}} (y_n - x_n)^2 \tag{8.3}$$

$$\mathrm{RMSE} = \sqrt{\mathrm{MSE}} \tag{8.4}$$

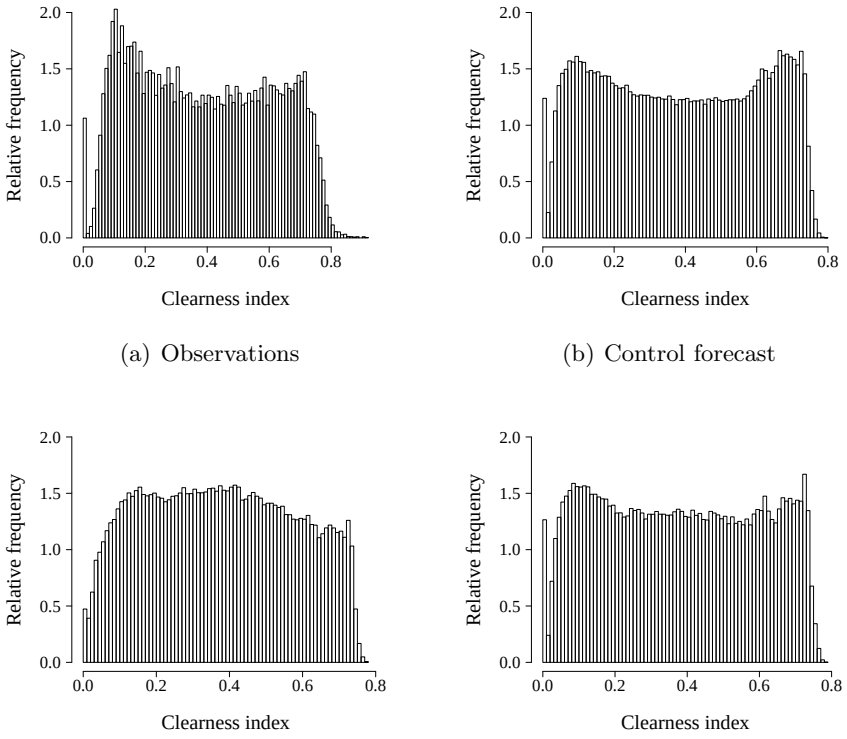

(a) Observations

(b) Control forecast

(c) Ensemble mean

(d) Ensemble median

FIGURE 8.2: Distribution of the clearness index for the observations (a), the control forecast (b), the ensemble mean (c), and the ensemble median (d) for the N forecast occasions and the K locations of the verifying observations; the distributions have been normalized.

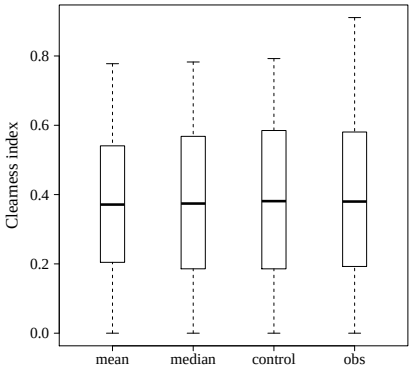

FIGURE 8.3: Distribution of the clearness index for ensemble mean (mean), the control forecast (control), the ensemble median (median), and the observations (obs) for all N forecast occasions and at all K verifying locations; in each box, the length of the box shows the interquartile range — i.e. values between the 25 % and the 75 % percentile of the distribution — bottom and top of the box, respectively; the thick horizontal line marks the median of the distribution; the ends of the whiskers mark the minimum and the maximum value.

according to equation (7.1) and (7.2), but here $\mathfrak{n}$ is the number in the total number of $\mathcal{N} = N \cdot K$ time and space combinations in the data set over which to average — in figure 8.4, this is determined by the forecast lead time —, and y_n and x_n are the forecast and the observation, respectively, at time-space point n. Both the measure of forecast bias (ME), the measure of forecast accuracy (MSE and RMSE), (and forecast skill score) are applicable to scalar forecasts (Wilks, 2006, Chap. 7) (see e.g. chapter 7). They are all here defined to incorporate the multidimensionality of the data set by averaging over a pooled data (sub)set consisting of both time and space points.

In generating the ME and the RMSE, illustrated in figure 8.4, the following procedure has been applied — here illustrated for the ensemble mean:

1. the ensemble mean is calculated for all $\mathcal{N}$ time-space combinations, and

2. for the ME the difference, and for the MSE the squared difference between the ensemble mean and the matching observation is calculated at each of the $\mathcal{N}$ time-space combinations, and

3. the average of this quantity is calculated for each lead time, that is, over n time-space combinations.

Taking the square root of the MSE gives the root mean squared error, RMSE. In calculating the bias and the MSE for the ensemble median, the median is

calculated in point 1 above instead of the ensemble mean and in calculating the bias and the MSE for the control forecast, point 1 is skipped. Note that in squaring the deviation between a forecast and the corresponding observation, the MSE and the RMSE become highly sensitive to large deviations in the data set. In forecasting accurately the global radiation received at solar collector, penalising large deviation between a forecast and a corresponding observation is desirable.

In general, the biases in figure 8.4(a) are modest. A strong declining trend is seen in the first ≈12 hours of the forecast lead time. This is related to spin-up effects[1], which might appear in the first hours of an NWP forecast as, for instance, clouds build up. From a turning point occurring at a forecast lead time of about 16 hours for the control forecast and 24 hours for the ensemble mean and the ensemble median an increasing trend is seen. The control forecast with its much faster rise towards zero performs better compared to both the ensemble mean and the control forecast. Over forecast lead times of 6 – 48 hours, the biases are negative with the ensemble mean displaying the largest absolute bias. This suggest a degree of, although modest, overall or systematic under-forecasting for all three forecasts, but most pronounced for the ensemble mean and the ensemble median. This corresponds with the figures in the "ME" column of table 8.1.

Values of RMSE found in this study and displayed in figure 8.4(b) are comparable with values reported in Díaz et al. (2012), in Lorenz et al. (2011) for single deterministic forecasts (compare for example with the high-resolution bias-corrected HIRLAM-CI data, the pixel-averaged WRF-MT data, or the direct model output WRF-UJAEN data), and in (Lorenz et al., 2012). This lends support to the three forecasts: the control, the ensemble mean, and the ensemble median from DMI-EPS. From the figure, accuracy is seen to decrease with lead time. The control forecast shows a larger RMSE for all lead times compared to both the ensemble median and the ensemble mean, which has the lowest RMSE. The overall values are shown in the "RMSE" column in table 8.1.

The strong diurnal variation in the squared forecast deviation symmetric around 12 UTC in figure 8.5 combined with the 6 hour interval between two consecutive forecasts (issued at 00, 06, 12, 18 UTC every day), causes the 6 hour variation in RMSE (thin dotted lines) seen in figure 8.4(b). A given

[1]The equation governing the state of the atmosphere are differential equations describing changes within the atmosphere. To use these equations in NWP forecasts, an initial state of the atmosphere must be specified. Typically, this initial state is based on observations, which compared with the NWP grid are sparse in coverage and must be interpolated to the forecast grid. This introduces errors in the initial state of the NWP forecast and initially the NWP model might predict large changes of the atmospheric state. This is referred to as spin-up effects and these are illustrated by the strongly declining bias in figure 8.4(a). As the effects of this initial state disappear, the changes of the atmospheric state reach a certain level. Information from `http:www.drjack.info/INFO/model-basics.html`

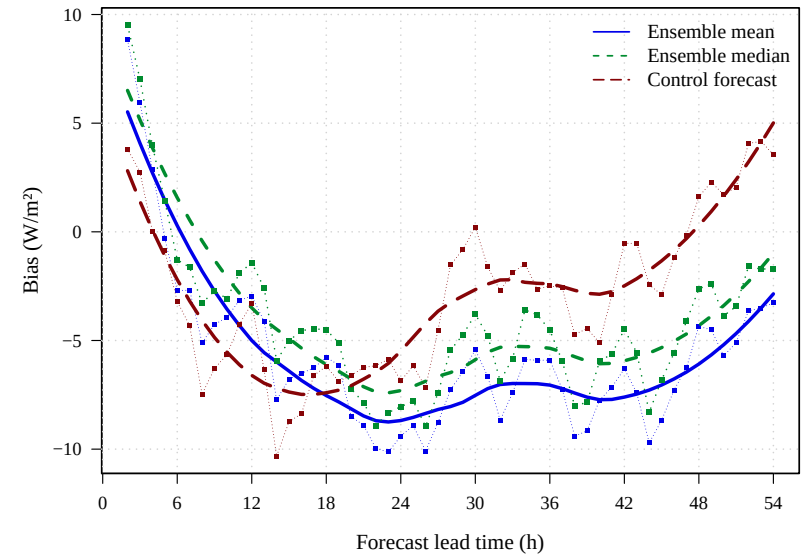

(a) Bias

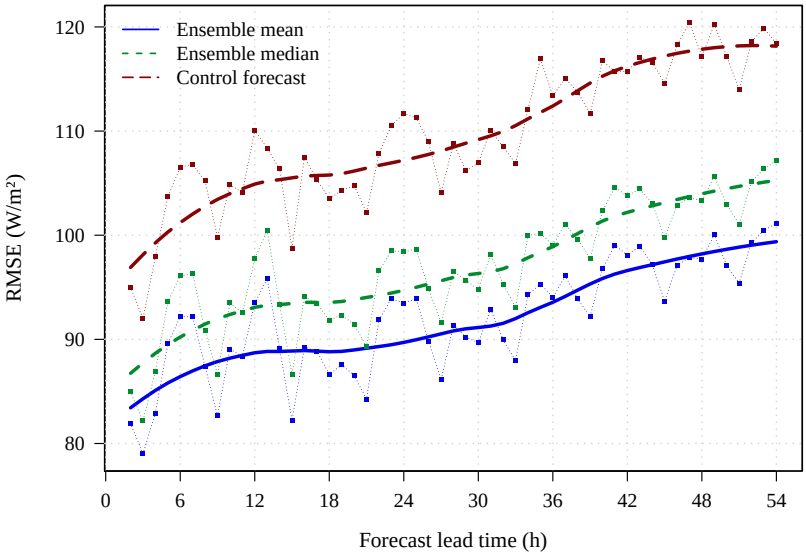

(b) RMSE

FIGURE 8.4: Bias (a) and RMSE (b) of global radiation calculated as an average per lead times; a Loess smoothing has been applied to emphasize trends.

	ME (bias)	RMSE
Ensemble mean	−5.7	92
Control forecast	−2.9	110
Ensemble median	−4.2	97

TABLE 8.1: An average over all $\mathcal{N}$ time space combinations of ME and RMSE in $\frac{W}{m^2}$

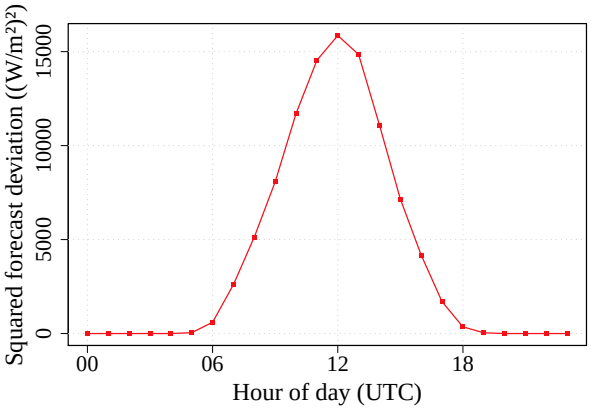

FIGURE 8.5: Mean of the squared forecast deviation as a function of time of day (UTC) for the ensemble mean; the squared forecast deviation enters into the calculation of both the MSE and the RMSE.

lead time (of say 3 hours) will with four forecasts per day (00, 06, 12, and 18 UTC) result in four different times of the day (03, 09, 15, and 21 UTC). The complete data set for a given lead time consists exclusively of those four times of the day. How these four distinct times are distributed in figure 8.5, affects the value of the MSE (and of the RMSE) according to the generation of them (equation (8.3) and (8.4)). With the 6 hour cycle in the forecasts, two lead times with a 6 hour interval result in the same four hours of the day (that is, a lead time of 9 hours result in 09, 15, 21, and 03 UTC), which are equal to the times of the 3 hour lead time. On average and according to figure 8.5, the same squared deviations enters the calculation of the RMSE, and this induces the 6 hour variation in the RMSE seen in figure 8.4(b).

In this work, the accuracy measure used in calculating the skill score is the MSE defined in equation (8.3). The sample climatology[2], or sample

[2]The climatology is estimated by the mean of the observations (or a set of observations), which is called the sample climatology (Wilks, 2006, Chap. 7).

mean, defined as

$$\bar{x} = \frac{1}{\mathfrak{n}} \sum_{\substack{n=1 \\ \mathfrak{n} \in \mathcal{N}}}^{\mathfrak{n}} x_n$$

is used as the references forecast and $\mathfrak{n}$ is the number in the $\mathcal{N}$ time-space combinations matching a given lead time. This gives the following accuracy measure for the unskillful reference forecasts

$$\mathrm{MSE}_{ref} = \mathrm{MSE}_{clima} = \frac{1}{\mathfrak{n}} \sum_{\substack{n=1 \\ \mathfrak{n} \in \mathcal{N}}}^{\mathfrak{n}} (\bar{x} - x_n)^2 \tag{8.5}$$

(Wilks, 2006, Chap. 7), and the following skill score

$$\mathrm{SS} = \left(1 - \frac{\mathrm{MSE}}{\mathrm{MSE}_{clima}}\right) \cdot 100\ \% \tag{8.6}$$

according to equation (7.4).

For MSE_{clima}, it is implied that the climatology, estimated by $\bar{x}$, does not change in the course of the $\mathfrak{n}$ forecast occasions (i.e. during either space or time of the $\mathfrak{n}$ forecasts) (Wilks, 2006, Chap. 7). Failing to account for a time varying climatology can according to equation 8.5 produce an unrealistically large MSE_{clima} (Wilks, 2006, Chap. 7). During the verification period of several months, the true climatology (or level) of global radiation is expected to change[3] as illustrated in figure 8.6(a). To reduce the effects of a changing climatology in the course of the verification period (August 5 to November 14), the clearness index is used in calculating skill scores. Despite a changing clearness index throughout this period, a clear and unambiguous trend is not seen in figure 8.6(b). The clearness index seems to more fluctuate around a mean value compared to the global radiation in figure 8.6(a).

Figure 8.7 displays the skill score as a function of lead time. With increasing lead time, the skill score is seen to decrease. Table 8.2 shows a selection of values found in figure 8.7. It is seen that the ensemble mean performs better in skill score (based on MSE with climatological values as the reference forecasts) compared to the control forecast. A value of 0.461 in skill score is interpreted as a 46.1 % increase in performance of the ensemble mean compared to the unskillful climatology, $\bar{x}$. For the control forecast, this value is 27 %. The decreasing trend in skill score with lead time is highly expected. It is more surprising that the 48 hour horizon skill score for the ensemble mean (0.380) corresponds to the 6 hour horizon for the control forecast (0.382). The modest skill scores — especially pronounced

[3]The annual period in the global radiation caused by astronomical constellations gives, in the course of the verification period, a gradual change in the climatology of the global radiation.

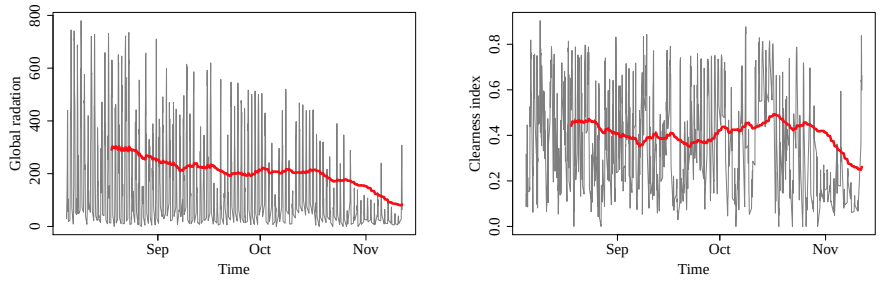

(a) Global radiation (b) Clearness index

FIGURE 8.6: Time evolution in the observed global radiation (a) and from this the computed clearness index (b) for verification station 6135; a moving average has been applied (red curve) to underline the variability of the climatology.

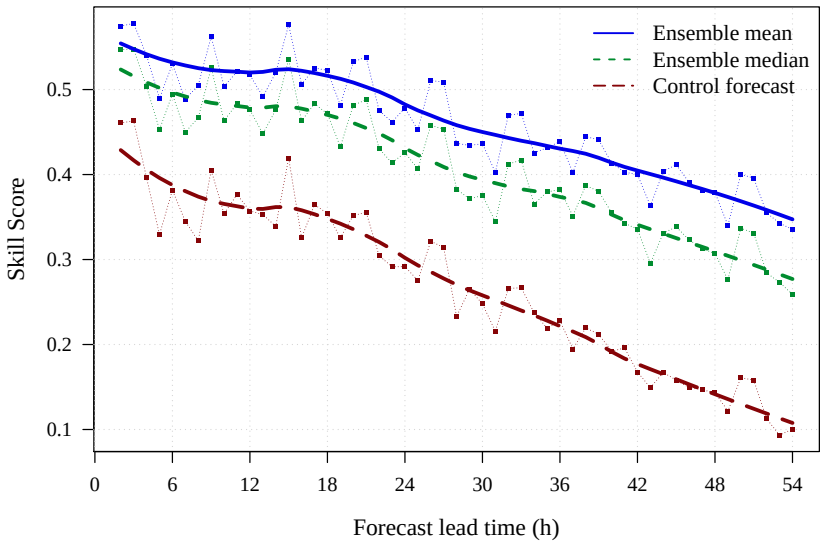

FIGURE 8.7: Skill score as a function of lead time; the MSEs, on which the skill score is based, is averaged over a data set defined by the lead time (see e.g. section 8.2.2). A Loess smoothing has been applied to emphasize trends.

Lead time(s)	Ensemble mean	Control forecast
All ($n = \mathcal{N}$)	0.461	0.270
6 hours	0.530	0.382
24 hours	0.478	0.292
48 hours	0.380	0.143

TABLE 8.2: Overall skill score (SS) for the ensemble mean and the control forecast for different lead times; the MSEs that form the basis of the skill scores are calculated as described in section 8.2.2 as an average in a data set consisting of $\mathcal{N} = N \cdot K$ time-space combinations over all data points (All), and over a data set consistent with a lead time of 6 hours, of 24 hours, and of 48 hours.

for the control forecast — might be related to the use of the clearness index for which the highly predictable astronomical signal present in the global radiation is eliminated leaving a "pure" weather signal.

8.2.3 Reliability

Recall from section 7.1.2 that a set of forecasts is said to be completely reliable if $E(x|y = Y) = Y$ for all forecast values Y, where $E(x|y = Y)$ is the mean value of the observations associated with a particular forecast value Y (Murphy et al., 1989). The conditional distribution $p(x|y = Y)$ of observations for a given forecast value Y together with the marginal distribution of forecasts $p(y = Y)$ for selected or binned values of Y provide information about unconditional as well as conditional biases in the forecasts — information that becomes available in the graphical representations in figure 8.8.

Within the distribution of observations associated with (or conditional on) a forecast value Y, $p(x|y = Y)$, displayed in figure 8.8, the thick line shows the median of this distribution, the two dashed lines the 25th and 75th percentiles, and the two dotted lines the 10th and the 90th percentile. The blue histograms displayed in figure 8.8(b) illustrates the distribution of forecasts $p(y = Y)$ also found in figure 8.2(b). The diagonal line in both figure 8.8(a) and 8.8(b) is the line of perfect correspondence between forecasts and observations (Murphy et al., 1989), that is, of completely reliable forecasts, is included to compare with the median values of the observations. Deviations of the conditional medians from this diagonal line are assumed to indicate that the forecasts contain bias (Murphy et al., 1989) either conditionally or unconditionally, and, hence, that they not completely reliable.

Inspecting the conditional quantile plots in figure 8.8, reveals both a presence of a condition bias, that is, a forecast bias that depends on the forecast value and an absence of unconditional biases, that is a systematic

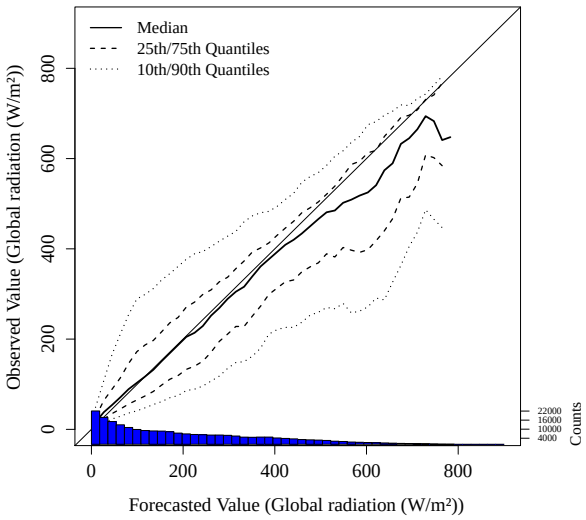

(a) Global Radiation

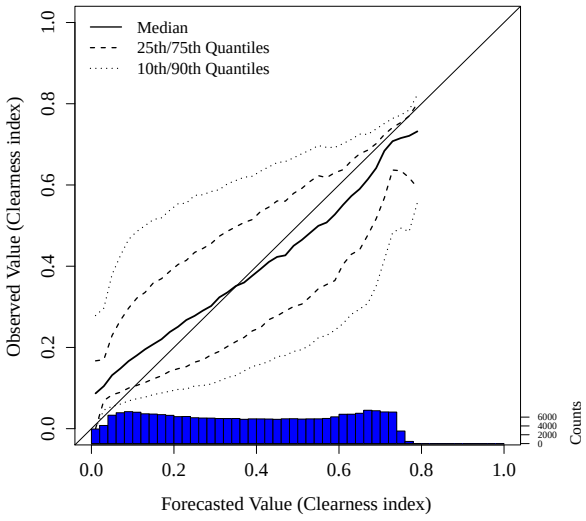

(b) Clearness index

FIGURE 8.8: The conditional distribution $p(x|y)$ of the control forecast for global radiation (a) and the clearness index (b) calculated for all N forecast occasions at each of the K verifying locations. The "conditional quantile plots" of quantiles of the conditional distribution $p(x|y)$ are inspired by Murphy et al. (1989).

bias irrespective of the forecast value that is appearent in figure 8.4(a). An unconditional bias in the forecasts would in figure 8.8 appear as a line of the observation medians entirely to one side of the diagonal line — above the line in case of systematic under-forecasting and below the line in case of systematic over-forecasting. For the control forecast in figure 8.8(a), the median lies along the diagonal line of perfect correspondence a least below a forecast value of about 500 $\frac{W}{m^2}$. A value of global radiation below $\approx 150 \frac{W}{m^2}$ is associated with some degree of under-forecasting and a value above $\approx 150 \frac{W}{m^2}$ (most pronounced for forecast values from about 500 to about 800 $\frac{W}{m^2}$) with over-forecasting, which agrees with HIRLAM's tendency to underestimate the cloud cover (Bent Hansen Sass, personal communication) and thereby over-estimating the amount of global radiation reaching the surface. From this plot, an area of focus could be to reduce high values (in the interval from 500 to 800 $\frac{W}{m^2}$) of global radiation caused by the underestimate of clouds — a problem that is not easily alleviated in NWP models because of the difficulties in forecasting the exact timing and location of small-scale clouds, some of which appear on a scale too small to be resolved by the grid of the NWP model.

A change of variable to the clearness index reveals a strong conditional bias with under-forecasting for small values of the clearness index and a similar degree of over-forecasting for high values of the clearness index. A value of ≈ 0.4 — the central value in the distribution of forecasts of clearness index — separates under-forecasting (for values below ≈ 0.4) from over-forecasting (for values above ≈ 0.4). In a situation of light cloud cover corresponding to a high clearness index, the forecasts over-estimate the clearness index in correspondence with HIRLAM's tendency to under-estimate clouds. Conversely, in a situation of heavy cloud cover corresponding to a low clearness index, the forecasts seem to overestimate the cloud cover and hence underestimate the clearness index (observed values are higher than forecasted values). The focus area from this figure would probably be more evenly distributed over both low values and high values of the clearness index and, hence, more evenly distributed between situations of a low to modest cloud cover associated with over-forecasting of the clearness index and thereby under-forecasting of the cloud cover and situations of a modest to an extended cloud cover associated with under-forecasting of the clearness index and thereby over-forecasting of the cloud cover.

While the conditional biases in figure 8.8(a) are modest at least until a forecast value of about 500 $\frac{W}{m^2}$ — indicating relatively unbiased forecasts in the range 0 – 500 $\frac{W}{m}$ —, the picture is different for the clearness index in figure 8.8(b). Here, the slope of the median values is different from the line of perfect correspondence between forecasts and observations. This deteriorate appearance is believed to be caused by a combination of the rearrangement of data using the clearness index instead of the measured values of global

radiation and by the resulting change of scale.

Similar "conditional quantile" plots of the ensemble mean and the ensemble median as well as individual ensemble members correspond qualitatively to the plots for the control forecasts and are therefore not shown. However, the ensemble mean displays somewhat less conditional bias compared to the control forecast.

8.2.4 Discrimination

To investigate the ability of a set of forecasts to discriminate between observations, both the approach of Murphy et al. (1989) based on the conditional distribution $p(y|x)$ and the approach of Manson and Weigel (2009) based on the general discrimination score, D, (described in section 7.1.2) have been applied.

Assessed by the conditional distribution $p(y|x)$

In figure 8.9(a) and 8.9(b), the conditional distribution, $p(y|x)$, is plotted for three different values of the observation, X: the lower quartile (25 %), the median (50 %), and the upper quartile (75 %) of the distribution of the observations. For the data subset corresponding to the 12 UTC global radiation, these are 73 $\frac{W}{m^2}$, 320 $\frac{W}{m^2}$, and 589 $\frac{W}{m^2}$, respectively. To reduce sampling variability, only forecasts associated with an observation within a 5 % interval of the observed value are considered. The number of forecasts used to estimate the conditional distribution $p(y|x)$ is between 350 and 1000 depending on the value of the observation and is a combination of time and space points. In figure 8.9, data for the ensemble mean (a) and for the control forecast (b) is seen. For each of the three observation values, the distributions of the corresponding forecasts have distinct peaks (modes) at values matching the observations for both the ensemble mean in figure 8.9(a) and the control forecast in figure 8.9(b). The distributions of forecasts associated with observations of 73 $\frac{W}{m^2}$ and 589 $\frac{W}{m^2}$, respectively, are well separated for both the ensemble mean in figure 8.9(a) and the control forecast in figure 8.9(b).

According to Murphy et al. (1989), a forecast Y is perfectly discriminatory if $p(y = Y|x) = 0$ for all values of X except one, that is, for perfect discrimination, all observations associated with a given forecast Y, should be equal to a given observation X. In figure 8.9(a), this is equivalent to requiring that for a given forecast, say $Y = 100$, the relative frequencies $p(y = 100|x = 320)$ and $p(y = 100|x = 589)$ both be equal to zero and $p(y = 100|x = 73)$ different from zero. This is nearly the case here for forecast in the range 0-150 $\frac{W}{m^2}$. The relative frequencies of $p(y = 100|x = 320)$

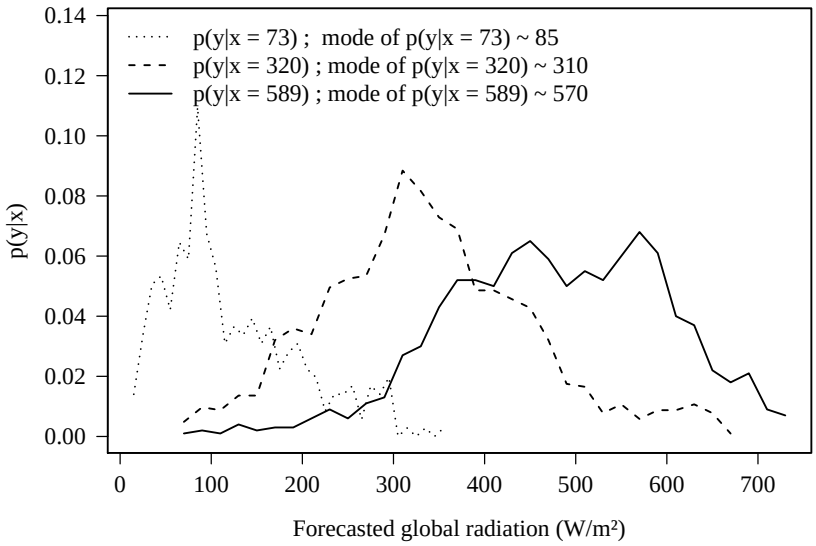

(a) Ensemble Mean

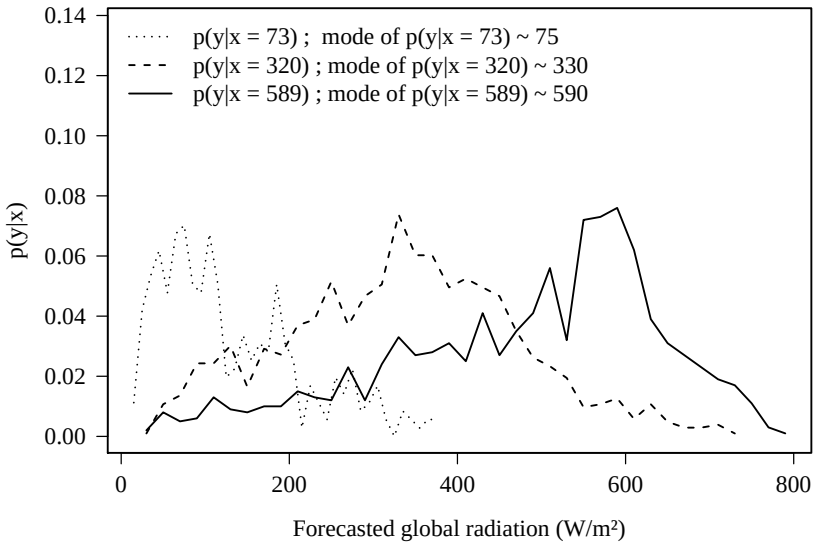

(b) Control Forecast

FIGURE 8.9: The conditional probability $p(y|x)$ for the ensemble mean (a) and the control forecast (b) for a data subset within the $\mathcal{N}$ time-space points consistent with the 12 UTC global radiation; the figure is inspired by Murphy et al. (1989, Fig. 8).

and $p(y = 100|x = 589)$ are both close to zero, while $p(y = 100|x = 73)$ is well above. However, this is not the case from values of about 300 to 500 $\frac{W}{m^2}$, where both figures reveal some overlap between the forecasts distributions corresponding to observations of 320 $\frac{W}{m^2}$ and 589 $\frac{W}{m^2}$. For those values, both forecasts distributions, $p(y|x = 320)$ and $p(y|x = 589)$, contain relative frequencies above zero and display a modest ability of both the ensemble mean and the control forecast to discriminate between those two well separated observation values.

From the two plots in figure 8.9, the assessment of which, the ensemble mean or the control forecast, is best at discriminating is not obvious. The modes of the three forecast distributions correspond better with the observations for the control forecast compared to the ensemble mean, for which the forecast distributions tend to be more peaked — at least for the two forecast distributions corresponding to $x = 73$ and $x = 320$ $\frac{W}{m^2}$.

Assessed by the generalised discrimination score

To avoid having trivial discriminations — for example a forecasting system being able to discriminate between global radiation in the morning and at midday or to discriminate between the global radiation in different parts of the country at a given time — influencing the evaluation of the discriminative power of global radiation, the calculation of the generalised discrimination score, D, is based on the clearness index, which allows the inclusion of the $K = 24$ verifying locations. The reason for this is that by using the clearness index, time, date and location are eliminated leaving only a weather component.

The generalised discrimination score, D, is in essence a scalar verification score, but by using the clearness index, the N forecast-observation pairs at each of the K verifying locations are included in the calculation of D.

Eliminating night values, leaves for each lead time between ≈ 3500 and ≈ 4500 data points (including the K verifying locations) for which any forecast-observation pair must be compared with any other forecast-observation pair.

The generalised discrimination score is seen to decrease with lead time. For all lead times, both the ensemble mean and the ensemble median score higher in the generalised discrimination score compared to the control forecast. Both the ensemble mean and the control forecast show a strong resemblance in the value of D, which decreases from about 78 % to 72 % for the ensemble mean and the ensemble median and from about 77 % to 70 % for the control forecast. Compared to the control forecast, the ensemble mean (and the ensemble median) scores about 3 % higher in discrimination score, D.

Each lead time is associated with between 3500 and 4500 forecast-observation pairs. Of these observations, nearly just as many are distinct corresponding to weather situations that might be very similar, but seldom

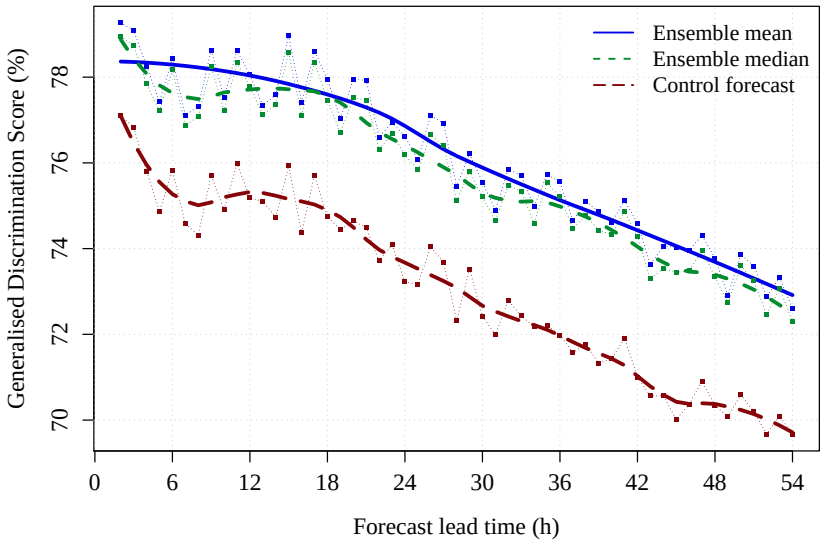

FIGURE 8.10: The generalised discrimination score as defined by Manson and Weigel (2009); a Loess smoothing has been applied to emphasize trends.

identical. This results in observations that might differ by tiny amounts. This might explain the somewhat modest discrimination score seen in figure 8.10. A higher precision of the forecasts is required to discriminate between continuous observations that differ by only small amounts. Another reason for the modest discrimination score might be related to the data set consisting of the clearness index for which the highly predictable astronomical signal present in the global radiation is eliminated leaving the more stochastic weather component. This might imply a conservative estimate of the discriminative power of the forecasts.

The two different ways of assessing the discriminative power of the ensemble mean and the control forecast have resulted in different outcomes. Using the generalised discrimination score, the ensemble mean performs better compared to the control forecast. This is, however, not evident using the conditional distribution $p(y|x)$ to assess the discriminative power.

8.3 Assessing the Performance of DMI-EPS

A central aspect of ensemble forecasting is its capacity to give information about the uncertainty in a forecast (Wilks, 2006, Chap. 6). The second part of this chapter is devoted to assessing the quality of DMI-EPS' ensemble forecasts of global radiation.

8.3.1 Application of quality measures applicable to single forecasts

Treating each ensemble member as an individual deterministic forecast, the deviation $y_i - x_i$ for each forecast-observation pair $i = 1, \ldots, N$, with $N = 19,002$, is computed at each of the $K = 24$ verifying locations and this is generated for each of the $M = 25$ ensemble forecasts. The resulting distribution of this pooled data set is divided after the hour of the day (UTC), and the result can be seen in figure 8.11. For each hour, the forecast deviations are generally distributed around zero with no forecast deviation at night — when both observations and model calculations are zero. Despite large deviations between forecasts and observations, no deviations seem physically impossible. A strong symmetry is present in the distributions in figure 8.11. Around 12 UTC, the distributions broaden and at 12 UTC, the distribution contains the largest absolute forecast deviations. A prevailing small negative forecast deviation is seen indicating a modest degree of under-forecasting. However, as suggested by figure 8.8, this picture might be more complicated with a presence of conditional bias.

Two quality measures of deterministic forecasts are applied to all 25 ensemble members. In figure 8.12, the forecast accuracy measure, the RMSE (see e.g. section 8.2.2), is seen, and in figure 8.13, the measure of forecast skill, the skill score is seen. The ensemble members are grouped according to the applied cloud scheme (STRACO and KF/RK), to "stochastic physics" and "no stochastic physics" of applied stochastic physics and no applied stochastic physics, respectively, and to their initial conditions (IC1 - IC5) (see e.g. table 6.2).

In general, the RMSE in figure 8.12 increases with lead time (this was also the case for the RMSEs of the control forecast, of the ensemble mean, and of the ensemble median in figure 8.4(b)). In using no stochastic physics (lower panels in figure 8.12), the two cloud schemes have different impacts on the RMSE with a high degree of clustering and little mixing and with the STRACO scheme in general superior to KF/RK. Without the application of stochastic physics, the RMSE for the two cloud scheme are slightly more adjacent for IC2 and IC4 compared to IC1, IC3, and IC5. In applying stochastic physics (upper panels), a considerable degree of overlap between the two cloud schemes is seen. In this case, however, the KF/RK scheme performs somewhat better with lower RMSEs. Differences in RMSE between

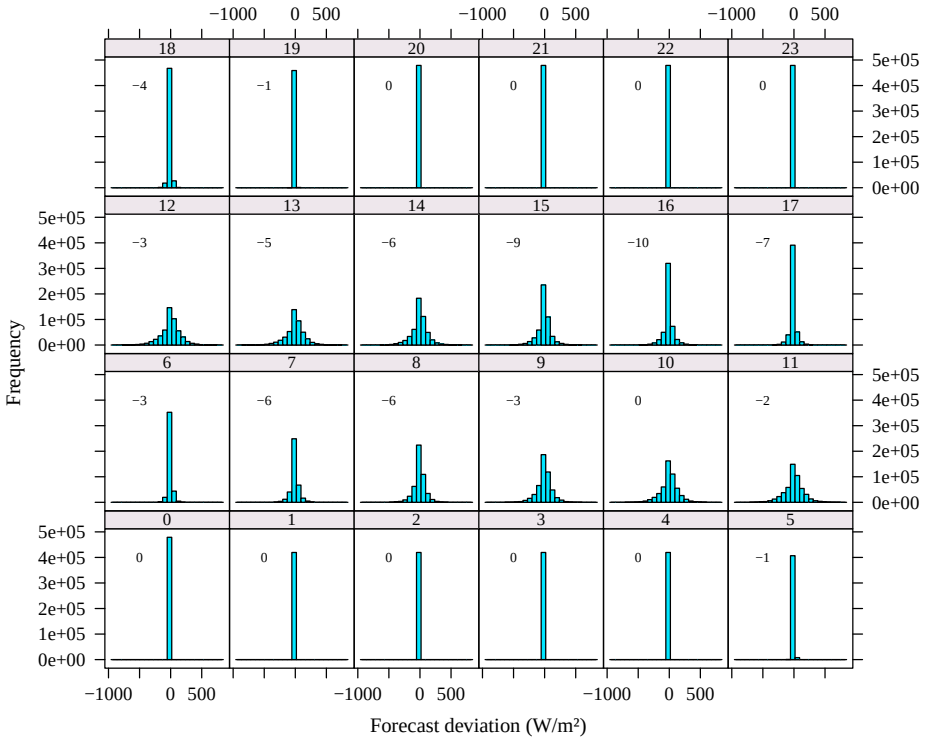

FIGURE 8.11: The distribution of the forecast deviations — difference between a forecast and the corresponding observation, $y_i - x_i$, for each i forecast occasion with $i = 1, \ldots, N$. The deviations are calculated for each $j = 1, \ldots, M$ ensemble forecast and for each location of the verifying observations $k = 1, \ldots, K$; the forecast deviations have been spilt by hour of day (UTC) indicated in the strips (0-23); night values are included; in each panel, the mean of the corresponding distribution is indicated; in each panel, the distribution contains 19002 x 24 (simultaneously predicted locations) x 25 (ensemble forecasts)/24 (hours) = 475,050 values.

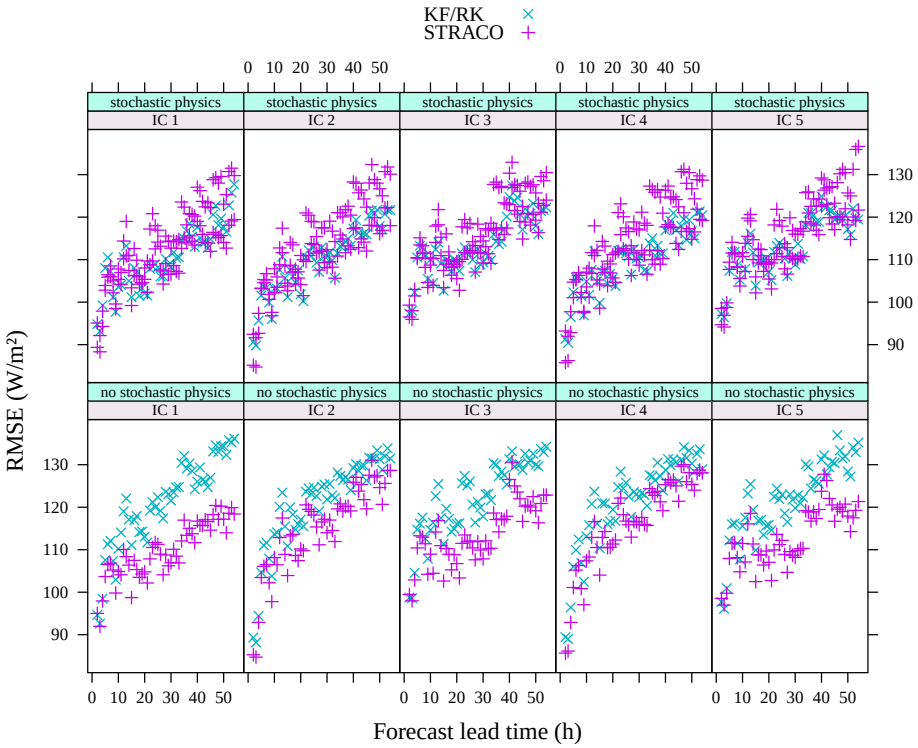

FIGURE 8.12: RMSE as a function of lead time calculated for each of the $M = 25$ ensemble members; the data set consists of all N forecast-observation pairs at each of the $K = 24$ verifying locations matching a given lead time. The RMSE for the ensemble members are grouped according to applied cloud scheme (the "STRACO" cloud scheme and the " KF/RK" cloud scheme), no application of stochastic physics ("no stochastic physics") and application of stochastic physics ("stochastic physics"), and initial conditions (see e.g. table 6.2); note that in the upper panel, two ensemble members fulfill the requirements of application of stochastic physics and STRACO cloud scheme for each initial condition, and this results in twice as many points for the STRACO scheme (purple "+") compared to the KF/RK scheme (cyan "x") — for IC1 ensemble members 6 and 21 contribute and for IC2 ensemble members 7 and 22 contribute, etc. (consult e.g. table 6.2).

the initial conditions are not pronounced for either cloud scheme. From the above analysis of RMSE, the application of stochastic physics seems to be able to convert groups of ensemble members into a more unified distribution, in which one cannot tell from the group of ensembles (I to V — see e.g. table 6.2), the value of the RMSE (for a given value of the lead time). Without stochastic physics, the different cloud schemes result in some clustering of the RMSEs with distinct relationships between RMSE and lead time.

Figure 8.13 shows a decreasing trend in the skill score, SS, with lead time (which was also the case for the skill scores for the control forecast and the ensemble mean in figure 8.7). Here, only the part of the data set corresponding to 12 UTC is included, which gives the following lead times: 0, 6, 18, 24, 30, 36, 42, 48, 54. In general, the conclusions of the figure resembles the conclusions of figure 8.12, but the limited data set emphasizes features of the ensemble forecasts somewhat more concealed in figure 8.12. A clear distinction in the skill scores of the two cloud schemes between applying stochastic physics (upper panel) and not applying stochastic (lower panel) exists. The application of stochastic physics brings the two cloud schemes closer regarding the skill score as defined here. With no application of stochastic physics, there is little mixing in skill scores between the two cloud schemes. The STRACO cloud scheme performs better (with higher skill score) than the KF/RK cloud scheme, but the closeness in skill score between the two cloud schemes depends, to some degree, on the initial condition perturbations. At the 54 hour lead time, the difference in skill score between the two cloud schemes is, for the initial conditions IC1, IC3, and IC5, substantial with no application of stochastic physics.

Considering the ensemble as reliable and the ensemble members as a random sample from the PDF, both the RMSE and its associated skill score (here based on MSE with climatology as the unskillful reference forecast) will deviate from one ensemble member to the next, but supposedly more in a statistical sense — in line with the upper panels in figure 8.12 and 8.13 — and probably less in line with the lower panels of these figures.

Among ensemble members with no application of stochastic physics in figure 8.12 and 8.13, a clear pattern in the different initial conditions is seen in both figure 8.12 and 8.13. The quality measure (RMSE or SS) of the two cloud schemes resembles each other more for IC2 and IC4 compared with IC3 and IC5. With respect to both RMSE and SS, using a 6 hour old forecast to generate the ensemble members gives the same pattern as using a 12 hour old forecast. Rather, the similarity in performance of the two cloud schemes seems to be related more to the sign of the perturbation in generating the initial conditions (see e.g. table 6.2 and equation (6.8)).

Values of RMSE of the individual ensemble members are comparable with values reported in Díaz et al. (2012), Lorenz et al. (2011) and Lorenz et al. (2012), which lends support to the individual forecasts of DMI-EPS.

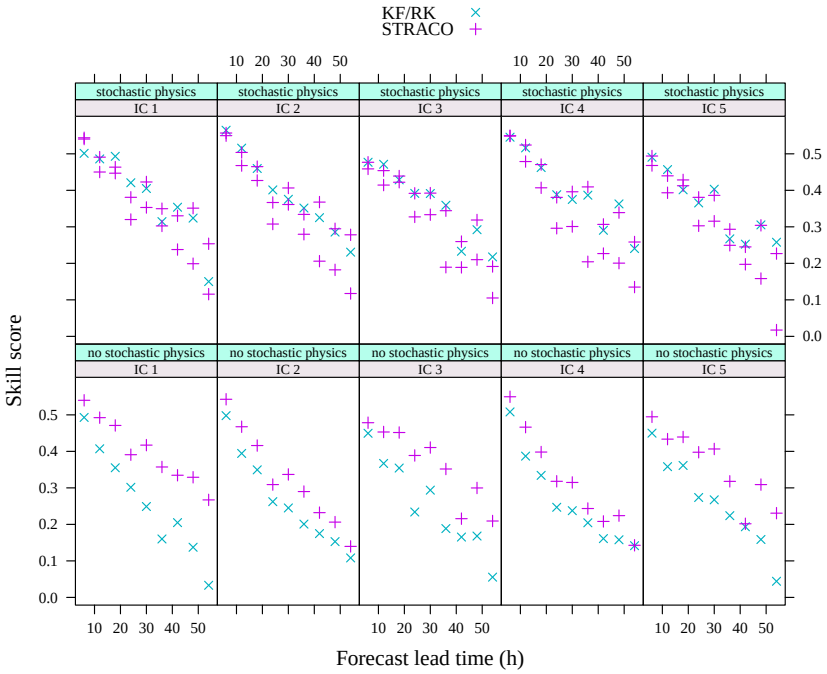

FIGURE 8.13: Skill scores (based on MSE_{clima}) as a function of lead time calculated for each of the $M = 25$ ensemble members; the data set consists of 12 UTC data at all K verifying locations matching a given lead time. The skill scores are grouped according to applied cloud schemes (STRACO and KF/RK), no application of stochastic physics ("no stochastic physics") and application of stochastic physics ("stochastic physics"), and initial conditions (see e.g. table 6.2); note that in the upper panel, two ensemble members fulfill the requirements of application of stochastic physics and STRACO cloud scheme for each initial condition, and this results in twice as many points for the STRACO scheme (purple "+") compared to the KF/RK scheme (cyan "x") — for IC1, ensemble members 6 and 21 contribute and for IC2, ensemble members 7 and 22 contribute, etc. (consult e.g. table 6.2).

8.3.2 Application of quality measures applicable to ensemble forecasts

For EPSs, the future state of a meteorological parameter should ideally fall within the ensemble spread, or the ensemble range or the ensemble dispersion, and the amount of spread should ideally be related to the uncertainty of the forecast (Toth and Kalnay, 1993). A small ensemble spread, that is, a high degree of agreement between the individual ensemble members, would intuitively imply a high confidence in the forecasts.

In figure 8.14(a), the capture rate is shown as a function of forecast lead time both excluding and including uncertainties on the observations. Due to sampling variability, the expected capture rate for a reliable ensemble of size M is $\frac{M-1}{M+1}$ (Feddersen, 2009; Jolliffe and Stephenson, 2012) — less than 100 %. Including 10 % uncertainty on the observations, increases the capture rate, but it is about 10 % off compared to the expected capture rate of $\frac{M-1}{M+1}$, which is about 92 %. Both curves (of including and not including observational uncertainties), increase with lead time until a lead time of about 18 hours. From then on, the curves increase only slightly. In figure 8.14(b), the spread of, or the dispersion of, the ensemble, here expressed as one standard deviation, is plotted against lead time. The ensemble spread increases until a lead time of about 42 hours, whereafter the ensemble spread seems to stabilise. Beyond a lead time of about 18 hours, the further divergence of the ensemble members, that is, the increase in ensemble spread (figure 8.14(b)) seems to be able to ensure that the capture rate is kept at a certain level throughout the forecast period despite the typical deterioration of forecasts with increasing lead time as illustrated in figure 8.4(b) and 8.12 for the RMSE and in figure 8.7 and 8.13 for the skill score.

Scalar Reliability

According to Jolliffe and Stephenson (2012, Chap. 8) and Bowler (2008), the RMSE of the ensemble mean should in case of consistency of the ensemble match the mean of the standard deviation of the ensemble — apart from a factor $\sqrt{\frac{M+1}{M}}$ that depends on the size of the ensemble. In figure 8.15, the RMSE as defined by equation (7.2) is plotted as a function of the mean ensemble standard deviation. The multidimensionality is here eliminated by averaging over the N time points in calculating the RMSE and the mean ensemble standard deviation. This gives a pair of values for each of the 24 verifying locations.

The ensemble standard deviation is about 20 % lower than the RMSE. Complete consistency of the ensemble forecasts of global radiation is not evident from the "RMSE versus ensemble spread"-relation.

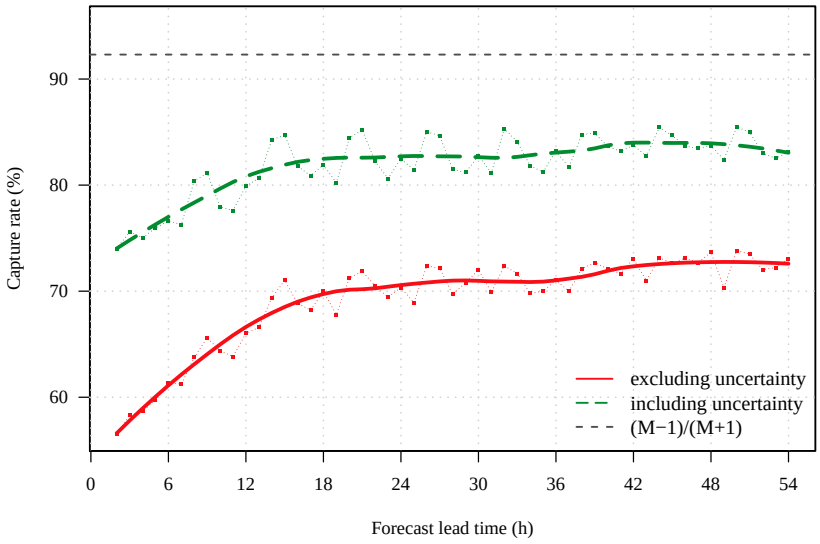

(a) Capture Rate

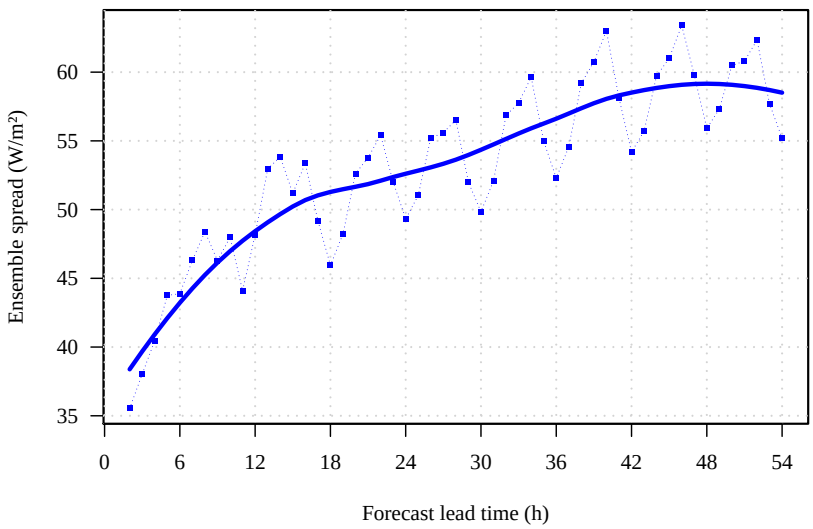

(b) Ensemble Spread

FIGURE 8.14: The capture rate (a) and ensemble spread (b) — expressed by one standard deviation from mean — as an average per lead time in a data set consisting of global radiation for $\mathcal{N}$ forecast-observation pairs; a Loess smoothing has been applied to emphasize trends.

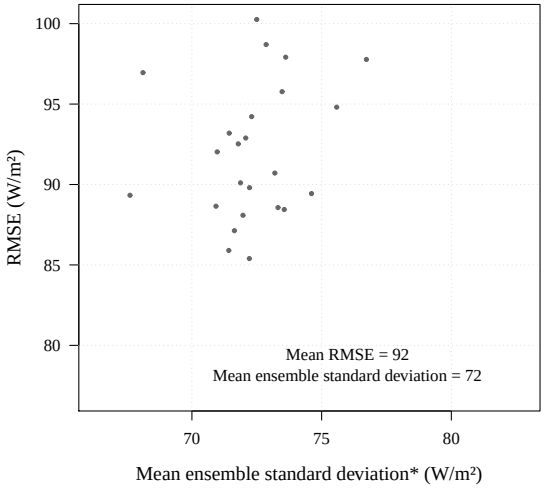

FIGURE 8.15: RMSE versus mean of the ensemble standard deviation multiplied by $\sqrt{\frac{M+1}{M}}$ (indicated by an asterisk (*)); an average of the 24 values is indicated.

Multidimensional Reliability

Multivariate Rank Histogram To evaluate the multidimensional reliability of the $K = 24$ simultaneously ensemble predictions each consisting of N ensemble forecasts with matching observations (see e.g. section 8.1), a multivariate rank (MVR) histogram has been constructed according to Gneiting et al. (2008); Jolliffe and Stephenson (2012) and is displayed in figure 8.16.

From the MVR histogram, both a slight tendency of the ensemble forecasts to over-forecast and a number of events, where the observation is exceeded by all ensemble members is seen. The highly overpopulated rank, $r = 1$, together with the slightly negative slope in the distribution suggests a degree of over-forecasting of the ensemble (see e.g. Gneiting et al. (2008, Figure 3)), which corresponds with HIRLAM's tendency to underestimate the cloud extent (Bent Hansen Sass, personal communication).

In the MVR histogram (figure 8.16), all rank values — except rank 1 — are close to being equally populated. One could argue that the requirement that for any two ensemble "vectors" $\mathcal{V}_j$ and $\mathcal{V}_l$, $\mathcal{V}_j$ must exceed $\mathcal{V}_l$ for all K dimensions for the coefficient $q_{j,l}$ to be different from zero (and for the pre-rank, ρ_j, to be different from 1), is in this case difficult to fulfil for $K = 24$ dimensions. This would imply that most "pre-ranks", ρ_j with $j \in \{0, 1, \ldots, M\}$ will be equal to 1 according to equation (7.11). The "pre-

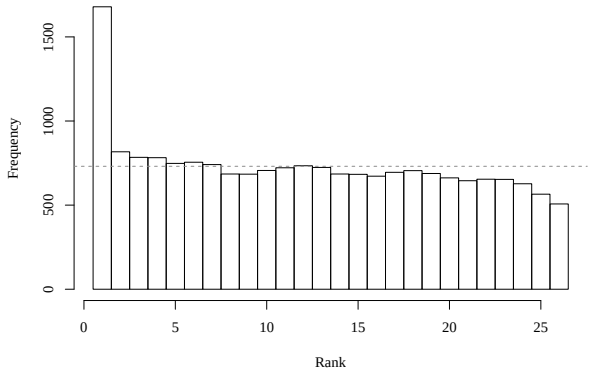

FIGURE 8.16: MVR rank histograms for all N forecast-observation pairs; the dashed line indicates the expected population of the rank values.

rank" of the observation, ρ_0, will then often be tied and its multivariate rank, r, solved at random. This will tend to populate all rank values, $1, \ldots, 26$, equally, which will result in a uniform multivariate rank histogram.

Minimum Spanning Tree Histogram The other method to evaluate the reliability of multidimensional ensemble forecasts is the minimum spanning tree (MST) histogram (Jolliffe and Stephenson, 2012, Chap. 8). It is applicable if a number of locations are simultaneously predicted (Jolliffe and Stephenson, 2012), which is the situation in this work with $K = 24$ simultaneously predicted ensemble forecasts (see e.g. section 8.1).

The distances of the spanning tree can be calculated in several ways applicable to different characteristics of the data set. In this case, the minimum spanning trees have been calculated using a Euclidean distance in a $K = 24$ dimensional space. The Euclidean distance might not be appropriate if the variances in the data set are different for some of the K dimensions[4], and if further a covariance between (some of) the K dimensions exists (Gombos and Hansen, 2007). The K dimensions of the data consist of the 24 locations measuring the same quantity, and it is therefore assumed that the variances of the data in different dimensions on average are similar. The use of the clearness index should reduce some of the covariance between dimensions[5].

[4]The situation is different if the K dimensions consists of $K = 2$ meteorological variables — like temperature and precipitation at the same location, since temperature and precipitation might not have the same variance.

[5]Concerning global radiation, a covariance between the K verifying locations exists due to the latitude and longitude dependence of the solar radiation. By use of the clearness index, this is eliminated, but a covariance due to a similar weather situation at two or

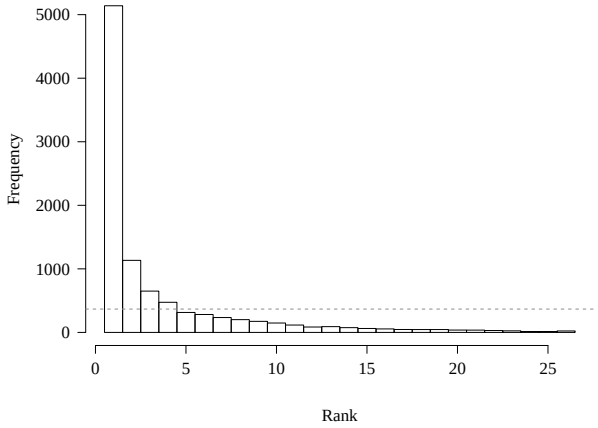

FIGURE 8.17: MST histograms for all N forecast-observation pairs; the dashed line indicates the expected population of rank values.

With the large number of forecast realizations, N, available here, it is believed that the similarity of the two distributions — the distribution at a certain forecast time of the ensemble forecasts and of the observation (considered as a random sample) — will not be sensitive to the choice of norm (Gombos and Hansen, 2007). From those considerations, the Euclidean distance has been applied in the minimum spanning tree.

The strong negative slope (see e.g. section 7.2) suggests an under-dispersive ensemble. Of the rank values $\{1, \ldots, M+1\}$, the smallest rank value, that is, $r = 1$, is highly overpopulated as seen in figure 8.17 indicating that the inclusion of the verifying observation increases the total length of the MST and hence that the notion of the ensemble members and the verifying observation being statistically indistinguishable is not evident.

Discrimination

To avoid having trivial discriminations — for example a forecasting system being able to discriminate between the 12 UTC global radiation on August 23 and on November 12 — influencing the evaluation of the discriminative power of global radiation from DMI-EPS, the calculation of the generalised discrimination score, D, is based on the clearness index, which allows the inclusion of the $K = 24$ verifying locations, since the clearness is a normalised quantity sensitive to only the weather situation — for example the amount of and distribution of clouds.

The generalised discrimination score, D, is a scalar verification score, but by using the clearness index, the N forecast-observation pairs at each

more neighbouring locations will still be present.

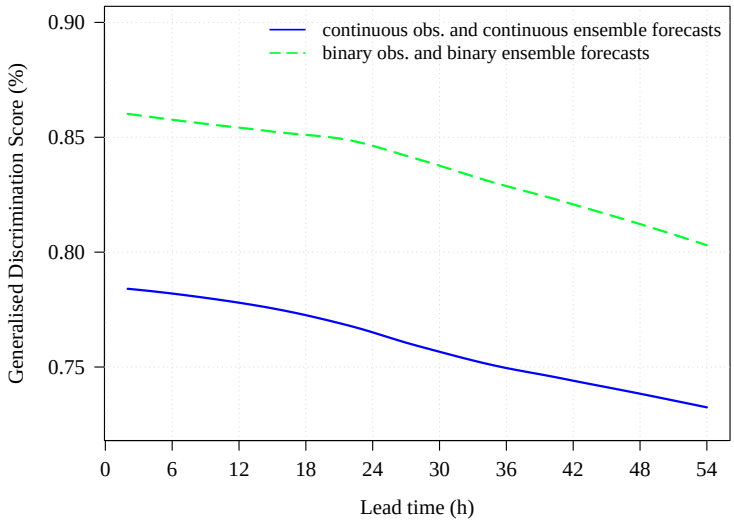

FIGURE 8.18: The generalised discrimination score as a function of lead time; a Loess smoothing has been applied; the binary events are generated by setting valued above or equal to the observational mean equal to 1 and values below the observational mean equal to 0.

of the K verifying locations are included in the calculation of D.

Eliminating night values, leaves for each lead time between ≈3500 and ≈4500 data points (including K verifying locations) from which any forecast-observation pair must be compared with any other forecast-observation pair. With ≈4000 values for each lead time, the process of ranking ensemble forecasts (described in section C)) is quite time-consuming. To reduce computational time, a sample of 1000 randomly selected data points is generated for each lead time, and from those values, the generalised discrimination score is calculated

As the number of distinct observations increases, the discriminative power of forecasts usually decreases because of the higher precision required in the continuous case to discriminate between a large number of observations that may differ by only small amounts (Weigel and Manson, 2011). To compare with ensemble forecasts of continuous observations, binary observations are generated by discerning between observations above or below the observation mean.

In figure 8.18, the generalised discrimination score is seen to decrease with lead time for both the continuous and the binary observations as expected. For the continuous observations the generalised discrimination score decreases from about 78 % and ends at about 72 % at a 54 hour forecast lead time. In the case of binary observations, the generalised discrimina-

tion score is about 8 % high throughout the forecast period. It decreases from about 86 % to about 85 % in the first 24 hours of the forecast. From then on, a faster decrease is seen, and at a 54 hour forecast lead time, the generalised discrimination score has dropped to about 80 %, which is highly comparable with D calculated for the ensemble mean and the ensemble median in figure 8.10. In this case, the sample of 1000 values corresponds to 1000 (or just below) discrete observations, so here, the forecasts have to discriminate between observations that may differ by only tiny amounts, which might explain the generally modest discrimination score, D. From figure 8.18, the generalised discrimination score for binary observations is for all lead times above the score for the continuous observations as a result of the higher precision required for the forecasts to discriminate between observations that differ by only small amounts in the continuous case compared to the binary case with only two observation values. Another reason for the modest discrimination score for both the continuous and the binary observations might be related to the use of the clearness index for which the highly predictable astronomical signal present in the global radiation is eliminated leaving only a weather component. This might give a modest estimate of the discriminative power of the forecasts.

9 Discussion

9.1 Verification of Global Radiation from DMI-EPS

An important goal in ensemble prediction is to approximate by the ensemble members the forecast PDF, which contains information on the forecast uncertainty. Through verification techniques, the consistency, or reliability, of the ensemble forecasts of global radiation has been investigated.

9.1.1 Assessing the Performance of DMI-EPS

Generating an EPS that takes into account both the uncertainty in the analysis, which is unknown, and the imperfections of the NWP model, which might be difficult to assess, poses a challenge to ensemble prediction.

Consistency of DMI-EPS forecasts of global radiation

The immediate conclusion on the ensemble consistency, or the ensemble reliability, of DMI-EPS global radiation forecasts is somewhat ambiguous.

However, the strong negative slope in the MST histogram in figure 8.17 and the values of the "RMSE versus ensemble spread"-relation shown in figure 8.15 both suggest an under-dispersive ensemble as caused by a conditional forecast bias. Under-dispersion is not evident from the MVR histogram in figure 8.16. One could in case of the the MVR histogram argue that the requirement that for any two ensemble "vectors" $\mathcal{V}_j$ and $\mathcal{V}_l$, $\mathcal{V}_j$ must exceed $\mathcal{V}_l$ for all K dimensions for the coefficient $q_{j,l}$ to be different from zero (and for the pre-rank, ρ_j, to be different from 1 — see e.g. equation (7.11)), is in this case difficult to fulfil for $K = 24$ dimensions. Most "pre-ranks", ρ_j would then be equal to 1 according to equation (7.11). The "pre-rank" of the observation, ρ_0, will then often be tied and its multivariate rank, r, solved at random. This will tend to populate all rank values, $1, \ldots, 26$, equally, which will result in a uniform multivariate rank histogram.

The under-dispersiveness derived from the MST histogram and the "RMSE versus ensemble spread"-relation corresponds with the too low capture rate seen in figure 8.14(a). In DMI-EPS, the capture rate is about 20 % off the

expected rate excluding uncertainties on the observations. This number is reduced to about 10 % including observational uncertainty. This illustrates the importance of including uncertainties on observations in all kind of verification. These capture rates correspond to figures reported in Bowler (2008) for the MOGREPS (Bowler et al., 2008) limited area ensemble prediction system of 24 ensemble members. Under-dispersion is ensemble forecasts is a common problem in ensemble prediction (Bowler, 2008; Buizza, 1997; Wilks, 2006), and how to alleviate it is not straightforward as it necessitates a better simulation of the uncertainty in the analysis and/or of the uncertainties relating to deficiencies in the NWP model formulation.

On those occasions when the observation lies just outside the ensemble range, the effect of excluding or including uncertainties on observations in evaluating ensemble dispersion either through rank histograms or through capture rates may be considerable (Bowler, 2008).

Except in a few cases, observational uncertainties have not been addressed, and this might permeate most results. Whether the inclusion of uncertainties on observations alone will increase the dispersion is yet to be investigated, but the results obtained here point toward an under-dispersive ensemble and ensemble forecasts that will give too little uncertainty on the forecast values.

Over-forecasting or under-forecasting

The MVR histogram in figure 8.16 suggests a strong degree of over-forecasting (from the highly over-populated lowest rank value, $r = 1$, indicating that the observation is too often exceeded by all ensemble members), which by comparing with Gneiting et al. (2008, Figure 4), seems to be the case in the MST histogram in figure 8.17. A tendency of the ensemble to over-forecast corresponds with HIRLAM's tendency to under-forecast clouds (Bent Hansen Sass, personal communication) and, hence, over-forecast global radiation at the surface. However, the slight under-forecasting evident from figure 8.11 and the over-forecasting established from figure 8.16 and 8.17 might seem contradictive. This difference in over-all bias is related to the difference between real values — as used in figure 8.11 and rank values — as used in figure 8.16 and 8.17 — for which information on the distance of the ensemble members to the observation is lost. To illustrate this, consider table 9.1. At time point "a", the contribution to the deviation between the ensemble members and the observation amounts to $2 - 18 + 1 = -15$, while the observation only exceeds one ensemble member resulting in rank 2 of the observation. At time point "b", the contribution to the deviation between ensemble members and observation is $1 + 1 + 1 = 3$ with all ensemble members exceeding the observation, which then has rank 1. The difference between rank 1 and rank 2 of the observation, might therefore contribute significantly to the difference between the ensemble forecasts and

	Ensemble member			
Time	mbr1	mbr2	mbr3	observation
$t = a$	32 (**4**)	12 (**1**)	31 (**3**)	30 (**2**)
$y_a - x_a$	2	-18	1	
$t = b$	21	21	21	20 (**1**)
$y_b - x_b$	1	1	1	

TABLE 9.1: An example illustrating how a low rank value of the observation can be associated with a large negative difference between a forecast and the matching observation; in parentheses, the rank value is shown.

the observation.

On those occasions, when all ensemble members exceed the observation, the contribution to the forecast deviation in figure 8.11 will be positive, but on those occasions when the observation exceed one or more of the ensemble members, the contribution to the forecast deviation in figure 8.11 might be considerable negative as illustrated in table 9.1. It is therefore possible to establish over-forecasting from the rank histograms in figure 8.16 and 8.17 and under-forecasting looking at the deviation between a given ensemble member and the observation.

As opposed to the rank histograms, the distributions shown in figure 8.11 are more sensitive to the actual values of the ensemble members. However, dispersion of the ensemble members is a necessary condition for ensemble consistency, and if the ensemble members were to be sampled from the PDF, all values would be valid, but, of course, not equally likely. From these considerations, I have most faith in the results from the MVR histogram with the reservations that all rank histograms should be interpreted with care and that despite searching the literature, a similar shape of a MVR histogram has not been found, which further complicates interpretation.

Initial Condition Perturbations

Several ways of generating initial condition perturbations simulating the uncertainty in the analysis exist. These methods differ in approach and complexity. In DMI-EPS, a SLAF method to generate ensemble perturbations is applied. Despite Boeing a simple way of generating the initial condition perturbations, results endorsing the SLAF method have been reported (Feddersen, 2009). Feddersen (2009) speculates, however, that a way of increasing the ensemble spread and thereby improve DMI-EPS forecasts could be to use a different method to perturb the initial conditions — for example, a breeding method (described in Toth and Kalnay (1993)).

Among ensemble members with no application of stochastic physics, two distinct patterns in the different initial conditions are seen in both figure 8.12

and 8.13 with a common pattern between IC3 and IC5, and a common pattern for IC2 and IC4. An explanation for this distinct pattern in terms of the generation of the initial conditions using a 6 hour and a 12 hour old forecast is not evident. These distinct patterns might suggest a degree of clustering of the ensemble members. However, by application of stochastic physics this apparent clustering seems to disappear.

Accessing model deficiency by use of multiple models

The use of multiple models beside the initial condition perturbations in generating ensemble members is reported to both cluster the ensemble members by model with a PDF dictated more by parametrisation scheme and less by the forecast uncertainty (Bowler et al., 2008) and improve the ensemble forecasts by increasing the ensemble dispersion (Wilks, 2006, Chap. 6). From figure 8.12 and 8.13, the use of multiple models in terms of cloud schemes seems to cluster the ensemble members by model. However, application of stochastic physics seems to alleviate this clustering. Whether the use of multiple cloud schemes improves the ensemble forecasts by increasing the ensemble dispersion is not easily assessed by the results obtained here, but the RMSE in figure 8.12 and the skill score in figure 8.13, might be distributed over a larger span of values compared to corresponding values with an application of stochastic physics in both figures. This is most pronounced for IC1, IC3, and IC5.

9.1.2 Assessing the Performance of the Ensemble Mean

An early goal of ensemble prediction was to obtain a forecast superior to a traditional forecast by averaging the ensemble members. In averaging, some of the errors present in a traditional forecast should cancel and, in general, provide an improved forecast (Tracton and Kalnay, 1993). However, this will only be the case if initially the ensemble members represent the PDF of the analysis and if the NWP model is perfect (Toth and Kalnay, 1993; Tracton and Kalnay, 1993). Imperfect NWP models and imperfect representations of the analysis PDF have shown to limit the effect of cancelling the errors (Tracton and Kalnay, 1993), and, averaging the ensemble members is now considered to be a simple application of ensemble forecasts (Wilks, 2006, Chap. 6).

Within the task of assessing the full potential of DMI-EPS, the ensemble mean has, nevertheless, been computed to be compared with the control forecast. Being a more robust measure of centre, the ensemble median has, in addition, been computed. However, the ensemble median does not, as speculated, perform better than — but highly comparable to — the ensemble mean. Concerning RMSE (figure 8.4(b)), skill score (table 8.2), reliability (assessed by the conditional quantile plots (illustrated in figure 8.8 for the

control forecast)), and discrimination as measured by the general discrimination score, D, (figure 8.10), the ensemble mean performs better than the control forecast. The superiority of the ensemble mean compared to the control forecast might be an effect of reducing by averaging some of the errors present in the control forecast. From the conditional quantile plots in figure 8.8, the character of the forecast bias has been revealed.

A source of the modest skill score, SS, of the control forecast might be related to the use of the clearness index in calculating the score. By use of the clearness index, the highly predictable signals relating to astronomical effects present in the global radiation is eliminated leaving the more stochastic weather component, which might give a conservative estimate of the forecast skills score. Another source of the modest skill score might be related to the limited time (5 August 2011 - 14 November 2011) over which the sample climatology (or observation mean) used as the unskillful reference forecast in computing the skill score is estimated (Jolliffe and Stephenson, 2012, Chap. 1).

Discrimination

The somewhat modest generalised discrimination score evident from figure 8.10 might be related to i) the vast amount of distinct observations for the forecasts to discriminate between and to ii) the use of the clearness index in estimating the discriminative power by the generalised discrimination score. By use of the clearness index, the highly predictable astronomical signal is eliminated leaving only a weather component. This might imply a highly cautions estimate of the discriminative power of the forecasts.

In general, the discrimination score, D, is about 3 % higher for the ensemble mean compared to the control forecast. This number might not be exceptional, but I find it nevertheless surprising. I would have expected that the smoothing by averaging introduced by the ensemble mean would imply a loss of discriminative power compared to the control forecasts. However, a clear distinction in the discriminative power between the ensemble mean and the control forecast using the conditional distribution $p(y|x)$ in figure 8.9 is not seen. The difference between the two methods in evaluating the discriminative power of the ensemble mean and the control forecast might be explained by the different approaches based on each their distribution: the conditional distribution $p(y|x)$ in figure 8.9 and the joint distribution $p(x, y)$ in figure 8.10.

9.2 Performance of Global Radiation Forecasts

Evaluation of single forecasts of global radiation has led to a revision of the HIRLAM shortwave parametrisations, which consists of simple, yet successful, parametrisation of the transmission of solar radiaiton through the

atmosphere. Concerning direct radiation, the revised parametrisations performs most satisfying compared with a highly detailed model describing transfer of radiation within the atmosphere.

9.3 High-Resolution, Limited-Area Models

With increased resolution in limited area NWP models, more details on the atmospheric state can be resolved including small-scale clouds, which might not appear in a model of lower resolution. If, however, one of these small-scale clouds were to be forecasted at one grid point, but show up at a neighbouring grid point, both grid points are forecasted wrong in terms of cloud cover. In this way, high-resolution models might because of their degree of detail suffer a double penalty compared to lower resolution models. The high-resolution limited area ensemble prediction system at DMI may, as a high-resolution model, in some cases suffer from this double penalty, which might reduce the quality of forecasts of global radiation.

9.4 The Solar Heating Unit

The full implementation of the advanced control system making use of all state-of-the-art forecast models developed within the project "Solar/electric heating systems in the future energy system" has not been feasible. It is planned, in a highly desirable prolongation of the project, to extend the advanced control system to make use of all developed forecast methods and available information.

10 Conclusion & Outlook

DMI-EPS

For most considered aspects of forecast quality, DMI-EPS is documented to perform better than or comparable to the global ensemble prediction system at ECMWF (Feddersen, 2009) and is a highly valuable forecast tool at the weather service at DMI.

From the investigation of the consistency of the ensemble forecasts of global radiation, there seems to be evidence of some under-dispersiveness. Whether the inclusion of uncertainties on the observations will reduce this under-dispersiveness is still an open question, but the ensemble memebers will tend to express too little uncertainty on forecast values (Wilks, 2006, Chap. 6). Often in EPSs, the ensemble dispersion will be too small to capture the observation at the expectable fraction (Bowler, 2008; Buizza, 1997; Wilks, 2006). How to alleviate this under-dispersiveness is not straightforward as it requires better simulation of the uncertainty in the analysis and, maybe, better simulation of the uncertainties relating to deficiencies in the NWP model formulation.

Concerning global radiation forecasts, the effect of simulating model deficiencies by use of multiple cloud schemes seems modest, and in a future revision of DMI-EPS, simulating model deficiencies by the application of two cloud schemes might be reconsidered and compared to the effect on ensemble dispersion of using a more complex way of generating the initial condition perturbations.

In DMI-EPS, the tendencies of temperature, wind speed, humidity, and cloud condensate are subjected to stochastic perturbations, which is a combination of meteorological variables of the primitive equations and variables of high impact and interest to common users of meteorological forecasts. A vast number of meteorological variables and parameters exist, each of which can be perturb stochastically. Bowler et al. (2008) apply stochastic perturbation to adjustable parameters in the physical parametrisations necessary in NWP models and introducing uncertainties in the NWP model. However, the stochastic perturbations applied in DMI-EPS seem highly successful as they are able to make ensemble members clustered by either model or initial condition un-clustered. Alternative, or additional, meteorological variables

to subject to stochastic perturbations could still be considered in a revision of DMI-EPS. Inspired by (Bowler et al., 2008), these could be poorly know parameters in some of the parametrisations. Which parametrisations to select for stochastic perturbations should be deliberated.

Application of statistical post-processing might be a way to improve the ensemble forecasts of global radiation. However, more research into the character of the bias and its variation with weather patterns is necessary.

DMI-EPS — The Ensemble Mean

From the superiority of the ensemble mean compared to the control forecast, the value of the operational forecast might, maybe also for other parameters, benefit from complementing it with the value of the ensemble mean. A cluster analysis may, in addition to providing valuable information on the distribution of the ensemble members, also provide information on the appropriateness of the ensemble mean as characterising the ensemble.

Revision of the Radiation Scheme

In consequence of the evaluation of global radiation from DMI's operational HIRLAM model, revisions of the radiation scheme have been implemented. The implementation has resulted in a radiation scheme that concerning direct radiation performs most satisfying compared to a detailed model describing the transmission of radiation through the atmosphere.

Appendices

I

A Derivation of Beer's Law

When radiation enters a medium containing optically active matter, interactions between the radiation and the matter will weaken or attenuate the radiation traversing the medium by either absorbing or scatter the radiation. This attenuation or extinction depends on the optical characteristic of the medium (Thomas and Stamnes, 1999, Chap. 2) and is described by Beer's law the derivation of which is found below.

In figure A.1(a) a small slap of volume dV, thickness ds and surface area dA. The slap contains matter of dN particles that are all optically active, that is, they interact with radiation passing through dV. A beam of radiation of a given wavelength λ is incident normally to the slap — as illustrated to the left in figure A.1 (a). As the beam of radiation passes through the slap, it interacts with the particles through either absorption or scattering and less radiation escapes at the opposite site of the slap (Thomas and Stamnes, 1999, Chap. 2) — the right side in figure A.1 (a). The beam of radiation has been subjected to attenuation (or to extinction).

It has been found experimentally that the weakening or attenuation of a radiation beam depends linearly upon both the incident radiation and the amount of optically active matter along the beam direction (Thomas and Stamnes, 1999, Chap. 2). This amount must be proportional to the length ds. That is, the amount of optically active matter along the beam direction is proportional to the distance within the medium traversed by the beam, which in figure A.1 (a) is ds. This gives

$$dI_\lambda \propto -I_\lambda ds$$

with the change in radiation to the left of the proportionality sign and the dependent quantities to the right. The constant of proportionality is denoted by k_λ and called the extinction coefficient. It is a characteristic of the matter and might vary with wavelength. The above equation then becomes

$$dI_\lambda = -k_\lambda I_\lambda ds, \tag{A.1}$$

which is known as Beer's law. By integrating equation (A.1) over a finite path from 0 to S along the beam direction (figure A.1 (b)), the more common

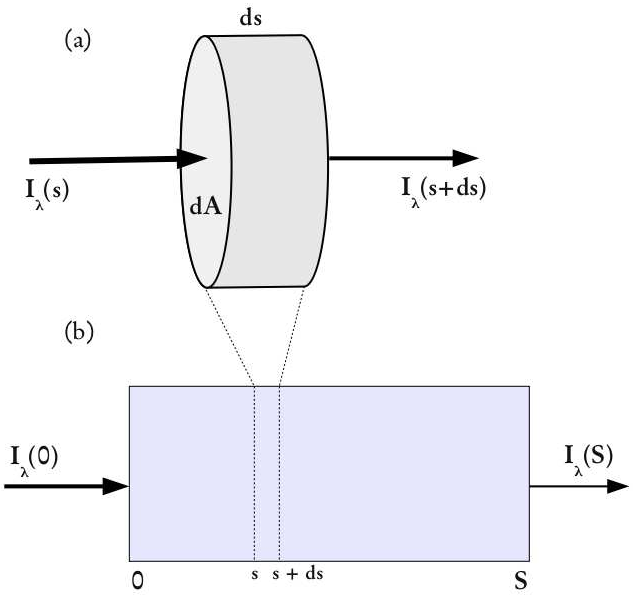

FIGURE A.1: (a) Radiation passing through a thin slab; (b) Radiation passing through a medium. The figure is inspired by Thomas and Stamnes (1999, Figure 2.4)

form of Beer's law is obtained

$$I_\lambda(S, \hat{\Omega}) = I_\lambda(0, \hat{\Omega}) \cdot \exp\,(-\int_0^S k_\lambda ds). \tag{A.2}$$

This form gives the radiation leaving the medium, $I_\lambda(S, \hat{\Omega})$, as a function of the radiation entering the medium $I_\lambda(0, \hat{\Omega})$, where $\hat{\Omega}$ is direction of propagation of the beam — which can be determined by a zenith and an azimuth angle. In an inhomogeneous medium, the extinction coefficient, k_λ, might change along the beam direction.

Defining an optical path τ_λ results in the following expression of Beer's law

$$I_\lambda(S, \hat{\Omega}) = I_\lambda(0, \hat{\Omega}) \cdot \exp\,(-\tau_\lambda).$$

(Paltridge and Platt, 1976; Thomas and Stamnes, 1999), where τ_λ, is a measure of the strength and number of optically active particles (that scatter or absorb radiation) along the beam of radiation, and the radiation is seen to decay exponentially with τ_λ along the beam direction (Thomas and Stamnes, 1999, Chap. 2). Note that τ_λ may change along the path of the beam.

I_λ is the spectral radiance, which is the energy with wavelengths in the interval $\{\lambda, \lambda + d\lambda\}$ that in the time interval dt passes the area element dA

and flows into a solid angle $d\omega$ centered on the direction $\hat{\Omega}$

$$I_\lambda = \frac{d^4E}{dA \cdot \cos\theta \cdot dt \cdot d\lambda \cdot d\omega} \tag{A.3}$$

where θ is the angle between the normal to the area dA and $\hat{\Omega}$. The quantity $dA \cdot \cos\theta$ is the projection of dA onto the direction $\hat{\Omega}$ (Thomas and Stamnes, 1999, Chap. 2) (see e.g. figure A.2).

The spectral irradiance, F_λ, expresses the energy with wavelengths in the interval $\{\lambda, \lambda + d\lambda\}$ that crosses an area dA in the time interval $\{t, t + dt\}$

$$F_\lambda = \frac{d^3E}{dA \cdot dt \cdot d\lambda}, \tag{A.4}$$

(Thomas and Stamnes, 1999, Chap. 2). Combining equation (A.4) and (A.3), the following relation between spectral radiance and spectral irradiance is obtained

$$F_\lambda = \int_{4\pi} I_\lambda \cos\theta d\omega. \tag{A.5}$$

From integrating the spectral radiance, I_λ, times $\cos\theta$ over all 4π solid angles, the total (or net) spectral irradiance F_λ is obtained.

The total downward irradiance (that is, the global radiation), $\mathrm{F}^\downarrow$, is obtained by integrating the spectral irradiance, F_λ, over a hemisphere.

$$\mathrm{F}^\downarrow = \int_0^\infty \int_{2\pi} I_\lambda \cos\theta \, d\omega d\lambda \tag{A.6}$$

The inner integral ($\int_{2\pi} I_\lambda \cos\theta d\omega$) is the downward spectral irradiance according to equation (A.5), which is then integrated over all wavelengths.

Integrating both the spectral radiance, I_λ, and the spectral irradiance, F_λ, over wavelengths gives the radiance I and the irradiance F, respectively, with units of $\frac{W}{m^2 \cdot sr}$ and $\frac{W}{m^2}$, respectively (Thomas and Stamnes, 1999; Wallace and Hobbs, 2006). Equation (A.5) then becomes

$$\begin{aligned} \mathrm{F} &= \int_0^\infty F_\lambda d\lambda && \text{(A.7)} \\ &= \int_0^\infty \int_{4\pi} I_\lambda \cos\theta d\omega d\lambda && \text{(A.8)} \\ &= \int_{4\pi} I \cos\theta && \text{(A.9)} \end{aligned}$$

This equation illustrates the relation between radiance and irradiance with unit of $\frac{W}{m^2 sr}$ and $\frac{W}{m^2}$, respectively. The irradiance, F, is the radiance integrated over some solid angle — for example a hemisphere as in equation (A.6), or, to obtain the net irradiance, over all solid angles as in equation (A.7).

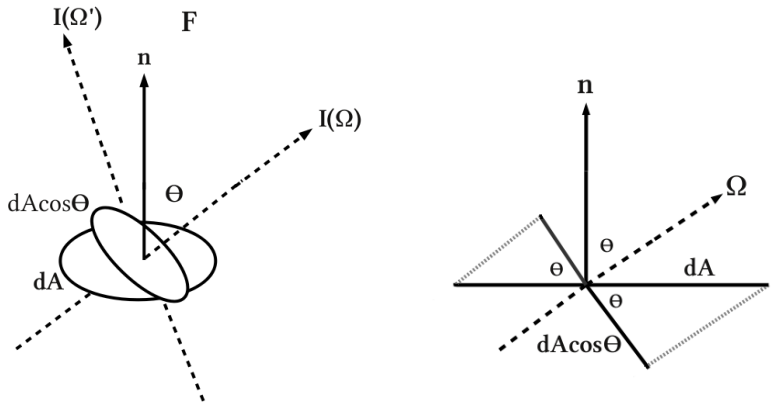

(a) (b)

FIGURE A.2: In (a), the irradiance (in $\frac{W}{m}$), F, would be all radiant energy passing through the area dA per second. The radiance $I(\Omega)$ (in $\frac{W}{m \cdot sr}$) in (a) is the radiant energy passing through an area $dA\cos\theta$ in the direction Ω (or into an infinitesimal cone centered at Ω) per second. Because of the lack of perspective in (a), the projection in one dimension of dA onto the direction of Ω, which is at an angle θ with $\mathbf{n}$, is illustrated in (b). The projection of dA onto the direction Ω becomes $dA\cos\theta$.

B Discrimination

Consider the set of forecast-observation pairs in table B.1.

Forecast	Observation
2.0	1.0
2.0	1.0
2.0	1.0
5.0	3.0
5.0	3.0
8.0	9.0

TABLE B.1: A simple example illustrating forecasts that are not completely reliable, but possess discrimination. The values could be *mm* of rain.

Because that neither

$$\begin{aligned} E(x|y &= 2.0) = 1.0 \neq 2.0 \\ &\text{nor} \\ E(x|y &= 5.0) = 3.0 \neq 5.0 \\ &\text{nor} \\ E(x|y &= 8.0) = 9.0 \neq 8.0, \end{aligned}$$

the requirements to complete reliability are not fulfilled (see e.g. equation

(7.7)). The conditional distributions $p(y|x)$ become

$$p(y = 2.0|x = 1.0) = 1.0$$
$$p(y = 2.0|x = 3.0) = 0.0$$
$$p(y = 2.0|x = 9.0) = 0.0$$

$$p(y = 5.0|x = 1.0) = 0.0$$
$$p(y = 5.0|x = 3.0) = 1.0$$
$$p(y = 5.0|x = 9.0 = 0.0$$

$$p(y = 8.0|x = 1.0) = 0.0$$
$$p(y = 8.0|x = 3.0) = 0.0$$
$$p(y = 8.0|x = 9.0) = 1.0$$

For each forecast value Y, $p(y = Y|x)$ equals zero for all values of X except for one, and Y is therefore perfect discriminatory (Murphy et al., 1989), which should become clear from the following consideration: a forecast value of 2.0 mm is always followed by an observation of 1.0 mm, and a forecast of 5.0 mm is always followed by an observation of 3.0 mm, and a forecast of 8.0 mm is always followed by an observation of 9.0 mm. Although the forecasts are not reliable, each forecast Y is able to discriminate between the three different events of 1.0 mm, 3.0 mm, and 9.0 mm.

C Generalized Discrimination Score

For two ensemble forecasts $\mathbf{y}_s$ and $\mathbf{y}_t$ of size M (i.e. $\mathbf{y}_s = (y_{s,1}, \ldots, y_{s,M})$ and $\mathbf{y}_t = (y_{t,1}, \ldots, y_{t,M})$), the following value is constructed:

$$F_{s,t} = \frac{\sum_{j=1}^{M} r_{s,t,j} - \frac{M(M+1)}{2}}{M^2}, \tag{C.1}$$

with $r_{s,t,j}$ begin the rank of $y_{s,j}$ with respect to the set of pooled ensemble members $y_{s,1}, y_{s,2}, \ldots, y_{s,M}, y_{t,1}, y_{t,2}, \ldots, y_{t,M}$, if sorted in ascending order (Weigel and Manson, 2011).

)

If in the pooled sample of $2M$ ensemble members, the ensemble members of $\mathbf{y}_s$ occupy the M smallest ranks $(1, \ldots, M)$ — which will sum to $\frac{M}{2}(M+1)$[1], all ensemble members of $\mathbf{y}_s$ are exceeded by those of $\mathbf{y}_t$ and the numerator will be 0, which corresponds to the intuitive. If the converse is true (if all ensemble members of $\mathbf{y}_s$ exceeds those of $\mathbf{y}_t$), the first term of the numerator will be equal to $\frac{M}{2}(2M + (M+1))$ (M ranks occupying ranks from $M+1$ to $2M$) and so $F_{s,t}$ will be 1. If every second of the ranks from 1 to $2M$ is occupied by $\mathbf{y}_s$ (the others occupied by $\mathbf{y}_t$), $F_{s,t} = 0.5$. In such a situation, it cannot be determine which ensemble forecast $\mathbf{y}_s$ or $\mathbf{y}_t$ is greater. If more than half of the ensemble members of $\mathbf{y}_s$ ($\mathbf{y}_t$) exceeds those of $\mathbf{y}_t$ ($\mathbf{y}_s$), $F_{s,t} > (<) 0.5$.

Determining the rank of $\mathbf{y}_s$, R_s, within the set of N ensemble forecasts $\mathbf{y}_1, \mathbf{y}_2, \ldots, \mathbf{y}_N$

$$\begin{aligned} R_s &= 1 + \sum_{\substack{t=1 \\ t \neq s}}^{N} u_{s,t} \quad \text{with} \\ u_{s,t} &= \begin{pmatrix} 1 & \text{if} & F_{s,t} > 0.5 \\ 0.5 & \text{if} & F_{s,t} = 0.5 \\ 0 & \text{if} & F_{s,t} < 0.5. \end{pmatrix} \end{aligned} \tag{C.2}$$

[1] A sum of integers is the number of integers in the sum $(n-k+1)$ times the sum of the last term in the sum (n) and the first term (k), and then this number is divided by 2. The sum of integers from k to n, $\sum_{i=k}^{n} i$ is $\frac{(n-k+1)(n+k)}{2}$.

The rank of $\mathbf{y}_s$ When all ensemble members of $\mathbf{y}_t$ exceeds those of $\mathbf{y}_s$ and $F_{s,t} = 0$, $u_{s,t} = 0$. Comparing the two ensemble forecasts $\mathbf{y}_s$ and $\mathbf{y}_t$ will in this case not increase the rank, R_s, of ensemble forecast $\mathbf{y}_s$. In a case when it cannot be determined if $\mathbf{y}_s > \mathbf{y}_t$ or vice verse, $F_{s,t} = 0.5$ and the contribution to R_s is 0.5.

With N observations ($x = x_1, \ldots, x_N$) and N ensemble ranks ($R = R_1, \ldots, R_N$), the following generalized discrimination score is obtained

$$D = \frac{1}{2}(\tau_{R,x} + 1) \tag{C.3}$$

as defined in equation (C.2).

Summary

To comply with an increasing demand for sustainable energy sources, a solar heating unit is being developed at the Technical University of Denmark. To make optimal use — environmentally and economically —, this heating unit is equipped with an intelligent control system using forecasts of the heat consumption of the house and the amount of available solar energy. In order to best make use of this solar heat unit, accurate forecasts of the available solar radiation are esstential. However, because of its sensitivity to local meteorological conditions, the solar radiation received at the surface of the Earth can be highly fluctuating and challenging to forecast accurately.

Within the project on developing a solar heating unit, it is the role of the Danish Meteorological Institute (DMI) — and thus of my Ph.D. project — to deliver accurate forecasts of the global, direct, and diffuse radiation. An evaluation of these forecasts has revealed shortcomings in the radiation scheme of DMI's HIRLAM models, which has subsequently been revised adjusting the ratio of direct to diffuse radiation penetrating a cloud layer and reaching the surface of the Earth.

As a mean of complying with the accuracy requirements to forecasts of global, direct, and diffuse radiation, the uncertainty of these forecasts is of interest. Forecasts uncertainties become accessible by running an ensemble of forecasts. To this end, global, direct, and diffuse radiation have sine August 2011 been output parameters from DMI's high-resolution ensemble prediction system — aimed at capturing small-scale weather features of which a solar heating unit can be expected to be sensitive.

From the investigation of the degree to which the ensemble members and the truth — here materialised by the verifying observation — are statistically indistinguishable, the appropriateness of complementing forecast values with uncertainty estimates derived from the ensemble forecasts has been assessed. A degree of under-dispersion of the ensemble members is evident, and the ensemble forecasts will tend to express too little uncertainty in the forecast values of global radiation. Under-dispersiveness of ensemble forecasts is a familiar problem in ensemble prediction. Some of the under-dispersiveness might be attributed to uncertainties on the observations.

Concerning RMSE, skill score, and discrimination, the ensemble mean is

seen to perform well compared to the control forecasts. It might be valuable, also for other parameters, to somehow complement the operational forecast with the value of the ensemble mean.

Bibliography

Peder Bacher. *Models for efficient integration of solar energy*. PhD thesis, Danish Technical University, 2012.

Peder Bacher, Henrik Madsen, and Bengt Peres. Short-term solar collector power forecasting. In *ISES Solar World Congress*, 2011.

Viorel Badescu. *Modelling Solar Radiation at the Earth Surface: Recent Advances*. Springer-Verlag Berlin Heidelberg, 2008.

Bhattacharyya and Johnson. *Statistical Concepts and Methods*. John Wiley & Sons, 1977.

Neil E. Bowler, Alberto Arribas, Kenneth B. Myle, Kelvyn B. Robertson, and Sarah E. Beare. The MOGREPS short-range ensemble prediction system. *Quarterly Journal of the Royal Meteorological society*, 134, 2008.

Neill E. Bowler. Accounting for the effect of observational errors of verification of Mogreps. *Meteorological Applications*, 15:199–205, 2008.

R. Buizza, M. Miller, and T. S. Palmer. Stochastic representation of model uncertainties in the ECMWF Ensemble Prediction System. *Q. J. R. Meteorol. Soc.*, 125:2887–2908, 1999.

Robert Buizza. Potential Forecast Skill of Ensemble Prediction and Spread and Skill Distributilns of the ECMWF Ensemble Prediction System. *Monthly Weather Review*, 125, 1997.

D. Díaz, J. A. Souto, A. Rodríguez, S. Saavedra, and J. J. Caseres. An ensemble-in-time forecast of solar irradiance. In *International Conference of Renewable Energies and Power Quality*, Department of Chemical Engineering, University of Santiago de Compostela, 2012. EA4EPQ.

Ebisuzaki and Kalnay. A modified lagged-average-forecast ensemble. Technical Report 17, WMO, 1992. Research activities in atmospheric and oceanic modellling.

Edward S. Epstein. Stochastic dynamic prediction. *Tellus XXI*, 6:739–759, 1969.

Henrik Feddersen. A Short-Range Limited Area Ensemble Prediction System. Technical Report 09-14, Danish Meteorological Institute, 2009.

Simon Furbo and Else Andersen. Udvikling af fremtidsikret solvarmeanlæg. *HVAC Magasin for klima- & energiteknik, miljø, bygninsinstallationer & netværk*, 45(3), 2009.

Tilmann Gneiting, Larissa I. Stanberry, Eric P. Grimit, Leonhard Held, and Nicholas A. Johnson. Assessing probabilistic forecasts of multivariate quantities, with an application to ensemble predictions of surface winds. Technical Report 537, Department of Statistics, University of Washington, 2008.

Daniel Gombos and James A. Hansen. Theory and Applications of the Minimum Spanning against Tree Histogram. *Monthy Weather Review*, 135, 2007.

Thomas M. Hamil and Stephen J. Colucci. Verification of Eta-Rms Short-Range Ensemble Forecast. *Monthly Weather Review*, 125, 1997.

Thomas M. Hamill. Intepretation of Rank Histograms for Verifying Ensemble Forecasts. *Monthy Weather Review*, 129, 2001.

A. Hammer, D. Heinemann, E. Lorenz, and B. Lückehe. Short-term forecasting of solar radiation: a statistical approach using satellite data. *Solar Energy*, 67(1-3):139–150, 1999.

Ian T. Jolliffe and David B. Stephenson, editors. *Forecast Verification: A Practitioner's Guide in Atmospheric Sicence*. John Wiley & Sons, second edition, 2012.

Huo Juan and Lu Da-Ren. Characteristics of solar radiation and the impact of clouds and Yangbjing, tibet. *Atmospheric and ocean science letters*, 3: 235–239, 2012.

John S. Kain. The Kain-Fritsch Convective Parameterization: An Update. *Journal of Applied Meteorology*, 43, 2004.

Fritz Kasten and Gerhard Czeplak. Solar and terrestrial radiation dependent on the amount and type of cloud. *Solar Energy*, 24:177–189, 1980.

C. E. Leith. Theoretical Skill of Monte Carlo Forecasts. *Monthly Weather Review*, 102(6), 1974.

E. Lorenz, J. Kühnert, and D. Heinemann. Short Term Forecasting of Solar Irradiance by Combining Satellite Data and Numerical Weather Predictions. In *Proceeding of the 27th European Photovoltaic Solar Energy Conference and Exhibition*, 2012.

E. N. Lorenz. Atmospheric predictability experiments with a large numerical model. *Tellus*, 34:505–513, 1982.

Edward N. Lorenz. Deterministic Nonperiodic Flow. *Journal of Atmospheric Science*, 20:130–141, 1963.

Elke Lorenz, Stefan, C. Müller, Wolfgang Traunmüller, Gerald Steinmaurer, David Pozo, José Antonio Ruiz-Arias, Vicente Lara Fanego, Lourdes Ramirez, Martin Gaston Romeo, Christian Kurz, Luis Martin Pomares, and Carlos Geijo Guerrero. Benchmarking of different approaches to forecast solar irradiance. International Energy Agency's (IEA) task "Solar Resources Knowledge Management", 2011.

Simon J. Manson and Andreas P. Weigel. The Generic Verification Framework for Administrative Purposes. *Monthly Weather Review*, 137, 2009.

F. Molteni, R. Buizza, T. N. Palmer, and T. Petroliagis. The ECMWF Ensemble Prediction System: Methology and validation. *Q. J. R. Meteorol. Soc.*, 122:73–119, 1996.

Allan Murphy. What Is a Good Forecast? An Essay on the Nature of Goodness in Weather Forecasting. *Monthy Weather Review*, 8, 1993.

Allan H. Murphy and Robert L. Winkler. A General Framework for Forecast Verification. *Monthy Weather Review*, 115, 1987.

Allan H. Murphy, Barbara G. Brown, and Yin-Sheng Chen. Diagnostic Verification of Temperature Forecasts. *Weather and Forecasting*, 4, 1989.

NCAR - Research Application Program. *verification: Forecasts verification utilities.*, 2010. URL `http://CRAN.R-project.org/package=verification`. R package version 1.31.

Maja Kjørup Nielsen. Solskinstimer i Pituffik, Verifikation af metode til beregning af solskinstimer ud fra globalstrålingsdata. Teknisk Rapport 05-18, Danmarks Meteorologiske Institut, 2005.

Claus Nordstrøm. Målinger af globalstråling og solskinsvarighed ved DMI. *Vejret*, 2005(105):12–16, 2005.

Claus Nordstrøm, Jens Quirin Hansen, Claus Nehring, and Paul Eriksen. Kalibreringspraksis og sporbarhed for instrumenter i DMI's netværk af meteorologiske målestationer. Teknisk Rapport 05-12, Danmarks Meteorologiske Institut, 2005.

G. W. Paltridge and C. M. R. Platt. *Radiative Processes in Meteorology and Climatology*. Elsevier Scienctific Publishing Company, Amsterdam, The Netherlands, 1976.

B. Perers, S. Furbo, E. Andersen, and J. Fan. Solar/electric heating system for the future energy system. In *ISES Solar World Conference Proceedings*, Johannesburg, South Africa, 2009. ISES Solar World Conference.

B. Perers, S. Furbo, E. Andersen, and J. Fan. Solar/electric heating systems using smart solar taks and variable electricity costs. In *EuroSun 2010*, Graz, Austria, 2010. EuroSun2010.

B. Perers, S. Furbo J. Fan, E. Andersen, and Z. Chen. Solar combisystems with forecast control to increase the solar fraction and lower the auxilary energy cost. In *Solar World Congress Proceedings*, Kassel, Germany, 2011. ISES Solar World Congress.

Richard Perez, Mark Beauharnois, Karl Hemker Jr., Sergey Kivalov, Elke Lorenz, Sophie Pelland, Jim Schlemmer, and Glenn Van Knowe. Evaluation of numerical weather prediction solar irradiance forecasts in the Us. In *Proceedings of ASES Annual Conference*, Raleigh, NC, 2011. American Solar Energy Society. Americal Solar Energy Society.

R Development Core Team. *R: A Language and Environment for Statistical Computing*. R Foundation for Statistical Computing, Vienna, Austria, 2011. URL `http://www.R-project.org/`. ISBN 3-900051-07-0.

P. J. Rasch and J. E. Kristjánsson. A Comparison of the Ccm3 Model Climate Using Diagnosed and Predicted Condensated Parameterisations. *Journal of Climate*, 11, 1998.

Bent Hansen Sass. A research version of the STRACO cloud scheme. Technical Report 02-10, Danish Meteorological Institute, 2002.

Bent Hansen Sass, Laura Rontu, and Petri Räisänen. Hirlam-2 radiation scheme: Documentation and tests. Technical Report 16, HIRLAM, Norrköping, 1994.

Hannu Savijärvi. Fast Radiation Parameterization Schemes for Mesoscale and Short-Range Forecast Models. *Journal of Applied Meteorology*, 29, 1990.

Knut Stamnes, S-Chee Tsay, Warren Wiscombe, and Kolf Jayaweera. Numerically stable algorithm for discrete-ordinate-method radiative transfer in multiple scattering and emitting layered media. *Applied Optics*, 27(12), 1988.

Graeme L. Stephens. The Parametrization of Radiation for Numerical Weather Prediction and Climate Models. *Monthly Weather Review*, 112, 1984.

John R. Taylor. *Error Analysis: The study of uncertainties in physical measurements*. Univerisity Science Books, Sausalito, California, second edition, 1997.

Gary E. Thomas and Knut Stamnes. *Radiative Transfer in the Atmosphere and Ocean*. Cambridge University Press, 1999.

Zoltan Toth and Eugenia Kalnay. Ensemble Forecasting at NMC: The Generation of Perturbations. *Bulletin of the American Meteorological Society*, 74(12), 1993.

M. Steven Tracton and Eugenia Kalnay. Operational Ensemble Prediction at the National Meteorological Center: Practical Aspects. *Weather and Forecasting*, 8:379–398, 1993.

John M. Wallace and Peter V. Hobbs. *Atmospheric Science An Introductory Survey*. Academic Press, second edition, 2006.

Andreas Weigel. *afc: Calculate afc*, 2010. URL `http://CRAN.R-project.org/package=afc`. R package version 1.03.

Andreas P. Weigel and Simon J. Manson. The Generalized Discrimination Score for Ensemble Forecasts. *Monthly Weather Review*, 139, 2011.

D. S. Wilks, editor. *Statistical Methods in the Atmospheric Sciences*. Elsevier, second edition, 2006.

Klaus Wyser, Laura Rontu, and Hannu Savijärvi. Introducing the Effective Radius into Fast Radiation Scheme of a Mesoscale Model. *Contributions to Atmospheric Physics*, 72(3), 1999.

DTU Civil Engineering
Department of Civil Engineering
Technical University of Denmark

Brovej, Building 118
2800 Kgs. Lyngby
Telephone 45 25 17 00

www.byg.dtu.dk

ISBN 9788778773739